

# SWITCHED RELUCTANCE MOTOR DRIVES

---

Modeling, Simulation, Analysis,  
Design, and Applications

# INDUSTRIAL ELECTRONICS SERIES

Series Editor

J. David Irwin, *Auburn University*

## TITLES INCLUDED IN THE SERIES

**Supervised and Unsupervised Pattern Recognition:  
Feature Extraction and Computational Intelligence**

Evangelia Micheli-Tzanakou, *Rutgers University*

**Switched Reluctance Motor Drives: Modeling,  
Simulation, Analysis, Design, and Applications**

R. Krishnan, *Virginia Tech*

**The Power Electronics Handbook**

Tim L. Skvarenina, *Purdue University*

**The Handbook of Applied Computational Intelligence**

Mary Lou Padgett, *Auburn University*

Nicolaos B. Karayannidis, *University of Houston*

Lofti A. Zadeh, *University of California, Berkeley*

**The Handbook of Applied Neurocontrols**

Mary Lou Padgett, *Auburn University*

Charles C. Jorgensen, *NASA Ames Research Center*

Paul Werbos, *National Science Foundation*

INDUSTRIAL ELECTRONICS SERIES

# SWITCHED RELUCTANCE MOTOR DRIVES

---

Modeling, Simulation, Analysis,  
Design, and Applications

R. KRISHNAN — Fellow, IEEE

The Bradley Department of Electrical and Computer Engineering  
Fellow, Center for Organizational and Technological Advancement (COTA)  
Virginia Tech, Blacksburg, Virginia



CRC Press

Boca Raton London New York Washington, D.C.

## Library of Congress Cataloging-in-Publication Data

Ramu, Krishnan.

Switched reluctance motor drives: modeling, simulation, analysis, design, and applications / Krishnan Ramu.

p. cm.—(Industrial electronics series)

Includes bibliographical references and index.

ISBN 0-8493-0838-0 (alk. paper)

1. Reluctance motors. I. Title. II. Series.

TK2787 .R35 2001

621.46—dc21

2001025727

This book contains information obtained from authentic and highly regarded sources. Reprinted material is quoted with permission, and sources are indicated. A wide variety of references are listed. Reasonable efforts have been made to publish reliable data and information, but the author and the publisher cannot assume responsibility for the validity of all materials or for the consequences of their use.

Neither this book nor any part may be reproduced or transmitted in any form or by any means, electronic or mechanical, including photocopying, microfilming, and recording, or by any information storage or retrieval system, without prior permission in writing from the publisher.

Direct all inquiries to CRC Press LLC, 2000 N.W. Corporate Blvd., Boca Raton, Florida 33431.

**Trademark Notice:** Product or corporate names may be trademarks or registered trademarks, and are used only for identification and explanation, without intent to infringe.

**Visit the CRC Press Web site at [www.crcpress.com](http://www.crcpress.com)**

---

© 2001 by CRC Press LLC

No claim to original U.S. Government works

International Standard Book Number 0-8493-0838-0

Library of Congress Card Number 2001025727

Printed in the United States of America 1 2 3 4 5 6 7 8 9 0

Printed on acid-free paper

*For*  
*Madhivanan and Ilankeeran*

---

# Preface

Industrial interest in switched reluctance motor (SRM) drives has varied since 1850s. The recent surge of activity since the 1980s has spurred university and industrial research and product development in the U.K. and U.S. and in a very small measure in some other countries. This interest has been primarily due to the emerging markets for variable speed drives in consumer and industrial products, such as home appliances, air conditioning, hand tools, fans, pump motor drives, extruders, and automotive and railway accessory drives. These new applications for variable speed drives are very cost sensitive while demanding higher reliability and an equivalent performance of dc and induction motor drives at the minimum. SRM drive systems promise to meet such demands in some select high-volume applications, hence the spurt of activity in this field. The expansion of knowledge in this field has been great, and it is timely to summarize in this book some of the key results in modeling, simulation, analysis, and design procedures for SRMs; their converter topologies; system integration; control techniques with and without position sensors; the much talked-about noise issue; and, finally, their applications. With that perspective, this book has been in preparation for the last 12 years, and the material has been taught in a number of IEEE forums, at industrial sites, and at the graduate level at the author's university and at Padova University in Italy.

The book presumes a familiarity with fundamentals of electromechanics, introductory power electronics, and linear control system theory, all at the undergraduate level. The intended audience for the book is electrical engineers in industrial and federal laboratories and students at the senior/graduate level in universities. Traditional trappings of worked examples and exercise problems are done away with, as this subject demands complete immersion and therefore much more intensive study and initiative to do extensive work by the readers on their own. The book is organized as follows.

Chapter 1 contains the introduction to SRM, its principle of operation, various types of SRM configurations including linear SRM, and the equivalent circuit. Chapter 2 discusses the magnetic equivalent circuit derivation and an analytical approach to the evaluation of the key three-dimensional relationships among flux linkages, excitation current, and rotor position in the SRM. The nonlinear material characteristics are preserved in this approach. These machine characteristics are central to the analysis and design of SRMs.

Chapter 3 contains an analytical design procedure for the SRM based on the output power equation that is prevalent in the design of electrical machines. The resistive and core losses for thermal consideration, criteria for the selection of stator and rotor back iron thickness, pole height, number of phases, ratio of pole arc to pole pitch, self-starting requirements to be fulfilled in the design, inductance measurement, and design of linear SRM from an equivalent rotary SRM are addressed

from fundamentals. Steady-state computation of air gap torque is also derived in this chapter.

Converters and their classification, principle of operation, design considerations, and merits and demerits of each converter and their impact on the machine output form the core of Chapter 4. Converters that have some merit from the point of view of industrial applications are considered in this selection.

The converter, SRM, and load are integrated through a controller. The basic drive system control is developed and illustrated with an implementation to demonstrate the similarity of this drive to dc and ac drives. The inadequacy of such controllers for high-performance applications is discussed, and contributing factors are identified. The heart of a high-performance system is current control, and various methods of current control such as the conventional linearized controller, linearizing and decoupling controller, and hybrid controller are systematically derived and developed. An alternative to current control is the flux linkages control, and its merits and demerits are discussed. The torque controller to produce very little torque ripple using torque distribution function-based control is introduced and its performance is studied in detail. Finally, analytic derivations of the speed controller gain and time constants are made using the symmetric optimum method. Throughout this chapter, an analytical approach is emphasized to understand the relationship between machine parameters and output variables. Usually the literature neglects mutual coupling in performance prediction. It is shown in the text that its omission may lead to as much as 6% torque ripple even in very good machine designs. Methods to include mutual coupling effects in performance prediction and in the linearized and decoupled current controller, flux linkage controller, and torque controller designs are presented.

Dynamic modeling, simulation, and analysis play crucial roles in the drive system analysis and design and are considered in Chapter 6. The subsystems modeling and their integration are developed step by step. The simulation procedure is illustrated with results to enhance the understanding of the SRM drive.

The SRM drive has been plagued with the acoustic noise problem. To understand this issue, the sources of acoustic noise are explained in Chapter 7. Measures to mitigate noise from magnetic, mechanical, aerodynamic, and electronic sources are presented. Active noise cancellation techniques using the power converter control are also described. A brief summary of qualitative measures to reduce noise is given. In order to facilitate noise quantification in laboratories, an introduction to measurement is included in this chapter.

The necessity for absolute rotor position information in SRM drives increases the complexity of motor manufacture, with the mounting of position sensors resulting in higher costs compared to other drives that do not require rotor position sensors for their operation, such as dc and ac motor drives. Various electronic methods for estimating or predicting the rotor position information are discussed along with their algorithms in Chapter 8. These methods are not invasive mechanically and use only the voltage applied across the winding and the current flowing in it. Many of the methods discussed in the literature are classified and their implementations are discussed to enable readers to assess the suitability of a particular method in the context of an application. Low-cost current sensing to obtain a completely sensorless SRM drive system is also included.

Application considerations and particular applications of the SRM drive systems are described in Chapter 9. The SRM drive system is reviewed for merits and demerits in regard to each of its subsystems. By doing so, the strengths and weaknesses of the SRM drive become apparent and hence their suitability for a given application. Applications are discussed in terms of the power categories of low, medium, and high and high-speed drives. Emerging applications in the high-volume, underwater, and linear-drive areas, particularly in machine tool drives, are identified.

This book contains significant results from my research students, past and present. They are Prof. R. Arumugam, Dr. Peter Materu, Dr. Guen-Hie Rim, Dr. Aravind Bharadwaj, Mr. A. Bedingfield, Mr. Prasad Ramakrishna, Mr. Terry Jackson, Dr. H. K. Bae, Dr. B. S. Lee, Dr. Praveen Vijayraghavan, Mr. Phil Vallance, and Ms. Amanda Staley. They have permitted me to draw generously from their theses. Parts of Chapters 1 and 3 are from Dr. Lee's thesis, parts of Chapters 5 and 6 are from Dr. Bae's thesis, part of Chapter 5 is from Mr. Jackson's thesis, and part of Chapter 2 is from Dr. Vijayraghavan's thesis. To them, I owe my gratitude. When there was hardly any interest in this subject matter nearly two decades back, my mentor Dr. J. F. Lindsay encouraged me to pursue this research topic. I am very grateful to him for his advice and insight. Initial funding from A. O. Smith Corp., Whirlpool Corp., and Black & Decker Corp. to initiate SRM research is gratefully acknowledged. Portions of this book were written while the author was on sabbatical in INPG, France, at the kind invitation of Prof. Jean Claude Sabonnadiere. I thank him for it. Earlier versions of this text have been taught at the University of Padova at the invitation of Prof. S. Bolognani, and I am grateful for his hospitality. My department provided excellent facilities to carry on the work related to this text. I am grateful for this to Profs. F. W. Stephenson, the Dean of Engineering, and L. A. Ferrari, Vice Provost for Special Initiatives. Monique Johnson helped me in all editorial work and with correcting part of the manuscript and her help is gratefully acknowledged. This manuscript preparation was partially supported by the Center for Organizational and Technological Advancement (COTA) at Virginia Tech in the form of a fellowship. For that I am grateful to Prof. Gregg Boardman, the center's director.

My sincere thanks to all at CRC Press who interacted with me during advance marketing for their time and help. I am also grateful to the project editor, Ms. Samar Haddad, for making amazing progress with the manuscript in a record time and for smoothing out the rough edges. Her patience made possible an enjoyable and wonderful journey through various steps in production.

The patience and gentle prodding of Nora Konopka, my editor, helped to maintain my focus on the book in the last year. It has been very enjoyable working with her on this book, and I am very grateful to her for the talented team that she assembled to make this book possible.

I owe immense gratitude to my wife, Vijaya, for her cheer and encouragement throughout this endeavor.

**R. Krishnan**

---

# About the Author

**R. Krishnan** received his Ph.D. in electrical engineering from Concordia University, Montreal, Canada, in 1982. He started his teaching career with the University of Madras in 1972. He was a staff engineer and then principal engineer at Gould Research Center from 1982 to 1985, and since then he has been with Virginia Tech. He is a professor of electrical and computer engineering, and his research interests include electric motor drives and applied control. He has developed many proprietary motor drives, an electronic stunner, uninterruptible power supplies, converters for PM brushless dc, switched reluctance and induction motor drives, controllers for ac and switched reluctance motor drives, and personal medical monitors. Some are in industrial use and others are under consideration for market.

Dr. Krishnan has organized and conducted short courses on vector-controlled induction motor drives, PM synchronous and brushless dc motor drives, and switched reluctance motor drives in the U.S., France, Italy, Korea, and Denmark. He is the author of *Electric Motor Drives* (Prentice-Hall, 2001).

He is a Fellow of the Institute of Electrical and Electronic Engineers (IEEE), cited for his contributions to the development of ac and switched reluctance motor drives. He is also a Fellow of the Center for Organizational & Technological Advancement (COTA) at Virginia Tech. He is the director of the Center for Rapid Transit Systems (CRTS), pursuing unique, safe, high-speed, energy-efficient, and personal electric transit solutions and their implementations in the U.S.

---

# Contents

## Chapter 1 Principle of Operation of the Switched Reluctance Motor

- 1.1 Introduction
- 1.2 Background
- 1.3 Elementary Operation of the Switched Reluctance Motor
- 1.4 Principle of Operation of the Switched Reluctance Motor
- 1.5 Derivation of the Relationship between Inductance and Rotor Position
- 1.6 Equivalent Circuit
- 1.7 SRM Configurations
  - 1.7.1 Rotary SRM
  - 1.7.2 Single-Phase SRM
- 1.8 Linear Switched Reluctance Machines
  - 1.8.1 Introduction
  - 1.8.2 Machine Topology and Elementary Operation of LSRMs

## References

## Chapter 2 Steady-State Performance and Analytic Derivation of SRM Characteristics

- 2.1 Introduction
- 2.2 Data for Performance Computation
- 2.3 Analytic Method for the Computation of Motor Flux Linkages
  - 2.3.1 Method of Inductance Calculation
    - 2.3.1.1 Flux Density Evaluation
    - 2.3.1.2 mmf Evaluation
    - 2.3.1.3 Calculation of Reluctance
    - 2.3.1.4 Assumptions
  - 2.3.2 Unaligned Inductance
    - 2.3.2.1 Flux Path 1
      - 2.3.2.1.1 Rotor Back Iron
      - 2.3.2.1.2 Stator Pole
      - 2.3.2.1.3 Stator Back Iron
    - 2.3.2.2 Flux Path 2
      - 2.3.2.2.1 Air Gap
      - 2.3.2.2.2 Stator Pole
      - 2.3.2.2.3 Rotor Pole
      - 2.3.2.2.4 Rotor Back Iron
      - 2.3.2.2.5 Stator Back Iron

- 2.3.2.3 **Flux Path 3**
  - 2.3.2.3.1 Air Gap
  - 2.3.2.3.2 Stator Pole
  - 2.3.2.3.3 Rotor Pole
  - 2.3.2.3.4 Rotor Back Iron
  - 2.3.2.3.5 Stator Back Iron
- 2.3.2.4 **Flux Path 4**
  - 2.3.2.4.1 Air Gap
  - 2.3.2.4.2 Stator Pole
  - 2.3.2.4.3 Rotor Pole
  - 2.3.2.4.4 Rotor Back Iron
  - 2.3.2.4.5 Stator Back Iron
- 2.3.2.5 **Flux Path 5**
  - 2.3.2.5.1 Air Gap
  - 2.3.2.5.2 Stator Pole
  - 2.3.2.5.3 Rotor Pole
  - 2.3.2.5.4 Rotor Back Iron
  - 2.3.2.5.5 Stator Back Iron
- 2.3.2.6 **Flux Path 6**
  - 2.3.2.6.1 Air Gap
  - 2.3.2.6.2 Stator Pole
  - 2.3.2.6.3 Stator Back Iron
  - 2.3.2.6.4 Magnetic Equivalent Circuit
- 2.3.2.7 **Flux Path 7**
  - 2.3.2.7.1 Unaligned Inductance
- 2.3.3 **Aligned Inductance**
  - 2.3.3.1 Flux Path 1
  - 2.3.3.2 Flux Path 7
- 2.3.4 **Results and Comparison**
- 2.3.5 **Performance Evaluation**
- 2.3.6 **Inductances at Intermediate Positions**
  - 2.3.6.1 **Region 1**
    - 2.3.6.1.1 Flux Path 1
    - 2.3.6.1.2 Flux Path 2
    - 2.3.6.1.3 Flux Path 3
    - 2.3.6.1.4 Flux Path 4
    - 2.3.6.1.5 Flux Path 5
    - 2.3.6.1.6 Flux Path 6
    - 2.3.6.1.7 Inductance in Region 1
  - 2.3.6.2 **Region 2**
    - 2.3.6.2.1 Flux Path 1
    - 2.3.6.2.2 Flux Path 2
    - 2.3.6.2.3 Flux Path 3
    - 2.3.6.2.4 Flux Path 4
    - 2.3.6.2.5 Flux Path 5
    - 2.3.6.2.6 Inductance Evaluation

- 2.4 Secondary Flux Paths
- 2.5 Computation of Inductance
- References

## Chapter 3 Design of SRM

- 3.1 Introduction
- 3.2 Derivation of Output Equation
- 3.3 Selection of Dimensions
  - 3.3.1 Diameter and Length
  - 3.3.2 Number of Turns
  - 3.3.3 Thermal Consideration
    - 3.3.3.1 Stator Copper Losses
    - 3.3.3.2 Approximate Evaluation of  $T_r$
    - 3.3.3.3 Approximate Evaluation of  $T_f$
  - 3.3.4 Stator Back Iron Thickness
  - 3.3.5 Stator Coil Dimensions
  - 3.3.6 Stator Pole Height
  - 3.3.7 Outer Diameter of Stator Lamination
  - 3.3.8 Rotor Back Iron Thickness
  - 3.3.9 Rotor Pole Height
  - 3.3.10 Estimation of Core Losses
  - 3.3.11 Flux Density Waveforms
    - 3.3.11.1 Stator
    - 3.3.11.2 Rotor
    - 3.3.11.3 Core Losses
    - 3.3.11.4 Calculation Procedure
- 3.4 Design Verification
- 3.5 Operational Limit
- 3.6 Selection of Number of Phases
- 3.7 Selection of Poles
- 3.8 Ratio of Pole Arc to Pole Pitch
- 3.9 Selection of Pole Arcs
  - 3.9.1 Minimum Rotor and Stator Pole Arcs to Achieve Self-Starting
  - 3.9.2 Overlap Angle ( $\theta_0$ ) Limits
  - 3.9.3 Upper Limit on  $\beta_r$
  - 3.9.4 Computation of Turn-Off Angle
  - 3.9.5 Selection of Pole Base
- 3.10 Effect of Air Gap on Torque
- 3.11 Measurement of Inductance
- 3.12 Calculation of Torque
  - 3.12.1 Average Torque
  - 3.12.2 Instantaneous Torque
- 3.13 Design of the Linear Switched Reluctance Machine
  - 3.13.1 Introduction

- 3.13.2 LSRM Configurations
  - 3.13.2.1 Three-Phase LSRM with Active Stator and Passive Translator Structure
  - 3.13.2.2 Four-Phase LSRM with Active Translator and Passive Stator Structure
- 3.13.3 LSRM Design
  - 3.13.3.1 Specifications of the LSRM
  - 3.13.3.2 Design of Rotary SRM
  - 3.13.3.3 Conversion of RSRM Dimensions to LSRM Dimensions
  - 3.13.3.4 Example 1: Design of Three-Phase LSRM with Active Stator and Passive Translator
  - 3.13.3.5 Example 2: Four-Phase LSRM Prototype with Active Translator and Passive Stator
- 3.13.4 Design Verification
  - 3.13.4.1 Analytical Inductance Calculation
    - 3.13.4.1.1 Aligned Inductance Calculation
    - 3.13.4.1.2 Intermediate Inductance Calculation—One-Third Shift of Translator from Fully Aligned Position
    - 3.13.4.1.3 Intermediate Inductance Calculation—Two-Thirds Shifting of Translator from Fully Aligned Position
    - 3.13.4.1.4 Fully Unaligned Inductance Calculation
  - 3.13.4.2 Analytical Force Calculation
  - 3.13.4.3 Finite Element Analysis Verification
  - 3.13.4.4 Experimental Setup for Measurements
    - 3.13.4.4.1 Inductance Measurement
    - 3.13.4.4.2 Force Measurement
  - 3.13.4.5 Results and Comparison

#### Appendix 3A: Calculation of Air gap Permeance

- Parallelepiped
- Semicircular Cylinder
- Half Annulus
- Spherical Quadrant
- Spherical Shell Quadrant

Total Permeance Value of the Air gap Flux Paths

#### Appendix 3B: Flux Paths and Associated Variables

- in the Stator and Translator
- Aligned Position Region
  - MMF per Path
  - Mean Path Length and Mean Cross-Section Area
- Intermediate Position Region I
  - MMF Per Path
  - Mean Path Length and Mean Cross-Section Area

Intermediate Position Region II

MMF per Path

Mean Path Length and Mean Cross-Section Area

Unaligned Position Region

MMF per Path

Mean Path Length and Mean Cross-Section Area

References

## Chapter 4 Converters for SRM Drives

### 4.1 Converter Configurations

#### 4.1.1 Asymmetric Bridge Converter

4.1.1.1 Switching Strategy

4.1.1.2 Device Ratings

4.1.1.3 Switch rms Current

4.1.1.4 Diode Average Current

4.1.1.5 Selection of Device Current Ratings

#### 4.1.2 Asymmetric Converter Variation

#### 4.1.3 Energy Recovery Snubber

### 4.2 Single-Switch-per-Phase Converters

#### 4.2.1 R-Dump

4.2.1.1 Device Current Ratings

4.2.1.2 Switch Current

4.2.1.3 Diode Current

4.2.1.4 Power Rating of Dump Resistor

#### 4.2.2 Bifilar Type

#### 4.2.3 Split dc Supply Converter

#### 4.2.4 $q$ Switches and $2q$ Diodes

#### 4.2.5 $q$ Switch and $2q$ Diode Configuration with Independent Phase Current Control

### 4.3 ( $q + 1$ ) Switch and Diode Configurations

#### 4.3.1 Configuration with Equal Sharing

#### 4.3.2 C-Dump Converter

##### 4.3.2.1 Modes of Operation and Mode Equations

4.3.2.1.1 Mode 1:  $T_1$  On and  $T_r$  Off

4.3.2.1.2 Modes 2 and 3:  $T_1$  and  $T_r$ , Both  
On and Then Off

4.3.2.1.3 Mode 4: Phase Current Commutation

4.3.2.1.4 Mode 5:  $T_1$  Off,  $T_r$  On

##### 4.3.2.2 Design Procedure

4.3.2.2.1 Device Ratings

4.3.2.2.2 Dump Capacitor Rating

4.3.2.2.3 Incremental Current in Machine Phases

4.3.2.2.4 Switching Frequency

4.3.2.2.5 Rating of  $L_r$

4.3.2.2.6 Recovery Current

- 4.3.2.2.7 Voltage and Current Control in Energy Recovery Circuits
- 4.3.3 C-Dump with Freewheeling
- 4.3.4 One Common Switch Configuration
- 4.3.5 Minimum Switch Topology with Variable dc Link
  - 4.3.5.1 Operational Modes of the Converter Circuit
  - 4.3.5.2 Design Considerations of the Chopper Circuit Components
  - 4.3.5.3 Performance Constraints and Design of the Converter
    - 4.3.5.3.1 Current Commutation Time
    - 4.3.5.3.2 Voltage Rise in the dc Source Capacitor
    - 4.3.5.3.3 Results and Analysis
  - 4.3.5.4 Merits and Demerits of the Converter
  - 4.3.5.5 Variable dc Link Voltage with Buck-Boost Converter Topology
- 4.3.6 (1.5q) Switches and Diodes Configuration
- 4.4 Comparison of Some Power Converters
- 4.5 Two-Stage Power Converter
  - 4.5.1 Front-End Converter
  - 4.5.2 Machine-Side Converter
  - 4.5.3 Operation of the Scheme
- 4.6 Resonant Converter Circuits
- References

## Chapter 5 Control of SRM Drive

- 5.1 Introduction
- 5.2 Control Principle
- 5.3 Closed-Loop, Speed-Controlled SRM Drive
  - 5.3.1 Design Example
  - 5.3.2 Solution
  - 5.3.3 Current Loop
  - 5.3.4 Current Comparator
  - 5.3.5 Carrier Signal
  - 5.3.6 Incorporation of Rotor Position Information
  - 5.3.7 Speed Loop
- 5.4 Design of Current Controllers
  - 5.4.1 Voltage and Torque Equations for the SRM
  - 5.4.2 Derivation of the SRM Small-Signal Model
  - 5.4.3 System Block Diagram
  - 5.4.4 Design of Current Controller
    - 5.4.4.1 Example 1: 5-hp SRM Drive System
    - 5.4.4.2 Current Controller Design
    - 5.4.4.3 Nonlinear Dynamic Simulation of Current Loop

- 5.4.5 Linearized Decoupling Current Controller Neglecting Mutual Inductance
- 5.4.6 Design of Current Controller Including Mutual Coupling Effects
- 5.5 Flux Linkage Controller
- 5.5.1 Machine without Mutual Coupling
- 5.6 Torque Control
  - 5.6.1 Methods of Torque Control
    - 5.6.1.1 Torque Distribution Neglecting Mutual Inductance and Saturation
    - 5.6.1.2 Torque Distribution Including Mutual Inductance and Neglecting Saturation
    - 5.6.1.3 Torque Distribution Including Mutual Inductance and Saturation
  - 5.6.2 Simulation Results
  - 5.6.3 Implementation of Torque Controller
- 5.7 Design of the Speed Controller
  - 5.7.1 Features of the Symmetric Optimum Function
  - 5.7.2 Simulation Results

## References

- ## Chapter 6 Modeling and Simulation of the SRM Drive System
- 6.1 Introduction
  - 6.2 Modeling
    - 6.2.1 Machine Model
      - 6.2.1.1 Per Phase Model
      - 6.2.1.2 Representation of Machine Magnetic Characteristics
      - 6.2.1.3 Method 1
      - 6.2.1.4 Method 2
      - 6.2.1.5 Torque Representation and Its Computation
      - 6.2.1.6 Mutual Inductance
    - 6.2.2 Converter
      - 6.2.2.1 Effect of Source Impedance and dc Link Filter
      - 6.2.2.2 Device-T transient Model
    - 6.2.3 Load
    - 6.2.4 Controller
      - 6.2.4.1 Speed Controller
      - 6.2.4.2 Torque Controller
      - 6.2.4.3 Current Command Controller
      - 6.2.4.4 Current Controller
        - 6.2.4.4.1 PWM Current Controller
        - 6.2.4.4.2 Hysteresis Current Controller

## 6.3 Simulation

### 6.3.1 Simulation Results

## References

# Chapter 7 Acoustic Noise and Its Control in SRMs

## 7.1 Introduction

## 7.2 Sources of Acoustic Noise in Electrical Machines

### 7.2.1 Noise Sources

#### 7.2.1.1 Magnetic Sources of Noise

#### 7.2.1.2 Mechanical Sources of Noise

##### 7.2.1.2.1 Self

##### 7.2.1.2.2 Load-Induced

##### 7.2.1.2.3 Auxiliaries

##### 7.2.1.2.4 Rotor Unbalance

#### 7.2.1.3 Aerodynamic Sources of Noise

#### 7.2.1.4 Electronic Sources of Noise

## 7.3 Noise Mitigation

### 7.3.1 Magnetic Noise Mitigation

### 7.3.2 Mechanical Noise Mitigation

### 7.3.3 Aerodynamic Noise Mitigation

### 7.3.4 Electronic Noise Mitigation

### 7.3.5 Active Noise-Cancellation Techniques

#### 7.3.5.1 Two-Stage Commutation Method

#### 7.3.5.2 Voltage-Smoothing Method

#### 7.3.5.3 Three-Stage Commutation Method

#### 7.3.5.4 Extended Freewheeling Method

#### 7.3.5.5 Disadvantages of Noise-Cancellation Techniques

## 7.4 Qualitative Design Measures to Reduce Noise

### 7.4.1 Machine Design Considerations

### 7.4.2 Torque-Smoothing Control

### 7.4.3 Converters with a High Degree of Freedom

### 7.4.4 Varying Input Voltage

## 7.5 Measurement of Acoustic Noise and Vibrations

## 7.6 Future Directions

# Appendix 7A: Derivation of First-Mode Frequency of an SRM

### Potential Energy

### Kinetic Energy

### Natural Frequency

## References

# Chapter 8 Sensorless Operation of SRM Drives

## 8.1 Introduction

## 8.2 Current Sensing

### 8.2.1 Current-Sensing Methods

- 8.2.2 Current Sensing with Resistors
- 8.2.3 Drive Scheme with Current Limiter
- 8.3 Rotor Position Measurement and Estimation Methods
- 8.3.1 Sensor-Based Measurement
- 8.4 Sensorless Rotor Position Estimation
  - 8.4.1 Inductance-Based Estimation
    - 8.4.1.1 Incremental Inductance Measurement
      - 8.4.1.1.1 Current Rise Time Method
      - 8.4.1.1.2 Current Fall Time Method
    - 8.4.1.2 Sensing with Inactive Phases
    - 8.4.1.3 Estimation Based on Constant Current/Flux Linkages
    - 8.4.1.4 Resonant Circuit Method
    - 8.4.1.5 Synchronous Demodulation Method
    - 8.4.1.6 Variation of the Demodulation Method
    - 8.4.1.7 Mutual Flux Linkages Method
  - 8.4.2 Direct Inductance-Sensing Methods
    - 8.4.2.1 Current Gradient Method
    - 8.4.2.2 Flux Linkages Estimation Method Based on Reference Position
    - 8.4.2.3 Flux-Linkages-Based Method with Hesitation-Free Starting
  - 8.4.3 Observer-Based Rotor Position Estimation
  - 8.4.4 Intelligent-Control-Based Estimation
    - 8.4.4.1 Artificial Neural Networks
    - 8.4.4.2 Fuzzy Control Estimator
  - 8.4.5 Sensing Coil Approach

## References

## Chapter 9 Application Considerations and Applications

- 9.1 Introduction
- 9.2 Review of SRM Drive Features for Application Consideration
  - 9.2.1 Motor
    - 9.2.1.1 Advantages
    - 9.2.1.2 Disadvantages
  - 9.2.2 Converter
    - 9.2.2.1 Advantages
    - 9.2.2.2 Disadvantages
  - 9.2.3 Control
- 9.3 Applications
  - 9.3.1 Low-Power Drives
  - 9.3.2 Medium-Power Drives
  - 9.3.3 High-Power Drives
  - 9.3.4 High-Speed Drives

## 9.4 Emerging Applications

### 9.4.1 High-Volume Applications

### 9.4.2 Underwater Applications

### 9.4.3 Linear Drive Applications

## References

---

# Nomenclature

Subscripts  $a$ ,  $b$ ,  $c$ , and  $d$  denote phases  $a$ ,  $b$ ,  $c$ , and  $d$ . Additional subscript  $n$  indicates a normalized variable (in p.u.).

$a_a$	Acceleration in LSRM (m/sec <sup>2</sup> )
$a_c$	Area cross section of the conductor (m <sup>2</sup> )
$a_d$	Deceleration in LSRM (m/sec <sup>2</sup> )
$A_g$	Air gap area; an additional numeral subscript indicates the flux path (m <sup>2</sup> )
$A_{rp}$	Rotor pole area; an additional numeral subscript indicates the flux path (m <sup>2</sup> )
$A_{ry}$	Rotor back iron area; an additional numeral subscript indicates the flux path (m <sup>2</sup> )
$A_s$	Specific electric loading (amp-con/m)
$A_{sp}$	Stator pole area; an additional numeral subscript indicates the flux path (m <sup>2</sup> )
$A_{sy}$	Stator back iron area; an additional numeral subscript indicates the flux path (m <sup>2</sup> )
$B$	Friction constant (N·m/rad/sec) or stator pole flux density at aligned position (T)
$B_g$	Air gap flux density (Wb/m <sup>2</sup> ); a numeral subscript indicates the flux path
$B_m$	Maximum flux density (T)
$B_{rp}$	Rotor pole flux density (Wb/m <sup>2</sup> ); a numeral subscript indicates the flux path
$B_{ry}$	Rotor back iron flux density (Wb/m <sup>2</sup> ); a numeral subscript indicates the flux path
$B_{sp}$	Stator pole flux density (Wb/m <sup>2</sup> ); a numeral subscript indicates the flux path
$B_{sy}$	Stator back iron flux density (Wb/m <sup>2</sup> ); a numeral subscript indicates the flux path
$B_t$	Total friction constant of the motor and load (N·m/rad/sec)
$b_{ry}$	Rotor back iron thickness (m)
$b_{sy}$	Stator yoke thickness (m)

$C_d$	Capacitor of the C-dump (F)
$C_{ry}$	Translator back iron thickness in LSRM (m)
$C_{sy}$	Stator back iron thickness in LSRM (m)
$D$	Bore diameter and stator inner diameter (m)
$d$	Rotor outer diameter
$d_c$	Diameter of conductor (m)
$d_1$	Average duty cycle per phase conduction
$d_2$	Average duty cycle for energy recovery circuit
$D_f$	Diameter of the fan mounting arm (m)
$D_o$	Stator outer diameter (m)
$D_{sh}$	Rotor shaft diameter (m)
$\frac{dL}{d\theta}, k(\theta)$	Rate of change of inductance with respect to rotor position only (H/rad/sec)
$dW_e$	Incremental electrical input energy (J)
$dW_m$	Incremental mechanical energy (J)
$dW_{mx}$	Incremental mechanical energy in propulsive direction in LSRM (J)
$dW_{mz}$	Incremental mechanical energy in normal direction in LSRM (J)
$dW_s$	Incremental field energy (J)
$dW_{sx}$	Incremental stored magnetic energy in LSRM (J)
$D_x$	Horizontal deflection (m)
$D_y$	Change in vertical part of the diameter or vertical deflection (m)
$E$	C-dump capacitor ( $C_o$ ) voltage (V) and Young's modulus
$e$	Instantaneous induced emf/phase (V)
$e_{as}, e_{bs}, e_{cs}$	Phase $a, b$ , and $c$ induced voltages (V)
$E_k$	Kinetic energy in the stator ring (J)
$E_p$	Potential energy per unit length (J) or peak induced emf (V)
$F$	MMF per pole pair, A-T
$F_a$	Acceleration force in LSRM (N)
$F_d$	Deceleration force in LSRM (N)
$F_{em}$	Motoring force in linear machines (N)
$F_{er}$	Regenerative force in linear machines (N)
$F_f$	Fill factor of the stator winding

$F_1, F_2$	Applied mmf of the stator pole 1 and 2 in LSRM (AT or A)
$f_c$	Pulse width modulation (PWM) frequency (Hz)
$f_f$	Pure tone frequency caused by fan blades (Hz)
$f_m$	Mechanical rotor frequency (Hz)
$f_n$	Natural frequency (Hz)
$F_n$	Radial or normal force (N)
$f_p$	Phase frequency (Hz)
$f_r$	Radial force harmonics frequency (Hz)
$f_s$	ac input supply frequency (Hz)
$f_x$	Propulsion force in LSRM (N)
$f_y$	Lateral force in LSRM (N)
$f_z$	Normal force in LSRM (N)
$F_t$	Tangential force (N)
$f_v$	Vortex frequency (Hz)
$F_y$	Lateral force (N)
$g_i$	Stator to rotor interpolar space height (m)
$g_{mi}$	Incremental mechanical energy per unit current (J/A)
$g_x$	Incremental slope of the inductance vs. rotor position for phase $x$ (H/rad)
$h$	Ratio between ( $E-V_{dc}$ ) and $E$ (V)
$h_c$	Height of the stator coil (m)
$h_r$	Rotor pole height (m)
$h_s$	Height of stator pole (m)
$H_c$	Gain constant of the current transducer (V/A)
$H_g$	Air gap field intensity (A/m); a numeral subscript indicates the flux path
$H_{rp}$	Rotor pole field intensity (A/m); a numeral subscript indicates the flux path
$H_{ry}$	Rotor back iron field intensity (A/m); a numeral subscript indicates the flux path
$H_{sp}$	Stator pole field intensity (A/m); a numeral subscript indicates the flux path
$H_{sy}$	Stator back iron field intensity (A/m); a numeral subscript indicates the flux path
$H_\omega$	Speed feedback gain (V/rad/sec)
$I$	rms phase current or polar moment of inertia

$i$	Stator current (A)
$i_{1q}$	Quadrature component of current (A)
$i_a, i_b, i_c$	Instantaneous phase $A, B, C$ currents (A)
$i_{as}, i_{bs}, i_{cs}$	Phase $a, b,$ and $c$ currents (A)
$i_a^*, i_b^*, i_c^*$	Phase current command (A)
$I_b$	Base current (A)
$I_D$	rms current in the diode (A)
$I_d$	Average diode current (A)
$i_{dn}$	Instantaneous current in diode $n$ (A)
$i_{en}$	$n$ th phase error current (A)
$i_i$	Input current of the energy recovery circuit (A)
$i_n$	$n$ th phase current (A)
$I_p$	Phase peak current (A)
$I_r$	Average current in the energy recovery chopper (A)
$I_T$	rms switch current (A)
$i_r$	Instantaneous current in the energy recovery chopper (A)
$I_s$	Average dc source current (A)
$i_s$	Instantaneous dc source current (A)
$i_{sn}$	$n$ th phase observer phase current (A)
$I_{sr}$	rms dc source current (A)
$J$	Rotor inertia ( $\text{Kg}\cdot\text{m sec}^2$ )
$J_c$	Current density ( $\text{A}/\text{m}^2$ )
$K$	Spring constant per unit length of the stator (m)
$k$	Ratio between axial length to bore diameter
$k(\theta)$	Slope of inductance to rotor position ( $\text{H}/\text{rad}$ )
$k(\theta, \lambda)$	Incremental slope of rotor position vs. flux linkages at constant current ( $\text{rad}/\text{H}$ )
$k_d$	Duty cycle
$k_e$	Efficiency
$K_b$	Small signal back or induced emf or torque constant ( $\text{V}/\text{rad/sec}$ )
$K_c$	Gain constant of the PI current controller ( $\text{V}/\text{V}$ )
$K_{is}$	Integral gain of the speed controller ( $\text{V}/\text{V}$ )
$K_{ps}$	Proportional gain of the speed controller ( $\text{V}/\text{V}$ )
$K_r$	Product of the resistivity and mean length of one turn of the winding or converter gain

$K_s$	Gain constant of the PI speed controller (V/V)
$L$	Stator core length (m)
$L(\theta, i)$	Self inductance as a function of rotor position and current (H)
$L_a^s, L_a$	Aligned saturated inductance per phase (H)
$L_a^u$	Aligned unsaturated inductance per phase (H)
$L_e$	Equivalent series inductance per phase (H)
$\ell_g$	Air gap, when stator and rotor poles are aligned (m)
$\ell_{g1-7}$	Length of air gap between stator and rotor poles with the number indicating the flux path
$\ell_{g1\ell}$	Length of air gap between stator and rotor poles at the lower side; number 1 indicates the associated flux path
$\ell_{g1u}$	Length of air gap between stator and rotor poles at the upper side; number 1 indicates the associated flux path
$\ell_{ry}$	Flux path length in rotor back iron, a numeral subscript indicates the flux path (m)
$\ell_{rp}$	Flux path length in rotor pole, a numeral subscript indicates the flux path (m)
$\ell_{sy}$	Flux path length in stator back iron, a numeral subscript indicates the flux path (m)
$\ell_{sp}$	Flux path length in stator pole, a numeral subscript indicates the flux path (m)
$\ell(\theta, i)$	Incremental inductance of a phase winding (H)
$l_m$	Average length of one turn of the winding (m)
$L_r$	Inductance of the inductor in energy recovery chopper circuit (H)
$L_t$	Stack length of the stator in LSRM (m)
$L_{tr}$	Stack length of the translator in LSRM (m)
$L_w$	Stack width of the LSRM (m)
$L_u$	Unaligned inductance per phase (H)
$M$	Mutual inductance per phase (H)
$m$	Mode number or number of phases active at a time
$m_1$	Linear slope of the inductance vs. rotor position characteristic (H/rad)
$M_{ab}$	Mutual inductance between phases $a$ and $b$ (H)
$M_{xy}$	Mutual inductance between $x$ and $y$ phases (H)
$N_b$	Number of fan blades
$N_h$	Number of horizontal layers in a stator coil

$N_g$	Number of grooves in the sleeve bearings
$N$	Number of turns in the solenoid
$n$	Total number of stator poles in LSRM
$N_r$	Rotor speed (rpm)
$N_{sc}$	Number of sectors in LSRM stator
$N_v$	Number of vertical layers in a stator coil
$P$	Specific resistivity of the coil (m) or power output in LSRM (W)
$P_a$	Air gap power in LSRM (W)
$p_a$	Instantaneous air gap power (W)
$P_{am}$	Air gap power during motoring (W)
$P_{ar}$	Air gap power during regeneration (W)
$P_c$	Total core loss (W)
$P_d$	Power output (W)
$P_f$	Form or packing factor of the winding
$P_g$	Permeance of the flux path in air, a numeral subscript indicates the path number (Wb/A)
$P_{ck}$	Core loss coefficient of the $k$ th segment (W/kg)
$P_{cu}$	Stator copper losses (W)
$P_d$	Developed power (W)
$P_r$	Number of rotor poles
$P_s$	Number of stator poles
$p_i$	Instantaneous input power (W)
$q$	Number of stator phases
$r$	Outer radius of the rotor (m)
$R$	Dump resistance ( $\Omega$ )
$R_c$	Core loss resistance ( $\Omega$ )
$R_{cr}$	Rotor core reluctance per pole pair
$R_{cs}$	Stator back iron reluctance per side
$R_e$	Equivalent series resistance per phase ( $\Omega$ )
$R_{eq}$	Equivalent resistance per phase ( $\Omega$ )
$R_g$	Air gap reluctance; an additional numeral subscript indicates the flux path
$R_{sn}$	Normalized stator phase resistance (p.u.)
$R_{tp}$	Reluctance of the translator pole (A/Wb)

$R_{ty}$	Reluctance of the translator back iron or yoke (A/Wb)
$r_i$	Inner contact surface radius of the ball bearing
$R_{em}$	Motor equivalent resistance for emf term ( $k(\theta)\omega_m$ ) ( $\Omega$ )
$r_o$	Outer contact surface radius of the ball bearing
$R_{rp}$	Rotor pole reluctance; an additional numeral subscript indicates the flux path (A/Wb)
$R_{ry}$	Rotor back iron reluctance; an additional numeral subscript indicates the flux path (A/Wb)
$R_s$	Resistance per phase ( $\Omega$ )
$R_{s1}, R_{s2}, R_{s3}, R_{s4}$	Current sensing resistors ( $\Omega$ )
$R_{sp}$	Reluctance of stator pole; an additional numeral subscript indicates the flux path (A/Wb)
$R_{sy}$	Stator back iron reluctance; an additional numeral subscript indicates the flux path (A/Wb)
$r_y$	Mean radius of the stator core (m)
$s$	Laplace transform variable; also represents time in seconds
$t_a$	Advance time for the gate pulse (sec)
$T_1, T_2$	Equivalent electrical time constant of the SRM system (sec)
$T_a$	Acceleration torque (N·m)
$T_{av}$	Average electromagnetic torque (N·m)
$T_{cc}$	Time constant of the PI current controller (sec)
$T_c$	One carrier cycle time (period) (sec)
$T_e$	Electromagnetic torque (N·m)
$T_f$	Fall time of the current (sec)
$T_l$	Load torque (N·m)
$T_m$	Mechanical time constant (sec)
$T_{\max}$	Maximum torque limit (N·m)
$T_{pc}$	Duration of varying phase inductance (sec)
$T_{ph}$	Number of turns per phase
$t_p$	One phase period (sec)
$T_r$	Rise time of the current or time constant of the converter (sec)
$t_r$	Rise time for $\Delta I$ (sec)
$T_s$	Sampling time or time constant of PI speed controller (sec)
$T_x$	Torque due to phase $x$ (N·m)
$T_{xy}$	Torque due to mutual coupling of phases $x$ and $y$ (N·m)

$T_y$	Torque due to phase $y$ (N·m)
$T_\omega$	Time constant of the speed transducer (sec)
$t_s$	Width of stator pole
$u$	Fan blade tip speed (m/sec)
$v$	Air-stream velocity (m/sec)
$v_{1q}$	Quadrature component of voltage (V)
$v_a, v_b, v_c$	Instantaneous phase $A, B, C$ voltage input (V)
$V_{ac}$	ac input supply voltage, line to line (V)
$V_b$	Base voltage (V)
$v_c$	Control voltage (V)
$V_{cm}$	Maximum control voltage (V)
$V_d$	Diode voltage drop (V)
$V_{dc}$	Applied voltage to a phase or dc source voltage (V)
$V_{dcn}$	Normalized applied or dc link voltage (p.u.)
$V_i$	Step-down voltage of the front-end chopper (V)
$V_m$	Peak ac line input voltage (V)
$V_{ro}$	Diode bridge rectifier output voltage (V)
$v_{ramp}$	PWM (carrier) voltage signal (V)
$V_t$	Power switch voltage drop (V)
$w$	Wedge height (m)
$W$	Vertical load (Kg)
$w_c$	Width of the stator coil (m)
$w_{cs}$	Space between two stator coils (m)
$W_e$	Electrical input energy (J)
$W_f$	Field energy (J)
$W'_f$	Coenergy (J)
$w_k$	Weight of the iron segment $k$ (kg)
$W_m$	Mechanical energy (J)
$W_s, W_f$	Field energy (J)
$w_{ss}$	Stator slot width in LSRM (m)
$w_{sp}$	Stator pole width in linear machines (m)
$w_{tp}$	Translator pole width in LSRM (m)
$w_{ts}$	Translator slot width in LSRM (m)
$Z_b$	Number of balls in the ball bearing or base impedance ( $\Omega$ )

$Z_r$	Number of rotor slots
$Z_s$	Number of stator slots
$\beta_s$	Stator pole arc (rad)
$\beta_{s1}$	Stator pole arc at its base (rad)
$\beta_r$	Rotor pole arc (rad)
$\beta_{r1}$	Rotor pole arc at its base (rad)
$\gamma$	Poisson's ratio or $\tan^{-1}$ of machine impedance angle
$\Delta$	Radial deflection
$\Delta F$	Error between applied and calculated mmf (AT)
$\Delta I$	Peak to peak current ripple (A)
$\Delta i$	Hysteresis window (A)
$\Delta V_o$	C-dump capacitor ripple voltage (V)
$\delta$	Variation of radius (m)
$\delta L$	Incremental inductance (H)
$\delta\theta$	Incremental rotor position (rad)
$\delta W_e$	Incremental electrical energy (J)
$\delta W_f$	Incremental field energy (J)
$\delta W'_f$	Incremental coenergy (J)
$\delta W_m$	Incremental mechanical energy (J)
$\theta$	Rotor position (rad)
$\theta_a$	Advance angle (rad)
$\theta_{a1}, \theta_{a2}$	Double valued rotor position for $\lambda_a$ , phase A (rad)
$\theta_{b1}, \theta_{b2}$	Double valued rotor position for $\lambda_b$ , phase B (rad)
$\theta_{co}$	Advance commutation angle (rad)
$\theta_d$	Current dwell angle (rad)
$\theta_e$	Error in rotor position (rad)
$\theta_{fr}$	Current fall angle at rated operating point (rad)
$\theta_o$	Overlap of phase flux linkages or inductances (rad)
$\theta_m$	Rotor position when $i = i_m$ (rad)
$\theta_{pc}$	Angle of significant inductance variation (rad)
$\theta_{rf}$	Reference rotor position (rad)
$\theta_{rp}$	Rotor pole pitch (rad)
$\theta_{rs}$	Phase shift between phase flux linkages or inductances (rad)
$\theta_s$	Phase current displacement angle (rad)

$\theta_{st}$	Initial rotor position at starting (rad)
$\lambda$	Flux linkage
$\lambda_a$	Flux linkages at aligned position (Wb-T)
$\lambda_e$	Expected phase flux linkages (volt-sec)
$\lambda_{en}$	$n$ th phase flux linkages error (volt-sec)
$\lambda_m$	Phase flux linkages (volt-sec)
$\lambda_n$	$n$ th phase flux linkages (volt-sec)
$\lambda_{sn}$	Observer $n$ th-phase flux linkages (volt-sec)
$\lambda_u$	Flux linkages at unaligned position (Wb-T)
$\rho$	Mass density of the lamination material (Kg/m <sup>3</sup> )
$\sigma_s$	Ratio between aligned and unaligned inductance at saturation
$\sigma_u$	Ratio between aligned unsaturated inductance and unaligned inductance
$\tau$	Time constant for linear operation (sec)
$\tau_a$	Aligned time constant (sec)
$\tau_c$	Core loss time constant (sec)
$\tau_f$	Current fall time (sec)
$\tau_r$	Current rise time (sec)
$\tau_u$	Unaligned time constant (sec)
$\phi$	Flux in the air gap during overlap of stator and rotor poles in rotary SRM or flux in stator pole in LSRM (Wb)
$\omega$	Angular natural frequency (rad/sec)
$\omega_c$	Angular switching frequency (rad/sec)
$\omega_{cs}$	PWM carrier frequency in inactive phases for probing (rad/sec)
$\omega_e$	Error rotor speed (rad/sec)
$\omega_m$	Rotor speed (mechanical) (rad/sec)
$\omega_{mr}$	Rated mechanical speed (rad/sec)
$\omega_n$	Natural frequency of oscillation (rad/sec)
$\omega_r$	Rotor speed signal (V)
$\omega_r^*$	Rotor speed reference signal (V)
$\omega_{rs}$	Resonant frequency (rad/sec)
$\omega_{sm}$	Observer rotor speed (rad/sec)
$\mu_r$	Relative permeability of the iron
$\zeta$	Damping ratio

---

# 1 Principle of Operation of the Switched Reluctance Motor

## 1.1 INTRODUCTION

The switched reluctance motor (SRM) drives for industrial applications are of recent origin. This chapter contains a brief introduction to SRM and its principle of operation. Key to an understanding of any machine is its torque expression, which is derived from first principles. The implications of machine operation and its salient features are inferred from the torque expression. The torque expression requires a relationship between machine flux linkages or inductance and the rotor position; for the sake of brevity and to illustrate the basic theory, only unsaturated operation is considered here. The machine operation in all of its four quadrants of torque vs. speed is derived from the inductance vs. rotor position characteristic of the machine, and, in line with other machines, the dynamic equivalent circuit for SRM is formulated. Its use may be limited in design but it has a larger impact on the high-performance controller derivations and understanding. Various configurations of the rotary SRM, including single-phase machines, are described. The single-phase machines have applications in low-performance but high-volume applications. An SRM capable of linear motion is introduced and its principles of operation and many of its configurations are presented in this chapter.

## 1.2 BACKGROUND

Since 1969, a variable reluctance motor<sup>1</sup> has been proposed for variable speed applications. The origin of this motor can be traced back to 1842, but the “reinvention” has been possible due to the advent of inexpensive, high-power switching devices. Even though this machine is a type of synchronous machine, it has certain novel features. It has wound field coils of a dc motor for its stator windings and has no coils or magnets on its rotor. Both the stator and rotor have salient poles, hence the machine is referred to as a doubly salient machine. Such a typical machine<sup>2,3</sup> is shown in [Figure 1.1a](#), and a modified version with two teeth per pole is shown in [Figure 1.1b](#).<sup>4,5</sup>

The rotor is aligned whenever diametrically opposite stator poles are excited. In a magnetic circuit, the rotating member prefers to come to the minimum reluctance position at the instance of excitation. While two rotor poles are aligned to the two stator poles, another set of rotor poles is out of alignment with respect to a different

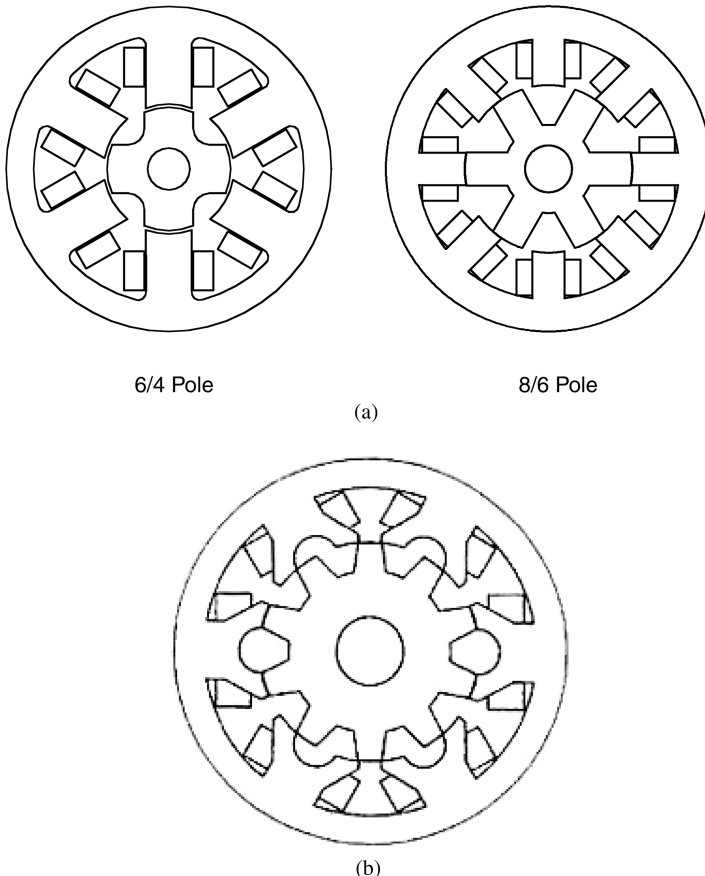


**FIGURE 1.1** Switched reluctance motor configurations. (a) One tooth per pole. (b) Two teeth per pole (12/10 poles).

set of stator poles. Then, this set of stator poles is excited to bring the rotor poles into alignment. Likewise, by sequentially switching the currents into the stator windings, the rotor is rotated. The movement of the rotor, hence the production of torque and power, involves switching of currents into stator windings when there is a variation of reluctance; therefore, this variable speed motor drive is referred to as a switched reluctance motor drive.

### 1.3 ELEMENTARY OPERATION OF THE SWITCHED RELUCTANCE MOTOR

Consider that the rotor poles  $r_1$  and  $r'_1$  and stator poles  $c$  and  $c'$  are aligned. Apply a current to phase  $a$  with the current direction as shown in [Figure 1.2a](#). A flux is established through stator poles  $a$  and  $a'$  and rotor poles  $r_2$  and  $r'_2$  which tends to pull the rotor poles  $r_2$  and  $r'_2$  toward the stator poles  $a$  and  $a'$ , respectively. When they are

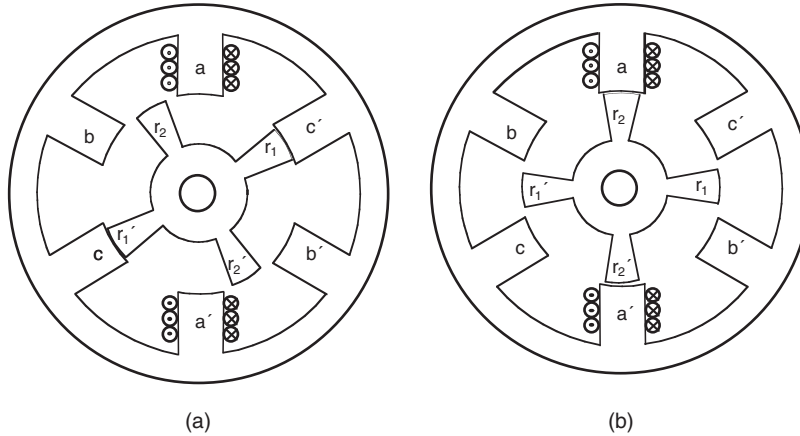


**FIGURE 1.2** Operation of an SRM. (a) Phase  $c$  aligned. (b) Phase  $a$  aligned.

aligned, the stator current of phase  $a$  is turned off and the corresponding situation is shown in Figure 1.2b. Now the stator winding  $b$  is excited, pulling  $r_1$  and  $r'_1$  toward  $b$  and  $b'$ , respectively, in a clockwise direction. Likewise, energization of the  $c$  phase winding results in the alignment of  $r_2$  and  $r'_2$  with  $c$  and  $c'$ , respectively. Hence, it takes three phase energizations in sequence to move the rotor by  $90^\circ$ , and one revolution of rotor movement is effected by switching currents in each phase as many times as there are number of rotor poles. The switching of currents in the sequence  $acb$  results in the reversal of rotor rotation is seen with the aid of Figures 1.2a and b.

#### 1.4 PRINCIPLE OF OPERATION OF THE SWITCHED RELUCTANCE MOTOR

The torque production in the switched reluctance motor is explained using the elementary principle of electromechanical energy conversion in a solenoid, as shown in Figure 1.3a. The solenoid has  $N$  turns, and when it is excited with a current  $i$ , the coil sets up a flux  $\Phi$ . Increasing the excitation current will make the armature move towards the yoke, which is fixed. The flux vs. magnetomotive force (mmf) is plotted for two values of air gap,  $x_1$  and  $x_2$ , where  $x_1 > x_2$ , and is shown in Figure 1.3b. The flux vs. mmf characteristics for  $x_1$  are linear because the reluctance of the air gap is dominant, making the flux smaller in the magnetic circuit. The electrical input energy is written as:

$$W_e = \int e i dt = \int i dt \frac{dN\Phi}{dt} = \int Ni d\Phi = \int F d\Phi \quad (1.1)$$

where  $e$  is the induced emf and  $F$  is the mmf. This input electrical energy,  $W_e$ , is equal to the sum of energy stored in the coil,  $W_f$ , and energy converted into mechanical

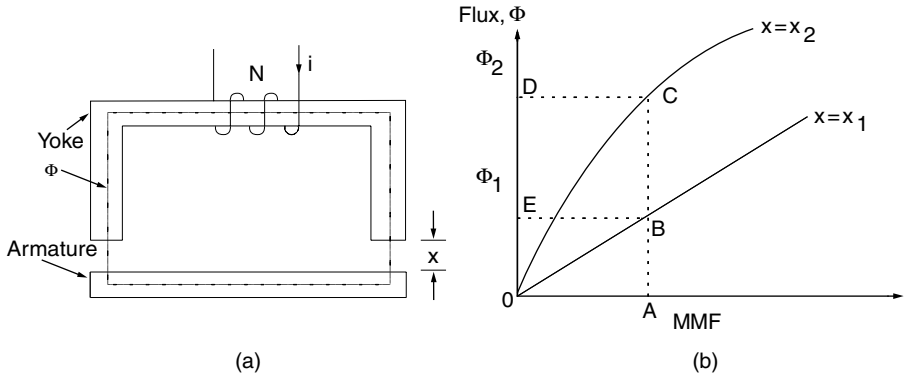


**FIGURE 1.3** Solenoid and its characteristics. (a) A solenoid. (b) Flux v. mmf characteristics.

work,  $W_m$ . It is written as:

$$W_e = W_f + W_m \quad (1.2)$$

When no mechanical work is done, as in the case of the armature starting from position  $x_1$ , the stored field energy is equal to the input electrical energy given by Eq. (1.1). This corresponds to area OBEO in Figure 1.3b. The complement of the field energy, termed *coenergy*, is given by area OB $A$ O in Figure 1.3b and mathematically expressed as  $\int \Phi dF$ . Similarly, for the position  $x_2$  of the armature, the field energy corresponds to area OCDO and the coenergy is given by area OCAO. For incremental changes, Eq. (1.2) is written as:

$$\delta W_e = \delta W_f + \delta W_m \quad (1.3)$$

For a constant excitation of  $F_1$  given by the operating point A in Figure 1.3b, the various energies are derived as:

$$\delta W_e = \int_{\phi_1}^{\phi_2} F_1 d\phi = F_1(\phi_2 - \phi_1) = \text{area(BCDEB)} \quad (1.4)$$

$$\delta W_f = \delta W_{f|_{x=x_2}} - \delta W_{f|_{x=x_1}} = \text{area(OCDO)} - \text{area(OBEO)} \quad (1.5)$$

Using Eqs. (1.3) to (1.5), the incremental mechanical energy is derived as:

$$\delta W_m = \delta W_e - \delta W_f = \text{area(OBCO)} \quad (1.6)$$

and that is the area between the two curves for a given magnetomotive force. In the case of a rotating machine, the incremental mechanical energy in terms of the electromagnetic torque and change in rotor position is written as:

$$\delta W_m = T_e \delta \theta \quad (1.7)$$

where  $T_e$  is the electromagnetic torque and  $\delta\theta$  is the incremental rotor angle. Hence, the electromagnetic torque is given by:

$$T_e = \frac{\delta W_m}{\delta\theta} \quad (1.8)$$

For the case of constant excitation (i.e., when the mmf is constant), the incremental mechanical work done is equal to the rate of change of coenergy,  $W'_f$ , which is nothing but the complement of the field energy. Hence, the incremental mechanical work done is written as:

$$\delta W_m = \delta W'_f \quad (1.9)$$

where

$$W'_f = \int \Phi dF = \int \Phi d(Ni) = \int (N\Phi) di = \int \lambda(\theta, i) di = \int L(\theta, i) i di \quad (1.10)$$

where the inductance,  $L$ , and flux linkages,  $\lambda$ , are functions of the rotor position and current. This change in coenergy occurs between two rotor positions,  $\theta_2$  and  $\theta_1$ . Hence, the air gap torque in terms of the coenergy represented as a function of rotor position and current is

$$T_e = \frac{\delta W_m}{\delta\theta} = \frac{\delta W'_f}{\delta\theta} = \left. \frac{\delta W'_f(i, \theta)}{\delta\theta} \right|_{i=\text{constant}} \quad (1.11)$$

If the inductance is linearly varying with rotor position for a given current, which in general is not the case in practice, then the torque can be derived as:

$$T_e = \frac{dL(\theta, i)}{d\theta} \cdot \frac{i^2}{2} \quad (1.12)$$

where

$$\frac{dL(\theta, i)}{d\theta} = \left. \frac{L(\theta_2, i) - L(\theta_1, i)}{\theta_2 - \theta_1} \right|_{i=\text{constant}} \quad (1.13)$$

and this differential inductance can be considered to be the torque constant expressed in  $\text{N}\cdot\text{m}/\text{A}^2$ . It is important to emphasize at this juncture that this is not a constant and that it varies continuously. This has the implication that the switched reluctance motor will not have a steady-state equivalent circuit in the sense that the dc and ac motors have.

Equation (1.12) has the following implications:

1. The torque is proportional to the square of the current, hence the current can be unipolar to produce unidirectional torque. Note that this is quite

- contrary to the case for ac machines. This unipolar current requirement has a distinct advantage in that only one power switch is required for control of current in a phase winding. Such a feature greatly reduces the number of power switches in the converter and thereby makes the drive economical.
- 2. The torque constant is given by the slope of the inductance vs. rotor position characteristic. It is understood that the inductance of a stator winding is a function of both the rotor position and current, thus making it nonlinear. Because of its nonlinear nature, a simple equivalent circuit development for this motor is not possible.
  - 3. Since the torque is proportional to the square of the current, this machine resembles a dc series motor; hence, it has a good starting torque.
  - 4. A generating action is made possible with unipolar current due to its operation on the negative slope of the inductance profile.
  - 5. The direction of rotation can be reversed by changing the sequence of stator excitation, which is a simple operation.
  - 6. Due to features 1, 4, and 5, this machine is suitable for four-quadrant operation with a converter.
  - 7. Torque and speed control is achieved with converter control.
  - 8. This machine requires a controllable converter for its operation and cannot be operated directly from a three-phase line supply. Hence, for constant speed applications, this motor drive is expensive in comparison to induction and synchronous motors.
  - 9. Because of its dependence on a power converter for its functioning, this motor drive is an inherently variable-speed motor drive system.
  - 10. There is very little mutual inductance between machine phase windings in SRM, and for all practical purposes it is considered to be negligible. Since mutual coupling is absent, each phase is electrically independent of other phases. This is a feature unique to this machine only. Due to this feature, note that a short-circuit fault in one phase winding has no effect on other phases. For one thing, it makes possible operation of other healthy phases of the machine and their operation will not be derated, as the voltage requirement is the same before and after the fault. Such independence of machine phases has tremendous consequence in aircraft actuators and generators, actuators used in defense applications, motors used in coolant pumps in nuclear power plants, and traction and electric vehicles, to mention a few applications. In extreme contrast to the operation of SRM under short-circuit fault, consider a permanent magnet synchronous motor with a single-phase, short-circuit fault condition.
  - 11. Because the current only needs to be unidirectional for all quadrants of operation, unlike in other machines, all power converter configurations for this machine have a switch in series with a machine phase winding facing the dc source voltage. In case of a machine partial-winding fault or switch misfiring, or short circuit, there is a significant delay time in the rise of the current which allows the protection circuit to be activated to isolate the faults. Also, there is no shoot-through failure mode even when the power switch fails. In contrast, all other ac machine drives require the placement

of two power switches in series facing the dc source, with the center point connection of the switches connected to one end of the machine phase winding. Such an arrangement for one phase is called a *phase leg* or the *inverter*. Only one switch in a phase leg can be on at any time. Failure in another switch leading to a short circuit or misfiring will lead to a short circuit of the dc source. Such a fault is known as a shoot-through fault.

From the above description, it is deduced that the switched reluctance motor is similar to the step motor except that it has

1. Fewer poles
2. Larger stepping angle
3. Usually one tooth per pole
4. Higher power output capability

The comparison should not be carried too much further due to the nonlinearity of the magnetic circuit.

## 1.5 DERIVATION OF THE RELATIONSHIP BETWEEN INDUCTANCE AND ROTOR POSITION

Since the torque characteristics are dependent on the relationship between flux linkages and rotor position as a function of current,<sup>6-10</sup> it is worthwhile to conceptualize the control possibilities and limitations of this motor drive. For example, a typical phase inductance vs. rotor position is shown in [Figure 1.4](#) for a fixed phase current. The inductance corresponds to that of a stator-phase coil of the switched reluctance motor neglecting the fringe effect and saturation. The significant inductance profile changes are determined in terms of the stator and rotor pole arcs and number of rotor poles. The rotor pole arc is assumed to be greater than the stator pole arc for this illustration, which is usually the case. From [Figures 1.4a](#) and [b](#), the various angles are derived as:

$$\theta_1 = \frac{1}{2} \left[ \frac{2\pi}{P_r} - (\beta_s + \beta_r) \right] \quad (1.14a)$$

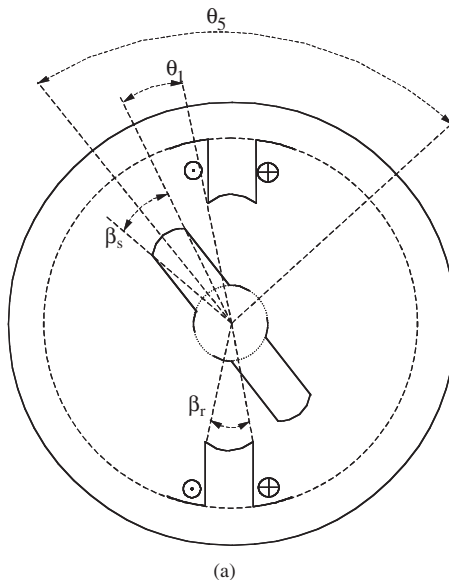
$$\theta_2 = \theta_1 + \beta_s \quad (1.14b)$$

$$\theta_3 = \theta_2 + (\beta_r - \beta_s) \quad (1.14c)$$

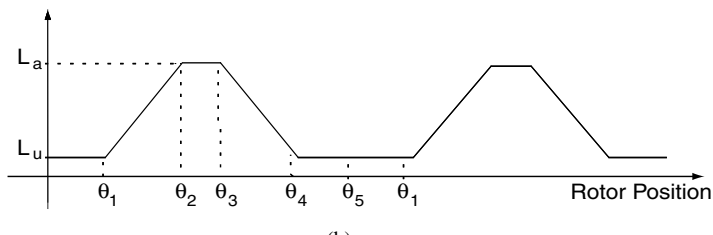
$$\theta_4 = \theta_3 + \beta_s \quad (1.14d)$$

$$\theta_5 = \theta_4 + \theta_1 = \frac{2\pi}{P_r} \quad (1.14e)$$

where  $\beta_s$  and  $\beta_r$  are stator and rotor pole arcs, respectively, and  $P_r$  is the number of rotor poles.



(a)



(b)

**FIGURE 1.4** Derivation of inductance vs. rotor position from rotor and stator pole arcs for an unsaturated switched reluctance machine. (a) Basic rotor position definition in a two pole SRM. (b) Inductance profile.

Four distinct inductance regions emerge:

1.  $0 - \theta_1$  and  $\theta_4 - \theta_5$ : The stator and rotor poles are not overlapping in this region and the flux is predominantly determined by the air path, thus making the inductance minimum and almost a constant. Hence, these regions do not contribute to torque production. The inductance in this region is known as unaligned inductance,  $L_u$ .
2.  $\theta_1 - \theta_2$ : Poles overlap, so the flux path is mainly through stator and rotor laminations. This increases the inductance with the rotor position, giving it a positive slope. A current impressed in the winding during this region produces a positive (i.e., motoring) torque. This region comes to an end when the overlap of poles is complete.

3.  $\theta_2 - \theta_3$ : During this period, movement of rotor pole does not alter the complete overlap of the stator pole and does not change the dominant flux path. This has the effect of keeping the inductance maximum and constant, and this inductance is known as aligned inductance,  $L_a$ . As there is no change in the inductance in this region, torque generation is zero even when a current is present in this interval. In spite of this fact, it serves a useful function by providing time for the stator current to come to zero or lower levels when it is commutated, thus preventing negative torque generation for part of the time if the current has been decaying in the negative slope region of the inductance.
4.  $\theta_3 - \theta_4$ : The rotor pole is moving away from overlapping the stator pole in this region. This is very much similar to the  $\theta_1 - \theta_2$  region, but it has decreasing inductance and increasing rotor position contributing to a negative slope of the inductance region. The operation of the machine in this region results in negative torque (i.e., generation of electrical energy from mechanical input to the switched reluctance machine).

It is not possible to achieve the ideal inductance profiles shown in [Figure 1.4](#) in an actual motor due to saturation. Saturation causes the inductance profile to curve near the top and thus reduces the torque constant. Hence, saturating the machine beyond a point produces a diminishing return on torque and power output.

For rectangular currents, it can be seen that the motoring torque is produced for a short duration in pulsed form, resulting in a large torque ripple. This can create problems of increased audible noise, fatigue of the shaft, and possible speed oscillations. The torque ripples are minimized by designing the machine such that the inductance profiles of two succeeding phases overlap during the ending of one and the beginning of the other. In turn this requires the correct choice of number of stator and rotor poles and their pole arcs. An alternative technique to reduce the torque ripples is to shape the currents (see Chapter 5).

## 1.6 EQUIVALENT CIRCUIT

An elementary equivalent circuit for the SRM can be derived neglecting the mutual inductance between the phases as follows. The applied voltage to a phase is equal to the sum of the resistive voltage drop and the rate of the flux linkages and is given as:

$$V = R_s i + \frac{d\lambda(\theta, i)}{dt} \quad (1.15)$$

where  $R_s$  is the resistance per phase, and  $\lambda$  is the flux linkage per phase given by:

$$\lambda = L(\theta, i)i \quad (1.16)$$

where  $L$  is the inductance dependent on the rotor position and phase current. The phase voltage equation, then, is

$$\begin{aligned} v &= R_s i + \frac{d\{L(\theta, i)i\}}{dt} = R_s i + L(\theta, i) \frac{di}{dt} + i \frac{d\theta}{dt} \cdot \frac{dL(\theta, i)}{d\theta} \\ &= R_s i + L(\theta, i) \frac{di}{dt} + \frac{dL(\theta, i)}{d\theta} \omega_m i \end{aligned} \quad (1.17)$$

In this equation, the three terms on the right-hand side represent the resistive voltage drop, inductive voltage drop, and induced emf, respectively, and the result is similar to the series excited dc motor voltage equation.

The induced emf,  $e$ , is obtained as:

$$e = \frac{dL(\theta, i)}{d\theta} \omega_m i = K_b \omega_m i \quad (1.18)$$

where  $K_b$  may be construed as an emf constant similar to that of the dc series excited machine and is given here as:

$$K_b = \frac{dL(\theta, i)}{d\theta} \quad (1.19)$$

Note that the emf constant is dependent on operating point and is obtained with constant current at the point. From the voltage equation and the induced emf expression, the equivalent circuit for one phase of the SRM is derived and shown in [Figure 1.5](#).

Substituting for the flux linkages in the voltage equation and multiplying with the current results in instantaneous input power given by:

$$p_i = vi = R_s i^2 + i^2 \frac{dL(\theta, i)}{dt} + L(\theta, i) i \frac{di}{dt} \quad (1.20)$$

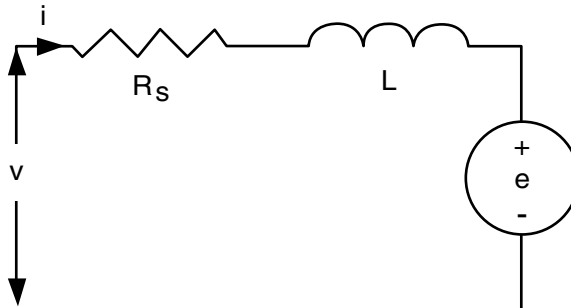


**FIGURE 1.5** Single-phase equivalent circuit of the SRM.

Here, the last term is physically uninterpretable; to draw a meaningful inference, it may be cast in terms of known variables as in the following:

$$\frac{d}{dt} \left( \frac{1}{2} L(\theta, i) i^2 \right) = L(\theta, i) i \frac{di}{dt} + \frac{1}{2} i^2 \frac{dL(\theta, i)}{dt} \quad (1.21)$$

Substituting the above into Eq. (1.20) gives:

$$p_i = R_s i^2 + \frac{d}{dt} \left( \frac{1}{2} L(\theta, i) i^2 \right) + \frac{1}{2} i^2 \frac{dL(\theta, i)}{dt} \quad (1.22)$$

where  $p_i$  is the instantaneous input power. This equation is in the familiar form found in introductory electromechanics texts, implying that the input power is the sum of the winding resistive losses given by  $R_s i^2$ , the rate of change of the field energy given by  $p[L(\theta, i) \cdot i^2/2]$ , and the air gap power,  $p_a$ , which is identified by the term  $[i^2 pL(\theta, i)]/2$ , where  $p$  is the differential operator,  $d/dt$ . Substituting for time in terms of the rotor position and speed, with

$$t = \frac{\theta}{\omega_m} \quad (1.23)$$

in the air gap power results in:

$$p_a = \frac{1}{2} i^2 \frac{dL(\theta, i)}{dt} = \frac{1}{2} i^2 \frac{dL(\theta, i)}{d\theta} \cdot \frac{d\theta}{dt} = \frac{1}{2} i^2 \frac{dL(\theta, i)}{d\theta} \omega_m \quad (1.24)$$

The air gap power is the product of the electromagnetic torque and rotor speed given by:

$$p_a = \omega_m T_e \quad (1.25)$$

from which the torque is obtained by equating these two equations as:

$$T_e = \frac{1}{2} i^2 \frac{dL(\theta, i)}{d\theta} \quad (1.26)$$

This completes development of the equivalent circuit and equations for evaluating electromagnetic torque, air gap power, and input power to the SRM both for dynamic and steady-state operations.

## 1.7 SRM CONFIGURATIONS

Switched reluctance motors are classified as shown in [Figure 1.6](#). Initial classification is made on the basis of the nature of the motion (i.e., rotating or linear). The linear SRMs have found application in the marketplace by catering to machine tool servos.

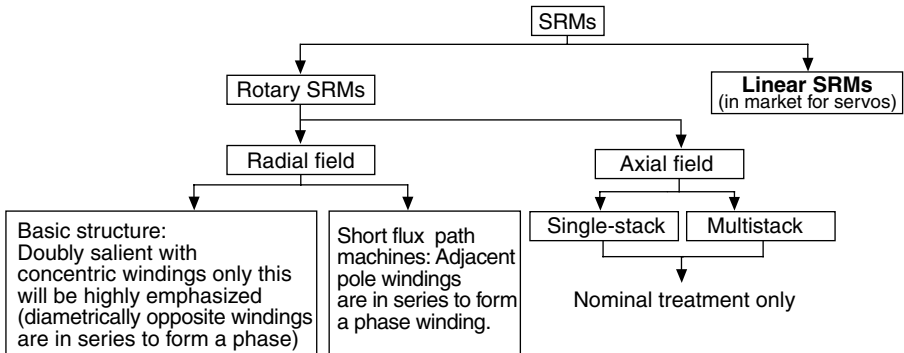
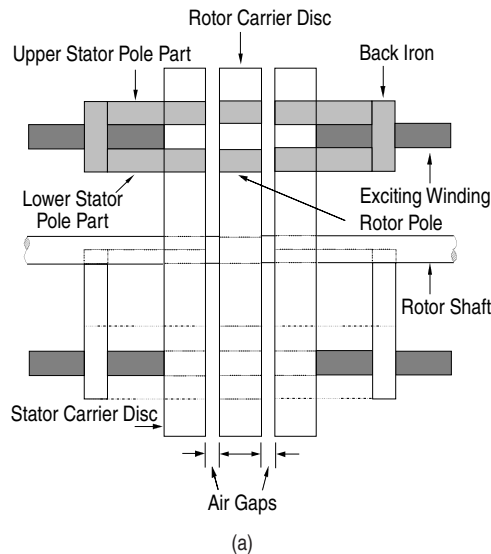


**FIGURE 1.6** Classification of SRMs.

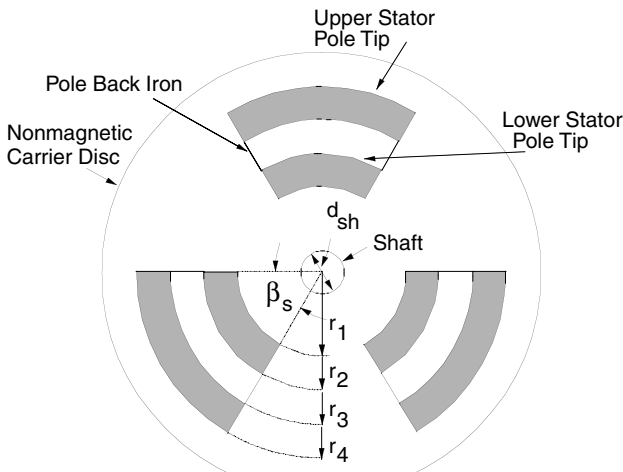
### 1.7.1 ROTARY SRM

The rotary machine-based SRMs are further differentiated by the nature of the magnetic field path as to its direction with respect to the axial length of the machine. If the magnetic field path is perpendicular to the shaft, which may also be seen as along the radius of the cylindrical stator and rotor, the SRM is classified as radial field. Such radial field SRMs are shown in [Figure 1.1](#). When the flux path is along the axial direction, the machine is called an *axial field SRM*.

The axial configuration of an SRM<sup>11</sup> is shown in [Figure 1.7a](#), and the stator and rotor discs are shown in [Figures 1.7b](#) and [c](#), respectively. The flux pattern is shown in [Figure 1.7d](#). The flux path is through the upper stator pole tip, air gap 1, upper rotor pole tip, air gap 2, upper opposite stator pole tip, back iron, stator lower pole tip, air gap 2, rotor lower pole tip, air gap 1, stator lower pole tip, and its back iron. Note that the flux path is parallel to the shaft, a configuration known as axial field SRM. Note that there are six stator poles but only two rotor poles in this axial field SRM. The number of stator discs can be reduced to one, but in that case the rotor laminations have to carry a back iron to provide a closed iron path for the flux. A pair of one rotor and one stator stacks or one rotor and two stator stacks or two rotor and one stator stacks constitutes a single-stack axial field SRM. Multiples of such single stacks can be arranged on the same shaft to augment the power rating. Such a machine is known as a multiple-stack axial field SRM and was the first of the viable axial prototypes in the early 1970s for electric vehicle propulsion.<sup>12</sup> Another example of an axial field SRM with two types of claw pole design for single-phase operation is shown in [Figure 1.8](#).<sup>13,14</sup> Both these designs are intended for ceiling-fan applications. Ingenious designs are possible in the axial type SRMs, as seen by the limited designs in the discussion. Emerging applications are the driving forces behind the quest for design variations and novel designs. The axial field SRMs are ideal for applications where the total length may be constrained, such as in a ceiling fan or in a propulsion application. The disadvantage of this configuration is that the stator laminations have to be folded one on top of the other unlike the simple stacking of laminations in the radial field configuration. The converter configurations and controller algorithms for both configurations of the SRMs are the same.



(a)

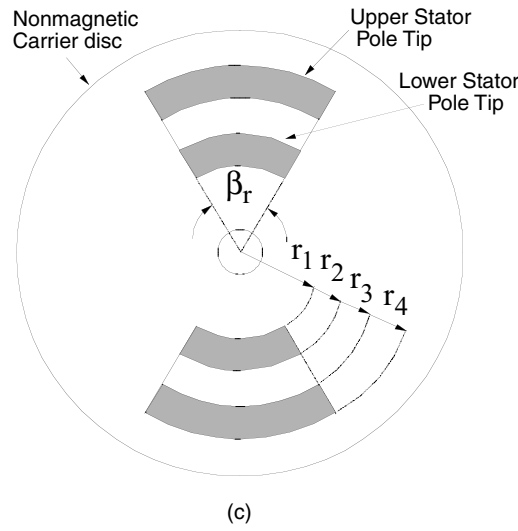


(b)

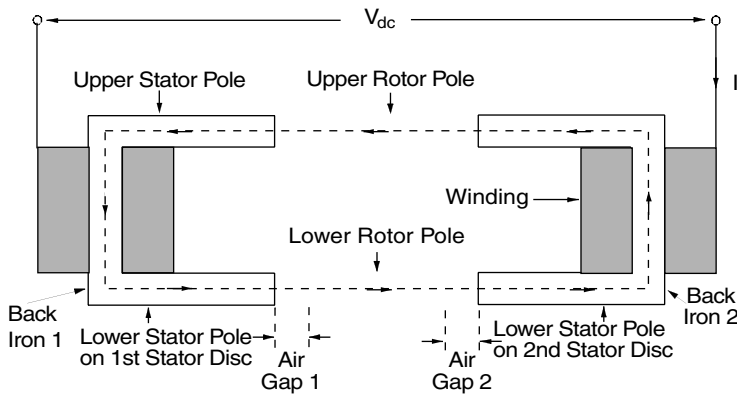
**FIGURE 1.7** (a) Axial field SRM. (b) Endview of the stator. (c) Endview of the rotor. (d) Flux path in the axial field SRM.

The developments in theory, principle, and operation are equally applicable to both the SRM configurations.

Radial field SRMs have emerged with both shorter and longer flux paths. This development is based on whether a phase coil is placed in the slots adjacent to each other to obtain a pair of poles as shown in [Figure 1.9](#) or the coil is placed in the diametrically opposite slots, as shown in [Figure 1.1](#). Short flux path SRMs<sup>15</sup> have



(c)



(d)

**FIGURE 1.7** (Continued)

the advantage of lower core losses due to the fact that flux reversals do not occur in stator back iron in addition to having short flux paths. They have the disadvantages of having a slightly higher mutual inductance compared to conventional radial field SRMs and a possible higher uneven magnetic pull on the rotor.

Conventional radial field SRMs with longer flux paths have been established for many applications due to overwhelming research and development data available on these machines. A recent variation of this type has full pitch coils. A hybridized version of radial field SRMs with permanent magnets placed either in the back iron or on the stator poles, similar to pole shoes in configuration, has been studied and is known as a flux reversal machine. By bringing the permanent magnets onto the stator, the machines can have the high-speed and high-response operational advantages unique to the SRMs.<sup>16–18</sup> They also carry the disadvantages of having magnets

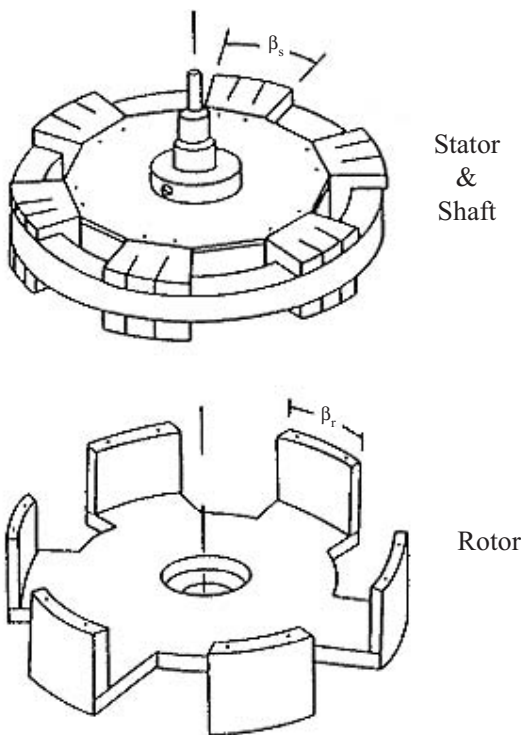


**FIGURE 1.8** Single-phase axial field SRM.

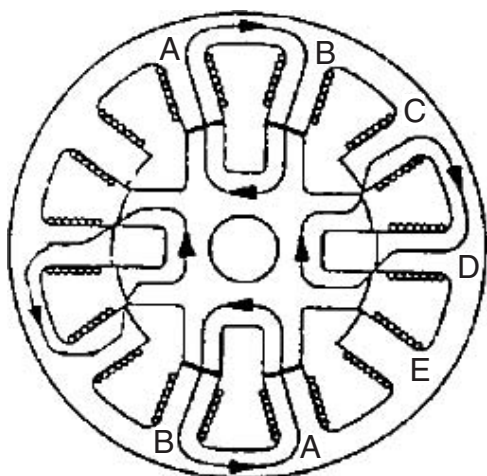


**FIGURE 1.9** Short flux path five-phase SRM with 10/8 pole.

sensitive to temperature, increased manufacturing complexity, and higher cost. These factors may not exclude the development of these and other novel SRM machine configurations as they may satisfy some special application requirements. The search for newer forms of SRMS will continue to overcome shortcomings in its current designs and to meet optimally the specifications of newer applications which may not be met efficiently and or cost effectively by existing forms of SRMs.

### 1.7.2 SINGLE-PHASE SRM

Single-phase SRMs<sup>16–18</sup> are of interest as they bear a strong resemblance to single-phase induction and universal machines and share their low-cost manufacture as well. High-speed applications are particularly appealing for single-phase SRMs. The single-phase SRMs have 2/2, 4/4, 6/6, and 8/8 stator and rotor poles. When the stator and rotor poles are aligned, the current is turned off and the rotor keeps moving due to stored kinetic energy. As the stator poles become unaligned, the stator winding again is energized, producing an electromagnetic torque. A problem with single-phase SRM operation arises only when the stator and rotor poles are in alignment at standstill (i.e., at the time of starting) or the rotor is at a position where the torque produced may be lower than that of the load torque at starting. This problem is overcome by having a permanent magnet on the stator to pull the rotor away from alignment, or to the appropriate position, to enable the generation of maximum electromagnetic torque; such a construction is shown in [Figure 1.10](#). The permanent magnet must be capable of pulling the rotor with its load. The magnet location is chosen so as to allow the stator windings on excitation to produce the maximum torque. Specific loads such as for an indoor fan may require little starting torque, resulting in smaller permanent magnets on the stator. The disadvantage of this configuration is that the magnet takes up space and its cost.

Starting from any rotor can also be achieved by shifting one pole from its normal position<sup>19</sup> by as much as  $20^{\circ}/P_s$ , where  $P_s$  is the number of stator poles, by having two different gaps (steps) in the rotor poles for each half of the pole arc as shown

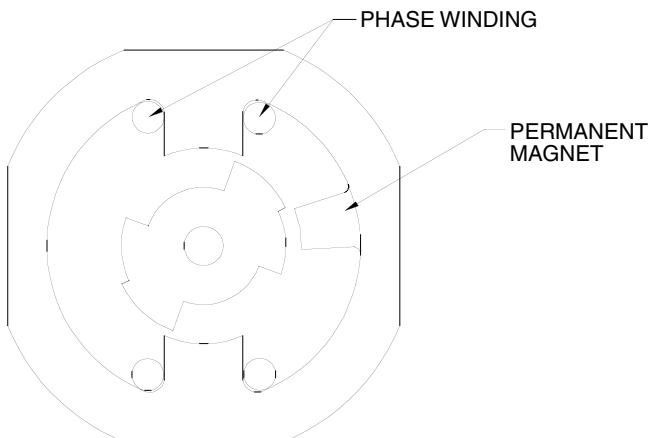


**FIGURE 1.10** Single-phase motor with permanent magnet to enable starting.

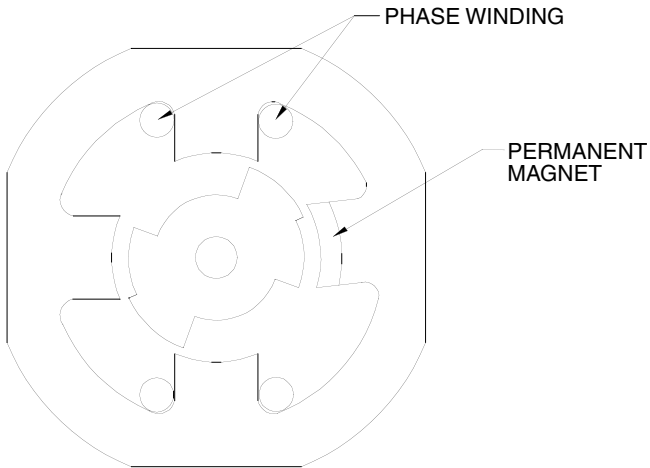


**FIGURE 1.11** Single-phase machine with shifted pole pair and parking magnet.

in Figure 1.11, by shaping the stator poles with side shifts and pole horns, by shaping the stator and rotor pole, or by shaping the stator poles to provide graded air gaps.<sup>20</sup> All of these methods provide unsymmetric saturation in the stator and rotor, resulting in shifting of the flux axis and hence variation in the capability to provide electromagnetic torque at all positions.

Single-phase motors have also been designed with a claw pole structure, with six poles on the stator and rotor having both radial and axial air gaps,<sup>21</sup> offering higher efficiency than that of standard single-phase machines with only radial air gaps. The construction of this machine is a little more intricate than its counterpart and may not be attractive for large-scale production.

The single-phase SRMs operate with a maximum duty cycle of 0.5, as only the rising inductance slope is utilized to generate torque; therefore, they have a torque discontinuity that results in high torque ripple and noise. Applications that are insensitive to this drawback are ideal for these machines, which may be found in hand tools and home appliances.

## 1.8 LINEAR SWITCHED RELUCTANCE MACHINES

### 1.8.1 INTRODUCTION

Linear motor drives are being increasingly considered for machine tool drives because they reduce the need for mechanical subsystems of gears and rotary-to-linear motion converters, such as lead screws. Positioning accuracy is improved by the absence of gears that contribute to the backlashes in the linear motor drives. Linear machine drives combined with electromagnetic levitation are strong candidates for conveyor applications in semiconductor fabrication plants and possibly in low- and high-speed transit applications because of their ability to produce propulsion force on the rotating part, known as the translator, without mechanical contact and friction. Linear switched reluctance machines (LSRMs) are the counterparts of the rotating

switched reluctance machines. In fact, the linear switched reluctance machine is obtained from its rotary counterpart by cutting, along the shaft over its radius, both the stator and rotor and then rolling them out. In this section, various linear switched reluctance machine configurations are introduced. Further, the ideal inductance profile is related to the stator and translator lamination dimensions. A similar relationship for the rotary switched reluctance machine that has been derived earlier is worth noting.

### 1.8.2 MACHINE TOPOLOGY AND ELEMENTARY OPERATION OF LSRMs

A linear SRM may have windings either on the stator or translator (the moving part), whereas in the rotary switched reluctance machine the windings are always on the stator and the rotor contains no windings. Regardless of the location of phase windings, the fixed part is called either a *stator* or *track* and the moving part is called a *translator*. There are two distinct configurations of linear SRM in the literature: longitudinal flux and transverse flux. These two configurations can be obtained by unrolling both the stator and rotor of a rotary SRM with a radial magnetic flux path and axial magnetic flux path, respectively. Figure 1.12 shows the longitudinal flux<sup>22–32</sup> and axial magnetic flux path,<sup>33</sup> respectively. Figure 1.12 shows the longitudinal flux<sup>22–32</sup>

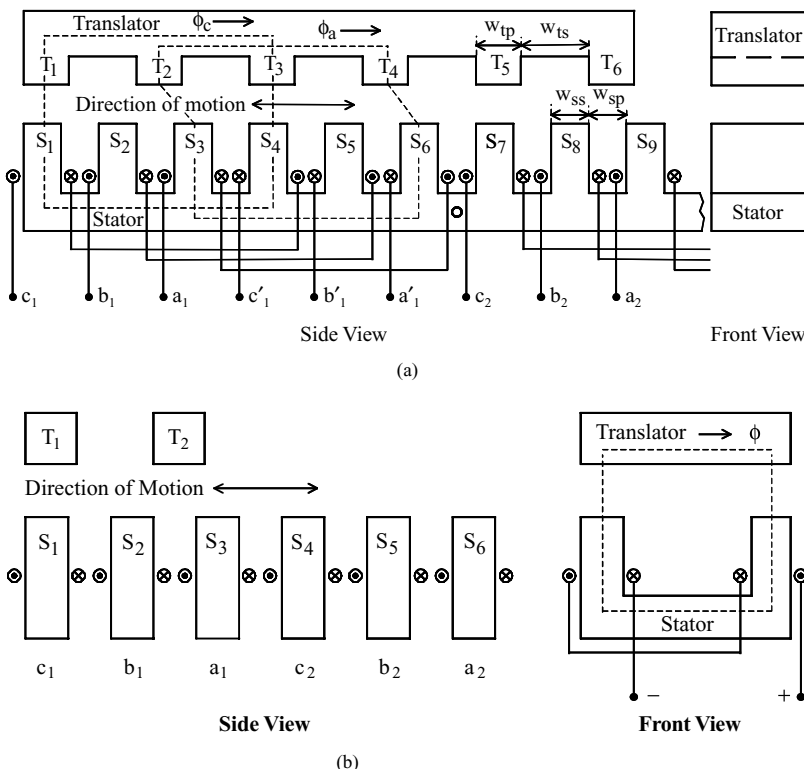


**FIGURE 1.12** Three-phase linear SRMs with longitudinal and transverse flux paths. (a) Three-phase longitudinal linear SRM. (b) Three-phase transverse linear SRM.

and transverse flux<sup>33–35</sup> configurations for three-phase LSRM with an active (containing windings) stator and passive (with no windings) translator topology. The longitudinal magnetic flux path configuration (Figure 1.12a) is a linear counterpart of three-phase radial flux rotary SRM. The flux path in this machine is in the direction of the vehicle motion. This machine is simpler to manufacture, is mechanically robust, and has lower eddy current losses as the flux is in the same direction as the translator motion. A transverse flux design (Figure 1.12b) has the flux path perpendicular to the direction of vehicle motion. It allows a simple track consisting of individually mounted transverse bars. As the flux is perpendicular to the direction of motion, an emf is induced in the core, resulting in high eddy current losses. Longitudinal flux and transverse flux configurations for four-phase LSRM with an active translator and passive stator structure are shown in Figure 1.13. The active stator and passive translator SRM configuration has the advantage of having the power supply and power converters being stationary, resulting in reduced

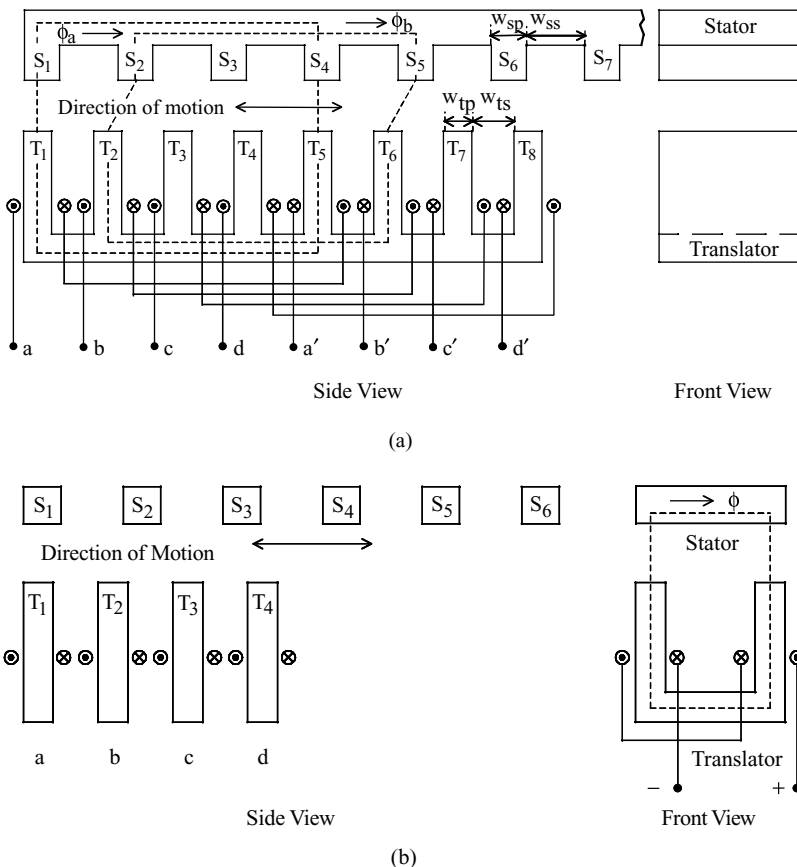


**FIGURE 1.13** (a) Four-phase longitudinal linear SRM with active translator and passive stator. (b) Four-phase transverse linear SRM with active translator and passive stator.

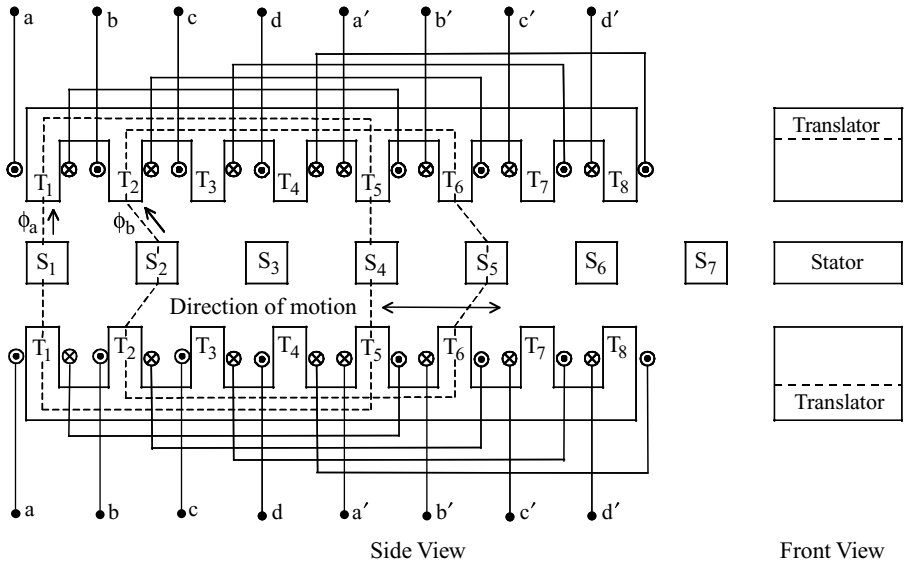


**FIGURE 1.14** Double-sided longitudinal linear SRM.

weight of the vehicle. This design, however, requires a large number of power converter sections along the track, resulting in high costs. On the other hand, a structure with an active translator and passive stator structure requires only one section of the power converter, but the power to the converter in the translator requires transfer by means of contact brushes which is not desirable for high-speed applications or by inductive transfer with additional power-converter circuits, with consequent complexity and higher costs.

Also, the LSRM may have either two stators or two translators or vice versa to make a double-sided LSRM, as shown in Figure 1.14. The double-sided linear SRM does not have as much freedom in the air gap tolerance as the single-sided linear SRM. The single-sided linear SRM provides a net levitation force that can be exploited in Maglev systems, but the double-sided LSRM does not produce a net levitation force; therefore, it is unsuitable for such applications. Its advantages are high force density and lower inductance, as it has four air gaps in its flux path. In contrast, the single-sided LSRM has two air gaps, higher inductance, and lower force density compared to the double-sided LSRM.

When a pair of stator windings connected in series is excited, the translator tends to move so as to align itself with the magnetic flux axis of the excited stator phase windings. This position is referred to as the fully aligned position and has the maximum phase inductance. The position corresponding to maximum reluctance value and hence minimum phase inductance is called the *unaligned position* and occurs when a corresponding pair of translator poles that eventually will be aligned is half a translator pole pitch away from the axis of the excited stator poles. The translator goes forward smoothly when the stator windings are switched in sequence. Depending on the converter topology and the mode of operation, the previously excited phase may be turned off before

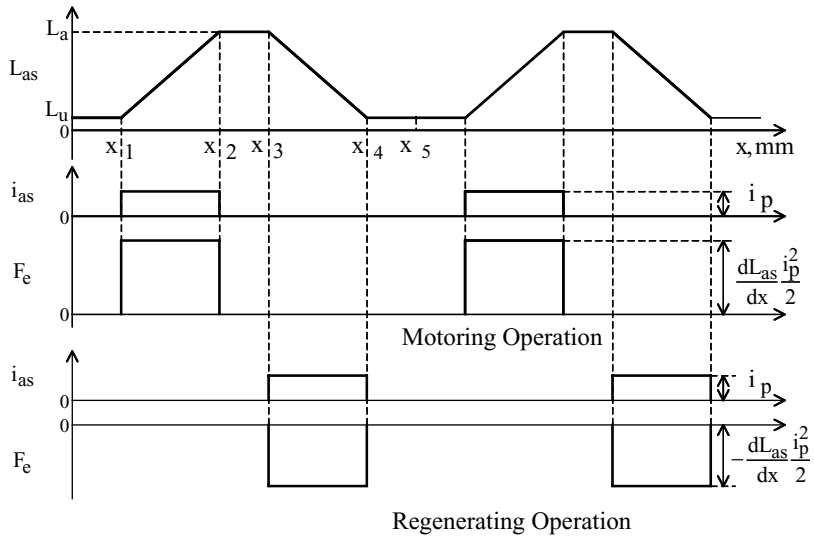


**FIGURE 1.15** Inductance profile and force generation for the linear SRM.

or after the succeeding phase is excited. Reverse motion of the translator can be achieved by reversing the excitation sequence of the stator phases.

Operation of the LSRM is based on the inductance profile of the machine. The inductance of the machine is related to machine dimensions such as the stator and translator pole and slot widths, excitation currents, and rotor position. Assuming that the magnetic circuit is linear and therefore the inductance characteristics are independent of stator current excitation, a relationship between the machine dimensions and inductance, shown in Figure 1.15, is derived.

The inductance of a phase winding is its self-inductance. Five translator positions are necessary to derive the inductance profile:

$$x_1 = \frac{w_{ts} - w_{sp}}{2} \quad (1.27a)$$

$$x_2 = x_1 + w_{sp} = \frac{w_{ts} + w_{sp}}{2} \quad (1.27b)$$

$$x_3 = x_2 + (w_{tp} - w_{sp}) = w_{tp} + \left( \frac{w_{ts} - w_{sp}}{2} \right) \quad (1.27c)$$

$$x_4 = x_3 + w_{sp} = w_{tp} + \left( \frac{w_{ts} + w_{sp}}{2} \right) \quad (1.27d)$$

$$x_5 = x_4 + \frac{w_{ts} - w_{sp}}{2} = w_{tp} + w_{ts} \quad (1.27e)$$

where  $w_{tp}$  is the width of the translator pole,  $w_{ts}$  is the width of the translator slot,  $w_{sp}$  is the width of the stator pole, and  $w_{ss}$  is the width of the stator slot. Between  $x_2$  and  $x_3$ , there is complete overlap of the stator and translator poles, and inductance during this interval corresponds to the aligned value and is a maximum. As there is no change in the inductance in this region, zero force is generated with an excitation current in the winding. But, it is important to have this flat inductance region to give time to commutate the current and prevent the generation of a negative force. The unequal stator and translator pole widths contribute to the flat-top inductance profile. On the other hand, the regions corresponding to  $0 \sim x_1$  and  $x_4 \sim x_5$  have no overlap between the stator and translator poles. These positions have the minimum phase inductance, known as *unaligned inductance*. The rate of change of inductance is zero, hence these regions also do not contribute to force production.

The force production for motoring and regeneration is shown in Figure 1.16. The forward direction of motion of the translator is assumed to be positive when

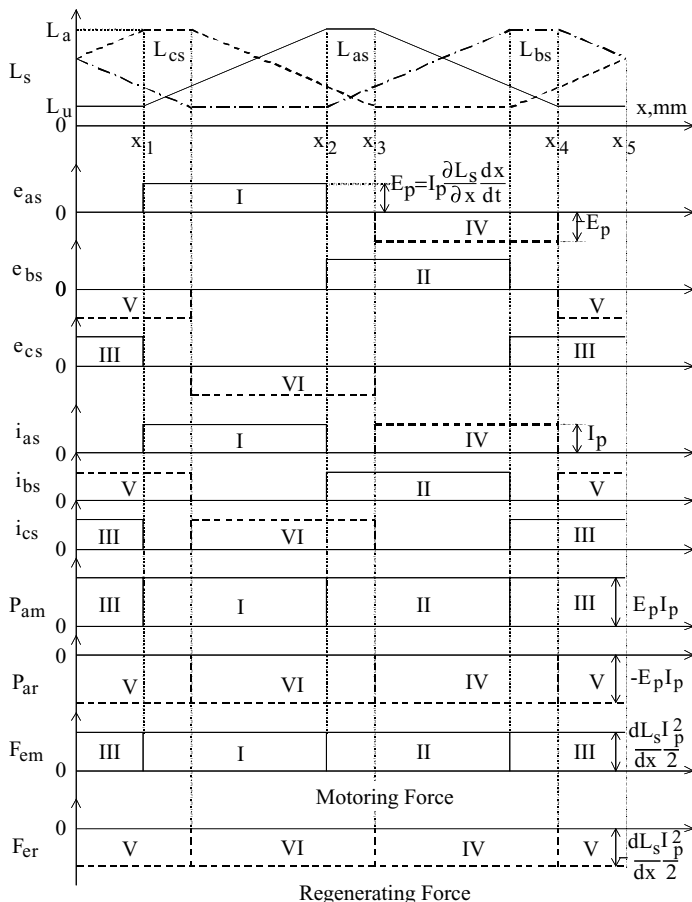


**FIGURE 1.16** Operation of a three-phase linear SRM and its key variables.

the phase excitation sequence is *abc*. For forward direction of motion, regions I to III represent forward motoring operation and regions IV to VI represent forward regenerative operation for the phase sequence *abc*. Similarly, for reverse direction of motion, regions I to III represent reverse regenerative operation and regions IV to VI represent reverse motoring operation for the phase sequence *acb*. The duty cycle of each phase is only 1/3, and the induced emfs are constant between  $x_2$  and  $x_1$ . The air gap power and hence the generated electromagnetic force can be made constant by exciting the stator phases with  $(x_2 - x_1)$  wide pulses of currents.  $P_{am}$  represents the motoring air gap power, and  $P_{ar}$  represents the regenerative air gap power.  $F_{em}$  is the motoring force and  $F_{er}$  is the regenerative force. Note that one half of the air gap power is stored in the form of magnetic field energy in phase windings and the other half of the air gap power is converted to mechanical power output. Ideal inductance profiles and ideal current generation are assumed in the discussion so far, but ideal currents with step rise and fall are not feasible due to the machine inductance; therefore, compensation to obtain the desired current is achieved by advancing the energization of the windings. Note the similarity between the LSRM and permanent magnet (PM) brushless dc machine emf, current, air gap power, and force waveforms. This clearly demonstrates that their controls are identical, hence the permanent magnet (PM) brushless dc machine controller, which is available in a chip form, can be used in the control of SRM for low-cost and high-volume applications.

## REFERENCES

1. Nasar, S.A., D.C.-switched reluctance motor, in *Proceedings of the Institution of Electrical Engineers (London)*, Vol. 116, No. 6, June 1969, pp. 1048.
2. Byrne, J. and J.C. Lacy, Electrodynamic system comprising a variable reluctance machine, U.S. Patent 3956678, May 1976.
3. Lawrenson, P.J., J.M. Stephenson, P.T. Blenkinsop, J. Corda, and N.N. Fulton, Variable-speed switched reluctance motors, *IEEE Proc. Electrical Power Appl. B*, 127(4), 253–265, 1980.
4. Finch, J.W., M.R. Harris, and H.M.B. Metwally, Variable speed drives using multitooth per pole switched reluctance motors, in *Proc. 13th Annual Symposium on Incremental Motion Control Systems and Devices*, May 1984, pp. 293–301.
5. Lindsay, J.F., R. Arumugan, and R. Krishnan, Finite-element analysis characterization of a switched reluctance motor with multitooth per stator pole, *IEEE Proc. Electrical Power Appl. B*, 133(6), 347–353, 1986.
6. Corda, J. and J.M. Stephenson, Analytical estimation of the minimum and maximum inductances of a double-salient motor, in *Proc. of Int. Conf. on Stepping Motors and Systems*, Sept. 1979, Leeds, pp. 50–59.
7. Materu, P. and R. Krishnan, Analytical prediction of SRM inductance profile and steady-state average torque, in *Conf. Rec. of the 1990 IEEE IAS Ann. Mtg.*, Oct. 1990, Seattle, WA, pp. 214–223.
8. Arumugan, R., D.A. Lowther, R. Krishnan, and J.F. Lindsay, Magnetic field analysis of a switched reluctance motor using a two-dimensional finite-element model, *IEEE Trans. on Magnetics*, 21(5), 1883–1885, 1985.
9. Miller, T.J.E., *Switched Reluctance Motors and Their Control*, Magna Physics Publishing/Clarendon Press, Oxford, 1993.

10. Krishnan, R., R. Arumugan, and J.F. Lindsay, Design procedure for switched-reluctance motors, *IEEE Trans. on Industry Appl.*, 24(3), 456–461, 1988.
11. Krishnan, R., M. Abouzeid, and X. Mang, A design procedure for axial field switched reluctance motors, in *Conf. Rec. of the 1990 IEEE IAS Ann. Mtg.*, Vol. 1, Oct. 1990, Seattle, WA, pp. 241–246.
12. Unnewehr, L.E. and W.H. Koch, An axial air-gap reluctance motor for variable speed applications, *IEEE Trans. on Power Apparatus and Systems*, PAS-93, 1974, pp. 367–376.
13. Chan, S. and H.R. Bolton, Development of sub-kW single phase switched reluctance motor drives, in *Proc. Int. Conf. on Electrical Machines*, Vol. 2, Sept. 1992, Manchester, U.K., pp. 527–531.
14. Chan, S. and H.R. Bolton, Performance enhancement of single phase switched reluctance motor by dc link voltage boosting, *IEEE Proc. B*, 140(5), 316–322, 1993.
15. Hendershot, J.R., Jr., Switched reluctance brushless DC motors with low loss magnetic circuits, *Proc. Sixteenth International Intelligent Motion (Motor-Con) Conference*, Intertec Commun., 1989, pp. 482–497.
16. Chatratana, S. and H.R. Bolton, Investigations into small, single phase switched reluctance motors, in *Proc. IEEE Conf. on Small and Special Electrical Machines*, Sept. 1981, pp. 99–102.
17. Compter, J.C., Microprocessor controlled single phase reluctance motor, in *Proc. Drives/Motors/Controls Conf.*, Oct. 1984, pp. 64–68.
18. Compter, J.C., Single Phase Reluctance Motor, U.S. Patent No. 4,616,165, Oct. 1986.
19. Horst, G.E., Shifted Pole Single Phase Variable Reluctance Motor, U.S. Patent No. 5,294,856, March 15, 1994.
20. Stephenson, J.M., Apparatus and Method for Starting a Single-Phase Variable Reluctance Motor, U.S. Patent No. 5,808,389, Sept. 15, 1998.
21. Lim, J.Y., H.S. Kim, J.Y. Oh, D.H. Cheong, and J.C. Kim, A performance of single switched reluctance having both radial and axial air gap, in *IEEE Industrial Electronics Conf. Rec.*, Nov. 1998, Aachen, Germany, pp. 905–910.
22. Adamiak, K., D. Barlow, C.P. Choudhury, P.M. Cusack, G.E. Dawson, A.R. Eastham, B. Grady, E. Ho, Y. Hongping, L. Pattison, and J. Welch, The switched reluctance motor as a low-speed linear drive, in *Int. Conf. on Maglev and Linear Drives*, May 1987, Las Vegas, NV, pp. 39–43.
23. Deshpande, U.S., J.J. Cathey, and E. Richter, A high force density linear switched reluctance machine, in *Conf. Rec. of the 1993 IEEE IAS Ann. Mtg.*, Vol. 1, Oct. 1993, Toronto, Canada, pp. 251–257.
24. Corda, J. and E. Skopljak, Linear switched reluctance actuator, in *Sixth Int. Conf. on Electrical Machines and Drives*, Sept. 1993, Oxford, U.K., pp. 535–539.
25. Matt, D., R. Goyet, J. Lucidarme, and C. Rioux, Longitudinal-field multi-air gap linear reluctance actuator, *Electric Machines Power Syst.*, 13(5), 299–313, 1987.
26. Lucidarme, J., A. Amouri, and M. Poloujadoff, Optimum design of longitudinal field variable reluctance motors—application to a high performance actuator, *IEEE Trans. on Energy Conversion*, 8(3), 357–361, 1993.
27. Boldea, I. and S.A. Nasar, *Linear Electric Actuators and Generators*, Cambridge University Press, Cambridge, U.K., 1997, 163–178.
28. Lee, Byeong-Seok, Han-Kyung Bae, Praveen Vijayraghavan, and R. Krishnan, Design of a linear switched reluctance machine, in *Conf. Rec. of the 1999 IEEE IAS Ann. Mtg.*, Oct. 1999, Phoenix, AZ, pp. 2267–2274.
29. Bae, Han-Kyung, Byeong-Seok Lee, Praveen Vijayraghavan, and R. Krishnan, Linear switched reluctance motor: converter and control, in *Conf. Rec. of the 1999 IEEE IAS Ann. Mtg.*, Oct. 1999, Phoenix, AZ, pp. 547–554.

30. Krishnan, R., B.-S. Lee, and P. Vallance, Integral linear switched reluctance machine based guidance, levitation and propulsion system, in *Proc. Maglev 2000 Conf.*, June 7–10, 2000, Rio de Janeiro, Brazil, pp. 281–286.
31. Corda, J. and M. Wilkinson, Prediction and measurement of magnetic parameters of cylindrical linear switched reluctance actuator, in *Proc. of Int. Conf. on Electrical Machines*, Vol. 3, Sept. 1994, Paris, pp. 479–484.
32. Corda, J. and M. Wilkinson, Modelling of static thrust characteristics of cylindrical linear switched reluctance actuator, in *Seventh Int. Conf. on Electrical Machines and Drives*, Sept. 1995, Durham, U.K., pp. 354–358.
33. Liu, C.T. and Y.N. Chen, On the feasible polygon classifications of linear switched reluctance machines, *1997 IEEE Int. Electric Machines and Drives Conf. Rec.*, May 1997, Milwaukee, WI, pp. TB1/11.1–11.3.
34. Liu, C.T., K.S. Su, and M.H. Lee, Three dimensional field and side-force design analyses of a transverse flux linear switched-reluctance machine, *IEEE Trans. on Magnetics*, 34(4), 2132–2134, 1998.
35. Liu, C.T. and N. Sheu, Optimal pole arrangement design of a linear switched-reluctance machine for magnetic levitation and propulsion system, *IEEE Trans. on Magnetics*, 32(5), 5067–5069, 1996.

---

# 2 Steady-State Performance and Analytic Derivation of SRM Characteristics

## 2.1 INTRODUCTION

The requirement for finding the performance characteristics of the SRM is to generate the relationships between the flux linkages vs. rotor position as a function of the machine phase currents. This section develops a procedure for analytically deriving the machine characteristics given the motor dimensions and excitation conditions along with the number of turns per phase. Notably, the nonlinear characteristics of the lamination material are preserved in this method to get a meaningful characterization of the SRM.

## 2.2 DATA FOR PERFORMANCE COMPUTATION

The area enclosed between the curves  $\lambda$  vs.  $i$  for unaligned and aligned positions of the rotor poles with a set of stator poles gives the maximum work done for one stroke of the motor. The electromagnetic torque can then be calculated if the angular movement is known from the mechanical work. Even though the calculation of torque and work done appears to be simple, the data generation for their calculation is a complex process. The data required for this procedure are the flux linkages vs. stator excitation currents for discrete positions of the rotor.

The aligned position corresponds to the center of the stator and rotor poles coinciding, and the unaligned position with the midpoint of the interpolar rotor gap facing the stator pole. It is possible to calculate the flux linkages for the aligned position analytically due to the fact that the leakage flux is negligible in the aligned position. The same is not true for the unaligned position; because the leakage paths are not known *a priori*, it is not easy to calculate the leakage flux analytically. Finite element analysis techniques are used to estimate the flux linkages.

Figures 2.1 and 2.2 show the flux at the unaligned position in a 6/4-pole<sup>6,7,8</sup> and 12/10-pole SRM,<sup>2</sup> respectively. It is clear from these figures that the flux paths in the unaligned positions are very difficult to predict, thus the complexity of the steady-state performance evaluation. It is usual to use finite element analysis techniques to map the flux in the unaligned position and for positions in between the aligned and unaligned stator and rotor poles. The flux leakage in the aligned position is practically

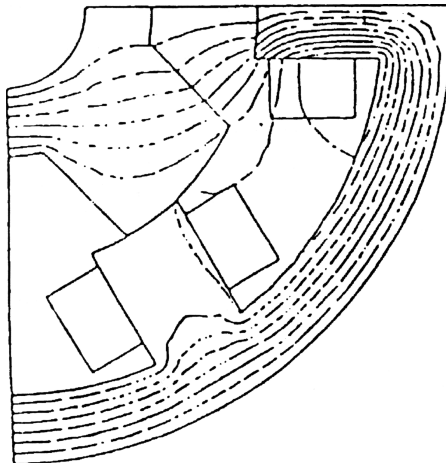


**FIGURE 2.1** Flux plot at fully unaligned position for 6/4 SRM.

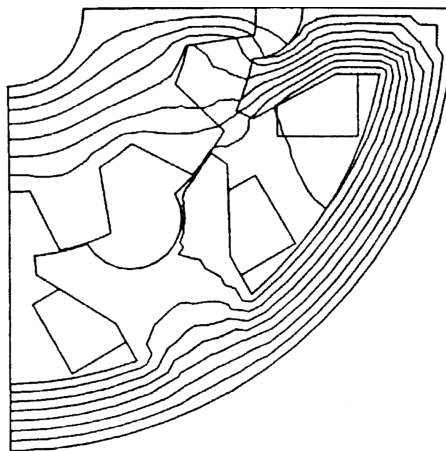


**FIGURE 2.2** Flux plot at fully unaligned position for 12/10 SRM.

negligible (as shown in [Figures 2.3](#) and [2.4](#)) for the 6/4 and 12/10 SRMs, respectively; therefore, the analytical calculation of the stator flux linkages at the aligned position is very accurate. The accuracy usually is within 2% of the finite element solution.

### 2.3 ANALYTIC METHOD FOR THE COMPUTATION OF MOTOR FLUX LINKAGES

The performance of the switched reluctance motor can be computed by finite element analysis techniques, but there are some disadvantages in resorting to them routinely. The relationship of motor output variables to motor dimensions, number of poles, number of turns per phase, excitation current, and current conduction angle

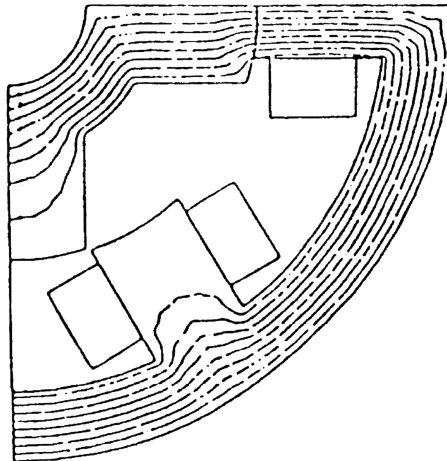


**FIGURE 2.3** Flux plot at fully aligned position for 6/4 SRM.

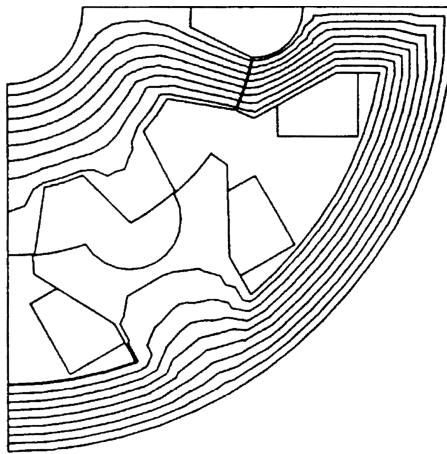


**FIGURE 2.4** Flux plot at fully aligned position for 12/10 SRM.

is not explicit. Hence, a change in one or many of the motor and control variables requires an entire finite element analysis computation which is either in two or three dimensions. Each set of finite element computations takes a considerable amount of time. Needless to say, such results are not valid for up and down scaling of the motor design. The scaling of the motors is very essential in a design environment, as the design of the motor is continually assessed to optimize a performance index. The performance index can be cost, efficiency, weight, volume, torque, output, or a combination of these for the switched reluctance motor and converter combination. In such a case, a design process to obtain a size and to evaluate variables of interest for the machine will be mandatory. The process has to be based on a set of implicit and

explicit analytical expressions involving the motor dimensions and inputs to performance variables.<sup>1,3,4,5,10,11,12,14,15</sup> The final design emerging from this analytic design approach can be analyzed with finite element modeling to improve the accuracy of the performance prediction. The following section gives an analytic approach that uses numerical iteration to obtain inductance vs. current characteristics of the motor from machine variables that are used to predict the torque and power output.

The procedure outlined in this chapter is to find inductance vs. rotor position vs. excitation current; that data is necessary to design the converter and controllers. The inductances are easier to deal with in the context of power electronics networks than flux linkages, but the flux linkages are very crucial to find the air gap torque and hence performance of the machine. Obtaining flux linkages from inductance and the excitation current by taking their product is fairly straightforward. From now on, the evaluation of flux linkages will not be mentioned in this chapter; only inductance evaluation is emphasized.

### 2.3.1 METHOD OF INDUCTANCE CALCULATION

For various positions of the rotor, a fixed number of flux paths is assumed. In order to minimize the number of flux maps for evaluation of inductance, only four flux maps are considered: the extreme positions of unalignment and alignment of rotor and stator poles and, in between these two extremes, two regions defined for overlapping and nonoverlapping rotor and stator poles. A generalization for various numbers of stator and rotor poles can be made in the derivation of relevant equations required in the inductance calculation (not considered in detail here).

Flux maps are usually derived based on the experience of the designer and can be fine tuned with the finite element analysis tool to improve the accuracy of the flux paths. A two-dimensional field analysis using finite element software is sufficient for most applications. Critical applications with a high power-density requirement for SRMs can be met with a three-dimensional field analysis. To a degree, the three-dimensional effects can also be included in the analytic procedure and will be indicated at appropriate instances in the derivations.

An SRM with an 8/6-pole combination is considered for deriving the analytic procedure for inductance evaluation. Assume a certain flux density in the stator pole and flux densities in other parts of the machine such as rotor pole, rotor back iron, stator yoke, and air gap are derived as the areas of cross sections of these parts for assumed flux paths are obtained from the machine geometry and the assumed stator pole flux density. From the flux densities in various parts of the machine and the flux density vs. magnetic field intensity ( $B$ - $H$ ) characteristics of the lamination material, corresponding magnetic field intensities are obtained. Given the magnetic field intensities and the length of the flux path in each part, their product gives the magnetomotive force (mmf). The mmfs for various parts are likewise obtained, and for the magnetic equivalent circuit and stator excitation Ampere's circuital law is applied. If an error between the applied stator mmf and that given equivalently by various parts of the machine reveals a discrepancy, then that error is used to adjust the assumed flux density in the stator pole and the entire iteration continues until the error is reduced to a set tolerance value.

### 2.3.1.1 Flux Density Evaluation

For example, consider the complete unaligned position and flux path 1 shown in [Figure 2.5](#) to illustrate the procedure for evaluating flux densities in various parts of the machine. The flux paths are equiflux lines (i.e., equal amount of flux lines are represented by each flux path). The flux distribution is symmetric with respect to the center line of the excited stator poles. The flux path 1 is assumed to have a flux of  $\phi_1$  in the stator pole. It crosses the air gap, splits evenly in the rotor back iron, and then recrosses the air gap to the southern pole and splits evenly to flow in the stator back iron (yoke). The reluctances of the stator pole, air gap, rotor back iron, and stator back iron for the flux path are denoted as  $R_{sp1}$ ,  $R_{g1}$ ,  $R_{ry1}$ , and  $R_{sy1}$ , respectively. The magnetic equivalent circuit for flux path 1 in terms of the reluctances and stator mmf,  $F_1$ , is shown in [Figure 2.6](#). The equivalent circuit is then simplified and given in [Figure 2.7](#). From [Figure 2.6](#), the flux in each segment of the machine is known and accordingly the flux densities for these segments are evaluated. Let the area of cross section of flux path 1 in the stator pole, air gap, rotor back iron, and stator back iron be  $A_{sp1}$ ,  $A_{g1}$ ,  $A_{ry1}$ , and  $A_{sy1}$ , respectively. If the stator flux density is  $B_{sp}$ , then the flux in path 1 in the stator is found if the area of cross section for the flux path is known. The flux path encloses one quarter of the stator pole arc; therefore, the area of cross section is

$$A_{sp1} = \frac{1}{4}(\text{stator pole area}) = \frac{1}{4}\left(\frac{D}{2}\beta_s \cdot L\right) = \frac{1}{8}(DL)\beta_s \quad (2.1)$$

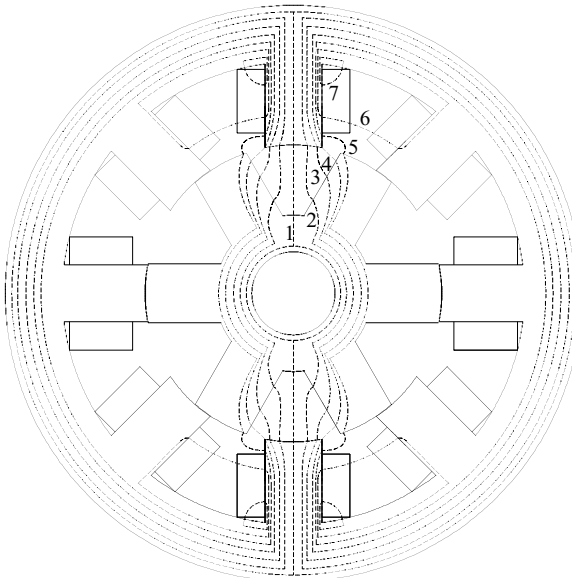


**FIGURE 2.5** Identification of seven flux paths for analytical calculation of unaligned inductance.

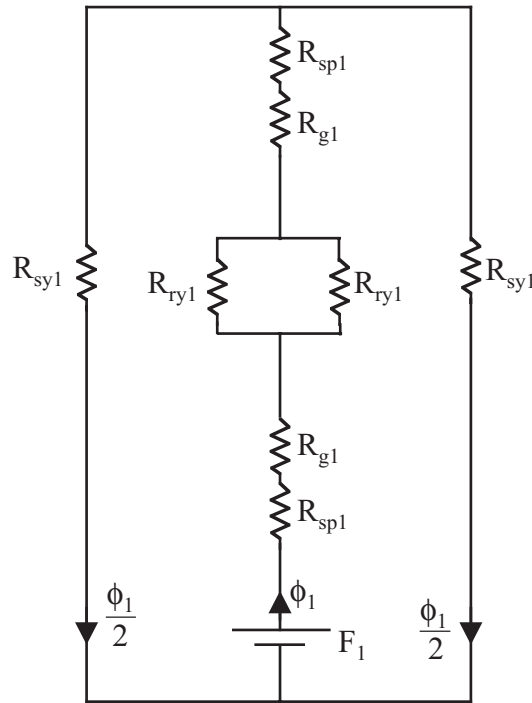


**FIGURE 2.6** Magnetic equivalent circuit for flux path 1 at fully unaligned position.

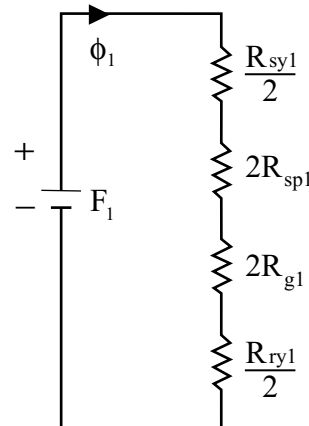


**FIGURE 2.7** Simplified magnetic equivalent circuit for flux path 1 at fully unaligned position.

where  $D$  is the inner stator lamination diameter,  $\beta_s$  is the stator pole arc, and  $L$  is the stator iron stack length.

Then the stator pole flux in path 1 is

$$\phi_1 = B_{sp} \cdot A_{sp1} \quad (2.2)$$

Let the mean area of the cross section of the air gap, rotor back iron, and stator back iron be,  $A_{g1}$ ,  $A_{ry1}$ , and  $A_{sy1}$ , respectively. Then the flux densities in these segments are

$$B_{g1} = \frac{\phi_1}{A_{g1}} = B_{sp} \cdot \left( \frac{A_{sp1}}{A_{g1}} \right) \quad (2.3)$$

$$B_{ry1} = \frac{\phi_1}{2A_{ry1}} = \frac{B_{sp}}{2} \cdot \left( \frac{A_{sp1}}{A_{ry1}} \right) \quad (2.4)$$

$$B_{sy1} = \frac{\phi_1}{2A_{sy1}} = \frac{B_{sp}}{2} \cdot \left( \frac{A_{sp1}}{A_{sy1}} \right) \quad (2.5)$$

$$B_{sp1} = B_{sp} \quad (2.6)$$

### 2.3.1.2 mmf Evaluation

The mmf for each segment of the flux path is evaluated by finding the magnetic field intensities from the flux densities of the segments using the B-H characteristics of the lamination material and average length of the flux path in the segments. Let the magnetic field intensities of the stator pole, air gap, rotor back iron, and stator back iron segments be  $H_{sp1}$ ,  $H_{g1}$ ,  $H_{ry1}$ , and  $H_{sy1}$ , respectively. The average lengths of the flux path 1 in the stator pole, air gap, rotor back iron, and stator back iron are  $\ell_{sp1}$ ,  $\ell_{g1}$ ,  $\ell_{ry1}$ , and  $\ell_{sy1}$ , respectively. Then, the Ampere circuital equation for this path is

$$F_1 = T_{ph}i = \Sigma H\ell = 2[H_{sp1}\ell_{sp1} + H_g\ell_{g1}] + \frac{1}{2}[H_{ry1}\ell_{ry1} + H_{sy1}\ell_{sy1}] \quad (2.7)$$

If the computed right-hand side is not equal to the applied mmf,  $F_1$ , then the error between them is a mark of incorrect flux densities in various segments of the machine. The error between the applied and computed mmf can be reduced to a level that is acceptable by an iterative adjustment of the stator pole flux density,  $B_{sp}$ , and then recalculating all the other variables. Let the error mmf be defined as:

$$\Delta F_1 = F_1 - \Sigma H\ell = T_{ph}i - \Sigma H\ell \quad (2.8)$$

If the error mmf is negative, then the stator pole flux density is reduced for the next iteration; in the case of a positive error, the stator pole flux density is increased for the next iteration. Nulling the mmf error is not attempted in practice due to the large number of iterations; therefore, the mmf error is reduced to a lower tolerance limit.

### 2.3.1.3 Calculation of Reluctance

From the final flux densities in the various segments of flux path 1 and the magnetic field intensities, the reluctances are computed. The reluctance of the stator pole segment is

$$R_{sp1} = \frac{\ell_{sp1}}{A_{sp1}\mu_o\mu_r} = \frac{\ell_{sp1}}{A_{sp1} \cdot \left(\frac{B_{sp1}}{H_{sp1}}\right)} = \frac{H_{sp1}\ell_{sp1}}{B_{sp1}A_{sp1}} \quad (2.9)$$

Similarly, the reluctances of the air gap, rotor back iron, and stator back iron are

$$R_{g1} = \frac{\ell_{g1}}{\mu_o A_{g1}} \quad (2.10)$$

$$R_{ry1} = \frac{H_{ry1}\ell_{ry1}}{B_{ry1}A_{ry1}} \quad (2.11)$$

$$R_{sy1} = \frac{H_{sy1}\ell_{sy1}}{B_{sy1}A_{sy1}} \quad (2.12)$$

In all these computations for all the flux paths, the mean length and their area of cross section are required, which we derive in the following.

### 2.3.1.4 Assumptions

The equations derived in this chapter apply to all levels of excitation under the assumptions stated below:

1. The air gap flux lines consist of concentric arcs and straight-line segments.
2. The flux lines enter and leave the iron normally.
3. The flux lines in the stator and rotor poles are parallel to the pole axes.
4. The flux lines in the stator back iron and rotor body are concentric.
5. The windings are rectangular blocks and the stator interpolar space is only partially filled with windings.
6. The shaft is purely nonmagnetic.

These assumptions make analytic derivations easier and approximate real conditions in the machine.

## 2.3.2 UNALIGNED INDUCTANCE

Aligned inductance for a given excitation current is derived in this section using the procedure outlined in the previous section. The flux paths at a completely unaligned position are shown in [Figure 2.5](#). Each of the flux paths is considered separately and inductance contributed by it is derived. The computational procedure to evaluate the path inductance is developed, along with a flow chart for mechanization. Various angles defined are only relevant to the flux path under consideration, so care needs to be exercised when defining them for various flux paths for programming.

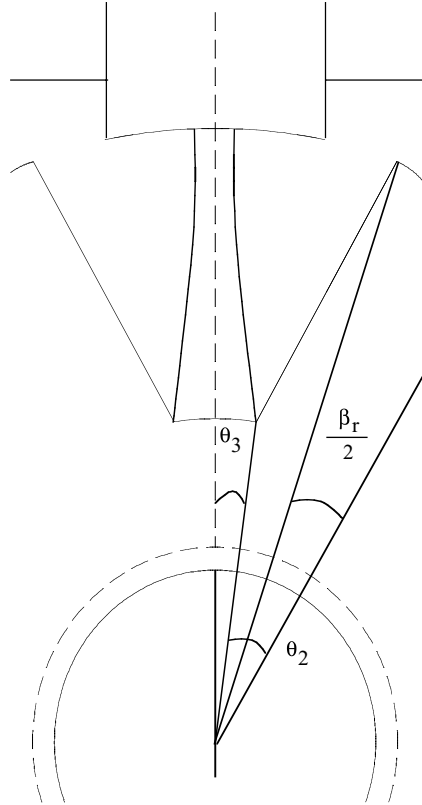


**FIGURE 2.8** Flux path 1 in fully unaligned position.

### 2.3.2.1 Flux Path 1

The calculation of the mean flux path in the air gap between the stator and rotor poles is considered first. That segment is expanded and shown in Figure 2.8. The area of cross section at the stator pole for the path has been derived in Eq. (2.1). The length of the flux path in the air gap is

$$\ell_{g1} = \frac{D}{2} - \ell_g - h_r \quad (2.13)$$

where  $\ell_g$  is the air gap during alignment, and  $h_r$  is the rotor pole height.

The area of cross section of flux path 1 is varying throughout the air gap so its mean is considered for calculation. The cross section of the flux path at the rotor is obtained as follows:

$$\theta_2 = \frac{\frac{\beta_r}{2} \left( \frac{D}{2} - \ell_g \right)}{\left( \frac{D}{2} - \ell_g - h_r \right)} \quad (2.14)$$

It is assumed that the rotor pole width remains constant over its length, which usually is the case. Then,  $\theta_3$  is derived as:

$$\theta_3 = \frac{1}{2} \left( \frac{2\pi}{P_r} \right) - \theta_2 = \frac{\theta_{rp}}{2} - \theta_2 \quad (2.15)$$

where  $\theta_{rp}$  is the rotor pole pitch, and  $P_r$  is the number of rotor poles. The area of cross section on the rotor periphery is

$$A_{r1} = 2\theta_3 \left( \frac{D}{2} - \ell_g - h_r \right) L \quad (2.16)$$

and the average area of cross section of flux path 1 is

$$A_{g1} = \frac{A_{sp1} + A_{r1}}{2} = \frac{\beta_s D L}{16} + \theta_3 \left( \frac{D}{2} - \ell_g - h_r \right) L \quad (2.17)$$

#### 2.3.2.1.1 Rotor Back Iron

The length of the flux path on each side of the rotor back iron is

$$\begin{aligned} \ell_{ry1} &= \frac{1}{2} [\text{average of } \{\text{periphery of shaft} + \text{periphery of inner rotor pole base}\}] \\ &= \frac{1}{2} \left[ \frac{\pi D_{sh}}{2} + \pi \left( \frac{D}{2} - \ell_g - h_r \right) \right] = \pi \left( \frac{D_{sh}}{4} + \frac{D}{4} - \frac{\ell_g}{2} - \frac{h_r}{2} \right) \end{aligned} \quad (2.18)$$

where  $D_{sh}$  is the rotor shaft diameter. The area of cross section of the rotor back iron for this flux path is

$$A_{ry1} = \left( \frac{D}{2} - \ell_g - h_r - \frac{D_{sh}}{2} \right) L \quad (2.19)$$

where the quantity inside the parentheses is the thickness of the rotor back iron.

#### 2.3.2.1.2 Stator Pole

The length of the flux path in the stator is

$$\ell_{sp1} = h_s \quad (2.20)$$

where  $h_s$  is the stator pole height. Its cross section has been already derived.

#### 2.3.2.1.3 Stator Back Iron

The length of the flux path in the stator back iron is

$$\ell_{sy1} = \frac{\pi(D_o - b_{sy})}{2} = \frac{\pi(D + 2h_s + 2b_{sy} - b_{sy})}{2} = \frac{\pi(D + 2h_s + b_{sy})}{2} \quad (2.21)$$

where  $b_{sy}$  is the stator back iron thickness. Its area of cross section is

$$A_{sy1} = b_{sy} L \quad (2.22)$$

This completes the relevant variables and constants for the computation of reluctances for flux path 1. The inductance contributed by the flux path 1 at unaligned inductance, then, is

$$L_{u1} = \frac{T_{ph} \cdot \phi_1}{i} = \frac{T_{ph} \cdot \frac{F_1}{\left(2R_{sp1} + 2R_{g1} + \frac{R_{sy1}}{2} + \frac{R_{ry1}}{2}\right)}}{i} = \frac{T_{ph}^2}{\left(2R_{sp1} + 2R_{g1} + \frac{R_{sy1}}{2} + \frac{R_{ry1}}{2}\right)} \quad (2.23)$$

The flux  $\phi_1$  is computed from the magnetic equivalent circuit in the final iteration to satisfy Ampere's circuital law, as discussed earlier in this section. A flow chart of the procedure involved in the computation of inductance is shown in [Figure 2.9](#). For relevant equations in each block of the flow chart, refer to the derivations in this section.

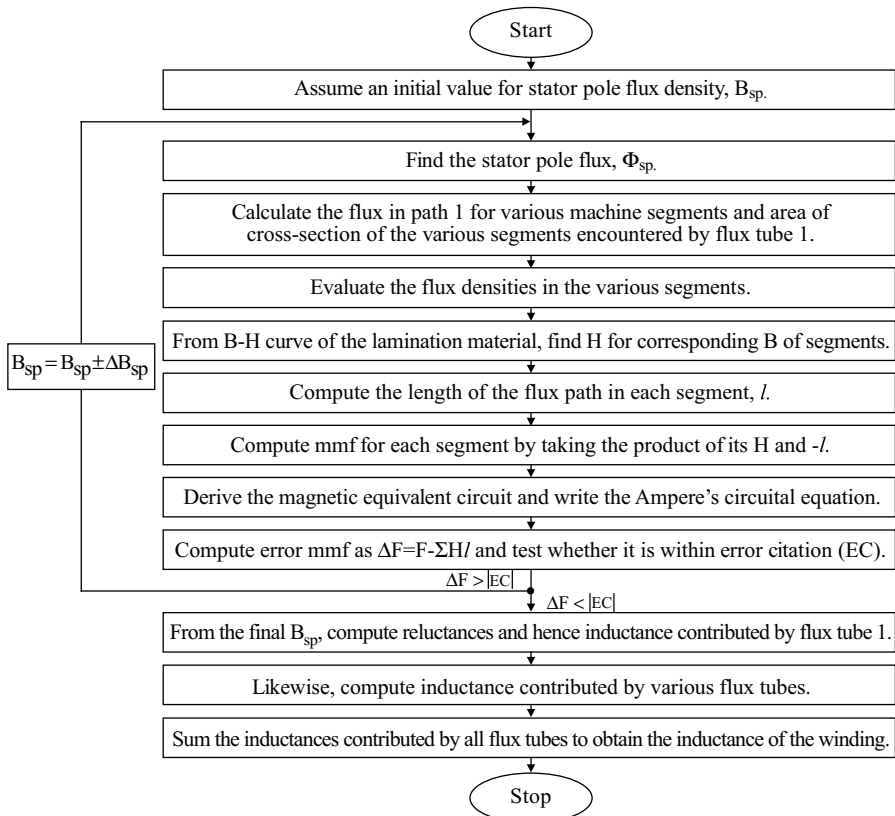


**FIGURE 2.9** Flow chart for the evaluation of machine inductance.

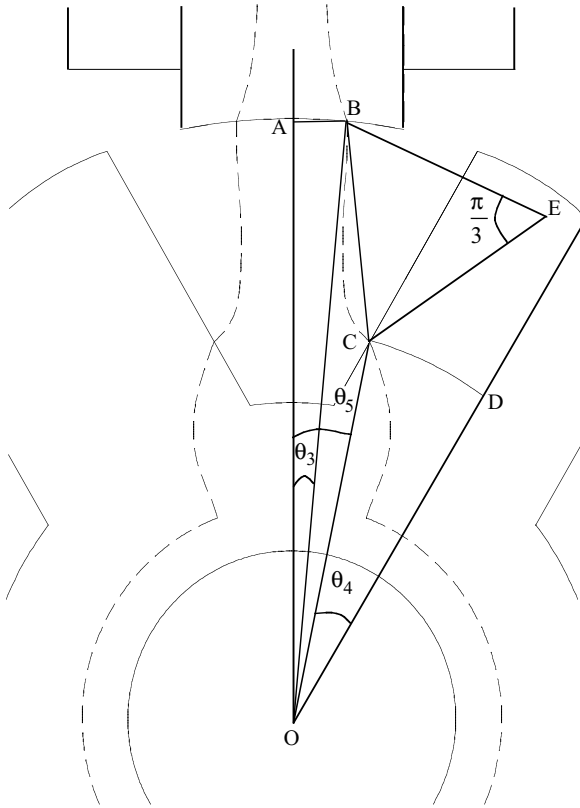


**FIGURE 2.10** Flux path 2 in fully unaligned position.

### 2.3.2.2 Flux Path 2

An enlarged upper part of flux path 2 is shown in Figure 2.10, and the magnetic equivalent circuit is shown in Figure 2.11, where  $F_2$  is the mmf applied on the stator pole. Only one side is considered for the equivalent circuit. For flux path 2,  $R_{sp2}$  is the stator pole reluctance,  $R_{g2}$  is the air gap reluctance,  $R_{rp2}$  is the rotor back iron reluctance, and  $R_{sy2}$  is the reluctance of the stator back iron. For these segments, the area of cross section and length of the flux path are derived in the following. It is assumed that the flux enters at  $(h_r/4)$  from the inner radius at the rotor pole.

#### *2.3.2.2.1 Air Gap*

Consider the length of flux path 2 to be the arc  $BC$ . It is computed by finding the chord length  $BC$  and using this as a radius by constructing an equilateral triangle,  $BCE$ . Assume that the center of the shaft is origin  $(0, 0)$ . The steps are as follows:

$$OB = \frac{D}{2} \quad (2.24)$$

$$\theta_3 = \frac{\beta_s}{4} \quad (2.25)$$

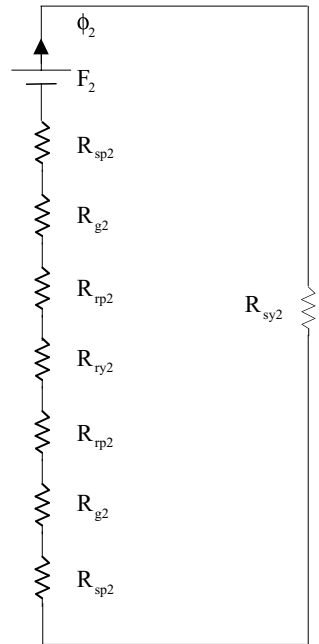


**FIGURE 2.11** Magnetic equivalent circuit for flux path 2 for one side of the machine.

The coordinates of  $B$  with  $O$  as origin are

$$(x_1, y_1) = \left[ \frac{D}{2} \sin(\theta_3), \frac{D}{2} \cos(\theta_3) \right] \quad (2.26)$$

The coordinates of  $C(x_2, y_2)$  are found as:

$$OD = \left( \frac{D}{2} - \ell_g - \frac{3}{4}h_r \right) \quad (2.27)$$

$$CD = \left( \frac{D}{2} - \ell_g \right) \frac{\beta_r}{2} \quad (2.28)$$

$$\theta_4 = \frac{CD}{OD} \quad (2.29)$$

$$\underline{|COA|} = \theta_5 = \frac{\theta_{rp}}{2} - \theta_4 \quad (2.30)$$

$$(x_2, y_2) = [OD \sin(\theta_5), OD \cos(\theta_5)] \quad (2.31)$$

The chord  $BC$  is, then:

$$BC = \sqrt{(x_2 - x_1)^2 + (y_2 - y_1)^2} \quad (2.32)$$

Then, the length of the flux in path 2 may be considered as arc  $BC$ . The arc is evaluated by considering an equilateral triangle  $BCE$  with the length of each side  $BC$ , and the arc is part of the circle centered at  $E$ . It is, then:

$$\ell_{g2} = \text{Arc } BC = [BC] \left( \frac{\pi}{3} \right) \quad (2.33)$$

The area of cross section of the flux path is calculated as the average of the stator and rotor area of cross sections and is given as:

$$A_{g2} = \frac{A_{sp2} + A_{rp2}}{2} \quad (2.34)$$

where

$$A_{sp2} = \frac{1}{2} \left( \frac{\beta_s D}{4} \cdot L \right) \quad (2.35)$$

$$A_{rp2} = \frac{h_r}{4} L \quad (2.36)$$

### 2.3.2.2.2 Stator Pole

The length of the flux path is

$$\ell_{sp2} = h_s \quad (2.37)$$

The area of cross section is

$$A_{sp2} = \frac{1}{2} \left( \frac{D}{2} \frac{\beta_s}{4} L \right) \quad (2.38)$$

### 2.3.2.2.3 Rotor Pole

The length of the flux path is

$$\ell_{rp2} = \frac{h_r}{4} \quad (2.39)$$

The area of cross section is  $A_{rp2}$ , given in Eq. (2.36).

#### 2.3.2.2.4 Rotor Back Iron

The length and area of the cross section of the flux path are

$$\ell_{ry2} = \ell_{ry1} \quad (2.40)$$

$$A_{ry2} = A_{ry1} \quad (2.41)$$

as given in the flux path 1 section.

#### 2.3.2.2.5 Stator Back Iron

The length and area of cross section of the flux path are

$$\ell_{sy2} = \ell_{sy1} \quad (2.42)$$

$$A_{sy2} = A_{sy1} \quad (2.43)$$

The Ampere's circuital equation for flux path 2 is written from the magnetic equivalent circuit as:

$$F_2 = [2(R_{sp2} + R_{g2} + R_{rp2}) + (R_{ry2} + R_{sy2})]\phi_2 \quad (2.44)$$

which can be written in terms of flux densities, corresponding magnetic field intensities, and length of the flux paths as:

$$R_{g2} = \frac{\ell_{g2}}{\mu_0 A_{g2}} \quad (2.45)$$

$$R_{sp2} = \frac{H_{sp2}\ell_{sp2}}{B_{sp2}A_{sp2}} \quad (2.46)$$

$$R_{rp2} = \frac{H_{rp2}\ell_{rp2}}{B_{rp2}A_{rp2}} \quad (2.47)$$

$$R_{ry2} = \frac{H_{ry2}\ell_{ry2}}{B_{ry2}A_{ry2}} \quad (2.48)$$

$$R_{sy2} = \frac{H_{sy2}\ell_{sy2}}{B_{sy2}A_{sy2}} \quad (2.49)$$

The error mmf is

$$\Delta F = T_{ph}i - \{2(R_{sp2} + R_{g2} + R_{rp2}) + R_{ry2} + R_{sy2}\}\phi_2 \quad (2.50)$$

which is checked against the error criterion to adjust the stator flux density and to go through the iteration to reduce the mmf error to an acceptable level. The inductance

contributed by flux path 2 is

$$L_{u2} = \frac{2T_{ph}\phi_2}{i} \quad (2.51)$$

where the multiplication factor 2 is inserted as our calculation of  $\phi_2$  is only for one side of the machine.

From this point on, enlarged figures for flux paths at one set of rotor and stator poles, derivation of the magnetic equivalent circuits, and evaluation of the length and area of the cross section are derived in a manner very similar to that in the previous section.

### 2.3.2.3 Flux Path 3

The flux path is enlarged and shown in [Figure 2.12](#). The magnetic equivalent circuit is similar to that for flux path 2 and hence not shown here. It is assumed that the flux enters the rotor pole at  $(h_r/4)$  from top and leaves the stator pole at  $\frac{5}{64}\beta_s$  from the tips. The width of the flux path is over an arc of  $\frac{3}{32}\beta_s$  in the stator.

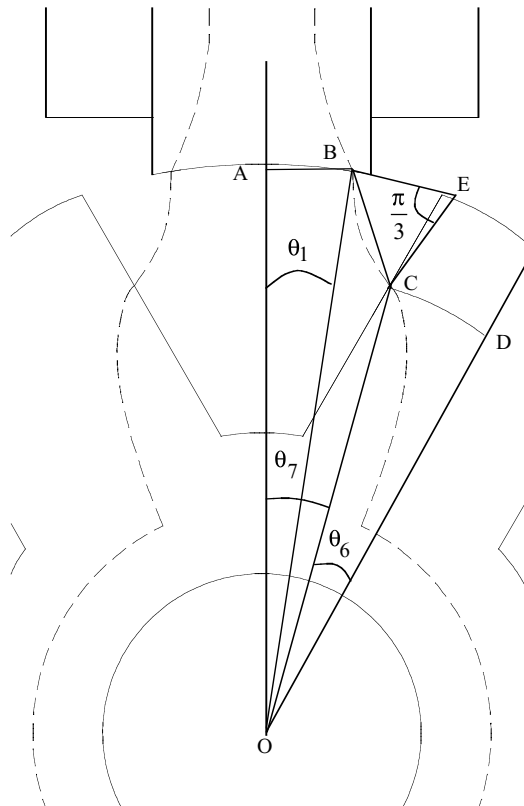


**FIGURE 2.12** Flux path 3 at fully unaligned position.

### 2.3.2.3.1 Air Gap

From [Figure 2.12](#),

$$OD = \left( \frac{D}{2} - \ell_g - \frac{h_r}{4} \right) \quad (2.52)$$

$$CD = \left( \frac{D}{2} - \ell_g \right) \frac{\beta_r}{2} \quad (2.53)$$

$$OB = \frac{D}{2} \quad (2.54)$$

$$\theta_1 = \left( \frac{\beta_s}{2} - \frac{5}{64} \beta_s \right) = \frac{27}{64} \beta_s \quad (2.55)$$

$$\theta_6 = \frac{CD}{OD} \quad (2.56)$$

$$\theta_7 = \theta_{rp} - \theta_6 \quad (2.57)$$

$$\text{coordinates of } B = (x_1, y_1) = [(OB) \sin \theta_1, (OB) \cos \theta_1] \quad (2.58)$$

$$\text{coordinates of } C = (x_2, y_2) = [(OD) \sin \theta_7, (OD) \cos \theta_7] \quad (2.59)$$

$$\text{chord}(BC) = \sqrt{(x_2 - x_1)^2 + (y_2 - y_1)^2} \quad (2.60)$$

$$\ell_{g3} = \text{arc } BC = \text{chord}(BC) \left( \frac{\pi}{3} \right) \quad (2.61)$$

$$A_{g3} = \frac{1}{2} (A_{rp3} + A_{sp3}) \quad (2.62)$$

### 2.3.2.3.2 Stator Pole

$$\ell_{sp3} \simeq h_s \quad (2.63)$$

$$A_{sp3} = \frac{3}{32} \beta_s \frac{D}{2} L \quad (2.64)$$

### 2.3.2.3.3 Rotor Pole

$$\ell_{rp3} \simeq \frac{3}{4} h_r \quad (2.65)$$

$$A_{rp3} = \frac{h_r}{4} L \quad (2.66)$$

### 2.3.2.3.4 Rotor Back Iron

$$\ell_{ry3} \simeq \ell_{ry1} \quad (2.67)$$

$$A_{ry3} \simeq A_{ry1} \quad (2.68)$$

### 2.3.2.3.5 Stator Back Iron

$$\ell_{sy3} = \ell_{sy1} \quad (2.69)$$

$$A_{sy3} = A_{sy1} \quad (2.70)$$

$$L_{u3} = \frac{T_{ph} \cdot [2\phi_3]}{i} = 2 \frac{T_{ph}\phi_3}{i} \quad (2.71)$$

where  $\phi_3$  is the flux in path 3 for one side of the machine.

### 2.3.2.4 Flux Path 4

The enlarged flux path nearer one stator and rotor pole is shown in [Figure 2.13](#). The flux leaves the stator at the tips and enters at  $(7/8)h_r$  from the rotor pole base. The width of the flux path at the stator pole is assumed to be

$$\left( \frac{\beta_s}{32} \frac{D}{2} + \frac{1}{4} \left( \frac{1}{4} h_s \right) \right)$$

From the figure, the following are derived:

$$\theta_1 = \frac{\beta_s}{2} \quad (2.72)$$

$$\text{coordinates of pole tip } B = (x_3, y_3) = \left[ \frac{D}{2} \sin\left(\frac{\beta_s}{2}\right), \frac{D}{2} \cos\left(\frac{\beta_s}{2}\right) \right] \quad (2.73)$$

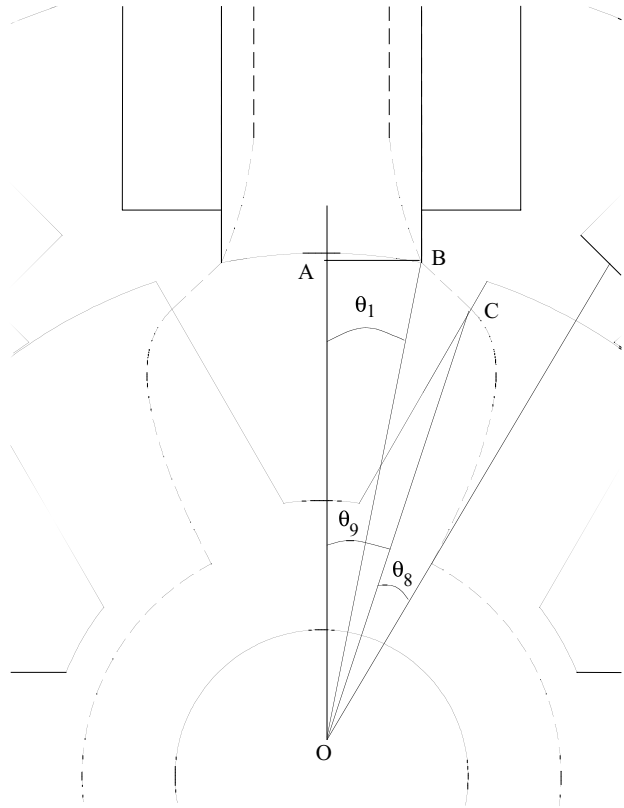


**FIGURE 2.13** Flux path 4 in fully unaligned position.

$$OC = \left( \frac{D}{2} - \ell_g - \frac{h_r}{8} \right) \quad (2.74)$$

$$\theta_8 = \frac{\frac{\beta_r}{2} \left( \frac{D}{2} - \ell_g \right)}{\left( \frac{D}{2} - \ell_g - \frac{h_r}{8} \right)} \quad (2.75)$$

$$\theta_9 = \frac{\theta_{rp}}{2} - \theta_8 \quad (2.76)$$

$$\text{coordinates of } C = (x_4, y_4) = [(OC)\sin\theta_9, (OC)\cos\theta_9] \quad (2.77)$$

$$BC = \sqrt{(x_3 - x_4)^2 + (y_3 - y_4)^2} \quad (2.78)$$

#### 2.3.2.4.1 Air Gap

$$\ell_{g4} = BC \quad (2.79)$$

$$A_{g4} = \frac{1}{2}[A_{sp4} + A_{rp4}] \quad (2.80)$$

for which the stator and rotor areas of the cross section for the flux path are given below.

#### 2.3.2.4.2 Stator Pole

$$\ell_{sp4} \simeq h_s \quad (2.81)$$

$$A_{sp4} \simeq \frac{\beta_s}{32} \frac{D}{2} L + \frac{1}{4} \frac{h_s}{4} L \quad (2.82)$$

#### 2.3.2.4.3 Rotor Pole

$$\ell_{rp4} = \frac{7h_r}{8} \quad (2.83)$$

$$A_{rp4} = \frac{h_r}{4} L \quad (2.84)$$

#### 2.3.2.4.4 Rotor Back Iron

$$\ell_{ry4} \simeq \ell_{ry1} \quad (2.85)$$

$$A_{ry4} \simeq A_{ry1} \quad (2.86)$$

#### 2.3.2.4.5 Stator Back Iron

$$\ell_{sy4} = \ell_{sy1} \quad (2.87)$$

$$A_{sy4} = A_{sy1} \quad (2.88)$$

The magnetic equivalent circuit is similar to that of flux path 2. The flux in the path is  $\phi_4$ , hence the inductance contributed by the two flux paths with path 4 is

$$L_{u4} = \frac{2T_{ph}\phi_4}{i} \quad (2.89)$$

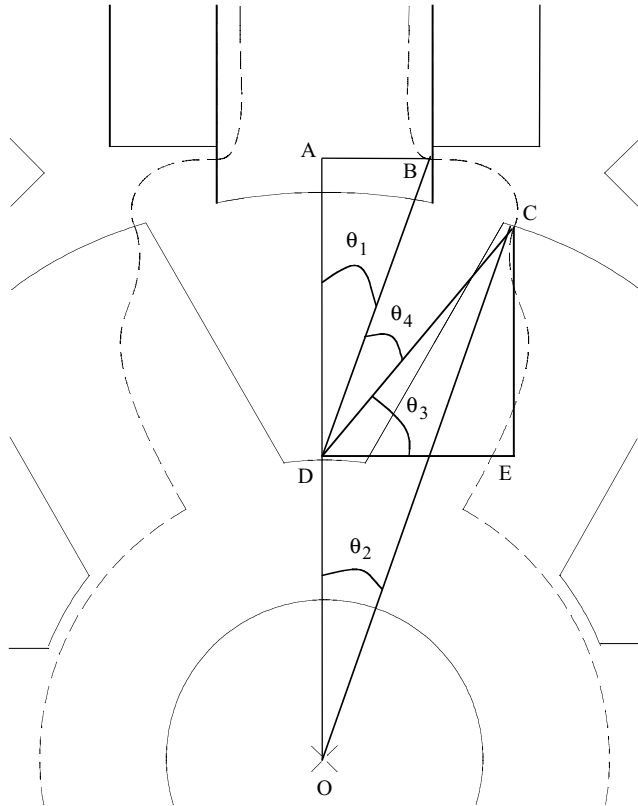


**FIGURE 2.14** Flux path 5 in fully unaligned position.

### 2.3.2.5 Flux Path 5

The flux path has a width of  $\frac{3}{4}(\frac{h_s}{4})$  on exit at the stator pole and is confined to one eighth of the rotor pole arc on entry. The enlarged flux path is shown in Figure 2.14. The magnetic equivalent circuit is similar to that for flux path 2. From Figure 2.14, the following are derived:

$$x_1 = AB = \frac{D}{2} \sin\left(\frac{\beta_s}{2}\right) \quad (2.90)$$

$$y_1 = OA = \frac{D}{2} \cos\left(\frac{\beta_s}{2}\right) + \frac{5h_s}{32} \quad (2.91)$$

Note that the coordinate is derived at the mean of the flux path that is  $(3/16)h_s$  wide but situated above  $(1/16)h_s$ .

$$\text{coordinates of } B = (x_5, y_5) = \left[ \frac{D}{2} \sin\left(\frac{\beta_s}{2}\right), \left\{ \frac{D}{2} \cos\left(\frac{\beta_s}{2}\right) + \frac{5h_s}{32} \right\} \right] \quad (2.92)$$

$$\theta_1 = \tan^{-1}\left(\frac{x_5}{AD}\right) = \tan^{-1}\left\{ \frac{x_5}{y_5 - \left(\frac{D}{2} - \ell_g - h_r\right)} \right\} \quad (2.93)$$

$$OC = \left( \frac{D}{2} - \ell_g \right) \quad (2.94)$$

$$\theta_2 = \left( \frac{\theta_{rp}}{2} - \frac{7}{16}\beta_r \right) \quad (2.95)$$

$$\text{coordinates of } C = (x_6, y_6) = [(OC)\sin\theta_2, (OC)\cos\theta_2] \quad (2.96)$$

$$\text{coordinates of } D = (x_7, y_7) = \left[ 0, \left( \frac{D}{2} - \ell_g - h_r \right) \right] \quad (2.97)$$

$$DC = \sqrt{(x_7 - x_6)^2 + (y_7 - y_6)^2} \quad (2.98)$$

$$DB = \sqrt{(x_7 - x_5)^2 + (y_7 - y_5)^2} \quad (2.99)$$

$$\theta_3 = \tan^{-1}\left(\frac{CE}{DE}\right) = \tan^{-1}\left(\frac{y_6 - y_7}{x_6}\right) \quad (2.100)$$

$$\theta_4 = \frac{\pi}{2} - \theta_3 - \theta_1 \quad (2.101)$$

### 2.3.2.5.1 Air Gap

The length of flux path 5 in the air gap can be approximated as the arc of a circle with an average radius of  $DB$  and  $DC$  and subtended by  $\theta_4$  as:

$$\ell_{g5} = \frac{1}{2}(DB + DC)\theta_4 \quad (2.102)$$

The area of cross section is the mean of the stator and rotor pole cross sections encountered by the flux path and is given as:

$$A_{g5} = \frac{1}{2}(A_{sp5} + A_{rp5}) \quad (2.103)$$

#### 2.3.2.5.2 Stator Pole

$$\ell_{sp5} \simeq h_s \quad (2.104)$$

$$A_{sp5} = \frac{3}{4} \frac{h_s}{4} L \quad (2.105)$$

#### 2.3.2.5.3 Rotor Pole

$$\ell_{rp5} = h_r \quad (2.106)$$

$$A_{rp5} = \left( \frac{D}{2} - \ell_g \right) \frac{\beta_r}{8} L \quad (2.107)$$

#### 2.3.2.5.4 Rotor Back Iron

$$\ell_{ry5} = \ell_{ry1} \quad (2.108)$$

$$A_{ry5} = A_{ry1} \quad (2.109)$$

#### 2.3.2.5.5 Stator Back Iron

$$\ell_{sy5} = \ell_{sy1} \quad (2.110)$$

$$A_{sy5} = A_{sy1} \quad (2.111)$$

The inductance contributed by the flux in path 5 is

$$L_{u5} = 2 \frac{T_{ph} \phi_5}{i} \quad (2.112)$$

where  $\phi_5$  is the flux in path 5.

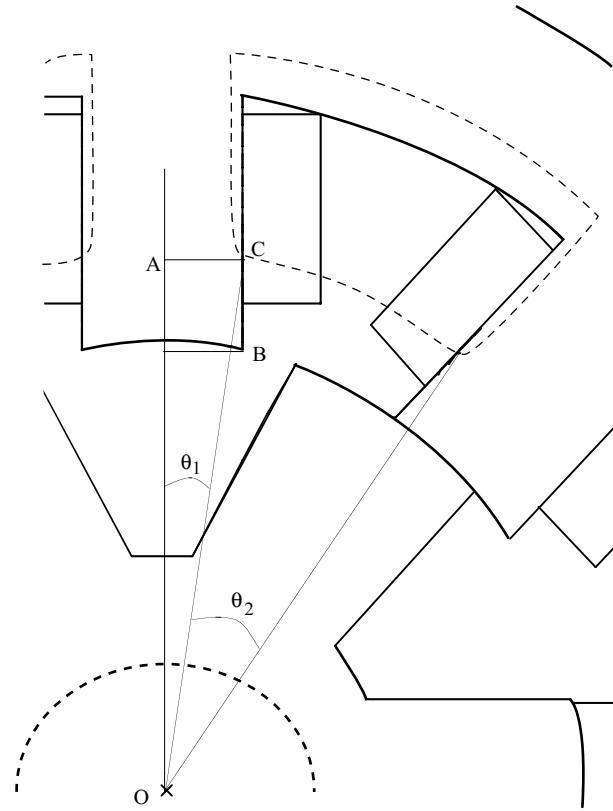


**FIGURE 2.15** Flux path 6 in fully unaligned position.

### 2.3.2.6 Flux Path 6

Flux path 6 is shown in detail in [Figure 2.15](#). The flux path can be assumed to be an arc centered at the center of the shaft. The flux path is  $(h_s/4)$  wide and is at a height of  $\left(\frac{h_s}{4} + \frac{1}{2} \frac{h_s}{4}\right)$ . The coordinates of  $OC$  are

$$y_1 = OA = \frac{D}{2} \cos\left(\frac{\beta_s}{2}\right) + \frac{3h_s}{8} \quad (2.113)$$

$$x_1 = AC = \frac{D}{2} \sin\left(\frac{\beta_s}{2}\right) \quad (2.114)$$

and  $\theta_1$  is

$$\theta_1 = \sin^{-1}\left(\frac{x_1}{\sqrt{(x_1^2 + y_1^2)}}\right) \quad (2.115)$$

$\theta_2$  is obtained as:

$$\theta_2 = \left( \frac{2\pi}{P_s} - 2\theta_1 \right) \quad (2.116)$$

where  $P_s$  is the number of stator poles.

#### 2.3.2.6.1 Air Gap

The length of the air gap for flux path 6 is

$$\ell_{g6} = (OC)\theta_2 = \left[ \sqrt{(x_1^2 + y_1^2)} \right] \theta_2 \quad (2.117)$$

The area of the cross section for the flux path is

$$A_{g6} = \frac{1}{2} [A_{sp6} + A_{rp6}] \quad (2.118)$$

#### 2.3.2.6.2 Stator Pole

The length of the flux path in stator pole is approximated as:

$$\ell_{sp6} \doteq \frac{5}{8} h_s \quad (2.119)$$

$$A_{sp6} = \frac{h_s}{4} L \quad (2.120)$$

#### 2.3.2.6.3 Stator Back Iron

The length and area of the cross section are

$$\ell_{sy6} \doteq \left( \frac{D}{2} + h_s + \frac{b_{sy}}{4} \right) \left[ \frac{2\pi}{P_s} - 2\theta_1 \right] \quad (2.121)$$

$$A_{sy6} \doteq A_{sy1} \quad (2.122)$$

#### 2.3.2.6.4 Magnetic Equivalent Circuit

The magnetic equivalent circuit for flux path 6 contains reluctances due to the stator poles, air gap, and stator back iron as shown in [Figure 2.16](#). It is noted that there are four flux paths 6 in this machine. The flux in them encloses only three eighths of the stator turns. The flux in path 6 is

$$\phi_6 = \frac{F_6}{2R_{sp6} + R_{g6} + R_{sy6}} = \frac{\frac{3}{8}(T_{ph}i)}{2R_{sp6} + R_{g6} + R_{sy6}} \quad (2.123)$$

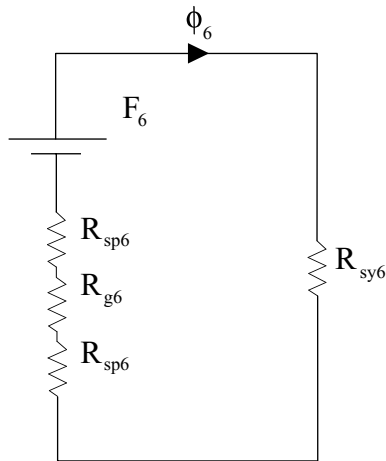


**FIGURE 2.16** Magnetic equivalent circuit for flux path 6.

The inductance contributed by the flux path 6 is

$$L_{u6} = \frac{4 \left\{ \frac{3}{8} (T_{ph} \phi_6) \right\}}{i} \quad (2.124)$$

as there are four paths of path 6.

### 2.3.2.7 Flux Path 7

An enlarged flux path 7 is shown in [Figure 2.17](#), and its magnetic equivalent circuit for one path is shown in [Figure 2.18](#). For the calculation of flux path length, the flux path is centered at  $B$  with a radius of  $(h_s/4)$  and an angle of  $(\pi/2)$ . Various lengths of the pole, air gap, and back iron segments are

$$\ell_{sy7} \simeq \frac{h_s}{4} + \frac{b_{sy}}{4} \quad (2.125)$$

$$\ell_{g7} \simeq \frac{h_s}{4} \frac{\pi}{2} \quad (2.126)$$

$$\ell_{sy7} \simeq \frac{h_s}{4} \quad (2.127)$$

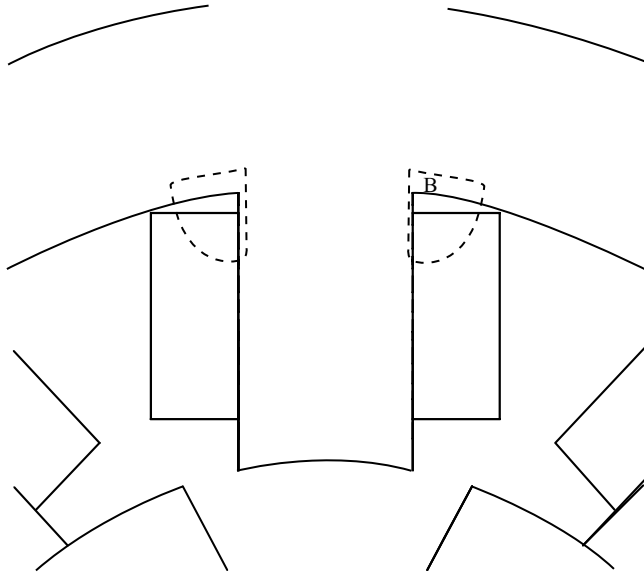


**FIGURE 2.17** Flux path 7 in fully unaligned position.

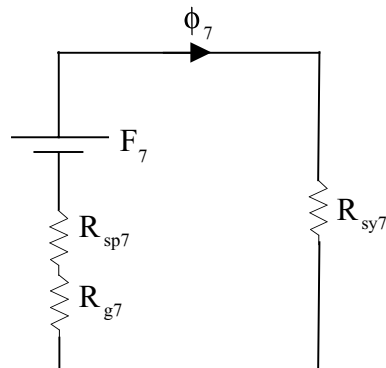


**FIGURE 2.18** Magnetic equivalent circuit for flux path 7.

The areas of cross section for the segments are

$$A_{sp7} = \frac{h_s}{2}L \quad (2.128)$$

$$A_{g7} = A_{sp7} \quad (2.129)$$

$$A_{sy7} = A_{sy1} \quad (2.130)$$

The flux in path 7 is  $\phi_7$ ; the mmf causing this is  $F_7$  and is equal to one fourth of the per-phase mmf,  $T_{ph}i$ . The inductance contributed by the four flux paths 7 is

$$L_{u7} = 4 \frac{T_{ph}}{2} \frac{\phi_7}{i} = \frac{2T_{ph}\phi_7}{i} \quad (2.131)$$

#### 2.3.2.7.1 Unaligned Inductance

The unaligned inductance is obtained by the sum of all the inductances contributed by the flux paths and it is given by:

$$L_u = \sum_{j=1}^7 L_{uj} \quad (2.132)$$

### 2.3.3 ALIGNED INDUCTANCE

The derivation of inductance is much simpler for the stator and rotor pole aligned positions than for unaligned positions. The flux lines, about 90 to 98%, pass the air gap between the stator and rotor. There is a small flux due to leakage between adjacent poles. The fringing is not very significant and can be accounted for, if necessary. For example, consider the flux plot of the 8/6 machine considered for illustration in the derivations and shown in [Figure 2.19](#). The flux in the machine consists of flux path 1 and flux path 7, identified for the unaligned position. Flux path 1 consists of the majority of the flux and is mutual flux connecting the stator and rotor.

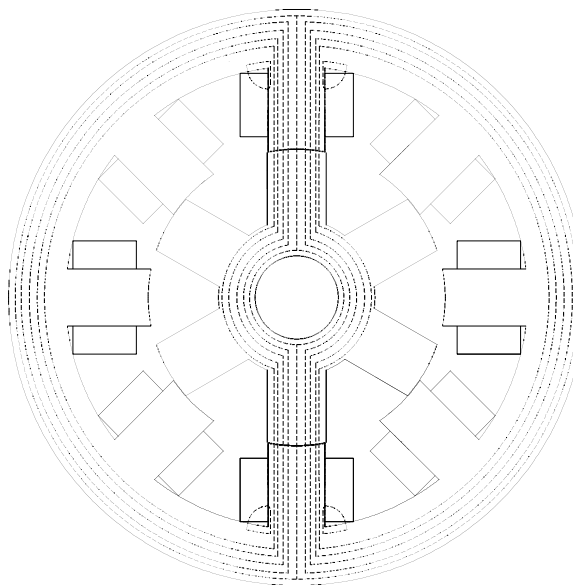


**FIGURE 2.19** Flux paths at fully aligned position.

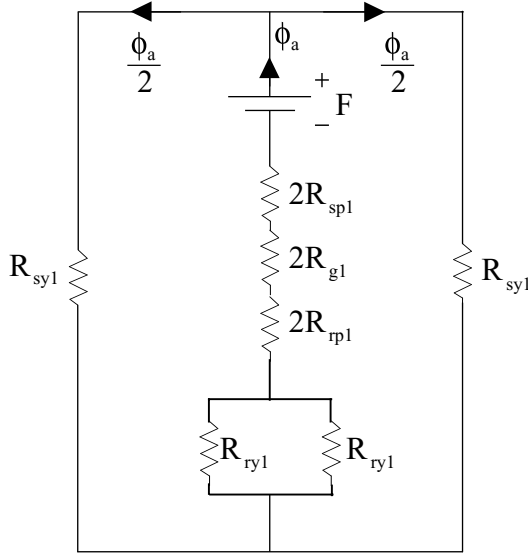


**FIGURE 2.20** Magnetic equivalent circuit for aligned position.

Flux path 7 has leakage flux only when connecting the excited poles with adjacent poles and carries only a small flux. The derivations for these two flux paths are given separately.

### 2.3.3.1 Flux Path 1

For the sake of simplicity, the magnetic equivalent circuit of the SRM at the aligned position can be deduced and shown in [Figure 2.20](#), for mutual flux path 1. The derivations for the length and area of cross section of the mutual flux path (i.e., flux path 1) are given in [Table 2.1](#).

Applying Ampere's circuital law, mmf calculated for each path are summed and given as:

$$F_c = 2[H_{sp1}\ell_{sp1} + H_{g1}\ell_{g1} + H_{rp1}\ell_{rp1}] + H_{ry1}\ell_{ry1} + H_{sy1}\ell_{sy1} \quad (2.133)$$

The magnetic field intensities are extracted from the B-H characteristics using the flux densities calculated in parts of the machine. From the calculated and applied mmf, the error mmf is found as:

$$\Delta F = F - F_c = T_{ph}i - F_c \quad (2.134)$$

It is reduced by iteration as described earlier. The flux in flux path 1 is found as:

$$\phi_a = \frac{T_{ph}i}{2[R_{sp1} + R_{g1} + 2R_{p1}] + \frac{1}{2}R_{y1} + \frac{1}{2}R_{sy1}} \quad (2.135)$$

---

**TABLE 2.1**  
**Length and Area of Cross Section of Flux Path 1 in the Aligned Position**

Segment	Path Length	Area of Cross Section of Flux Path
Air gap	$\ell_{g1} = \ell_g$	$A_{g1} = \frac{\beta_s \frac{D}{2} L + \beta_r (\frac{D}{2} - \ell_g) L}{2}$
Stator pole	$\ell_{sp1} = h_s$	$A_{sp} = \beta_s \frac{D}{2} L$
Rotor pole	$\ell_{rp1} = h_r$	$A_{rp1} = \beta_r \left( \frac{D}{2} - \ell_g \right) L$
Rotor back iron	$\ell_{ry1} = \frac{\pi}{2} \left[ \frac{D}{4} - \ell_g - h_r + \frac{D_{sh}}{2} \right]$	$A_{ry1} = \left( \frac{D}{2} - \ell_g - h_r \right) L$
Stator back iron	$\ell_{sy1} = \frac{\pi}{2} [D + h_s + b_{sy}]$	$A_{sy1} = b_{sy} L$

---

**TABLE 2.2**  
**Length and Area of Cross Section of Flux Path 7 in the Aligned Position**

Segment	Path Length	Area of Cross Section
Air gap	$\ell_{g7} = \frac{3h_s}{4} \frac{\pi}{2}$	$A_{g7} = \frac{3h_s}{4} L$
Stator pole	$\ell_{sp7} = \frac{1}{2} \frac{3h_s}{4} + \frac{b_{sy}}{2}$	$A_{sp7} = \frac{1}{2} \left[ \frac{3h_s}{4} L \right]$
Stator back iron	$\ell_{sy7} = \ell_{sp7}$	$A_{sy7} = b_{sy} L$

---

And this flux contributes an inductance,

$$L_{a1} = \frac{T_{ph} \phi_a}{i} \quad (2.136)$$

### 2.3.3.2 Flux Path 7

For leakage flux path 7, the length and area of the cross sections of various parts in the flux path are derived similarly and given in [Table 2.2](#). The magnetic equivalent circuit for this flux path is the same as that for the fully unaligned position given earlier. The circuital equation is

$$F_c = [H_{sp7} \ell_{sp7} + H_{g7} \ell_{g7} + H_{sy7} \ell_{sy7}] \quad (2.137)$$

and the mmf error for this calculated value is derived as:

$$\Delta F = \frac{3}{4}T_{ph}i - F_c \quad (2.138)$$

as only three quarters of the stator mmf are involved with this flux path.

The flux in this path is derived as:

$$\phi_{7a} = \frac{\frac{3}{4}T_{ph}i}{R_{sp7} + R_{g7} + R_{sy7}} \quad (2.139)$$

and the inductance due to four flux paths in path 7 is

$$L_{a7} = 4 \left[ \frac{\frac{3}{4}T_{ph}i}{i} \right] = \frac{3T_{ph}\phi_{7a}}{i_a} \quad (2.140)$$

Total aligned inductance is then obtained as:

$$L_a = L_{a1} + L_{a7} \quad (2.141)$$

### 2.3.4 RESULTS AND COMPARISON

The validity of similar analytical procedures for predicting aligned and unaligned inductances is evaluated by comparing finite element analysis results and measurements obtained from a prototype 6/4-pole SRM for which the details are given below:

---

Number of stator poles	6
Number of rotor poles	4
Stator diameter (outer)	19 cm
Rotor diameter (bore)	10.206 cm
Core length	6.037 cm
Air gap	0.025 cm
Back iron thickness	1.0515 cm
Stator pole arc	0.418 rad
Rotor pole arc	0.628 rad
Turns per phase	536
Wire size	AWG #19
Core material	M19 steel

---

The comparison is made for three currents, and the base value for the current is the prototype's rated current of 10A. This makes the range of observations from 0.1 to 2 p.u. sufficient for a reasonable comparison (see [Table 2.3](#)). The analytical results are closer to the measurements than the results of the finite element method.

**TABLE 2.3**  
**Comparison of Inductance by Various Methods**

Phase Current ( $I_p$ , A)	Unaligned Inductance ( $L_{uA}$ , mH)			Aligned Inductance ( $L_{aA}$ , mH)			Average Electromagnetic Torque (N · m)		
	Analytical	FEM <sup>a</sup>	Measured	Analytical	FEM <sup>a</sup>	Measured	Analytical	FEM <sup>a</sup>	Measured
1	23.2	25.8	35.5	923	843	879	0.88	0.80	0.90
10	28.3	25.8	40.7	130	133	155	18.77	18.50	20.30
20	29.5	25.8	35.6	82.4	75.5	89	38.60	37.80	41.60

<sup>a</sup> FEM = finite element method.

The close correlation, however, between the analytical and experimental results validates the magnetic circuit approach and derivations.

A second machine with 8/6 poles is considered for verifying the algorithm developed for predicting aligned and unaligned inductances, for which the details are given below:

Number of stator poles	8
Number of rotor poles	6
Power output	5 hp
Stator pole arc	18 degrees
Rotor pole arc	22 degrees
Air gap length	0.5 mm
Outer stator diameter	190 mm
Bore diameter	100.6 mm
Stack length	200 mm
Shaft diameter	28 mm
Speed	1500 rpm
Stator back iron thickness	12 mm
Height of stator pole	32.7 mm
Height of rotor pole	19.8 mm
Turns per phase	154
Conductor area of cross section	1.588 mm <sup>2</sup>
Rated current	13 A
Lamination material	M43

Comparison between finite element analysis and analytical results for the 8/6-SRM at the rated current is given in the following table:

	Finite Element Analysis (mH)	Analytical (mH)
Aligned inductance	65.41	66.79
Unaligned inductance	11.35	11.38

The close correlation at the rated (nominal) current for this machine validates the method.

### 2.3.5 PERFORMANCE EVALUATION

Having determined the aligned and unaligned inductances as a function of excitation current, an approximate output capability of the machine can be found. It requires some approximations, such as:

1. The phase inductance variation is linear from the initial overlap to full overlap positions of the stator and rotor poles. The beginning of the overlap of the stator and rotor poles is given by:

$$\theta_i = \frac{\pi}{P_r} - \left( \frac{\beta_s + \beta_r}{2} \right) = \frac{\theta_{rp} - (\beta_s + \beta_r)}{2} \quad (2.142)$$

The full overlap position is given by:

$$\theta_o = \frac{\theta_{rp}}{2} \quad (2.143)$$

where the initial and full overlap are measured from the fully unaligned position.

2. The phase inductance at the initial overlap position is equal to the phase inductance at the unaligned position.

Then, for a given excitation, the aligned and unaligned flux linkages vs. excitation current are obtained by the product of the inductance with the excitation current. From the area enclosed between the aligned and unaligned flux linkages vs. excitation current characteristics, the work done and torque can be evaluated.

This is very approximate, as most of the time in a variable-speed SRM drive current injection up to the full alignment position at a constant excitation level is rare, as issues such as advance commutation of current arise to avoid operation in the regeneration mode and torque ripple minimization require current programming as a function of rotor position (discussed in [Chapter 5](#)).

Variable current vs. rotor position and variable on times with variable phase displacement of the current with respect to fully unaligned and aligned positions are required to deliver desired performance. The performance computation requires the complete set of flux linkages or inductance vs. rotor position vs. excitation current. Such a set of characteristics can be analytically derived by using the procedure developed for fully unaligned and aligned inductance computations. A few intermediate positions between completely unaligned and aligned can be chosen and the characteristics computed. Then the inductance between two computed positions can be extrapolated to obtain the inductances for intermediate positions. The accuracy in the case may be compromised when the inductance at only a few intermediate positions are known. An alternative method is to derive the analytic relationships of various flux paths as a function of rotor position, in which case extrapolation of inductances is avoided and computation of inductances is carried out for any desired rotor position and excitation current. The latter method is chosen here and derivations are made and presented in the next section.

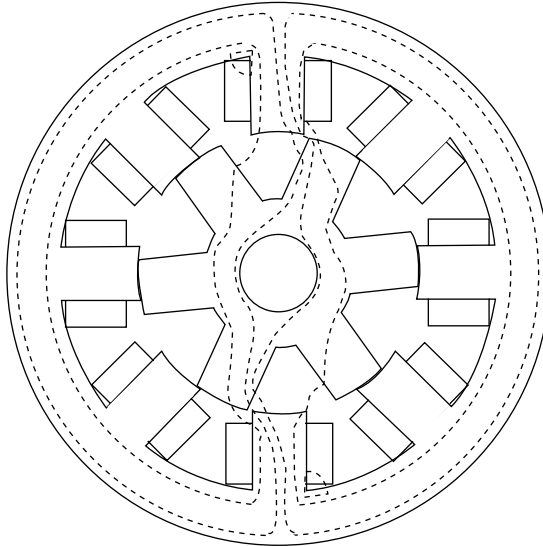


**FIGURE 2.21** Flux distribution in region 1.

### 2.3.6 INDUCTANCES AT INTERMEDIATE POSITIONS

Within the intermediate position between completely unaligned and aligned stator and rotor poles, there are two distinct regions in which the flux patterns change in the machine: from the fully unaligned position to initial overlap of the stator and rotor poles (region 1) and from the initial overlap to complete overlap of the stator and rotor poles (region 2). Sample flux maps for each of these regions are shown in Figures 2.21 and 2.22, respectively.

When the poles start barely overlapping (i.e., region 1), the flux is diverted entirely to the closer rotor pole and the leakage flux path starts to increase at the base of the stator pole on one side. In overlapping region 2, the flux density increases in the stator poles and the leakage flux path increases resulting in the leakage flux connecting the adjacent stator poles on either side. This leakage flux path variation is difficult to predict with the magnetic equivalent circuit approach; therefore, it will be included by one simple path at the base of the excited stator poles.

#### 2.3.6.1 Region 1

The region 1 is defined by:

$$0 \leq \theta \leq \left( \frac{\theta_{rp} - (\beta_r + \beta_s)}{2} \right) \quad (2.144)$$

Only the flux paths, including leakage, are considered for illustration (see Figure 2.23), for region 1. Paths 1 to 5 are for mutual flux and path 6 is for leakage flux at the base of the excited stator poles. The flux paths in the stator back iron and rotor body

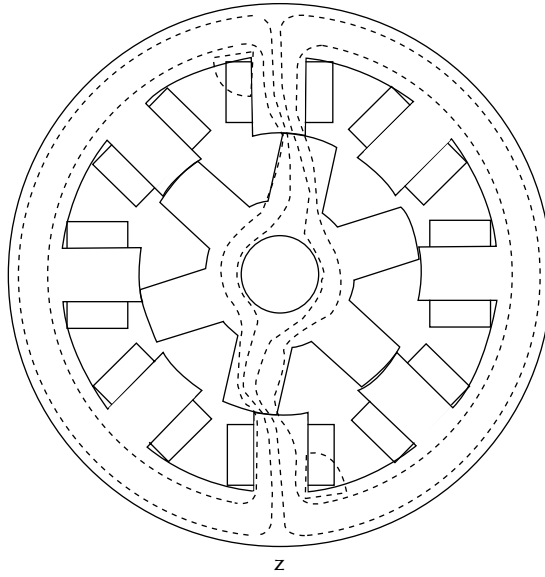


**FIGURE 2.22** Flux distribution in region 2.

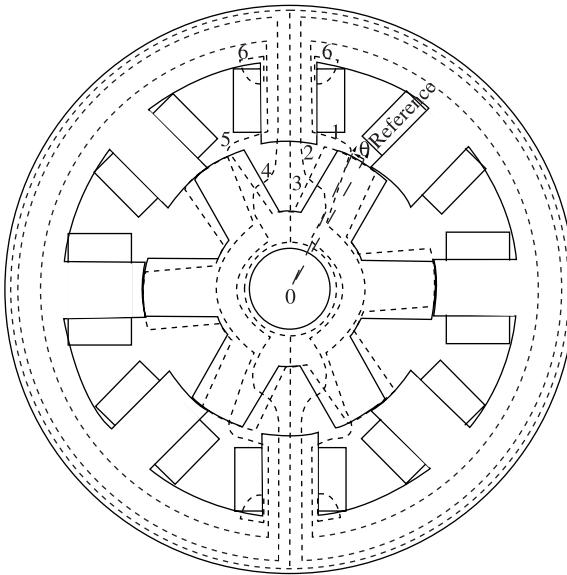


**FIGURE 2.23** Flux distribution in region 1.

are very similar to those of the aligned and unaligned position flux maps, so they are not shown in the figure. Derivations for path 6 have been made in the aligned inductance section. It is assumed here that flux path 6 is independent of rotor position; therefore, only derivations for flux paths 1 to 5 as a function of rotor position are developed in the following section.

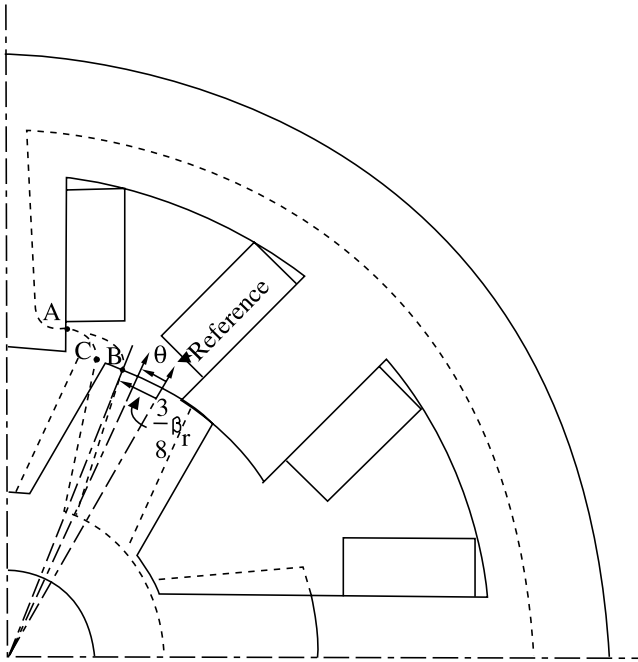


**FIGURE 2.24** Flux path 1 in region 1.

#### 2.3.6.1.1 Flux Path 1

The flux path in the air gap is enlarged and shown in [Figure 2.24](#). The mean flux line leaves the stator pole at one eighth of the stator pole height from the air gap, denoted by point A, and enters the rotor pole at  $(1/8)\beta_r$  from its leading edge. Even though only one flux line is shown, the width of this flux path is one quarter of the stator pole height and, therefore, is centered around  $(1/8)h_s$ . The length of the flux path is given by the arc AB at the fully unaligned position. As the rotor is moved by  $\theta$ , its length is given by arc AC. The key to obtaining the inductance contributed by this path is to formulate the length of flux path 1 in the air gap as a function of rotor position and machine dimensions. Note also that there is no symmetry of flux path 1 as seen from the upper stator pole and its diametric opposite pole at the lower side. This needs to be considered for calculation of the length of flux path 1 in the air between the stator and rotor poles at both the upper and lower poles. The corresponding values will be indicated by subscripts  $u$  and  $\ell$ . It is derived as follows with other relevant parameters to compute the reluctance.

The linear distance between A and C is found by finding their coordinates with the origin,  $O$ , at the center of the shaft. Then, the arc AC is found by making an equilateral triangle with length AC. From that arc AC is evaluated. The steps are

$$\text{coordinates of } O = (0, 0) \quad (2.145)$$

$$\text{coordinates of } A = (x_1, y_1) \quad (2.146)$$

where

$$x_1 = \frac{D}{2} \sin\left(\frac{\beta_s}{2}\right) \quad (2.147)$$

$$y_1 = \frac{D}{2} \cos\left(\frac{\beta_s}{2}\right) + \frac{h_s}{8} \quad (2.148)$$

$$\text{coordinates of } C = (x_2, y_2) \quad (2.149)$$

where

$$x_2(\theta) = \left(\frac{D}{2} - \ell_g\right) \sin\left(\frac{\theta_{rp}}{2} - \frac{1}{8}\beta_r - \theta\right) \quad (2.150)$$

$$y_2(\theta) = \left(\frac{D}{2} - \ell_g\right) \cos\left(\frac{\theta_{rp}}{2} - \frac{1}{8}\beta_r - \theta\right) \quad (2.151)$$

Note that  $x_2$  and  $y_2$  have been expressed as a function of rotor position,  $\theta$ . From the coordinates of  $A$  and  $C$ , the distance between  $A$  and  $C$  is calculated as:

$$AC = \sqrt{(x_2 - x_1)^2 + (y_2 - y_1)^2} \quad (2.152)$$

Then, the arc  $AC$  may be thought of as the air gap at the upper pole and approximated in terms of the chord  $AC$  as:

$$\ell_{g1u} = \text{arc } AC = AC \cdot \left(\frac{\pi}{3}\right) \quad (2.153)$$

Similarly, the length of the mean flux line in path 1 at the lower pole is evaluated by:

$$x_3 = \left(\frac{D}{2} - \ell_g\right) \sin\left(\frac{\theta_{rp}}{2} - \frac{1}{8}\beta_r + \theta\right) = x_2(-\theta) \quad (2.154)$$

$$y_3 = \left(\frac{D}{2} - \ell_g\right) \cos\left(\frac{\theta_{rp}}{2} - \frac{1}{8}\beta_r + \theta\right) = y_2(-\theta) \quad (2.155)$$

$$\ell_{g1l} = \frac{\pi}{3} \cdot \sqrt{(x_3 - x_1)^2 + (y_3 - y_1)^2} \quad (2.156)$$

Therefore, the total length of flux path 1 in air at the lower side is

$$\ell_{g1} = \ell_{g1u} + \ell_{g1\ell} \quad (2.157)$$

The area of the flux path in the air gap is

$$A_{g1} = \left[ \frac{h_s}{4} + \frac{1}{4} \beta_r \left( \frac{D}{2} - \ell_g \right) \right] \frac{L}{2} \quad (2.158)$$

Similarly, the length and area of the core section of the flux path in the stator poles, rotor poles, and stator and rotor back iron are derived and given below:

1. **Stator pole:** For both stator poles,

$$\ell_{sp1} = 2 \frac{7}{8} h_s \quad (2.159)$$

$$A_{sp1} = \frac{h_s L}{4} \quad (2.160)$$

2. **Rotor pole:** For both rotor poles,

$$\ell_{rp1} = 2 h_r \quad (2.161)$$

$$A_{rp1} = \frac{\beta_r}{4} \left( \frac{D}{2} - \ell_g \right) L \quad (2.162)$$

3. **Stator back iron:**

$$\ell_{sy1} = \pi \left( \frac{D}{2} + h_s + \frac{b_{sy}}{2} \right) \quad (2.163)$$

$$A_{sy1} = b_{sy} L \quad (2.164)$$

4. **Rotor back iron:**

$$\ell_{ry1} = \frac{\pi}{2} \left( \frac{D}{2} - \ell_g - h_r - \frac{D_{sh}}{2} \right) \quad (2.165)$$

$$A_{ry1} = \left( \frac{D}{2} - \ell_g - h_r - \frac{D_{sh}}{2} \right) L \quad (2.166)$$

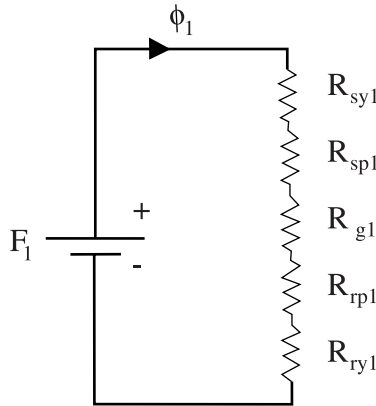


**FIGURE 2.25** Magnetic equivalent circuit for flux path 1 in region 1.

The magnetic equivalent circuit is shown in [Figure 2.25](#), where the excitation mmf is given by:

$$F_1 = T_{ph}i \quad (2.167)$$

The total stator pole reluctance is computed for both the flux paths as:

$$R_{sp1} = \frac{\ell_{sp1}}{\mu_o \mu_{r1} A_{sp1}} \quad (2.168)$$

where  $\mu_{r1}$  is the relative permeability in the stator pole. Similarly, for both rotor pole paths, the reluctance is

$$R_{rp1} = \frac{\ell_{rp1}}{\mu_o \mu_{r2} A_{rp1}} \quad (2.169)$$

where  $\mu_{r2}$  is the relative permeability in the rotor pole. The stator and rotor back iron reluctances, respectively, for path 1 are

$$R_{sy1} = \frac{\ell_{sy1}}{\mu_o \mu_{r3} A_{sy1}} \quad (2.170)$$

$$R_{ry1} = \frac{\ell_{ry1}}{\mu_o \mu_{r4} A_{ry1}} \quad (2.171)$$

where  $\mu_{r3}$  and  $\mu_{r4}$  are relative permeabilities for the stator and rotor back iron, respectively. The reluctance of flux path 1 for both air gaps combined is

$$R_{g1} = \frac{\ell_{g1}}{\mu_o A_{g1}} \quad (2.172)$$

The procedure to calculate the stator flux density and all other variables of interest are very much similar to the procedure developed in the previous section; therefore, for the sake of brevity, it will not be repeated here. The inductance contributed by the flux path for the considered rotor position,  $\theta$ , is

$$L_1 = \frac{T_{ph}\phi_1(\theta)}{i} \quad (2.173)$$

where  $\phi_1(\theta)$  is the flux in path 1.

#### 2.3.6.1.2 Flux Path 2

This flux path is subtended by one-fifth stator pole arc and it crosses to the rotor pole from its side with a width of  $(1/3)h_r$  at a height of  $(1/4)h_r$  (see Figure 2.23). As for its flow to the diametrically opposite rotor pole and then to the diametrically opposite stator pole, it is identical to the upper part just described. The stator back iron on the right-hand side carries the flux in path 2. Flux path 2 enlarged for the upper part is shown in Figure 2.26. Note the similarity of the flux path in the lower part of the stator and rotor poles as this flux passes through the diametrically opposite rotor pole. The relevant lengths of the mean flux lines and the area of cross section of the flux paths are derived similar to the procedure developed in the previous section. The steps involved for the path in the air gap are

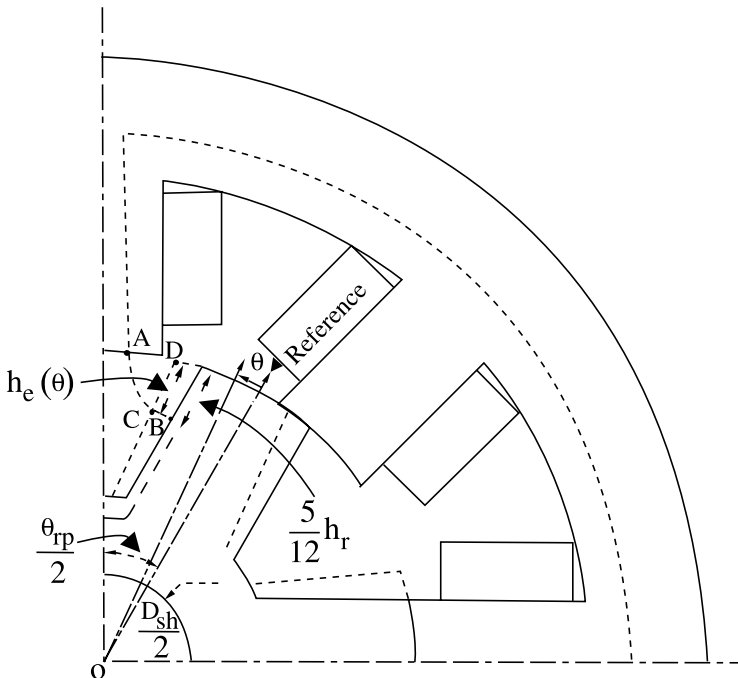


**FIGURE 2.26** Flux path 2 in region 1.

For the coordinates of  $A = (x_1, y_1)$ ,

$$x_1 = \frac{D}{2} \sin\left(\frac{\beta_s}{5}\right) \quad (2.174)$$

$$y_1 = \frac{D}{2} \cos\left(\frac{\beta_s}{5}\right) \quad (2.175)$$

$$\text{coordinates of } C = (x_2, y_2) \quad (2.176)$$

$$x_2(\theta) = \left(\frac{D}{2} - \ell_g - h_{eu}(\theta)\right) \sin\left(\frac{\theta_{eu}}{2} - \frac{\beta_r}{2} - \theta\right) \quad (2.177)$$

$$y_2(\theta) = \left(\frac{D}{2} - \ell_g - h_{eu}(\theta)\right) \cos\left(\frac{\theta_{rp}}{2} - \frac{\beta_r}{2} - \theta\right) \quad (2.178)$$

$$AC = \sqrt{(x_2 - x_1)^2 + (y_2 - y_1)^2} \quad (2.179)$$

$$\ell_{g2u} \simeq \frac{\pi}{3} \cdot AC \quad (2.180)$$

where the height,  $h_{eu}(\theta)$ , at which the flux enters the side of the rotor pole as it draws to the end of region 1, becomes half its original height at unalignment. It can be approximately represented as:

$$h_{eu}(\theta) = \frac{5}{12} h_r \left(1 - \frac{\theta}{2\left(\frac{\theta_{rp}}{2} - \frac{\beta_s + \beta_r}{2}\right)}\right) \quad (2.181)$$

The length of the flux path in the air between the lower stator and rotor poles is

$$\ell_{g2\ell} = \sqrt{(x_3 - x_1)^2 + (y_3 - y_1)^2} \quad (2.182)$$

where  $x_1$  and  $y_1$  are given by Eqs. (2.174) and (2.175), respectively, and  $x_3$  and  $y_3$  are derived by modifying Eqs. (2.177) and (2.178) in the section on flux path 2;

$$x_3(\theta) = \left(\frac{D}{2} - \ell_g - h_{e\ell}(\theta)\right) \sin\left(\frac{\theta_{rp}}{2} - \frac{\beta_r}{2} + \theta\right) \quad (2.183)$$

$$y_3(\theta) = \left( \frac{D}{2} - \ell_g - h_{e\ell}(\theta) \right) \cos\left(\frac{\theta_{rp}}{2} - \frac{\beta_r}{2} + \theta\right) \quad (2.184)$$

$$h_{e\ell}(\theta) = \frac{5}{12} h_r \left( 1 + \frac{\theta}{2 \left( \frac{\theta_{rp} - (\beta_s + \beta_r)}{2} \right)} \right) = h_{eu}(-\theta) \quad (2.185)$$

The total mean length of the flux lines in the air then is

$$\ell_{g2} = \ell_{g2u} + \ell_{g2\ell} \quad (2.186)$$

The length of the flux path in rotor pole is

$$\ell_{rp2u} = h_r - h_{eu}(\theta) \quad (2.187)$$

$$\ell_{rp2\ell} = h_r - h_{e\ell}(\theta) \quad (2.188)$$

The total length of flux line in rotor pole is

$$\ell_{rp2} = \ell_{rp2u} + \ell_{rp2\ell} \quad (2.189)$$

The area of cross section of the flux path in the air is the average of the stator and rotor pole areas of cross section and is given as:

$$A_{g2} = \left( \frac{\beta_s}{5} \frac{D}{2} + \frac{1}{3} h_r \right) \frac{L}{2} \quad (2.190)$$

All other values are straightforward and are not elaborated here. The magnetic equivalent circuit is identical to that of path 1 shown in [Figure 2.26](#).

#### 2.3.6.1.3 Flux Path 3

Flux from one fifth of the stator pole arc flows into the rotor interpolar space, the mean of which is indicated by the line *AB* at the center of the stator pole in [Figure 2.27](#). It is so until the rotor interpolar space moves away or a short air path to the side of the rotor pole emerges. The latter case arises only in region 2 and never in region 1; therefore, two cases arise for flux path 3. When rotor pole movement is less than half, the interpolar arc is given as:

$$\theta \leq \frac{\theta_{rp} - \beta_r}{2}$$

in which case, the flux path is in the air and is indicated by *AB*. Then, the mean length of flux path 3 in the air for the upper and lower parts is

$$\ell_{g3u} = AB = \left( \frac{D}{2} - \ell_g - h_r \right) = \ell_{g3\ell} \quad (2.191)$$

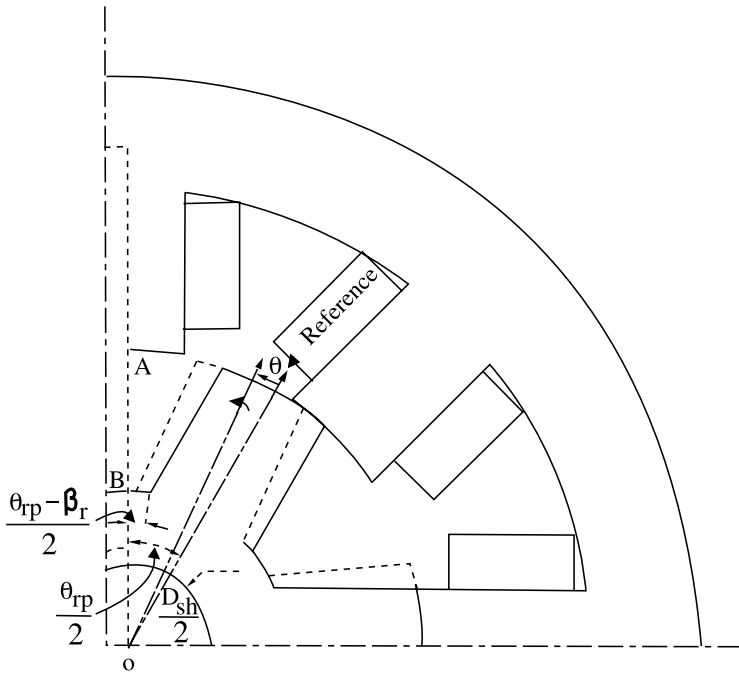


**FIGURE 2.27** Flux path 3 in region 1.

Hence, the total air length in path 3 is

$$\ell_{g3} = \ell_{g3u} + \ell_{g3\ell} = 2(AB) = 2\left(\frac{D}{2} - \ell_g - h_r\right) \quad (2.192)$$

It is tacitly assumed that a path to the leading side of the rotor pole is greater than  $AB$  and is not considered. Such an assumption is very valid in practice.

Note that the upper and lower stator and rotor pole paths are similar and the equivalent circuit is identical to that for flux path 1 shown in [Figure 2.25](#). The area of cross section of flux path 3 in the air is

$$A_{g3} = \frac{1}{5} \beta_s \frac{D}{2} L \quad (2.193)$$

in region 1. The air gap area is considered equal to the stator pole area for flux path 3, as the flux path is straight and does not warrant consideration like other paths. All other variables for other parts of the machine are easy to derive and are not given here.

#### 2.3.6.1.4 Flux Path 4

The flux pattern in path 4 resembles that of the flux in path 2 except that it is advanced by  $-\theta$  in all the computations of length and other variables; therefore, the derivations of flux path 2 can be referred to. The length of the flux lines and the cross section of their path in magnetic parts of the machine may be derived easily and are not given here. The length of the flux path in the back iron is given by the arc angle of  $2\pi/3$  and not  $\pi$ . The magnetic equivalent circuit is identical to that of flux path 1 shown in [Figure 2.25](#).

#### 2.3.6.1.5 Flux Path 5

This is identical to flux path 1 in the stator pole. When it comes to the upper air gap between the stator and rotor poles, the length of the flux lines in the air gap increases; the length decreases in the lower stator and rotor pole pair. The length of the flux lines in the lower stator and rotor pole exactly corresponds to that of flux path 1 at the upper stator and rotor pole; therefore,

$$\ell_{g5\ell} = \ell_{g1u} \quad (2.194)$$

where  $\ell_{g1u}$  has been derived in an earlier section and is given by Eq. (2.152). The cross section of the flux path is

$$A_{g5} = A_{g1} \quad (2.195)$$

As for the air gap length between the upper stator and rotor pole pair, it is identical to flux path 1 of the lower part stator and rotor pole pair, hence its length is given by:

$$\ell_{g5u} = \ell_{g1\ell} \quad (2.196)$$

The lengths of the flux path in the rotor pole and rotor back iron are identical to those of flux path 1. The equivalent circuit for this flux path is identical to the equivalent circuits of flux paths 1, 2, 3, and 4.

#### 2.3.6.1.6 Flux Path 6

This flux path is dealt with in [Section 2.3.2.7](#), and the equations and equivalent circuit from the same section are directly applicable here.

#### 2.3.6.1.7 Inductance in Region 1

The inductance in region 1 is arrived at as:

$$L_a = \sum_{n=1}^6 L_n \quad (2.197)$$

where  $L_1, L_2, \dots, L_6$  are the inductances contributed by the flux linkages associated with paths 1, 2, ..., 6, respectively.

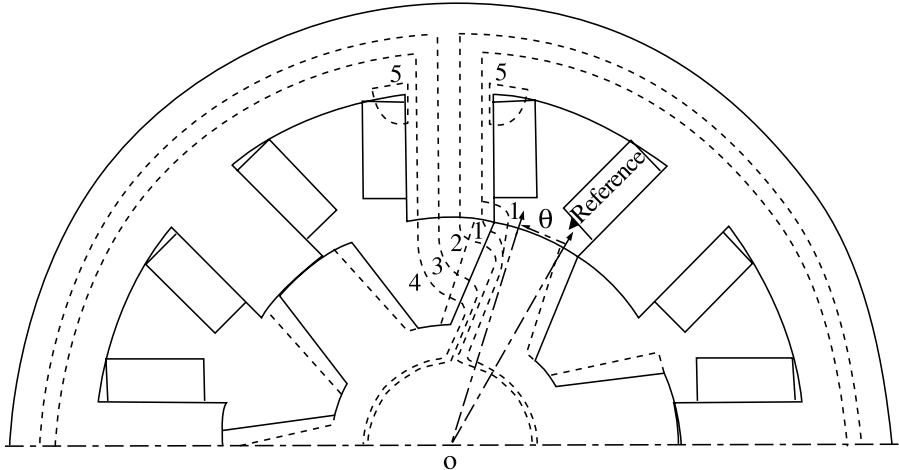


**FIGURE 2.28** Flux distribution in region 2.

### 2.3.6.2 Region 2

Region 2 is defined by the rotor movement from its completely unaligned position,  $\theta$ , as:

$$\frac{\theta_{rp} - (\beta_s + \beta_r)}{2} \leq \theta \leq \frac{\theta_{rp}}{2} \quad (2.198)$$

The typical flux distribution at an intermediate position in region 2 is shown in [Figure 2.28](#). Only five flux paths are considered here. Many more can be included to improve the accuracy of predicting the machine characteristics. The chosen flux paths are explained in the following and their relevant lengths in the air gap are given.

#### 2.3.6.2.1 Flux Path 1

This is similar to flux path 1 in region 1 in terms of its length and area of cross section in the stator and rotor poles. It is symmetric with respect to its diametrically opposite rotor pole and hence is not shown in the figure. Flux path 1 has two subpaths in the air gap with half of the flux lines in each subpath. The area of cross section of the flux path in the air is the average of the stator pole exit and rotor pole entrance cross sections and for subpath 1 is given by:

$$A_{g1} = \frac{1}{2} [A_{sp1} + A_{rp1}] = \frac{1}{2} \left[ \frac{h_s}{4} + \frac{\beta_r}{4} \left( \frac{D}{2} - \ell_g \right) \right] L \quad (2.199)$$

For subpath 1', the area of cross section is

$$A_{g1'} = \frac{1}{2} \left[ \frac{\beta_s D}{4} + \frac{h_r}{4} \right] L; \quad \left( \frac{\theta_{rp}}{2} - \frac{\beta_r}{2} - \frac{\beta_s}{2} \right) \leq \theta \leq \left( \frac{\theta_{rp}}{2} - \frac{\beta_r}{2} - \frac{3\beta_s}{8} \right)$$

$$= \frac{\beta_s D}{4} L; \quad \left( \frac{\theta_{rp}}{2} - \frac{\beta_r}{2} - \frac{3\beta_s}{8} \right) \leq \theta \leq \frac{\theta_{rp}}{2} \quad (2.200)$$

Note that the area of cross section of subpath 1' is dependent on the rotor position and so also its reluctance. The lengths of the mean flux in these subpaths are derived assuming that the flux subpath entrance is at  $\beta_r/4$  from the tip of the stator pole and are given as:

$$\ell_{g1u} = \ell_{g1\ell} = \frac{\pi}{3} \sqrt{(x_2 - x_1)^2 + (y_2 - y_1)^2}; \quad \left( \frac{\theta_{rp}}{2} - \frac{\beta_r + \beta_s}{2} \right) \leq \theta \leq \left( \frac{\theta_{rp}}{2} - \frac{\beta_s}{2} - \frac{1}{4}\beta_r \right)$$

$$= 0; \quad \left( \frac{\theta_{rp}}{2} - \frac{\beta_s}{2} - \frac{1}{4}\beta_r \right) \leq \theta \leq \frac{\theta_{rp}}{2} \quad (2.201)$$

$$\ell_{g1'u} = \ell_{g1'\ell} = \frac{\pi}{3} \sqrt{(x_4 - x_3)^2 + (y_4 - y_3)^2}; \quad \left( \frac{\theta_{rp}}{2} - \frac{\beta_r + \beta_s}{2} \right) \leq \theta \leq \left( \frac{\theta_{rp}}{2} - \frac{3\beta_s}{8} - \frac{\beta_r}{2} \right)$$

$$= \ell_g; \quad \left( \frac{\theta_{rp}}{2} - \frac{3\beta_s}{8} - \frac{\beta_r}{2} \right) \leq \theta \leq \frac{\theta_{rp}}{2} \quad (2.202)$$

where

$$x_1 = \frac{D}{2} \sin\left(\frac{\beta_s}{2}\right) \quad (2.203)$$

$$y_1 = \frac{h_r}{8} + \frac{D}{2} \cos\left(\frac{\beta_s}{2}\right) \quad (2.204)$$

$$x_2 = \left(\frac{D}{2} - \ell_g\right) \sin\left(\frac{\beta_s}{2} + \frac{\beta_r}{4}\right) \quad (2.205)$$

$$y_2 = \left(\frac{D}{2} - \ell_g\right) \cos\left(\frac{\beta_s}{2} + \frac{\beta_r}{4}\right) \quad (2.206)$$

$$x_3 = \frac{D}{2} \sin\left(\frac{3\beta_s}{8}\right) \quad (2.207)$$

$$y_3 = \frac{D}{2} \cos\left(\frac{3\beta_s}{8}\right) \quad (2.208)$$

$$x_4 = c_1 \sin \theta \quad (2.209)$$

$$y_4 = c_1 \cos \theta \quad (2.210)$$

$$c_1 = \frac{D}{2} - \ell_g - \frac{h_r}{8} \left\{ 1 - \frac{\theta}{\left( \frac{\theta_{rp}}{2} - \frac{\beta_r}{2} - \frac{3\beta_s}{8} \right)} \right\} \quad (2.211)$$

Therefore, the total length of the mean flux line in air is

$$\ell_{g1} = \ell_{g1u} + \ell_{g1\ell} = 2\ell_{g1u} \quad (2.212)$$

$$\ell_{g1'} = \ell_{g1'u} + \ell_{g1'\ell} = 2\ell_{g1'u} \quad (2.213)$$

The magnetic equivalent circuit is very similar to [Figure 2.25](#) for subpaths 1 and 1' and also for flux paths 2, 3, and 4. For brevity, it is omitted from now on.

### 2.3.6.2.2 Flux Path 2

The area of cross section for this flux path in the stator pole is

$$A_{sp2} = \frac{\beta_s}{4} \frac{D}{2} L \quad (2.214)$$

and in the rotor pole is

$$\begin{aligned} A_{rp2} &= \frac{h_r}{4} L; \quad \left( \frac{\theta_{rp}}{2} - \frac{(\beta_s + \beta_r)}{2} \right) \leq \theta \leq \left( \frac{\theta_{rp}}{2} - \frac{\beta_r}{2} - \frac{1}{8}\beta_s \right) \\ &= A_{sp2}; \quad \left( \frac{\theta_{rp}}{2} - \frac{\beta_r}{2} - \frac{1}{8}\beta_s \right) \leq \theta \leq \frac{\theta_{rp}}{2} \end{aligned} \quad (2.215)$$

The area of cross section of the flux path in the air gap is

$$A_{g2} = \frac{A_{sp2} + A_{rp2}}{2} \quad (2.216)$$

The length of the mean flux in air gap is

$$\ell_{g2u} = \ell_{g2\ell} = \sqrt{(x_6 - x_5)^2 + (y_6 - y_5)^2} \quad (2.217)$$

where

$$x_5 = \frac{D}{2} \sin\left(\frac{1}{8}\beta_s\right) \quad (2.218)$$

$$y_5 = \frac{D}{2} \cos\left(\frac{1}{8}\beta_s\right) \quad (2.219)$$

$$x_6 = c_2 \sin \theta \quad (2.220)$$

$$y_6 = c_2 \cos \theta \quad (2.221)$$

$$c_2 = \frac{D}{2} - \ell_g - \frac{3}{8}h_r \left( 1 - \frac{\theta}{\frac{\theta_{rp}}{2} - \frac{\beta_r}{2} - \frac{1}{8}\beta_s} \right); \quad \left( \frac{\theta_{rp}}{2} - \frac{\beta_r}{2} - \frac{\beta_s}{2} \right) \leq \theta \leq \left( \frac{\theta_{rp}}{2} - \frac{\beta_r}{2} - \frac{1}{8}\beta_s \right) \quad (2.222)$$

$$\ell_{g2u} = \ell_g; \quad \left( \frac{\theta_{rp}}{2} - \frac{\beta_r}{2} - \frac{1}{8}\beta_s \right) \leq \theta \leq \frac{\theta_{rp}}{2} \quad (2.223)$$

The total air gap length for both the upper and lower rotor and stator poles for this path is

$$\ell_{g2} = \ell_{g2u} + \ell_{g2l} = 2\ell_{g2u} \quad (2.224)$$

### 2.3.6.2.3 Flux Path 3

This path has a width of  $(\beta_s/4)(D/2)$  in the stator pole, as the flux paths 2 and 3, and has the same width at the rotor entrance when the rotor interpolar space is closer than a side of the rotor pole. If the side of the rotor pole is nearer, the width of its entry is  $(h_r/4)$ . The area of cross section of the flux path in air is

$$A_{g3} = \frac{1}{2}[A_{sp3} + A_{rp3}] \quad (2.225)$$

where

$$A_{sp3} = \frac{\beta_s}{4} \frac{D}{2} \cdot L \quad (2.226)$$

$$\begin{aligned} A_{rp3} &= \frac{h_r}{4}L; \quad \text{if flux path is through rotor side} \\ &= A_{sp3}; \quad \text{if flux path is through rotor interpolar} \\ &\quad \text{space or directly through rotor pole face} \end{aligned} \quad (2.227)$$

Whether the flux path is through the rotor side or rotor interpolar (between two rotor poles) space is determined by the following algorithm for the air gap length:

$$\ell_{g3u} = \ell_{g3\ell} = \frac{\ell_{g3}}{2} \quad (2.228)$$

where

$$\frac{\ell_{g3}}{2} = \frac{\pi}{3} \sqrt{(x_8 - x_7)^2 + (y_8 - y_7)^2}; \quad \text{if } \frac{\ell_{g3}}{2} \leq \left( \frac{D}{2} - \ell_g - h_r \right) \quad (2.229)$$

otherwise,

$$\frac{\ell_{g3}}{2} = \left( \frac{D}{2} - \ell_g - h_r \right) \quad (2.230)$$

and

$$x_7 = \frac{D}{2} \sin \left( \frac{-\beta_s}{8} \right) \quad (2.231)$$

$$y_7 = \frac{D}{2} \cos \left( \frac{-\beta_s}{8} \right) \quad (2.232)$$

$$x_8 = c_3 \sin \left( \frac{\theta_{rp}}{2} - \frac{\beta_r}{2} - \theta \right) \quad (2.233)$$

$$y_8 = c_3 \cos \left( \frac{\theta_{rp}}{2} - \frac{\beta_r}{2} - \theta \right) \quad (2.234)$$

$$c_3 = \frac{D}{2} - \ell_g - \frac{5}{8} h_r \left( 1 - \frac{\theta}{\frac{\theta_{rp}}{2} - \frac{\beta_r}{2} + \frac{1}{8} \beta_s} \right); \quad \left( \frac{\theta_{rp}}{2} - \frac{\beta_s + \beta_r}{2} \right) \leq \theta \leq \left( \frac{\theta_{rp}}{2} - \frac{\beta_r}{2} + \frac{1}{8} \beta_s \right) \quad (2.235)$$

Flux path 3 presents three air gap choices when (1) it enters interpolar space, (2) it enters the side of the rotor pole, and (3) it enters on the rotor pole face. Both case (1) and (2) have been addressed in Eqs. (2.229) and (2.230). When the leading rotor pole barely reaches the exit of the mean flux path in the stator pole, note that the air gap is reduced to the air gap during alignment, giving rise to case (3), hence the air gap at that time is

$$\frac{\ell_{g3}}{2} = \ell_g; \quad \left( \frac{\theta_{rp}}{2} - \frac{\beta_r}{2} + \frac{1}{8} \beta_s \right) \leq \theta \leq \frac{\theta_{rp}}{2} \quad (2.236)$$

This is the third case for the air gap length of flux path 3.

#### 2.3.6.2.4 *Flux Path 4*

This flux path has characteristics very similar to flux path 3, with the same three possibilities for its air gap. Derivations for its air gap length and area of cross section are omitted for the sake of brevity.

#### 2.3.6.2.5 *Flux Path 5*

This flux path is identical to flux path 7 in the case of unaligned inductance evaluation; therefore, it is not further reviewed here.

#### 2.3.6.2.6 *Inductance Evaluation*

The procedure for inductance and flux linkages determination is very similar to that for the unaligned and aligned cases covered earlier in this chapter. No further consideration is given here for application to regions 1 and 2 to avoid repetition.

### 2.4 SECONDARY FLUX PATHS

Hitherto, the inductance evaluation has been based only on two-dimensional flux distribution. The various flux paths at both ends of the stator and rotor poles and the varieties of ways they can traverse have been ignored. In terms of their influence, the studies have indicated their contribution to inductances can amount to as much as 15% of unaligned inductance. Their significance near aligned positions is relatively very small compared to the inductance value at these positions, even though their absolute magnitude may remain constant. Small errors can arise due to the omission of such fringing and end effects in performance evaluations, and the error introduced may be on the order of 3 to 5% of the peak rating of the machine. Studies have yet to emerge to predict very precisely the effects of secondary flux path omissions on the computation of machine performance. To alleviate this circumstance, we resort to three-dimensional finite element analysis. It provides very little insight to a designer seeking the cause–effect relationships among a set of machine dimensions, excitation and rotor positions, and the resulting set of machine characteristics and performance.

An analytical method similar to the approach developed using magnetic equivalent circuits allows inclusion of the inductance contribution of the secondary flux paths. A number of such predetermined paths have been developed in earlier texts,<sup>13</sup> and Appendix 3A contains some flux path and permeance computational formula that can be used to enhance the accuracy of prediction. In Chapter 3, they are used for inductance prediction of linear switched reluctance machines. The equations and approach are easier to use for linear machines than for rotary machines (see Chapter 3).

### 2.5 COMPUTATION OF INDUCTANCE

The algorithms derived for inductance prediction in this chapter have to be carefully coded. The transitions between regions 1 and 2 and the varying length of flux paths in the stator, rotor and air gap require special attention, as they involve various cases for different rotor positions. The algorithms for regions 1 and 2 indicate, in general, a simple procedure for the derivation of equations for inductance prediction. They should

be used more as a guideline rather than for direct use in the design process. For higher accuracy in prediction, a larger number of flux paths is necessary and are therefore strongly recommended for those interested in mechanizing this procedure for their day-to-day SRM design use.

The accuracy of prediction of the three-dimensional characteristics of the flux linkages vs. excitation current vs. rotor position is within 5 to 10% of the measured results. The accuracy can be improved with selecting a higher number of flux paths. The only advantage of this method of finding machine characteristics is in assessing new machine configurations and their impact on the machine characteristics. For example, the machine characteristics can be changed by modifying only a segment of the stator or rotor or both of them in the machine and changing its flux path. In such a circumstance, the direct relationship between the machine dimensional changes and the machine characteristic changes can be captured using the method developed in this chapter, leading to a qualitative and quantitative understanding of the machine and its design.

## REFERENCES

1. Miller, T.J.E. and M. McGilp, Nonlinear theory of the switched reluctance motor for rapid computer-aided design, *IEE Proc. B*, 137(6), 337–346, 1990.
2. Lindsay, J.F., R. Arumugam, and R. Krishnan, Finite element analysis characterization of a switched reluctance motor with multi-tooth per stator pole, *IEE Proc. B*, 133(6), 347–353, 1986.
3. Corda, J. and J.M. Stephenson, An analytical estimation of the minimum and maximum inductances of a double-salient motor, in *Proc. of the Int. Conf. on Stepping Motors and Systems*, Leeds, 1979, pp. 50–59.
4. Radun, A., Analytical calculation of the switched reluctance motor's unaligned inductance, *IEEE Trans. on Magnetics*, 35(6), 4473–4481, 1999.
5. Stephenson, J.M. and J. Corda, Computation of torque and current in doubly salient reluctance motors from nonlinear magnetization data, *IEEE Proc.*, 127(5), 393–396, 1979.
6. Esatham, A.R., H. Yuan, G.E. Dawson, P.C. Choudhury, and P.M. Cusack, A finite element evaluation of pole shaping in switched reluctance motors, *Electrosoft*, 1(1), 55–67, 1990.
7. Arumugam, R., D.A. Lowther, R. Krishnan, and J.F. Lindsay, Magnetic field analysis of a switched reluctance motor using a two-dimensional finite element model, *IEEE Trans. on Magnetics*, Vol. MAG-21, No. 5, 1883–1885, 1985.
8. Arumugam, R., Design and Finite Element Analysis of Switched Reluctance Motors, Ph.D. thesis, Concordia University, Montreal, Canada, December 1987.
9. Lee, B.-S., H.-K. Bae, P. Vijayraghavan, and R. Krishnan, Design of a linear switched reluctance machine, in *IEEE Ind. Appl. Soc. Conf. (IAS '99)*, Vol. 4, Oct. 3–7, 1999, Phoenix, AZ, pp. 2267–2274.
10. Krishnan, R., M. Abou-Zeid, and X. Mang, A design procedure for axial field switched reluctance motors, in *IEEE Ind. Appl. Soc. Ann. Mtg. Conf. Rec.*, Oct. 1990, Seattle, WA, pp. 241–246.
11. Materu, P. and R. Krishnan, Analytical prediction of SRM inductance profile and steady state average torque, in *IEEE Ind. Appl. Soc. Ann. Mtg. Conf. Rec.*, Oct. 1990, Seattle, WA, pp. 214–223.

12. Deshpande, U.S., J.J. Cathey, and E. Richter, A high force density linear switched reluctance machine, in *Conf. Rec. of the 1993 IEEE IAS Ann. Mtg.*, Vol. 1, Oct. 1993, Toronto, Canada, pp. 251–257.
13. Roters, H.C., *Electromagnetic Devices*, Wiley, New York, 1941.
14. Corda, J. and M. Wilkinson, Prediction and measurement of magnetic parameters of cylindrical linear switched reluctance actuator, in *Proc. of Int. Conf. on Electrical Machines*, Vol. 3, Sept. 1994, Paris, France, pp. 479–484.
15. Lee, B.S., Linear Switched Reluctance Machine Drives with Electromagnetic Levitation and Guidance Systems, Ph.D. thesis, The Bradley Department of Electrical and Computer Engineering, Virginia Tech., Blacksburg, VA, Nov. 2000.

---

# 3 Design of SRM

## 3.1 INTRODUCTION

Performance analysis of the SRM requires the dimensions for stator and rotor laminations, winding details, pole numbers, and pole arcs. An approximate sizing of the SRM is obtainable using a power output equation familiar to machine designers. The resulting machine dimensions form the starting point in design evaluation, and final design is achieved through an iterative process of steady-state performance calculations described in this chapter. This chapter contains the derivation of the output equation and selection of various machine variables such as number of poles, rotor and stator pole arcs, core length, bore diameter, back iron thickness, number of turns in each phase, and air gap for rotary switched reluctance machines. The design trade-offs emerging from conflicting requirements are discussed in great detail.

A procedure to calculate resistive and core losses is presented. Flux densities at various parts of the machine are derived from first principles. Measurement of winding inductance is crucial to the validation of machine design and is briefly described here. The computation of torque for ideal and practical currents is developed, and the procedure is equally applicable to both steady-state and dynamic processes.

A step-by-step design of linear motion SRMs is considered in detail. In order to utilize the knowledge base of the rotary SRM, the linear machine design is achieved using the rotary SRM design process developed in this chapter. In order to accomplish it, the design specifications of the linear machine are converted to rotary machine design specifications. Then, an equivalent rotary SRM is designed and the design outcomes are translated into linear machine dimensions and variables by simple algebraic relationships. The design verification with analysis using magnetic equivalent circuits, finite element method, and experimental measurements is developed in detail. The procedure for inductance and force measurements is also described in this chapter for the linear SRM.

## 3.2 DERIVATION OF OUTPUT EQUATION

The output equation relates the bore diameter, length, speed, and magnetic and electric loadings to the output of a machine. In general, the conventional machines are designed starting from the output equation. A similar development of the output equation for SRM will make its design systematic.<sup>22,33</sup> Moreover, the experience of the machine designers can be effectively used in the design of these new machines, as they could use the commonality between these and the conventional machines to start with. While the output equation of SRM will be significantly different from that of the conventional machine, the emphasis here is placed on their similarities.

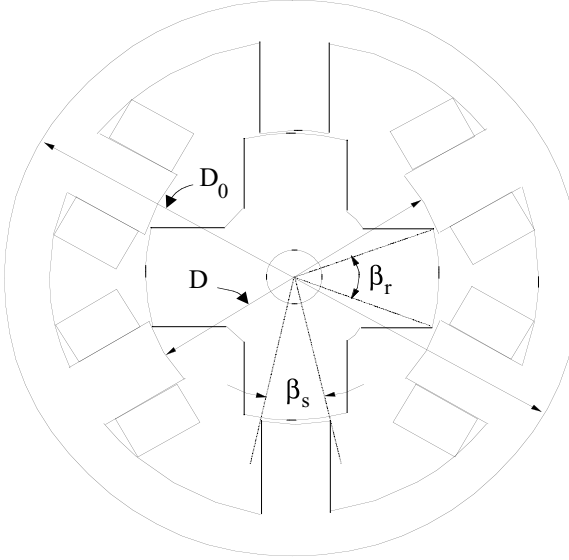


**FIGURE 3.1** A three-phase SRM with major dimensional variables.

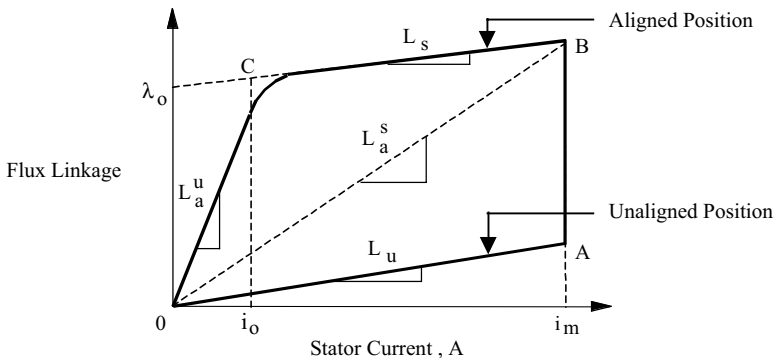


**FIGURE 3.2** Flux linkages vs. stator current for SRM.

An SRM with six stator poles and four rotor poles is shown in [Figure 3.1](#). The flux linkages vs. current characteristics for the unaligned and perfectly aligned position of the stator and rotor poles are shown in [Figure 3.2](#). The unaligned position of the stator and rotor poles means that the center of the stator pole is in between the two rotor poles. The area enclosed by  $OABC$  denotes the output mechanical energy of the motor for one stroke. Neglecting the resistive voltage drop in the machine winding, the applied voltage then equals the rate of change of flux linkages. Then, the flux linkage–voltage relationship for a flat-topped phase current  $i$  is obtained by

neglecting resistive voltage drop as:

$$V \equiv \frac{d\lambda}{dt} = \frac{(\lambda_a - \lambda_u)}{\lambda_u} = \frac{(L_a^s - L_u)i}{t} \quad (3.1)$$

where  $L_a^s$  is the aligned saturated inductance per phase,  $L_u$  is the unaligned inductance per phase,  $V$  is the applied voltage and  $t$  is the time taken for the rotor to move from the unaligned to aligned position. That time can be expressed in terms of the stator pole arc and rotor speed as:

$$t = \frac{\beta_s}{\omega_m} \quad (3.2)$$

where  $\beta_s$  is the stator pole arc in rad, and  $\omega_m$  is the rotor speed in rad/s.

We define:

$$\sigma_s = \frac{L_a^s}{L_a^u} \quad (3.3)$$

and

$$\sigma_u = \frac{L_a^u}{L_u} \quad (3.4)$$

where  $L_a^u$  is the aligned but unsaturated inductance. Substituting Eqs. (3.3) and (3.4) in Eq. (3.1), the applied voltage becomes:

$$V = \frac{\omega_m L_a^s i}{\beta_s} \left( 1 - \frac{1}{\sigma_s \sigma_u} \right) \quad (3.5)$$

We write the flux linkages in the aligned position in terms of flux and number of turns and then in terms of flux density and machine dimensions as:

$$L_a^s i = \phi T_{ph} = B \times A_{sp} \times T_{ph} = B \times D \times L \times \beta_s \times T_{ph} / 2 \quad (3.6)$$

where  $\phi$  is the aligned flux,  $A_{sp}$  is the area of the stator pole,  $D$  is the bore diameter,  $L$  is the axial length of the stator pole,  $B$  is the stator pole flux density at the aligned position, and  $T_{ph}$  is the number of turns per phase. The stator current may be obtained from the specific electric loading  $A_s$ , which is defined as:

$$A_s = \frac{2T_{ph}im}{\pi D} \quad (3.7)$$

where  $m$  is the number of phases conducting simultaneously. In the case of a 6/4 motor, such as the example being considered, only one phase conducts at a time.

The power developed then is

$$P_d = k_e k_d V i \text{ Vim} \quad (3.8)$$

where  $V$  and  $i$  are peak phase values,  $k_d$  is the duty cycle defined in Eq. (3.9), and  $k_e$  is the efficiency. The duty cycle can be expressed as:

$$k_d = \frac{\theta_i \cdot q P_r}{360} \quad (3.9)$$

where  $\theta_i$  is the current conduction angle for each rising inductance profile,  $q$  is the number of stator phases given by  $P_s/2$ ,  $P_s$  is the number of stator poles, and  $P_r$  is the number of rotor poles.

Combining Eqs. (3.5) and (3.6), the power developed is given by:

$$P_d = k_e \cdot k_d \left( \frac{\pi^2}{120} \right) \left( 1 - \frac{1}{\sigma_s \sigma_u} \right) B A_s D^2 L N_r \quad (3.10)$$

where  $N_r$  is the rotor speed in revolutions per minute (rpm). Equation (3.10) can be rearranged to resemble that of the conventional output equation of ac machines and is given by:

$$P_d = k_e k_d k_1 k_2 B A_s D^2 L N_r \quad (3.11)$$

where

$$k_1 = \frac{\pi^2}{120} \quad (3.12)$$

$$k_2 = 1 - \frac{1}{\sigma_s \sigma_u} \quad (3.13)$$

The torque can be obtained from Eq. (3.10) and expressed as:

$$T = k_d k_e k_3 k_2 \cdot (B A_s) D^2 L \quad (3.14)$$

where

$$k_3 = \frac{\pi}{4} \quad (3.15)$$

Note that the torque and power output are proportional to the product of specific electric and magnetic loadings and bore volume given by  $(\pi D^2 L)/4$ .  $k_2$  is the only variable dependent on the operating point of the motor and is determined by the stator

phase current, magnetic characteristics of the core materials, and dimensions of the motor. For a given operating point,  $k_2$  is a constant. Hence, to extract the maximum output power from the SRM,  $k_2$  needs to be calculated at the maximum stator current. For that matter, the flux linkages vs. current for the aligned and unaligned positions are to be estimated for various values of stator currents. For  $k_d = 1$ , the power developed is maximum for a given stator current. It is usual to find that the maximum possible duty cycle is less than one. Furthermore, torque and power control are exercised by the duty cycle similar to a chopper-controlled dc motor. The speed is controlled by the frequency of switching of the phases resembling that of a synchronous motor.

### 3.3 SELECTION OF DIMENSIONS

#### 3.3.1 DIAMETER AND LENGTH

Since the SRM is normally used as a variable-speed device, it is appropriate to have a base speed specification. At the base speed, the motor is expected to deliver the rated torque and hence the rated output power. Using Eq. (3.11) to correspond to the rated power output and keeping the stack length as a multiple or submultiples of rotor bore diameter, the following is obtained:

$$L = k \cdot D \quad (3.16)$$

which on substitution in the output power equation results in:

$$P_d \propto k_2 \cdot D^3 \quad (3.17)$$

From Eq. (3.17),  $D$  is evaluated if the rated speed  $B$ ,  $A_{sp}$ ,  $k_2$ ,  $k_d$ , and  $k$  are known. It is possible to start the iterative process of design with reasonable values. In general, at the rated operating point, the range of  $k_2$  is given by:

$$0.65 < k_2 < 0.75 \quad (3.18)$$

The values of  $B$  for the aligned position can be taken as the allowable maximum for the core material. The specific electric loading in amp-conductors per meter is usually in the range of:

$$25000 < A_s < 90000 \quad (3.19)$$

The duty cycle  $k_d$  can be assumed to be one to start with. Using the above starting values, bore diameter  $D$  is obtained. The air gap is determined from constraints imposed by the manufacturing techniques employed. Small machines have air gaps from 0.18 to 0.25 mm. Integral horsepower machines may have air gaps from 0.3 to 0.5 mm. The ratio of the lengths to bore  $k$  need not be arbitrary; it is decided

by the nature of the application and space constraints. For nonservo applications, the range of  $k$  can be

$$0.25 < k < 0.70 \quad (3.20)$$

and for servo applications it is usually in the range given by:

$$1 < k < 3 \quad (3.21)$$

### 3.3.2 NUMBER OF TURNS

Using Eq. (3.7), the number of turns per phase,  $T_{ph}$ , is calculated for a given current. The conductor size is chosen such that the available winding space will be filled. The resulting current density is calculated and checked against the maximum permissible value, which is dependent on the cooling methods employed in the motor. If there is no restriction on the outer diameter the winding space can be calculated from the number of turns, the area of cross-section of the conductor, and the insulation thickness. The height of the stator pole is then derived from the winding space.

From Eq. (3.7), for a given specific electric loading and bore diameter, it can be seen that the product of  $T_{ph}$  and  $i$  is a constant. The best values are those that would satisfy the following mutually contradictory demands:

1. Small current implying a larger number of turns
2. Small values of resistance and inductance of the winding implying a smaller number of turns

An engineering trade-off has to be made keeping thermal considerations in perspective. Again, it must be emphasized here that the selection of  $i$  and  $T_{ph}$  is also dependent on the ac supply available for rectification and subsequent input to the converter to control the SRM.

### 3.3.3 THERMAL CONSIDERATION

The thermal capability of the motor is one of the important characteristics. The thermal capability is determined by the losses in the machine, the available surface area for cooling, and additional cooling arrangements provided by a fan or a blower or water- or liquid-circulated cooling. Evaluations of copper and core losses are given in the following sections to determine the thermal rating of the machine.

#### 3.3.3.1 Stator Copper Losses

If  $R_s$  is the per-phase resistance of the stator winding, the total copper losses for nonoverlapping currents in the stator is given by:

$$P_{cu} = q \cdot I^2 \cdot R_s \quad (3.22)$$

where  $q$  is the number of stator phases, and  $I$  is the rms value of the current given by:

$$I = \frac{I_p}{\sqrt{q}} \quad (3.23)$$

where  $I_p$  is the peak value of phase current. Hence, the copper losses are

$$P_{cu} = I_p^2 \cdot R_s \quad (3.24)$$

We can write the resistance in terms of the number of turns and area of cross section of the conductor as:

$$R_s = \rho \cdot \frac{\ell}{a_c} = K_r \cdot \frac{T_{ph}}{a_c} \quad (3.25)$$

where  $a_c$  is the area of cross section of the conductor,  $\rho$  is the specific resistivity,  $\ell$  is the total length of the winding,  $K_r$  is the product of the resistivity, and the mean length of turn given by  $\ell_m$ .

Substituting Eq. (3.25) in (3.24),

$$P_{cu} = K_r \left( \frac{I_p}{a_c} \right) (T_{ph} i) \quad (3.26)$$

In terms of the current density given by:

$$J_c = \frac{I_p}{a_c} \quad (3.27)$$

the copper losses are derived as:

$$P_{cu} \propto (J_c)(T_{ph} I_p) \quad (3.28)$$

Since the maximum ( $T_{ph} \cdot I_p$ ) is a constant for a design, copper losses are proportional to current density. Note that to minimize copper losses, the current density has to be decreased.

Consider the case where phase currents are overlapping with both the previous and succeeding phases. This is the most realistic condition in an SRM drive. The phase currents for a three-machine neglecting switching transients and assuming a linear rise and fall are shown in [Figure 3.3](#). Note that the stator copper losses at any time are the sum of the copper losses contributed by the instantaneous phase currents. This amounts to building the equivalent rms current in a phase for the time duration

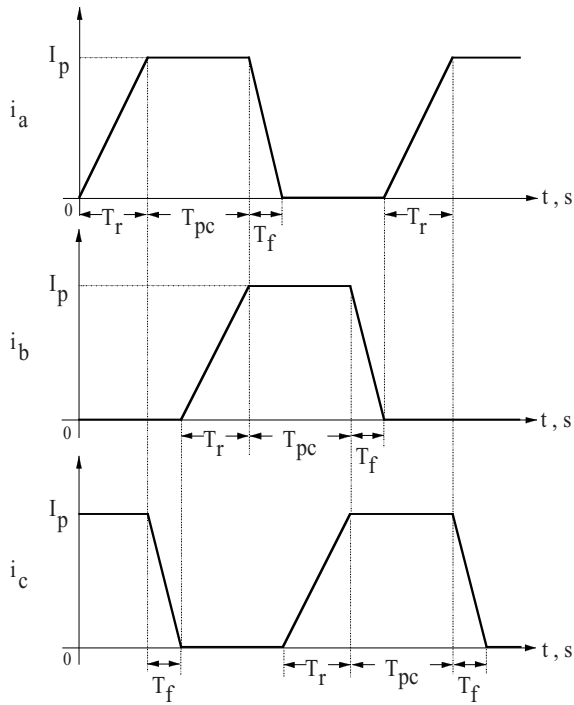


**FIGURE 3.3** Typical but simplified phase currents with an overlap in a three-phase SRM.

$T_{pc}$  when the phase inductance is varying and for which duration only a constant current is desired, as given by:

$$T_{pc} = \frac{\theta_{pc}}{\omega_m} = \frac{2\pi}{\left(\frac{P_s P_r}{2}\right) \omega_m} = \frac{4\pi}{\omega_m P_s P_r}, \text{ s} \quad (3.29)$$

During this interval, one phase has the maximum assumed to be the constant current, the current in the preceding phase is decaying, and the succeeding phase has a rising current. The resistive losses are the result of the cumulative effect of all these three currents, evaluated as follows:

$$P_{cu} = I^2 \cdot R_s = \frac{R_s}{T_{pc}} \left[ I_p^2 T_{pc} + \frac{1}{3} I_p^2 T_r + \frac{1}{3} I_p^2 T_f \right] = I_p^2 R_s \left[ 1 + \frac{(T_r + T_f)}{3 T_{pc}} \right], \text{ W} \quad (3.30)$$

where  $T_r$  and  $T_f$  are the current rise and fall times, respectively.  $T_r$  and  $T_f$  can be evaluated approximately using the equivalent circuit of the SRM as follows. A comment is in order here. Note that when  $T_{pc}$  is substituted for in terms of speed and stator and rotor poles from Eq. (3.29) into Eq. (3.30), the copper losses are

dependent on speed. Therefore, a copper loss only at the highest machine speed has to be considered. This is important for the thermal design of the machine.

### 3.3.3.2 Approximate Evaluation of $T_r$

The current in a phase is initiated when the machine is past the unaligned position so as to have the desired current magnitude  $I_p$  at the instant when the inductance slope begins. During this rise time, the inductance of the phase is at its unaligned value and its change with respect to rotor position is considered to be zero. It is also assumed that a constant voltage  $V_{dc}$  is applied during the current rise interval. Then, the phase voltage equation is approximated by:

$$V_{dc} \approx R_s i + L_u \frac{di}{dt} \quad (3.31)$$

as the induced emf term becomes zero. The current rises in time interval  $T_r$  from zero to the desired value,  $I_p$ . Using these initial and final conditions in the solution for current from Eq. (3.31), the rise time is obtained as:

$$T_r = \tau_u \ln \left[ \frac{1}{1 - \frac{R_s I_p}{V_{dc}}} \right], s \quad (3.32)$$

where the time constant at the unaligned position is given as:

$$\tau_u = \frac{L_u}{R_s}, s \quad (3.33)$$

### 3.3.3.3 Approximate Evaluation of $T_f$

During the current turn-off, a negative voltage is usually applied to the machine phase winding. In most converter topologies, the voltage equals the negative of the dc source voltage itself. During turn-off, the machine phase has an inductance equal to its aligned value throughout the current decay, as assumed in the following derivation. Note that the induced emf term goes to zero with these assumptions. The machine phase equation is given by:

$$R_s i + L_a \frac{di}{dt} = -V_{dc} \quad (3.34)$$

The initial and final conditions are

$$i(0) = I_p \quad (3.35)$$

$$i(T_f) = 0 \quad (3.36)$$

from which the fall time for the phase current is evaluated as:

$$T_f = \tau_a \ln \left[ 1 + \frac{R_s I_p}{V_{dc}} \right], s \quad (3.37)$$

where the electrical time constant of machine phases at the aligned position is given by:

$$\tau_a = \frac{L_a}{R_s}, s \quad (3.38)$$

### 3.3.4 STATOR BACK IRON THICKNESS

The stator back iron thickness,  $b_{sy}$ , is determined on the basis of maximum flux density in it and by the additional factor of vibration minimization to reduce acoustic noise. More on the latter factor is given in Chapter 7. The flux density in the stator back iron is approximately half that of the stator poles. An allowance is given to have a slightly greater share of the pole flux. The stator pole arcs have to be chosen to accommodate the pole flux density. If  $\omega_{sp}$  is the pole width given in terms of pole arc as follows:

$$\omega_{sp} = D \sin\left(\frac{\beta_s}{2}\right) \quad (3.39)$$

then the back iron thickness has to be a minimum of 0.5  $\omega_{sp}$ . Due to considerations of mechanical robustness and minimization of vibration it could have a value in the range of:

$$\omega_{sp} > b_{sy} \geq 0.5 \omega_{sp} \quad (3.40)$$

in practice. It is recommended to choose a higher value for  $b_{sy}$  than its minimum.

### 3.3.5 STATOR COIL DIMENSIONS

The stator coil dimensions given by its width,  $\omega_c$ , and length,  $h_c$ , emerge from the area of cross section of the conductor,  $a_c$ , determined by the current density and the number of turns per phase,  $T_{ph}$ . Let  $\omega_{cs}$  is the width or gap to be left between the two adjacent coils in a slot at the bore including the slot liners. A stator coil area is given, in terms of number of turns and area of cross section of the conductor, by:

$$h_c \omega_c = \frac{a_c T_{ph}}{2} \quad (3.41)$$

The maximum  $\omega_c$  is obtained by taking the stator bore periphery and subtracting the motor pole arcs and gap between coils and dividing the remaining by  $2P_s$  coils. Then,

$$\omega_c = \frac{\pi D - P_s [\beta_s \cdot \frac{D}{2} + \omega_{cs}]}{2P_s} = \frac{\pi D}{2P_s} - \frac{1}{2} \left\{ \frac{D}{2} \beta_s + \omega_{cs} \right\} \quad (3.42)$$

Combining Eqs. (3.42) and (3.41), the available coil height is determined from:

$$h_c = \frac{a_c T_{ph}}{2\omega_c} = a_c T_{ph} \left[ \frac{P_s}{\pi D - P_s \left\{ \frac{D}{2} \beta_s + \omega_{cs} \right\}} \right] \quad (3.43)$$

### 3.3.6 STATOR POLE HEIGHT

The minimum stator pole height is approximately equal to the coil height, but the coil has to be held in place and for that a small space is required near the pole face. The coil seating at the root of the pole is not usually tight fitting; therefore, some additional space is lost which must be accounted for to calculate the stator pole height. Taking into consideration all these factors and the need for a smaller length of the pole, the pole height in terms of the coil height  $h_c$  is given by:

$$h_c < h_s < 1.4h_c \quad (3.44)$$

### 3.3.7 OUTER DIAMETER OF STATOR LAMINATION

If the outer diameter is prespecified, the design is carried out from the outer to inner dimensions. Machines used in special variable-speed applications may not fall under frame numbers categorized by NEMA and other agencies and organizations. In that case, design details may start from bore diameters and then work their way up to determine the outer diameter of the stator lamination by adding to it the pole heights and back iron thickness. It then is given by:

$$D_0 = D + 2b_{sy} + 2h_s \quad (3.45)$$

### 3.3.8 ROTOR BACK IRON THICKNESS

The rotor back iron thickness,  $b_{ry}$ , is based on structural integrity and operating flux density. It need not be as much as the stator back iron thickness and neither has to be equal to the minimum value equal to half the stator pole width. The range of values to be chosen from has to account for the larger interpolar air gap to provide a high ratio between the aligned and unaligned inductances, but at the same time it is desirable to have shorter rotor poles to generate minimum vibration in the rotor. Based on these considerations, the rotor back iron thickness in terms of stator pole width is

$$0.5\omega_{sp} < b_{ry} < 0.75\omega_{sp} \quad (3.46)$$

### 3.3.9 ROTOR POLE HEIGHT

Given the bore diameter, air gap length,  $\ell_g$ , rotor back iron thickness, and rotor shaft diameter, the rotor pole height is written as:

$$h_r = \left[ \frac{D - 2\ell_g - D_{sh} - 2b_{ry}}{2} \right] \quad (3.47)$$

where  $D_{sh}$  is the rotor shaft diameter.

### 3.3.10 ESTIMATION OF CORE LOSSES

Core loss prediction plays an important role in design of the machine and in determination of its thermal rating. Efficiency optimization of the machine requires the sources of losses in the machine and their relationships between the lamination material characteristics, machine dimensions, excitation conditions, and losses. It is fairly straightforward to evaluate the stator resistive losses in an SRM, as indicated elsewhere, but core losses are difficult to predict in the SRM due to the presence of flux densities with various frequencies in stator segments. Further, these flux densities are neither pure sinusoids nor constants.<sup>2,37</sup>

The core losses in an SRM consist of hysteresis and eddy current losses. To reduce the eddy current losses, the stator and rotor cores are laminated. As for the hysteresis losses, the frequency of flux reversal and its path determine its magnitude. The first step in the computation of machine core losses is to derive the flux densities in various paths of the machine. Note that the flux path segments in the stator consist of  $P_s$  segments in the back iron and  $P_s$  in the poles. For the rotor laminations, the segments consist of poles and the back iron. For one-phase excitation, only two stator poles and two rotor poles carry the flux along with the entire stator back iron and the non-flux-carrying poles' back iron in the rotor contributing to the flux path.

The number of distinct iron segments for an  $q$ -phase SRM is derived as:

$$j = q + 2 \quad (3.48)$$

The total number of iron segments in use at a time for nonoverlapping stator currents is given as:

$$k = 2q + 6 = 2(j + 1) \quad (3.49)$$

If  $B_j$  is the flux density in the  $j$  segment of the iron, then the flux density in the  $k$  section,  $B_k$ , can be evaluated in terms of  $B_j$ . Such a step will lead to a graphical derivation of flux density waveforms for various segments of the SRM. Various segments of the machine are shown in [Figure 3.4](#) for a three-phase SRM with six stator and four rotor poles.

### 3.3.11 FLUX DENSITY WAVEFORMS

#### 3.3.11.1 Stator

The flux densities in various iron segments are derived starting from the stator poles.<sup>37</sup> The flux density of stator pole  $A$ ,  $B_7$ , vs. rotor position is shown in [Figure 3.5](#). The flux densities of other poles are identical but are phase shifted by  $\theta_s$  (i.e., the delay angle between phases when energizing the corresponding phase windings). Each phase current is conducting for  $\theta_c$  (conduction angle) and falls to zero in  $\theta_f$  (fall angle) duration.

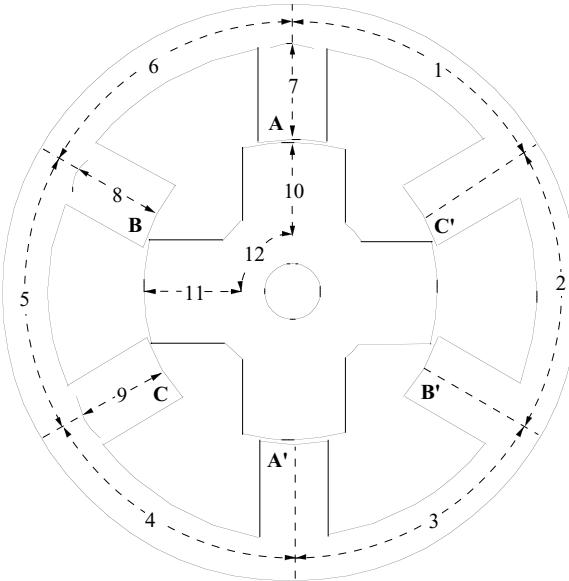


**FIGURE 3.4** Iron segments in a 6/4 SRM.

The conduction and fall angles are not usually equal, but for the sake of illustration they are considered to be equal in the following discussion. The flux density in the stator back iron segment,  $B_1$ , is proportional to the sum of the stator pole flux densities (i.e.,  $B_7 + B_8 + B_9$ ). The rotor pole pitch  $\theta_{rp}$  is given by:

$$\theta_{rp} = \frac{2\pi}{P_r} \quad (3.50)$$

Phase current displacement angle  $\theta_s$  in terms of  $\theta_{rp}$  is

$$\theta_s = \frac{\theta_{rp}}{(P_s/2)} = \frac{\theta_{rp}}{q} \quad (3.51)$$

The flux density in stator pole segment  $B_7$  is

$$B_7 = \begin{cases} B_m \frac{\theta}{\theta_c}, & 0 \leq \theta \leq \theta_c \\ B_m \left[ 1 - \frac{(\theta - \theta_c)}{\theta_f} \right], & \theta_c \leq \theta \leq (\theta_c + \theta_f) \end{cases} \quad (3.52)$$

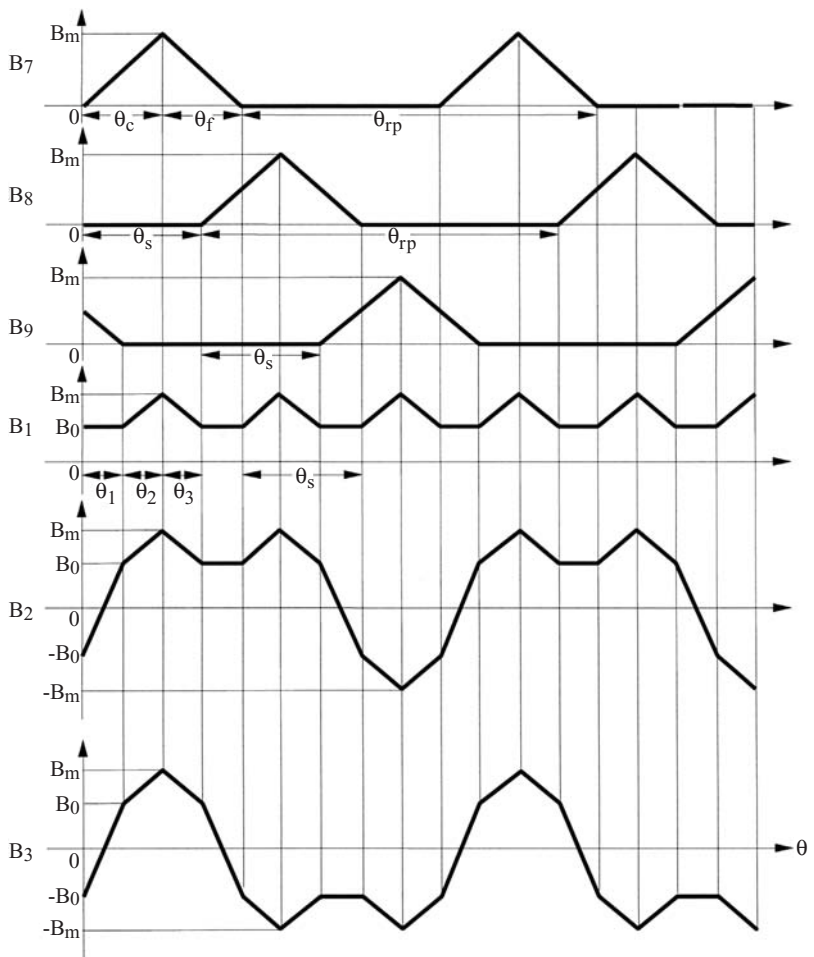


**FIGURE 3.5** Stator flux density waveform for the 6/4 SRM shown in [Figure 3.4](#).

The flux density in the back iron segment adjacent to the stator pole,  $B_1$ , is repetitive for each  $\theta_s$  radians and could be compactly expressed as:

$$B_1 = \begin{cases} aB_m \left[ \frac{\theta}{\theta_c} + \frac{\theta_f - (\theta + \theta_s - \theta_c)}{\theta_f} \right], & 0 \leq \theta \leq \theta_1 \\ aB_m \frac{\theta}{\theta_c}, & \theta_1 \leq \theta \leq \theta_c \\ aB_m \left[ \frac{\theta_f - (\theta - \theta_c)}{\theta_f} \right], & \theta_c \leq \theta \leq \theta_s \end{cases} \quad (3.53)$$

where  $a$  is a constant that accounts for the area of cross-section differential to provide a lower flux density in the stator core than the flux density in the stator poles in order to mitigate the acoustic noise in the SRM.

It may be noted that:

$$\theta_1 = \theta_c + \theta_f - \theta_s \quad (3.54)$$

$$\theta_2 = \theta_c - \theta_1 \quad (3.55)$$

$$\theta_3 = \theta_s - \theta_c \quad (3.56)$$

$$\theta_s = \theta_1 + \theta_2 + \theta_3 \quad (3.57)$$

$$B_0 = aB_m \left[ \frac{\theta_c + \theta_f - \theta_s}{\theta_c} \right] \quad (3.58)$$

The flux density in stator back iron segments 2 and 3 are derived as:

$$B_2 = a(B_7 + B_8 - B_9) \quad (3.59)$$

$$B_3 = a(B_7 - B_8 - B_9) \quad (3.60)$$

Note that from symmetry it can be shown that:

$$B_4 = B_1 \quad (3.61)$$

$$B_5 = B_2 \quad (3.62)$$

$$B_6 = B_3 \quad (3.63)$$

Even though  $B_2$  and  $B_3$  are similar, they are not identical. They have the same frequency, as given by:

$$f_2 = f_3 = \frac{\omega_m}{\theta_{rp}} = \frac{2\pi n_r}{(2\pi/P_r)} = n_r P_r \quad (3.64)$$

where  $n_r$  is the rotor speed in revolutions per second. The frequency of  $B_1$  is

$$f_1 = \frac{\omega_m}{\theta_s} = \frac{2\pi n_r}{2\pi/(qP_r)} = qP_r n_r = qf_2 \quad (3.65)$$

The frequency of the stator pole flux density is given by:

$$f_7 = \frac{\omega_m}{\theta_{rp}} = n_r P_r = f_2 \quad (3.66)$$

In general, for a machine with phases greater than or equal to 3, there are  $m$  distinct flux densities in the stator including its poles and back iron segments. While  $B_1$ ,  $B_7$ ,  $B_8$ , and  $B_9$  have unidirectional flux densities, they also have ripples that cause increased core losses.  $B_2$  and  $B_3$  are both bidirectional and hence cause much higher core losses.

### 3.3.11.2 Rotor

For an  $q$ -phase SRM with  $P_r$  rotor poles, each pair of rotor poles aligns with a pair of stator poles at a periodic interval given by:

$$\theta_{r1} = \frac{(q-1)}{q} \cdot \theta_{sp} = (q-1)\theta_s \quad (3.67)$$

where  $\theta_{sp}$  is the stator pole pitch given as:

$$\theta_{sp} = \frac{2\pi}{P_s} = \frac{\theta_s \cdot P_r}{2} \quad (3.68)$$

The rotor pole flux reverses every half a revolution of the rotor. Over a complete revolution, the rotor pole flux density waveform shown as  $B_{10}$  in [Figure 3.6](#) is a bipolar envelope with a frequency:

$$f_{10} = \frac{\omega_r}{2\pi} = n_r \quad (3.69)$$

But it has a carrier (ripple) content whose frequency is given by:

$$f_{10r} = 2qn_r = n_r P_s \quad (3.70)$$

Note that the rotor pole flux density peak is  $bB_m$  to account for the difference between stator and rotor pole cross-sectional area. Similarly, a factor  $c$  has been introduced for the rotor pole core section.

The flux density of the rotor back iron,  $B_{12}$ , is obtained by subtracting the rotor pole flux densities  $B_{10}$  and  $B_{11}$  and multiplying by  $c$ . Its fundamental frequency is  $n_r$  and with a minor loop flux reversal in one revolution. Note that  $B_{11}$  lags  $B_{10}$  by  $\theta_{rp}$ .

### 3.3.11.3 Core Losses

Very few procedures for core loss calculation have emerged and are very difficult to apply in practice,<sup>1,18,37</sup> but a method using Steimetz's equations for eddy current losses and Preisach's model for hysteresis losses is a viable approach using a physical

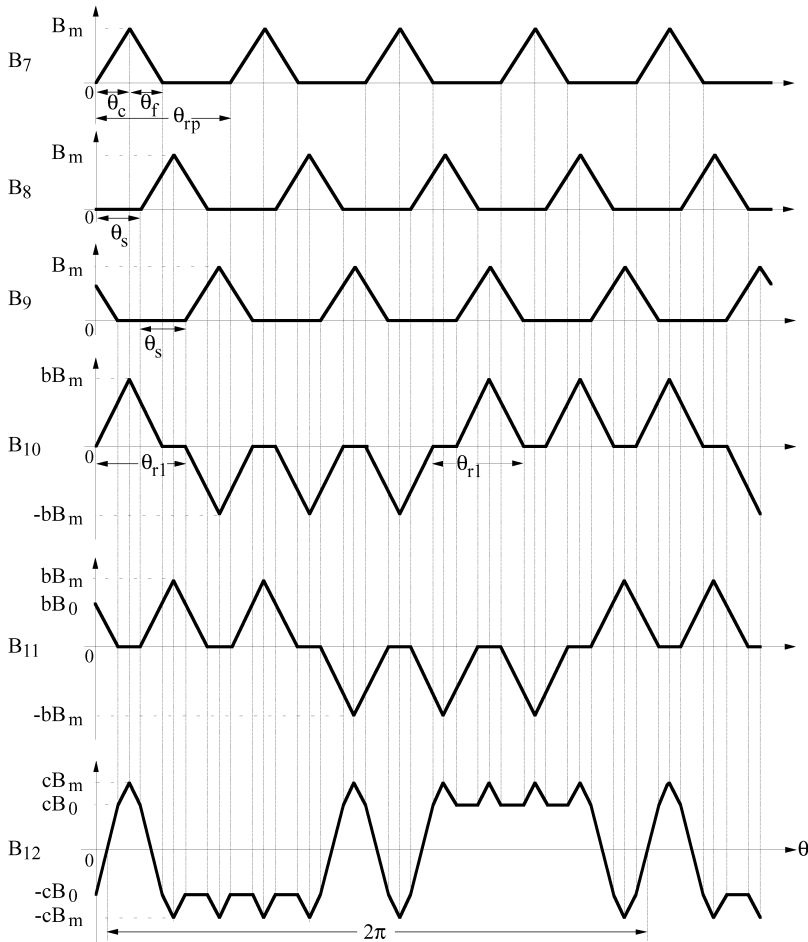


**FIGURE 3.6** Rotor flux density waveforms of the 6/4 SRM.

understanding of correlating the machine parameters and variables analytically to the losses. For the sake of simplicity, a simple procedure for core losses calculation is given below. Note that it may be used for an approximate estimation but not for applications where precision in predicting efficiency or thermal rise is a requirement. Then, finite element analysis (FEA) has to be resorted to.

#### 3.3.11.4 Calculation Procedure

The flux density waveforms are derived for each iron segment of the SRM as shown above. Their frequencies are also evaluated. The weights of the iron segments,  $W_k$ , are evaluated. The rms values of the flux densities,  $B_k$ , are evaluated for each section  $k$ .

From loss characteristics of the material, the loss coefficient  $P_{ck}$  considering the frequency of the flux densities  $f_k$  is evaluated. Then, total core losses is obtained as:

$$P_c = \sum_{n=1}^k P_{cn} W_n \quad (3.71)$$

### 3.4 DESIGN VERIFICATION

The design of an SRM using the output equation is to be verified from the flux linkages vs. current characteristics for both the aligned and unaligned positions. The flux linkages, and hence the values of inductances, are analytically obtained using the procedure discussed in Chapter 2. While the evaluation of aligned flux linkages can be very accurate, the same cannot be said for the unaligned values. The leakage fluxes and the path of the mutual flux complicate accurate estimation of the unaligned flux linkages and unaligned inductance. Finite element analysis techniques have been used to accurately estimate the unaligned flux linkages and inductances. The inaccuracy of the unaligned inductance introduces an error in the computation of  $k_2$  and in the output equation. Note that,

$$k_2 = 1 - \frac{L_u}{L_a^s} \quad (3.72)$$

The analytical technique to calculate the unaligned inductance may have a 50 to 100% error compared to its actual value, thereby introducing a 10 to 15% prediction error in the motor output. The dimensions of an SRM are given in [Table 3.1](#). The flux linkages vs. current characteristics are calculated and are shown in [Figure 3.7](#) for M19 steel. [Figure 3.8](#) displays the inductance at the aligned position as a function of the stator current.  $k_2$  and the ratio of the aligned to unaligned inductances vs. stator current are shown in [Figure 3.9](#). Such a wide variation of  $k_2$  affects the power

---

**TABLE 3.1**  
**Dimensions of an SRM**

Number of stator poles	6
Number of rotor poles	4
Stator outside diameter	19.4 cm
Rotor bore diameter	10.205 cm
Core length	5.076 cm
Air gap length	0.025 cm
Back iron width	1.25 cm
Number of turns/phase	536
Stator pole arc	0.418 rad
Rotor pole arc	0.628 rad

---

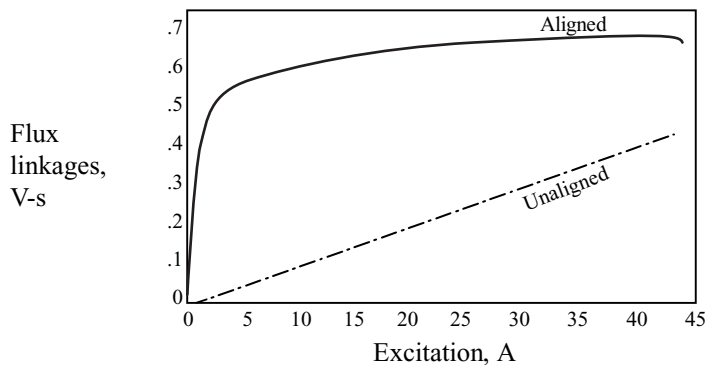


**FIGURE 3.7** Flux linkages vs. excitation current for designed SRM.

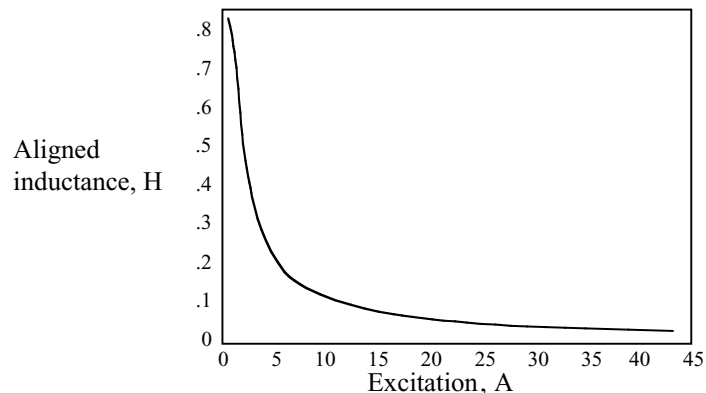


**FIGURE 3.8** Inductance at aligned position vs. stator excitation.

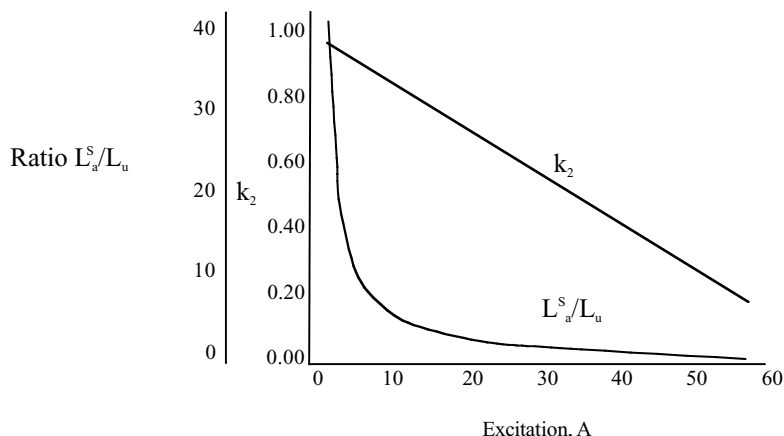


**FIGURE 3.9**  $k_2$  and ratio of aligned to unaligned inductance vs. stator current.

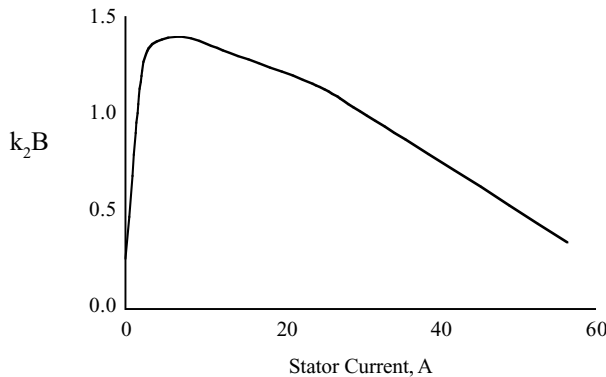


**FIGURE 3.10**  $k_2 B$  vs. stator current for designed SRM.

developed per ampere input if all other machine variables are constant, as shown in Figure 3.10, which relates the product of flux density and  $k_2$  vs. stator current. From the output equation, it could be realized that the power developed per ampere is proportional to the product of flux density and  $k_2$ . The design verification for inductances and torque are presented in Chapter 2 and Section 2.3.4.<sup>22,29,34</sup>

### 3.5 OPERATIONAL LIMIT

An increase in the stator current results in enhanced mechanical power output of the SRM, but the enhancement of mechanical energy is not uniform for all the operating points, particularly in the saturated region. At those points, the return diminishes, necessitating an operational limit on the maximum excitation current. The incremental mechanical energy per input current can be written as:

$$g_{mi} = \frac{\Delta W_m}{\Delta i} = \lambda_o + i_{so}(L_s - L_u) + \frac{\Delta i}{2}(L_s - L_u) \quad (3.73)$$

where  $\lambda_o$  is the intercept on the flux linkages axis from the saturated portion of the aligned position curve, shown in Figure 3.7;  $i_{so}$  is the operating stator current at which the incremental values are calculated;  $\Delta i$  denotes the incremental stator current;  $\Delta W_m$  is the resulting mechanical energy per stroke; and the inductances are given as the slopes of the characteristics shown in Figure 3.7. It can be seen that  $L_u > L_s$  in the present design example, and hence the incremental gain  $g_{mi}$ , decreases with increasing stator current. It can be proved that the maximum value of  $g_{mi}$  occurs when  $L_s = L_u$  and is given by:

$$\hat{g}_{mi} = \lambda_o \quad (3.74)$$

### 3.6 SELECTION OF NUMBER OF PHASES

The number of phases is usually determined by the following factors:

1. *Starting capability*: For example, a single-phase machine cannot start if the rotor and stator poles are aligned. It usually requires a permanent magnet on the stator at an intermediate position to the stator poles to keep the rotor poles at an unaligned position.
2. *Directional capability*: Whether the machine needs to run in one or two directions dictates the minimum number of stator phases. For example, a 4/6 machine is capable of only one direction of rotation, whereas a 6/4 is capable of two-direction rotation. The former case is a two-phase machine and the latter case is a three-phase SRM.
3. *Reliability*: A higher number of phases means higher reliability because a failure of one or more phases will still allow the running of the machine with the remaining healthy phases. This factor may be highly relevant in critical applications where safety of human beings or successful mission completion is the predominant factor. Examples are an aircraft generator,<sup>14</sup> a defense mission, actuators in nuclear power plants, and icebreakers for research missions.
4. *Cost*: A higher number of phases requires a corresponding number of converter phase units, their drivers, logic power supplies, and control units. All these are likely to impact the cost and packaging size and therefore have to be considered concurrently with the machine design.
5. *Power density*: A higher number of phases tends to give higher power density (say, three-phase compared to two-phase) in many applications.<sup>13</sup>
6. *Efficient high-speed operation*: Efficiency is enhanced by reducing the core loss at high speed by decreasing the number of stator phases and lowering the number of phase switchings per revolution.<sup>14</sup> Three phases is preferred over four phases in an aircraft starter/generator SRM because of its high-speed operation and the need to keep the size smaller, which requires a great reduction in losses to maintain thermal robustness.

### 3.7 SELECTION OF POLES

It is preferred to have the ratio between stator and rotor poles be a noninteger even though some integer values have been attempted. Based on this guideline, the stator and rotor pole combinations common in industrial designs are given below:

	Poles			
Stator	6	12	8	12
Rotor	4	8	6	10

The limiting factors in the poles selection are the number of converter power switches and their associated cost of gate drives and logic power supplies and the control

requirement in terms of small rise and fall times of the phase currents. Note that a 12/8 SRM is a three-phase machine with four stator poles per phase. If the maximum speed of the machine is  $\omega_{rm}$  rad/sec, then the stator frequency for a phase is

$$f_s = \left( \frac{\omega_{rm}}{2\pi} \right) P_r, \text{ Hz} \quad (3.75)$$

Therefore, increasing the rotor poles increases the stator frequency in proportion, resulting in higher core losses and more importantly greater conduction time to provide the rise and fall of the current compared to that of an SRM drive with a smaller number of rotor poles. The latter contributes to higher copper losses and to larger phase conduction overlaps. Due to increased switching frequency, the commutation torque ripple frequency is also increased, thus making its filtering easier. Further due to the overlapping phase conductances and their effective control, note that the commutation torque ripple magnitude could be attenuated very significantly, leading to a quiet operation. It should be understood that this comes at the expense of efficiency and simplicity in control. In many applications such as fans or pumps and even in off- and on-highway vehicle propulsion this may not be necessary, as they can stand higher commutation torque ripples, for example, as compared to position servos.

The cost of motor production rises with higher pole numbers due to increased winding insertion costs and terminal costs and most of all due to the increased cost of the converter, with its greater number of power switches and diodes and cost of packaging.

### 3.8 RATIO OF POLE ARC TO POLE PITCH

The pole arcs of the stator and rotor are important variables in the switched reluctance machine design. Guidelines for their selection in this section are developed<sup>36</sup> from the study of a particular machine whose details are given elsewhere.

The stator and rotor pole arcs are varied for a given current, and their effect on the average torque developed in the machine is studied to give a clearly identifiable range of practical pole arcs for the stator and rotor poles. A nondimensional parameter is derived to generalize the results by defining pole enclosure as the ratio of pole arc to pole pitch where pole pitch is the angle between two stator (or rotor, as the case may be) poles. The base current in the current example is 10A. Figure 3.11 shows the average torque vs. pole arc to pole pitch ratio, when the stator and rotor pole enclosures are equal, for three currents. From these, it is seen that a ratio of pole arc to pole pitch of 0.3 to 0.45 produces the highest average torque in the machine.

Figure 3.12 shows the average torque vs. stator pole enclosure for various values of rotor pole enclosures. This figure makes it clear that lower values of rotor pole enclosure are preferable. The most suitable stator pole enclosure lies in the range of 0.35 to 0.45. Consideration has to be given not only for the maximization of average torque but also to the circuit parameter, the aligned inductance,  $L_a$ . The aligned inductance determines the peak current possible in the motor and hence in the torque generation in the machine. Its sensitivity to the ratio of the rotor to stator

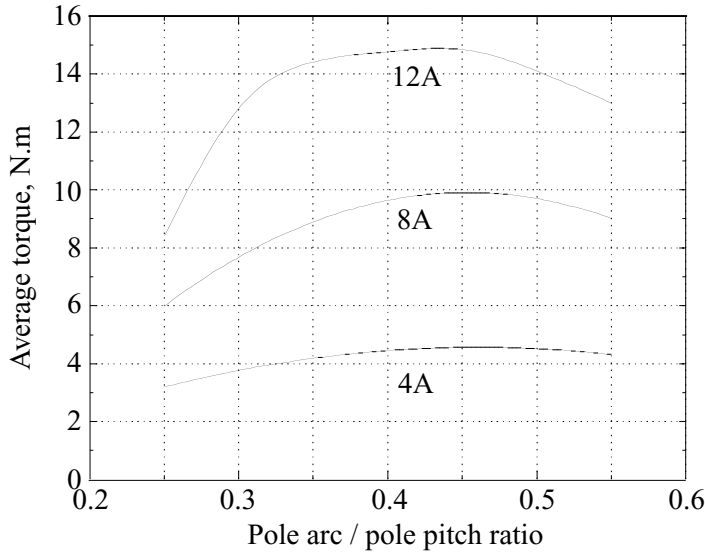


**FIGURE 3.11** Average torque vs. pole arc to pole pitch ratio.

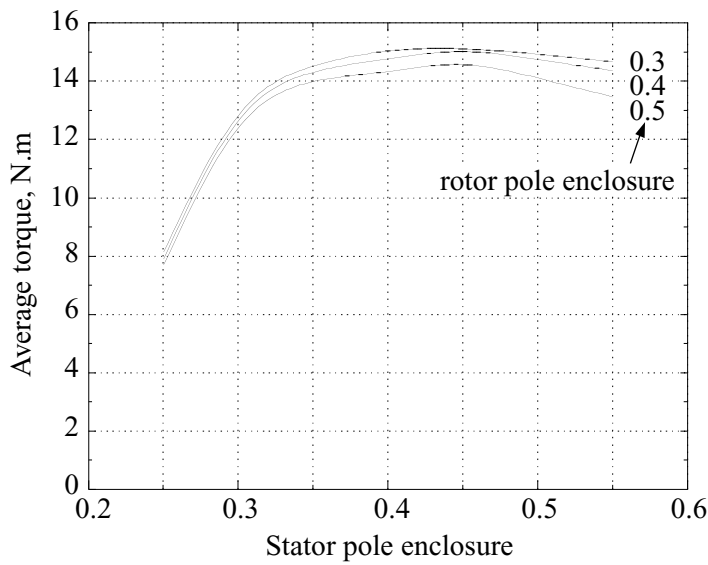


**FIGURE 3.12** Average torque vs. stator pole enclosure for various values of rotor pole enclosures.

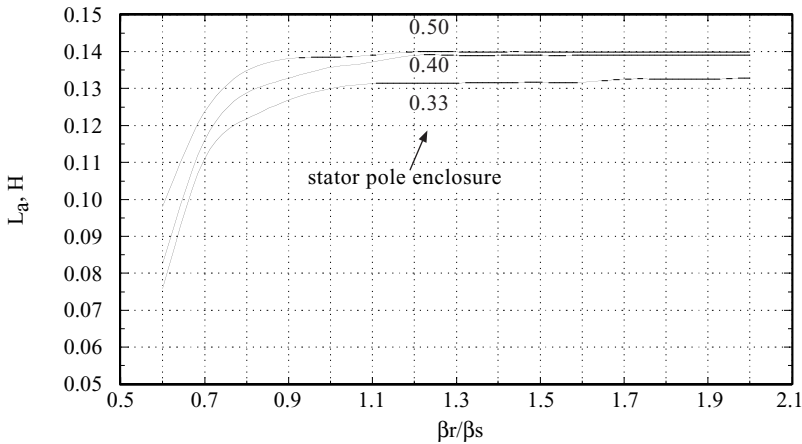


**FIGURE 3.13** Sensitivity of aligned inductance vs. rotor to stator pole arc ratio and for various values of stator pole enclosure.

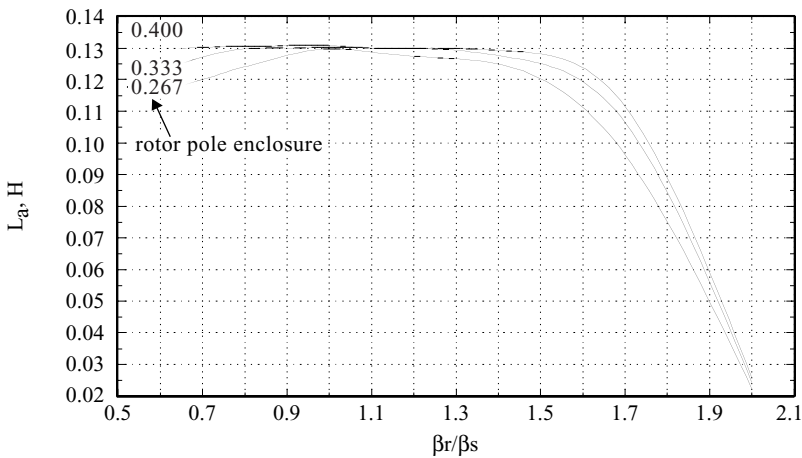


**FIGURE 3.14** Sensitivity of aligned inductance vs. rotor to stator pole arc ratio for various rotor pole enclosure factors.

pole arc as a function of various stator pole enclosures is shown in [Figure 3.13](#), and the sensitivity as a function of various rotor pole enclosures is shown in [Figure 3.14](#). The range of interest for the ratio of the rotor to stator pole arc is 0.5 to 1.5, and in this region the aligned inductance is insensitive to the rotor pole enclosure factor. The variation of the stator pole enclosure is very significant in the same region of interest. From these observations, it can be recommended that the rotor to stator pole arc ratio should be confined to 0.85 to 1.2, with only a variation of 15% in the aligned inductance value.

The guidelines that follow from these observations are that the rotor pole enclosure factor should be in the range of 0.3 to 0.45 and the stator pole enclosure factor in the range of 0.35 to 0.5. Any further increase in the rotor pole enclosure will end up in more iron volume and higher inertia. A higher value than the recommended value for the stator pole enclosure factor will reduce the space for stator windings and increase the stator weight, resulting in poorer utilization of the material.

### 3.9 SELECTION OF POLE ARCS

The primary selection criteria for the stator and rotor pole arcs are

1. Self-starting requirement
2. Shaping of static torque vs. rotor position characteristics

These requirements can be incorporated into the machine design by computing the minimum rotor and stator pole arcs to achieve self-starting (i.e., without any additional means to keep the rotor poles at an unaligned position with respect to a set of stator poles). In addition, an upper limit is placed on the overlap and rotor pole arcs. They are derived analytically to satisfy the aforementioned requirements. These design factors are derived as follows.

#### 3.9.1 MINIMUM ROTOR AND STATOR POLE ARCS TO ACHIEVE SELF-STARTING

Let the mechanical rotor pole pitch be defined as:

$$\theta_{rp} = \frac{2\pi}{P_r}, \text{ rad} \quad (3.76)$$

The phase shift between successive stator phase inductances or flux linkages is given as:

$$\theta_{rs} = \left( \frac{2\pi}{P_r} \right) \cdot \frac{1}{q} = \frac{\theta_{rp}}{q}, \text{ rad} \quad (3.77)$$

where

$$q = \frac{P_s}{2} \quad (3.78)$$

in simple structures (i.e., with one tooth per pole).

Consider the inductance profiles of successive phases shown in [Figure 3.15](#). From the figure, it can be seen that for the continuous starting torque requirement the overlap angle denoted as  $\theta_o$  should be less than or equal to zero; that is,

$$\theta_o \leq 0 \quad (3.79)$$

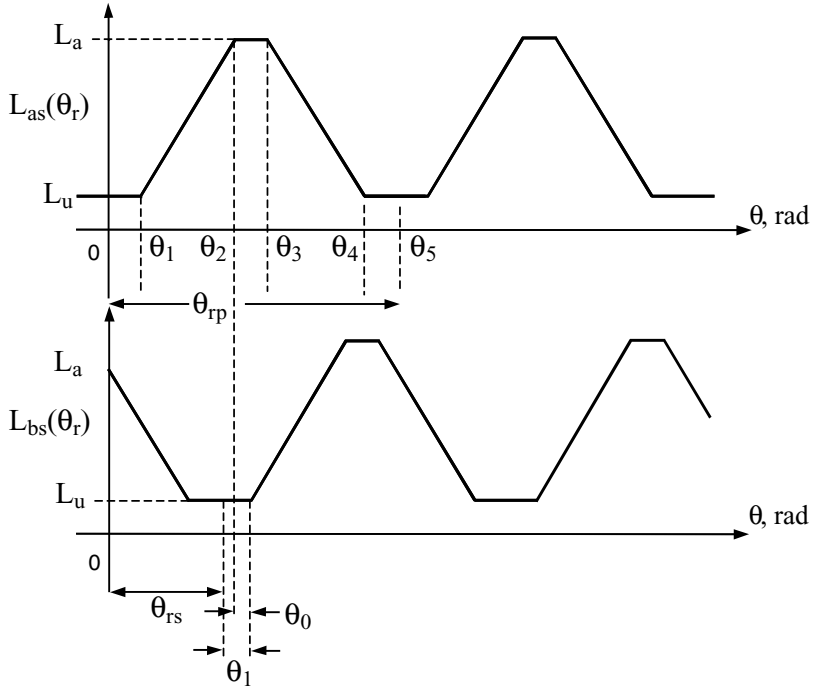


**FIGURE 3.15** Stator inductance vs. rotor position for two successive stator phases.

Consider the minimum condition of  $\theta_0$  being equal to zero and write  $\theta_o$  in terms of other angles as:

$$\theta_0 = \theta_{rs} + \theta_1 - \theta_2 = \theta_{rs} - (\theta_2 - \theta_1) = 0 \quad (3.80)$$

from which the minimum of  $(\theta_2 - \theta_1)$  is obtained as:

$$(\theta_2 - \theta_1) = \theta_{rs} = \frac{\theta_{rs}}{q} = \frac{2\pi}{qP_r} = \frac{4\pi}{P_s P_r} \quad (3.81)$$

where  $P_s$  and  $P_r$  are stator and rotor pole numbers, respectively. The angles on the left-hand side of Eq. (3.81) could be written in terms of stator and rotor pole arcs as:

$$\theta_1 = \frac{1}{2}[\theta_{rp} - (\beta_s + \beta_r)] \quad (3.82)$$

$$\theta_2 = \theta_1 + \beta_s \quad (3.83)$$

from which  $(\theta_2 - \theta_1)$  is written as:

$$\theta_2 - \theta_1 = \beta_s \quad (3.84)$$

Combining Eqs (3.81) and (3.84), the minimum pole arc is given by:<sup>2</sup>

$$\min [\beta_s] = \frac{4\pi}{P_s P_r} \quad (3.85)$$

assuming linear magnetic characteristics.

### 3.9.2 OVERLAP ANGLE ( $\theta_0$ ) LIMITS

The limits on overlap angle for self-starting are

$$\left. \begin{aligned} \min [\theta_0] &= 0 \\ \max [\theta_0] &= -\frac{2\pi}{P_r} \left( \frac{1}{2} - \frac{1}{q} \right) \end{aligned} \right\} \quad (3.86)$$

Hence,

$$\frac{2\pi}{P_r} \left( \frac{1}{q} - \frac{1}{2} \right) \leq \theta_0 \leq 0 \quad (3.87)$$

and  $\theta_0$  is derived as follows:

$$\begin{aligned} \theta_0 &= \theta_{rs} - (\theta_2 - \theta_1) = \frac{\theta_{rp}}{q} - (\theta_2 - \theta_1)|_{\max} = \frac{2\pi}{qP_r} - \frac{2\pi}{2P_r} \\ &= \frac{2\pi}{qP_r} \left( 1 - \frac{q}{2} \right) = \theta_{rs} \left( 1 - \frac{q}{2} \right); \quad \text{for } q > 2 \end{aligned} \quad (3.88)$$

where negative values of  $\theta_0$  mean overlap and positive values signify nonoverlap. Note that:

$$\theta_3 = \theta_2 + (\beta_r - \beta_s) \quad (3.89)$$

from which,

$$(\beta_r - \beta_s) = (\theta_3 - \theta_2) \quad (3.90)$$

From the figure, it can be seen that  $(\theta_3 - \theta_2)$  has to be greater than or equal to zero, thus making Eq. (3.90):

$$(\beta_r - \beta_s) \geq 0 \quad (3.91)$$

This equation signifies that the rotor pole arc has to be greater than or at least equal to the stator pole arc, symbolically represented as:

$$\beta_r \geq \beta_s \quad (3.92)$$

Equations (3.85) and (3.90) give the minimum stator and rotor pole arcs, respectively, for the self-starting requirement, with Eq. (3.87) giving the minimum stator pole pairs and hence phases equal to or greater than two. The next design issue to be addressed is the upper limit on the rotor pole arc.

### 3.9.3 UPPER LIMIT ON $\beta_r$

When the rotor pole arc is greater than that of the stator pole arc, there is no tangible benefit in terms of torque production on the SRM if ideal current turn-off is assumed. Further, this adds to the lamination iron volume and weight. Therefore, many of the practical designs have rotor pole arcs slightly greater or almost equal to stator pole arcs in the SRMs.

Ideal current turn-off (i.e., zero time for current to go to zero from an operating value) is impossible with SRMs, as they have significant inductance. In fact, the largest inductance is encountered at turn-off, where it is most likely at the completely aligned position of the stator and rotor poles where the inductance is at its maximum. Therefore, it becomes necessary to turn off the currents even before they reach the completely aligned position. Hence, to utilize the torque-producing positive inductance slope region completely, it is important that the current be maintained in the region. If the current continues beyond the positive slope region, then a negative torque is produced in SRMs with equal stator and rotor pole arcs, because there is no zero slope inductance region, as seen from [Figure 3.16](#).

Due to the negative torque generation, the average  $T_{av}$  per stator phase is reduced. To eliminate the negative torque generation, phase current must be made zero beyond  $\theta_2$ . That requires the current fall angle calculation and use of that information to advance the current commutation. Such a step involves an on-line fall angle ( $\theta_f$ ) calculator, which is dependent on motor parameters, current, voltage, and speed, thus making it difficult to calculate with great precision. Even if it is precisely computed and used, it must be noted that the advanced turn-off forces a reduction in the average torque, as it is not possible to maintain a constant peak current in the positive inductance slope region. All these factors contribute to reduced average torque generation compared to the peak capacity of the machine even if a peak current had been maintained.

Consider the case when the rotor pole arc is greater than the stator pole arc, overcoming all the disadvantages discussed above due to equal stator and rotor pole arcs. [Figure 3.17](#) shows the torque generation features of the SRM with  $\beta_r > \beta_s$  assuming linear magnetic characteristics as in the previous case; only one rotor pole pitch is considered for our illustration. A number of observations could be made from this figure:

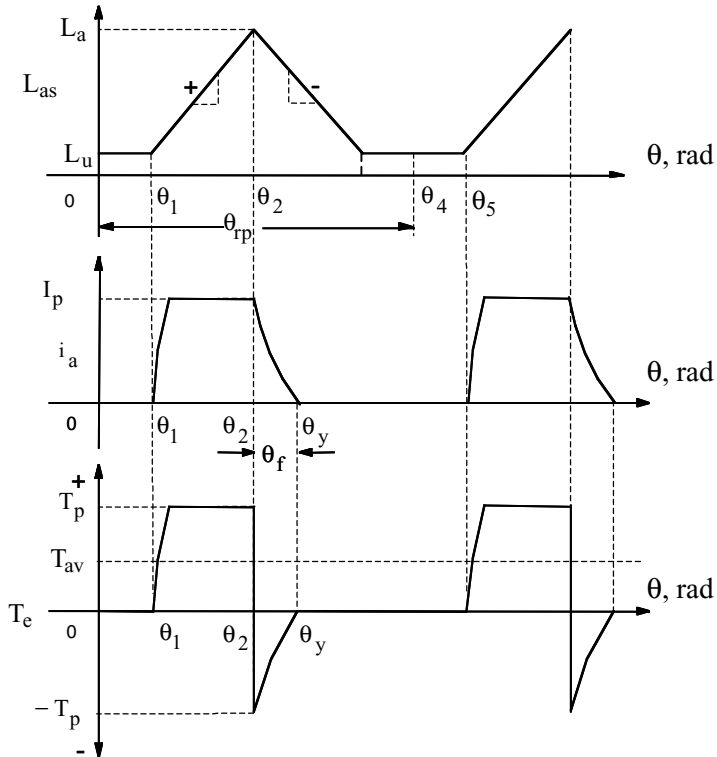


**FIGURE 3.16** Effect of equal stator and rotor pole arcs on torque generation.

1. Negative torque generation can be avoided entirely with a dead zone (i.e.,  $\theta_3$  to  $\theta_2$ ), given by  $(\beta_r - \beta_s)$ ; where no torque is produced even when there is current. This increases the average torque contribution of a phase winding as opposed to the previous case with  $\beta_r = \beta_s$ .
2. Precise calculation of fall angle  $\theta_f$  is not necessary for every operating condition in the control of the machine once  $\beta_r$  is designed to provide the fall angle for the maximum operating condition, which is derived later in the text. Because precise computation of the fall angle is not required with these designs, note that the computation burden for control is very much reduced. This enhances the operational simplicity of the drive.
3. By advancing the turn-on angle of the current, peak current could be maintained during the entire positive torque-producing region with  $\beta_r > \beta_s$ . This will increase the average torque produced in the machine much more than that of an SRM with equal stator and rotor pole arcs. This is an immense advantage both in steady-state and transient operating conditions. The effect is illustrated in [Figure 3.18](#), in which the torque-producing regions and phase peak currents are assumed to be equal in each case. Turn-on and turn-off are advanced in both cases, so as not to produce any negative

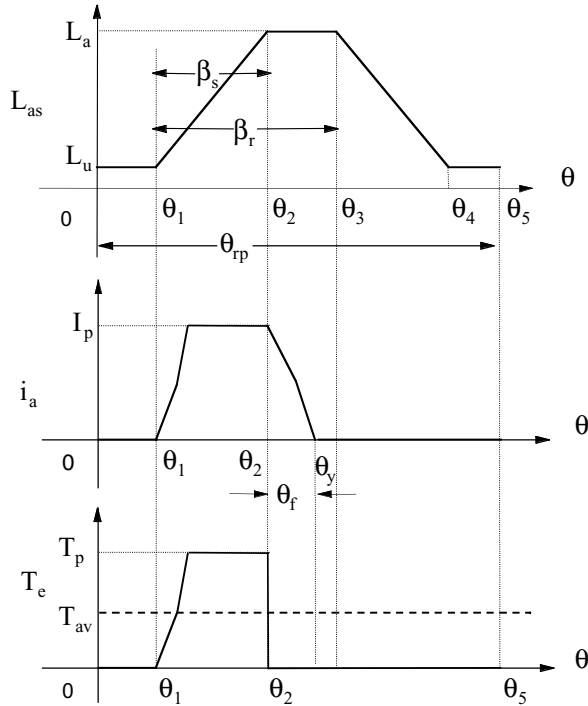


**FIGURE 3.17** Effect of rotor pole arc greater than the stator pole arc on torque generation.

torque. Even though the torque produced in case 2 (i.e., with  $\beta_r > \beta_s$ ) is greater than in case 1 with  $\beta_r = \beta_s$ , note that the rms currents are different, with the rms current in 2 being higher than that of case 1. If a different criterion, such as maximum torque per unit current, is required to be met, then even in case 2, advance turn-off has to be initiated to minimize the non-torque-producing component (or what is known as reactive component) of the current.

4. Elimination of negative torque generation reduces the torque ripples and hence the audible noise generation.

Given all these factors, it can be seen that it is very advantageous to have the rotor pole arc greater than the stator pole arc. Then, the question that needs to be addressed in design is by how much the rotor pole arc has to be greater than the stator pole arc.

The upper limit on rotor pole arc is

$$\beta_r = \beta_s + \theta_{fr}$$

where  $\theta_{fr}$  is the current fall angle at the rated operating conditions. Such a condition allows maximum torque production but does not optimize efficiency and maximum

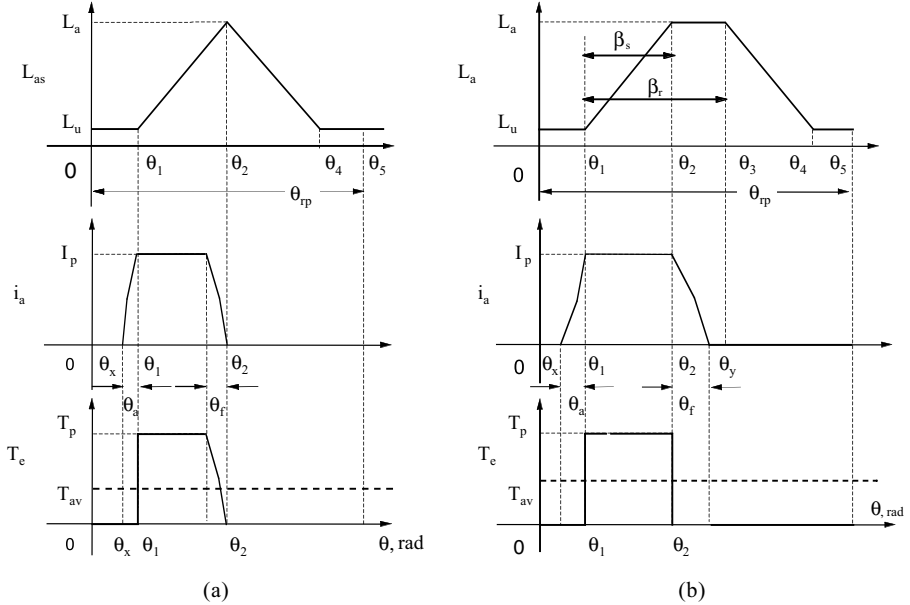


**FIGURE 3.18** Effect of pole arcs on torque generation for same peak currents. (a)  $\beta_r = \beta_s$ ; (b)  $\beta_r > \beta_s.z$

torque per unit rms current. The current fall angle has to be for the rated condition, implying that the stator phase peak current, speed, and applied voltage are all at rated (nominal values) values. Based on linear magnetic characteristics, the current fall angle, at the rated operating point,  $\theta_{fr}$ , is computed as follows. It is assumed that, when the current has to be commutated, a negative voltage with a magnitude of dc link voltage  $V_{dc}$  is applied at the beginning of commutation where current is  $I_p$  and the inductance during the commutation is equal to the aligned inductance,  $L_a$ . The time taken for the current to fall to zero,  $T_f$ , is derived in Eq. (3.37) as:

$$T_f = \tau_a \ln \left[ 1 + \frac{R_s I_p}{V_{dc}} \right] \quad (3.93)$$

Note that the fall angle at rated speed,  $\omega_{mr}$ , is given as:

$$\theta_{fr} = \omega_{mr} T_f = [\omega_{mr} \tau_a] \ln \left\{ 1 + \frac{R_s I_p}{V_{dc}} \right\} \quad (3.94)$$

The product  $(\omega_{mr} \tau_a)$  is the tangent of the impedance angle of the machine at the aligned condition for the current  $I_p$ , hence it can be represented as:

$$\tan(\gamma) = \omega_{mr} \tau_a = \frac{\omega_{mr} L_a}{R_s} = \frac{x_a}{R_s} \quad (3.95)$$

where  $\gamma$  is the impedance angle at the aligned condition. If  $I_b$  and  $V_b$  are the rated current and voltage, respectively, then the normalized armature resistance is given by:

$$R_{sn} = \frac{R_s I_b}{V_b} = \frac{R_s}{Z_b} \quad (3.96)$$

where the base impedance  $Z_b$  is

$$Z_b = \frac{V_b}{I_b} \quad (3.97)$$

Substituting the above two expressions into the current fall angle, the following is obtained:

$$\theta_{fr} = [\tan \gamma] \ln \left[ 1 + \frac{R_{sn} I_{pn}}{V_{dcn}} \right], \text{ rad} \quad (3.98)$$

where the last subscript  $n$  indicates normalized values of the parameters and variables. A set of normalized curves in the form of  $\theta_{fr}$  vs.  $(R_{sn} I_{pn} / V_{dcn})$  for various impedance angles,  $\gamma$ , is shown in [Figure 3.19](#) for design use.

The range of the rotor pole arc then is given by:

$$\beta_s \leq \beta_r \leq (\beta_s + \theta_{fr}) \quad (3.99)$$

where  $\theta_{fr}$  is given by the previous expression, Eq. (3.98), in terms of machine constants.

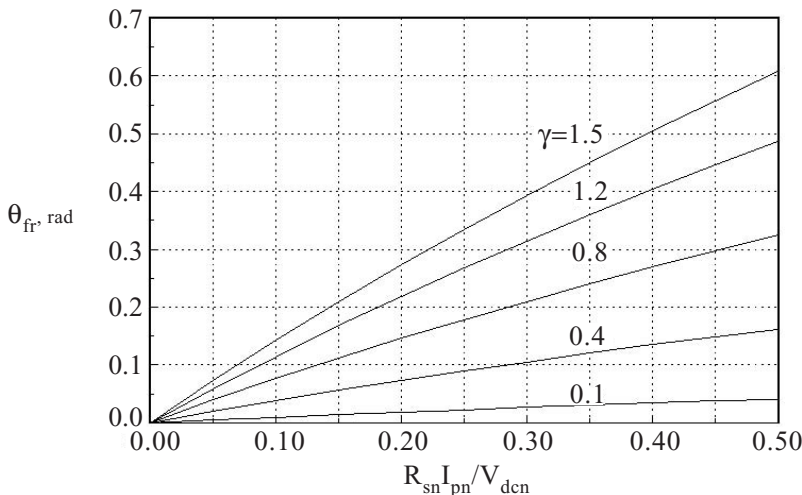


**FIGURE 3.19** Current fall angle at rated speed vs.  $(R_{sn} I_{pn} / V_{dcn})$  for various machine impedance angles  $\gamma$ .

Instances may arise when  $\theta_{fr}$  could be as much as 50% of the stator pole arc or even higher. In such cases, it is not advantageous (from the viewpoint of increasing iron volume and weight in the rotor) to keep increasing the rotor pole arc to satisfy the elimination of negative torque generation. The other alternative is afforded by the control of advanced current commutation in the machine phases,<sup>4,5,13,17,23</sup> even though it is likely to reduce the average torque as pointed out earlier. Then the advance turn-off angle,  $\theta_f$ , has to be calculated for every operating point to initiate the current commutation in the machine phases.

### 3.9.4 COMPUTATION OF TURN-OFF ANGLE

An approximate procedure to calculate the advance turn-off angles is derived with the following assumptions:

1. The SRM has linear magnetic characteristics.
2.  $\beta_r = \beta_s$ , though other cases when  $\beta_r > \beta_s$  are very well covered by the derivation with some simple modifications.
3. The current becomes zero just at the instance where the inductance slope changes from positive to negative, thus preventing negative torque generation in the motoring mode.

Consider the machine phase inductance and current waveform where, at  $\theta_y$ , the commutation is initiated as shown in Figure 3.20. Since commutation is attempted when there is induced emf, the current fall angle is very much different from the previous calculation. Let the inductance slope,  $m_1$ , be given by:

$$m_1 = \frac{dL}{d\theta} = \frac{L_a - L_u}{\theta_2 - \theta_1} \quad (3.100)$$

at the desired current operation (say, at an average value of  $I$ ) and the difference between the peak and average currents is considered to be very small. The current commutation is initiated at  $\theta = \theta_y$  when  $i_{as} = I_p$  with a voltage of  $-V_{dc}$  across the machine winding. The corresponding operational mode is given by the differential equation,

$$R_s i + L(\theta) \frac{di}{dt} + i \frac{dL(\theta)}{dt} = -V_{dc} \quad (3.101)$$

with

$$i(\theta_y) = I_p \quad (3.102)$$

Note that

$$\theta = \omega_m t \quad (3.103)$$

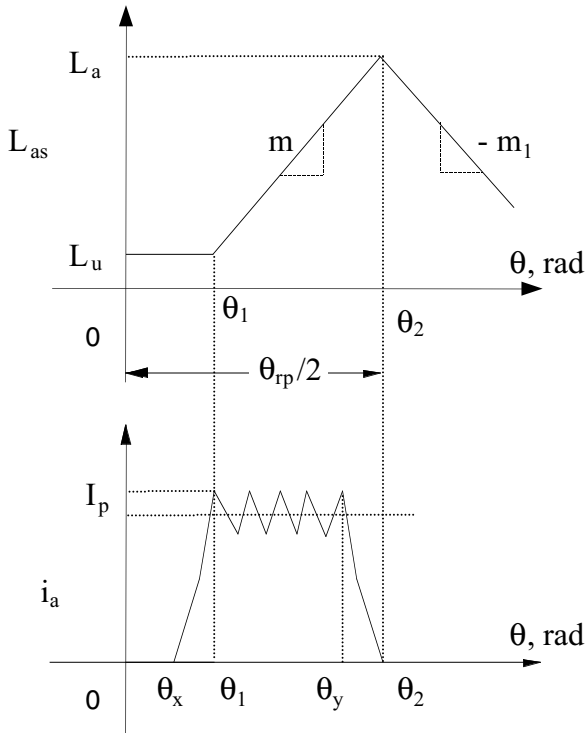


**FIGURE 3.20** Inductance profile and current waveform with advance turn-on and turn-off in an SRM phase winding.

where  $\omega_m$  is the rotor speed. Combining Eqs. (3.100), (3.101), and (3.103),

$$(R_s + \omega_m m_1)i + L(\theta_r) \frac{di}{dt} = -V_{dc} \quad (3.104)$$

where

$$m_1 = \frac{dL(\theta)}{d\theta} \quad (3.105)$$

as given by Eq. (3.100). It is assumed that the current goes to zero in  $t_f$  seconds from the instant of commutation initiation and that time is divided into  $n$  equal intervals of  $\Delta t$  where  $\Delta t$  is the unknown while  $n$  can be arbitrarily chosen. Further, it is assumed that to solve the time-varying Equation (3.101) that inductances for  $\Delta t$  remain constant and speed is constant throughout the commutation time. The general solution of Eq. (3.101) with the initial current  $I(0)$  is

$$i(t) = I(0)e^{-t/\tau} - \frac{V_{dc}}{R_{eq}}(1 - e^{-t/\tau}) \quad (3.106)$$

where

$$\tau = \frac{L(\theta)}{R_{eq}} \quad (3.107)$$

$$R_{eq} = R_s + \omega_m m_1 \quad (3.108)$$

and  $I(0)$  is the initial current for each of the  $\Delta t$  interval times. The currents for various  $\Delta t$  intervals are obtained from Eq. (3.106):

$$i(\Delta t) = I_p e^{-\Delta t/\tau} - \frac{V_{dc}}{R_{eq}} (1 - e^{-\Delta t/\tau}) = e^{-\Delta t/\tau} \left[ I_p + \frac{V_{dc}}{R_{eq}} \right] - \frac{V_{dc}}{R_{eq}} \quad (3.109)$$

$$\begin{aligned} i(2\Delta t) &= e^{-\Delta t/\tau_1} \left[ i(\Delta t) + \frac{V_{dc}}{R_{eq}} \right] - \frac{V_{dc}}{R_{eq}} \\ &= e^{-\Delta t/\tau_1} \left[ e^{-\Delta t/\tau} I_p + e^{-\Delta t/\tau} \frac{V_{dc}}{R_{eq}} + \frac{V_{dc}}{R_{eq}} \right] - \frac{V_{dc}}{R_{eq}} \\ &= e^{-\Delta t \left\{ \frac{1}{\tau} + \frac{1}{\tau_1} \right\}} \left[ I_p + \frac{V_{dc}}{R_{eq}} \right] + \frac{V_{dc}}{R_{eq}} [e^{-\Delta t/\tau_1} - 1] \end{aligned} \quad (3.110)$$

$$i(3\Delta t) = e^{-\Delta t \left\{ \frac{1}{\tau} + \frac{1}{\tau_1} + \frac{1}{\tau_2} \right\}} \left[ I_p + \frac{V_{dc}}{R_{eq}} \right] + \frac{V_{dc}}{R_{eq}} \left[ e^{-\Delta t \left\{ \frac{1}{\tau_1} + \frac{1}{\tau_2} \right\}} - 1 \right] \quad (3.111)$$

Similarly,

$$i(n\Delta t) = i(t_f) = e^{-\Delta t \left\{ \frac{1}{\tau} + \frac{1}{\tau_1} + \frac{1}{\tau_2} + \dots + \frac{1}{\tau_{n-1}} \right\}} \left[ I_p + \frac{V_{dc}}{R_{eq}} \right] + \frac{V_{dc}}{R_{eq}} \left[ e^{-\Delta t \left\{ \frac{1}{\tau_1} + \frac{1}{\tau_2} + \dots + \frac{1}{\tau_{n-1}} \right\}} - 1 \right] \quad (3.112)$$

where

$$\left. \begin{aligned} \tau &= \frac{L(\theta_y)}{R_{eq}} = \frac{L(t_o)}{R_{eq}} \\ \tau_1 &= \frac{L(\theta_y + \Delta\theta)}{R_{eq}} = \frac{L(t_o + \Delta t)}{R_{eq}} \\ &\dots \\ \tau_{n-1} &= \frac{L(t_o + \overline{n-1}\Delta t)}{R_{eq}} \end{aligned} \right\} \quad (3.113)$$

Expanding  $\tau_1$  and using the value of  $\tau$ ,

$$\begin{aligned}\tau_1 &= \frac{L(\theta_y) + m_1 \Delta\theta}{R_{eq}} = \tau + \frac{m_1}{R_{eq}} \Delta\theta = \tau + \frac{m_1}{R_{eq}} \omega_m \Delta t \\ &= \tau + \left( \frac{R_{eq} - R_s}{R_{eq}} \right) \Delta t = \tau + \left( 1 - \frac{R_s}{R_{eq}} \right) \Delta t = \tau + c_2 \Delta t\end{aligned}\quad (3.114)$$

where

$$c_2 = 1 - \frac{R_s}{R_{eq}} \quad (3.115)$$

Similarly,

$$\tau_2 = \tau + c_2[2\Delta t] \quad (3.116)$$

...

$$\tau_{n-1} = \tau + c_2[\overline{n-1} \Delta t] \quad (3.117)$$

To compute Eq. (3.112), the inverses of the time constants are required, and they are approximated by:

$$\frac{1}{\tau_1} = \frac{1}{\tau + c_2 \Delta t} = \frac{1}{\tau \left( 1 + c_2 \frac{\Delta t}{\tau} \right)} \quad (3.118)$$

It must be noted that  $c_2$  is close to unity; hence, with  $\Delta t$  being very small, it is seen that:

$$c_2 \frac{\Delta t}{\tau} \ll 1 \quad (3.119)$$

This gives way to the binomial expansion of Eq. (3.118), resulting in:

$$\frac{1}{\tau_1} = \frac{1}{\tau} \left[ 1 - c_2 \frac{\Delta t}{\tau} \right] \quad (3.120)$$

Similarly,

$$\frac{1}{\tau_2} = \frac{1}{\tau} \left[ 1 - c_2 \frac{2\Delta t}{\tau} \right] \quad (3.121)$$

...

$$\frac{1}{\tau_{n-1}} = \frac{1}{\tau} \left[ 1 - c_2 \frac{\overline{n-1} \Delta t}{\tau} \right] \quad (3.122)$$

Substituting Eqs. (3.120), (3.121), and (3.122) into Eq. (3.112) results in:

$$i(n\Delta t) = i(t_f) = 0 = \left[ e^{c_3\Delta t} \cdot e^{c_4\Delta t^2} \right] \left[ I_p + \frac{V_{dc}}{R_{eq}} \right] + e^{c_5\Delta t} \cdot e^{c_4\Delta t^2} \left[ \frac{V_{dc}}{R_{eq}} \right] - \frac{V_{dc}}{R_{eq}} \quad (3.123)$$

where

$$c_3 = -\frac{n}{\tau} \quad (3.124)$$

$$c_4 = \frac{c_2}{\tau^2} \left[ \frac{n(n+1)}{2} - 1 \right] \quad (3.125)$$

$$c_5 = \frac{1-n}{\tau} \quad (3.126)$$

In Eq. (3.123), the only unknown is  $\Delta t$  which could be obtained either by an iterative solution or by judicious approximation that may be sufficient for practical application. Resorting to approximation and expanding the exponentials up to second-order terms only, the following is obtained:

$$\Delta t \left\{ \frac{1}{\tau} + c_3 \right\} + \frac{\Delta t^2}{2} \left\{ \frac{1}{\tau^2} - c_3^2 \right\} \equiv -[1 + R_{eqn}] \quad (3.127)$$

where

$$R_{eqn} = \frac{I_p R_{eq}}{V_{dc}} \quad (3.128)$$

Substituting for  $c_3$  from Eq. (3.124) into Eq. (3.127) solving for  $\Delta t$ , the current advance commutation time is obtained as:

$$t_f = n\Delta t \equiv -n(n-1)\tau + n\tau\sqrt{(n-1)^2 + 2(n^2-1)(1+R_{eqn})} \quad (3.129)$$

from which the fall or advance commutation angle is obtained as:

$$\theta_f = t_f \omega_m, \text{ rad} \quad (3.130)$$

### 3.9.5 SELECTION OF POLE BASE

Shaping of torque vs. rotor position characteristics is possible<sup>10,11,32</sup> with different widths at the tip and base of the stator poles, as shown in [Figure 3.21](#). It is found that variation of such widths on the rotor poles has very little effect on torque shape characteristics.<sup>32</sup> Increasing the stator pole width at the base has the effect of increasing

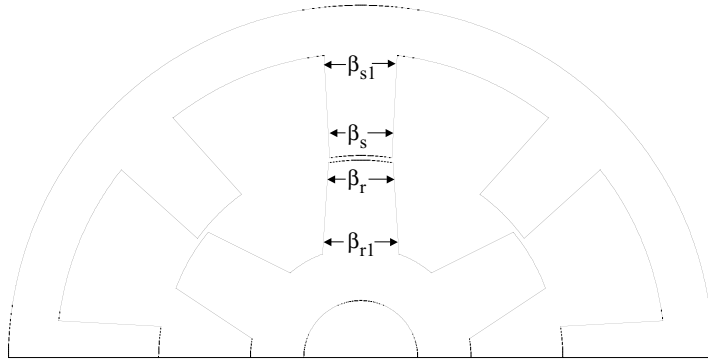


**FIGURE 3.21** Pole base and arc shaping of the SRM.

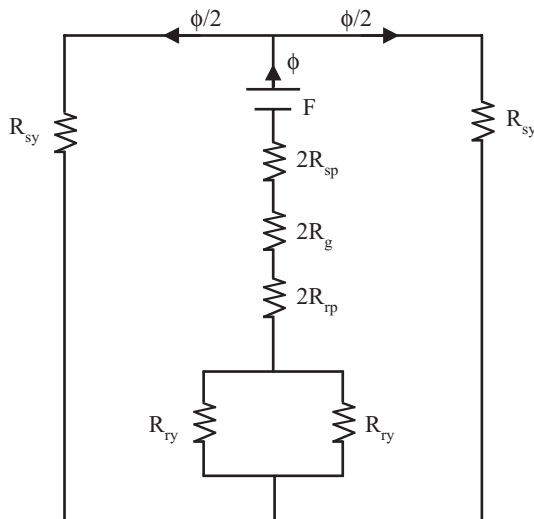


**FIGURE 3.22** Magnetic equivalent circuit of the SRM assuming half symmetry.

the overall area of the cross section, leading to a decrease in the reluctance of the stator pole sections. Considering the magnetic equivalent circuit and assuming half-symmetry, as shown in Figure 3.22, the effect of said variation may be inferred as follows.  $F$  is the mmf,  $R_{sp}$  is the stator pole reluctance,  $R_g$  is the air gap reluctance,  $R_{rp}$  is the rotor pole reluctance,  $R_{ry}$  is the rotor core reluctance per side, and  $R_{sy}$  is the stator back iron reluctance per side. As  $R_{sp}$  decreases for increasing base width of the stator poles, the equivalent circuit reluctance decreases and allows an increased flux to flow in the circuit. This increases the torque while at the same time increasing the phase inductance. These effects are particularly more pronounced near the aligned position where the stator pole tends to be saturated than at the unaligned position where the magnetic circuit is in the linear range of operation. Even though the flux increases, the flux density decreases due to the increased area of the cross

section of the stator pole base. This in turn increases the permeability of the steel laminations, which further reduces the reluctance and increases flux and consequently generates higher torque.

For example, the effect of varying the pole base width in comparison to constant pole width is illustrated with the following SRM prototype:

Poles	
Stator	8
Rotor	6
Pole arcs	
Stator	18°
Rotor	22°
Air gap	0.3 mm
Interpolair air gap	22 mm
Bore diameter	100 mm
Stator outer diameter	190 mm
Shaft diameter	28 mm
Back iron thickness	12.5 mm
Core length	114 mm
Turns/phase	144
Wire cross section area	1 mm <sup>2</sup>
Coil fill factor	0.7
Coil cross section area	103 mm <sup>2</sup>
Peak current	12A (1 p.u.)
Voltage	500V (1 p.u.)
Lamination material	M19 steel

The stator pole base is varied from 1 to 3.5 times the pole arc at the tip, and results obtained from using finite element software are shown in [Figure 3.23](#)<sup>32</sup> for phase inductance and torque vs. rotor position, respectively. Note the enhancement of torque near the aligned position due to an increase in the inductances. The current is maintained at 1 p.u. (i.e., 12A) for this simulation throughout. The shaping of the torque vs. rotor position to make it almost rectangular has the benefit of reducing the effects of commutation torque ripple to obtain an ideal and continuous torque as in other machines. The demand on the torque-smoothing controller and hence on the current controllers is minimized by this torque shaping. Further, for many low-performance applications, any additional torque smoothing other than the torque shaping provided by variation of pole arc base may not be necessary. The torque vs. rotor position has been made a half-wave sinusoid to enable ripple-free operation; such a drive has been developed for machine tool applications, for which pole base shaping was crucial.<sup>10,11</sup> In recent times, efforts at current and hence torque control are becoming predominant over approaches using machine design. A hybrid method of both pole shaping and torque control using modern techniques will enhance the SRM drive system performance to suit almost all high performance applications.

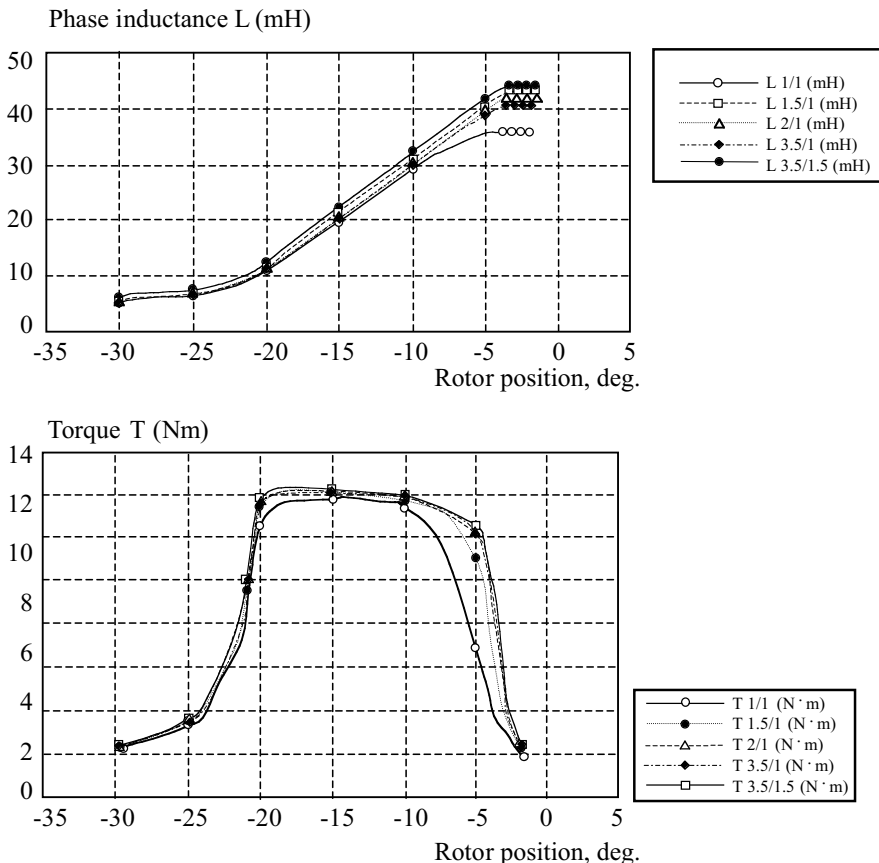


**FIGURE 3.23** Machine characteristics for stator pole base variation from 1 to 3.5 times the pole arcs.

### 3.10 EFFECT OF AIR GAP ON TORQUE

The effect of air gap length on the electromagnetic torque is derived in the following to assess its importance and to explore the influence of other determining variables on torque generation.

Consider a linear magnetic characteristic of the machine. The electromagnetic torque for a pair of poles then is given by:

$$T_e = \frac{1}{2} i^2 \frac{dL}{d\theta} = \frac{1}{2} i^2 \frac{L_a - L_u}{\beta_s} = \frac{1}{2} i^2 \frac{L_a}{\beta_s} \left( 1 - \frac{L_u}{L_a} \right) \quad (3.131)$$

It is usual to find the range of the ratio between unaligned and aligned inductance as:

$$0.07 < \frac{L_u}{L_a} < 0.18 \quad (3.132)$$

Hence, treating this factor as a constant,  $k_1$ , the torque is given by:

$$T_e = \frac{1}{2} k_1 i^2 \frac{L_a}{\beta_s} \quad (3.133)$$

where the aligned inductance is expressed in terms of the key machine dimensions and number of turns per phase as:

$$L_a = \frac{T_{ph}^2}{R_g} \quad (3.134)$$

where  $T_{ph}$  is the number of turns per phase and  $R_g$  is the reluctance of the air gap given by:

$$R_g = \frac{2\ell_g}{\frac{D}{2} \times L \times \beta_s \times \mu_o} \quad (3.135)$$

where  $\ell_g$  is the air gap length,  $D$  is the bore diameter, and  $L$  is the stack length. Combining Eqs. (3.133), (3.134), and (3.135), the electromagnetic torque is derived as:

$$T_e = \left[ \frac{1}{8} k_1 \mu_o \right] \left[ \frac{T_{ph}^2 D L}{\ell_g} \right] i^2 \quad (3.136)$$

It can be observed from Eq. (3.136) that the smaller the air gap the larger the torque produced, with the rest of the variables remaining the same. Further to be noted is the fact that the aligned inductance is inversely proportional to the air gap length, hence any decrease in the air gap results in an increase in the aligned inductance. This may not be acceptable where the available dc link voltage is not sufficient to force and maintain the desired current in the machine phase. Then the only recourse is to decrease the bore diameter or stack length or the number of turns in the phase winding. Depending upon the design criterion, only one of them is decreased or a simultaneous decrease of all the variables is coordinated to keep the aligned inductance within an acceptable level.

The manufacturing tolerances and minimum air gap that could be supported in the production environment are two important factors driving the minimum air gap length determination. The tolerance in turn affects the maximum eccentricity in the air gap arising amongst the diametrically opposite poles. This determines the magnitude of the uneven pull on the rotor and hence the wear and tear on rotor bearings and their longevity. Further, this contributes to audible noise. To maintain a uniform air gap, which is essential to overcome these problems, the stator and rotor are ground on the inner and outer surfaces, respectively. That leads to disturbance of the magnetic alignment in the lamination material, resulting in higher core losses, which are more acceptable as compared to the problems wrought by the uneven air gap.

### 3.11 MEASUREMENT OF INDUCTANCE

The design and successful development of an SRM are dependent on the inductance profile of the motor and therefore on its measurement in prototypes. The measurement technique<sup>35</sup> is based on the voltage equation of the SRM in terms of the phase current and flux linkages,  $\lambda(t)$ , and is given for one rotor position by:

$$v(t) = R_s i(t) + \frac{d\lambda(t)}{dt} \quad (3.137)$$

which on integration gives the flux linkages as:

$$\lambda(t) - \lambda(0) = \int_0^t \{ v(t) - R_s i(t) \} dt \quad (3.138)$$

where  $v(t)$  is the applied voltage and  $R_s$  is the resistance per phase from which the inductance is obtained as:

$$L(t) = \frac{1}{i(t)} \left\{ \lambda(0) + \int_0^t \{ v(t) - R_s i(t) \} dt \right\} \quad (3.139)$$

Note that this inductance is a function of the fixed rotor position,  $\theta$ , and the current  $i(t)$  and therefore should be denoted rightly as  $L(i(t), \theta)$ . To obtain the inductance for various positions (known as an inductance profile), this experiment has to be repeated for various fixed rotor positions ranging from the aligned to completely unaligned position of the stator and rotor poles to plot the three-dimensional relationship of  $\lambda(i, \theta)$  vs.  $i$  and  $\theta$ . This is sufficient for the evaluation of instantaneous electromagnetic torque for a given current profile as a function of rotor position. Note that the rotor is locked for these measurements in each position.

The manner in which the flux linkages are obtained is very crucial to the accuracy of the results. Instrumenting the applied voltage and phase current for evaluating the flux linkages by software integration eliminates the hardware-based instrumentation errors. The measurements could be by monitoring either rising or decaying current in the machine winding. The latter method is appropriate for higher currents as the voltage during a falling current is very small and fairly constant. This is because the measurement during a decaying current is carried out by eliminating the applied voltage to the winding, and an alternative path to the winding current is provided through a freewheeling diode connected across the machine phase. The voltage across the winding during the decaying current is only the forward voltage drop of the diode. In the rising current method, the applied source voltage varies while the current is increasing, giving rise to errors due to quantization and its use in the evaluation of flux linkages.

Core losses complicate the measurement of inductances, as the core losses are not incorporated into the model using Eq. (3.137). A general technique to find only the reactive component of the current will be able to isolate the effects due to core losses, particularly those of the eddy current. Such a technique is described in Chapter 8.

## 3.12 CALCULATION OF TORQUE

Algorithms for evaluating steady-state and instantaneous electromagnetic torque are developed in this section.

### 3.12.1 AVERAGE TORQUE

Assuming that the flux linkages vs. current characteristics are available and current  $I_p$  is maintained constant between the unaligned and aligned positions of the rotor movement, the average torque is calculated as follows.<sup>38</sup> The area between these two curves is calculated and is denoted as  $\delta W_m$ , as shown in [Figure 3.24](#).  $\delta W_m$  is then the work done per stroke of the machine:

$$\delta W_m = W'_{m \text{ aligned}} - W'_{m \text{ unaligned}} = \Delta i \left( \lambda_1 + \lambda_2 + \dots + \frac{1}{2} \lambda_n \right) - \frac{1}{2} \lambda_u \times I_p \quad (3.140)$$

where the aligned co-energy is calculated using  $n$  points on the  $\lambda$  vs.  $i$  curve with the trapezoidal integration algorithm and

$$\Delta i = \frac{I_p}{n} \quad (3.141)$$

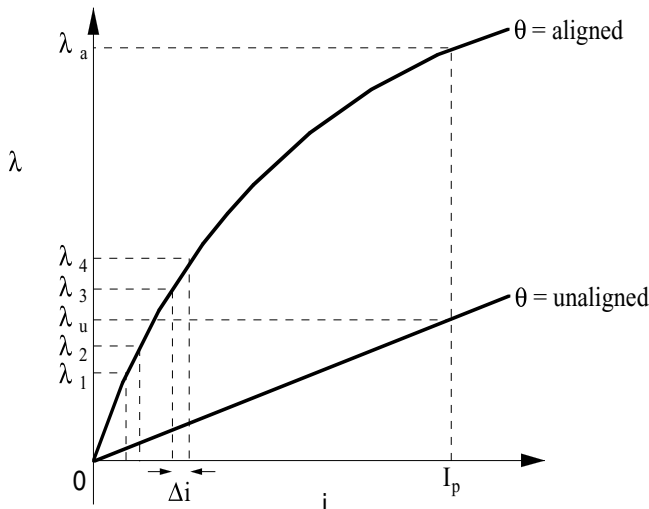


**FIGURE 3.24** Flux linkage vs. excitation current for aligned and unaligned rotor positions.

The average torque is

$$T_{av} = \frac{\text{Total work done/revolution}}{2\pi} \quad (3.142)$$

$$\begin{aligned} \text{Total work done/revolution} &= \delta W_m \times \text{Number of strokes/revolution} \\ &= \delta W_m \times q P_r \\ &= \delta W_m \times \frac{P_s}{2} \cdot P_r \end{aligned} \quad (3.143)$$

where  $P_s$  is the number of stator poles,  $P_r$  is the number of rotor poles, and  $q$  is the number of phases. Substituting Eq. (3.143) into Eq. (3.142) results in:

$$T_{av} = \frac{\delta W_m P_s P_r}{4\pi} = \frac{\delta W_m q P_r}{2\pi} N \cdot m \quad (3.144)$$

and the average air gap power is

$$P_a = T_{av} \times \omega_m = \frac{q \delta W_m P_r \omega_m}{2\pi} W \quad (3.145)$$

where  $\omega_m$  is the rotor speed in rad/sec. The torque at low and rated currents has a relationship that is approximately parabolic and linear, respectively, with regard to the current. Such torque characteristics make this drive unsuitable for open-loop servo applications where a linear relationship is required. A feedback control will overcome this nonlinearity.

### 3.12.2 INSTANTANEOUS TORQUE

The procedure for calculating the average torque can be applied to any operating conditions of the SRM. This is illustrated with a typical operating condition of the SRM for which the current vs. rotor position and the corresponding flux-linkages vs. current for various rotor positions are shown in Figure 3.25. Here, it is assumed that  $\theta_1$  is greater than the fully unaligned position and  $\theta_6$  is less than the completely aligned position. The phase current increases from zero to  $i_{p1}$ , which, in turn, produces a torque moving the rotor from position  $\theta_1$  to  $\theta_2$ . Correspondingly, the phase flux linkages rise from zero to reach point  $a$  in the figure through the trajectory  $0a$ . Then, the current decays from  $i_{p1}$  to  $i_{p2}$ . During this interval, the slope of the inductance is positive so will produce a motoring torque further moving the rotor from position  $\theta_2$  to  $\theta_3$ . The flux linkage trajectory pertinent to this step is the curve  $ab$ . Likewise, the change in the coenergy can be estimated for this stroke of the SRM and is shown as the area  $0abcd0$  in the figure. This area can be computed numerically and is equal to the work done per stroke of the machine,  $\delta W_m$ . From  $\delta W_m$  and other machine variables, average torque and air gap power are calculated using Eqs. (3.144) and (3.145), respectively.

In a similar way, the instantaneous torque can be found if the incremental area,  $\delta W_m$ , for each incremental rotor position is calculated. The torque then is the ratio of the  $\delta W_m$  and the incremental rotor position as given by Eq. (3.12).

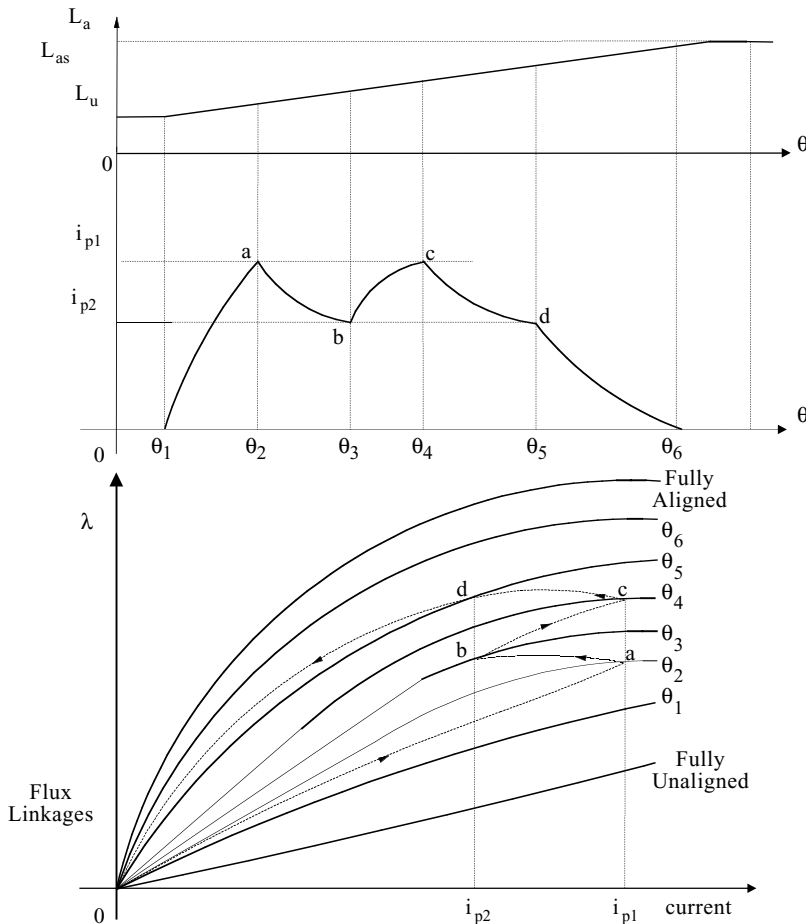


**FIGURE 3.25** Typical SRM phase current waveforms and flux linkages.

### 3.13 DESIGN OF THE LINEAR SWITCHED RELUCTANCE MACHINE

A standard design procedure for a single-sided and longitudinal-flux-based linear switched reluctance machine (LSRM) is developed in this section. The proposed design procedure utilizes the rotating switched reluctance machine (rotary SRM) design by converting the specifications of the linear machine into those of an equivalent rotating machine. The machine design is carried out in the rotary domain, which then is transformed back into the linear domain. Such a procedure brings to bear the knowledge base and familiarity of the rotary machine designers to design a linear machine effectively. This section contains illustrations of the proposed design procedure for a three-phase LSRM with an active stator and passive translator and a four-phase LSRM with an active translator and passive stator. Analysis procedures

for the phase winding inductance, and propulsion, and normal forces vs. translator position are developed with a lumped-parameter magnetic circuit model. The results from it are verified with finite element analysis. The experimental setup for measurements of inductance vs. position vs. current, propulsion force vs. position vs. current, and normal force vs. position vs. current is described.

### 3.13.1 INTRODUCTION

There are two distinct configurations of LSRM: transverse flux and longitudinal flux. Transverse flux machines have been explored in detail in the literature; however, the design of machines is not described in detail, although the calculation of inductances and force by finite element analysis is covered extensively.<sup>42</sup> The design of longitudinal-flux,<sup>39,40,41,43,48–51</sup> single-sided machines has been extensively studied,<sup>51</sup> and procedures developed from these studies are presented in this section.

A standard or classical design procedure begins with the power output equation relating the machine dimensions such as bore diameter, lamination stack length, speed, magnetic loading, and electric loading. Further, the machine dimensions and their impact on performance are characterized by implicit relationships and made available in a form to enable machine design. Such a procedure allows insight into the scaling of designs and enables the exercise of engineering judgment to select the best design with the least amount of computations. These advantages are not feasible with finite element analysis; therefore, a standard design procedure is preferable for design of LSRM.

To design an LSRM using a standard design procedure, analytical expressions relating machine dimensions to output variables are required. Recognizing that a standard design procedure is available for the rotary SRM, the design of an LSRM can proceed via the rotary SRM if the design specifications can be transformed from the linear to rotary domain, and the design is then carried out in the rotary domain.<sup>30,31</sup> The specifications can then be recovered in the linear domain by simple algebraic transformations.

### 3.13.2 LSRM CONFIGURATIONS

In this section, we will consider two longitudinal LSRM configurations: a three-phase LSRM with an active stator and passive translator and a four-phase LSRM with an active translator and passive stator.

#### 3.13.2.1 Three-Phase LSRM with Active Stator and Passive Translator Structure

[Figure 3.26](#) shows the three-phase LSRM structure and its winding diagram with an active stator, a passive translator, and a longitudinal flux configuration. The LSRM consists of six translator poles and  $n$  stator poles. This corresponds to the six stator/four rotor pole rotary SRM. One stator sector is composed of six stator poles, and the number of stator sectors  $N_{sc}$  is given by:

$$N_{sc} = \frac{n}{6} \quad (3.146)$$

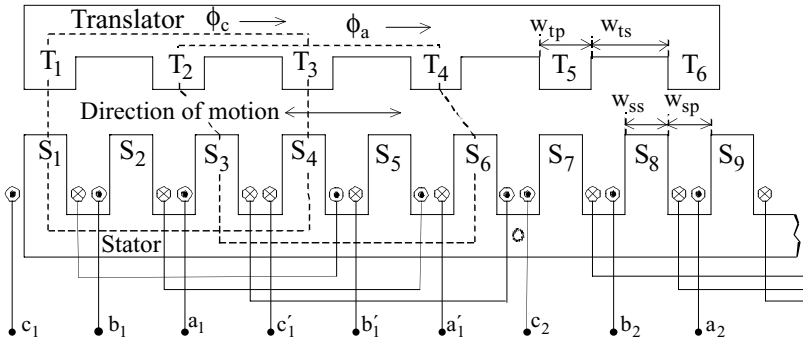


**FIGURE 3.26** Three-phase LSRM structure and winding diagram with six translator poles.

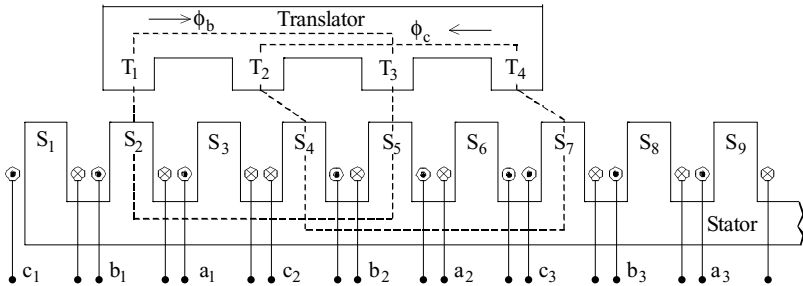


**FIGURE 3.27** Three-phase LSRM structure and winding diagrams with four translator poles.

A rotary SRM has four rotor poles, hence the corresponding LSRM should have four translator poles. However, in the LSRM structure with four translator poles, there is a reversal of flux at the instant of phase current commutation. For example, consider the LSRM in [Figure 3.27](#), which has only four translator poles. For the continuous forward movement of LSRM, the excitation sequence of  $a_1a_2 - b_1b_2 - c_2c_3 - \dots$  is necessary for motion in the increasing inductance region. However, this causes a flux reversal when the sequence is in between the excitation of  $b_1b_2 - c_2c_3$  and so on. This results in degradation of the LSRM performance with higher noise and increased core losses. If this topology is used, the converter design and the switching sequence are much more complicated. Therefore, the number of translator poles is increased from four to six to prevent the reversal of flux and to maintain the flux path in the same direction (see [Figure 3.26](#)). In the case of eight stator and six rotor poles in the rotary SRM, the number of translator poles should be increased from six to nine to maintain the flux in the same direction. The application of the sequence of  $c_1c_1' - a_1a_1' - b_1b_1' - c_2c_2' - \dots$  makes the translator move in the forward direction continuously. The generated flux directions resulting from excitation of phase  $a$  and phase  $c$  windings are shown in [Figure 3.26](#). Each sector operates in an independent manner, which means that there is no simultaneous excitation of poles in different sectors. For example, the simultaneous excitation of  $c_1'c_2$ ,  $b_1'b_2$ , and  $a_1'a_2$  is not permitted. Therefore, there is no flux flow in the back iron between  $S_6$  and  $S_7$ ,

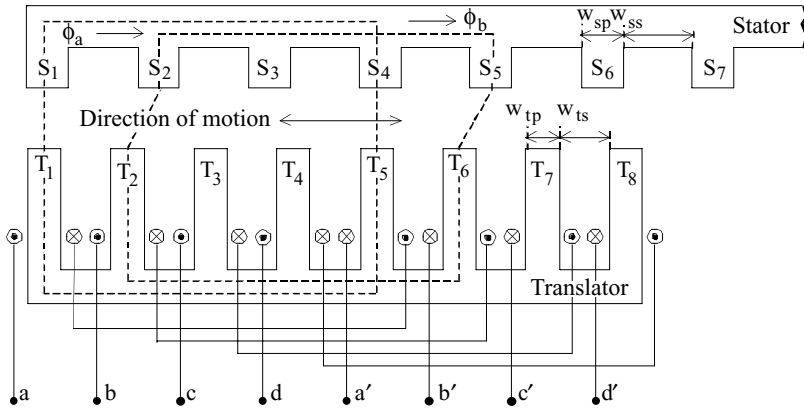


**FIGURE 3.28** Four-phase LSRM structure with active translator and passive stator.

hence the back iron portion between  $S_6$  and  $S_7$  can be used for other purposes such as stacking of laminations. As seen from [Figure 3.26](#),  $w_{tp}$  is the width of the translator pole,  $w_{ts}$  is the width of the translator slot,  $w_{sp}$  is the width of the stator pole, and  $w_{ss}$  is the width of the stator slot. The stacking width of the laminations is given by  $L_w$ .

### 3.13.2.2 Four-Phase LSRM with Active Translator and Passive Stator Structure

[Figure 3.28](#) shows a four-phase longitudinal LSRM with an active translator and a passive stator. The LSRM consists of eight translator poles, corresponding to the eight stator and six rotor poles in the rotary SRM. Contrary to the active stator and passive translator structure, there is no reversal of flux at the instant of phase current commutation, and the back irons of the stator and translator experience the same direction of magnetic flux regardless of the switching of the phase winding current. The energization sequence of  $aa' - bb' - cc' - dd' - aa' - \dots$  in the increasing inductance region makes the translator move in the forward direction continuously with the flux direction maintained the same. The flux paths and directions for phase  $a$  and phase  $b$  excitation are shown in [Figure 3.28](#).

### 3.13.3 LSRM DESIGN<sup>30,31</sup>

The design of LSRM is achieved by first translating its specifications into equivalent rotary SRM specifications, then the rotary SRM is designed from which the LSRM dimensions and design variables are recovered by inverse translation. The design procedure is derived in this section.

#### 3.13.3.1 Specifications of the LSRM

Consider an LSRM to be designed for a machine stator length  $L_s$ , with a maximum linear velocity of  $v_m$  and an acceleration time  $t_a$  required to reach the maximum velocity. The maximum mass of the translator is restricted to  $M_t$ . [Figure 3.29](#) shows the

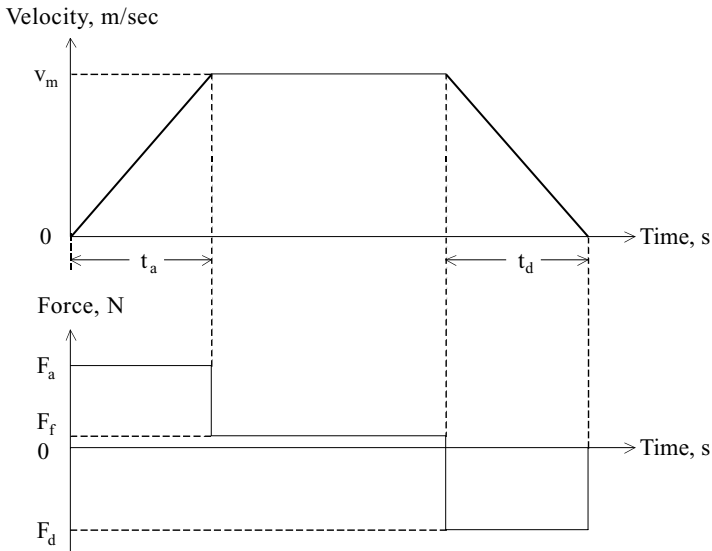


**FIGURE 3.29** Velocity and required force profile of LSRM.

required velocity profile of the LSRM. If the deceleration time  $t_d = t_a$ , the maximum acceleration is given by:

$$a_a = \frac{v_m}{t_a} \quad (3.147)$$

and the maximum deceleration  $a_d = -a_a$ . The instantaneous acceleration force  $F_a$  is given by:

$$F_a = M_t \cdot a_a \quad (3.148)$$

and the instantaneous deceleration force  $F_d = -F_a$ . Assuming a zero instantaneous friction force (that is,  $F_f = 0$ ), the maximum power capacity of the LSRM is given by:

$$P = F_a v_m \quad (3.149)$$

### 3.13.3.2 Design of Rotary SRM

A 6/4 rotary SRM (RSRM) is designed for a power capacity identical to that of the LSRM. The material used for the laminations is M19 steel, which is made of non-oriented silicon steel. The rotary SRM has a stator pole angle of  $\beta_s$  and a rotor pole angle of  $\beta_r$ . The speed of the rotary SRM,  $N_r$ , in rpm, is given by:

$$N_r = \frac{v_m}{D/2} \cdot \frac{60}{2\pi} \quad (3.150)$$

where  $D$  is the bore diameter of the rotary SRM. The power output equation of a rotary SRM in terms of key physical variables is described by:<sup>22</sup>

$$P = k_e k_d k_1 k_2 B A_s D^2 L N_r \quad (3.151)$$

where  $P$  is the power output,  $k_e$  is the efficiency,  $k_d$  is the duty cycle determined by the current conduction angle for each rising inductance profile,  $k_1 = \pi^2/120$ ,  $k_2$  is a variable dependent on the operating point and is determined by using aligned saturated inductance and unaligned inductance,  $B$  is the stator pole flux density at the aligned position,  $A_s$  is the specific electric loading which is defined as ampere conductor per meter of stator inner periphery,  $L$  is the stack length of the magnetic core, and  $N_r$  is the speed. Setting the stack length as a multiple or submultiple of the bore diameter,

$$L = kD \quad (3.152)$$

and converting the rotational angular velocity to linear velocity,

$$P = k_e k_d k_1 k_2 B A_s D^2 (kD) \left( \frac{V_m}{D/2} \cdot \frac{60}{2\pi} \right) = k_e k_d k_1 k_2 k B A_s D^2 v_m \frac{60}{\pi} \quad (3.153)$$

The bore diameter is obtained from the power output equation as:

$$D = \sqrt{\frac{P\pi}{60 \cdot k_e k_d k_1 k_2 k B A_s v_m}} \quad (3.154)$$

The air gap of the LSRM is usually much larger than that of the air gap of the rotary SRM. In the aligned portion, the B-H characteristic of the magnetic material is fairly linear and the reluctance of the steel core is small when compared to the reluctance of the air gap in the aligned position. The machine flux can be calculated as:

$$\phi = B_g A_g \quad (3.155)$$

where  $A_g$  is the cross-section area of the air gap and during alignment is approximately equal to

$$A_g = \left( \frac{D}{2} - \ell_g \right) \left( \frac{\beta_r + \beta_s}{2} \right) L \quad (3.156)$$

where  $\ell_g$  is the length of the air gap, but the air gap flux is equal to the stator pole flux neglecting leakage flux and hence

$$\phi = B A_{sp} \quad (3.157)$$

where  $A_{sp}$  is the stator pole area and given as:

$$A_{sp} = \frac{DL\beta_s}{2} \quad (3.158)$$

The magnetic field intensity in the air gap can be calculated as:

$$H_g = \frac{B_g}{\mu_0} = \frac{BA_{sp}}{\mu_0 A_g} \quad (3.159)$$

Assuming the existence of a large air gap, the ampere turns required to produce the air gap magnetic field intensity is given by:

$$T_{ph} I_p = H_g \cdot (2\ell_g) \quad (3.160)$$

where  $T_{ph}$  is the number of winding turns per phase, and  $I_p$  is the peak phase current. Assuming a value for the peak phase current allowable in the machine, the number of turns per phase of the rotary SRM can be calculated as:

$$T_{ph} = \frac{H_g \cdot (2\ell_g)}{I_p} \quad (3.161)$$

If  $J$  is the maximum allowable current density in the winding and  $q$  is the number of phases, the area of the conductor is calculated as:

$$a_c = \frac{I_p}{J\sqrt{q}} \quad (3.162)$$

Neglecting the leakage of flux, the area of the stator yoke, and the height of the stator pole can be calculated, respectively, as:

$$A_{sy} = b_{sy} \cdot L = \frac{A_{sp} B}{B_{sy}} \quad (3.163)$$

$$h_s = \frac{D_o}{2} - \frac{D}{2} - b_{sy} \quad (3.164)$$

where  $b_{sy}$  is the thickness of the stator yoke and  $D_o$  is the outer diameter of the stator lamination. The rotor pole area is given by:

$$A_{rp} = \left( \frac{D}{2} - \ell_g \right) L \beta_r \quad (3.165)$$

If the rotor yoke has a radius equal to the width of the rotor pole, the rotor yoke width and the height of the rotor pole are sequentially calculated as:

$$b_{ry} = \frac{A_r}{L} \quad (3.166)$$

$$h_r = \frac{D}{2} - \ell_g - b_{ry} \quad (3.167)$$

This completes the analytical relationships required for the rotary SRM design.

### 3.13.3.3 Conversion of RSRM Dimensions to LSRM Dimensions

The bore circumference of the rotary SRM forms the length of one sector of the LSRM. The total number of sectors of the LSRM is given by:

$$N_{sc} = \frac{L_t}{\pi D} \quad (3.168)$$

For the number of poles  $P_s$  in the stator of the rotary SRM, the number of stator poles is obtained by:

$$n = P_s N_{sc} \quad (3.169)$$

The width of stator pole and the width of stator slot are given by:

$$w_{sp} = \frac{A_{sp}}{L} = \left(\frac{D}{2}\right)\beta_s \quad (3.170)$$

$$w_{ss} = \frac{(\pi D - P_s w_{sp})}{P_s} \quad (3.171)$$

The translator pole width and the translator slot width are converted from the rotor pole area neglecting the air gap length and are given by:

$$w_{tp} = \left(\frac{D}{2}\right)\beta_r \quad (3.172)$$

$$w_{ts} = \frac{(\pi D - P_r w_{tp})}{P_r} \quad (3.173)$$

where  $P_r$  is the number of poles in the rotor of the rotary SRM. Now, the fill factor of the windings is verified to see if the slot size is sufficient to hold the windings. The fill factor is defined as:

$$F_f = \frac{\text{Stator winding area}}{\text{Stator slot window area}} \quad (3.174)$$

The diameter of the conductor is given by:

$$d_c = \sqrt{\frac{4a_c}{\pi}} \quad (3.175)$$

Assuming that a portion of the stator pole height is occupied by wedges to hold the windings in place, given by  $w$ , the number of vertical layers of winding is

$$N_v = P_f \frac{(h_s - w)}{d_c} \quad (3.176)$$

where  $P_f$  is the form factor or packing factor. If the number is a fraction, it is rounded off to a lower integer. The number of horizontal layers of the winding is given by:

$$N_h = \frac{T_{ph}}{2N_v} \quad (3.177)$$

The stator winding area is given by:

$$\text{Stator winding area} = 2 \frac{a_c N_h N_v}{P_f} \quad (3.178)$$

Finally, the fill factor is calculated as:

$$F_f = \frac{\text{Stator winding area}}{\text{Stator slot window area}} = \frac{2 \frac{a_c N_h N_v}{P_f}}{w_{ss}(h_s - w)} = \frac{2 a_c N_h N_v}{P_f w_{ss}(h_s - w)} \quad (3.179)$$

Consideration has to be given to keeping the two phase windings in the slot separated. Then, the normal range of the fill factor is  $0.2 \leq F_f < 0.7$ . The translator length for an LSRM with six translator poles is then calculated as:

$$L_{tr} = 6w_{tp} + 5w_{ts} \quad (3.180)$$

Since the core stack length of the LSRM equals the stator stack length of the rotary SRM, the core stack length is written as:

$$L_w = L = kD \quad (3.181)$$

Finally, the following condition has to be satisfied:

$$P_s(w_{sp} + w_{ss}) = P_r(w_{tp} + w_{ts}) \quad (3.182)$$

The winding details of the rotary SRM and LSRM are identical in this design. This need not be the case, as the duty cycle of a winding in the three-phase LSRM is  $1/(3N_{sc})$ , whereas that of the rotary SRM winding is  $1/3$ . Therefore, the windings in the LSRM can have much lower copper volume but take more losses.

### 3.13.3.4 Example 1: Design of Three-Phase LSRM with Active Stator and Passive Translator

An LSRM prototype is designed<sup>51</sup> for a length of 4.8 m, with a maximum linear velocity of 1.5 m/sec and acceleration time of 0.667sec. The maximum mass of translator assembly is restricted to 20 kg. The acceleration is then given by:

$$a_a = \frac{v_m}{t_a} = \frac{1.5}{0.667} = 2.25 \text{ m/s}^2$$

The force for initial acceleration is calculated as:

$$F_a = M_t \cdot a_a = 20 \cdot 2.25 = 45\text{N}$$

The deceleration  $a_d = -2.25 \text{ m/sec}^2$  and the deceleration force  $F_d = -45 \text{ N}$ . The power capacity of the LSRM is  $P = F_a v_m = 45 \cdot 1.5 = 67.5 \text{ W}$ . The rotary SRM is assumed to have a stator pole angle  $\beta_s = 30^\circ = 0.524 \text{ rad}$  and a rotor pole angle  $\beta_r = 36^\circ = 0.628 \text{ rad}$ . After fine-tuning the parameters, the constants are set as follows:  $k_e = 0.4$ ,  $k_d = 1$ ,  $k_2 = 0.7$ ,  $B = 1.1215 \text{ T}$ ,  $A_s = 23886.5$ , and  $k = 0.655$ . The bore diameter is obtained as:

$$D = \sqrt{\frac{P\pi}{60 \cdot k_e k_d k_1 k_2 k B A_s v_m}} = 76.39 \text{ mm}$$

The stack length of the rotary SRM is obtained as:

$$L = kD = 0.655 \cdot 76.39 = 50 \text{ mm}$$

The stator yoke thickness  $b_{sy}$  is given by:

$$b_{sy} = \frac{D\beta_s}{2} = 20 \text{ mm}$$

Assuming  $D_o = 190 \text{ mm}$ , the height of the stator pole,  $h_s$ , can be calculated as:

$$h_s = \frac{D_o}{2} - \frac{D}{2} - b_{sy} = \frac{190}{2} - \frac{76.39}{2} - 20 \approx 37 \text{ mm}$$

The rotor back iron width,  $b_{ry}$ , and the height of the rotor pole (the translator pole),  $h_{rp}$ , are then calculated as:

$$b_{ry} = \left(\frac{D}{2}\right)\beta_r = \left(\frac{76.39}{2}\right)0.628 = 24 \text{ mm}$$

$$h_r = \frac{D}{2} - \ell_g - b_{yr} = \frac{76.39}{2} - 1 - 24 \approx 15 \text{ mm}$$

The magnetic field intensity in the air gap is calculated as:

$$H_g = \frac{B}{\mu_0} = \frac{1.1215}{4\pi \cdot 10^{-7}} = 892461.3 \text{ A/m}$$

For a peak phase current of  $I_p = 8.5$  A, the number of turns per phase is

$$T_{ph} = \frac{H_g \cdot (2\ell_g)}{I_p} \approx 210 \text{ turns/phase}$$

Assuming a current density of  $J = 6$  A/mm<sup>2</sup>, the area of the conductor is calculated as:

$$a_c = \frac{I_p}{J\sqrt{q}} = \frac{8.5}{6\sqrt{3}} = 0.818 \text{ mm}^2$$

The closest wire size for this area of cross section of the conductor is AWG #18. It has an area of 0.817 mm<sup>2</sup> and is selected for the phase windings. The calculation of the winding turns completes the rotary SRM design. The conversion from rotary to linear domain follows.

The number of sectors of the LSRM and the resultant total number of stator poles are

$$N_{sc} = \frac{L_t}{\pi D} = \frac{4.8}{\pi \cdot 76.39 \cdot 10^{-3}} = 20$$

$$n = P_s N_{sc} = 6 \cdot 20 = 120$$

The width of the stator pole and the width of the stator slot are given by:

$$\begin{aligned} w_{sp} &= \frac{D\beta_s}{2} = \frac{76.394 \cdot 30}{2} \frac{\pi}{180} = 20 \text{ mm} \\ w_{ss} &= \frac{(\pi D - 6w_{sp})}{6} = \frac{(\pi \cdot 76.394 - 6 \cdot 20)}{6} = 20 \text{ mm} \end{aligned}$$

The translator pole width and the translator slot width are calculated as:

$$\begin{aligned} w_{tp} &= b_{yr} = 24 \text{ mm} \\ w_{ts} &= \frac{(\pi D - 4w_{tp})}{4} = \frac{(\pi \cdot 76.394 - 4 \cdot 24)}{4} = 36 \text{ mm} \end{aligned}$$

The total length of the translator is given by:

$$L_{tr} = 6w_{tp} + 5w_{ts} = 6 \cdot 24 + 5 \cdot 36 = 324 \text{ mm}$$

The core stack width of the LSRM is obtained from the stator stack length of the rotary SRM as:

$$L_w = L = kD = 50 \text{ mm}$$

Now, the fill factor of the windings is verified to see if the slot size is sufficient to hold the windings. The diameter of the conductor is given by:

$$d_c = \sqrt{\frac{4a_c}{\pi}} = \sqrt{\frac{4 \cdot 0.817}{\pi}} = 1.02 \text{ mm}$$

Assuming the width of the wedges  $w = 3$  and packing factor  $P_f = 0.8$ , the number of vertical layers of winding and the number of horizontal layers of winding are obtained as:

$$N_v = P_f \frac{(h_s - w)}{d_c} = 0.8 \frac{(37 - 3)}{1.02} = 26.6 \approx 26$$

$$N_h = \frac{T_{ph}}{2 \cdot N_v} = \frac{210}{2 \cdot 26} = 4.03 \approx 4$$

The winding area is given by:

$$\text{Stator winding area} = 2 \frac{a_c N_v N_h}{P_f} = 212.4 \text{ mm}^2$$

The fill factor is calculated as:

$$F_f = \frac{\text{Stator winding area}}{\text{Stator slot window area}} = \frac{212.4}{(37 - 3) \cdot 20} = 0.312$$

Finally, it can be observed that the condition outlined in Eq. (3.182) is satisfied with this design. [Figure 3.30](#) shows the dimensions of the designed three-phase LSRM.

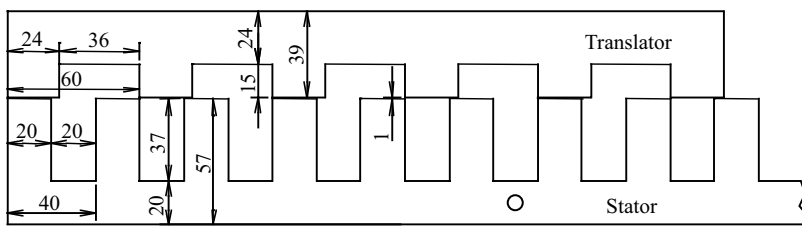


**FIGURE 3.30** Dimensions of the designed three-phase LSRM.

### 3.13.3.5 Example 2: Four-Phase LSRM Prototype with Active Translator and Passive Stator

An LSRM prototype is designed<sup>51</sup> for a length of 6 m, with a maximum linear velocity of 1 m/sec and acceleration time of 1.5 sec. The maximum mass of translator assembly is restricted to 60 kg. The acceleration is then given by:

$$a_a = \frac{v_m}{t_a} = \frac{1}{1.5} = 0.667 \text{ m/sec}^2$$

The instantaneous acceleration force is calculated as:

$$F_a = M_t \cdot a_a = 60 \cdot 0.667 = 40 \text{ N}$$

The deceleration  $a_d = -0.667 \text{ m/sec}^2$  and the instantaneous deceleration force  $F_d = -40 \text{ N}$ . The power capacity of the LSRM is  $P = F_a v_m = 40.1 = 40 \text{ W}$ . The rotary SRM is assumed to have a stator pole angle  $\beta_s = 18^\circ = 0.314 \text{ rad}$  and a rotor pole angle  $\beta_r = 22^\circ = 0.384 \text{ rad}$ . After fine-tuning the parameters, the constants are set as follows:  $k_e = 0.3$ ,  $k_d = 1$ ,  $k_2 = 0.7$ ,  $B = 0.65 \text{ T}$ ,  $A_s = 41456.7$ , and  $k = 0.8$ . The bore diameter is obtained as:

$$D = \sqrt{\frac{P\pi}{60 \cdot k_e k_d k_1 k_2 k B A_s v_m}} = 75 \text{ mm}$$

The stack length of the rotary SRM is obtained as:

$$L = kD = 0.8 \cdot 75 = 60 \text{ mm}$$

The stator yoke thickness  $b_{sy}$  is given by:

$$b_{sy} = \frac{D\beta_s}{2} \approx 12 \text{ mm}$$

Assuming  $D_o = 190 \text{ mm}$ , the height of the stator pole  $h_s$  can be calculated as:

$$h_s = \frac{D_o}{2} - \frac{D}{2} - b_{sy} = \frac{190}{2} - \frac{75}{2} - 12 \approx 44 \text{ mm}$$

The rotor back iron width  $b_{ry}$  and the height of the rotor pole  $h_r$  are then calculated as:

$$b_{ry} = \left(\frac{D}{2}\right)\beta_r = \left(\frac{75}{2}\right)0.384 \approx 15 \text{ mm}$$

$$h_r = \frac{D}{2} - g - b_{ry} = \frac{75}{2} - 3 - 15 \approx 15 \text{ mm}$$

The magnetic field intensity in the air gap is calculated as:

$$H_g = \frac{B}{\mu_0} = \frac{0.65}{4\pi \cdot 10^{-7}} = 517253.6 \text{ A/m}$$

For a peak phase current of  $I_p = 8.5 \text{ A}$ ,

$$T_{ph} = \frac{H_g \cdot (2g)}{I_p} \approx 360 \text{ turns/phase}$$

Assuming a current density of  $J = 6.5 \text{ A/mm}^2$ , the area of the conductor is calculated as:

$$a_c = \frac{I_p}{J\sqrt{q}} = \frac{8.5}{6.5\sqrt{4}} = 0.654 \text{ mm}^2$$

AWG #19 wire size is suitable as it has an area of  $0.653 \text{ mm}^2$ .

In the active translator and passive stator structure of LSRM, the stator and rotor of the rotary SRM correspond to the translator and stator of LSRM, respectively. The widths of stator pole and stator slot are given by:

$$\begin{aligned} w_{sp} &= b_{ry} \approx 15 \text{ mm} \\ w_{ss} &= \frac{(\pi D - 6w_{sp})}{6} = \frac{(\pi \cdot 75 - 6 \cdot 15)}{6} \approx 25 \text{ mm} \end{aligned}$$

The total number of stator poles is

$$n = \frac{L_t}{W_{sp} + W_{ss}} = \frac{6.0}{0.015 + 0.025} = 150$$

The translator pole width and the translator slot width are calculated as:

$$w_{tp} = b_{sy} \approx 12 \text{ mm}$$

$$w_{ts} = \frac{(\pi D - 8w_{tp})}{8} = \frac{(\pi \cdot 75 - 8 \cdot 12)}{8} \approx 18 \text{ mm}$$

The total length of the translator is given by:

$$L_{tr} = 8w_{tp} + 7w_{ts} = 8 \cdot 12 + 7 \cdot 18 = 222 \text{ mm}$$

The core stack width of the LSRM is obtained from the stator stack length of the rotary SRM as:

$$L_w = L = kD = 60 \text{ mm}$$

Now, the fill factor of the windings is verified to see if the slot size is sufficient to hold the windings. The diameter of the conductor is given by:

$$d_c = \sqrt{\frac{4a_c}{\pi}} = \sqrt{\frac{4 \cdot 0.817}{\pi}} = 0.912 \text{ mm}$$

Assuming the width of the wedges  $w = 3 \text{ mm}$  and packing factor  $P_f = 0.8$ , the number of vertical layers of winding and the number of horizontal layers of winding are given by:

$$N_v = P_f \frac{(h_s - w)}{d_c} = 0.8 \frac{(44 - 3)}{0.912} \approx 36$$

$$N_h = \frac{T_{ph}}{2 \cdot N_v} = \frac{360}{2 \cdot 36} \approx 5$$

The winding area is given by:

$$\text{Stator winding area} = 2 \frac{a_c N_v N_h}{P_f} = 293.9 \text{ mm}^2$$

The fill factor is calculated as:

$$F_f = \frac{\text{Stator winding area}}{\text{Stator slot window area}} = \frac{293.9}{(44 - 3) \cdot 18} = 0.398$$

Note that the condition outlined in Eq. (3.182) is also satisfied with this design. [Figure 3.31](#) shows the final dimensions of the designed four phase LSRM.

### 3.13.4 DESIGN VERIFICATION

The design verification process, very much similar to that for the rotary SRM, includes analytical and finite element analyses and experimental verification of the machine.<sup>51</sup> The analytical part of the verification is in finding the performance of the machine through its flux linkage vs. current vs. translator position characteristics

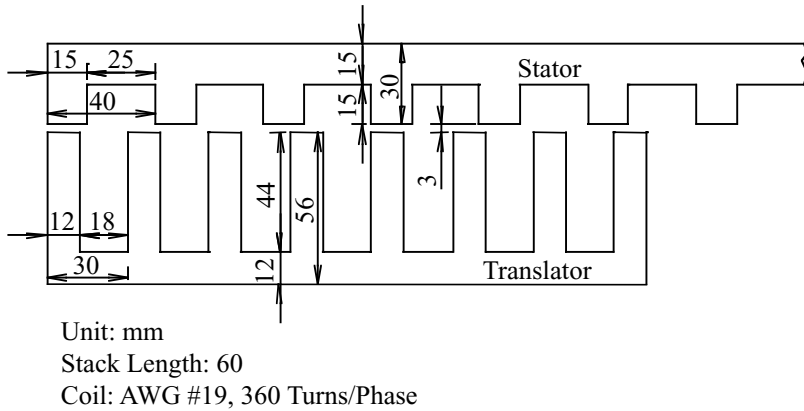


**FIGURE 3.31** Dimensions of the designed four-phase LSRM.

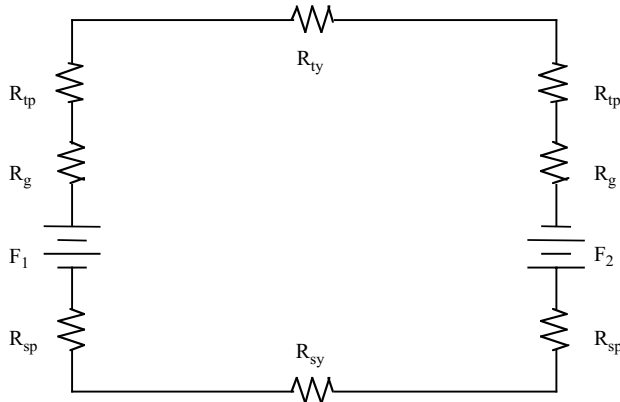
derived using a magnetic equivalent circuit approach. The finite element analysis is made using commercial software, and the design is fine-tuned with these results. Then, the prototype is usually built and tested. A strong correlation between the analytical, finite element, and experimental results assures confidence in the engineering analysis and the design methods adopted and enables confident scaling of the machine. A poor correlation of the results forces the designer to revisit the design methodology.

### 3.13.4.1 Analytical Inductance Calculation

Flux linkages in the machine are calculated for a given excitation and a translator position using magnetic equivalent circuit. The flux linkages can be obtained from the inductance and corresponding excitation current. In this section, the winding inductance is computed using the permeance of the magnetic flux paths. The magnetic flux path of an LSRM encompasses five parts of the machine: air gaps, stator poles, stator yoke, translator poles, and translator yoke. Each part experiences different flux densities and different lengths of flux line based on the chosen magnetic flux path. From the pattern of the flux path of the three-phase LSRM prototype shown in [Figure 3.26](#), the lumped parameter model of the equivalent magnetic circuit of the LSRM can be derived as shown in [Figure 3.32](#). The relevant reluctances are named for each flux path in one of the five parts of the machine. The mmf applied to a phase winding at any translator position is given by:

$$F = F_1 + F_2 = F_g + F_s + F_t \quad (3.183)$$

where  $F$  is the total mmf per phase applied and  $F_g$ ,  $F_s$ , and  $F_t$  are the mmf drops in the air gap, stator iron core, and translator iron core, respectively. The mmf equation can be rewritten in terms of the magnetic field intensity and flux path length using



$R_{tp}$ ,  $R_{ty}$ : Reluctances of the translator pole and translator yoke

$R_{sp}$ ,  $R_{sy}$ : Reluctances of the stator pole and stator yoke

$R_g$ : Reluctance of the air gap

$F_1$ ,  $F_2$ : Applied mmfs per pole

**FIGURE 3.32** Lumped parameter model of the equivalent magnetic circuit of LSRM.

Ampere's circuital law:

$$F = T_{ph}i = \sum H_g l_g + \sum H_s l_s + \sum H_t l_t \quad (3.184)$$

where  $H_g$ ,  $H_s$ ,  $H_t$ , and  $l_g$ ,  $l_s$ , and  $l_t$  are the magnetic field intensities and flux path lengths in the air gap, stator iron core, and translator iron core, respectively.

The following assumptions are made to compute the reluctances:

1. Only one phase is excited at any given time.
2. Flux distribution is uniform over the cross section of the core.
3. Hysteresis is negligible.
4. The flux lines enter and leave the iron surface normally.
5. The air gap sections of the flux lines consist of straight lines and concentric arc segments.
6. The flux lines in the stator and translator poles run parallel to each pole axis.
7. The flux lines in the stator and translator yokes run parallel to the longitudinal axis.

Then, the flux density  $B_k(i, x)$  in path  $k$  for current  $i$  and translator position  $x$  is given by:

$$B_k(i, x) = \frac{\phi_k(i, x)}{A_k} \quad (3.185)$$

where  $\phi_k(i, x)$  is the magnetic flux, and  $A_k$  is the cross-sectional area determined by the geometry of LSRM. In the air gap, the flux density can be represented in terms of the permeance equation as:

$$B_{gk}(i, x) = \frac{\phi_k(i, x)}{P_{gk}(x)} \cdot \frac{\mu_0}{l_{gk}}, \quad P_{gk}(x) = \frac{\mu_0 A_k}{l_{gk}} \quad (3.186)$$

where  $P_{gk}(x)$  is the air gap permeance, and  $l_{gk}$  is the average air gap length of flux lines in path  $k$ . Since the magnetic flux  $\phi_k(i, x)$  is an unknown variable, iterative procedures such as a bisection root-finding algorithm is introduced by assuming an arbitrary initial value of  $\phi_k(i, x)$ . The value of  $B_k(i, x)$  is obtained from Eq. (3.185) and is used in the B-H characteristics of the core material to obtain the magnetic field intensity  $H_k(i, x)$ , except in the air gap region of linear free space. Determination of magnetic field intensity in the iron core requires an accurate fit of the B-H nonlinear characteristic curve, and cubic spline interpolation is normally used. The value of  $H_k(i, x)$  thus obtained is used to test for convergence in the mmf equation 3.184. The iterative solution outlined above gives the value of magnetic flux  $\phi_k(i, x)$  associated with path  $k$ . Finally, the inductance  $L(i, x)$  for one phase with all magnetic flux paths is calculated as:

$$L(i, x) = \sum_k L_k(i, x) = \frac{T_{ph}}{i} \sum_k \phi_k(i, x) \quad (3.187)$$

A flow chart for the calculation procedure is shown in [Figure 3.33](#).

The selection of flux paths is usually accomplished based on the flux distribution in the air gap. The air gap predominantly determines the flux distribution, as most of the mmf and hence the magnetic energy is applied to the air gap as long as the core is not saturated. On this basis, four different translator regions are considered for evaluation of the permeance in the air gap. They are shown in [Figure 3.34](#) including the fringing flux paths in the air gap. The flux paths are chosen primarily based on the experience gained through finite element analysis (FEA). The air gap permeance path for the different locations of the translator can similarly be inferred by these four configurations. It is observed from [Figures 3.34b](#) and [c](#) that the local saturation occurs in the pole tips of both the stator and translator. The local saturation occurs when the relative position of the stator and translator is at the threshold of overlap or during partial overlap. This phenomenon is dependent on the level of excitation and the shape of the pole tips. To accommodate the pole tip saturation effect, the flux density in this region is assumed to be the maximum of the iron core material, and the effective pole width and pole height are approximated using the small rectangular area. Uniform distribution of the magnetic flux density in the core is assumed for fully aligned and unaligned positions, as shown in [Figures 3.34a](#) and [d](#), respectively.

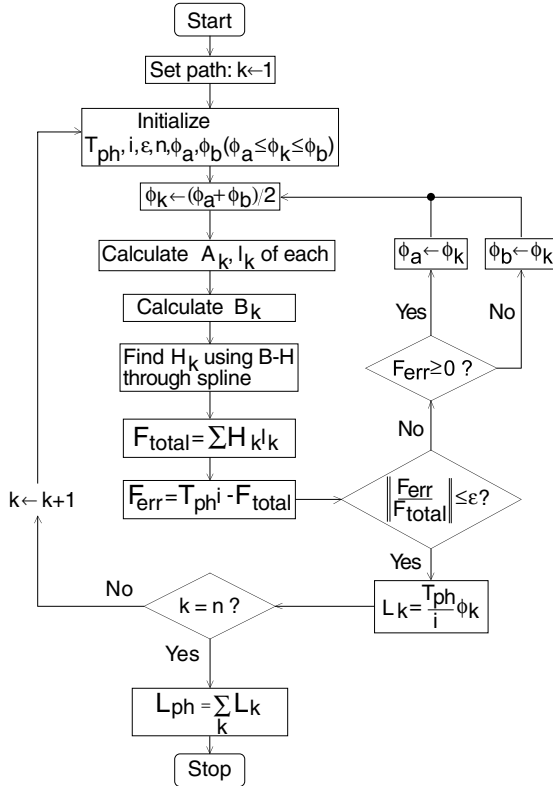


**FIGURE 3.33** Flow chart for calculation of the phase winding using bi-section root finding.

#### 3.13.4.1.1 Aligned Inductance Calculation

The air gap permeance of the aligned position considering the end effects generated by the end windings of the stator pole is derived in this section. Analytical estimation of the permeance of the air gap flux paths has been developed for use in electromagnetic devices<sup>44</sup> and is summarized in Appendix 3A. The air gap has seven different types of flux paths, as shown in Figure 3.34a. Each flux path consists of straight lines and concentric circular arc segments. Also, each flux path has a numeric label that is associated with the permeance expression. The paths from 1 to 3 are the main flux linkages for the air gap permeance evaluation, and the paths from four to seven are included to consider the three-dimensional end effect. The fringing flux paths of pole ends are indicated by a dashed oblique line and small dot because of the difficulty in showing them in a two-dimensional figure. Detailed equations for the permeance evaluation in the poles and back iron of the stator and translator are given in Appendix 3B. The derived air gap permeances are given in the following:

$$P_{g1} = \mu_0 \frac{L_w \cdot (w_{sp} + w_{tp}) / 2}{\ell_g} = \mu_0 L_w \left( \frac{w_{sp} + w_{tp}}{2 \cdot \ell_g} \right) \quad (3.188)$$

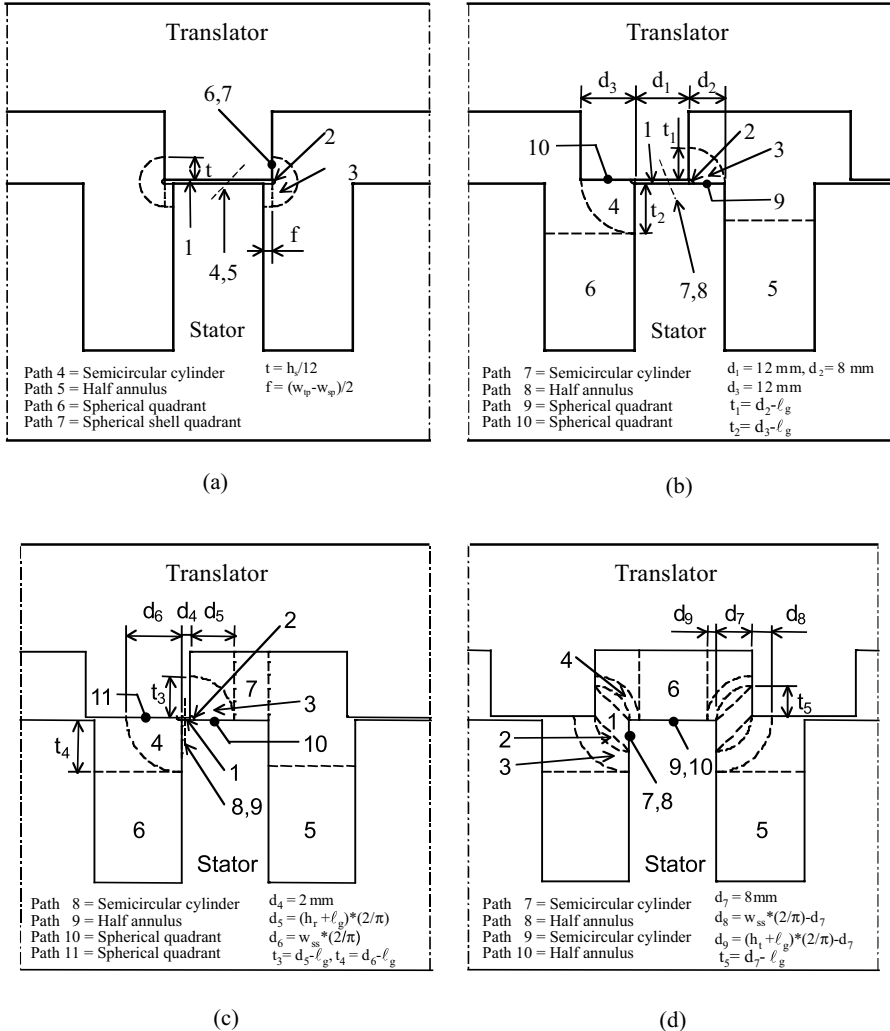


**FIGURE 3.34** Magnetic flux paths and permeance calculations in the four different translator positions. (a) Fully aligned position; (b) one third shift of translator from fully aligned position; (c) two thirds shift of translator from fully aligned position; (d) fully unaligned position.

$$P_{g2} = \mu_0 \left( \frac{L_w \cdot 0.322 \ell_g}{1.22 \ell_g} \right) = 0.268 \cdot \mu_0 L_w \quad (3.189)$$

$$P_{g31} = 0.318 \cdot \mu_0 L_w \cdot \ln \left( 1 + \frac{2t_0}{\ell_g} \right) \quad (3.190)$$

$$P_{g32} = \mu_0 \frac{L_w t_0}{f} = \mu_0 L_w \frac{t_0}{f_0} \quad (3.191)$$

$$P_{g3} = \frac{P_{g31} \cdot P_{g32}}{P_{g31} + P_{g32}} \quad (3.192)$$

$$P_{g4} = 0.268 \cdot \mu_0 \left( \frac{w_{sp} + w_{tp}}{2} \right) = 0.314 \cdot \mu_0 (w_{sp} + w_{tp}) \quad (3.193)$$

$$P_{g5} = 0.318 \cdot \mu_0 \left( \frac{w_{sp} + w_{tp}}{2} \right) \cdot \ln \left( 1 + \frac{2t_0}{\ell_g} \right) = 0.159 \cdot \mu_0 (w_{sp} + w_{tp}) \cdot \ln \left( 1 + \frac{2t_0}{\ell_g} \right) \quad (3.194)$$

$$P_{g6} = 0.076 \cdot \mu_0 \ell_g \quad (3.195)$$

$$P_{g7} = 0.25 \cdot \mu_0 t_0 \quad (3.196)$$

where

$$\begin{aligned} t_0 &= \frac{h_s}{12} \\ f_0 &= \frac{w_{tp} - w_{sp}}{2} \end{aligned} \quad (3.197)$$

By assuming the initial value for flux  $\phi_k$ , the flux density for each part can be obtained from Eqs. (3.185) and (3.186). The total mmf,  $F_t$ , at the rated phase current is calculated using Eq. (3.184) as:

$$F_t = 2 \cdot \left( \frac{\phi_k}{P_{gk}} + H_{spk} \cdot l_{spk} + H_{syk} l_{syk} + H_{tpk} \cdot l_{tpk} + H_{tyk} l_{tyk} \right) \quad (3.198)$$

where  $H_{spk}$ ,  $H_{syk}$ ,  $H_{tpk}$ , and  $H_{tyk}$  are the magnetic field intensities in the stator pole, stator back iron, translator pole, and translator back iron in path  $k$ , respectively. These values are obtained from the B-H characteristics of the lamination material, M19 steel. For example 1, after the convergence of the mmf equation with the designed value of  $F_t = T_{ph} i = 210 \cdot 8.5 = 1785$ , the aligned inductance for the rated phase current is calculated as:

$$\begin{aligned} L(i = 8.5 \text{ A}, x = 30 \text{ mm}) &= L_1 + 2 \cdot (L_2 + L_3) + 4 \cdot (L_4 + L_5 + L_6 + L_7) \\ &= \frac{T_{ph}}{i} \cdot [\phi_1 + 2 \cdot (\phi_2 + \phi_3) + 4 \cdot (\phi_4 + \phi_5 + \phi_6 + \phi_7)] \\ &= 32.608 \text{ mH} \end{aligned}$$

The flux density in the air gap is then obtained as:

$$B_{g1} = \frac{\phi_{k1}}{P_{g1}} \cdot \frac{\mu_0}{\ell_g} = \frac{1.196 \cdot 10^{-3}}{1.382 \cdot 10^{-6}} \cdot \frac{4\pi \cdot 10^{-7}}{0.001} = 1.087 \text{ T}$$

### 3.13.4.1.2 Intermediate Inductance Calculation—One-Third Shift of Translator from Fully Aligned Position

The air gap in this region has ten different types of flux paths and for each of these paths the permeance is derived as:

$$P_{g1} = \mu_0 L_w \cdot \frac{d_1}{\ell_g} \quad (3.199)$$

$$P_{g2} = 0.5356 \cdot \mu_0 L_w \quad (3.200)$$

$$P_{g3} = \frac{\mu_0 L_w}{(\pi/2)} \cdot \ln\left(\frac{\ell_g + t_1}{\ell_g}\right) = 0.637 \cdot \mu_0 L_w \cdot \ln\left(1 + \frac{t_1}{\ell_g}\right) \quad (3.201)$$

$$P_{g4} = \frac{\mu_0 L_w}{(\pi/2)} \cdot \ln\left(\frac{\ell_g + t_2}{\ell_g}\right) = 0.637 \cdot \mu_0 L_w \cdot \ln\left(1 + \frac{t_2}{\ell_g}\right) \quad (3.202)$$

$$P_{g5} = \mu_0 \frac{L_w \cdot (h_s - d_2)}{w_{ss}} = \mu_0 L_w \cdot \left(\frac{h_s - d_2}{w_{ss}}\right) \quad (3.203)$$

$$P_{g6} = \mu_0 \frac{L_w \cdot (h_s - t_2)}{w_{ss}} = \mu_0 L_w \cdot \left(\frac{h_s - t_2}{w_{ss}}\right) \quad (3.204)$$

$$P_{g7} = 0.268 \cdot \mu_0 d_1 \quad (3.205)$$

$$P_{g8} = \frac{\mu_0 d_1}{\pi} \cdot \ln\left(\frac{(\ell_g + t_1 + t_2)/2}{\ell_g/2}\right) = 0.318 \cdot \mu_0 d_1 \cdot \ln\left(1 + \frac{(t_1 + t_2)}{\ell_g}\right) \quad (3.206)$$

$$P_{g9} = 0.152 \cdot \mu_0 d_2 \quad (3.207)$$

$$P_{g10} = 0.152 \cdot \mu_0 d_3 \quad (3.208)$$

where

$$\begin{aligned} d_1 &= x - f_0 \\ d_2 &= w_{sp} - d_1 \\ d_3 &= w_{tp} - d_1 \\ t_1 &= d_2 - \ell_g \\ t_2 &= d_3 - \ell_g \end{aligned} \quad (3.209)$$

The computational procedure for inductance is very similar to that of the aligned inductance. The inductance for the rated phase current is calculated as:

$$L(i = 8.5 \text{ A}, x = 20 \text{ mm}) = 25.280 \text{ mH}$$

### 3.13.4.1.3 Intermediate Inductance Calculation—Two-Thirds Shifting of Translator from Fully Aligned Position

The air gap in this region is assumed to have 11 different types of flux paths and their permeances are given by:

$$P_{g1} = \mu_0 L_w \cdot \frac{d_4}{\ell_g} \quad (3.210)$$

$$P_{g2} = 0.5356 \cdot \mu_0 L_w \quad (3.211)$$

$$P_{g3} = \frac{\mu_0 L_w}{(\pi/2)} \cdot \ln\left(\frac{\ell_g + t_3}{\ell_g}\right) = 0.637 \cdot \mu_0 L_w \cdot \ln\left(1 + \frac{t_3}{\ell_g}\right) \quad (3.212)$$

$$P_{g4} = \frac{\mu_0 L_w}{(\pi/2)} \cdot \ln\left(\frac{\ell_g + t_4}{\ell_g}\right) = 0.637 \cdot \mu_0 L_w \cdot \ln\left(1 + \frac{t_4}{\ell_g}\right) \quad (3.213)$$

$$P_{g5} = \mu_0 \frac{L_w \cdot (h_s - d_5)}{w_{ss}} = \mu_0 L_w \cdot \left(\frac{h_s - d_5}{w_{ss}}\right) \quad (3.214)$$

$$P_{g6} = \mu_0 \frac{L_w \cdot (h_s - t_4)}{w_{ss}} = \mu_0 L_w \cdot \left(\frac{h_s - t_4}{w_{ss}}\right) \quad (3.215)$$

$$P_{g7} = \mu_0 \frac{L_w \cdot (w_{sp} - d_4 - d_5)}{\ell_g + h_r} = \mu_0 L_w \cdot \left(\frac{w_{sp} - d_4 - d_5}{\ell_g + h_r}\right) \quad (3.216)$$

$$P_{g8} = 0.268 \cdot \mu_0 d_4 \quad (3.217)$$

$$P_{g9} = \frac{\mu_0 d_4}{\pi} \cdot \ln\left(\frac{(\ell_g + t_3 + t_4)/2}{\ell_g/2}\right) = 0.318 \cdot \mu_0 d_4 \cdot \ln\left(1 + \frac{(t_3 + t_4)}{\ell_g}\right) \quad (3.218)$$

$$P_{g10} = 0.152 \cdot \mu_0 d_5 \quad (3.219)$$

$$P_{g11} = 0.152 \cdot \mu_0 d_6 \quad (3.220)$$

where

$$\begin{aligned}
 d_4 &= x - \left( \frac{w_{ts} - w_{sp}}{2} \right) \\
 d_5 &= \frac{2}{\pi} (h_r + \ell_g) \\
 d_6 &= \frac{2}{\pi} w_{ss} \\
 t_3 &= d_5 - \ell_g \\
 t_4 &= d_6 - \ell_g
 \end{aligned} \tag{3.221}$$

The inductance for the rated phase current from these equations is calculated as:

$$L(i = 8.5 \text{ A}, x = 10 \text{ mm}) = 11.680 \text{ mH}$$

#### 3.13.4.1.4 Fully Unaligned Inductance Calculation

The air gap in this section is assumed to have ten different types of flux paths and their permeances are given by:

$$P_{g1} = \mu_0 \frac{L_w \cdot t_5 / \sqrt{2}}{\sqrt{2} d_7} = \mu_0 L_w \cdot \frac{t_5}{2 d_7} \tag{3.222}$$

where

$$\begin{aligned}
 d_7 &= -d_4 \\
 t_5 &= d_7 - \ell_g
 \end{aligned} \tag{3.223}$$

The mean length of flux path 2 is equal to the length of a line drawn midway between the straight line and arc circumference and is equal to  $1.462 \cdot d_7$ . The mean cross-sectional area of the flux path is estimated by dividing the entire volume of flux path 2 by the mean length. The permeances are

$$P_{g2} = \mu_0 \frac{\left( \frac{0.285 \cdot d_7^2 L_w}{1.462 \cdot d_7} \right)}{1.462 \cdot d_7} = 0.134 \cdot \mu_0 L_w \tag{3.224}$$

$$P_{g3} = \frac{\mu_0 L_w}{(\pi/2)} \cdot \ln\left(\frac{d_7 + d_8}{d_7}\right) = 0.637 \cdot \mu_0 L_w \cdot \ln\left(1 + \frac{d_8}{d_7}\right) \tag{3.225}$$

$$P_{g4} = \frac{\mu_0 L_w}{(\pi/2)} \cdot \ln\left(\frac{d_7 + d_9}{d_7}\right) = 0.637 \cdot \mu_0 L_w \cdot \ln\left(1 + \frac{d_9}{d_7}\right) \tag{3.226}$$

$$P_{g5} = \mu_0 \frac{L_w \cdot (h_s - t_5 - d_8)}{w_{ss}} = \mu_0 L_w \cdot \frac{(h_s - t_5 - d_8)}{w_{ss}} \quad (3.227)$$

$$P_{g6} = \mu_0 \frac{L_w \cdot (w_{sp} - 2d_9)}{h_t + g} = \mu_0 L_w \cdot \frac{(w_{sp} - 2d_9)}{h_t + g} \quad (3.228)$$

$$P_{g7} = \mu_0 \frac{\left( \frac{0.393 \cdot d_7^2 t_5}{1.713 \cdot d_7} \right)}{1.713 \cdot d_7} = 0.134 \cdot \mu_0 t_5 \quad (3.229)$$

$$P_{g8} = \mu_0 \frac{\frac{t_5}{\sqrt{2}} \cdot \frac{(d_8 + d_9)}{2}}{\frac{\sqrt{2}\pi}{4} \cdot (2d_7 + d_8 + d_9)} = 0.318 \cdot \mu_0 \cdot \frac{t_5}{1 + \frac{2d_7}{(d_8 + d_9)}} \quad (3.230)$$

$$P_{g9} = 0.268 \cdot \mu_0 (w_{sp} - 2d_9) \quad (3.231)$$

$$P_{g10} = \frac{(w_{sp} - 2d_9) \cdot d_9}{\frac{\pi}{2} \cdot (h_t + \ell_g + d_9)} = 0.637 \cdot \mu_0 \cdot \frac{(w_{sp} - 2d_9)}{1 + \frac{(h_t + \ell_g)}{d_9}} \quad (3.232)$$

where

$$\begin{aligned} d_8 &= \frac{2}{\pi} w_{ss} - d_7 \\ d_9 &= \frac{2}{\pi} (h_r + \ell_g) - d_7 \end{aligned} \quad (3.233)$$

The unaligned inductance for the rated phase current is calculated for example 1 as:

$$L(i = 8.5 \text{ A}, x = 0 \text{ mm}) = 7.490 \text{ mH}$$

### 3.13.4.2 Analytical Force Calculation

The forces in the  $x$ ,  $z$ , and  $y$  directions, named as the propulsion force, normal force, and lateral force, respectively, and shown in [Figure 3.35](#), can be calculated using the principle of conservation of energy expressed as,

$$dW_e = dW_I + dW_s + dW_m \quad (3.234)$$

where  $dW_e$  is the incremental electric input energy,  $dW_I$  is the incremental loss energy dissipated by heat,  $dW_s$  is the incremental stored magnetic energy, and  $dW_m$  is the

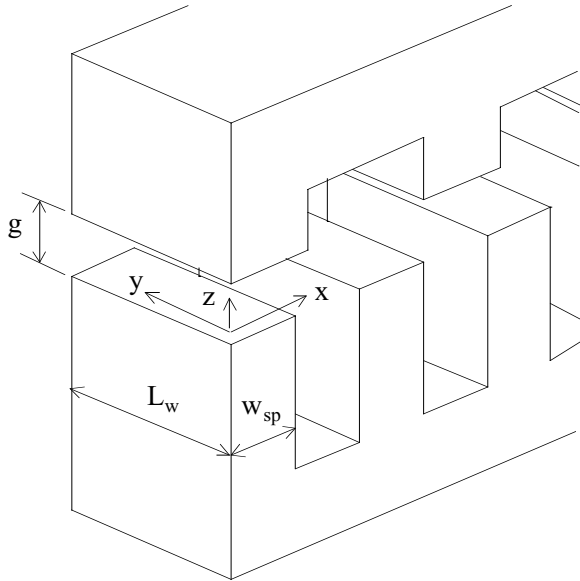


**FIGURE 3.35** Analytical force calculation using the principle of conservation of energy.

incremental mechanical energy. Assuming that the translator moves in the  $x$  direction by  $dx$ , the incremental mechanical energy is defined as:

$$dW_{mx} = f_x dx \quad (3.235)$$

where  $f_x$  is the propulsion force generated. The same expression is used for other forces with displacements in their directions. It is clear from the energy conservation principle that the force calculations in  $x$ ,  $y$ , and  $z$  directions require incremental values of electric input energy, energy loss, and stored energy in the magnetic field.

The flux density in the air gap is given by:

$$B_g = \frac{\phi}{XY} \quad (3.236)$$

where  $X$  and  $Y$  are the overlapped lengths in a particular position of the translator with respect to the stator in the  $x$  and  $y$  directions, respectively. As described in Section 3.13.3.2, assuming a large air gap in the linear machine structure, Eq. (3.155) can be written as:

$$\phi = B_g \cdot XY = \mu_0 H_g \cdot XY = \mu_0 \frac{T_{ph} i}{Z} \cdot XY \Rightarrow T_{ph} i = \frac{\phi Z}{\mu_0 XY} \quad (3.237)$$

The incremental electric input energy  $dW_e$  is given by the multiplication of flux linkage  $\lambda$  and constant excitation current  $i$  as:

$$dW_e = i \cdot d\lambda = i \cdot d(T_{ph}\phi) = T_{ph}i \cdot d\phi = \frac{\phi Z}{\mu_0 XY} \cdot d\phi \quad (3.238)$$

The stored energy in the magnetic field  $W_s$  is

$$W_s = \frac{B_g^2 \cdot XYZ}{2\mu_0} = \left(\frac{\phi}{XY}\right)^2 \cdot \frac{XYZ}{2\mu_0} = \frac{\phi^2 Z}{2\mu_0 XY} \quad (3.239)$$

The incremental stored magnetic energy  $dW_{sx}$  for the incremental displacement  $dx$ , and which causes the propulsion force, is given by:

$$dW_{sx} = -\frac{\phi^2 Z}{2\mu_0 X^2 Y} \cdot dx + \frac{\phi Z}{\mu_0 XY} d\phi \quad (3.240)$$

Ignoring incremental energy losses such as copper loss, core loss, and mechanical friction loss, the incremental mechanical energy  $dW_{mx}$  during the incremental displacement  $dx$  can be written as:

$$dW_{mx} = dW_e - dW_{sx} = \frac{\phi Z}{\mu_0 XY} \cdot d\phi + \frac{\phi^2 Z}{2\mu_0 X^2 Y} \cdot dx - \frac{\phi Z}{\mu_0 XY} \cdot d\phi = \frac{\phi^2 Z}{2\mu_0 X^2 Y} \cdot dx \quad (3.241)$$

From which the propulsion force is now obtained as:

$$f_x = \frac{dW_{mx}}{dx} = \frac{\phi^2 Z}{2\mu_0 X^2 Y} = \frac{(B_g XY)^2 Z}{2\mu_0 X^2 Y} = \frac{B_g^2}{2\mu_0} \cdot YZ \quad (3.242)$$

The incremental stored magnetic energy  $dW_{sz}$  during the incremental displacement  $dz$  is given by:

$$dW_{sz} = \frac{\phi^2}{2\mu_0 XY} \cdot dz + \frac{\phi Z}{\mu_0 XY} \cdot d\phi \quad (3.243)$$

Ignoring incremental energy losses, the incremental mechanical energy  $dW_{mz}$  due to incremental displacement  $dz$  can be written as:

$$dW_{mz} = dW_e - dW_{sz} = \frac{\phi Z}{\mu_0 XY} \cdot d\phi - \frac{\phi^2}{2\mu_0 XY} \cdot dz - \frac{\phi Z}{\mu_0 XY} \cdot d\phi = -\frac{\phi^2}{2\mu_0 XY} \cdot dz \quad (3.244)$$

The normal force is then obtained as:

$$f_z = \frac{dW_{mz}}{dz} = -\frac{\phi^2}{2\mu_0 XY} = -\frac{(B_g XY)^2}{2\mu_0 XY} = -\frac{B_g^2}{2\mu_0} \cdot XY \quad (3.245)$$

The negative sign indicates that the force generated tends to decrease the length of the air gap and in this case is the downward force experienced by the translator. Similarly, the lateral force can be calculated as:

$$f_y = \frac{B_g^2}{2\mu_0} \cdot XZ \quad (3.246)$$

In the design described in Example 1, with  $L_w = 50$  mm,  $w_{sp} = 20$  mm,  $\ell_g = 1$  mm, and  $B_g = 1.087$  T, the propulsion force due to excitation of a single pole is

$$f_{x1} = \frac{B_g^2}{2\mu_0} \cdot YZ = \frac{B_g^2}{2\mu_0} \cdot L_w \ell_g = 23.506 \text{ N}$$

The propulsion force due to the excitation of a phase is  $f_x = 2 \cdot f_{x1} = 47.01$  N. The normal force due to excitation of a single pole is calculated as:

$$f_{z1} = -\frac{B_g^2}{2\mu_0} \cdot XY = -\frac{B_g^2}{2\mu_0} \cdot w_{sp} L_w = -470.13 \text{ N}$$

The total downward force experienced by the translator is given by  $f_z = 2 \cdot f_{z1} = -940.26$  N. The normal force can be calculated at different translator positions by changing the overlap length  $X$ .

### 3.13.4.3 Finite Element Analysis Verification

In this section, two-dimensional finite element analysis is used to verify the design procedure of the LSRM and the accuracy of the analytical method. The flux linkages and inductances of the stator phase windings and the propulsion and normal forces developed by the machine for various excitation currents and translator positions are determined. Finite element analysis, in general, provides more accurate results than the magnetic equivalent circuit approach because it considers a large number of flux paths compared to the magnetic equivalent circuit method.

To determine the magnetic field distribution of the LSRM, the following assumptions are made: (1) The magnetic field distribution is constant along the longitudinal direction of the LSRM; (2) the magnetic field outside the LSRM periphery is negligible and has zero magnetic vector potential, as the Dirichlet boundary condition is assigned to the outer periphery of the LSRM surface; (3) in the two-dimensional analysis, the current density vector has a component only in the  $y$  direction, and, for this reason, the flux density vector has components only in the  $x$  and  $z$

directions; (4) hysteresis effects are neglected under the assumptions that the magnetic materials of the stator and translator are isotropic and the magnetization curve is single valued; (5) the end effects are neglected.

The field solution is obtained using the Flux-2D software package by Magsoft Corporation. The entire problem region is subdivided into triangular finite elements, with 14,916 nodes and 7149 elements. The LSRM translator is moved from an unaligned position with respect to the stator to an aligned position for different excitation currents, and, corresponding to each translator position, the inductance, propulsion force, and normal force are obtained. [Figure 3.36](#) shows the flux distributions

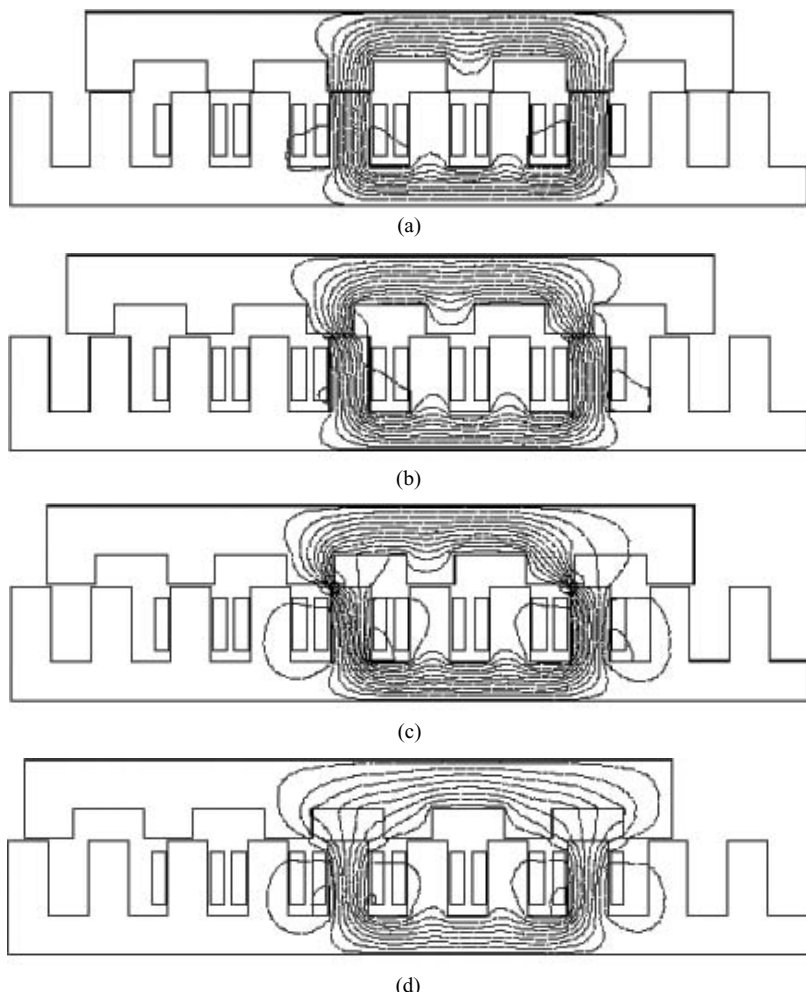


**FIGURE 3.36** Flux distribution of the three-phase LSRM prototype for the rated phase current. (a) Fully aligned position; (b) Intermediate position: one third shift of translator from fully aligned position; (c) Intermediate position: two thirds shift of translator from fully aligned position; (d) Fully unaligned position.

inside the LSRM for the fully aligned position, two intermediate positions of 10 mm and 20 mm shifted from the fully aligned position, and fully unaligned position of the translator. These plots are obtained for a current of 8.5 A in one phase winding. It is observed that the leakage flux lines cross the stator slot to the adjacent stator poles and complete their path through the stator back iron. The flux densities in the excited stator poles and the force producing translator poles are high for a given excitation. The flux densities in other parts of the machine are very low.

The force in a given direction is obtained by differentiating the magnetic coenergy of the system with respect to a virtual displacement of the translator in this direction using the calculated flux densities in each triangular element. Based on this approach, the propulsion forces at various currents for various translator positions are calculated. The results are presented in a later section along with experimental results.

### 3.13.4.4 Experimental Setup for Measurements

#### 3.13.4.4.1 Inductance Measurement

[Figure 3.37](#) shows the schematic diagram for the measurement of phase winding inductance.<sup>35</sup> After the translator is locked mechanically into the desired position, a dc voltage is applied to the test phase winding through a power semiconductor switch, thus a constant current is applied to the phase winding. Once the current reaches steady state, the power switch is turned off and the current is diverted through the diode. The current starts to decay and the falling current profile is captured using the triggering mode of the oscilloscope. The time constant is measured from the profile and the inductance is calculated. A metal oxide semiconductor field effect transistor (MOSFET) power switch with a fast turn-off characteristic is used for disconnecting the dc source from the phase winding. A freewheeling diode of the fast recovery type has to be connected across the test phase winding to provide a path for the stored energy after the winding is disconnected from the source. The voltage drop across the diode introduces a small discrepancy in evaluation of the time constant. In order to minimize its impact, a large external resistor can be connected in series with the winding. It has another advantage in that it minimizes the impact

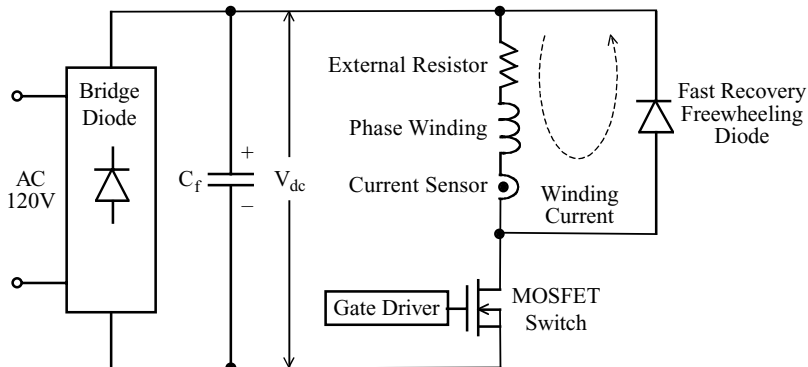


**FIGURE 3.37** Schematic diagram for the measurement of phase winding inductance.

of winding resistance variation in the evaluation of the time constant. Without the external resistor, a small change in stator resistance can cause a large variation in time constant.

#### 3.13.4.4.2 Force Measurement

Figures 3.38 and 3.39 show the experimental setup for the measurement of the propulsion and normal forces, respectively. They are measured after locking the

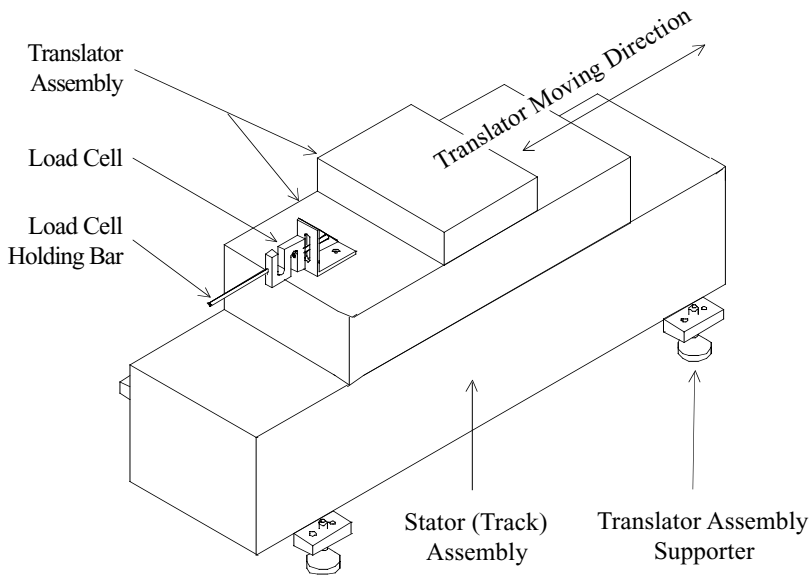


**FIGURE 3.38** Experimental setup for the propulsion force measurement.

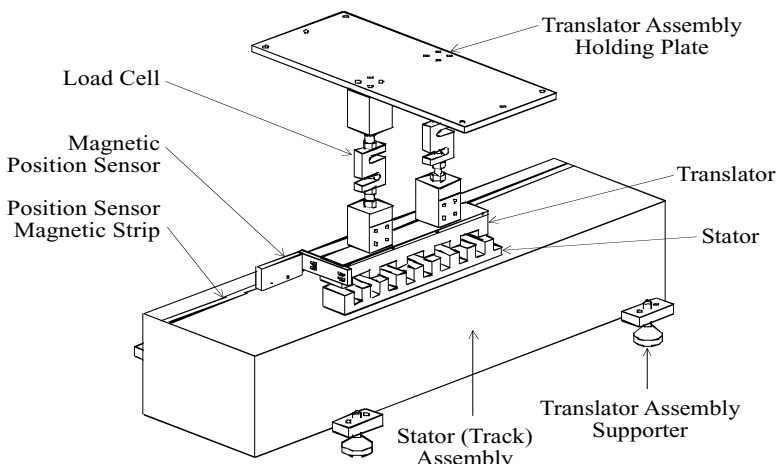


**FIGURE 3.39** Experimental setup for the normal force measurement.

translator at the desired position and energizing one phase winding with a constant current. When the current reaches steady state, the force is recorded. This test procedure is repeated for various currents and translator positions. The force is measured using an S-type load cell. The translator and its mechanical support are connected through the screws at each end of the S-type load cell to minimize any off-center pull or push. In the case of normal force measurement, two load cells of the same capacity are used, as shown in [Figure 3.39](#). For this reason, the two sensor outputs should be added to obtain the total normal force.

### 3.13.4.5 Results and Comparison

[Figure 3.40](#) shows the measured results along with finite element analysis results and also shows the correlation to the finite element analysis results. The inductance profiles at currents lower than the rated value are almost identical to the profile at the rated current due to the fact that the air gap usually is very large in the linear machine and the machine does not saturate at all. There is high correlation in the aligned inductance region, but small discrepancies in the unaligned inductance region may be due to the end effects. Note that they are not considered in the two-dimensional electromagnetic field analysis. A comparison of inductances by three different methods at fully aligned, two intermediate, and fully unaligned positions is given in [Table 3.2](#) at the rated phase current. In the aligned translator position, both the analytical and finite element results are very close to the measured inductance with

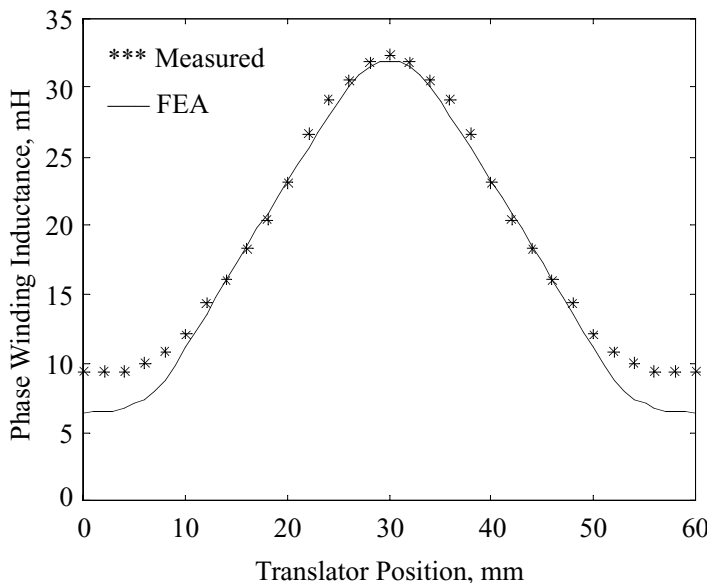


**FIGURE 3.40** Measured and finite element analysis results of inductance at the rated phase current of 8.5 A.

---

**TABLE 3.2**  
**Comparison of Winding Inductance Results by Three Methods**  
**at the Rated Phase Current**

Translator Position	Analytical Value without End Effect (mH)	Analytical Value with End Effect (mH)	Finite Element Analysis (mH)	Measured Value (mH)
Fully aligned position ( $x = 30 \text{ mm}$ )	31.459	32.608	31.961	32.375
Intermediate position ( $x = 20 \text{ mm}$ )	24.408	25.280	23.301	23.100
Intermediate position ( $x = 10 \text{ mm}$ )	11.392	11.680	11.073	12.110
Fully unaligned position ( $x = 0 \text{ mm}$ )	7.014	7.490	6.382	9.380

---

less than 2% error. On the other hand, in the unaligned translator position, the analytical and finite element results have errors of 20.1% and 31.9%, respectively. The error is attributable to the end effects and, to a smaller degree, to distortion of the magnetic properties of the core material due to punching stresses, inexact B-H characteristics provided by the steel manufacturers and nonuniformity of the air gap. End leakage effects are severe in the fully aligned position because the reluctance of the end paths becomes comparable to that of the air gap paths. Even though the end effect has been included in the analytical method, accurate modeling of the three-dimensional geometry of leakage flux tubes is difficult. It can be seen that the analytical results are closer to the measurements than the results of the finite element analysis.

Figure 3.41 shows the measured propulsion forces at different positions and currents together with the finite element analysis results. At smaller currents, there is high correlation between the finite element analysis and measured values, but at higher currents there is a minor discrepancy between the two sets of values. Figure 3.42 shows the measured and finite element analysis computed normal forces at different positions and currents. The discrepancy between the results by different methods is attributed to the side load acting on the S-type load cell. In the increasing inductance region, the translator receives not only the downward normal force but also the propulsion force. This propulsion force generated affects the S-type load cell as a side load, which is undesirable during the measurement of normal force. Figure 3.43 shows the analytical and finite element analysis results for various positions and currents. High correlation is observed between the two methods. Figure 3.44 shows the prototype LSRM discussed in Example 1.

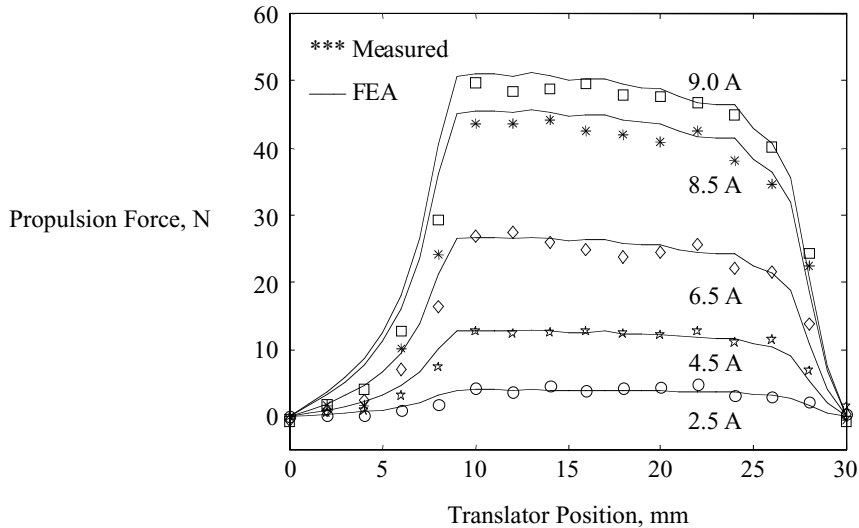


**FIGURE 3.41** Measured and finite element analysis results of propulsion force at different phase currents.

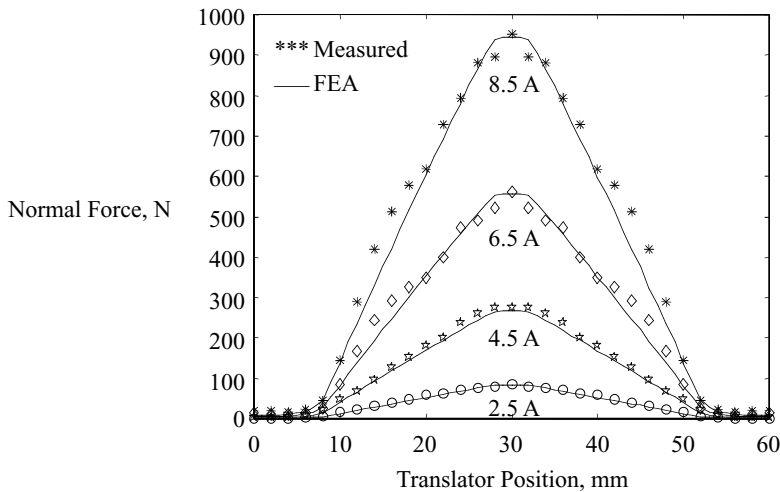


**FIGURE 3.42** Measured and finite element analysis results of normal force at different phase currents.

### APPENDIX 3A: CALCULATION OF AIR GAP PERMEANCE

The method for analytical estimation of the permeance of prefixed flux paths has been developed<sup>44</sup> for use in electromagnetic devices and is introduced here. In general, the lumped parameter magnetic circuit analysis requires reluctances computed from the permeances for various flux paths. The accuracy of the magnetic equivalent

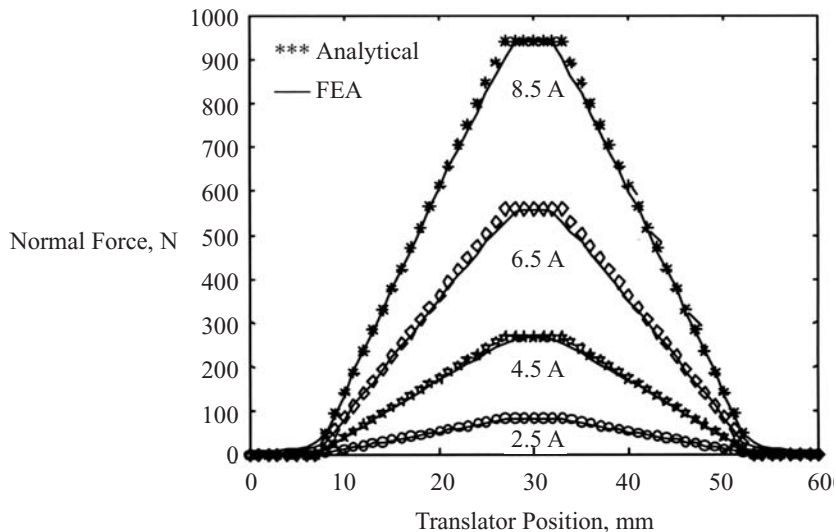


**FIGURE 3.43** Analytical and finite element analysis results of normal force at different phase currents.

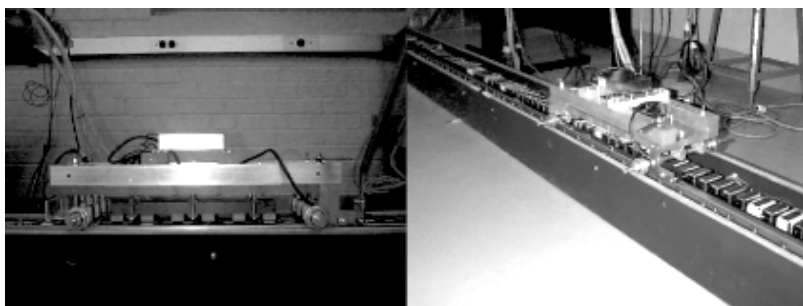


**FIGURE 3.44** Three-phase LSRM prototype setup.

circuits is dependent on the reluctances and hence on the permeances. However, three-dimensional flux distribution makes the task of the designer difficult when estimating the permeance accurately. For this reason, the analytical air gap permeance calculations use predetermined magnetic flux paths in between the poles, consisting of straight lines and concentric circular arc segments.

The stator and translator poles at a given position determine the air gap geometry. The poles are rectangular in shape and separated from each other by an air gap, as shown in [Figure 3.45](#).<sup>51</sup> The total flux linkages can be estimated using five basic forms of flux paths: parallelepiped, semicircular cylinder, half annulus, spherical quadrant, and spherical shell quadrant, as shown in [Figure 3.46](#).<sup>51</sup>

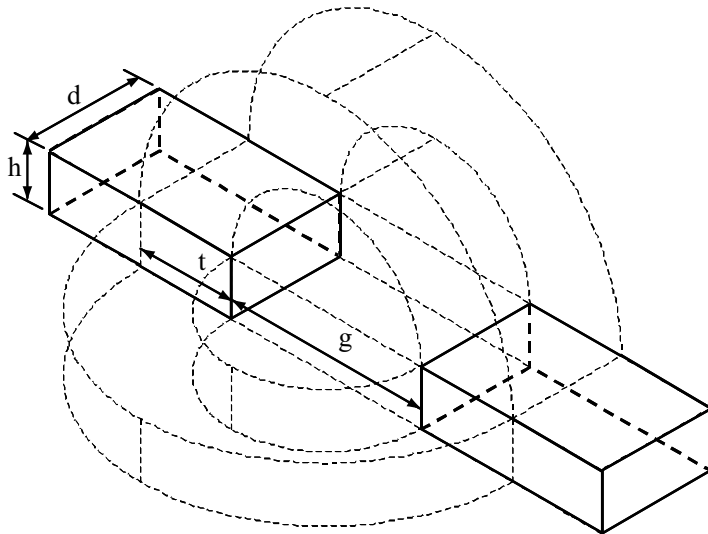


**FIGURE 3.45** Magnetic flux paths in the air gap of two rectangular poles.

### PARALLELEPIPED

This is the most basic geometry of the magnetic flux paths, and the flux lines are perpendicular to the material or plane surface. Calculation of the cross-section area and flux path length is simple, and the permeance is given by:

$$P_1 = \mu \cdot \frac{\text{Mean cross-section area}}{\text{Mean flux path length}} = \mu_0 \cdot \frac{hd}{\ell_g} \quad (3A.1)$$

where  $\mu_0$  is the permeability of free space,  $h$  is the height of the flux path,  $d$  is the depth of the flux path, and  $\ell_g$  is the air gap length.

### SEMICIRCULAR CYLINDER

The mean length of the flux path is equal to the length of a line drawn midway between the diameter and the semicircumference, equal to  $1.211 \cdot \ell_g$ . The mean cross-section area of the flux path is estimated by dividing the volume of the flux path by its mean length. The permeance is then derived as:

$$P_2 = \mu \cdot \frac{\text{Mean cross-section area}}{\text{Mean flux path length}} = \mu_0 \cdot \frac{\frac{\pi \ell_g^2 d}{8} \cdot \frac{1}{1.211 \ell_g}}{1.211 \ell_g} = 0.268 \cdot \mu_0 d \quad (3A.2)$$

### HALF ANNULUS

There are two different formulas for calculating the permeance of a half annulus determined by the ratio between the air gap length and annulus thickness.

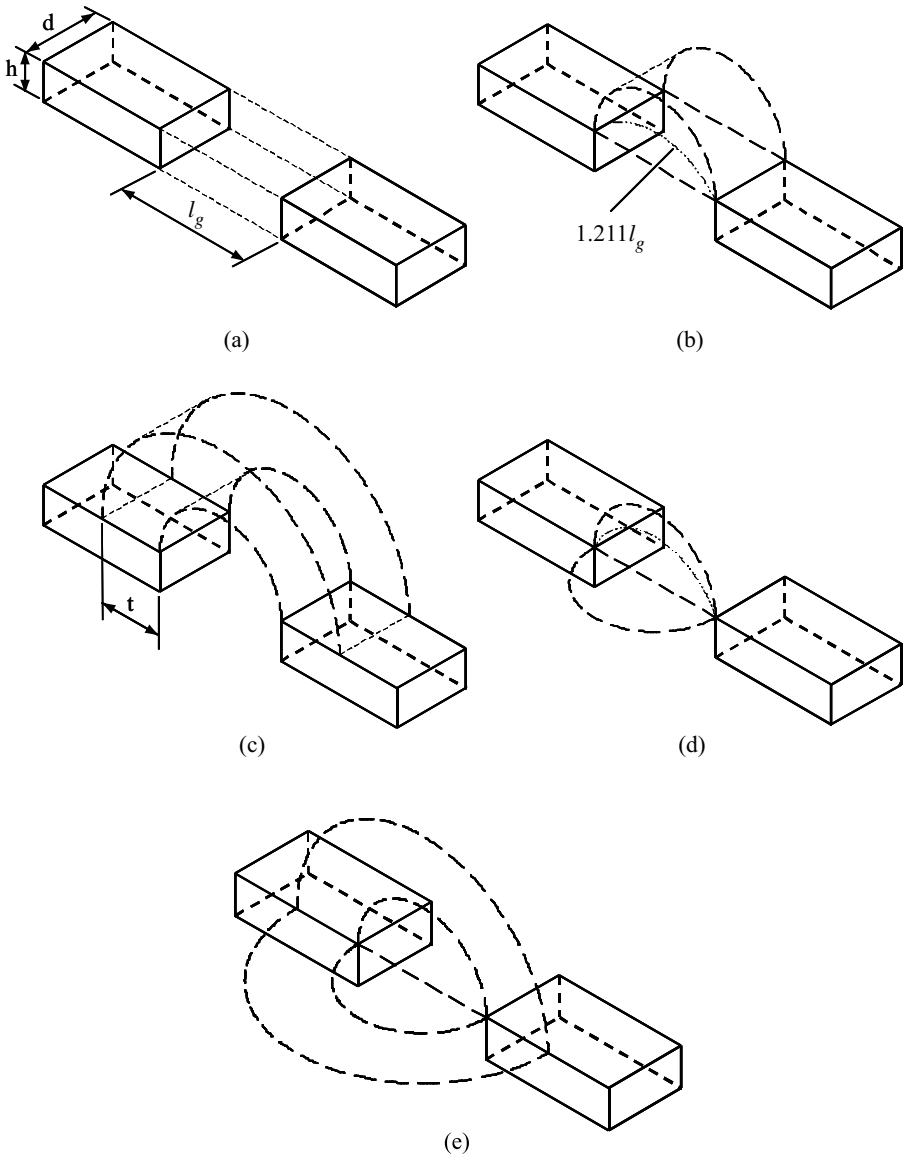


**FIGURE 3.46** Magnetic flux paths and plane surfaces of the five basic forms. (a) Parallelepiped; (b) semicircular; (c) half-annulus; (d) spherical quadrant; (e) spherical shell quadrant.

When  $\ell_g \geq 3t$ , where  $t$  is the width of the fringing flux path, the permeance is given by:

$$P_3 = \mu \cdot \frac{\text{Mean cross-section area}}{\text{Mean flux path length}} = \mu_0 \cdot \frac{td}{\pi \left( \frac{\ell_g + t}{2} \right)} = 0.637 \cdot \frac{\mu_0 td}{\ell_g + t} \quad (3A.3)$$

When  $\ell_g < 3t$ , the permeance is given by:

$$P_3 = \int_{g/2}^{(g+t)/2} \mu \cdot \frac{d \cdot dr}{\pi r} = \frac{\mu_0 d}{\pi} \cdot \ln \left( 1 + \frac{2t}{\ell_g} \right) = 0.318 \cdot \mu_0 d \cdot \ln \left( 1 + \frac{2t}{\ell_g} \right) \quad (3A.4)$$

### Spherical Quadrant

The mean length of the flux path is equal to the length of a line drawn 0.65 times the distance between the center of the sphere and the circumference, equal to  $1.311 \cdot \ell_g$ . The mean cross-section area of the flux path is also estimated by dividing the volume of the flux path by its mean length. Therefore, the permeance is given by:

$$P_4 = \mu \cdot \frac{\text{Mean cross-section area}}{\text{Mean flux path length}} = \mu_0 \cdot \frac{\frac{\pi \ell_g^3}{24} \cdot \frac{1}{1.13 \ell_g}}{1.13 \ell_g} = 0.076 \cdot \mu_0 \ell_g \quad (3A.5)$$

### Spherical Shell Quadrant

If the mean cross-section area is assumed to be half of the maximum cross-section area of the magnetic flux path, the permeance is given by:

$$P_5 = \mu \cdot \frac{\text{Mean cross-section area}}{\text{Mean flux path length}} = \mu_0 \cdot \frac{\frac{\pi t (\ell_g + t)}{8} \cdot \frac{1}{1.13 \ell_g}}{\pi \left( \frac{\ell_g + t}{2} \right)} = 0.25 \cdot \mu_0 t \quad (3A.6)$$

### Total Permeance Value of the Air Gap Flux Paths

By using Eqs. (3A.1) to (3A.6), the total permeance of the air gap flux paths shown in [Figure 3.45](#) can be calculated as:

$$\begin{aligned} P_{Total} = & \mu_0 \cdot \frac{hd}{\ell_g} + 0.536 \cdot \mu_0(h+d) + 0.636 \cdot \mu_0(h+d) \cdot \ln \left( 1 + \frac{2t}{\ell_g} \right) \\ & + 0.304 \cdot \mu_0 \ell_g + \mu_0 t \end{aligned} \quad (3A.7)$$

## APPENDIX 3B: FLUX PATHS AND ASSOCIATED VARIABLES IN THE STATOR AND TRANSLATOR<sup>51</sup>

Equations for the calculation of permeance in the poles and in the back iron of the stator and translator are given here. [Figure 3.47](#) shows the typical magnetic flux paths of the LSRM for four different translator position regions. With reference to [Figure 3.47](#), the equations for the mmf, mean length of the flux path, and its cross-section area are derived for all the four regions. Half-machine symmetry is assumed.

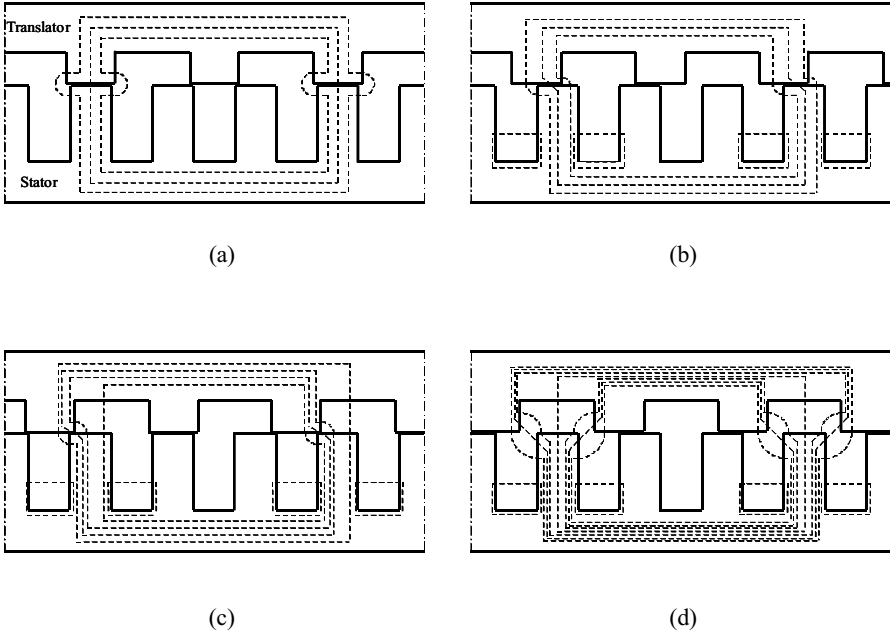


**FIGURE 3.47** Typical magnetic flux paths of the LSRM for four different translator position regions. (a) Aligned position region; (b) intermediate position region I; (c) intermediate position region II; (d) unaligned position region.

### ALIGNED POSITION REGION

#### MMF per Path

$$F_{1,2,4,6} = \frac{T_{ph}}{2} \cdot i \quad (3B.1)$$

$$F_{3,5,7} = \frac{(h_s - t/2)}{h_s} \cdot \frac{T_{ph}}{2} \cdot i \quad (3B.2)$$

where the subscript denotes the chosen flux path.

#### Mean Path Length and Mean Cross-Section Area

$$\text{Stator pole:} \quad l_{sp1,2,4,6} = h_s + C_{sy}/2 \quad (3B.3)$$

$$l_{sp3,5,7} = h_s - t/2 + C_{sy}/2 \quad (3B.4)$$

$$A_{sp1-7} = L_w w_{sp} \quad (3B.5)$$

$$Stator yoke: \quad l_{sy1\sim 7} = 1.5 \cdot (w_{sp} + w_{ss}) \quad (3B.6)$$

$$A_{sy1\sim 7} = L_w C_{sy} \quad (3B.7)$$

$$Translator pole: \quad l_{tp1,2,4,6} = h_r + C_{ry}/2 \quad (3B.8)$$

$$l_{tp3,5,7} = h_r - t/2 + C_{ry}/2 \quad (3B.9)$$

$$A_{tp1\sim 7} = L_w w_{tp} \quad (3B.10)$$

$$Translator yoke: \quad l_{ty1\sim 7} = w_{tp} + w_{ts} \quad (3B.11)$$

$$A_{tp1\sim 7} = L_w C_{ry} \quad (3B.12)$$

## INTERMEDIATE POSITION REGION I

### MMF per Path

$$F_{1,2,3,7} = \frac{T_{ph}}{2} \cdot i \quad (3B.13)$$

$$F_4 = \frac{(h_s - t_2/2)}{h_s} \cdot \frac{T_{ph}}{2} \cdot i \quad (3B.14)$$

$$F_5 = \frac{(h_s - d_2)}{h_s} \cdot \frac{T_{ph}}{2} \cdot i \quad (3B.15)$$

$$F_6 = \frac{(h_s - t_2)}{h_s} \cdot \frac{T_{ph}}{2} \cdot i \quad (3B.16)$$

$$F_8 = \frac{h_s - (t_1 + t_2)/4}{h_s} \cdot \frac{T_{ph}}{2} \cdot i \quad (3B.17)$$

$$F_9 = \frac{(h_s - d_2/2)}{h_s} \cdot \frac{T_{ph}}{2} \cdot i \quad (3B.18)$$

### Mean Path Length and Mean Cross-Section Area

$$Stator pole: \quad l_{sp1,2,3,5,7} = h_s + C_{sy}/2 \quad (3B.19)$$

$$l_{sp4,10} = h_s - t_2/2 + C_{sy}/2 \quad (3B.20)$$

$$l_{sp5} = 2 \cdot ((h_s - d_2)/2 + C_{sy}/2) \quad (3B.21)$$

$$l_{sp6} = 2 \cdot ((h_s - t_2)/2 + C_{sy}/2) \quad (3B.22)$$

$$l_{sp8} = h_s - (t_1 + t_2)/4 + C_{sy}/2 \quad (3B.23)$$

$$l_{sp9} = h_s - d_2 + C_{sy}/2 \quad (3B.24)$$

$$A_{sp1-10} = L_w w_{sp} \quad (3B.25)$$

*Stator yoke:*  $l_{sy1-4,7-10} = 1.5 \cdot (w_{sp} + w_{ss}) \quad (3B.26)$

$$l_{sy5,6} = w_{sp} + w_{ss} \quad (3B.27)$$

$$A_{sy1-10} = L_w C_{sy} \quad (3B.28)$$

*Translator pole:*  $l_{tp1,2,4,7} = h_r + C_{ry}/2 \quad (3B.29)$

$$l_{tp3} = h_r - t_1/2 + C_{ry}/2 \quad (3B.30)$$

$$l_{tp8} = h_r - (t_1 + t_2)/4 + C_{ry}/2 \quad (3B.31)$$

$$l_{tp9} = h_r - t_1/2 + C_{ry}/2 \quad (3B.32)$$

$$l_{tp10} = h_r - d_3/2 + C_{ry}/2 \quad (3B.33)$$

$$A_{tp1-4,7-10} = L_w w_{tp} \quad (3B.34)$$

*Translator yoke:*  $l_{ty1-4,7-10} = w_{tp} + w_{ts} \quad (3B.35)$

$$A_{ty1-4,7-10} = L_w C_{ry} \quad (3B.36)$$

*Pole tip:*  $l_{pt1,2,7} = t_1/2 \quad (3B.37)$

$$A_{pt1,2,7} = L_w d_1 \quad (3B.38)$$

## INTERMEDIATE POSITION REGION II

### MMF per Path

$$F_{1,2,3,7,8} = \frac{T_{ph}}{2} \cdot i \quad (3B.39)$$

$$F_{4,11} = \frac{(h_s - t_4/2)}{h_s} \cdot \frac{T_{ph}}{2} \cdot i \quad (3B.40)$$

$$F_5 = \frac{(h_s - d_5)}{h_s} \cdot \frac{T_{ph}}{2} \cdot i \quad (3B.41)$$

$$F_6 = \frac{(h_s - t_4)}{h_s} \cdot \frac{T_{ph}}{2} \cdot i \quad (3B.42)$$

$$F_9 = \frac{(h_s - (t_3 + t_4)/4)}{h_s} \cdot \frac{T_{ph}}{2} \cdot i \quad (3B.43)$$

$$F_{10} = \frac{(h_s - d_5/2)}{h_s} \cdot \frac{T_{ph}}{2} \cdot i \quad (3B.44)$$

### Mean Path Length and Mean Cross-Section Area

$$\text{Stator pole:} \quad l_{sp1,2,3,7,8} = h_s + C_{sy}/2 \quad (3B.45)$$

$$l_{sp4,11} = h_s - t_4/2 + C_{sy}/2 \quad (3B.46)$$

$$l_{sp5} = 2 \cdot ((h_s - d_5)/2 + C_{sy}/2) \quad (3B.47)$$

$$l_{sp6} = 2 \cdot ((h_s - t_4)/2 + C_{sy}/2) \quad (3B.48)$$

$$l_{sp9} = h_s - (t_3 + t_4)/4 + C_{sy}/2 \quad (3B.49)$$

$$l_{sp10} = h_s - d_5 + C_{sy}/2 \quad (3B.50)$$

$$A_{sp1\sim 11} = L_w w_{sp} \quad (3B.51)$$

*Stator yoke:*  $l_{sy1\sim 4,7\sim 11} = 1.5 \cdot (w_{sp} + w_{ss}) \quad (3B.52)$

$$l_{sy5,6} = w_{sp} + w_{ss} \quad (3B.53)$$

$$A_{sy1\sim 11} = L_w C_{sy} \quad (3B.54)$$

*Translator pole:*  $l_{tp1,2,4,8} = h_r + C_{ry}/2 \quad (3B.55)$

$$l_{tp3} = h_r - t_3/2 + C_{ry}/2 \quad (3B.56)$$

$$l_{tp7} = C_{ry}/2 \quad (3B.57)$$

$$l_{tp9} = h_r - (t_3 + t_4)/4 + C_{ry}/2 \quad (3B.58)$$

$$l_{tp10} = h_r - t_3/2 + C_{ry}/2 \quad (3B.59)$$

$$l_{tp11} = h_r - d_6/2 + C_{ry}/2 \quad (3B.60)$$

$$A_{tp1\sim 4,7\sim 11} = L_w w_{tp} \quad (3B.61)$$

*Translator yoke:*  $l_{ty1\sim 4,8\sim 11} = w_{tp} + w_{ts} \quad (3B.62)$

$$l_{ty7} = 1.5 \cdot (w_{tp} + w_{ts}) \quad (3B.63)$$

$$A_{ty1\sim 4,7\sim 11} = L_w C_{ry} \quad (3B.64)$$

*Pole tip:*  $l_{pt1,2,8} = d_4 \quad (3B.65)$

$$A_{pt1,2,8} = L_w d_5 \quad (3B.66)$$

## UNALIGNED POSITION REGION

### MMF per Path

$$F_{1,7,8} = \frac{(h_s - t_5/2)}{h_s} \cdot \frac{T_{ph}}{2} \cdot i \quad (3B.67)$$

$$F_2 = \frac{(h_s - t_5)}{h_s} \cdot \frac{T_{ph}}{2} \cdot i \quad (3B.68)$$

$$F_3 = \frac{(h_s - t_5 - d_8/2)}{h_s} \cdot \frac{T_{ph}}{2} \cdot i \quad (3B.69)$$

$$F_{4,6,9,10} = \frac{T_{ph}}{2} \cdot i \quad (3B.70)$$

$$F_5 = \frac{(h_s - d_7)}{h_s} \cdot \frac{T_{ph}}{2} \cdot i \quad (3B.71)$$

## Mean Path Length and Mean Cross-Section Area

*Stator pole:*  $l_{sp1,7,8} = h_s - t_5/2 + C_{sy}/2 \quad (3B.72)$

$$l_{sp2} = h_s - t_5 + C_{sy}/2 \quad (3B.73)$$

$$l_{sp3} = h_s - t_5 - d_8/2 + C_{sy}/2 \quad (3B.74)$$

$$l_{sp4,6,9} = h_s + C_{sy}/2 \quad (3B.75)$$

$$l_{sp5} = 2 \cdot ((h_s - t_5 - d_8)/2 + C_{sy}/2) \quad (3B.76)$$

$$l_{sp10} = h_s - d_9/2 + C_{sy}/2 \quad (3B.77)$$

$$A_{sp1-10} = L_w w_{sp} \quad (3B.78)$$

*Stator yoke:*  $l_{sy1-4,6-10} = 1.5 \cdot (w_{sp} + w_{ss}) \quad (3B.79)$

$$l_{sy5} = w_{sp} + w_{ss} \quad (3B.80)$$

$$A_{sy1-11} = L_w C_{sy} \quad (3B.81)$$

*Translator pole:*  $l_{tp1,7,8} = h_r - t_5/2 + C_{ry}/2 \quad (3B.82)$

$$l_{tp2,3} = h_r + C_{ry}/2 \quad (3B.83)$$

$$l_{tp4} = h_r - t_5 - d_9/2 + C_{ry}/2 \quad (3B.84)$$

$$l_{tp6,9} = C_{ry}/2 \quad (3B.85)$$

$$l_{tp10} = C_{ry}/2 - d_9/2 \quad (3B.86)$$

$$A_{tp1-4,6-10} = L_w w_{tp} \quad (3B.87)$$

$$\text{Translator yoke:} \quad l_{ty1-4,7,8} = 1.5 \cdot (w_{tp} + w_{ts}) \quad (3B.88)$$

$$l_{ty6,9,10} = w_{tp} + w_{ts} \quad (3B.89)$$

$$A_{ty1-4,6-10} = L_w C_{ry} \quad (3B.90)$$

## REFERENCES

1. Miller, T.J.E., *Switched Reluctance Motors and their Control*, Magna Physics Publishing and Oxford University Press, London, 1993.
2. Lawrenson, P.J., J.M. Stephenson, P.T. Blenkinsop, J. Corda, and N.N. Fulton, Variable-speed switched reluctance motors, *IEEE Proc. B*, 127(4), 253–265, 1980.
3. Harris, M.R., J.W. Finch, J.A. Mallick, and T.J.E. Miller, A review of the integral horsepower switched reluctance drive, in *IEEE IAS Conf. Proc.*, 1985, pp. 783–789.
4. Ray, W.F., P.J. Lawrenson, R.M. Davis, J.M. Stephenson, N.N. Fulton, and R.J. Blake, High performance switched reluctance brushless drives, in *IEEE IAS Conf. Proc.*, 1985, pp. 1769–1776.
5. Krishnan, R. and R. Bedingfield, Dynamic analysis of an SRM drive system, in *IEEE IAS Ann. Mtg.*, 1991, pp. 265–271.
6. Chappell, P.H., Current pulses in switched reluctance motor, *IEEE Proc. B*, 135(5), 1998.
7. Harris, M.R., J.W. Finch, J.A. Mallick, and T.J.E. Miller, A review of the integral horsepower switched reluctance drive, in *IEEE IAS Conf. Proc.*, 1985, pp. 783–789.
8. Stephenson, J.M., P.J. Lawrenson, and N.N. Fulton, High power switched reluctance drives, in *Int. Conf. on Elec. Machines*, 1986, pp. 1052–1055.
9. Harris, M.R. and T.J.E. Miller, Comparision of design and performance parameters in switched reluctance and induction motors, *EMD*, 303–556, 1989.
10. Byrne, J.V. and M.F. McMullin, Design of a reluctance motor as a 10-kW spindle drive, *ICI*, 407–421, 1982.
11. Bryne, J.V., Design and performance of a saturable variable reluctance servo motor, *MOTOR-CON*, 139–146, 1985.
12. Egan, M.G., J.M.D. Murphy, P.F. Kennelly, and J.V. Lawton, A high performance variable reluctance drive: achieving servomotor control, *MOTOR-CON*, 161–168, 1985.
13. Torrey, D.A. and J.H. Lang, Progress of the development of 60-kW variable reluctance motor drive for electric vehicle propulsion, *MOTOR-CON*, 169–178, 1985.
14. Ferreira, C.A. and W.D. Jones, Detailed design of a 30-kW switched reluctance starter/generator system for a gas turbine engine application, in *IEEE IAS Conf. Proc.*, 1993, 97–105.
15. Miller, T.J.E. and M. McGilp, Nonlinear theory of the switched reluctance motor for rapid computer-aided design, *IEEE Proc. B*, 137(6), 337–346, 1990.
16. Lindsay, J.F., R. Arumugam, and R. Krishnan, Finite element analysis characterization of a switched reluctance motor with multi-tooth per stator pole, *IEEE Proc. B*, 133(6), 347–353, 1986.

17. Miller, T.J.E., Ed., *Switched Reluctance Motor Drives*, Intertec Communications PCIM Series in Power Electronics and Intelligent Motion, Ventura, CA, 1988.
18. Fulton, N.N. and J.M. Stephenson, A review of switched reluctance machine design, Int. Conf. on Electric Machines, 1988.
19. Corda, J. and J.M. Stephenson, An analytical estimation of the minimum and maximum inductances of a double-salient motor, in *Proc. of the Int. Conf. on Stepping Motors and Systems*, Leeds, U.K., 1979, pp. 50–59.
20. Radun, A.V., Analytical calculation of the switched reluctance motor's unaligned inductance, *IEEE Trans. on Magnetics*, 35(6), 4473–4481, 1999.
21. Stephenson, J.M. and J. Corda, Computation of torque and current in doubly salient reluctance motors from nonlinear magnetization data, *IEEE Proc. B*, 127(5), 393–396, 1979.
22. Krishnan, R., R. Arumugam, and J.F. Lindsay, Design procedure for switched-reluctance motors, *IEEE Trans. on Industry Appl.* 24(3), 456–461, 1988.
23. Radun, A.V., Design considerations for the switched reluctance motor, *IEEE Trans. on Industry Appl.*, 31, 1049–1087, 1995.
24. Eastham, A.R., H. Yuan, G.E. Dawson, P.C. Choudhury, and P.M. Cusack, A finite element evaluation of pole shaping in switched reluctance motors, *Electrosoft*, 1(1), 55–67, 1990.
25. Arumugam, R., D.A. Lowther, R. Krishnan, and J.F. Lindsay, Magnetic field analysis of a switched reluctance motor using a two-dimensional finite element model, *IEEE Trans. on Magnetics*, 1883–1885, 1985.
26. Finch, J.W., M.R. Harris, A. Musoke, and H.M.B. Metwally, Variable speed drives using multi-tooth per pole switched reluctance motors, in *Proc. 13th Ann. Symp. on Incremental Motion Control Systems and Devices*, 1984, pp. 293–301.
27. Byrne, J. and J.C. Lacy, Electrodynamic System Comprising a Variable Reluctance Machine, U.S. Patent No. 3, 956, 678, May 1976.
28. Arumugam, R., Design and Finite Element Analysis of Switched Reluctance Motors, Ph.D. thesis, Concordia University, Montreal, Canada, December 1987.
29. Materu, P.N., Design and Steady-State Analysis of the Switched Reluctance Motor Drive, Ph.D. thesis, The Bradley Dept. of Electrical and Computer Engineering, Virginia Tech., Blacksburg, VA, July 1989.
30. Lee, B.-S., H.-K. Bae, P. Vijayraghavan, and R. Krishnan, Design of a linear switched reluctance machine, *IEEE Industry Appl. Conf. (IAS '99)*, Vol. 4, Oct. 3–7, 1999, Phoenix, AZ, pp. 2267–2274.
31. Bae, H.-K., B.-S. Lee, P. Vijayraghavan, and R. Krishnan, Linear switched reluctance motor: converter and control, *IEEE Industry Appl. Soc. Conf. (IAS '99)*, Vol. 1, Oct. 3–7, 1999, Phoenix, AZ, pp. 547–554.
32. Neagoe, C., A. Foggia, and R. Krishnan, Impact of pole tapering on the electromagnetic torque of the switched reluctance motor, in *IEEE Int. Electric Machines and Drives Conf.*, May 1997, Milwaukee, WI.
33. Krishnan, R., M. Abou-Zeid, and X. Mang, A design procedure for axial field switched reluctance motors, in *IEEE Ind. Appl. Soc. Ann. Mtg. Conf. Rec.*, Oct. 1990, Seattle, WA, pp. 241–246.
34. Materu, P. and R. Krishnan, Analytical prediction of SRM inductance profile and steady state average torque, in *IEEE Ind. Appl. Soc. Ann. Mtg. Conf. Rec.*, Oct. 1990, Seattle, WA, pp. 214–233.
35. Krishnan, R. and P. Materu, Measurement and instrumentation of a switched reluctance motor, in *IEEE Ind. Appl. Soc. Ann. Mtg. Conf. Rec.*, Oct. 1989, San Diego, CA, pp. 116–121.

36. Arumugam, R., J.F. Lindsay, and R. Krishnan, Sensitivity of pole arc/pole pitch ratio on switched reluctance motor performance, *IEEE Ind. Appl. Soc. Ann. Mtg. Conf. Rec.*, Oct. 1988, Pittsburgh, PA, pp. 50–54.
37. Materu, P.N. and R. Krishnan, Estimation of switched reluctance motor losses, *IEEE Trans. on Ind. Appl.*, 28(3), 668–697, 1992.
38. Krishnan, R., A.S. Bharadwaj, and P.N. Materu, Computer aided design of electrical machines for variable speed applications, *IEEE Trans. on Industrial Electronics*, 36(4), 560–571, 1988.
39. Adamiak, K., D. Barlow, C.P. Choudhury, P.M. Cusack, G.E. Dawson, A.R. Eastham, B. Grady, E. Ho, Y. Hongping, L. Pattison, and J. Welch, The switched reluctance motor as a low-speed linear drive, in *Int. Conf. on Maglev and Linear Drives*, May 1987, Las Vegas, NV, pp. 39–43.
40. Takayama, K., Y. Takasaki, R. Ueda, and T. Sonoda, Thrust force distribution on the surface of stator and rotor poles of switched reluctance motor, *IEEE Trans. on Magnetics*, 25(5), 3997–3999, 1989.
41. Cusack, P.M., G.E. Dawson, and T.R. Eastham, Design, control and operation of a linear switched reluctance motor, in *Canadian Conf. on Electrical and Computer Eng.*, Sept. 1991, Quebec, Canada, pp. 19.1.1–19.1.5.
42. Liu, C.T. and Y.N. Chen, On the feasible polygon classifications of linear switched reluctance machines, in *1997 IEEE Int. Electric Machines and Drives Conf. Rec.*, May 1997, Milwaukee, WI, pp. 11.1–11.3.
43. Deshpande, U.S., J.J. Cathey, and E. Richter, A high force density linear switched reluctance machine, in *Conf. Rec. of the 1993 IEEE IAS Ann. Mtg.*, Vol. 1, Oct. 1993, Toronto, Canada, pp. 251–257.
44. Roters, H.C., *Electromagnetic Devices*, Wiley, New York, 1941.
45. Corda, J. and E. Skopljak, Linear switched reluctance actuator, in *Sixth Int. Conf. on Electrical Machines and Drives*, Oxford, U.K., Sept. 1993, Oxford, U.K., pp. 535–539.
46. Corda, J. and M. Wilkinson, Prediction and measurement of magnetic parameters of cylindrical linear switched reluctance actuator, in *Proc. of Int. Conf. on Electrical Machines*, Vol. 3, Sept. 1994, Paris, France, pp. 479–484.
47. Corda, J. and M. Wilkinson, Modelling of static thrust characteristics of cylindrical linear switched reluctance actuator, in *Seventh Int. Conf. on Electrical Machines and Drives*, Sept. 1995, Durham, U.K., pp. 354–358.
48. Matt, D., R. Goyet, J. Lucidarme, and C. Rioux, Longitudinal-field multi-airgap linear reluctance actuator, *Electric Machines and Power Systems*, 13(5), 299–313, 1987.
49. Lucidarme, J., A. Amouri, and M. Poloujadoff, Optimum design of longitudinal field variable reluctance motors—application to a high performance actuator, *IEEE Trans. on Energy Conversion*, 8(3), 357–361, 1993.
50. Boldea, I. and S.A. Nasar, *Linear Electric Actuators and Generators*, Cambridge University Press, Cambridge, U.K., pp. 163–178, 1997.
51. Lee, B.S., Linear Switched Reluctance Machine Drives with Electromagnetic Levitation and Guidance Systems, Ph.D. thesis, The Bradley Dept. of Electrical and Computer Engineering, Virginia Tech., Blacksburg, VA, 2000.

---

# 4 Converters for SRM Drives

Since the torque in SRM drives is independent of the excitation current polarity, the SRM drives require only one switch per phase winding. This is contrary to the ac motor drives where at least two switches per phase are required for current control. Moreover, the windings are not in series with the switches in ac motor drives, leading to irreparable damage in shoot-through faults. The SRM drives always have a phase winding in series with a switch. In case of a shoot-through fault, the inductance of the winding limits the rate of rise in current and provides time to initiate protective relaying to isolate the faults. The phases of the SRM are independent and, in case of one winding failure, uninterrupted operation of the motor drive operation is possible, although with reduced power output. Some configurations of converters used in SRM drives are presented and discussed in this chapter. While many of these configurations have been known for some time, the rest are emerging from research laboratories.

## 4.1 CONVERTER CONFIGURATIONS

The mutual coupling between phases is negligible in SRMs. This gives complete independence to each phase winding for control and torque generation. While this feature is advantageous, a lack of mutual coupling requires a careful handling of the stored magnetic field energy. The magnetic field energy has to be provided with a path during commutation of a phase; otherwise, it will result in excessive voltage across the windings and hence on the power semiconductor switches leading to their failure. The manner in which this energy is handled gives way to unique but numerous converter topologies for SRM drives. The energy could be freewheeled, partially converting it to mechanical/electrical energy and partially dissipating it in the machine windings. Another option is to return it to the dc source either by electronic or electromagnetic means. All of these options have given way to power converter topologies with  $q$ ,  $(q + 1)$ ,  $1.5q$ , and  $2q$  switch topologies, where  $q$  is the number of machine phases. These converter configurations are classified and listed in [Figure 4.1](#) for easier reference. A two-stage power converter configuration which does not fit categorization based on the number of machine phases is also included. They are considered in detail in the following.

All the converter topologies except the two-stage power converter assume that a dc voltage source is available for their inputs. This dc source may be from batteries or most usually a rectified ac supply with a filter to provide a dc input source to the SRM converters. The derivation of such dc sources from ac input and reversal of power flow from this dc source to an ac source may be found in standard power electronics textbooks.

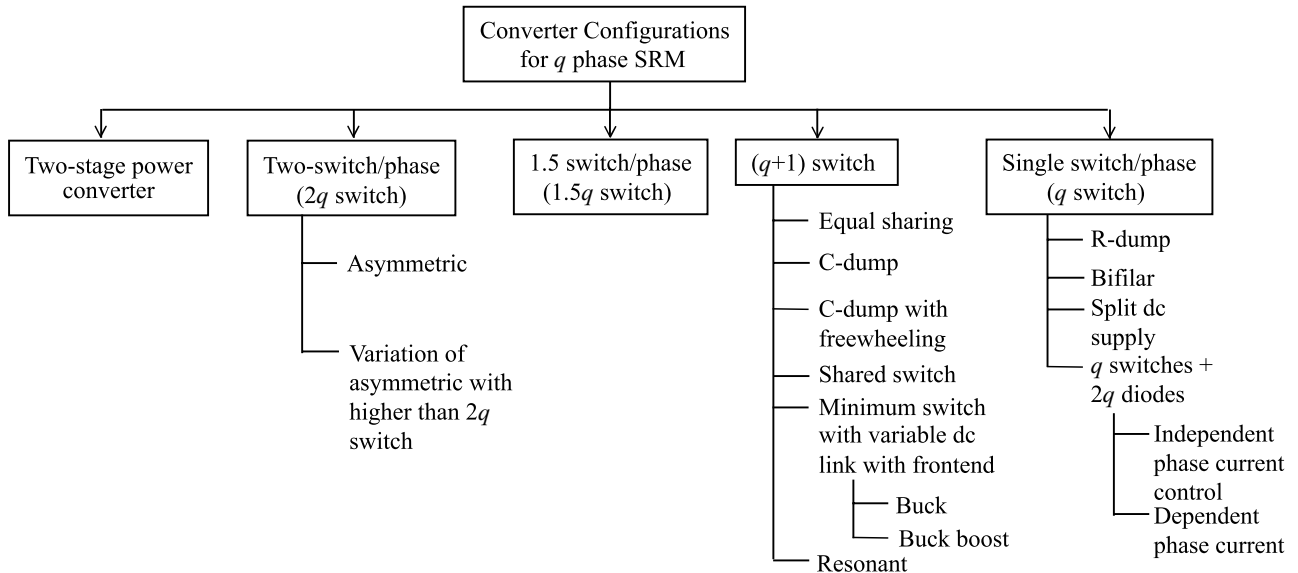


**FIGURE 4.1** Classification of power converters for switched reluctance machines.

### 4.1.1 ASYMMETRIC BRIDGE CONVERTER

Figure 4.2a shows the asymmetric bridge converter considering only one phase of the SRM.<sup>1,2,3,5</sup> The rest of the phases are similarly connected. Turning on transistors  $T_1$  and  $T_2$  will circulate a current in phase A of the SRM. If the current rises above the commanded value,  $T_1$  and  $T_2$  are turned off. The energy stored in the motor winding of phase A will keep the current in the same direction until it is depleted. Hence, diodes  $D_1$  and  $D_2$  will become forward biased leading to recharging of the source. That will decrease the current, rapidly bringing it below the commanded value. This operation is explained with the waveforms of Figure 4.2b. Assuming that a current of magnitude  $I_p$  is desired during the positive inductance slope for motoring action, the A-phase current command is generated with a linear inductance profile. Here, phase advancing both at the beginning and during commutation are neglected. The current command,  $i_a^*$ , is enforced with a current feedback loop where it is compared with the phase current,  $i_a$ . The current error is presumed to be processed through a hysteresis controller with a current window of  $\Delta i$ . When the current error exceeds  $-\Delta i$ , the switches  $T_1$  and  $T_2$  are turned off simultaneously. Hysteresis current controller is considered here due to its simplicity in concept and implementation. At that time, diodes,  $D_1$  and  $D_2$  take over the current and complete the path through the dc source.

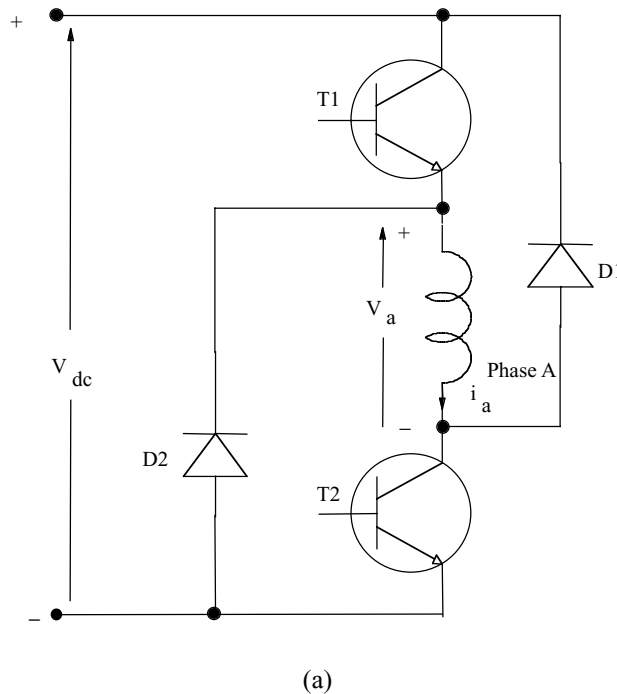
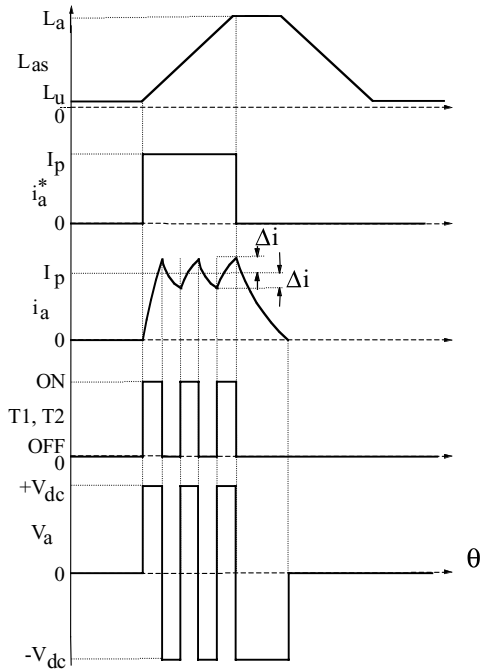


**FIGURE 4.2** (a) Asymmetric converter for SRM with freewheeling and regeneration capability. (b) Operational waveforms of the asymmetric bridge converter (strategy I); (c) Operational waveforms of the asymmetric bridge converter (strategy II).

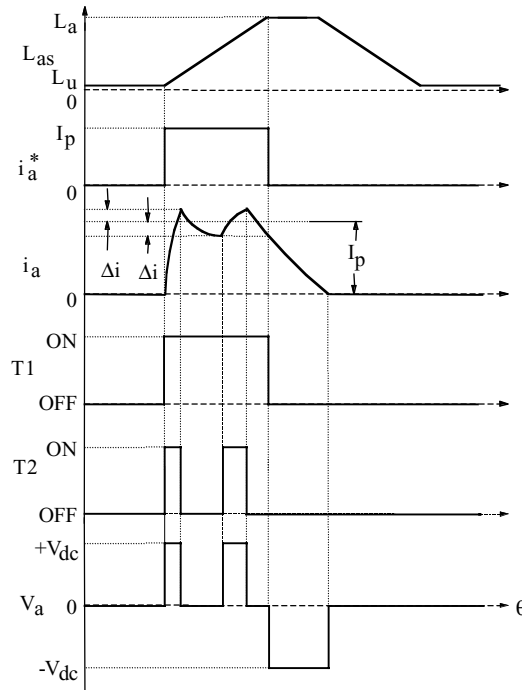


(b)

**FIGURE 4.2** (Continued)

Note that the voltage of phase A is then negative and will equal the source voltage,  $V_{dc}$ . During this interval, the energy stored in the machine inductance is sent to the source, thus exchanging energy between the load and source repeatedly in one cycle of a phase current. After the initial startup, during turn-on and turn-off of  $T_1$  and  $T_2$ , the machine phase winding experiences twice the rate of change of dc link voltage, resulting in a higher deterioration of the insulation. This control strategy (strategy I) hence puts more ripples into the dc link capacitor, thus reducing its life and also increasing the switching losses of the power switches due to frequent switching necessitated by energy exchange. These can be ameliorated with an alternate switching strategy.

The energy stored in the phase A can be effectively circulated in itself by turning off, say,  $T_2$  only (strategy II). In that case, the current will continue to flow through  $T_1$ , phase A, and  $D_1$ , the latter having forward biased soon after  $T_2$  is turned off. The voltage across the winding becomes zero if the diode and transistor voltage drops are neglected as shown in Figure 4.2c. That will take the phase current from  $I_p + \Delta i$  to  $I_p - \Delta i$  in a time greater than had it been forced against the source voltage using the previous strategy. This particular fact reduces the switching frequency and hence the switching losses. When the current command goes to zero, both  $T_1$  and  $T_2$  are turned off simultaneously. During this interval, the voltage across the winding is  $-V_{dc}$  as long as  $D_1$  and  $D_2$  conduct (i.e., until  $i_a$  goes to zero) and



(c)

**FIGURE 4.2** (Continued)

thereafter the winding voltage is zero. The voltage across  $T_2$  during its off time and when  $T_1$  is on is equal to the source voltage,  $V_{dc}$ . Hence, the power switches and diodes have to be rated to a minimum of source voltage at least. The current ratings of the switches are equal to or less than  $I_p/\sqrt{q}$  by interchanging the off times between  $T_1$  and  $T_2$  in one cycle of phase conduction. Similarly, the current rating of the diodes can be evaluated. While such a self-circulation will keep the current going for a longer time compared to recharging the source voltage, it has the advantage of converting the stored energy to useful mechanical work. While this form of control can be used for current control, the recharging of the source is advantageous when the current has to be turned off rapidly. Such an instance arises when the inductance profile becomes flat or is starting to have a negative slope. Any further conduction of current in such regions entails a loss of energy or production of negative torque, thus reducing the average motoring torque. Note that this converter requires two transistors and two diodes for each phase, resembling the conventional ac motor drives.

#### 4.1.1.1 Switching Strategy

A slight modification to the second strategy described above can give a negative voltage across the machine winding for negative current error signals in between a carrier or switching or pulse cycle, as shown in [Figure 4.3](#). This converter provides

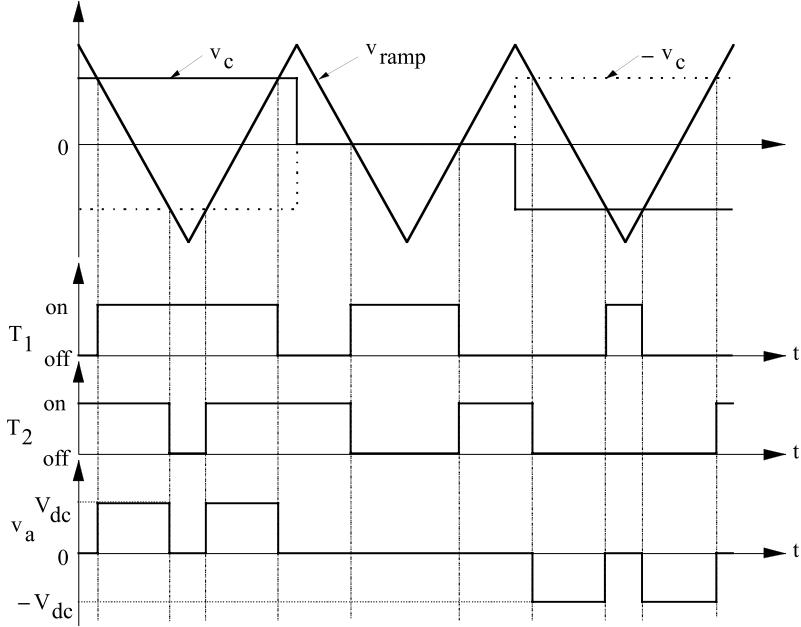


**FIGURE 4.3** Unipolar switching strategy.

an output voltage of the same polarity as the current error (i.e., the control signal). This is identified hereafter as a unipolar switching strategy and is utilized in other drive systems. This switching strategy handles negative current error signals in between the energization and commutation modes of the phases with judicious choice of negative or zero voltage across the winding to obtain a fast current response. Further, it effectively doubles the switching frequency contributing to mitigation of current ripple and hence reduction of the ripple torque. Due to these advantages, this switching strategy is ideal for high-performance current and torque control of SRM drive systems. Unipolar switching is possible only in converters that can provide bidirectional output voltages and therefore may not be possible with other types of converters with restrictions on their output voltages.

The algorithm for unipolar switching is as follows:

$$v_a = \begin{cases} V_{dc} & @ i_a^* > 0, \quad v_c \geq v_{ramp} \quad \& \quad -v_c < v_{ramp} \\ -V_{dc} & \quad v_c < v_{ramp} \quad \& \quad -v_c \geq v_{ramp} \\ 0 & \text{elsewhere} \\ -V_{dc} & @ i_a^* < 0, \quad v_c \geq v_{ramp} \quad \& \quad -v_c < v_{ramp} \\ V_{dc} & \quad v_c < v_{ramp} \quad \& \quad -v_c \geq v_{ramp} \\ 0 & \text{elsewhere} \end{cases}$$

where  $v_c$  is the control voltage,  $v_{ramp}$  is the carrier frequency voltage, and  $v_a$  is the output voltage of the converter phase (i.e., the phase winding input voltage).

The asymmetric converter is ideal for high-power applications. One of the challenges in high-power applications is that the switching losses have to be minimized. While snubbers are one way to overcome this problem, there are alternative solutions using resonant converter topologies.<sup>26,27</sup> The resonant converter topologies, discussed in Section 4.6, do not seem to be attractive at this juncture due to the fact that voltage and current stresses are higher than those of the equivalent pulse width modulation (PWM) switching converters. Therefore, a snubber-based solution is considered in Section 4.1.3.

#### 4.1.1.2 Device Ratings

The minimum voltage rating of the power devices is equal to the maximum of the dc link voltage. The current rating of the devices is not as simple as that of the voltage rating. To provide for equal rating of the rms current in the power switches and the average current in the diodes, it is to be noted that neither switching strategy I nor II is sufficient. A slight modification of switching strategy II is developed as shown in Figure 4.4 to give equal ratings for the power devices and diodes in each phase of the converter.

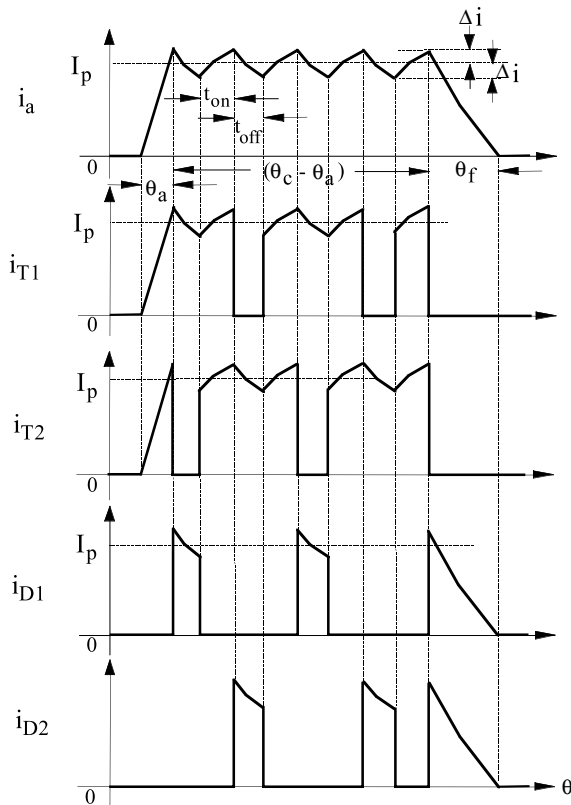


**FIGURE 4.4** Device currents with modification of switching strategy II.

The modified switching strategy uses alternate freewheeling with  $D_1$  and  $D_2$  by turning off  $T_2$  and  $T_1$ , respectively, in the conduction region, given as  $(\theta_c - \theta_a)$  in Figure 4.4. It is assumed that there are no switchings in the rising portion of the current in the region 0 to  $\theta_a$ . Each switch conducts for two on times and one off time and is turned off for one off time. Such a switching strategy enables equal rms current in the switches and equal average current in the diodes as seen from Figure 4.4.

The average duty cycle in region  $(\theta_c - \theta_a)$  may be derived as:

$$d_1 = \frac{I_p(R_s + \omega_m)}{V_{dc}} \quad (4.1)$$

This average duty cycle is assumed for each switching in this region to derive the switch and diode current ratings.

#### 4.1.1.3 Switch rms Current

Current ripple of  $2\Delta i$  within a switching cycle is assumed during switching. The rms current in the switch is

$$I_{T1} = \sqrt{\frac{1}{\theta_{rp}} \left\{ (I_p + \Delta i)^2 \cdot \frac{\theta_a}{3} + \left\{ I_p^2 + \frac{7}{3}(\Delta i)^2 \right\} \frac{(\theta_c - \theta_a)}{2} (1 + d_1) \right\}} \quad (4.2)$$

where  $\theta_c$  is the conduction angle,  $\theta_a$  is the advance (current rise) angle and the rotor pole pitch,  $\theta_{rp}$ , in terms of number of rotor poles,  $P_r$ , is

$$\theta_{rp} = \frac{2\pi}{P_r} \quad (4.3)$$

#### 4.1.1.4 Diode Average Current

The average current in the diode is derived approximately as:

$$I_{D1}(\text{ave}) \cong \frac{I_p}{\theta_{pr}} \left[ (1 - d_1) \frac{(\theta_c - \theta_a)}{2} + \frac{\theta_f}{2} \right] \quad (4.4)$$

where  $\theta_f$  is the current fall angle.

#### 4.1.1.5 Selection of Device Current Ratings

The device current ratings are dependent on the desired current  $I_p$ ; conduction and advance angles  $\theta_c$  and  $\theta_a$ , respectively; fall angle  $\theta_f$ ; and average duty cycle  $d_1$ , as shown in Eqs. (4.2) and (4.4). The devices have to be rated based on the maximum values they may experience in the variable speed operation. The maximum current

rating is determined by the maximum operating cycle of the drive determined by the maximum speed and minimum of dc link voltage, as seen from Eq. (4.1). Also, the device rating is determined based on the maximum advance, conduction, and fall angles.

#### 4.1.2 ASYMMETRIC CONVERTER VARIATION

Utilization of the power devices is poor in the asymmetrical converter. Their duty cycles can be increased while minimizing the number of self-commutating devices by introducing phase control devices<sup>15</sup> (i.e., silicon-controlled rectifiers, or SCRs), as shown in Figure 4.5. An even number of phases is required to take advantage of this configuration. The SCRs serve mainly to steer currents into selective phases but are not used for control, as they require auxiliary commutation circuit, which increases the component count, cost, and packaging size.

The number of diodes is reduced to one per phase which results in considerable savings compared to the two diodes per phase required in the asymmetrical converter discussed earlier. Note that alternate machine phases and not adjacent phases are grouped together under one set of self-commutating device pairs. This allows time for one phase current commutation up to one phase cycle and hence permits independent on and off control of each phase with overlapping currents not exceeding one phase cycle duration.

The working of this converter can be explained with reference to phase A. To energize the phase, transistors  $T_1$  and  $T_2$  and SCR  $S_1$  are all gated on. If the current exceeds its reference,  $T_1$  is turned off. The current freewheels and has the path of phase A,  $S_1$ ,  $T_2$ , and  $D_2$  and the voltage across the phase is zero if the devices are assumed ideal. In this mode, energy in the machine inductance is mostly converted to mechanical energy and the phase current decreases. When the phase current finally has to be commutated,  $T_1$  and  $T_2$  are turned off simultaneously which enables turning on of  $D_1$  and  $D_2$ , resulting in  $-V_{dc}$  voltage being applied across the machine phase. Also, the dc link current is reversed, initiating energy transfer from the machine to the dc source and partial conversion to mechanical energy. This reduces the current

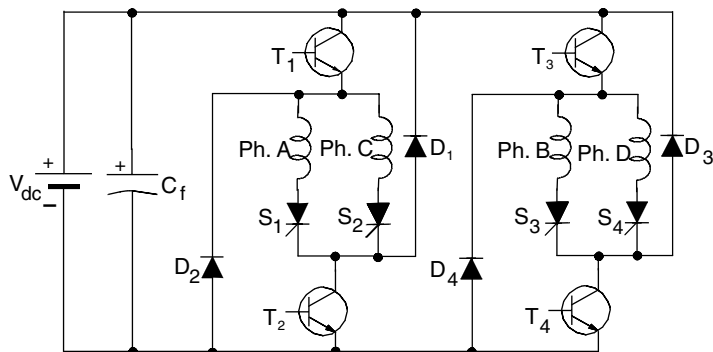


**FIGURE 4.5** Alternate asymmetrical converter topology.

very rapidly to zero. The SCR  $S_2$  blocks the current circulation from phase A to phase C during the commutation mode.

The advantages and disadvantages of this power topology are summarized in the following. The advantages include:

1. It has one self-commutating device, one SCR, and one diode per phase; this drive costs less compared to the two switches per phase asymmetrical converter.
2. Higher utilization of the self-commutating devices in this topology (i.e., once in two-phase cycles instead of once in four-phase cycles) decreases cost for high-power SRM drives.
3. The converter is capable of positive ( $+V_{dc}$ ), negative ( $-V_{dc}$ ), and zero voltage output capability and so it allows greater flexibility in controlling the machine current.
4. Phase current control is independent with a minimum number of self-commutating devices.

The disadvantages include:

1. An SCR is always in the current conduction path, thus increasing the losses in the converter and requiring a larger heatsink for cooling. This would further reduce the system efficiency much more noticeably in low-power SRM drives than in high-power SRM drives.
2. Parts count is higher due to SCR gate drive amplifiers with their own isolation requirements.

#### 4.1.3 ENERGY RECOVERY SNUBBER

Snubber studies for SRM drives are nonexistent even though the converter topologies are unique and do not fall under the category of inverter topologies applicable to ac motor drives. The importance of the snubbers does not come into the picture until either the power rating of the converter is high and in the multi-kW range or the switching frequency requirement is in the 20-kHz range. Such requirements have come to the forefront recently in many product development applications such as extruders, general purpose drives, integral starter generators for aircraft, electric vehicles, high-speed spindles and centrifuges, etc. This section presents an extension of the Undeland snubber configuration to the two-switches-per-phase converter topology of the SRM drive including the energy recovery feature. The impact of the proposed snubber on the converter efficiency and its comparison with a conventional snubber-based system such as with resistor, capacitor, and diode (RCD) is evaluated to assess the advantages of the proposed energy recovery snubber.

The energy recovery snubber<sup>35</sup> is shown in Figure 4.6 for one phase of the SRM drive. Other phases use identical snubbers. The series inductors  $L_{1T}$  and  $L_{1B}$  provide controlled turn-on and capacitors  $C_{1T}$  and  $C_{1B}$  provide controlled turn-off of the switches. They keep the rate of change of current and voltage within the safe limits of the power devices. The diodes  $D_{2T}$ ,  $D_{3T}$ ,  $D_{2B}$ , and  $D_{3B}$  carry the energy stored in

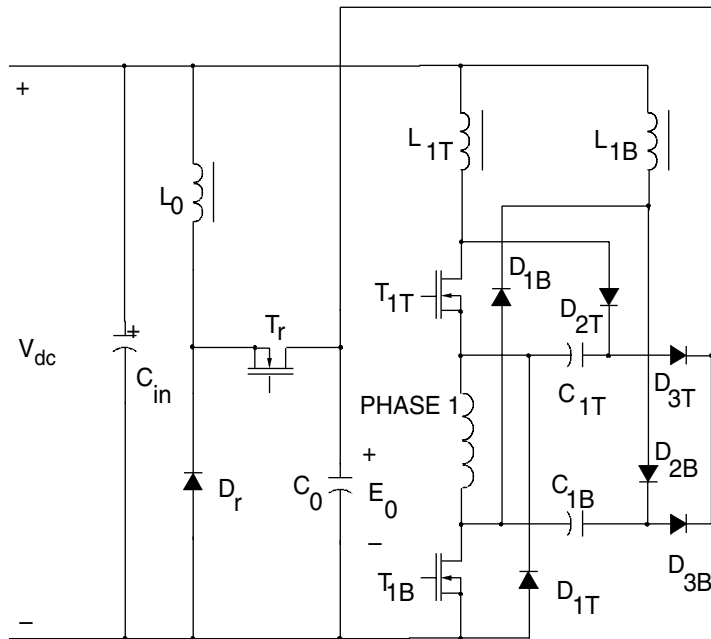


**FIGURE 4.6** One phase of SRM with energy recovery snubber circuit.

the inductors to the energy recovery capacitor  $C_o$  whenever the power devices  $T_{1T}$  or  $T_{1B}$  are turned on or off. The snubber has two inductors, two capacitors, and four diodes per phase which is more than that required for the RCD type of snubbers. A reduction in the number of components is possible if the snubbing protection is given only to one switch rather than both. One switch could be turned on for the entire cycle of phase winding conduction while the other switch could be turned on and off to control the current. This implies multiple switching in one conduction cycle for one switch and only one switching for the other. The snubber could be provided only for the highly switched device, thereby reducing the component count.

Energy trapped in the snubber inductors and capacitors is guided to the energy storage capacitor  $C_o$  and recovered from it by a recovery circuit consisting of a step-down, dc-to-dc converter which acts independently of the main power devices, and any circuit configuration can be used. The present circuit uses the dc-to-dc chopper. It consists of the power device  $T_r$ , inductor  $L_o$ , and diode  $D_r$ . The recovered energy is received by the dc link capacitor,  $C_{in}$ . By controlling the voltage on  $C_o$ , the maximum voltage of all the power devices is kept within safe operating limits. One such recovery circuit is sufficient for all the phases of the SRM drive.

This snubber has many advantages. Due to the series inductor, overcurrent protection can be assured for motor phase winding short-circuits, a requirement in many high-performance applications such as an aircraft starter generator. Hard turn-off of the freewheeling diodes is avoided, thereby saving some energy and removing a failure possibility.

## 4.2 SINGLE-SWITCH-PER-PHASE CONVERTERS

Single-switch-per-phase converters are appealing due to their compactness of converter package and hence a possible reduction in their cost compared to other converters. They also have the disadvantage of being unable to apply zero voltage across the machine phase during current conduction. Such an operational constraint increases the circulation of energy between the machine and dc link, resulting in higher losses and reduced system efficiency. Also, the rate of change of the voltage is doubled during current control, which causes insulation deterioration and increased acoustic noise in the machine. In spite of many shortcomings, a large number of single-switch-per-phase converter topologies has been proposed and tested. They have selective advantages that may suit an application. These converter topologies are described in this section.

### 4.2.1 R-DUMP

Figure 4.7 shows a converter configuration with one transistor and one diode per phase of the SRM.<sup>10</sup> When  $T_1$  is turned off, the current freewheels through  $D_1$ , charging  $C_s$ , and later flows through the external resistor  $R$ . This resistor partially dissipates the energy stored in phase A. This has the disadvantage that the current in phase A will take longer to extinguish compared to recharging the source. The energy, in addition, is dissipated in a resistor, thus reducing the overall efficiency of the motor drive.

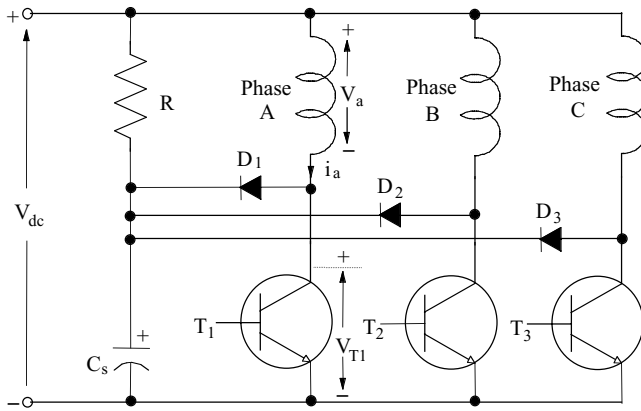
Figure 4.7b shows the timing waveforms of the circuit in detail. The hysteresis current controller turns off  $T_1$  when the phase current exceeds the current command,  $i_a^*$  by  $\Delta i$ . Turning off  $T_1$  will reduce the current, which in turn induces an emf in the winding to sustain  $i_a$  in the same direction. This emf forward biases diode  $D_1$ . The voltage across the resistor  $R$  is  $i_a R$ . Note that the voltage across the resistor has a positive polarity with respect to the positive rail of the source voltage. The voltage across  $T_1$  during off time is then the sum of the source voltage and the voltage drop across the resistor is expressed as:

$$V_{T1} = V_{dc} + i_a R \quad (4.5)$$

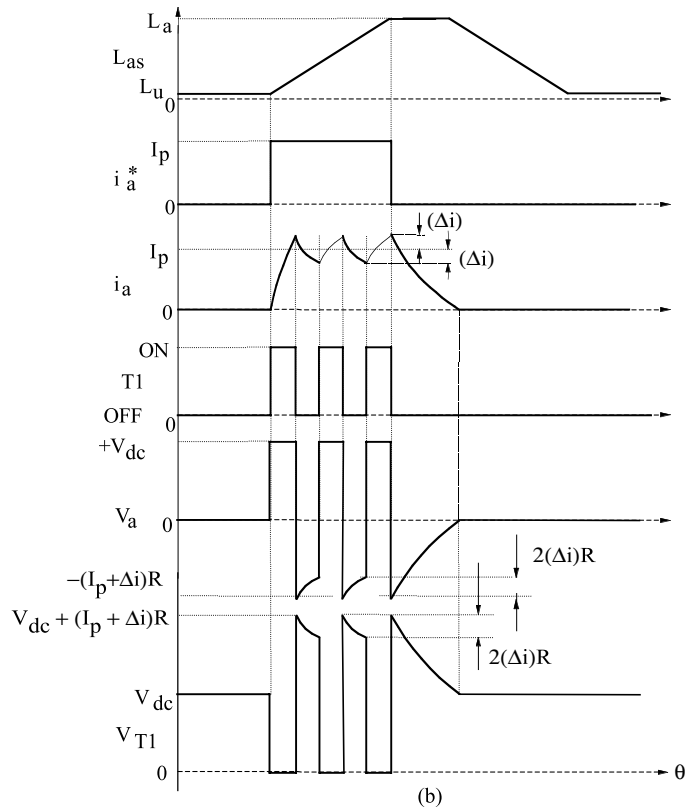
Design considerations such as the turn-off transient voltage have to be included in the rating of the switch  $T_1$ . The selection of  $R$  not only determines the power dissipation but also the switch voltage. A lower value of  $R$  increases the fall time of the current. If the current comes under the negative slope region of the phase inductance, negative torque will be generated, decreasing the average motoring torque. A high value of  $R$  increases the voltage drop across the winding and hence across  $T_1$ .

#### 4.2.1.1 Device Current Ratings

The power switch and diode current ratings can be derived from simplistic assumptions, such as the switch carries all the current until commutation is initiated. This gives rise to a maximum current rating of the switch, leading to a conservative design. A phase current with an advance angle of  $\theta_a$  is assumed for the waveforms



(a)



(b)

**FIGURE 4.7** (a) Converter for SRM with freewheeling path; (b) operational waveforms of R-dump converter; (c) simplified waveforms for calculation of switch and diode current ratings; (d) switch rms to peak current ratio vs.  $k_c$  characteristics for various  $k_a$ ; (e) a phase current with PWM switching; (f) normalized graph for the advance time of phase currents.

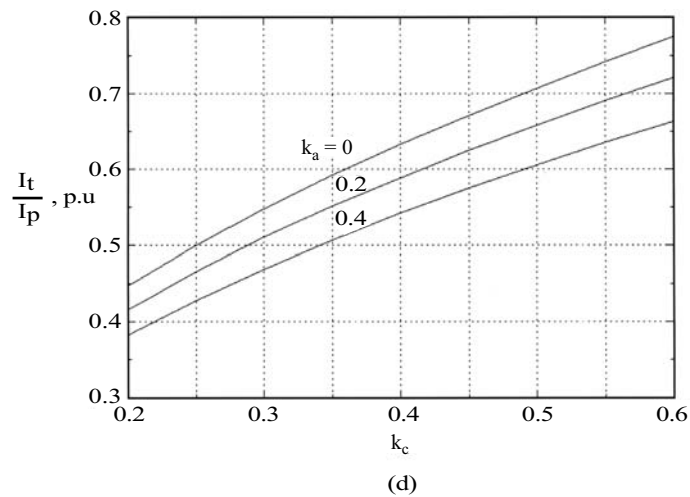
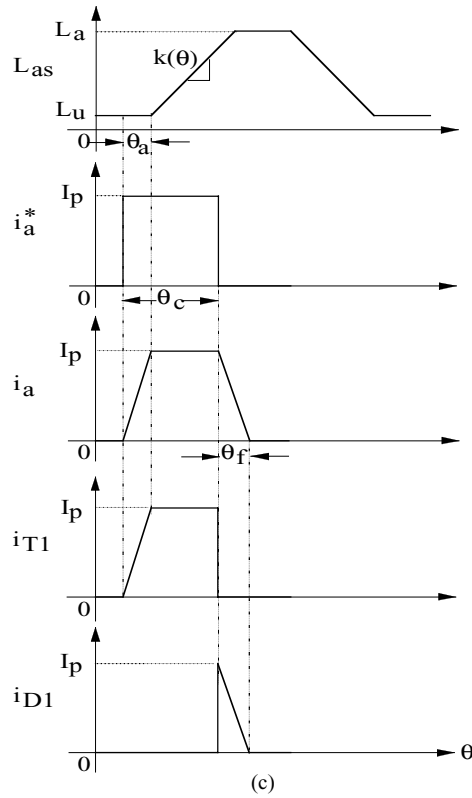


**FIGURE 4.7** (Continued)

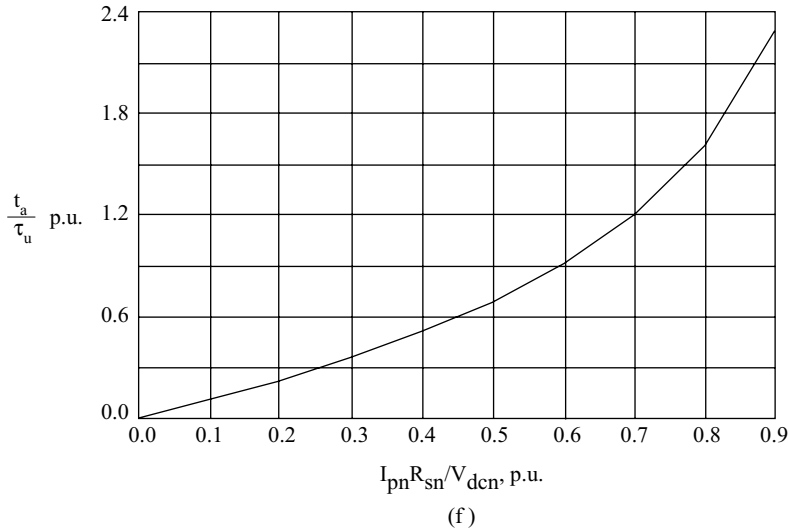
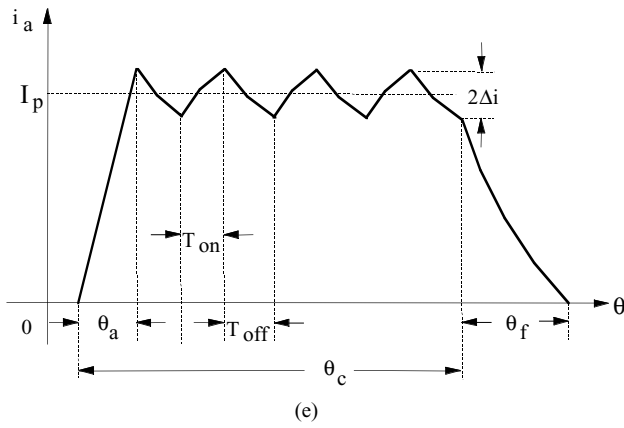


**FIGURE 4.7** (Continued)

shown in [Figure 4.7c](#). The current command is for the duration of  $\theta_c$  degrees with a constant current of  $I_p$ . PWM switching is neglected to derive the switch and diode current ratings.

#### 4.2.1.2 Switch Current

The rms current rating of the switch is derived from the figure as:

$$I_T = I_p \sqrt{\frac{\theta_c}{\theta_{rp}} \left\{ 1 - \frac{2}{3} \cdot \frac{\theta_a}{\theta_c} \right\}} \quad (4.6)$$

where  $\theta_{rp}$  is the rotor pole pitch. Eq. (4.6) is written in terms of only two variables,  $k_c$  and  $k_a$ , defined as:

$$k_c = \frac{\theta_c}{\theta_{rp}} \quad (4.7)$$

$$k_a = \frac{\theta_a}{\theta_c} \quad (4.8)$$

$$\frac{I_T}{I_p} = \sqrt{k_c \left(1 - \frac{2}{3} k_a\right)} \quad (4.9)$$

The variables  $k_c$  and  $k_a$  have the range of values for two- to four-phase machines given by:

$$0.2 \leq k_c \leq 0.6 \quad (4.10)$$

$$0 \leq k_a \leq 0.4 \quad (4.11)$$

for which the normalized relationships are drawn in [Figure 4.7d](#).

#### 4.2.1.3 Diode Current

To calculate the current in the diode, it is necessary to consider also the current during turn-off duration in the PWM switching cycle. Otherwise, the current estimate will be optimistic and may be unsuitable for design purposes. The phase current may be as shown in [Figure 4.7e](#) with PWM switching. The desired current is a rectangular current block of  $I_p$  as shown in [Figure 4.7c](#). Assuming a linear inductance slope with respect to rotor position and neglecting mutual inductance between phases, the system equations for phase A are

$$R_s i + \omega_m i k(\theta) + L \frac{di}{dt} = V_{dc}, \quad \text{for on time} \quad (4.12)$$

$$R_s i + R i + \omega_m i k(\theta) + L \frac{di}{dt} = 0, \quad \text{for off time} \quad (4.13)$$

where  $k(\theta)$  is the rate of change of inductance with respect to rotor position. During on time, note that

$$\frac{di}{dt} \cong \frac{2\Delta i}{T_{on}} \quad (4.14)$$

and during off time,

$$\frac{di}{dt} \cong -\frac{2\Delta i}{T_{off}} \quad (4.15)$$

Substituting Eqs. (4.14) and (4.15) in Eqs. (4.12) and (4.13) and for an average current of  $I_p$ , the duty cycle  $d_1$  is calculated as:

$$d_1 = \frac{I_p [R + R_s + \omega_m k(\theta)]}{V_{dc} + RI_p} \quad (4.16)$$

where

$$d_1 = \frac{T_{\text{on}}}{T_{\text{on}} + T_{\text{off}}} = \frac{T_{\text{on}}}{T_c} = t_1 f_c \quad (4.17)$$

where  $f_c$  is the carrier or PWM frequency. For the duration  $(\theta_c - \theta_a)$ , this duty cycle can be considered on an average basis. Hence, on that basis, the average diode current is obtained as:

$$I_d = I_p \{k_c(1 - k_a)(1 - d_1) + 0.982k_f\} \quad (4.18)$$

where

$$k_f = \frac{\theta_f}{\theta_{rp}} \quad (4.19)$$

and  $k_a$  and  $k_c$  are as defined in Eqs. (4.7) and (4.8). This includes the falling current for duration  $\theta_f$ . The commutation current is assumed to fall to 2% of  $I_p$  within four times the time constant, given by  $\tau_f$  as:

$$\tau_f \cong \frac{L_a}{(R_s + R)} \quad (4.20)$$

and the fall angle is derived as:

$$\theta_f = \omega_m t_f = \omega_m (4\tau_f) = 4\omega_m \tau_f \quad (4.21)$$

Diode current rating is determined by the advance, conduction, and fall angles of the current but most importantly by the average duty cycle. The duty cycle for calculation of the diode current rating has to be the minimum corresponding to the minimum speed of the drive, evaluated from Eq. (4.16). The advance angle is calculated assuming that the inductance at the current initiation is the unaligned value:

$$\theta_a = \omega_m \tau_u \ln \left[ \frac{1}{1 - \frac{I_p R_s}{V_{dc}}} \right], \text{ rad} \quad (4.22)$$

where time constant at unaligned rotor position is given by:

$$\tau_u = \frac{L_u}{R_s}, \text{ s} \quad (4.23)$$

The advance time for the current normalized to unaligned time constant is

$$\frac{t_a}{\tau_u} = \frac{\theta_a}{\omega_m \tau_u} = \ln \left[ \frac{1}{1 - \frac{I_{pn} R_{sn}}{V_{dcn}}} \right], \text{ p.u.} \quad (4.24)$$

and is shown in [Figure 4.7f](#) for design use.

#### 4.2.1.4 Power Rating of Dump Resistor

The power rating of the dump resistor is calculated from the number of phases and the rms current of the diode currents passing through the power resistor. The rms current of the diode is

$$I_D = I_p \sqrt{(1 - d_1)k_c(1 - k_d) + \frac{1}{2}k_f} \quad (4.25)$$

and the power of the dump resistor is

$$P = qI_D^2 R \quad (4.26)$$

This power is maximum for the minimum duty cycle, which would be at the minimum speed of the SRM drive system for a given  $I_p$ . Selection of  $R$  is based on the maximum switch and diode voltage, current fall time, and power dissipation capability. This completes the selection of various components of the  $R$ -dump converter circuit.

#### 4.2.2 BIFILAR TYPE

Figure 4.8a shows a converter configuration with one transistor and one diode per phase but regenerating the stored magnetic energy to the source.<sup>2</sup> This is achieved by having a bifilar winding with the polarity as shown in the figure. When the phase-A

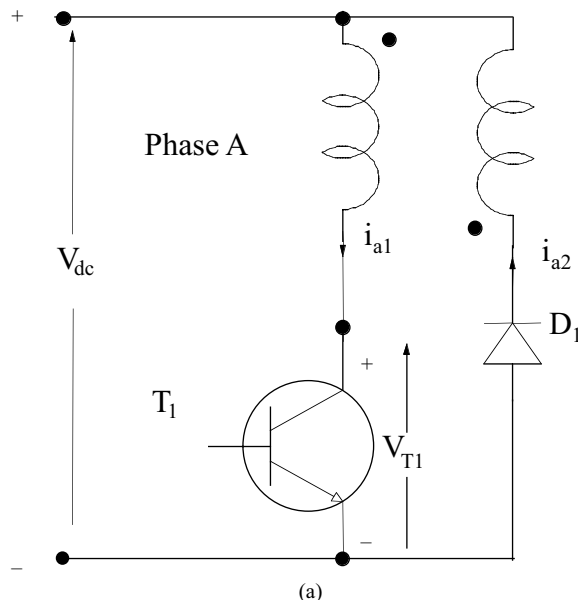


**FIGURE 4.8** (a) Converter for an SRM with bifilar windings; (b) operational waveforms of bifilar converter.

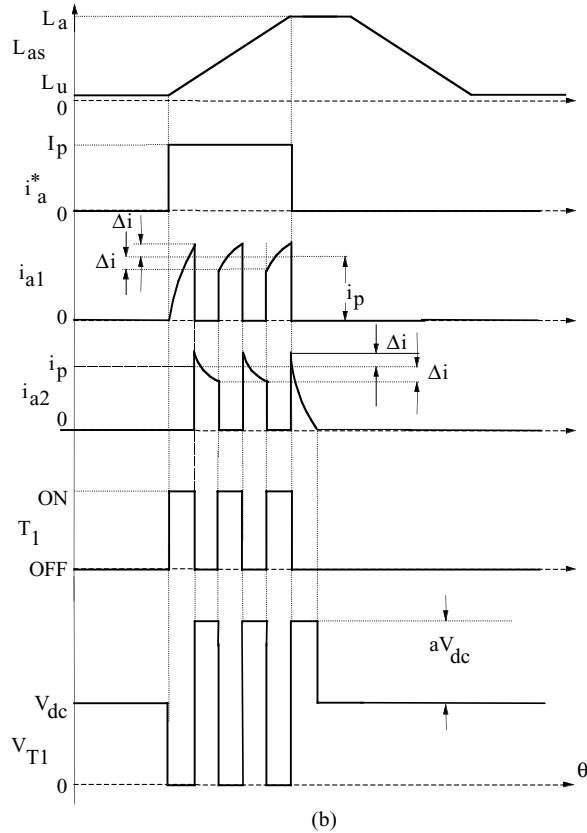


**FIGURE 4.8** (Continued)

current is turned off by removing the base drive signal to  $T_1$ , the induced emf in the winding is of such polarity that  $D_1$  is forward biased. This leads to the circulation of current through  $D_1$ , the bifilar secondary winding, and the source, thus transferring energy from the machine winding to the source.

The various timing waveforms of the circuit are shown in Figure 4.8b. During current turn-off, the applied voltage across the bifilar secondary winding is equal to the dc link voltage. The voltage reflected into the main winding is dependent upon the turns ratio of the windings. Considering the turns ratio between the main winding in series with the power switch and the auxiliary winding in series with the diode as  $a$ , the voltage across the power switch is

$$V_{T1} = V_{dc} + aV_{dc} = (1 + a)V_{dc} \quad (4.27)$$

This shows that the voltage across  $T_1$  can be very much greater than the source voltage. One switch per phase comes with a voltage penalty on the switch. The volt-ampere (VA) capability of the switch will not be very different for one switch compared to two switches per phase circuit. The disadvantage of this drive is that

the SRM needs a bifilar winding and such a form of winding is not economical for large motors. Also, the bifilar windings require additional slot volume, reducing the power density of the SRM.

#### 4.2.3 SPLIT DC SUPPLY CONVERTER

A split dc supply for each phase allows freewheeling and regeneration, as shown in [Figure 4.9a](#). This topology preserves one switch per phase; its operation is as follows. Phase A is energized by turning on  $T_1$ . The current circulates through  $T_1$ , phase A, and capacitor  $C_1$ . When  $T_1$  is turned off, the current will continue to flow through phase A, capacitor  $C_2$ , and diode  $D_2$ . In that process,  $C_2$  is being charged up and hence the stored energy in phase A is depleted quickly. Similar operation follows for phase B. The operation of this circuit for phase A is shown in [Figure 4.9b](#). A hysteresis current controller with a window of  $\Delta i$  is assumed. The phase voltage is  $V_{dc}/2$  when  $T_1$  is on, and when it is turned off with a current established in phase A, the phase voltage is  $-V_{dc}/2$ . The voltage across the transistor  $T_1$  during the on time is negligible, and it is  $V_{dc}$  when the current is turned off. That makes the switch voltage rating at least equal to the dc link voltage. As the stator current reference,  $i_a^*$  goes to zero, the switch  $T_1$  is turned off regardless of the magnitude of  $i_a$ . When the winding current becomes zero, the voltage across  $T_1$  drops to  $0.5 V_{dc}$  and so also does the voltage across  $D_2$ . Note that this converter configuration has the disadvantage of derating the supply dc voltage,  $V_{dc}$ , by utilizing only half its value at any time. Moreover, care has to be exercised in balancing the charge of  $C_1$  and  $C_2$  by proper design measures.

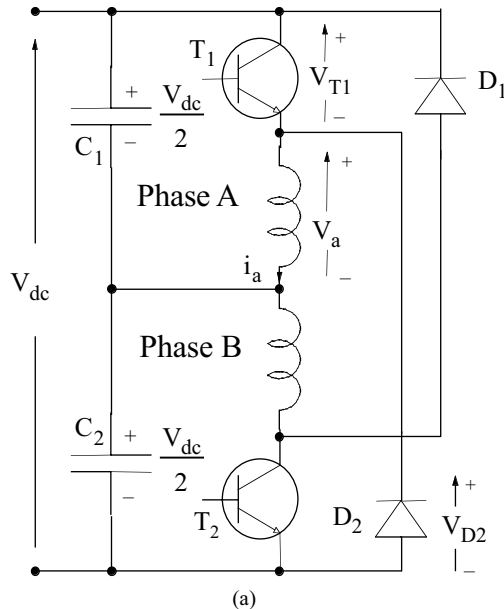


**FIGURE 4.9** (a) Converter for SRM with split dc supply; (b) operational waveforms of split dc supply converter.

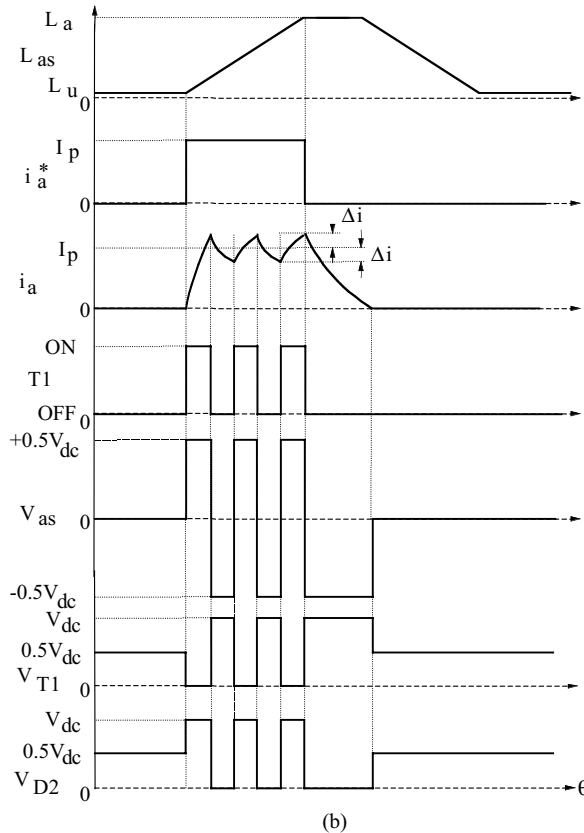


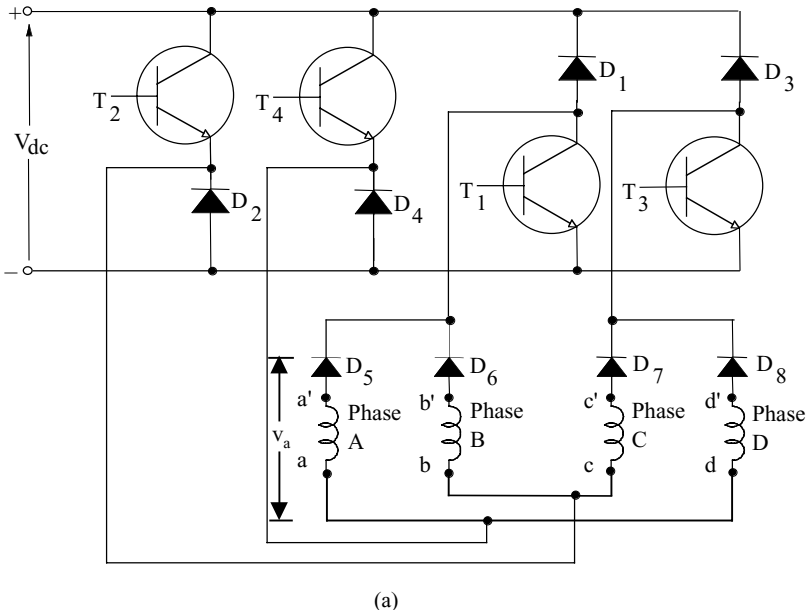
**FIGURE 4.9** (Continued)

For balancing the charge across the dc link capacitors, the number of machine phases has to be even and not odd. In order to improve the cost-competitive edge of the SRM drive, this converter was chosen in earlier integral horse power (hp) product developments, but its use in fractional hp SRM drives supplied by a single-phase 120-V ac supply is much more justifiable; the neutral of the ac supply is tied to the midpoint of the dc link and so capacitors can be rated to 200 V dc, thus minimizing the cost of the converter.

#### 4.2.4 $q$ SWITCHES AND $2q$ DIODES

Figure 4.10a shows another single-switch-per-phase converter configuration.<sup>8</sup> Note that  $D_1$ ,  $D_2$ ,  $D_3$ , and  $D_4$  are fast, freewheeling diodes and  $D_5$ ,  $D_6$ ,  $D_7$ , and  $D_8$  are slow diodes. The circuit operation can be explained as follows.

Phase A is energized by turning on switches  $T_4$  and  $T_1$ . If the current exceeds the reference current  $i_a^*$  by the current window  $\Delta i$ , switches  $T_4$  and  $T_1$  are turned off. That will enable the diodes  $D_1$  and  $D_4$  to carry the A-phase current. The voltage across the winding becomes  $-V_{dc}$ , which indicates that the energy is being transferred



(a)

**FIGURE 4.10** (a) Modified single-switch-per-phase converter; (b) strategy I (both switches on and off simultaneously); (c) strategy II (freewheeling); (d) waveforms for overlapping current conduction.

from the winding to the dc link. This will reduce the phase A current rapidly to zero, as shown in Figure 4.10b (denoted as strategy I). An alternative strategy is to turn off only one switch to reduce the current between switching cycles (denoted as strategy II). Consider  $T_4$  is on while  $T_1$  is turned off for one switching cycle and vice versa for the next switching cycle to reduce the rms rating of the switches  $T_1$  and  $T_4$  and for their equality. This action is shown in Figure 4.10c. Note that, during this operation, two diodes and one switch are in series with the winding. With the current in phase A winding, if phase B current is to be built up, then switches  $T_2$  and  $T_1$  have to be turned on. Turning on  $T_1$  will turn off the diode  $D_1$ , which implies that the decaying phase-A current will circulate through the A-phase winding, diode  $D_5$ , switch  $T_1$ , and freewheeling diode  $D_4$ . This reduces the voltage across the A-phase winding to zero. Further, this will increase the time for the phase-A current to decay to zero, as shown in Figure 4.10d. During overlapping currents in the succeeding winding phases, independent control of the currents is lost. That is undesirable in high-performance applications.

Even though this converter uses only four switches, each carries the current of two phases. Their maximum rms current rating is

$$I_{\max} = \frac{I_p}{\sqrt{2}} \quad (4.28)$$

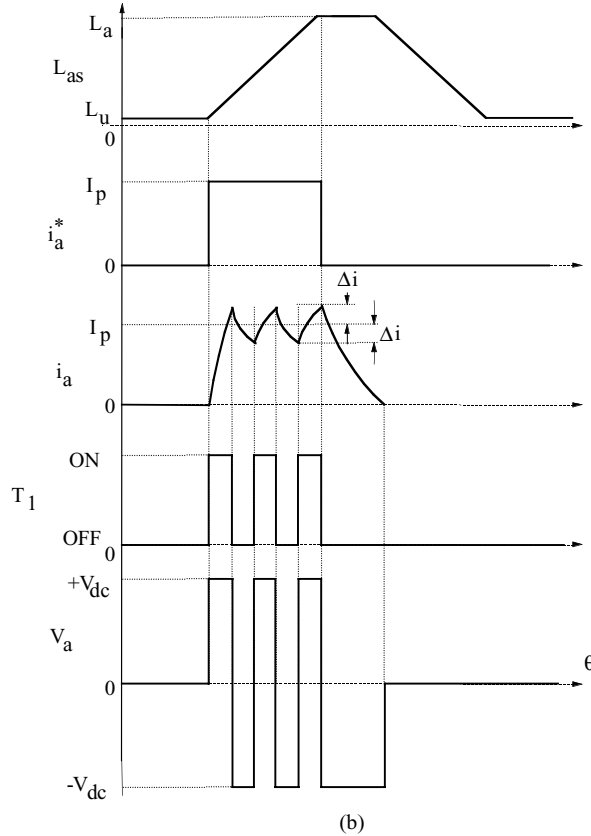


**FIGURE 4.10** (Continued)

where  $I_p$  is the peak value of the phase current, assuming the current is a single rectangular block. Because of its higher current rating per switch, this configuration may not be better than other configurations. Moreover, this configuration requires an even number of machine phases, which restricts its applicability in practice.

#### 4.2.5 $q$ SWITCH AND $2q$ DIODE CONFIGURATION WITH INDEPENDENT PHASE CURRENT CONTROL

Single-switch-per-phase converter topologies presented so far required modified/special bifilar windings and reduced dc link voltage to half for feeding a machine phase and involved higher losses and lower efficiency. A converter topology overcoming all the special requirements and drawbacks is shown<sup>19</sup> in Figure 4.11. It requires additional  $q$  diodes and dc link capacitors. The diodes  $D_a$ ,  $D_b$ , and  $D_c$  can be a slow type and their function is to create a separate dc link source voltage for each phase.

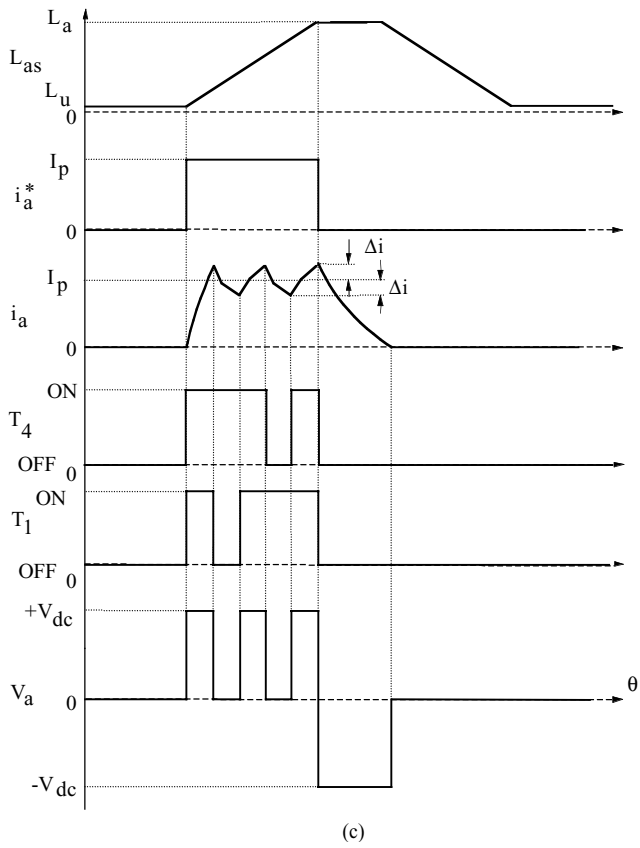
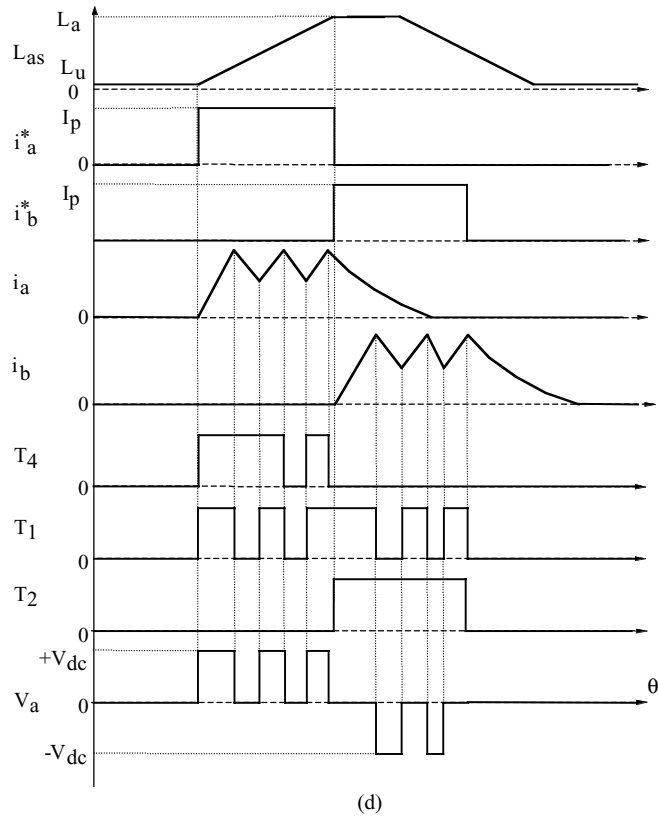


**FIGURE 4.10** (Continued)

The operation of the circuit is as follows. Consider phase A operation. To energize phase A,  $T_1$  is turned on. When phase-A current exceeds its reference, by hysteresis window  $\Delta i$ ,  $T_1$  is turned off. The current in phase A takes the path via diode  $D_1$  and capacitor  $C_{f3}$  connected between phase C and the dc source (equal to the voltage across  $C_{f1}$ ) negative rail of the dc source voltage. Energy from phase A is partially transferred to  $C_{f3}$ , increasing its voltage beyond  $V_{dc}$ , which can rise to a maximum value of  $2V_{dc}$ . The voltage across phase A during  $T_1$  turn-off is the difference between the source voltage and voltage across  $C_{f3}$ , which is negative. When A-phase current drops below the reference,  $T_1$  is turned on to keep the A-phase current around its reference value. For final commutation of phase-A current,  $T_1$  is turned off. Note that the energy stored in  $C_{f3}$  will be depleted during phase C energization. This happens because voltage across  $C_{f3}$  is much greater than  $V_{dc}$ , thus  $D_c$  is reverse biased, resulting in an energy transfer from  $C_{f3}$  to phase C. Since the voltage across  $C_{f3}$  is higher than  $V_{dc}$ , this will allow a faster current rise in phase C. Further, it implies smaller advance angle for phase C and higher efficiency of the machine. When voltage across  $C_{f3}$  becomes less than the source voltage, phase C draws energy



(d)

**FIGURE 4.10** (Continued)

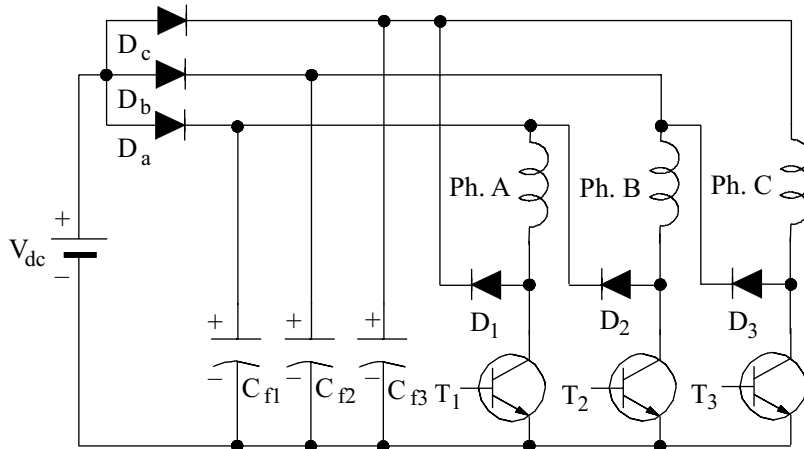


**FIGURE 4.11** Single-switch and two-diodes-per-phase SRM converter.

directly from the source itself. From this discussion, the advantages of the power converter circuit can be summarized in the following:

1. This circuit uses only one switch per phase with none of the disadvantages of other single-switch-per-phase topologies.
2. This topology endows independent phase current control in the SRM.
3. Energy transferred to dc link capacitors during current control and commutation of machine phases is utilized to provide a faster current response, resulting in faster dynamic torque and speed control of the SRM.

The disadvantages of this power converter are:

1. It requires additional  $q$  diodes and  $(q - 1)$  dc link capacitors, which may be obtained by splitting the single dc link capacitor into  $q$  capacitors of equal value.
2. This converter provides only a positive or a negative voltage but is not capable of zero voltage, resulting in higher losses due to the circulating energy and higher acoustic noise.
3. The voltage rating of all the switches and diodes  $D_1$ ,  $D_2$ , and  $D_3$  is  $2V_{dc}$  which increases the volt–ampere (VA) rating of the converter.
4. The number of terminals required of the SRM is  $2q$  for connection to the converter, whereas for most single-switch-per-phase topologies, it is  $(q + 1)$ . This will increase the cost of the machine and will increase the labor involved in the assembly of the motor converter set.
5. This converter is not suitable for purely generator applications of the SRM as there are  $q$  capacitors from which energy has to be recovered. This increases the rating and component count of the energy recovery circuits.

## 4.3 ( $q + 1$ ) SWITCH AND DIODE CONFIGURATIONS

### 4.3.1 CONFIGURATION WITH EQUAL SHARING

A  $(q + 1)$  switch configuration<sup>16</sup> is shown in [Figure 4.12](#). Consider that phase A has to be energized.  $T_1$  and  $T_2$  are turned on, applying the dc source voltage across the phase-A winding. When  $i_a$  exceeds its reference, one option is to turn off either  $T_1$  or  $T_2$ . This will result in current freewheeling with  $D_1$  and  $T_2$  or  $D_2$  and  $T_1$  with the voltage across phase A being zero. The second option is to turn off both  $T_1$  and  $T_2$ , resulting in  $-V_{dc}$  being applied to phase A and a consequent fall in current. To turn off the current in phase A altogether, note that the second option is chosen. Similarly for phase B, devices  $T_2$ ,  $T_3$ ,  $D_2$ , and  $D_3$  are used, and for phase C, devices  $T_3$ ,  $T_4$ ,  $D_3$ , and  $D_4$  are utilized for current control. Devices  $T_2$ ,  $T_3$ ,  $D_2$ , and  $D_3$  share two phase currents. This not only increases their current ratings but also places a constraint on the independent current control of the SRM phases, particularly for operation with overlapping phase currents. Let phase A be commutated and phase B energized with turn-off of  $T_1$  and turn-on of  $T_2$  and  $T_3$ . This results in zero voltage across phase A and  $+V_{dc}$  across phase B. Note that the preferred voltage during commutation is  $-V_{dc}$ .

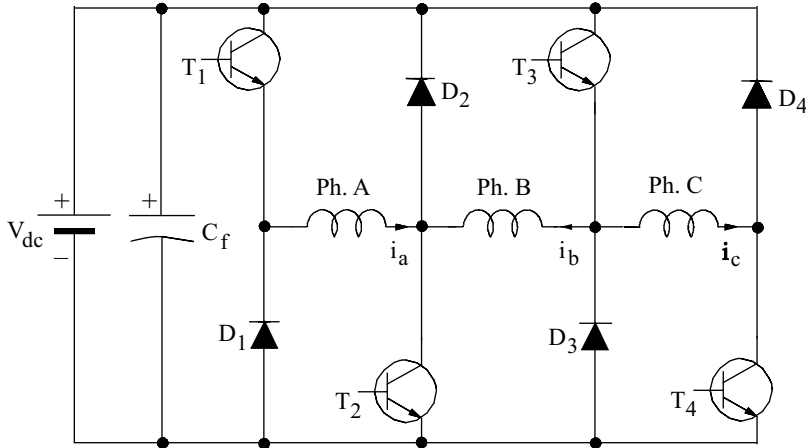


**FIGURE 4.12** A variant of  $(q + 1)$  switch topology.

for a faster current turn-off. The freewheeling of phase A now will prolong current conduction, possibly leading to regeneration and reducing the average electromagnetic torque.

The merits of this converter configuration are

1.  $(q - 1)$  switches and diodes have higher utilization due to shared switch operation.
2. This topology is applicable for any number of phases and has fewer constraints on overlapping phase currents in SRMs with  $q \geq 4$ .

The disadvantages of this converter arrangement are

1. The circuit provides restricted current control options during overlapping phase currents. For phases higher than or equal to four, two or more phases can be operated independently but not all phases independently.
2. The higher driver and power supply requirement in this configuration compared to other  $(q + 1)$  switch topologies is due to the fact that less than  $q$  switches have their emitters connected to the negative rail of the dc bus in this converter as opposed to  $q$  switches in other  $(q + 1)$  switch topologies.

A modification of this circuit<sup>11</sup> with additional diodes results in  $q$  switches and is shown in Figure 4.13. Note that this circuit has  $2q$  diodes, half of which (diodes  $D_a$ ,  $D_b$ ,  $D_c$ , and  $D_d$ ) are steering the currents into right phases and therefore could be of a slow rectifying type. This circuit has a greater restriction in controlling individual phase currents compared to the previous one and is likely to result in longer commutation times. Only machines with an even number of phases equal to or greater than four benefits using this configuration in general. All the switches

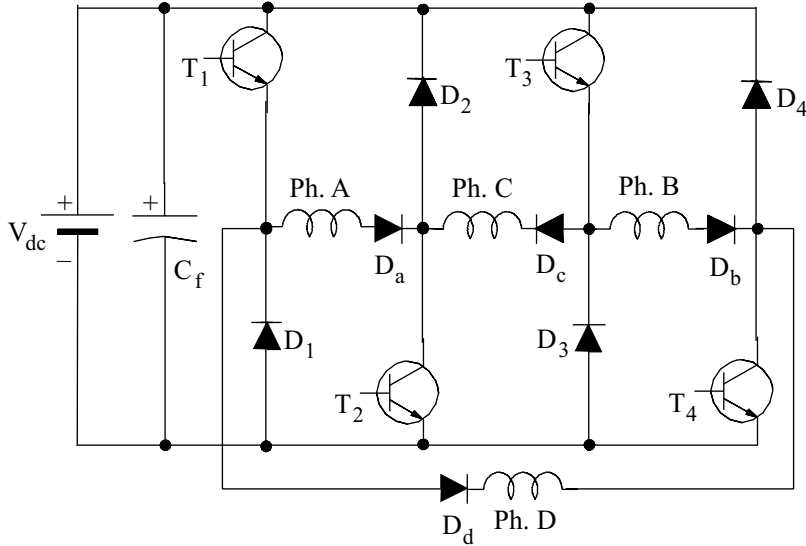


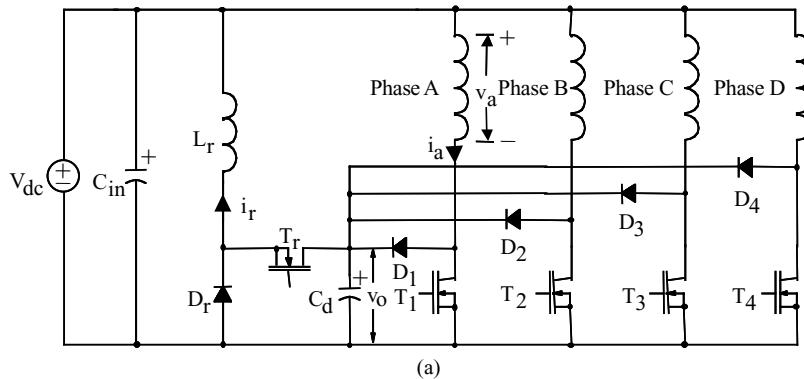
**FIGURE 4.13** Variation of the converter shown in [Figure 4.12](#).

have uniform current ratings, as each carries the sum of two phase currents. For example,  $T_1$  carries both phase  $A$  and  $B$  currents during the conduction of  $T_2$  and  $T_4$ , respectively.

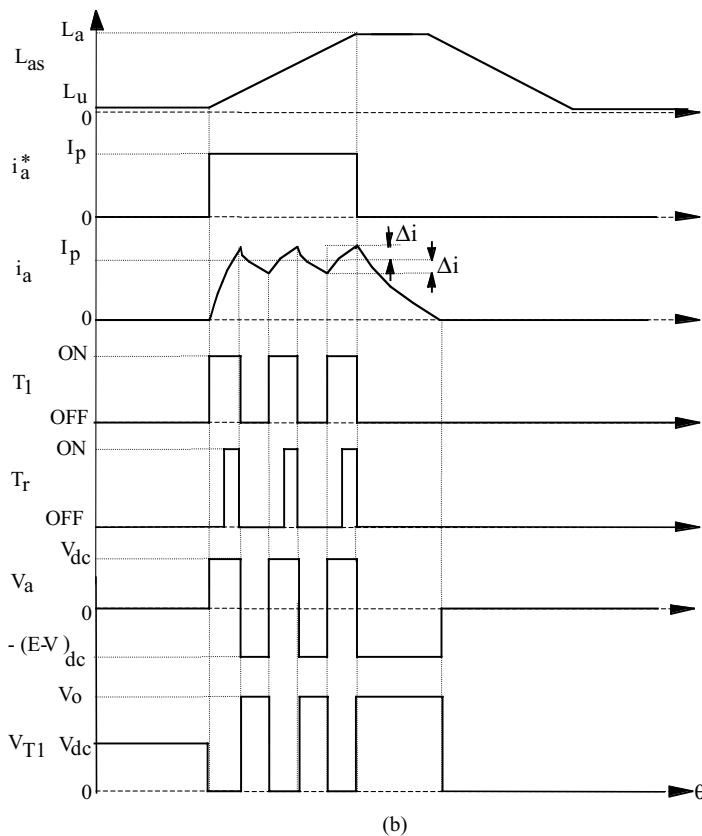
#### 4.3.2 C-DUMP CONVERTER

The C-dump converter<sup>3,6,7</sup> is shown in [Figure 4.14a](#) with an energy recovery circuit. The stored magnetic energy is partially diverted to the capacitor  $C_d$  and recovered from it by the single quadrant chopper comprising of  $T_r$ ,  $L_r$ , and  $D_r$ , and sent to the dc source. Assume that  $T_1$  is turned on to energize phase  $A$  and when the  $A$ -phase current exceeds the reference,  $T_1$  is turned off. This enables the diode  $D_1$  to be forward biased, and the current path is closed through  $C_d$  which increases the voltage across it. This has the effect of reducing the  $A$ -phase current, and, when the current falls below the reference by  $\Delta i$  (i.e., current window),  $T_1$  is turned on to maintain the current close to its reference. When current has to be turned off completely in phase  $A$ ,  $T_1$  is turned off, and partially stored magnetic energy in phase  $A$  is transferred to energy dump capacitor,  $C_d$ . The remaining magnetic energy in the machine phase has been converted to mechanical energy. [Figure 4.14b](#) shows the variables of interest in this converter.

This converter has the advantage of minimum switches allowing independent phase current control. The main disadvantage of this circuit is that the current commutation is limited by the difference between voltage across  $C_d$ ,  $v_o$ , and the dc link voltage. Speedy commutation of currents requires larger  $v_o$ , which results in increasing the voltage rating of the power devices. Further, the energy circulating between  $C_d$



(a)



(b)

**FIGURE 4.14** (a) C-dump converter with energy recovery circuit; (b) waveforms of C-dump converter with energy-recovery circuit.

and the dc link results in additional losses in the machine,  $T_r$ ,  $L_r$ , and  $D_r$ , thereby decreasing the efficiency of the motor drive.

The energy recovery circuit is activated only when  $T_1$ ,  $T_2$ ,  $T_3$ , or  $T_4$  switches are conducting to avoid freewheeling of the phase currents. The control pulses to  $T_r$  end with the turn-off of the phase switches. The control pulse is generated based on the reference and actual value of  $E$  with a window of hysteresis to minimize the switching of  $T_r$ .

This circuit has gained in popularity since its introduction in the early stages of SRM drive research and development; therefore, a detailed analysis of this circuit<sup>36</sup> is presented here. Analysis in the following sections considers computation of switching losses of the power devices, maximum voltage, and current ratings of the power devices for an SRM drive of known power rating; ratings of the energy recovery capacitor,  $C_d$ , inductor,  $L_o$ , and its duty cycle; and the efficiency of the overall circuit. The design procedure for the converter topology is derived from this analysis.

#### 4.3.2.1 Modes of Operation and Mode Equations

In one switching period, each phase encounters five distinct modes of operation as shown in [Figure 4.15](#). The five modes of operation are explained and respective mode equations are derived in this section.

##### 4.3.2.1.1 Mode 1: $T_1$ On and $T_r$ Off

The dc link voltage supplies the magnetizing energy to the motor winding in this mode. The current during this period can be expressed, assuming ideal devices, constant speed, and linear magnetic characteristics, as:

$$i_{ph}(t) = \frac{V_{dc} - e}{R_s} \cdot (1 - e^{-t/\tau_1}) + i_o(t) \cdot e^{-t/\tau_1} \quad (4.29)$$

where

$$\tau_1 = \frac{L(i, \theta)}{R_s} \quad (4.30)$$

$$e = \omega_m \cdot i \cdot \frac{dL(i, \theta)}{d\theta} \quad (4.31)$$

$L(i, \theta)$  is the motor winding inductance per phase,  $\omega_m$  is the motor speed,  $R_s$  is the motor winding resistance per phase,  $i_o(t)$  is the initial phase current,  $e$  is the induced emf, and  $\theta$  is the rotor angle. Note that  $L$ ,  $e$ , and  $\tau_1$  are current and time dependent (because of rotor position) so the initial current is time dependent. If the winding resistance is neglected and assuming that the current varies linearly, then the maximum

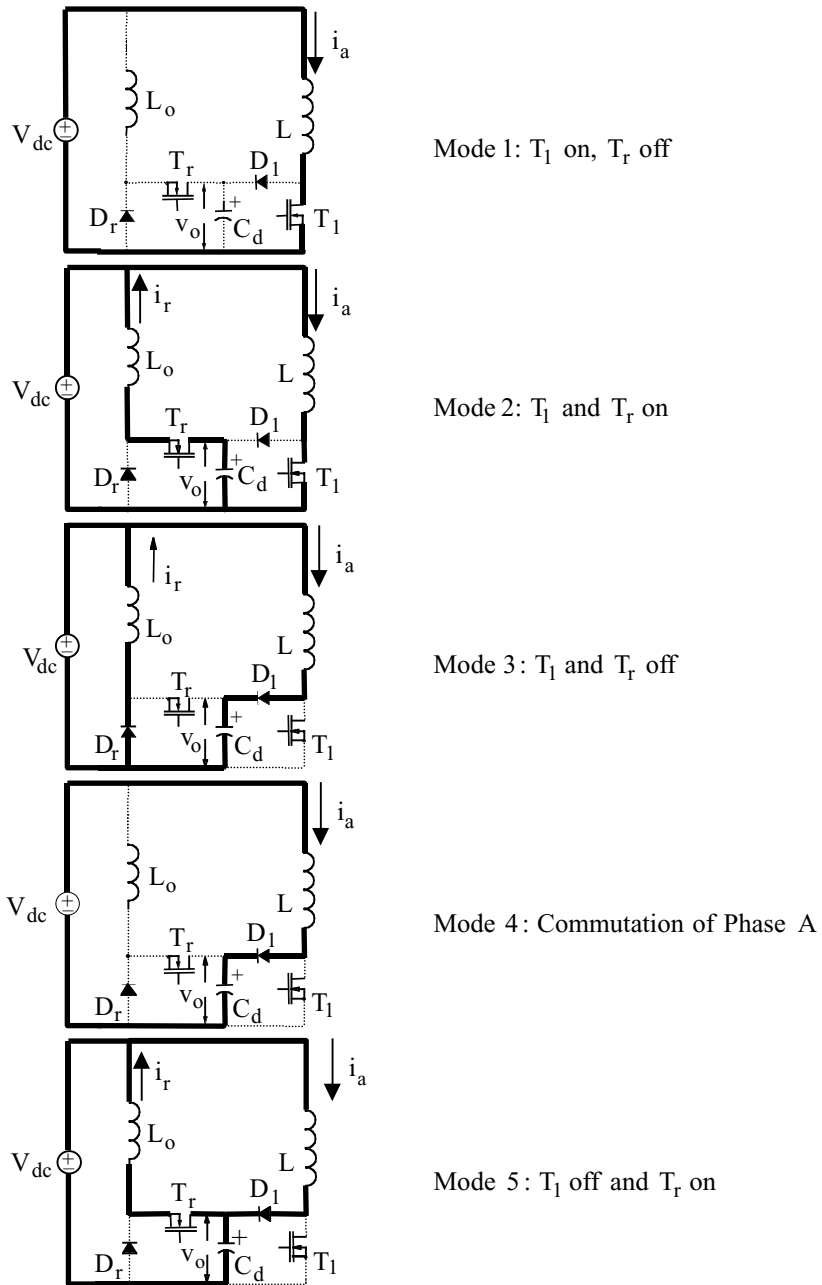


**FIGURE 4.15** Five modes of operation of a phase.

and the minimum (initial) phase currents are given by:

$$i_1(t) = i_o(t) + \frac{V_{dc} - e}{L} \cdot t_1 \quad (4.32)$$

$$i_o(t) \approx i_1(t) - \frac{v_o + e - V_{dc}}{L} \cdot t_2 \quad (4.33)$$

$$\left. \begin{array}{l} t_1 = d_1 \cdot T_c \\ t_2 = (1 - d_1) \cdot T_c \\ T_c = 1/f_c \end{array} \right\} \quad (4.34)$$

where  $t_1$  is the on time and  $t_2$  is the off time of the phase switch in each PWM cycle, and  $f_c$  is the PWM carrier frequency in Hz. Eqs. (4.32), (4.33), and (4.34) can be combined to find the average duty cycle of the phase switch if the induced emfs during on and off durations in a PWM cycle are approximately equal. Then, the duty cycle  $d_1$  is

$$d_1 = \frac{v_o - V_{dc} + E}{v_o} = h + \frac{E}{v_o} \quad (4.35)$$

where

$$h = \frac{v_o - V_{dc}}{v_o} \quad (4.36)$$

$$E = \omega_m \cdot I \cdot k(\theta) \quad (4.37)$$

where  $E$  is the average induced emf in the machine phase during current conduction,  $I$  is the average phase current in a PWM cycle, and  $\omega_m$  is the speed in rad/sec, and

$$k(\theta) = \frac{dL(i, \theta)}{d\theta} \quad (4.38)$$

If  $E$  is defined to be equal to base voltage  $V_b$ , then the steady-state C-dump voltage and approximated  $k(\theta)$  are written as:

$$\left. \begin{array}{l} V_o = V_b = k(\theta) \cdot I_b \cdot \omega_b \\ k(\theta) = \frac{L_a - L_u}{(\pi/3/q)} \end{array} \right\} \quad (4.39)$$

where  $I_b$  is the base current;  $L_a$  and  $L_u$  are the aligned and unaligned inductances, respectively; and  $\omega_b$  is the base speed.

By substituting Eq. (4.39) in Eq. (4.37) and then in Eq. (4.36), and taking the average, the duty cycle  $d_1$  is obtained as:

$$d_1 = h + \omega_m \cdot I_n \quad (4.40)$$

where normalized speed is

$$\omega_{mn} = \frac{\omega_m}{\omega_b}, \text{ p.u.} \quad (4.41)$$

and normalized current is

$$I_n = \frac{I}{I_b}, \text{ p.u.} \quad (4.42)$$

Eq. (4.40) clearly brings out the relationship between the energy storage capacitor voltage, dc link voltage, speed, phase current, and duty cycle of the phase switch. If speed increases,  $d_1$  has to be increased if  $h$  is maintained constant. Note that in practical applications  $h$  is a constant and may be in the range of 0.2 to 0.3. From this equation, the impact of increasing  $V_o$  becomes evident. Increasing  $V_o$  increases  $h$ , so for a given maximum duty cycle and current, the maximum machine speed will decrease. This sets a limit on the maximum speed of operation. It is preferable, then, to keep  $h$  at the minimum level. This will have other consequences as noted later. The maximum speed for a 1-p.u. current is given by:

$$\omega_{mn}(\max) = d_1(\max) - h(\min) = (1 - h), \text{ p.u.} \quad (4.43)$$

#### 4.3.2.1.2 Modes 2 and 3: $T_1$ and $T_r$ Both On and Then Off

The energy recovery switch is turned on after  $T_1$  starts conducting transferring energy from capacitor  $C_d$  to the dc source and inductor  $L_r$ . Let  $d_2$  be the duty cycle of the energy recovery switch. The duty cycle  $d_2$  is a variable and is determined by feedback control to keep the voltage across  $C_d$  constant.

#### 4.3.2.1.3 Mode 4: Phase Current Commutation

In this mode, the current in the machine phase has to be decreased rapidly to zero. During this time, the switch  $T_1$  is turned off and the energy in the machine is partially transferred to the capacitor  $C_d$ , as shown in Figure 4.15. During this mode, the voltage across the capacitor,  $C_d$ , increases. The current decays as the voltage difference between  $V_o$  and  $V_{dc}$  is impressed across the machine phase.

#### 4.3.2.1.4 Mode 5: $T_1$ Off, $T_r$ On

This mode arises when the current in the phase is controlled by turn-off of  $T_1$  while  $T_r$  is on, transferring energy from  $C_d$  to the dc source. This mode is a combination of modes 2 and 4.

### 4.3.2.2 Design Procedure

Evaluation of the device and passive component ratings and switching frequency selection form the design of the converter circuit. They are derived in the following.

#### 4.3.2.2.1 Device Ratings

The power devices have to withstand  $V_o + \Delta V_o$  where  $\Delta V_o$  is the rise in voltage across the dump capacitor during commutation of the phase current. The voltage  $V_o$  has to be conservatively estimated at  $2V_{dc}$ . The rating of the phase switches based on average current is its peak value divided by number of phases assuming that the turn-off interval during phase conduction is negligible. Note that this is not the case in practice; therefore, this is a conservative design value for the average current rating of the device. The phase diode is likewise conservatively rated.

#### 4.3.2.2.2 Dump Capacitor Rating

The dump capacitor rating is derived from calculating the incremental voltage rise in the dump capacitor. Considering the average current of the machine phase as  $I$  and the current ripple being small, the incremental voltage rise in  $C_d$  during the turn-off of  $T_1$  is approximated as:

$$\Delta V_o \cong \frac{1}{C_d} \cdot I \cdot t_{\text{off}} \cong \frac{1}{C_d} \cdot I \cdot (1 - d_1) \cdot T_c \cong \frac{(1 - d_1)}{f_c} \cdot \frac{I}{C_d} \quad (4.44)$$

The dump capacitor value is derived from this equation as:

$$C_d = \frac{(1 - d_1)}{f_c} \cdot \frac{I}{\Delta V_o} \quad (4.45)$$

where  $d_1$  corresponds to its minimum value obtained at no-load operation.

#### 4.3.2.2.3 Incremental Current in Machine Phases

During conduction of the machine phases, current rises from  $i_o$  to  $i_1$ , providing an incremental rise of  $\Delta i$  with application of the dc link voltage to the machine phases. During this time, inductance changes incrementally by  $\Delta L$ . Neglecting resistances of the machine phase and the switching devices, the following approximate relationship is obtained:

$$L\Delta i = V_{dc} d_1 T_c - I\Delta L \quad (4.46)$$

where  $L$  is the inductance at turn-on. From this the incremental current is derived.

The current ripple in the machine phases influences the torque pulsations, thus its magnitude is an important parameter in the SRM drive system.

#### 4.3.2.2.4 Switching Frequency

The switching frequency affects both incremental voltage rise and current as seen from Eqs. (4.45) and (4.46). Hence, the minimum switching frequency is derived by equating the duty cycle  $d_1$  from these two expressions, resulting in:

$$f_c = \frac{V_{dc}}{I\Delta L + L\Delta i + V_{dc} C_o \Delta V_o} \quad (4.47)$$

The relevant variables of the machine—energy recovery circuit, operating current, dc link voltage, current and voltage increments—are related to the switching frequency. The design value for  $f_c$  is chosen for maximum values of  $V_{dc}$  and minimum values of  $\Delta V_o$ ,  $L$ ,  $I$ , and  $\Delta i$ .

#### 4.3.2.2.5 Rating of $L_r$

$L_r$  is computed based on the ripple requirement in energy recovery current,  $i_r$ . It is given by,

$$L_r = \frac{d_2 T_c h E}{\Delta i_r} = \frac{d_2 h E}{f_c \Delta i_r} \quad (4.48)$$

It has to be evaluated for the least tolerable current ripple and maximum duty cycle,  $d_2$  of the recovery switch.

#### 4.3.2.2.6 Recovery Current

The recovery current in  $L_r$  is found by equating the charging and discharging energy in  $C_d$ . It is approximately given by neglecting the losses in the inductor and power device  $T_r$  as:

$$h V_o d_2 T_c I_r = V_o I (1 - d_1) T_c \quad (4.49)$$

from which

$$I_r = \frac{(1 - d_1)}{d_2} \cdot \frac{I}{h} \quad (4.50)$$

Note that  $d_2$  can almost be equal to  $d_1$  and the recovery current magnitude is influenced by  $I$ ,  $h$ , and  $d_1$ . Note that the recovery current identifies the volt–ampere (VA) rating of this subsystem circuit. Higher values of  $h$  are preferable in the design to minimize average energy recover current,  $I_r$ , to minimize the operational speed range, as seen from Eqs. (4.39) and (4.42). A design trade-off is inevitable between the conflicting choices. Further, it must be noted that higher  $h$  values also increase the switch and diode voltage ratings. These considerations along with maximum speed of operation have to be kept in perspective in the choice of  $h$ , which invariably affects  $I_r$  and other parameters.

The recovered energy circulates through the converter and machine, resulting in increased losses in machine windings, switches, and circuit passive components due to increased phase current. This is the cause for increased volt-ampere rating of the converter and for a slight drop in efficiency compared to two switches per phase converter based SRM drive system. The rating of the recovery circuit switch and its cooling play a critical role in the design of this converter circuit.

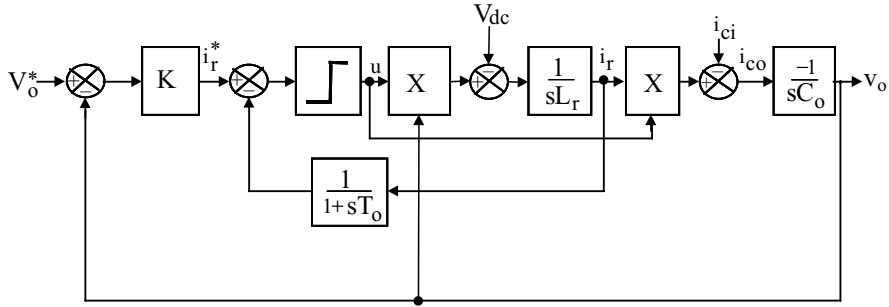


**FIGURE 4.16** Sliding mode-based controller for energy recovery chopper.

#### 4.3.2.2.7 Voltage and Current Control in Energy Recovery Circuits

One of the problems associated with energy recovery from the capacitor  $C_d$  and its transfer to the dc source is that there is a wide fluctuation of capacitor voltage due to the discontinuous current in the inductor  $L_r$ . High ripple currents in the capacitor and a large ratio of peak to average current in the inductor result, necessitating a larger rating and sizing of  $L_r$ . Both problems can be overcome by having current and voltage control in the energy recovery chopper circuit.<sup>38</sup> The inner loop is for current in the inductor and the outer is for the voltage control of the capacitor. Let the instantaneous voltage across  $C_d$  be denoted by  $v_o$ . Either PWM or hysteresis current control is possible for this purpose. A first-order filter is introduced in the current feedback path. A control schematic using sliding mode control with hysteresis is shown in Figure 4.16. The voltage error generates the current reference command after processing with a gain  $K$ . The current is fed back through a filter with a time constant of  $T_o$ . The current error is processed through a sign discriminator to produce the switching signals for energy recovery chopper. This signal is  $u$ , which is related to the switching of switch  $T_r$  as:

$$\begin{aligned} u &= 1, T_r \text{ is ON} \\ u &= 0, T_r \text{ is OFF} \end{aligned} \quad (4.51)$$

Whenever  $T_r$  is on, it forces a current through  $L_r$  which is due to the difference between  $v_o$  and  $V_{dc}$ . The difference between chopper stage input current  $i_i$  and  $i_r$  is the capacitor current  $i_{co}$  which determines the state of  $v_o$ .

#### 4.3.3 C-DUMP WITH FREEWHEELING

The C-dump SRM converter circuit is unable to provide zero voltage across the circuit, thus eliminating an additional degree of freedom in the control of the SRM. This results in a considerable increase in acoustic noise (see Chapter 7). Further, the machine phases experience either dc source voltage or a difference between the

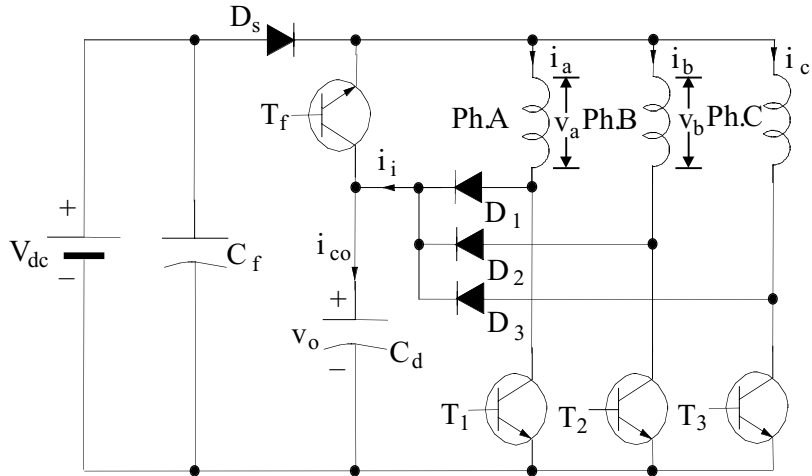


**FIGURE 4.17** Freewheeling C-dump SRM converter.

dc source and C-dump capacitor voltage resulting in a large rate of change of voltage, almost two times that of the dc source voltage, in a short time. This affects the life of the winding insulation and is a source of additional loss.

All these problems are overcome by adding a freewheeling transistor as shown in Figure 4.17 which could also be used to recover the energy in the C-dump if a diode  $D_s$  is introduced in the dc link current path.<sup>25</sup> Note that the energy recovery circuit is not needed for this configuration. In fact, this power converter topology has the same number of devices as the C-dump with an active energy recovery circuit. The energy recovery circuit is replaced in a different arrangement in this circuit and the inductor  $L_r$  is disposed of completely, which amounts to considerable savings in the drive system cost.

For energization of a phase, say phase A, transistor  $T_1$  is turned on and it is mode 1. When the phase current exceeds a set value,  $T_1$  is turned off and  $T_f$  is turned on. Mode 2 starts with the charging of  $C_d$ . When its voltage exceeds that of the dc source,  $T_f$  conducts and current takes the path of machine phase, diode  $D_1$ , and  $T_f$  (note that the voltage across the machine phase is almost zero). When the current in phase has to be commutated,  $T_1$  is turned off without turning on  $T_f$  which enables the transfer of the energy from the machine partially to  $C_d$  and partially for power conversion in the machine. This is mode 3, and during this mode the voltage across the machine phase is  $(V_{dc} - v_o)$ . Mode 4 is enabled when a phase is completely commutated, and the energy in  $C_d$  may be depleted by turning on  $T_f$  when phase B or C is conducting. Now diode  $D_s$  is reverse biased, allowing the C-dump voltage  $v_o$  to be applied across the conducting phase. During all these modes, independent control of phases is achieved except for overlapping phase currents. Turning on  $T_f$  during overlapping currents will prolong the commutation of current in the outgoing phase. The general waveforms of the circuit functioning without phase current overlap are shown in Figure 4.18. The energy

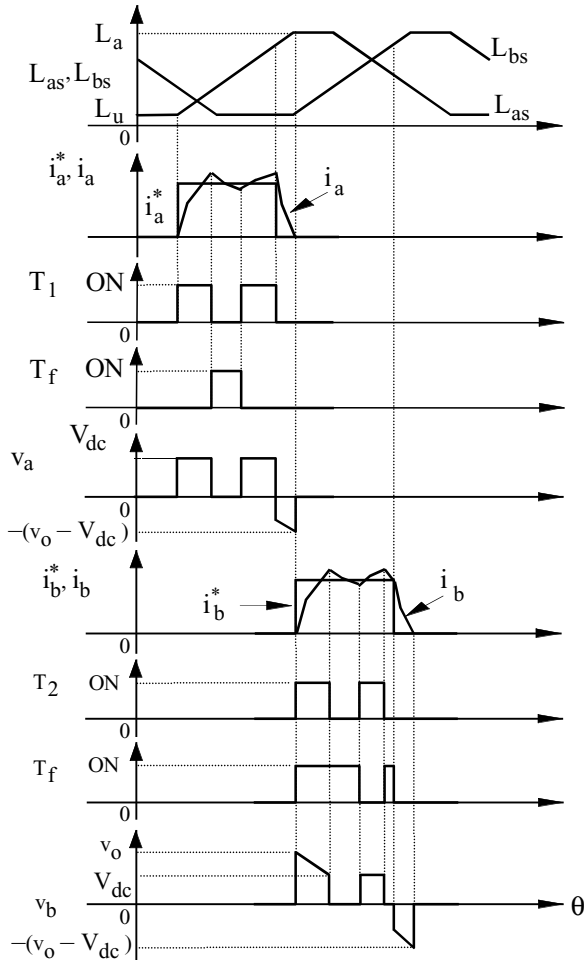


**FIGURE 4.18** Operational waveforms of freewheeling C-dump SRM converter with no overlapping phase currents.

accumulated in  $C_d$  during phase-A commutation is used in phase-B for faster current rise at the time of initiating the phase-B current. Alternatively, the energy could be used in the latter during rising phase inductance (say, at higher speeds) for good current and torque control. There is a fair amount of control flexibility in shaping the dynamics of the drive system by careful and timely utilization of the energy stored in  $C_d$  in every phase cycle. While all such control strategies cannot be enumerated here, for lack of space, it is noted that adequate flexibility in SRM drives control is possible with this topology.

The advantages of this power topology include:

1. The dc source capacitor has less ripple current as there is no energy transfer from the machine to the dc source.

2. It achieves positive, zero, and negative voltage across the machine phase. This has the positive effects of higher control flexibility, lower acoustic noise, lower dielectric losses in the machine, and longer life of the insulation.
3. Higher voltage of  $C_d$  could be used to greater benefit in current and torque control, particularly at higher speeds where voltage higher than the dc source is inadequate for high-quality dynamic and steady-state control.
4. This circuit achieves additional freedom in output voltages with the same number of devices as in the C-dump with an active energy recovery circuit and lends itself to a compact packaging.

This topology also has serious limitations, and some of the disadvantages are given in the following:

1. Only motoring operation is possible; if regenerative operation is desired, a regenerative brake circuit or some energy recovery circuit has to be incorporated with this circuit.
2. The rating of  $T_f$  is very much higher than that of phase switches.
3. Control coordination between the freewheeling switch and main phase switches during commutation with overlapping phase currents restricts control freedom and flexibility. This would result in a longer commutation time with possible regeneration and an increase in acoustic noise.

A slight modification of this type of converter dispenses with the dc link capacitor  $C_f$ , as shown in [Figure 4.19](#).  $C_d$  is charged through the machine phase windings, so a separate precharging circuit is not required to limit the surge current in the capacitor. This, in turn, reduces the peak ratings of the front-end rectifier diodes. It may be noticed that operational freedom is very much curtailed with this arrangement compared to the previous circuit due to the need to have  $C_d$  charged and the machine phases supplied with desired currents. Further, the ratings of  $T_f$  and  $D_s$  increase as their duty cycles increase. Diode  $D_s$  serves to block the antiparallel diode of the device  $T_f$  from charging  $C_d$  directly through diode bridge.

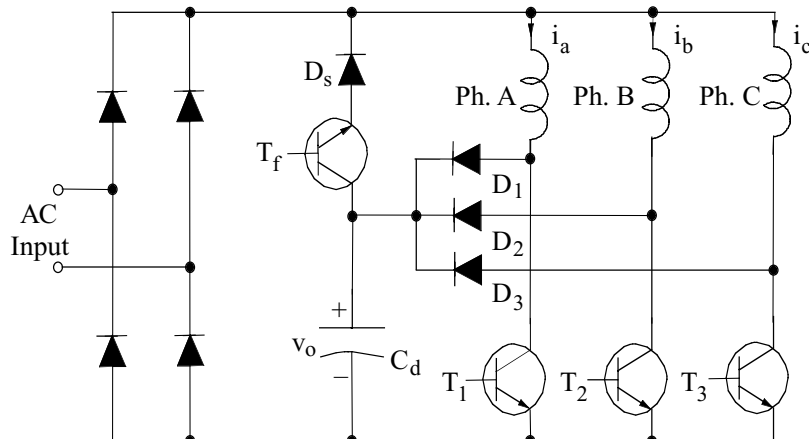


**FIGURE 4.19** Modification of circuit shown in [Figure 4.17](#) with one capacitor only.

#### 4.3.4 ONE COMMON SWITCH CONFIGURATION

Figure 4.20a shows a converter<sup>4,39,40</sup> overcoming some of the drawbacks associated with the converters discussed earlier. The line switch  $T_1$  isolates the common top terminals of phases A, B, and C to enable the transfer of energy to the capacitor  $C_1$ . For conduction of current in phase A,  $T_1$  and  $T_3$  are turned on. When the phase current exceeds the command value,  $T_1$  and  $T_3$  are turned off together or singly. The current will continue to flow in the same direction in phase A, through  $D_3$ ,  $C_1$ , and  $D_2$ , if  $T_1$  and  $T_3$  are turned off. The recovered energy in  $C_1$  can be sent to ac supply mains through an appropriate front-end converter. The converter operation is shown in Figure 4.20b. The disadvantage of the converter is that two phases of the SRM cannot be allowed to conduct simultaneously. At that time, the outgoing phase has to freewheel its energy through itself and the diode, prolonging the conduction time. For such a contingency, the operational waveforms are shown in Figure 4.20c.

Three switching strategies are possible to control the current in the machine phases:

1. *Strategy I*: Throughout phase conduction, the main switch  $T_1$  is on and the phase switch is turned on and off.
2. *Strategy II*: Throughout phase conduction, the phase switch is on and the main (common) switch is turned on and off.
3. *Strategy III*: Simultaneous switching (on and off) of both the common and phase switches.

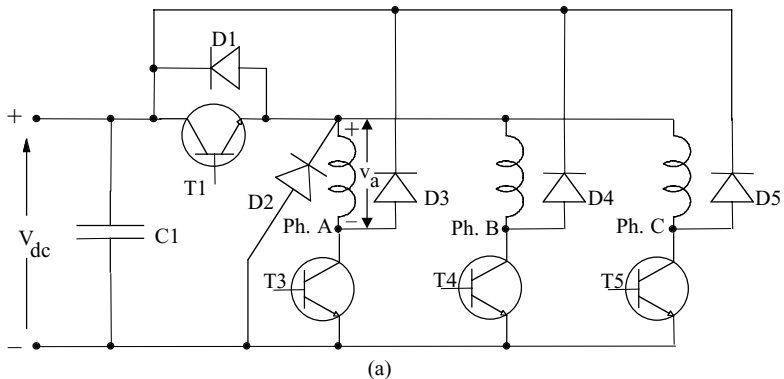
Strategy I increases the current rating of the common switch compared to strategies II and III and hence is undesirable. Even though strategy III provides for the same rating of the main switch as strategy II, it also gives a lower current rating of the phase switches, but it increases the switching losses of the converter. From these observations, it may be inferred that strategy II is the most desirable of the three switching strategies. The current waveforms using switching strategy II are shown in Figure 4.21.

The average current rating of  $T_1$  is approximately equal to  $I_p/2$ . The average current rating of phase switches is approximately  $I_p/q$ .

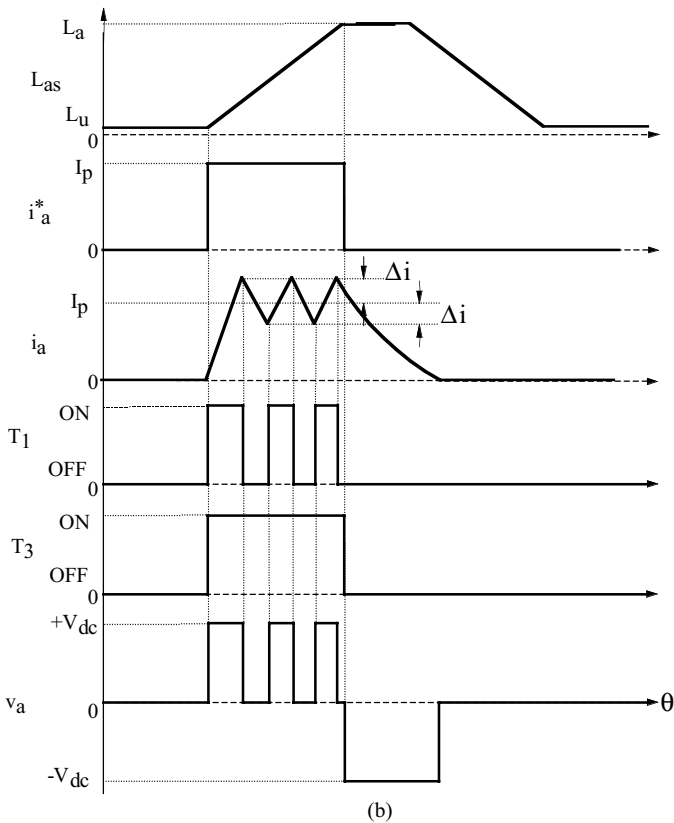
It can be seen that freewheeling diodes  $D_3$ ,  $D_4$ , and  $D_5$  carry a small fraction of the average current. The common diode and switch,  $D_2$  and  $T_1$ , respectively, are complementary in their current conduction. Their minimum voltage ratings are all equal to  $V_{dc}$ .

#### 4.3.5 MINIMUM SWITCH TOPOLOGY WITH VARIABLE DC LINK

Two  $(q + 1)$  switch configurations for switched reluctance motor drives have been advocated due to their simple power converter topology having a minimum number of power switches and attractive control features, in spite of their operational limitations. These topologies have full four-quadrant operational capacity and endow the same voltage rating on all the devices as that of the dc source but have no independent energization and commutation of the machine phases for overlapping conduction

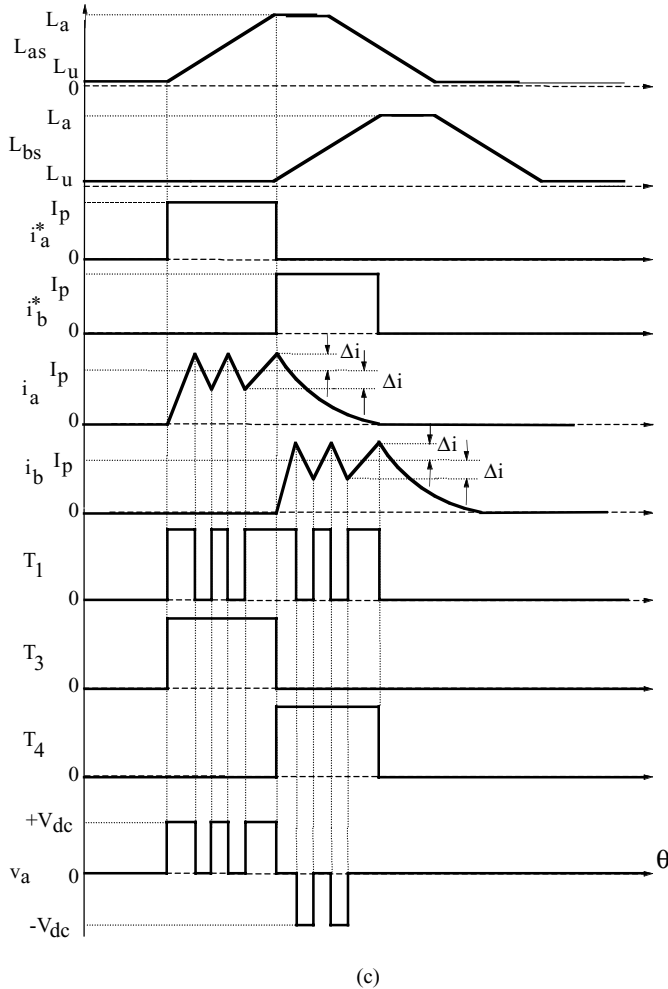


(a)



(b)

**FIGURE 4.20** (a) Converter for SRM with regenerative capability; (b) waveforms of the converter with no overlap of phase currents; (c) operational waveforms during overlapping current conduction.



(c)

**FIGURE 4.20** (Continued)

of the phases. The version with a C-dump has independent energization and commutation control of phases but a higher voltage rating for the devices compared to the topologies already discussed. It also has a greater circulating energy through the machine windings and attendant losses. These disadvantages have restricted the use of many of these converters in practice.

Shown in [Figure 4.22](#) for a three-phase SRM is an original power circuit topology<sup>41</sup> overcoming the restriction on the independent control of energization and commutation of the phase currents while maintaining the same number of power switching devices. The switch  $T_c$ , diode  $D_c$ , inductor  $L_c$ , and capacitor  $C_c$  form the step-down chopper power stage. This stage varies the input dc source voltage  $V_{dc}$  to  $V_i$  to obtain the desirable input voltage to the machine windings, such as for single-pulse voltage

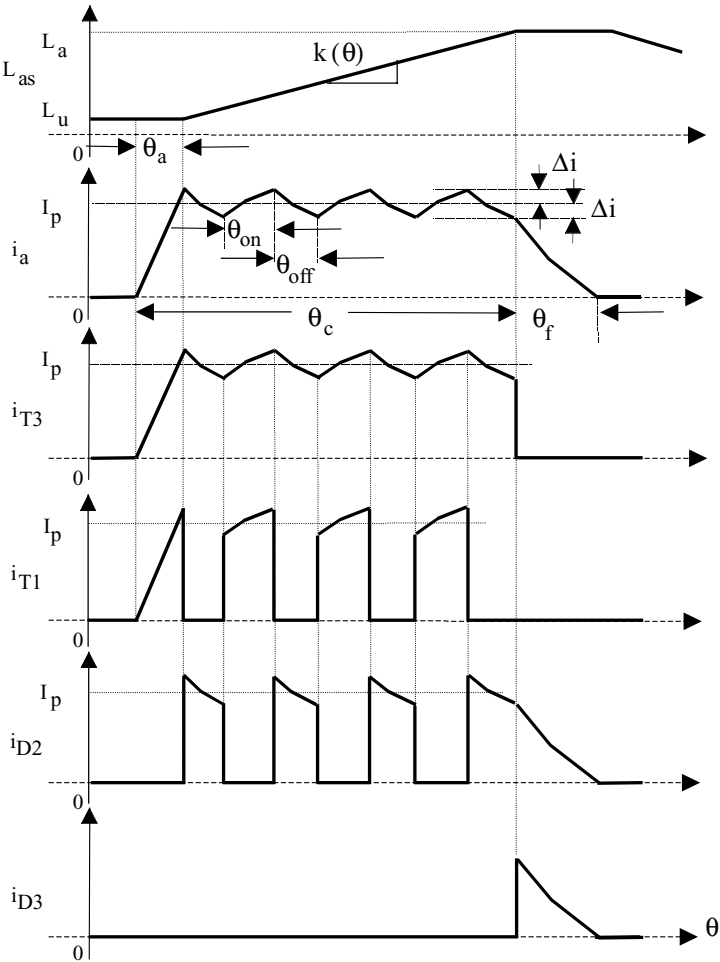


**FIGURE 4.21** Current waveforms for switching strategy II.

switching, to minimize switching and reduce the associated losses both in the phase switches of the SRM converter and the core losses in the machine windings. Further, this stage provides the isolation required for faster commutation of the current while limiting the voltage rating of all the power devices to the dc source voltage, unlike the case of the C-dump topology, which requires a switch voltage rating twice that of the dc source bus. A step-down front-end chopper stage has been advocated for use with an asymmetric converter, but requires  $(2q + 1)$  switching devices and diodes.<sup>29,31,33</sup>

The energization mode is initiated by switching on the phase switch (say,  $T_1$ ) which applies the voltage  $V_i$  to the machine phase A, assuming an ideal diode and switch. To regulate the current in the winding, switch  $T_1$  is turned off, which initiates the routing of the current through the freewheeling diode  $D_1$ , the source voltage  $V_{dc}$ ,

**TABLE 4.1**  
**Modes of Operation**

Mode	$T_c$	$D_c$	$i_c$	$T_1$	$D_1$	$i_a$
1	On	Off	>0	Off	Off	0
2	Off	On	>0	Off	Off	0
3	Off	Off	0	Off	Off	0
4	On	Off	>0	On	Off	>0
5	On	Off	>0	Off	On	>0
6	Off	On	>0	Off	On	>0
7	Off	Off	0	Off	On	>0
8	Off	On	>0	On	Off	>0
9	Off	Off	0	On	Off	>0

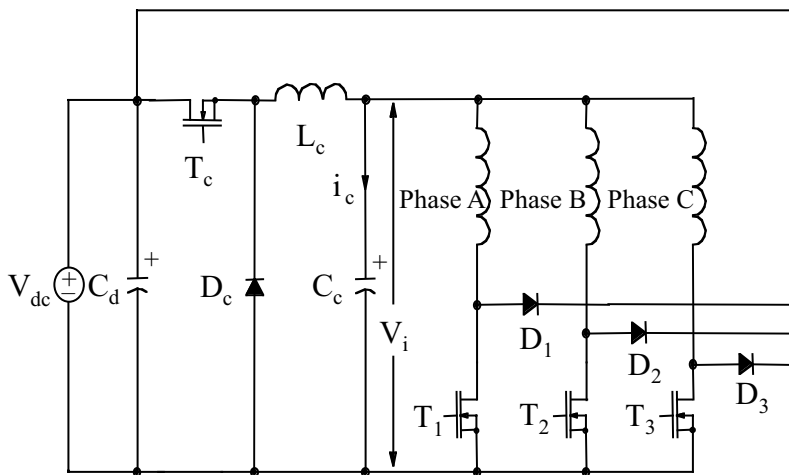


**FIGURE 4.22** Variable dc link converter topology for SRM drives.

and capacitor  $C_c$ , assuming that the chopper switch  $T_c$  is turned off during that time. That would apply a negative voltage equal to the difference between  $V_{dc}$  and  $V_i$  across the machine phase. The energy in the capacitor  $C_c$  will be able to cater to the oncoming phase (say, B) during the time that the switch  $T_c$  is turned off. In this manner, the independence between various machine phases is maintained.

#### 4.3.5.1 Operational Modes of the Converter Circuit

Various modes of operation of the circuit are derived by isolating the modes of the machine phase switch and its diode and the chopper which when combined provide all the modes of operation. This strategy works very well in determining the key modes of this converter circuit (see Table 4.1). Note that the first three modes correspond to the operation of the chopper in isolation and the next six modes when a machine phase (say, in this case, phase A) is energized. When machine phase B

is energized while machine phase A is continuing to conduct or being commutated, note that six additional modes similar to that of the modes 4 to 9 will exist with A- and B-phase machine currents greater than zero. As the last set of modes of operation are virtually the same if the machine mutual inductances are neglected, which could be safely done for the SRMs, then modes 1 to 9 are considered independent modes and are sufficient to fully understand the operation and hence to find analytical relationships between the converter and machine variables for the design of the converter.

#### 4.3.5.2 Design Considerations of the Chopper Circuit Components

The chopper plays a critical role in the operation of the SRM drive. It determines the freewheeling of the machine phases and the input voltage,  $V_i$ , to the machine phases. By setting  $V_i$ , the commutation voltage ( $V_{dc} - V_i$ ) across the machine phases and the speed of the current rise in the machine phases are affected. It is seen that the rising current response and current commutation have conflicting requirements in that the former requires maximum input and the latter requires the minimum of the input voltage. This conflict could be viewed as a design trade-off, which could be advantageously negotiated by advancing the subsequent phase current with respect to the commutating phase. Note that during the commutation phase the input voltage could be reduced substantially without affecting the current in the rising phase very much. Conflicting requirements such as faster rise of current in the incoming phase, faster decay of current in the outgoing phase, lower ripple current, and a required minimum energy storage are considerations for the chopper design. Details can be found in relevant publications.

#### 4.3.5.3 Performance Constraints and Design of the Converter

The critical performance variables of interest in the design are the commutation time of the current and the voltage rise in the source capacitor  $C_f$  due to the energy being transferred from the machine windings to the dc source capacitor of the converter. Both of these effects are quantified in the following sections to assess the control boundaries of the converter and the total drive system and to select the rating of the dc source capacitor. Note that during commutation, assuming that the chopper switch is turned off and the current in  $L_c$  is zero, the voltages across  $C_c$  and  $C_d$  are  $V_{io}$  and  $V_{dco}$ , respectively. With a machine current of  $i_o$  at the start of the commutation, the following analysis is made.

##### 4.3.5.3.1 Current Commutation Time

During commutation, the current has a path through the machine winding of  $a$ , diode  $D_1$ ,  $C_f$ , and  $C_c$  with the chopper current being zero, which is enforced ahead of the commutation starting time. The equivalent circuit for this condition is a resistor, inductor, and capacitor (RLC) circuit with initial conditions for the inductor and capacitors. The equivalent resistance of the network consists of the winding resistance and the constant associated with the induced emf of the machine winding as follows:

$$R_{eq} = R_s + \omega_m \cdot \frac{dL}{d\theta} \quad (4.52)$$

where the derivative term corresponds to the slope of the machine inductance to its rotor angle, which may be assumed constant for a fixed current. We define the natural frequency of the oscillation and damping factors in terms of the circuit variables as:

$$\omega_o = \frac{1}{\sqrt{(LC)}} \quad (4.53)$$

$$\zeta = \frac{1}{2} \cdot \frac{R_{eq}}{L\omega_o} = \frac{1}{2} \cdot R_{eq} \sqrt{C/L} \quad (4.54)$$

where the equivalent capacitance is given as:

$$C = \frac{C_d \cdot C_c}{C_d + C_c} \quad (4.55)$$

The current in the winding is derived by:

$$i(t) = \frac{V_{io} - V_{dco}}{\omega L} \cdot e^{-\zeta\omega_o t} \sin \omega t + i_o e^{-\zeta\omega_o t} \left\{ \cos \omega t - \zeta \frac{\omega_o}{\omega} \sin \omega t \right\} \quad (4.56)$$

where the damped frequency of oscillation is given as:

$$\omega = \omega_o \sqrt{1 - \zeta^2} \quad (4.57)$$

The current commutation time  $t_c$  is obtained by solving Eq. (4.56) with the condition that  $i(t_c) = 0$ , yielding:

$$t_c = \frac{\pi - \phi}{\omega} \quad (4.58)$$

where

$$\phi = \text{atan} \left[ \frac{i_o}{\left\{ \frac{V_{io} - V_{dco}}{\omega L} - i_o \zeta \frac{\omega_o}{\omega} \right\}} \right] \quad (4.59)$$

#### 4.3.5.3.2 Voltage Rise in the dc Source Capacitor

The rise in the dc link capacitor,  $C_d$ , is derived as follows from the current  $i(t)$ :

$$\delta V_{dc} = V_{dc}(t_c) - V_{dco} \quad (4.60)$$

where

$$V_{dc}(t_c) = \frac{C(V_{io} - V_{dco})}{C_d} \left[ 1 - e^{-\zeta\omega_o t_c} \left\{ \cos \omega t_c - \zeta \frac{\omega_o}{\omega} \sin \omega t_c \right\} \right] + \frac{i_o}{\omega C_d} \cdot e^{-\zeta\omega_o t_c} \sin \omega t_c \quad (4.61)$$

Similarly, derivation for damping factors greater than one are obtained.

#### 4.3.5.3.3 Results and Analysis

This analysis is illustrated by an SRM drive with a rating of 1/3 hp, 160 V, and 4 A. The base frequency is 60 Hz, maximum speed of the machine is 3600 rpm, and carrier frequency  $f_c = 20$  kHz in the converter. The base impedance is 40 ohms, and the base inductance and capacitance are 0.106 H and  $66.3 \mu F$ , respectively. The inductor  $L_c = 2$  mH and capacitor  $C_c = 10 \mu F$  are chosen.

Shown in Figure 4.23 for a machine inductance of 3 mH at the start of the commutation, which is the aligned inductance value, is a set of curves with commutation time vs. duty cycle of the chopper for various damping factors ranging from 0.01 to 3, covering all possible conditions in a practical SRM drive system. The commutation time is normalized by choosing the base time equal to the on time of a phase winding at maximum speed. As expected for higher duty cycles, and hence higher  $V_i$ , there is an increase in the commutation time. Note that the relationship between the commutation time and duty cycle is not linear and the preferred duty cycle is between zero (which is practically not possible) and up to 0.7 for commutation times lower than 0.2 p.u. Note that higher damping contributed by the induced emf term reduces the commutation time, indicating that initiation of commutation even before the machine reaches its aligned inductance value is beneficial to obtain a lower commutation time. The low damping factor of 0.01 gives the worst-case scenario in

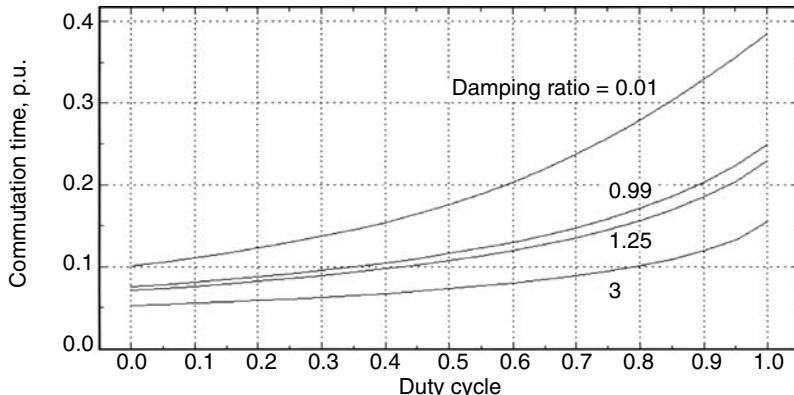


**FIGURE 4.23** Commutation time  $t_c$  (in p.u.) vs. duty cycle of the chopper for various damping ratios.

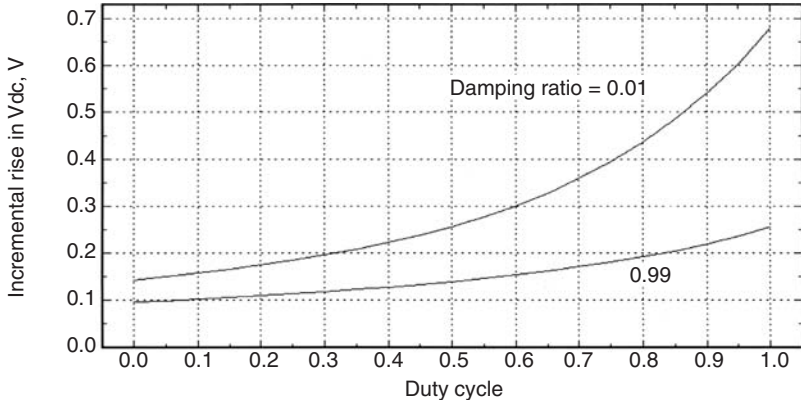


**FIGURE 4.24** Incremental rise in dc link voltage vs. duty cycle of the chopper for various damping ratios during current commutation.

that it corresponds to very low-speed operation such as around zero speed with practically no contribution from the induced emf term.

Figure 4.23 shows clearly that the commutation time can be limited to 0.2 p.u., provided that the duty cycle of the chopper is coordinated. It is done by turning off the chopper switch for a few PWM cycles before the commutation is initiated, which allows for the depletion of energy from  $C_c$ . Note that this is beneficial even for the rising current in an oncoming phase of the machine due to the fact that the unaligned inductance is much smaller than the aligned inductance for the outgoing phase, thus the smaller voltage  $V_i$  is sufficient to support a faster rise of current. Note that, with low  $V_i$ , the oncoming phase need not be switched on and off but may be allowed to be on continuously until the required current rises in the machine windings. That would save the switching losses in the phase switch and diode.

Shown in Figure 4.24 is the dc source capacitor voltage rise due to the commutation of current in machine windings and resulting transfer of energy from the machine windings to the capacitor  $C_d$  against the chopper duty cycle for damping factors of 0.01 and 0.99. The rise in the voltage across  $C_d$  is negligible, indicating that for practical motor drive systems this is a great advantage in that the ratings of all devices and capacitors have to be rated only for the dc source voltage of  $V_{dc}$ . This proves that this power converter topology will have the lowest voltage and lowest VA rating for a given SRM as compared to the C-dump converter-based drive system due to the fact the dump capacitor will have a greater voltage rating than the dc source.

#### 4.3.5.4 Merits and Demerits of the Converter

The merits of the topology are summarized as follows:

1. For an  $q$ -phase SRM, only  $(q + 1)$  switches and diodes are required for full four-quadrant operation.
2. Independent operation of the machine phases is guaranteed.

3. The commutation voltage is  $(v_i - V_{dc})$ , whereas the applied voltage is  $v_i$ , which is less than the source voltage, and a faster current turn-off in the machine phases is obtained by reducing  $v_i$  during the commutation phase only.
4. Single-pulse voltage operation of the machine phases is made possible by varying the input voltage  $v_i$  to provide the required current, thus minimizing the switching losses in the power devices and machine core losses, resulting in enhancement of the efficiency of the SRM drive system.
5. The advantages of the minimum logic power supplies requirement of the other  $(q + 1)$  switch topologies are preserved due to the fact that all the machine phase switch emitters are tied together.
6. Control and operation are very much similar to the C-dump topology without its disadvantages; for example, the link capacitor is rated for the same voltage as that of the dc source voltage with a margin unlike that of the capacitor ratings of the C-dump topology.
7. The topology is applicable to half-wave controlled PM brushless dc motor drives which makes the study of this topology very attractive for creating a set of universal converter drives for a line of variable speed motors.
8. The advantage of acoustic noise reduction is maintained due to the addition of the chopper in the front end, as described in the literature.<sup>29,31,33</sup>
9. The peak voltage rating of the power devices is equal to the dc link voltage,  $V_{dc}$ , unlike that of the C-dump converter.
10. A very small capacitor and inductor are required in the chopper power stage as compared to that of the C-dump converter passive components.
11. This configuration uniquely lends itself to freewheeling for current control in the machine phases by coordinating the chopper switching—not possible with the C-dump, which requires an additional power device.
12. Due to the common source or emitter connection of the phase switches, a truly sensorless drive could be realized as follows. The current could be sensed by monitoring the drain source voltage with no need for isolation and so could be used for current control. For position sensing, the inductance needs to be measured and is found by switching on any inactive phase and measuring the current and voltage, neither of which requires isolation for processing due to the common source or emitter connection of the phase switches. From the inductance, the rotor position is estimated. With current control and estimation of rotor position in this manner, a truly sensorless four-quadrant drive could be realized. Because of the above stated facts, the converter topology lends itself very well to such a low-cost sensorless implementation. Note that the sensorless implementation is crucial to the market introduction of the SRM in low-cost but high-volume applications.

The disadvantages of the proposed topology are

1. The commutation voltage is lower compared to the two-switch-per-phase configuration.

2. The step-down chopper circuit has to be rated for the SRM power rating which may preclude its use in integral horsepower drives, thus making it suitable only for fractional horsepower drive systems.
3. Coordinated control of the input voltage to the converter,  $v_i$ , during commutation to provide faster turn-off of the current in the machine phases and to minimize machine and switch losses is quite new and has not been attempted with other topologies, thus it must yet be developed for this drive.
4. Due to the additional stage of power processing in the chopper, the overall system efficiency of the SRM drive system is lower than that of the other schemes without the chopper stage. The reduction in system efficiency could be offset by resorting to single-pulse switching of the machine phases, thus boosting the efficiency of the machine converter stage and the machine.
5. This topology is unsuitable for continuous operation as a generator, as the oncoming phase has maximum (aligned) inductance and the outgoing phase has minimum (unaligned) inductance, which is contrary to the motoring operational mode. This phenomenon requires maximum voltage during commutation at the machine input, which will increase the commutation time and reduce the duration possible for generation, thus affecting the effectiveness of this operation.

#### 4.3.5.5 Variable dc Link Voltage with Buck-Boost Converter Topology

An alternate variable dc link voltage converter circuit with four switches and diodes<sup>15</sup> is shown in [Figure 4.25](#). There is only one switch per machine phase, and it is

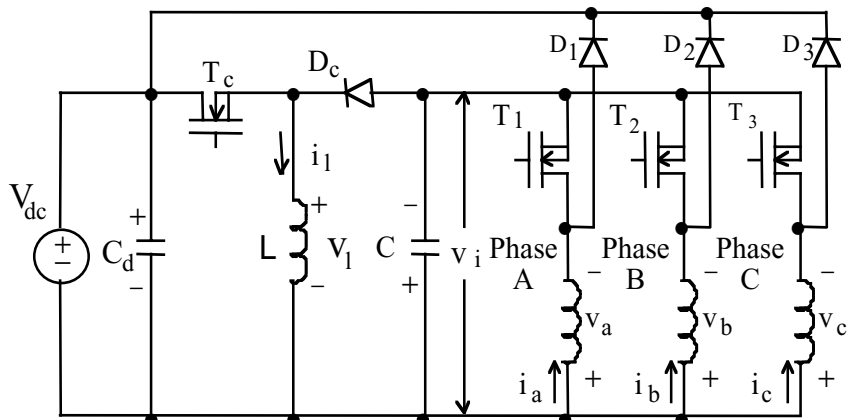


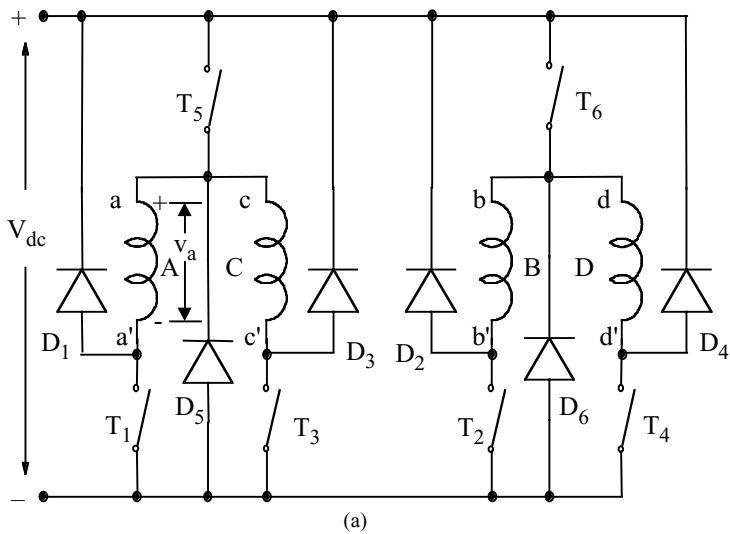
**FIGURE 4.25** Variable dc link with buck-boost converter topology for SRMs.

connected in series with the phase winding which prevents a shoot-through fault. The switch  $T_c$ , diode  $D_c$ , inductor  $L$ , and output capacitor  $C$  form the buck-boost, front-end power stage. The machine dc link voltage  $V_i$  can be varied from zero to greater than (say, two times) the dc source voltage  $V_{dc}$  to obtain the desirable input voltage to the machine windings. Further, this stage provides the isolation required for faster commutation of the current with the constant source voltage  $V_{dc}$ . The energization mode is initiated by turning on the phase switch (say,  $T_1$ ) and thereby applying the voltage  $V_i$  to machine phase A. To regulate the winding, switch  $T_1$  is turned off which initiates the routing of the current through the freewheeling diode  $D_1$ , the dc source voltage  $V_{dc}$ , and phase A winding, regardless of the on or off condition of the chopper switch  $T_c$ . That would apply a fixed negative dc source voltage  $V_{dc}$  across the machine phase winding. The energy in the output capacitor  $C$  will be able to cater to the oncoming phase (say,  $B$ ) during the time that the switch  $T_c$  is turned off. In this manner, the independence between various machine phases is maintained in this converter topology.

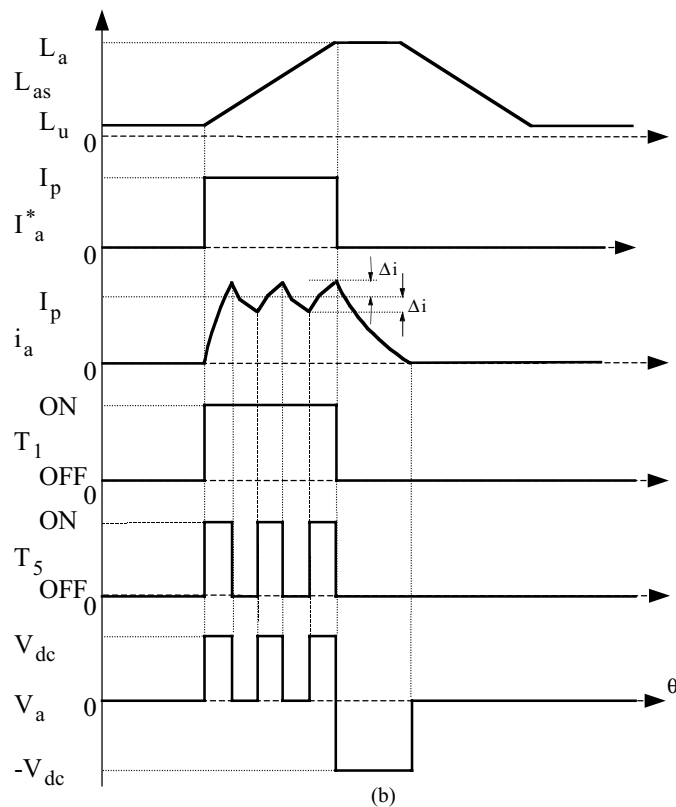
The distinct advantage of this power converter compared to the converter with a buck converter front end is that the input voltage to the machine phases could be increased over and above the dc source voltage to accelerate the buildup of the current in the machine phases. But a much greater advantage is found in the generation mode of the machine because the phase energization instance coincides near the rotor and stator pole alignment where the inductance is many times greater than the unaligned inductance encountered initially in the motoring mode of operation. These advantages come with a penalty in the voltage rating of the switches. All the machine phase switches have to be rated at least to the maximum output voltage of the chopper. The chopper switch voltage rating is equal to the sum of the dc source and machine input voltages. For example, assuming that the machine input voltage (i.e., the output voltage of the chopper circuit) is equal to, say, twice the source voltage, then the voltage rating of the chopper rises to three times that of the source voltage. In the buck mode of operation, when the machine input voltage is less than that of the source voltage, the switch ratings are still higher than that of the buck front-end converter while retaining the advantages of the buck front-end converter topology.

#### 4.3.6 (1.5q) SWITCHES AND DIODES CONFIGURATION

[Figure 4.26a](#) shows another variant of a converter<sup>17</sup> with less than two switches per phase but capable of independent phase current control. Note that this requires three switches and three freewheeling diodes for two phases. This converter configuration is limited to an even number of phases of switched reluctance motor designs. The switches  $T_5$  and  $T_6$  carry two-phase currents in one cycle of operation and accordingly their ratings are greater than the phase switches  $T_1$ ,  $T_2$ ,  $T_3$ , and  $T_4$ . Note also that the grouping of the windings is different from that of the previous converter configuration. This different grouping of two nonsucceeding phases guarantees the independent control of their currents. The performance waveforms of this converter are shown in [Figure 4.26b](#).



(a)



(b)

**FIGURE 4.26** (a) Converter with independent current control; (b) its operational waveforms.

## 4.4 COMPARISON OF SOME POWER CONVERTERS

A brief comparison of power converters is deduced from their descriptions. The comparison is based on the assumptions of an 8/6 pole SRM with a dc link voltage of  $V_{dc}$  and a peak current of  $I_p$  and the same machine is connected to the converters. Some approximations are made on the duty cycle of the shared switches. The voltage excursions in the machine windings are compared to obtain their rates of change of voltage and hence to determine the insulation strength of the windings. The comparison is summarized in [Table 4.2](#). The comparison examines only a few factors for the choice of power converters and ignores the control flexibility offered by them. This is an important consideration influencing the steady-state and dynamic operation of the SRM drive system. The cost optimization of the power converter for an SRM is an important step in the optimization of the SRM drives system and this is the most expensive subsystem in the SRM drive system. This comparison table gives an approximate total VA rating of the power switches and hence indirectly their cost. Note that switch voltage ratings have to be greater than  $V_{dc}$  to account for switching transient overvoltages, hence the VA rating will increase in actual design. Further, the availability of switch voltage ratings is not gradual but has large increments such as 60, 100, 150, 200, 250, 350, 400, 450, 600, 900, 1200 V, etc., leading to a further increase in the VA rating over the desired rating.

## 4.5 TWO-STAGE POWER CONVERTER

A scheme capable of transferring electrical power from the machine directly to the ac supply mains is shown in [Figure 4.27](#) with two-stage power conversion.<sup>37</sup> The first stage consists of a controllable converter with six switches and six diodes, and it interfaces input of a three-phase, 60-Hz ac supply to a single-phase, variable-frequency ac output. This stage is a controlled rectifier/inverter but without the drawbacks of a low power factor and high input line harmonics. The other power stage is the commutating stage through which each phase winding is energized.

Most of the SRM drives (the rectifier–capacitor source), except battery-source cases, cannot directly return the energy from the machine to the source due to the diode bridge and the current limitation of the electrolytic power capacitor, thus only a limited amount of returned energy is stored in the capacitors and reused. As a result, an extra circuit, such as a dump resistor across the capacitor, may be required to limit the voltage rise in the dc link, resulting in a low efficiency. In such cases, the current reversal affects the lifetime of the capacitor due to the frequent charging and discharging actions. However, this converter can return the power from the machine to the source directly without any limitations and eliminates the dc link capacitor. The elimination of dc link capacitor results in cost savings and in the enhancement of the reliability of the scheme and an increase in the power density of the scheme.

A disadvantage of this two-stage converter is its requirement for a higher number of power devices which results in higher costs. It is not economical if the regenerative power is not substantial. An application that may be suitable for this converter topology is in variable-speed, constant-frequency generation using wind energy.

**TABLE 4.2**  
**Comparison of Power Converters**

Items	Figure	4.2(a)	4.9(a)	4.7(a)	4.8(a)	4.10(a)	4.14(a)	4.20(a)	4.26(a)
Number of switches									
Phases	8	4	4	4	4	4	4	4	4
Common	—	—	—	—	—	1	1	2	
Number of diodes	8	4	4	4	8	5	5	6	
RMS phase currents ( $I$ )	$\frac{I_p}{2}$	$\frac{I_p}{2}$	$<\frac{I_p}{2}$	$<\frac{I_p}{2}$	$\frac{I_p}{\sqrt{2}}$	$\frac{I_p}{2}$	$\frac{I_p}{2}$	$\frac{I_p}{2}$	
Max. phase voltage ( $V_{ph}$ )	$\pm V_{dc}$	$\pm \frac{V_{dc}}{2}$	$\{V_{dc} - (I_p + \Delta I)R\}$	$> V_{dc}$	$\pm V_{dc}$	$-(V_o - V_{dc});$ $V_{dc}$	$\pm V_{dc}$	$\pm V_{dc}$	
Max. speed ( $\omega_m$ )	$\omega_m$	$\cong 0.5 \omega_m$	$\omega_m$	$\omega_m$	$\omega_m$	$\omega_m$	$\omega_m$	$\omega_m$	$\omega_m$
Torque ( $T_e$ )	$T_e$	$T_e$	$T_e$	$T_e$	$T_e$	$T_e$	$T_e$	$T_e$	$T_e$
Output power ( $P_o$ )	$P_o$	$0.5P_o$	$P_o$	$P_o$	$P_o$	$P_o$	$P_o$	$P_o$	$P_o$
Device voltage ( $V_T$ )	$V_{dc}$	$V_{dc}$	$V_{dc} + (I_p + \Delta i)R$	$1.5V_{dc}^a$	$V_{dc}$	$V_o$	$V_o$	$V_{dc}$	$V_{dc}$
Total switch VA ( $V_T I$ ) (rms)	$4V_{dc}I_p$	$2V_{dc}I_p$	$2V_{dc}I_p + 2I_p^2R$	$3V_{dc}I_p$	$2\sqrt{2}V_{dc}I_p$	$2.5EI_p$	$\equiv 2.7V_{dc}I_p^b$	$3.414V_{dc}I_p^b$	

<sup>a</sup> An assumption.

<sup>b</sup> A duty cycle of 0.5 is assumed for the common switch (es).

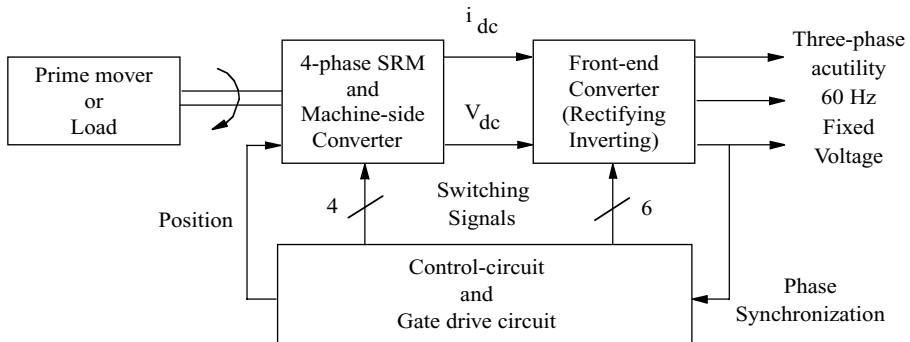


**FIGURE 4.27** Overall power conversion scheme using an SRM.

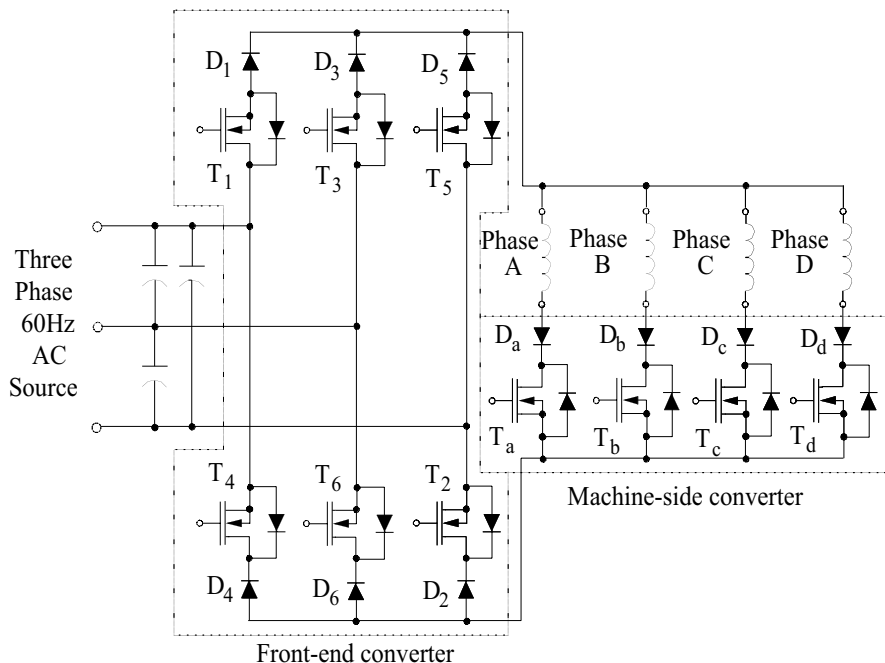


**FIGURE 4.28** The two-stage power converter.

#### 4.5.1 FRONT-END CONVERTER

The converter configuration is shown in Figure 4.28. It is realized by cascading one switch with a diode for a switching block. It is composed of six MOSFET switches ( $T_1$  to  $T_6$ ) and six diodes ( $D_1$  to  $D_6$ ). The three-phase ac is connected to the midpoint of each leg and the output is applied across the phase winding. The MOSFETs withstand the positive voltage, and the diodes block the negative voltage excursion. Each MOSFET is provided with a turn-off snubber circuitry (not shown in the figure) to

reduce the turn-off switching stress. The capacitors on the ac side provide current path when both a top and bottom switch are turned off. It is a two-quadrant converter. Note that the switching block eliminates shoot-through faults; that is, any number of switches can be activated simultaneously without a detrimental outcome. This feature is greatly advantageous in controlling the converter and will be discussed in detail in the section on converter control. The output voltage and switching signal in the PWM mode are very similar to a conventional three-phase diode bridge output with chopping. Peak currents through devices are determined primarily by the machine phase current. The voltage ratings are dependent on the peak voltage of the three-phase ac source.

#### 4.5.2 MACHINE-SIDE CONVERTER

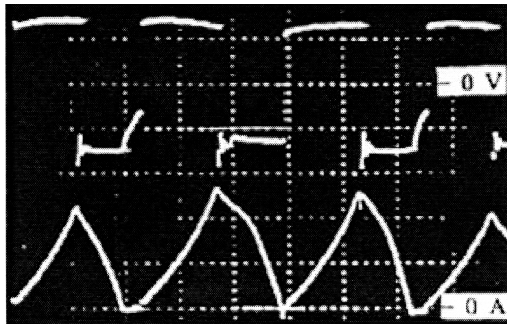
Each phase winding of the SRM is connected in series with a self-commutating device and a diode. The diodes prevent the phase current reversal, which may happen through the antiparallel diodes of the MOSFETs when the polarity of the applied voltage is changed by the front-end converter for generation. Compared to the front-end converter, the switching frequency of this converter is very low, because it is used only for phase commutation. At the point of commutation, there is no current flowing in the phase winding, which greatly reduces turn-off stresses of the MOSFET switches. Peak currents through the devices are determined primarily by the machine. The peak current and voltage ratings of the devices are the same as those of the front-end converter.

#### 4.5.3 OPERATION OF THE SCHEME

Basic operational waveforms are considered to look at the operation of the two-stage converter with an SRM. The front-end converter is basically phase controllable; therefore, the current can flow at any phase of the source voltage. The phase relationship between the phase voltage and current is set at  $\alpha = 0^\circ$ , similar to a thyristor-based, phase-controlled rectifier. Dc link voltage is maximized at the activation angle. The oscillograms of the dc link voltage and current are shown in [Figure 4.29a](#). With the same time scale at the machine speed of 1800 rpm (1 p.u.), the instantaneous power waveform shown in [Figure 4.29b](#) also contains the dc link current. [Figure 4.29c](#) shows the waveforms of the phase voltage and current of the ac mains. The humps in the voltage can be removed by using a low-pass filter on the supply side. The bipolarity current indicates that only one current path is provided for the winding energization and regeneration. In other words, only two phases out of the three phases of the supply are used as the current path at a given time.

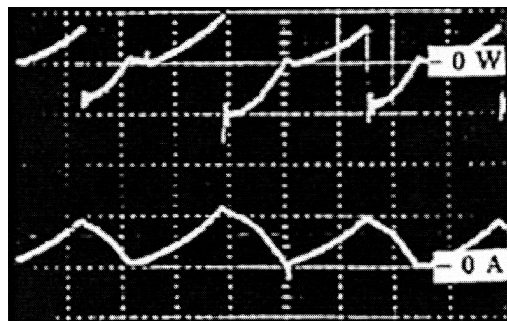
### 4.6 RESONANT CONVERTER CIRCUITS

The power converter topologies hitherto discussed are known as hard-switched topologies because during turn-on and turn-off the power switch and diode voltages and/or currents are nonzero, thus causing significant power loss in these devices. During the switching instant, if the current or voltage is zero, then the device loss is zero



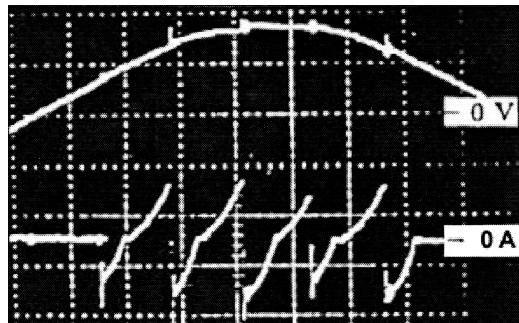
10 V/div  
0.2 A/div  
0.5 ms/div

(a)



11 W/div  
0.5 A/div  
0.5 ms/div

(b)



10 V/div  
0.5 A/div  
1 ms/div

(c)

**FIGURE 4.29** Experimental results of the scheme; (a) dc link voltage and current; (b) dc link power and current; (c) ac phase voltage and line current.

and topologies enabling such a condition are known as resonant circuits. Many variations of these topologies are available. Because the switching losses are theoretically zero in the resonant circuits, the circuit efficiency and hence the overall system efficiency is increased in the motor drive. Such a claim may seem correct *prima facie*, but it is difficult to sustain such a claim in the face of losses in the passive elements of the resonant circuit such as the inductor and capacitor, and experimental studies have not been encouraging. Further claims are being made as to the electromagnetic interference (EMI) reduction in these circuits compared to the hard-switched topologies that must be taken cautiously in the absence of good experimental correlation. Their main disadvantage is that the device voltage ratings have to be multiple times that of the source voltage due to the action of the resonant circuit. This increases the volt–ampere rating of the converter to multiple times that of the conventional hard-switched topologies, restricting its industrial use in switched reluctance motor drive systems. Its advantage is that the quality of the current waveform can be made very superior as the circuit can be operated at a higher frequency as the device switching losses are very small. Note that the switching losses can become a significant fraction of the conduction losses in the devices at very high frequencies, but at nominal frequencies of 20 kHz and lower that may not be true, hence the need for resonant circuits decreases and it has minimal impact on the motor drive.

For the sake of completeness, only one resonant topology is considered in this section and shown in [Figure 4.30](#). It is realized that this is nothing but a variant of the C-dump circuit topology with resonant commutation of the phase current. Its working is described below.

The resonant circuit consists of the inductor  $L_r$ , capacitor  $C_r$ , power switch  $T_r$ , and diode  $D_r$ . The machine windings are connected in series with power devices  $T_1$ ,  $T_2$ , and  $T_3$ , and diodes  $D_1$ ,  $D_2$ , and  $D_3$  steer the current of the machine phases during commutation and the excess current from the resonant circuit to the dc source,  $V_{dc}$ .

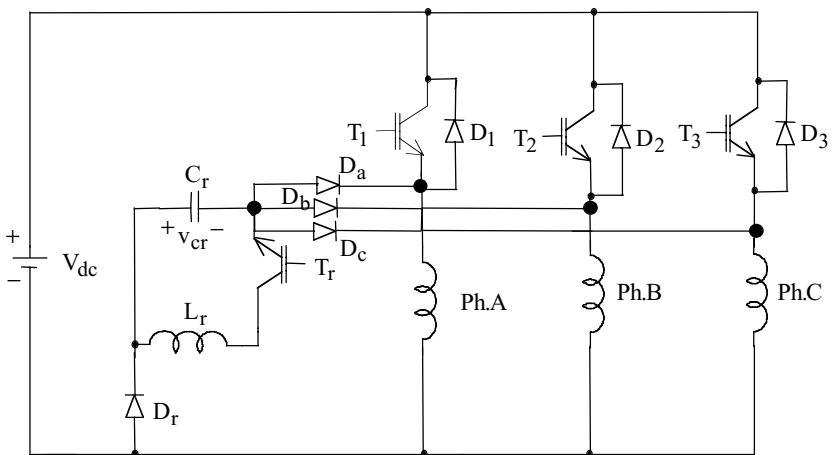


**FIGURE 4.30** Resonant topology of a C-dump converter variant for SRM drives.

Assume that the voltage across the resonant capacitor  $V_r$ , is positive and as indicated for positive polarity. The distinct modes of operation are outlined separately.

In mode 1, energization of the phase winding is achieved by switching the phase switch (say,  $T_1$ ). When the machine current exceeds the desired level, we wish to turn off the phase switch and reduce the energy transfer from the source to the machine.

In mode 2, turn-off of the phase switch results in the machine current being diverted via  $D_r$ ,  $C_r$ ,  $D_a$ , and the phase-A winding. This charges the resonant capacitor  $C_r$ , thus reducing the current in the machine winding. When the current nears the acceptable lower limit, the phase switch  $T_1$  is turned on to keep the winding current fairly a constant.

Mode 3 is the resonant mode. With turn-on of the resonant switch, the resonant capacitor and inductor are connected in series, resulting in resonant oscillation. The energy in the capacitor is transferred to the inductor, resulting in the forward biasing of diodes  $D_a$  and  $D_r$  and the current flows from the inductor to the load as well as to the dc source via the diode  $D_1$ , inductor, device  $T_r$ , and  $D_a$ . The current fed to the source current is the excess current that is over and above that of the load current. During the resonant oscillation, the voltage across the capacitor has reversed and is negative which is conducive for the takeover of current from the phase switch when it is being turned off. Note that turn-off of the main switches is achieved with zero voltage because its antiparallel diode  $D_1$  is conducting during the energy recovery period, thus eliminating the turn-off switching loss in the phase switch.

Because the voltage across the capacitor  $C_r$  is two to three times that of the source voltage, its application across the machine winding rapidly commutes the current. This in turn gives a much higher conduction angle for the SRM drive without any concern for regeneration when the desired operation is in the motoring region. Note that this is one of the circuit topologies where the antiparallel diode of the switching device is utilized, whereas in conventional hard-switched topologies they are seldom used.

## REFERENCES

1. Bedord, B.D., Compatible Brushless Reluctance Motors and Controlled Switch Circuits, U.S. Patent No. 3,679,953, July 25, 1972.
2. Davis, R.M. and R.J. Blake, Inverter drive for switched reluctance motor circuits and component ratings, *IEE Proc.*, 126–136, 1981.
3. Miller, T.J.E., Converter volt–ampere requirements of the switched reluctance motor drive, *IEEE Trans. Ind. Appl.*, Vol. 21, No. 5, 1136–1144, 1985.
4. Farzanehfard, H. and R. Krishnan, A fully controlled converter for switched reluctance motor, in *Proc. VPEC Ann. Sem.*, Nov. 4, 1986, Virginia Tech., Blacksburg, VA.
5. Davis, R.M. et al., Electric Power Converter Circuit, U.S. Patent No. 4,563,619, Jan. 7, 1986.
6. Ehsani, M., J.T. Bass, T.J.E. Miller, and R.L. Steigerwald, Development of a unipolar converter for variable reluctance motor drives, *IEEE Trans. Ind. Appl.*, Vol. 23, No. 3, 545–553, 1987.
7. Miller, T.J.E. et al., Regenerative Unipolar Converter for Switched Reluctance Motors Using One Switching Device per Phase, U.S. Patent No. 4,684,867, Aug. 4, 1987.
8. Pollock, C. and B.W. Williams, A unipolar converter for a switched reluctance motor, *IEEE IAS*, 44–49, 1988.

9. Dunlop, G.R., Power device reduction using negative torque sequences in switched reluctance motors, *ICEM*, 595–598, 1988.
10. Krishnan, R. and P. Materu, Design of a single-switch-per-phase converter for switched reluctance motor drives, *IEEE Trans. on Industrial Electronics*, 37(6), 469–476, 1990.
11. Krishnan, R. and P. Materu, Analysis and design of a new converter topology for switched reluctance motor drives, *IEEE IAS*, 1181–1185, 1989.
12. Huy, H.L., P. Viarouge, and B. Franouer, A novel unipolar converter for switched reluctance motor, *IEEE PESC*, 3–10, 1989.
13. Krishnan, R. and P. Materu, Analysis and design of a low cost converter for switched reluctance motor drives, *IEEE Trans. on Industry Appl.*, 29(2), 320–327, 1993.
14. Huy, H.L., P. Viarouge, and B. Franouer, Unipolar converter for switched reluctance motor, *IEEE IAS*, 551–560, 1989.
15. Vukosavic, S. and V.R. Stefanovic, SRM inverter topologies: a comparative evaluation, *IEEE IAS*, 946–958, 1990.
16. Pollock, C. and B.W. Williams, Power converter circuits for switched reluctance with the minimum number of switches, *IEE Proc.*, Vol. 137, Pt. B, No. 6, 373–384, 1990.
17. Pollock, C. and B.W. Williams, A unipolar converter for a switched reluctance motor, *IEEE Trans. Ind. Appl.*, Vol. 26, No. 2, 222–228, 1990.
18. Huy, H.L., P. Viarouge, and K. Slimani, A current controlled quasi-resonant converter for switched reluctance motor, *IEEE*, 1022–1028, 1990.
19. Harris, W.A., Switched reluctance motor control circuit with energy recovery capability, U.S. Patent No. 5,075,610, Dec. 24, 1991.
20. Ehsani, M., I. Husain, K.R. Ramani, and J.H. Galloway, Dual decay converter for switched reluctance motor drives in low voltage application, *IEEE PESC*, 620–624, 1991.
21. Hava, A., V. Blasko, and T.A. Lip, A Modified C-dump converter for variable reluctance machines, *IEEE IAS*, 886–891, 1991.
22. Doncker, R.W.D. and J.P. Lyons, An auxiliary quasi-resonant dc link inverter for switched reluctance machines, *EPE*, 18–23, 1991.
23. Vukosavic, S. and V.R. Stefanovic, SRM inverter topologies: a comparative evaluation, *IEEE*, 1034–1047, 1991.
24. Schramm, D.S., B.W. Williams, and T.C. Green, A new reluctance motor drive configuration, *EPE Proc.*, 394–397, 1991.
25. Sood, P.K., Power Converter for a Switched Reluctance Motor, U.S. Patent No. 5,115,181, May 9, 1992.
26. Park, S.S. and T.A. Lipo, New series resonant converter for variable reluctance motor drive, *IEEE PESC*, 833–838, 1992.
27. Hava, A., J.B. Wacknov, and T.A. Lipo, New ZCS resonant power converter topologies for variable reluctance machine drives, *IEEE PESC*, 432–439, 1993.
28. Chan, S. and H.R. Bolton, Performance enhanced of single phase switched reluctance motor by dc link voltage boosting, *IEE Proc.*, 316–322, 1993.
29. Pillay, P., R. Samudio, M. Ahmed, and R. Patel, A chopper controlled SRM drive for reduced acoustic noise and improved ride through capability using super capacitors, *IEEE IAS*, 313–321, 1994.
30. Rim, G.H. and W.H. Kim, A novel converter topology for switched reluctance motor drives improving efficiency and simplifying control strategy, *IEEE PESC*, 937–942, 1994.

31. Kim, E.S., K.C. Lee, G.H. Rim, and W.H. Kim, A choppingless converter for switched reluctance motor with unity power factor and sinusoidal input current, *IEEE PESC*, 500–507, 1994.
32. Jang, D.H., I. Husain, and M. Ehsani, Efficiency and performance analysis of the dual decay converter for switched reluctance motor drives, *IEEE IAS*, 658–664, 1994.
33. Pillay, P., R. Samudio, M. Ahmed, and R. Patel, A chopper controlled SRM drive for reduced acoustic noise and improved ride through capability using super capacitors, *IEEE Trans. on Industry Appl.* 31(5), 1029–1037, 1995.
34. Mir, S., I. Husain, and M. Elbuluk, Energy efficient C-dump converters for switched reluctance motors, *IEEE APEC*, 968–973, 1996.
35. Gharpure, V.S., R. Krishnan, and S. Lee, Analysis and design of energy recovery snubbers for switched reluctance motor drives, *IEEE IAS*, 1055–1062, 1994.
36. Krishnan, R. and S. Lee, Analysis and design of a single switch per phase converter for switched reluctance motor drives, *IEEE PESC*, 485–492, 1994.
37. Rim, G. and R. Krishnan, Variable speed constant frequency power conversion with a switched reluctance machine, *IEEE APEC*, 63–71, 1994.
38. Bolognani, S., E. Ognibeni, and M. Zigliotto, Sliding mode control of the energy recovery chopper in a C-dump switched reluctance motor drive, *IEEE APEC*, 188–194, March 1991.
39. Krishnan, R. and P.N. Materu, Design of a single-switch-per-phase converter for switched reluctance motor drives, *IEEE Trans. Ind. Electr.*, Vol. 37, No. 6, 469–476, Dec. 1990.
40. Materu, P., R. Krishnan, and H. Farzanehfard, steady-state analysis of the variable speed switched reluctance motor drive, *IEEE Ind. Electr. Conf.*, Conf. Record, Boston, 294–302, Nov. 1987.
41. Krishnan, R., A novel converter topology for switched reluctance motor drives, Conf. Rec., *IEEE PESC*, Baveno, Italy, 1811–1816, June 23–27, 1996.

---

# 5 Control of SRM Drive

## 5.1 INTRODUCTION

The switched reluctance machine has strong similarity to series-excited dc and synchronous reluctance machines, but in control it is very remotely connected to these machines and therefore analogous control development is not possible. The fact that the machine inductance is not only a function of the rotor but also the excitation current even for a fraction of the rated current complicates the development of control strategies for SRM drive systems. In contrast, for all other electrical machines, it is known that control strategies are derived based on the machine parameters being constant for most of the excitation range.<sup>1</sup> This may confound design of the drive system control for SRM initially, but by classifying the control requirement as low or high performance based on torque ripple and speed of response specification, it may be found that a majority of the applications fall into the low-performance category. Only a small fraction of the applications or a small fraction of the motor drives required demand high performance.

The concept of control from the machine characteristics of inductance vs. rotor position for a fixed excitation is introduced here. The variables of control such as advance rise and commutation angles are recognized and their dependence on machine inductance, speed, and the requirement to maximize torque are discussed. A low-performance, closed-loop, speed-controlled SRM is considered and a complete step-by-step design and implementation of the control system is given.

The heart of any motor drive's control system is current control. Two types of current controllers are developed, one based on the linearized model of an SRM delivering a reasonable performance and the other based on decoupling and linearization to give a high performance. For the high-performance current controller design, factors such as mutual coupling of the phases and nonlinearity of the system are included one at a time. Systematic design derivation, implementation, and verification of the current controller are developed. In most of the dc drives, torque control is synonymous with current control. Because of its nonlinearity, the SRM is significantly different in this regard. Multiphase switching is mandatory for minimization of torque ripple and to deliver high and quickly responsive torque performance. Also presented is torque control based on torque distribution functions to guarantee a linear torque amplifier out of the SRM drive throughout its excitation range.

With control of torque, speed control becomes a simple task. Analogous to other motor drives, the speed controller chosen for illustration is proportional plus integral. The derivation of the speed controller is achieved using a symmetric optimum technique.

All of the current, torque, and speed controller performances are illustrated amply with dynamic simulation results, and, wherever possible, linear control system techniques are used to bring the vast knowledge base of linear control systems to bear on the design.

## 5.2 CONTROL PRINCIPLE

Given the inductance profile shown in Figure 5.1 for motoring operation, the phase windings are excited at the onset of increasing inductance. The torque production for motoring and regeneration is also shown in Figure 5.1. The torques shown are for only one phase. An average torque will result due to the combined instantaneous values of electromagnetic torque pulses of all machine phases. The machine produces discrete pulses of torque and, by proper design of overlapping inductance profile, it is possible to produce a continuous torque. In actual practice, it will result in reduced power density of the machine and increased complexity of control of the SRM drive.

From Figure 5.1, it can be seen that the average torque is controlled by adjusting the magnitude of winding current,  $I_p$ , or by varying the dwell angle,  $\theta_d$ . To reduce the torque ripples, it is advisable to keep the dwell angle constant and vary the magnitude of the winding current. The latter approach requires a current controller in the motor drive which incidentally also ensures a safe operation.

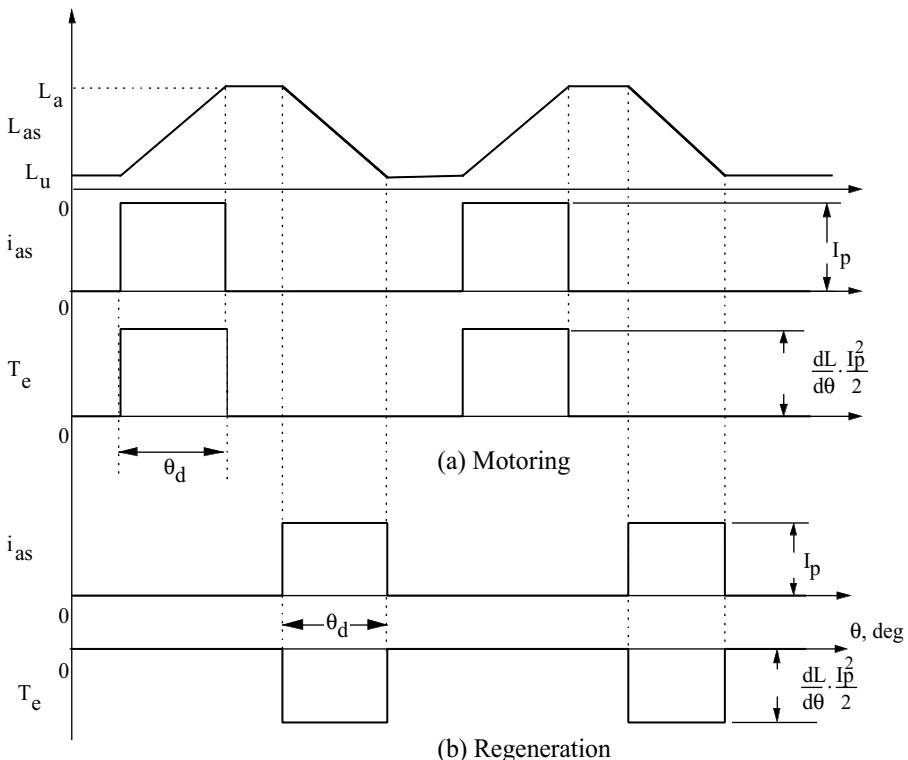
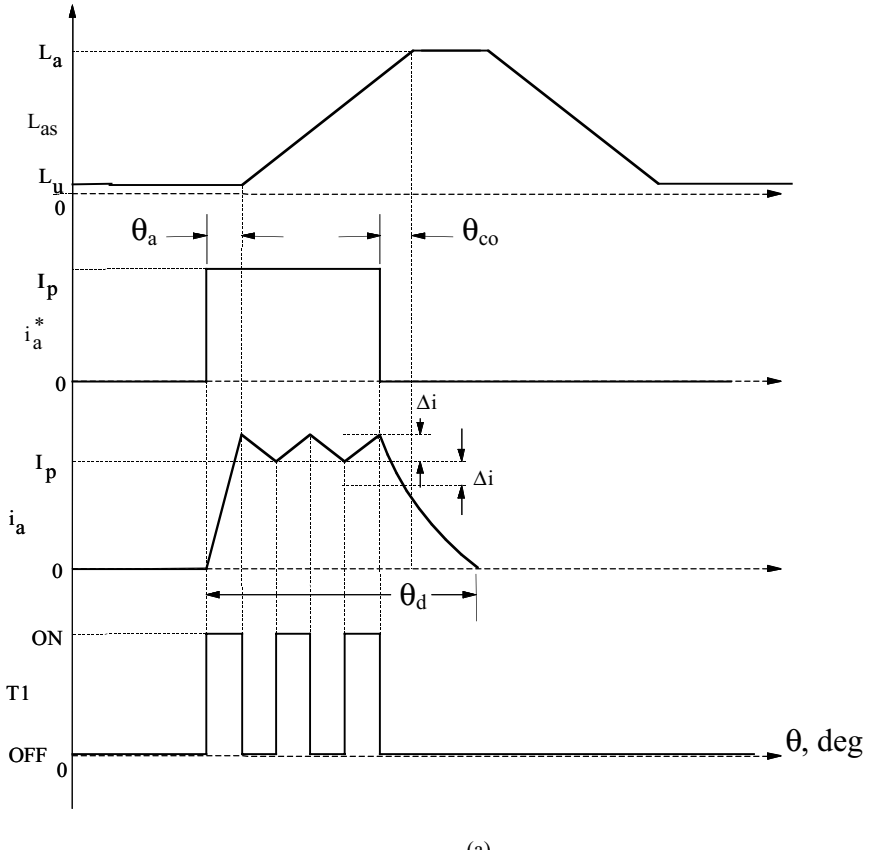


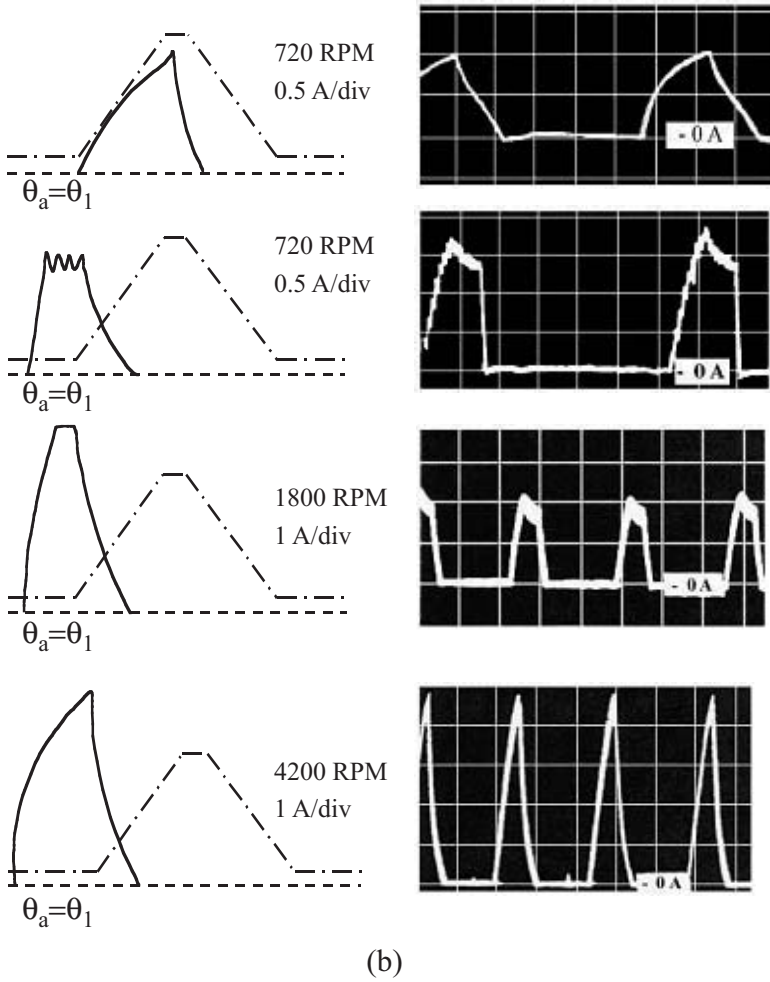
**FIGURE 5.1** Motoring and regenerative actions of the SRM.



(a)

**FIGURE 5.2** (a) Current control of the SRM drive; (b) typical current waveforms at different speeds and advance angles for an 8/6 SRM.

To ensure instantaneous torque production it is essential that the desired current comes on at the instant of increasing inductance. From a practical point of view, the current cannot instantaneously rise or fall in a resistor, inductor (RL) circuit. This necessitates advanced application of voltage for starting the current and advanced commutation to bring the current to zero before a negative sloping inductance profile is encountered. Hence, the actual current waveforms are likely to be as shown in Figure 5.2a. The voltage to the phase winding is applied in advance by  $\theta_a$  degrees and the current turn-off is initiated in advance by  $\theta_{co}$ . Note that  $\theta_a$  and  $\theta_{co}$  are dependent on the magnitude of the peak winding current  $i_p$  and the rotor speed. The current is maintained at  $i_p$  by switching on or off the transistors. The actual current is allowed to deviate by  $\pm \Delta i$ , and this window is adjusted to ensure minimum switching frequency and minimum turn-on and turn-off losses. Figure 5.2b shows the typical current waveforms for various advance angles and dwell angles and corresponding experimental waveforms for an 8/6 SRM.<sup>18</sup>



(b)

**FIGURE 5.2** (Continued)

### 5.3 CLOSED-LOOP, SPEED-CONTROLLED SRM DRIVE

A closed-loop, speed-controlled SRM drive is shown in Figure 5.3. The speed error is processed through a proportional plus integral (PI) controller and a limiter to yield the torque command,  $T_e^*$ . From the torque command, the current command  $i^*$  is obtained using the torque constant,  $K_t$ . This torque constant is for the linearized inductance vs. rotor position characteristics for a particular value of current. The current command is added and subtracted from the hysteresis window,  $\Delta i$ , to obtain the  $i_{\max}$  and  $i_{\min}$  that determine the switching of the phase and main switches of any converter. The currents are injected into respective windings based on their position information obtained from an encoder or a resolver or position estimator. The rise and fall angles are calculated from the magnitude of the stator current, rotor speed, and minimum and maximum

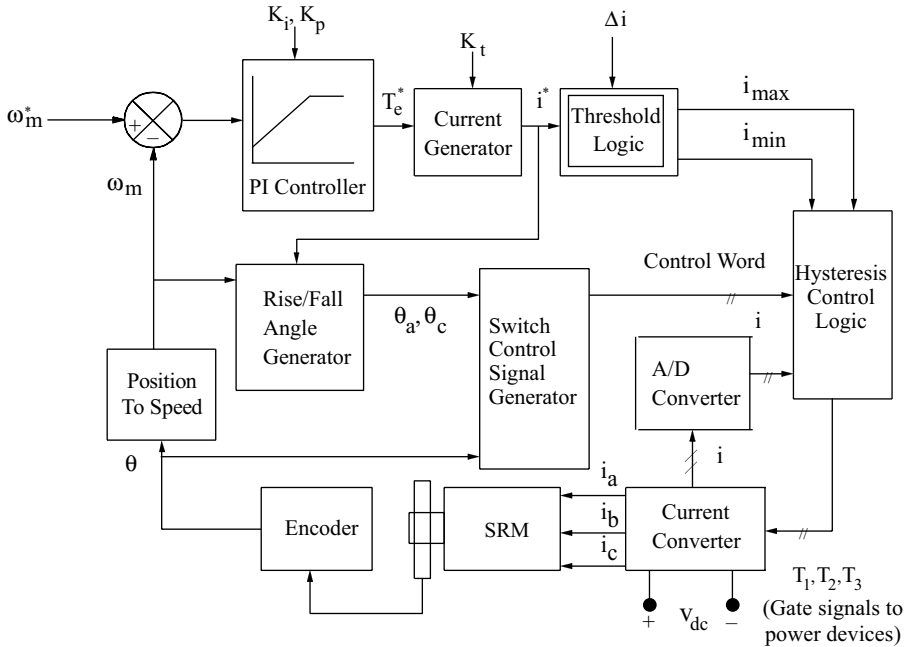


**FIGURE 5.3** Closed-loop SRM drive.

inductances. The rise and fall angles are incorporated with the rotor position information in the switch control signal generator block shown in the block diagram.

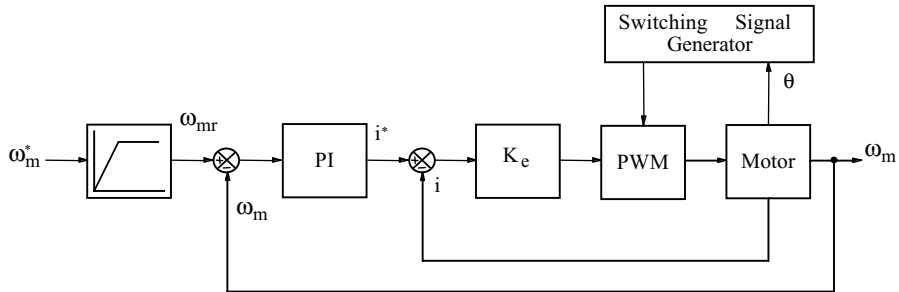
### 5.3.1 DESIGN EXAMPLE

Design a low-cost, one-quadrant SRM analog controller with a minimum number of parts and discuss the scheme and implementation details for a 6/4 SRM.<sup>2</sup>

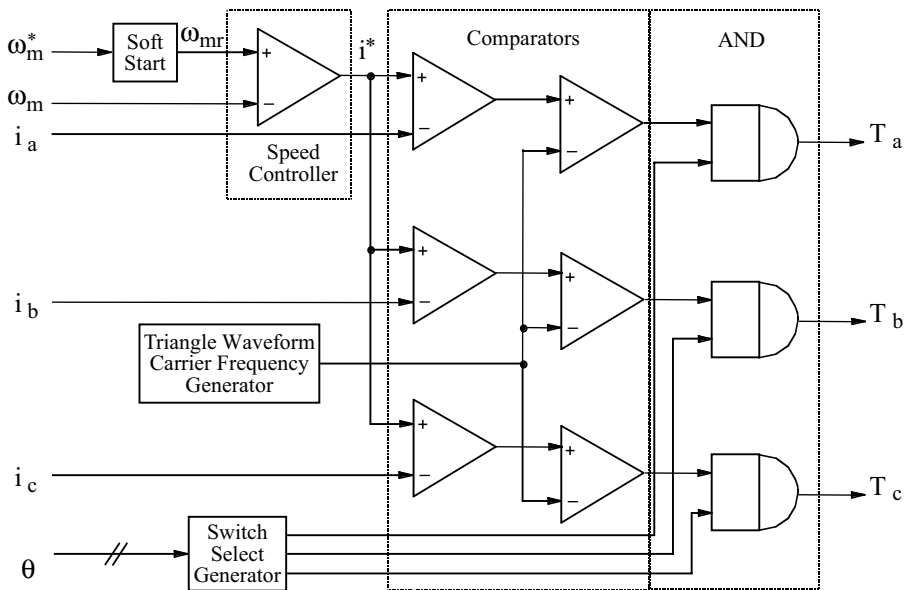
### 5.3.2 SOLUTION

Figure 5.4 shows the block diagram of such an SRM controller, and the detailed implementation schematic is given in Figure 5.5. The inputs to the controller are speed reference  $\omega_m^*$ ; motor winding currents  $i_a$ ,  $i_b$ , and  $i_c$ ; rotor position  $\theta$ ; and rotor speed  $\omega_m$ . The motor currents can be detected through the use of Hall sensors. The rotor position information can be obtained from transducers or by estimation.

The speed command,  $\omega_m^*$ , is processed through a soft-start circuit to provide a controlled acceleration/deceleration. The speed controller accepts the speed and its processed command value to find the current command with a proportional integral amplification of the speed error. The current command,  $i^*$ , is compared with the motor currents and their errors are merged with a triangular carrier frequency to generate the required pulse width modulation (PWM) control signals. These control signals are steered to the corresponding base/gate of the power switches by the



**FIGURE 5.4** Block diagram of the SRM control system.



**FIGURE 5.5** Implementation schematic of the SRM analog controller.

switch-select generator which has the actual rotor position information. The switch-select generator is implemented with a read-only memory.

### 5.3.3 CURRENT LOOP

Three identical current loops, one for each phase, are suggested for implementation. Each loop consists of the following

1. Current error signal generator
2. PWM circuit
3. Converter
4. Current feedback circuit

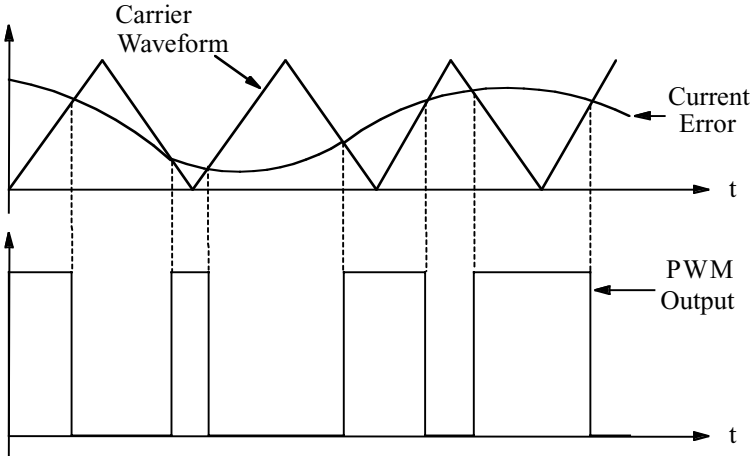


**FIGURE 5.6** Input–output waveform of the PWM circuit.

### 5.3.4 CURRENT COMPARATOR

The current error is obtained by using an operational amplifier as an inverting adder, the output of which is given as:

$$i_e = K_i(i^* - i) \quad (5.1)$$

where  $K_i$  is the gain of current loop. To obtain a high speed of response, the instrumented value is in the range of 30 to 70.  $i^*$  is the commanded current, and  $i$  is the actual winding current. Hall-effect current sensors with galvanic isolation are used for sensing the winding currents, and a circuit is built to process this feedback signal. In order to maintain a desired current in the phase windings, the PWM technique is used in the current loops. Each loop has a comparator to compare the amplitude of the current error with the carrier signal of the triangular waveform at 3 kHz. When the carrier amplitude is higher than the current error, the output is low and the switch is turned off. This is shown using the input and output waveforms of the comparator in [Figure 5.6](#).

### 5.3.5 CARRIER SIGNAL

The triangular waveform generator consists of three operational amplifiers and is shown in [Figure 5.7](#). A positive feedback amplifier is used as a square waveform oscillator which is then fed to an integrator to obtain a triangular waveform. The third amplifier works as an adder to add a dc offset to the waveform so that a positive triangular signal is generated. A zener diode is added in this circuit to reduce the trimming work during calibration.

The circuit has been designed such that the chopping occurs at all times. Even when high torque is required in cases such as acceleration and deceleration, the peak level of

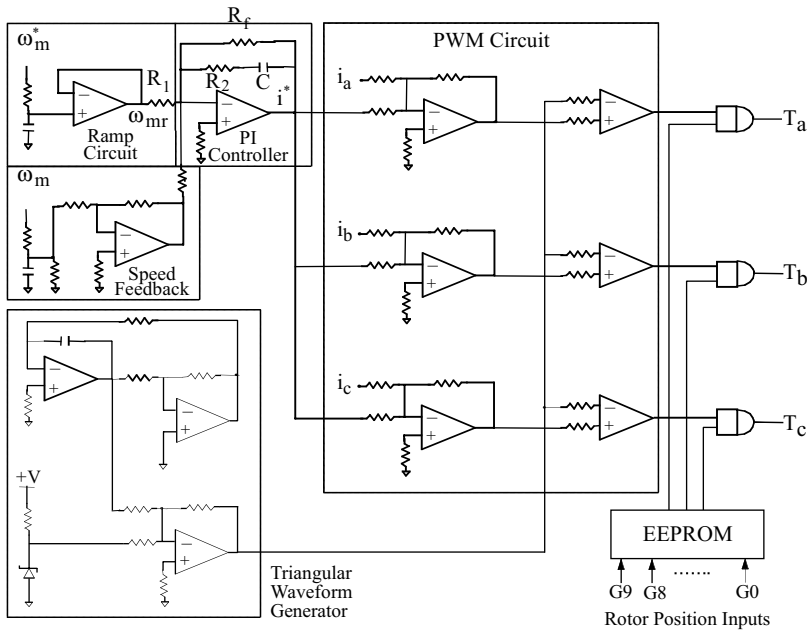


**FIGURE 5.7** Circuit diagram of the SRM analog controller.

the carrier can be adjusted such that it is always higher than the maximum value of the error signal,  $i_e$ . The difference between these two signals can be adjusted to a value such that chopping occurs only when the current error is greater than a set value.

### 5.3.6 INCORPORATION OF ROTOR POSITION INFORMATION

An encoder mounted on the shaft gives 10-bit absolute position information (in Gray code) to an erasable, programmable read only memory (EPROM), which then generates the phase switching signals. Several data tables stored in the EPROM are based on the direction of rotation and the advance and fall angles. At any instant, there is one input to the EPROM to output a three-bit phase switching signal. The zero reference point of the rotor position is the instant where the winding of phase A is in alignment with the rotor. With this reference, the computation of the entries in the tables is explained with the following example. Since the switching signal is periodic over every  $90^\circ$  for a 6/4-pole SRM, calculation for the first quadrant will satisfy all the cases. For an advance angle and fall angle value of zero, the switching signals should be changed at  $0^\circ$ ,  $30^\circ$ , and  $60^\circ$ . For the case where the fall angle and the advance angle are identical (say,  $12^\circ$ ), the conduction angle for each phase winding will still remain at  $30^\circ$ . The range of on time for switching the phase A winding will then be between  $48^\circ$  and  $78^\circ$  in the first quadrant in clockwise rotation. In hexadecimal code, this range equals 0090 to 00E0. Therefore, the contents of the

memories addressed from 0090 to 00E0 should be 100 in binary code. This code indicates that the winding of phase A will be excited when the rotor is driven within this range of  $30^\circ$ . Three of the eight output bits of the EPROM are used as switching signals. This signal is logically ANDed with the output of the PWM to produce the final phase switching signals which are output to the gate drive circuit of the converter.

### 5.3.7 SPEED LOOP

The output of the soft-start circuit, which is a ramp circuit (shown in [Figure 5.7](#)), provides the modified speed reference. A speed error is generated by subtracting the speed from its reference value. The speed error is amplified by a proportional plus integral (PI) controller. The speed reference is enforced by this controller and speed feedback. The PI controller is synthesized with analog circuitry and uses an operational amplifier. The PI controller output is current command given by:

$$i^* = K_p(\omega_{rm} - \omega_m) + K_i \int (\omega_{rm} - \omega_m) dt \quad (5.2)$$

where

$$K_p = \frac{R_2}{R_1}$$

$$K_i = \frac{1}{CR_1}$$

and  $\omega_{rm}$  and  $\omega_m$  are the modified speed reference and speed, respectively. Thus,  $K_p$  and  $K_i$  can easily be changed by varying the values of  $R_1$ ,  $R_2$ , and  $C$ . Typical values of  $R_1$ ,  $R_2$ , and  $C$  are 3.3 K $\Omega$ , 150 K $\Omega$ , and 10  $\mu\text{F}$ , respectively. The value of  $K_p$  can be chosen to lie between 30 and 50 while that of  $1/K_i$  should be about 0.05. For more stable operation,  $R_f$  is connected in parallel with  $R_2$  and  $C$ . It also serves as a dc bypass for the feedback loop of the operational amplifier. The output of the PI controller (i.e., the current command  $i^*$ ) is given to three current loops to generate the three-phase current commands  $i_a^*$ ,  $i_b^*$ , and  $i_c^*$ . To provide a smooth and soft starting of the SRM, a speed ramp circuit is activated after the controller receives the speed command  $\omega_m^*$ . This circuit maintains the rate of change of speed to a desired value.

From the ramp circuit diagram it is noted that the time constant  $RC$  controls the rate of change of the speed signal. The speed command  $\omega_m^*$  can be changed by a potentiometer. Final implementation of the controller is shown in [Figure 5.7](#).

If a tachogenerator is not available, a frequency-to-voltage converter chip (e.g., LM2917) can be used to generate the speed feedback signal. The frequency input signal for this purpose can be obtained from the least significant bit (LSB) of the position from the encoder output.

## 5.4 DESIGN OF CURRENT CONTROLLERS

The SRM is nonlinear as there is a term in the voltage equation containing the product of rotor speed and phase current. Nonlinearity in the system makes the controller design difficult. If the system is linearized, then the knowledge base of well-known linear control systems theory can be applied to the controller design. Further, such an approach is analytical and capable of providing insight into the system unlike the computer-aided design approach. This controller is not capable of high performance as its design was based on an operating point, whereas in a variable speed SRM drive system the operating point continually changes. A nonlinear controller enables linearization and decoupling of the current loop, resulting in high performance. Decoupling is essential as the current in one phase will affect other phase current due to the presence of mutual coupling. Normally two phases conduct for part of a phase conduction period; when the outgoing phase current is being commutated, the incoming phase current is in the process of rising to its required level. These currents contribute to mutual flux linkages, even though the mutual inductances are minimized in the machine design.

Accordingly, the current controller is designed using the approaches outlined above:

1. Linearized current controller design<sup>11,15</sup>
2. Nonlinear current controller design with feedback linearization and decoupling but without considering mutual inductance<sup>14,16</sup>
3. Approach 2 considering mutual inductance<sup>14</sup>

All of these approaches invariably use pulse width modulation to enforce current command, but a hysteresis current controller known as a bang–bang current controller<sup>1</sup> is sometimes encountered in practice. This controller is easy to implement and requires no proportional-plus-integral current controllers. For faster response, the hysteresis current controller is combined with a PWM controller, resulting in a hybrid controller.<sup>11</sup>

The design of the current controllers is an integral part of any drive system development. Due to the nonlinear nature of the SRM, the development of a block diagram is not as straightforward as in the case of the dc motor. Realizing that the SRM is very much similar to the series-excited dc machine (as seen from the torque and equivalent circuit development earlier in our text), it is feasible to proceed with linearization of the system equations to obtain a small signal model and a block diagram from which the transfer functions are developed. The transfer functions could be used, as in the case of other motor drives, to derive a proportional-plus-integral controller. Such a procedure is outlined in the following section.

### 5.4.1 VOLTAGE AND TORQUE EQUATIONS FOR THE SRM

The voltage and torque equations of an SRM are linearized about the rated current and speed or the most likely operating point. While this likely operating point is difficult to pinpoint in a variable-speed drive application, it is usual to consider it corresponding to the rated torque at the rated speed.

The small signal model of the SRM is derived from the voltage and torque equations given below:

$$v = R_s i + \frac{d\lambda(\theta, i)}{dt} \quad (5.3)$$

$$T_e(\theta, i) - T_\ell = J \frac{d\omega_m}{dt} + B \omega_m \quad (5.4)$$

In the above equations, the flux,  $\lambda$ , and the airgap torque,  $T_e$ , are dependent upon the phase current and rotor position. By using the relation  $L(\theta, i)i = \lambda(\theta, i)$  the voltage equation is written as:

$$v = R_s i + \frac{d[L(\theta, i)i]}{dt} = R_s i + L(\theta, i) \frac{di}{dt} + \frac{dL(\theta, i)}{d\theta} \omega_m i \quad (5.5)$$

In Eq. (5.5), the three terms in the right-hand side represent the resistive voltage drop, inductive voltage drop, and back emf, respectively, and the result is similar to the separately excited dc motor voltage equation. The electromagnetic torque assuming that the inductance varies as a function of rotor position for an assumed current is known to be

$$T_e = \frac{1}{2} i^2 \frac{dL(\theta, i)}{d\theta} \quad (5.6)$$

which on substitution into the mechanical equation results in the following:

$$\frac{1}{2} i^2 \frac{dL(\theta, i)}{d\theta} - T_\ell = J \frac{d\omega_m}{dt} + B \omega_m \quad (5.7)$$

### 5.4.2 DERIVATION OF THE SRM SMALL-SIGNAL MODEL<sup>15</sup>

The states of the SRM plant are the rotor speed,  $\omega_m$ , and the phase current,  $i$ . By examining the SRM voltage and torque equations, there are terms where states are multiplied together resulting in a nonlinear system. It is desirable to derive a linearized model to utilize a vast amount of knowledge on linear systems to synthesize the current and speed controllers. This section contains the derivation of a linearized model of the SRM.

The inductance  $L = L(\theta, i)$  is assumed to be constant for the sake of simplification. The inductance is chosen as the mean value between the aligned inductance and the unaligned inductance at the rated current. The derivative of inductance with respect to rotor position is also assumed to be a constant and calculated between the conduction angles at the rated current value. This derivative has only a small change over the operating range of the motor.

Perturbing the system around a steady-state operating point with small signals, the new system states and inputs are

$$i = i_o + \delta i \quad (5.8)$$

$$\omega_m = \omega_{mo} + \delta\omega_m \quad (5.9)$$

$$v = v_o + \delta v \quad (5.10)$$

$$T_l = T_{lo} + \delta T_l \quad (5.11)$$

where the extra subscript  $o$  indicates steady-state values of the states and inputs, and the small signals are indicated by  $\delta$  preceding the variables. Substituting the perturbed variables in the system equations, it is seen that the steady-state terms cancel and the residual of these equations gives:

$$\frac{d\delta i}{dt} = \left( -\frac{R_s}{L} - \frac{1}{L} \frac{dL}{d\theta} \omega_{mo} \right) \delta i - \frac{1}{L} \frac{dL}{d\theta} i_o \delta\omega_m + \frac{\delta V}{L} \quad (5.12)$$

$$\frac{d\delta\omega_m}{dt} = \left( -\frac{1}{J} \frac{dL}{d\theta} i_o \right) \delta i - \frac{B}{J} \delta\omega_m + \frac{\delta T_\ell}{J} \quad (5.13)$$

Hereafter, the following substitutions are used:

$$R_{eq} = R_s + \frac{dL}{d\theta} \omega_{mo} \quad (5.14)$$

$$K_b = \frac{dL}{d\theta} i_o \quad (5.15)$$

$$\delta e = \frac{dL}{d\theta} i_o \delta\omega_m \quad (5.16)$$

where  $R_{eq}$  is the equivalent resistance,  $K_b$  is the emf constant, and  $\delta e$  is the induced emf. By using the small signal voltage and torque equations, the following block diagram is derived for the linearized SRM plant model. Note that this model is similar to the separately excited dc machine model. The block diagram of the linearized SRM is shown in [Figure 5.8](#).

The load is assumed to be frictional; that way, the load torque is treated as an integral component of the system but not as a disturbance. For the sake of simplicity, only one current feedback loop is shown in [Figure 5.8](#), even though for an  $q$ -phase SRM there will be  $q$  current feedback loops. These current loops are identical but shifted in phase, so there is no need to consider more than one phase for control modeling, analysis, and design.

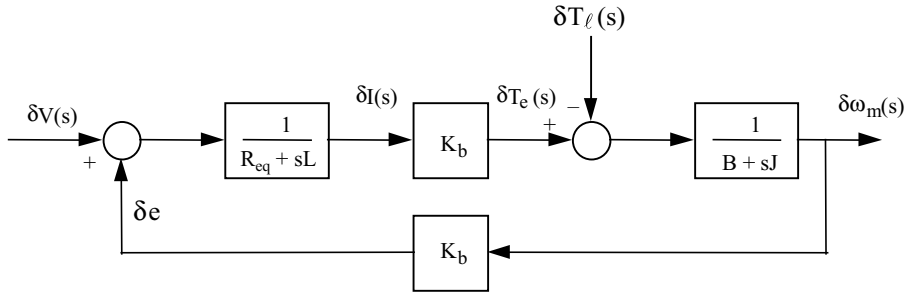


**FIGURE 5.8** Block diagram of the linearized SRM.

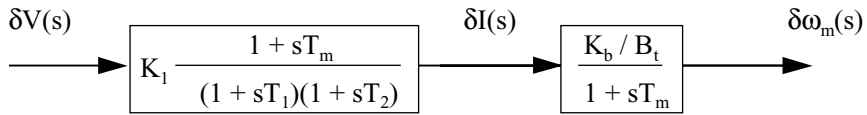


**FIGURE 5.9** Reduced block diagram of the SRM.

The back emf and current feedback loops cross each other, resulting in cross-coupling of these loops. Further, it makes the task of designing a current controller and later the speed controller very difficult. For this reason, the SRM block diagram is cast in a different form by removing the back emf feedback loop but absorbing it in a form which leads to a two-stage transfer function as shown in [Figure 5.9](#), very much similar to dc machines, where

$$B_t = B + B_\ell \quad (5.17)$$

$$K_1 = \frac{B_t}{K_b^2 + R_{eq}B_t} \quad (5.18)$$

$$T_m = \frac{J}{B_t} \quad (5.19)$$

$$-\frac{1}{T_1}, -\frac{1}{T_2} = -\frac{1}{2} \left[ \frac{B_t}{J} + \frac{R_{eq}}{L} \right] \pm \sqrt{\frac{1}{4} \left( \frac{B_t}{J} + \frac{R_{eq}}{L} \right)^2 - \frac{K_b^2 + R_{eq}B_t}{JL}} \quad (5.20)$$

### 5.4.3 SYSTEM BLOCK DIAGRAM

A speed-controlled SRM drive system is shown in [Figure 5.10](#). Rotor speed is converted to a voltage signal through a tachogenerator which then is filtered to provide  $\omega_r$ , which is then compared with its reference  $\omega_r^*$ . The speed error signal is amplified and conditioned with the speed controller which normally is a proportional-plus-integral type. The output of this speed controller is a voltage signal proportional to current command signal  $I^*$ . A current feedback signal in volts is compared with this command signal to generate a current error. The current error is processed through

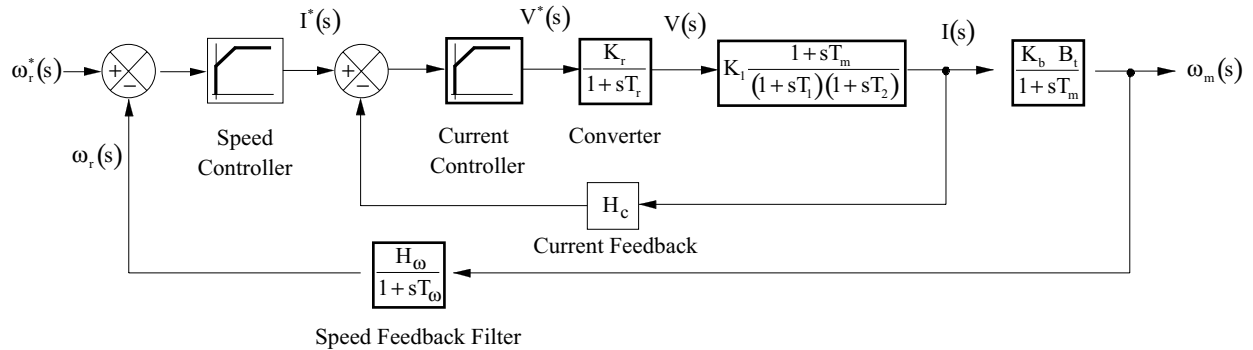


**FIGURE 5.10** Block diagram of the speed-controlled SRM drive.

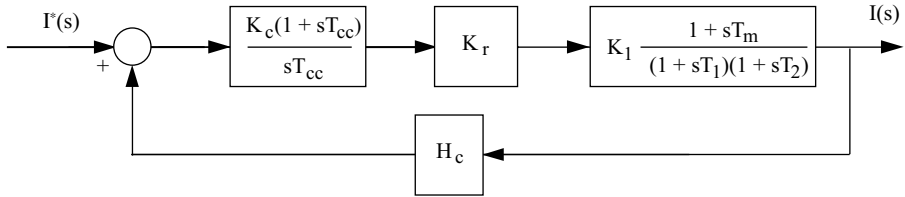


**FIGURE 5.11** Block diagram of the current control loop.

a PI controller to produce a command signal for the power converter. The power converter is modeled as a gain with a first-order lag, and both of these constants may be measured or evaluated in the design stage. The power converter gain is

$$K_r = \frac{V_{dc}(\text{nominal})}{V_{cm}} \quad (5.21)$$

where  $V_{cm}$  is the maximum control voltage. The time constant of the converter,  $T_r$ , assuming PWM control of the converter with a carrier frequency of  $f_c$ , is given by:

$$T_r = \frac{T_c}{2} = \frac{1}{2f_c} \quad (5.22)$$

#### 5.4.4 DESIGN OF CURRENT CONTROLLER<sup>15</sup>

A PI controller is selected for the current controller because of its simplicity to implement and its widespread industrial use. The block diagram of the current loop is shown in [Figure 5.11](#). The transfer function of the current controller is

$$G_c(s) = \frac{K_c(1+sT_{cc})}{sT_{cc}} \quad (5.23)$$

The time delay of the converter is neglected here due to the assumption that the switching frequency is at least 10 times greater than that of the electrical time constant in the current loop. Further, such an assumption simplifies the block diagram.

Since the mechanical time constant of the system,  $T_m$ , is large,  $(1+sT_m)$  can be approximated as  $sT_m$ . With this approximation, the current loop becomes a second-order system. The approximated system is given below:

$$\frac{I(s)}{I^*(s)} = \frac{K_c K_r K_1 T_m (1 + sT_{cc})}{T_c (1 + sT_1) (1 + sT_2) + H_c K_c K_r K_1 T_m (1 + sT_{cc})} \quad (5.24)$$

In designing the current controller gain and time constant, it is desirable to specify a bandwidth for the current loop based on the switching frequency of the converter. In order to approximate the converter as a simple gain, the bandwidth of the converter must be ten times faster than the bandwidth of the current loop.

To design the current controller using the bandwidth method, the characteristic equation of the approximated current loop is used, as shown below:

$$s^2 + s \left( \frac{T_1 + T_2 + H_c K_c K_r K_1 T_m}{T_1 T_2} \right) + \frac{H_c K_c K_r K_1 T_m + T_{cc}}{T_{cc} T_1 T_2} \quad (5.25)$$

Since it is a second-order equation, the natural frequency of oscillation,  $\omega_n$ , and damping ratio,  $\zeta$ , of a second-order system may be used to obtain the current controller gain and time constant. Given below are the equations which specify the damping (5.26) and the natural frequency of the approximated system (5.27):

$$2\zeta\omega_n = \frac{T_1 + T_2 + H_c K_c K_r K_1 T_m}{T_1 T_2} \quad (5.26)$$

$$\omega_n^2 = \frac{H_c K_c K_r K_1 T_m + T_{cc}}{T_{cc} T_1 T_2} \quad (5.27)$$

The gain,  $K_c$ , and the time constant,  $T_c$ , may be solved from Eqs. (5.26) and (5.27), respectively, for a given natural frequency and damping ratio. The following are equations for  $K_c$  and  $T_c$ :

$$K_{cc} = \frac{2\zeta T_1 T_2 \omega_n - T_1 - T_2}{H_c K_r K_1 T_n} \quad (5.28)$$

$$T_{cc} = \frac{H_c K_c K_r K_1 T_m}{T_1 T_2 \omega_n^2 - 1} \quad (5.29)$$

#### 5.4.4.1 Example 1: 5-hp SRM Drive System

To validate the design technique using the linearized model, a 5-hp SRM is considered for the current and speed controller designs.<sup>15</sup> The specifications for the 5-hp SRM drive are listed below:

---

<b>Motor and System Parameters</b>	
Command signal levels	±10 V
Dc link voltage	400 V
Max. current	15 A
PWM chopping frequency	8 kHz
Phase resistance	0.931 Ω
Power	5 hp
Rated current	10 A (1 p.u.)
Rated speed	2500 rpm
Rotor friction constant	0.001 N · m/rad/sec
Rotor inertia	0.006 kg·m <sup>2</sup>
Speed feedback gain	0.0383 V/rad/sec
Speed feedback time constant	0.1 sec

---

Inductance of the SRM phases is assumed to be the mean value of the unaligned inductance and aligned inductance at the rated current. This value turns out to be 22.1 mH. The slope of the inductance curve is needed in order to calculate the linearized torque/back emf constant. Using the inductance values at the rated current, the approximate slope of the inductance profile is 0.234 H/rad. By using Eqs. (5.26) and (5.27), the linearized torque/back emf constant,  $K_b$ , and the linearized phase resistance,  $R_{eq}$ , are calculated:

$$R_{eq} = R_s + \frac{dL}{d\theta} \omega_{mo} = 0.931 + (0.234)(261) = 62 \Omega \quad (5.30)$$

$$K_b = \frac{dL}{d\theta} i_o = (0.234)(10) = 2.34 \quad (5.31)$$

The following constants are calculated in order to begin the design of the controllers:

1. Converter gain:

$$K_r = \frac{V_{dc}}{v_c} = \frac{400}{10} = 40 \quad (5.32)$$

2. Current transducer gain:

$$H_c = \frac{v_c}{i_{max}} = \frac{10}{15} = 0.667 \text{ V/A} \quad (5.33)$$

3. Motor transfer function:

$$B_t = B + B_t = 0.001 + 0 = 0.001 \quad (5.34)$$

$$K_1 = \frac{B_t}{K_b^2 + RB_t} = 0.000182 \quad (5.35)$$

$$T_m = \frac{J}{B_t} = \frac{0.006}{0.001} = 6 \text{ s} \quad (5.36)$$

$$-\frac{1}{T_1}, -\frac{1}{T_2} = -\frac{1}{2} \left[ \frac{B_t}{J} + \frac{R_{eq}}{L} \right] \pm \sqrt{\frac{1}{4} \left( \frac{B_t}{J} + \frac{R_{eq}}{L} \right)^2 - \frac{K_b^2 + R_{eq}B_t}{JL}} \quad (5.37)$$

$$T_1 = 0.0668 \text{ s} \quad T_2 = 0.000358 \text{ s}$$

#### 5.4.4.2 Current Controller Design

To design the current controller gain and time constant, Eqs. (5.27) and (5.28) are used. For a bandwidth of 1600 Hz and damping ratio of 0.707 for the current loop performance, the controller gains are

$$K_c = \frac{1.414 T_1 T_2 \omega_n - T_1 - T_2}{H_c K_r K_1 T_m} = 9.36 \quad (5.38)$$

$$T_{cc} = \frac{H_c K_c K_r K_1 T_m}{T_1 T_2 \omega_n^2 - 1} = 0.000113 \text{ s} \quad (5.39)$$

Shown in [Figure 5.12](#) are the responses of the current loop. Both the approximated and unapproximated current loop responses were identical, so the unapproximated model-based response is shown here. The frequency response is shown in [Figure 5.12b](#) and the bandwidth of the system is approximately 1600 Hz.

#### 5.4.4.3 Nonlinear Dynamic Simulation of Current Loop

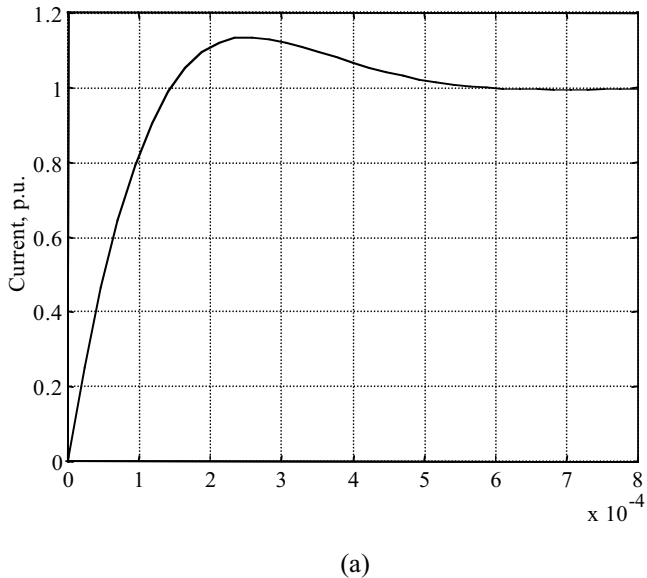
To verify the validity of the current controller design, nonlinear dynamic simulation of the drive system is presented in this section. Shown in [Figure 5.13](#) is the step response of the current loop at the rated speed of 2500 rpm and rated current of 10 A. The first plot shows the phase-A current along with an idealized inductance profile for reference. The second plot shows the phase-B current; the third plot, the torque generated; and the fourth plot, the PWM signal to the converter.

With a dc link voltage of 400 V and the maximum PWM duty cycle of 90%, the current controller cannot maintain a commanded current of 10 A because of the back emf generated and the sharp rise in inductance. The currents of phase A and phase B trail off into the negative inductance slope region where negative torque is generated, although the magnitude of the negative torque does not seem to be significant. By increasing the dc link voltage, the current error is reduced at the rated speed and rated current. [Figure 5.14](#) shows the current loop response for a dc link of 500 V.

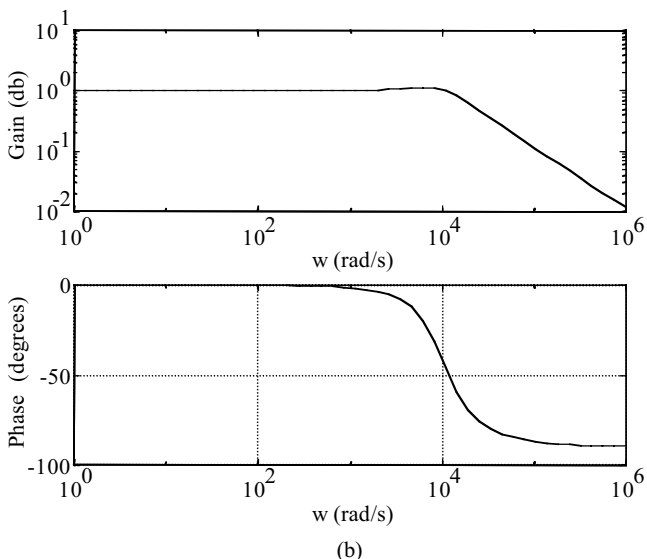
[Figures 5.15](#) and [5.16](#) show the current loop response for a speed of 1250 rpm and current command of 10 A and a speed of 2500 rpm and a current command of 5 A, respectively. Even at different current commands and at different speeds, the time response of the current loop meets or exceeds the designed system current loop step response. The current loop simulation also shows that an advanced angle is not necessary, unless the phase current is advanced in order to advance the commutation and prevent the current from trailing off into the negative slope region.

#### 5.4.5 LINEARIZED DECOUPLING CURRENT CONTROLLER NEGLECTING MUTUAL INDUCTANCE<sup>13,14</sup>

The design of the linearized current controller presumed that only one phase is conducting current at any time in a SRM. This assumption is very limiting and does not truly reflect the SRM operation. For part of a phase conduction period, two phases are active. This happens when one phase current is being commutated and the succeeding



(a)



(b)

**FIGURE 5.12** Step and frequency response of current loop. (a) Step response of current loop transfer function; (b) frequency response of the current loop transfer function.

phase has initiation of current. Because of mutual coupling of the phase windings, the currents influence each other. The mutual coupling is minimized at the machine design stage. In spite of best efforts, the mutual inductances are approximately 2 to 5% of the aligned self-inductances. If mutual coupling is ignored, then the phase currents are only dependent upon their respective phase voltage inputs only. Then the current loop

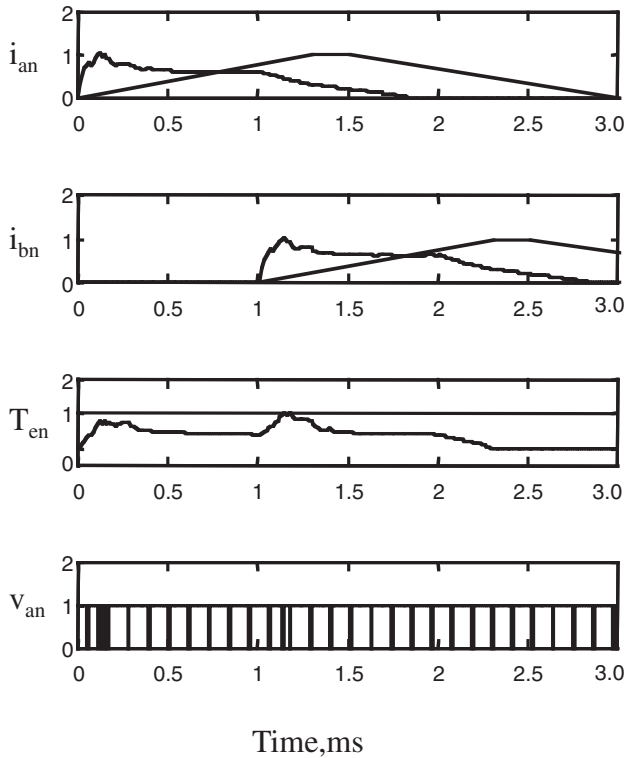


**FIGURE 5.13** Normalized step current responses at 2500 rpm with a dc link voltage of 400 V (step current command = 1 p.u.).

design becomes easier as only one phase at a time has to be considered. But it is seen from the machine equation that it is coupled through the induced emf and is nonlinear because of the term containing the product of the speed and current. It can be decoupled as follows: Consider the voltage equation given for phase  $x$  as:

$$\begin{aligned} v_x &= R_s i_x + L_x \frac{di_x}{dt} + i_x \frac{dL_x}{dt} = R_s i_x + L_x \frac{di_x}{dt} + i_x \frac{\partial L_x}{\partial \theta} \cdot \frac{\partial \theta}{\partial t} \\ &= R_s i_x + L_x \frac{di_x}{dt} + \omega_m i_x \frac{\partial L_x}{\partial \theta} = R_s i_x + L_x \frac{di_x}{dt} + g_x \omega_m i_x \end{aligned} \quad (5.40)$$

where  $R_s$  is the phase resistance,  $L_x$  is the self-inductance for a given current and rotor position,  $g_x$  is the incremental inductance slope with respect to rotor position, and  $v_x$  is the applied voltage to the phase winding. The machine inductance is a function of both the current and rotor position. In state space form, this equation is written as:

$$\frac{di_x}{dt} = -\frac{R_s}{L_x} i_x - \frac{g_x}{L_x} \omega_m i_x + \frac{v_x}{L_x} = -a_1 i_x - a_2 \omega_m i_x + a_0 v_x \quad (5.41)$$

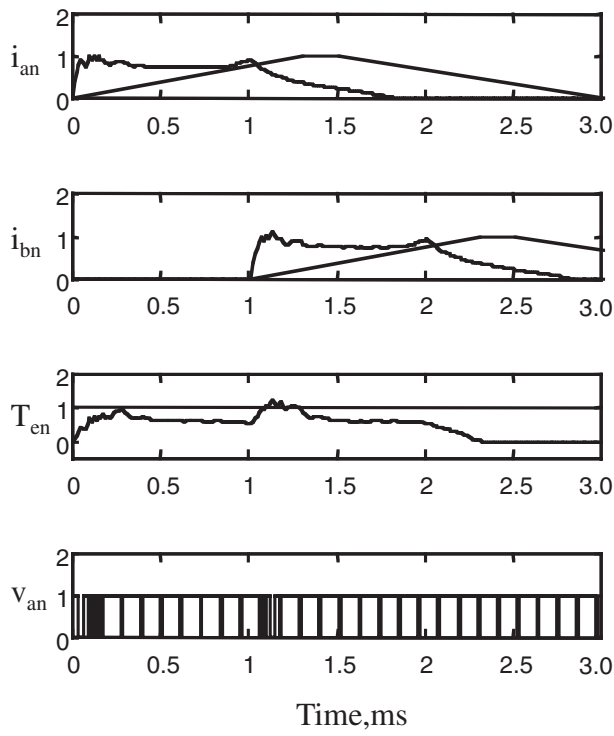


**FIGURE 5.14** Normalized step current responses at 2500 rpm with a dc link voltage of 500 V (step current command = 1 p.u.).

where

$$a_0 = \frac{1}{L_x} \quad (5.42)$$

$$a_1 = \frac{R_s}{L_x} \quad (5.43)$$

$$a_2 = \frac{g_x}{L_x} = \frac{1}{L_x} \cdot \frac{\partial L_x}{\partial \theta} \quad (5.44)$$

The block diagram representation of one phase of the SRM is shown in Figure 5.17. It can further be simplified as shown in Figure 5.18. The nonlinearity due to the product of current and speed does not allow linear control techniques to be applied for design of the current controller.

The effect of that term is decoupled<sup>8,13</sup> by defining a new input with the relationship to the old input as:

$$v_x = \bar{v}_x + \frac{a_2}{a_0} \omega_m i_x \quad (5.45)$$

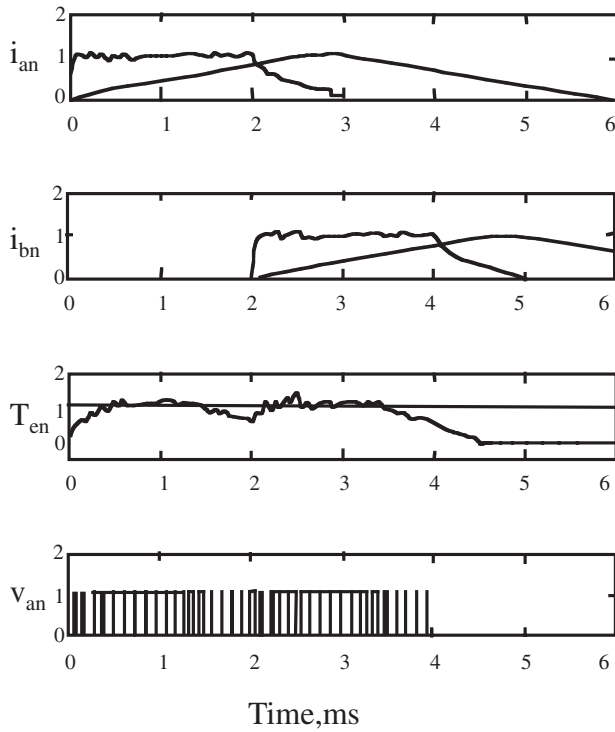


**FIGURE 5.15** Normalized step current responses at 1250 rpm with a dc link voltage of 400 V (step current command = 0.5 p.u.).

which, when substituted into the voltage equation, results in:

$$\frac{di_x}{dt} = -a_1 i_x - a_2 \omega_m i_x + a_0 \left\{ \bar{v}_x + \frac{a_2}{a_0} \omega_m i_x \right\} = -a_1 i_x + a_0 \bar{v}_x \quad (5.46)$$

The block diagram for this appears in Figure 5.19, and it is linear in the new input plane. Note that the system is linear time varying because of the coefficient  $a_1$ .

The linearization is achieved if the new input voltage is considered to subtract the product term of speed and current from the original input. This linearization may be appropriately termed pseudo-linearization. In contrast, real linearization can be achieved by actually subtracting from the phase voltage command input the term  $\frac{a_2}{a_0} \omega_m i_x$  and using the resultant as the new input. It has serious consequences on the implementation, and the computational burden will be significant enough that the pseudo-linearization appears an attractive alternative. This approach is taken throughout this chapter.

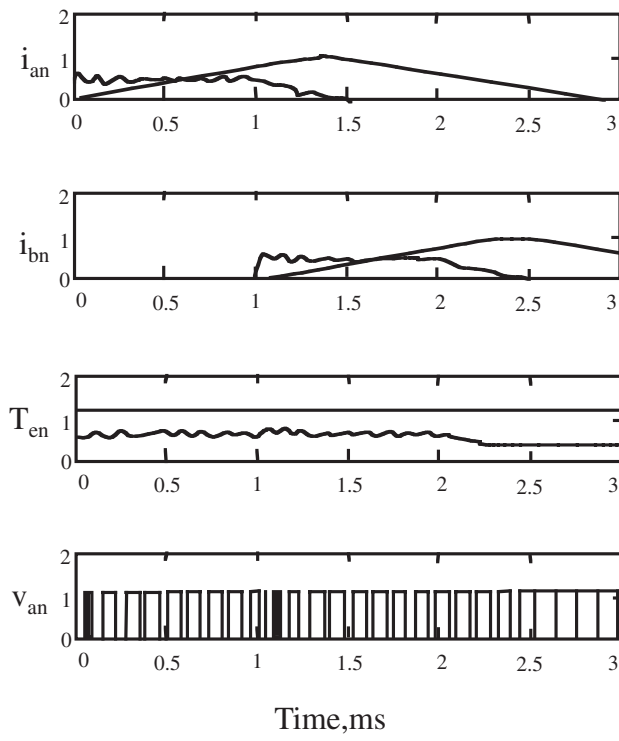


**FIGURE 5.16** Normalized step current responses at 2500 rpm with a dc link voltage of 400 V (step current command = 0.5 p.u.).

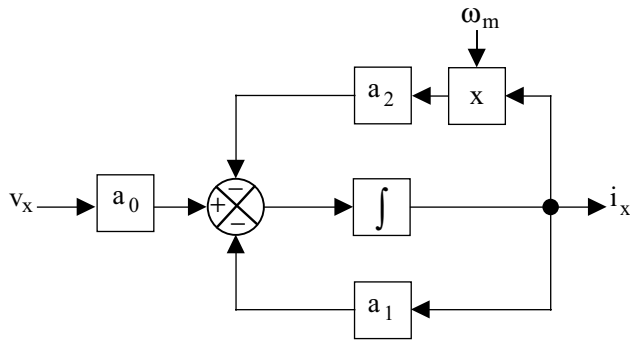


**FIGURE 5.17** Block diagram of one phase of the SRM

For use in current control loop design, consider that the new input  $\bar{v}_x$  is obtained from a control voltage,  $\bar{v}_c$ , through the power converter transfer function as:

$$\bar{v}_x(s) = \frac{K_r}{1 + sT_r} v_c(s) \quad (5.47)$$

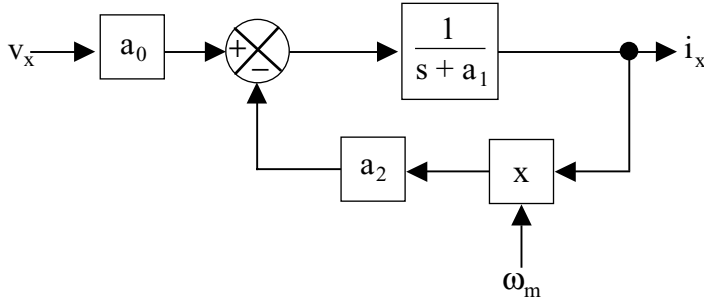


**FIGURE 5.18** Simplified block diagram of one phase of the SRM.

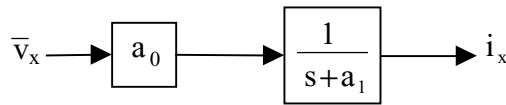


**FIGURE 5.19** Linear SRM for one phase.

The control voltage is generated by the PI current controller whose input is the current error (in voltage):

$$\bar{v}_c^* = K_{px}(i_x^* - i_x) + K_{ix} \int_0^t (i_x^* - i_x) dt \quad (5.48)$$

where  $i_x^*$  is the phase current command,  $K_{px}$  is the proportional gain, and  $K_{ix}$  is the integral control of the current controller. The current transducer gain can be absorbed in  $K_{px}$  and  $K_{ix}$ , and thereby an extra constant is eliminated in the symbolic representation.

The controller gains can be evaluated by the conventional design procedure based on the frequency response characteristics. The time constant of the converter is negligible compared to the electrical time constant of the machine; therefore, the converter transfer function is conveniently reduced to  $K_r$ . The current control loop with the PI controller is shown in Figure 5.20. The closed loop transfer function may then be derived as

$$\begin{aligned}
 \frac{i_x}{i_x^*} &= \frac{a_0 K_r (K_{ix} + s K_{px})}{s^2 + a_1 s + a_0 H_c K_r (K_{ix} + s K_{px})} \\
 &= \frac{1}{H_c} \cdot \frac{a_0 H_c K_r (K_{ix} + s K_{px})}{s^2 + (a_1 + a_0 H_c K_r K_{px}) s + a_0 H_c K_r K_{ix}} \\
 &= \frac{1}{H_c} \cdot \frac{a_0 H_c K_r K_{ix} + s a_0 H_c K_r K_{px}}{s^2 + a_0 H_c K_r K_{px} s + a_0 H_c K_r K_{ix}} \\
 &= \frac{1}{H_c} \cdot \frac{2 \zeta \omega_n s + \omega_n^2}{s^2 + 2 \zeta \omega_n s + \omega_n^2} \quad (5.49)
 \end{aligned}$$

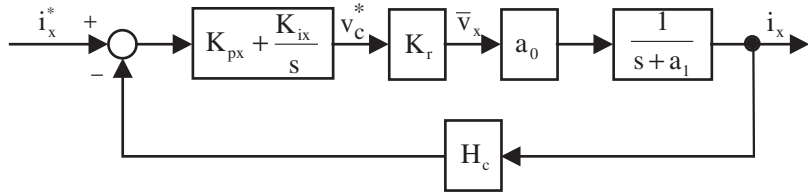


**FIGURE 5.20** Block diagram of the linearized current control loop.

as  $a_0 H_c K_r K_{px} \gg a_1$ , and

$$\omega_n^2 = a_0 H_c K_r K_{px} \quad (5.50)$$

$$2\zeta\omega_n = a_0 H_c K_r K_{ix} \quad (5.51)$$

The controller gains are selected from the required damping ratio,  $\zeta$ , and bandwidth,  $\omega_c$ . Bandwidth is related to the damping ratio and the natural frequency of oscillation,  $\omega_n$ , and is derived as follows.<sup>11</sup> The transducer gain does not enter into the picture as the conversion of  $i_x^*$  from ampere to volt will cancel it. Therefore, consider a transfer function of the type:

$$G_c(s) = \frac{2\zeta\omega_n s + \omega_n^2}{s^2 + 2\zeta\omega_n s + \omega_n^2} \quad (5.52)$$

The gain at frequency corresponding to bandwidth is

$$G_c(j\omega)|_{\omega=\omega_c} = \sqrt{\frac{(\omega_n^2)^2 + (2\zeta\omega_n\omega_c)^2}{(\omega_n^2 - \omega_c^2) + (2\zeta\omega_n\omega_c)^2}} = \frac{1}{\sqrt{2}} \quad (5.53)$$

which is simplified as:

$$\omega_c^4 - 2(1 + 2\zeta^2)\omega_n^2\omega_c^2 - \omega_n^4 = 0 \quad (5.54)$$

The bandwidth is obtained from this in terms of the damping ratio and natural frequency of oscillation as:

$$\omega_c = \omega_n \sqrt{(1 + 2\zeta^2) + \sqrt{(1 + 2\zeta^2)^2 + 1}} \quad (5.55)$$

Note that this derivation was helped by the fact that the bandwidth has to be positive. Then, the current controller gains are obtained as:

$$K_{ix} = \frac{\omega_n^2}{a_0 H_c K_r} = \left[ \frac{1}{a_0 H_c K_r} \right] \left[ \frac{\omega_c^2}{(1 + 2\zeta^2) + \sqrt{(1 + 2\zeta^2)^2 + 1}} \right] \quad (5.56)$$

$$K_{px} = \frac{2\zeta\omega_n}{a_0 H_c K_r} = \left[ \frac{1}{a_0 H_c K_r} \right] \left[ \frac{2\zeta\omega_c}{(1 + 2\zeta^2) + \sqrt{(1 + 2\zeta^2)^2 + 1}} \right] \quad (5.57)$$

To evaluate the gains, the damping ratio and bandwidth are chosen and substituted in the equations derived. A few comments are in order here:

1.  $a_0$  is not a constant but is dependent on machine self-inductance and subject to continuous variation as rotor position changes; therefore, for a constant integral current controller gain, the natural frequency changes, thus making the bandwidth also vary. This invariably affects the current response.
2. Similar is the effect of constant proportional gain on the current response.
3. In order to have a constant bandwidth as well as a constant damping ratio, it is important to vary the current controller gains as a function of rotor position. This is in contrast to constant current controller gains encountered in dc and ac motor drives. The variation of controller gains as a function of rotor position is known as gain scheduling. The disadvantage of gain scheduling is that additional computational steps are required in controller software execution, leading to a higher sampling interval in the current control loop execution.
4. If the dependence of the inductance on the current also is included, as it must be, gain scheduling has to be employed to maintain the performance of the current at desired levels.
5. The same procedure that has been employed in the derivation of current loop linearization can be utilized when considering mutual inductance. Decoupling of the inputs is also necessary for this particular case and is illustrated in the following section.

#### **5.4.6 DESIGN OF CURRENT CONTROLLER INCLUDING MUTUAL COUPLING EFFECTS<sup>14,16</sup>**

Mutual coupling of the phase windings results in making the phase current dependent on other phase currents. Further, it has the deleterious effect of augmenting the ripple torque. Since mutual coupling is due to simultaneous conduction in at least two phases, the SRM model is derived assuming that only two phases conduct at any given time and its features are commented on. From the system model, the need for linearization and decoupling becomes evident and a method to achieve them is described in this section. The performance of the current controller is presented and

contrasted to that of the conventional current controller without the linearization and decoupling of inputs.

As only two phases are excited, the equations for those phases are written as:

$$v_x = R_s i_x + \frac{d\lambda_x}{dt} \quad (5.58a)$$

$$v_y = R_s i_y + \frac{d\lambda_y}{dt} \quad (5.58b)$$

where the flux linkages are expressed as the product of inductances and currents and the inductances are expressed as a function of rotor position and current:

$$\lambda_x(i_x, i_y, \theta) = L_x(i_x, \theta)i_x + M_{xy}(i_x, i_y, \theta)i_y \quad (5.59a)$$

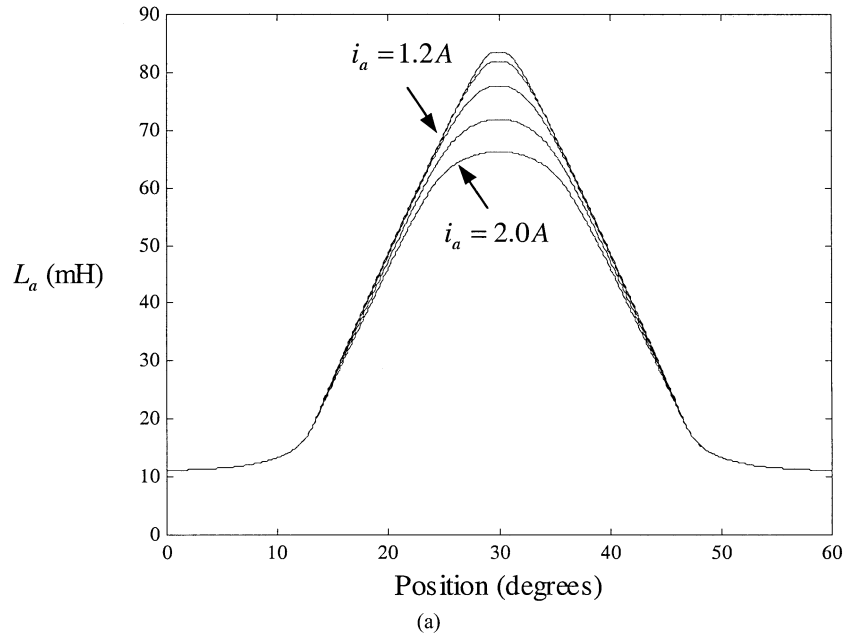
$$\lambda_y(i_x, i_y, \theta) = M_{xy}(i_x, i_y, \theta)i_x + L_y(i_y, \theta)i_y \quad (5.59b)$$

Phase flux is the sum of the self-flux and the mutual flux. The self-flux is dominant as it goes through mostly iron and two airgaps across the phase poles and the corresponding rotor poles. In contrast, the mutual flux path is constituted by the airgap between the stator poles and the interpolar part of the rotor poles. The net result is this path has a higher effective air gap, resulting in high reluctance and lower flux contribution to the phase flux. Therefore, it is fair to presume that only the rotor position and related phase current determine the self-inductance of a phase. However, rotor position and two adjacent phase currents determine the mutual inductance as given in Eq. (5.59), although the variation in the mutual inductance due to the phase currents is practically negligible. As the mutual flux linkage is very small compared to self-flux linkages, their summation is valid even under saturation to obtain a phase flux linkage.

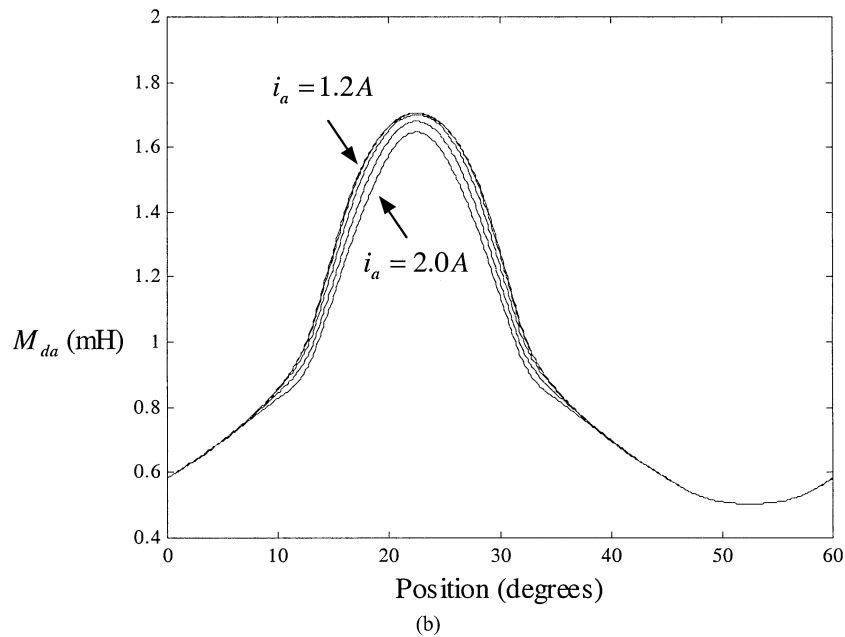
There is no variation in the self-inductance when the rotor is unaligned but it significantly decreases when the rotor is near the aligned position. The variation in the mutual inductance is not significant compared with the variation in the self-inductance. For example,  $L_{a,max}$  at  $i_a = 2.0$  A is 79.4% of  $L_{a,max}$  at  $i_a = 1.2$  A, and  $M_{da,max}$  at  $i_d = 0$  A and  $i_a = 2.0$  A is 95.9% of  $M_{da,max}$  at  $i_d = 0$  A and  $i_a = 1.2$  A, respectively, for a four-phase machine.

The self- and mutual inductances at various current levels are shown in [Figures 5.21a](#) and [b](#), respectively, for a four-phase machine. The lowest and highest currents are 1.2 and 2.0 A, respectively; the current is incremented by 0.2 A. When the magnetic circuit is saturated, the self-inductance decreases around the aligned position, whereas the mutual inductance decreases slightly. Practically, the mutual inductance can be considered only as a function of rotor position due to negligible variation in the mutual inductance.

It is instructive to find the nature of partial derivatives of self- and mutual inductances with respect to the rotor position shown in [Figures 5.21c](#) and [d](#). They are required to compute torque. The changes in the derivatives of self-inductance are very high compared to the changes in derivatives of mutual inductance for variations in current. The latter is negligible compared to the former. The partial derivatives of self- and mutual inductances with respect to current are shown in [Figures 5.22a](#) and [b](#), respectively.

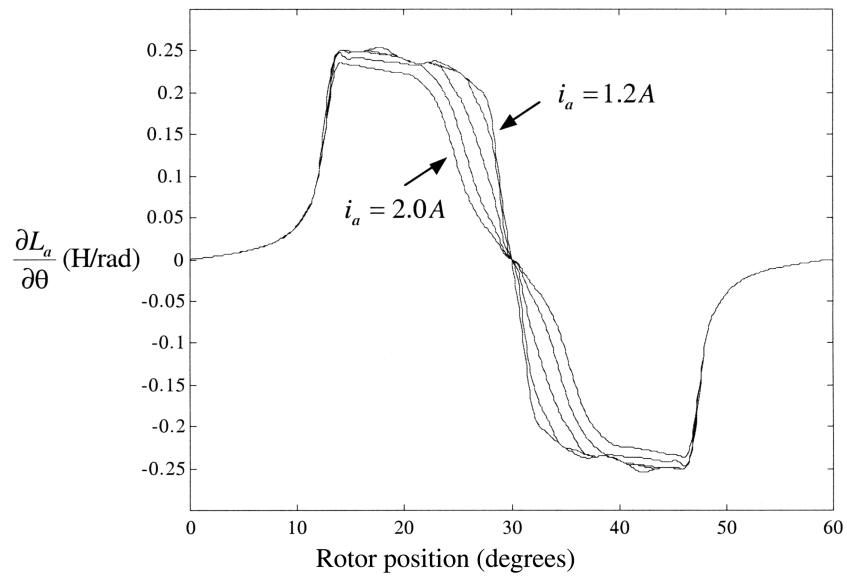


(a)

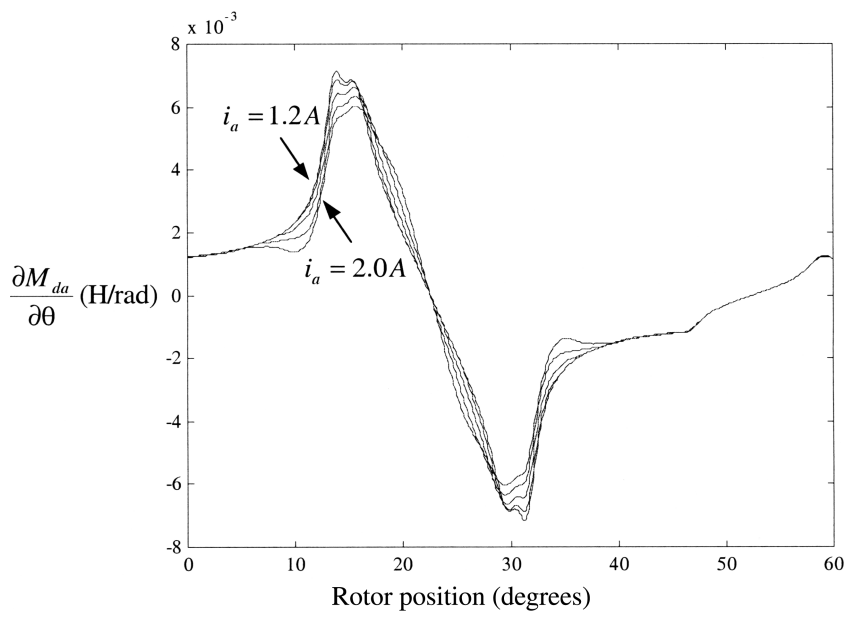


(b)

**FIGURE 5.21** Inductances and their rates of change at various current levels. (a)  $L_a(i_a, \theta)$ ; (b)  $M_{da}(i_a, 0, \theta)$ ; (c)  $\partial L_a(i, \theta)/\partial \theta$ ; (d)  $\partial M_{da}(0, i_a, \theta)/\partial \theta$ .

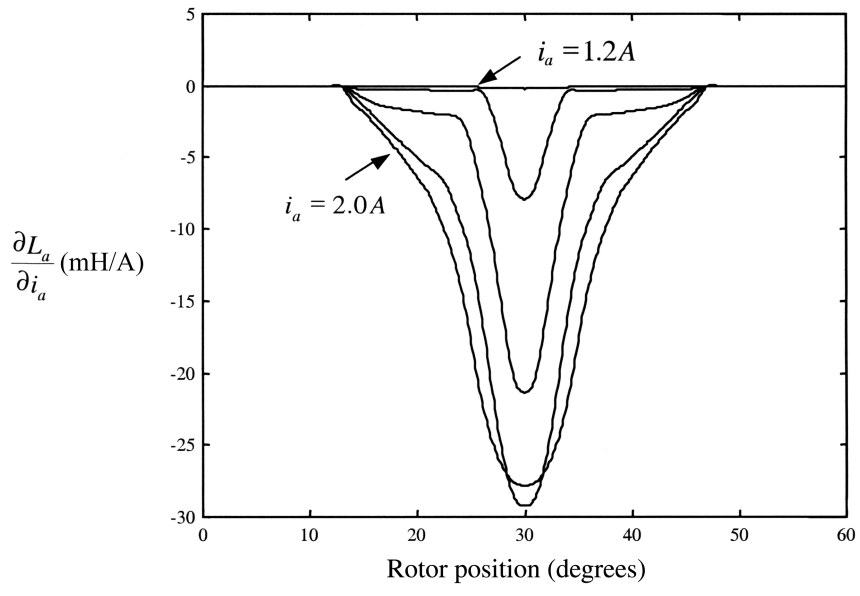


(c)

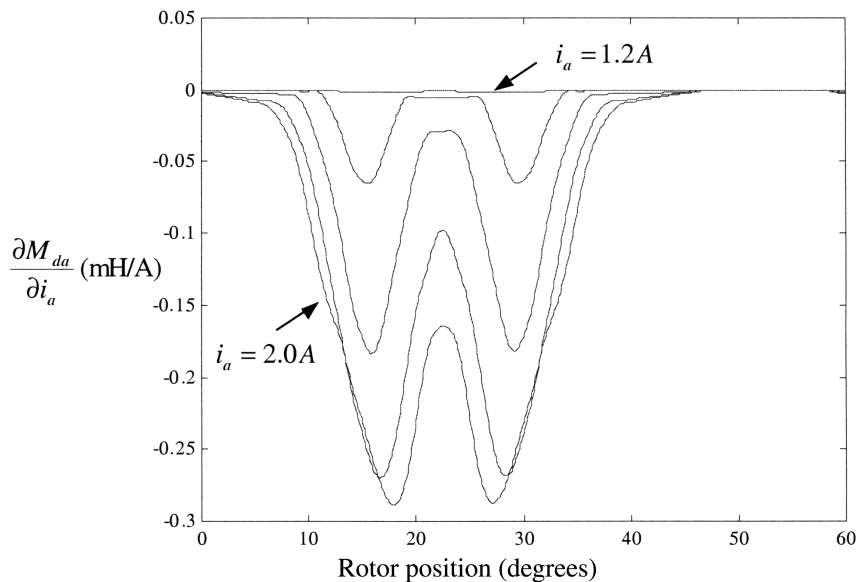


(d)

**FIGURE 5.21** (Continued)



(a)



(b)

**FIGURE 5.22** Rates of change of inductances with respect to phase current at various current levels. (a)  $\frac{\partial L_a(i_a, \theta)}{\partial i_a}$ ; (b)  $\frac{\partial M_{da}(0, i_a, \theta)}{\partial i_a}$ .

Here, again, the latter is negligible compared to the former. Therefore, it is usual to ignore the partial derivatives of mutual inductances with respect to excitation current, which we will do in the development of system equations in this chapter.

By differentiating Eq. (5.59) we have

$$\begin{aligned}\frac{d\lambda_x}{dt} &= \left(L_x + \frac{\partial L_x}{\partial i_x} i_x\right) \frac{di_x}{dt} + \frac{\partial L_x}{\partial \theta} \omega_m i_x + M_{xy} \frac{di_y}{dt} + \frac{\partial M_{xy}}{\partial \theta} \omega_m i_y \\ &\quad + \frac{\partial M_{xy}}{\partial i_x} i_y \frac{di_x}{dt} + \frac{\partial M_{xy}}{\partial i_y} i_y \frac{di_y}{dt}\end{aligned}\quad (5.60a)$$

$$\begin{aligned}\frac{d\lambda_y}{dt} &= M_{xy} \frac{di_x}{dt} + \frac{\partial M_{xy}}{\partial \theta} \omega_m i_x + \left(L_y + \frac{\partial L_y}{\partial i_y} i_y\right) \frac{di_y}{dt} + \frac{\partial L_y}{\partial \theta} \omega_m i_y \\ &\quad + \frac{\partial M_{xy}}{\partial i_x} i_x \frac{di_x}{dt} + \frac{\partial M_{xy}}{\partial i_y} i_x \frac{di_y}{dt}\end{aligned}\quad (5.60b)$$

If the equivalent self-inductances  $L'_x$  and  $L'_y$  are defined as:

$$L'_x = L_x + \frac{\partial L_x}{\partial i_x} i_x \quad (5.61a)$$

$$L'_y = L_y + \frac{\partial L_y}{\partial i_y} i_y \quad (5.61b)$$

electromagnetic torque is

$$T_e = \frac{1}{2} g_x i_x^2 + \frac{1}{2} g_y i_y^2 + \frac{1}{2} g_{xy} i_x i_y \quad (5.62)$$

where partial derivatives of self-inductances for phases  $x$  and  $y$  and mutual inductances with respect to rotor position are denoted as  $g_x$ ,  $g_y$ , and  $g_{xy}$ , respectively. Ignoring the terms with  $\frac{\partial M_{xy}}{\partial i_x}$  and  $\frac{\partial M_{xy}}{\partial i_y}$ , as they are small in comparison with other terms, the equation of the two current conducting phases are:

$$\frac{di_x}{dt} = -a_1 i_x - a_2 \omega_m i_x + a_3 i_y + a_4 \omega_m i_y + a_0 \left( v_x - \frac{M_{xy}}{L'_y} v_y \right) \quad (5.63a)$$

$$\frac{di_y}{dt} = -b_1 i_y - b_2 \omega_m i_y + b_3 i_x + b_4 \omega_m i_x + b_0 \left( -\frac{M_{xy}}{L'_y} v_x + v_y \right) \quad (5.63b)$$

where

$$D = L'_x L'_y - M_{xy}^2 \quad (5.64)$$

$$\begin{aligned} a_0 &= \frac{L'_y}{D} & b_0 &= \frac{L'_x}{D} \\ a_1 &= a_0 R_s & b_1 &= b_0 R_s \\ a_2 &= a_0 \left( \frac{\partial L_x}{\partial \theta} - \frac{M_{xy}}{L'_y} \cdot \frac{\partial M_{xy}}{\partial \theta} \right) & b_2 &= b_0 \left( \frac{\partial L_y}{\partial \theta} - \frac{M_{xy}}{L'_x} \cdot \frac{\partial M_{xy}}{\partial \theta} \right) \\ a_3 &= a_0 \frac{M_{xy} R_s}{L'_y} & b_3 &= b_0 \frac{M_{xy} R_s}{L'_x} \\ a_4 &= a_0 \left( \frac{M_{xy}}{L'_y} \cdot \frac{\partial L_y}{\partial \theta} - \frac{\partial M_{xy}}{\partial \theta} \right) & b_4 &= b_0 \left( \frac{M_{xy}}{L'_x} \cdot \frac{\partial L_x}{\partial \theta} - \frac{\partial M_{xy}}{\partial \theta} \right) \end{aligned} \quad (5.65)$$

Current in one winding is dependent on the other winding current and also the input voltages of both the windings as seen from Eq. (5.63). The equation set is nonlinear, also. It can be linearized and decoupled by having a new set of inputs that cancels all the nonlinear terms and cross-coupling voltages— $u_x$  and  $u_y$ . Then the two phase equations are

$$\frac{di_x}{dt} = -a_1 i_x + a_0 u_x \quad (5.66)$$

$$\frac{di_y}{dt} = -b_1 i_y + b_0 u_y \quad (5.67)$$

These equations are linear and decoupled. They are shown in block diagram form in [Figure 5.23](#).

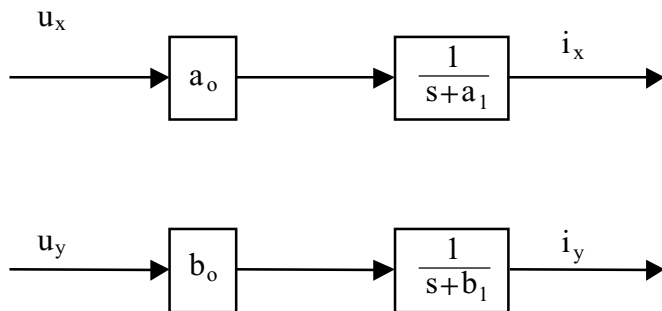


**FIGURE 5.23** Linearized and decoupled current loop.

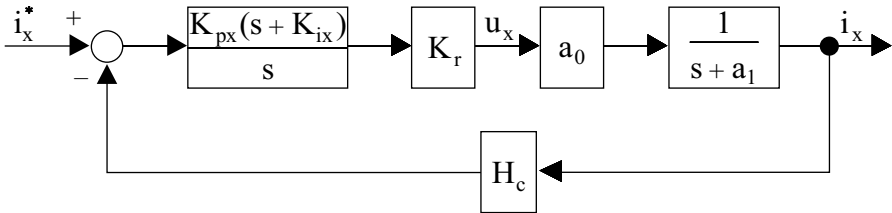


**FIGURE 5.24** Current control loop with PI controller.

It is assumed that the new inputs  $u_x$  and  $u_y$  are generated by the power converters in tandem with PI controllers with the current errors from phase  $x$  and  $y$ , respectively. The closed current control loop is shown in Figure 5.24 for phase  $x$  and a similar one for phase  $y$  can be drawn. The closed current loop transfer function is derived as:

$$G_{cx}(s) = \frac{i_x(s)}{i_x^*(s)} = \frac{1}{H_c s^2 + K_{1x} K_{px} s + K_{1x} K_{ix}} \quad (5.68)$$

where

$$K_{1x} = a_o H_c K_r$$

and

$$a_o H_c K_r K_{px} \gg a_1$$

The proportional and integral gains of the controller can be derived in a manner very much similar to that given in the previous section. The controller constants all have the term  $K_{1x}$  in the denominator. Note that this term depends on  $a_o$ , which is dependent on self-inductance and hence on rotor position and current. Therefore, computation of the current controllers has to be done for every rotor position and current.

The performance of this current controller compared to a conventional current controller is shown in Figure 5.25 for a four-phase machine. The conventional controller has a significant lag during commutation which is persistent during the turn-on but on a much reduced level. The conventional controller's ability to provide high accuracy in tracking even when the current reference is more or less constant is not very high. On both these measures, the performance of the linearized and decoupled controller is striking.

## 5.5 FLUX LINKAGE CONTROLLER

Instead of a current control loop, a flux linkage feedback control loop is attractive from the point of view of its high bandwidth and its decoupling of the influence of other phases on the phase under control.<sup>14</sup> Flux linkage controller design ignoring mutual coupling and saturation is treated in this section. Extension of this approach to include

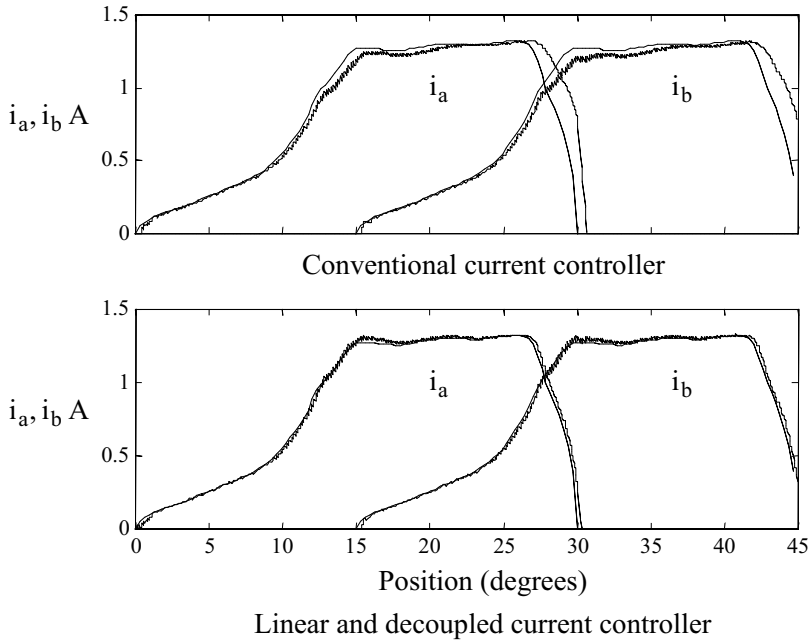


**FIGURE 5.25** Performance of the conventional and devised current controller.

mutual coupling and saturation is straightforward and similar to the procedure given in the previous section.

### 5.5.1 MACHINE WITHOUT MUTUAL COUPLING

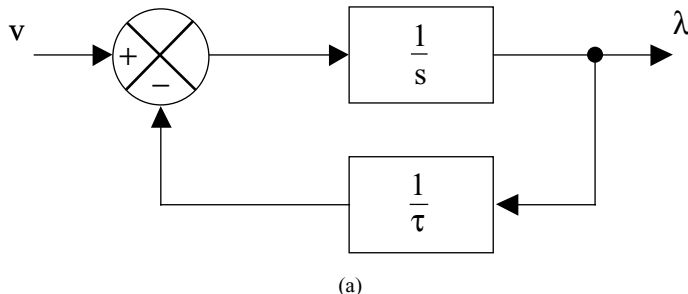
In the case without mutual coupling of phase winding, only one phase needs to be considered for designing the controller. The phase equation in flux linkages is

$$\frac{d\lambda}{dt} = v - Ri = v - \frac{R}{L}\lambda = v - \frac{\lambda}{\tau} \quad (5.69)$$

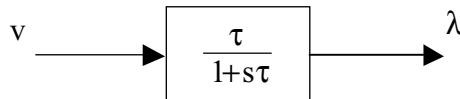
where  $L$  is the phase inductance and is a function of current and rotor position. It can be represented in a block diagram as shown in Figure 5.26. Note that the time constant is a function of current and rotor position, which in turn are time dependent. The transfer function between the flux linkages and input voltage is much simpler compared to the transfer function between the current and input voltage. This clearly indicates that the flux linkage feedback control is much simpler than the current feedback control.

The dependence of the flux linkage control loop on the resistive voltage drop is removed by defining a new input  $u$  as:

$$u = v + Ri \quad (5.70)$$



(a)



(b)

**FIGURE 5.26** Block diagram of one phase of an SRM and its transfer function. (a) Block diagram; (b) transfer function.

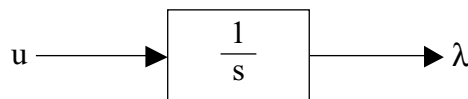


**FIGURE 5.27** Decoupled block diagram of an SRM phase.

Then, the machine equation is written in terms of flux linkage and new input as:

$$\frac{d\lambda}{dt} = v - Ri = u \quad (5.71)$$

This equation represents a linear system. The decoupled system block diagram is shown in [Figure 5.27](#).

The new input  $u$  can be made the output of a proportional-plus-integral controller in tandem with the power converter for which the input is the flux linkage error, given as:

$$u = \frac{K_r}{1 + sT_r} \cdot \frac{K_{p\lambda}(1 + sK_{i\lambda})}{s} [\lambda^* - \lambda] \quad (5.72)$$

This is represented in block diagram form with the machine in [Figure 5.28](#).

Neglecting the converter time constant, the transfer function of the system is of second order and very similar to the transfer function between the current and its command derived in the earlier sections. The gains of the flux linkage controller can be derived using a procedure similar to that outlined earlier in Section 5.4.5. For a

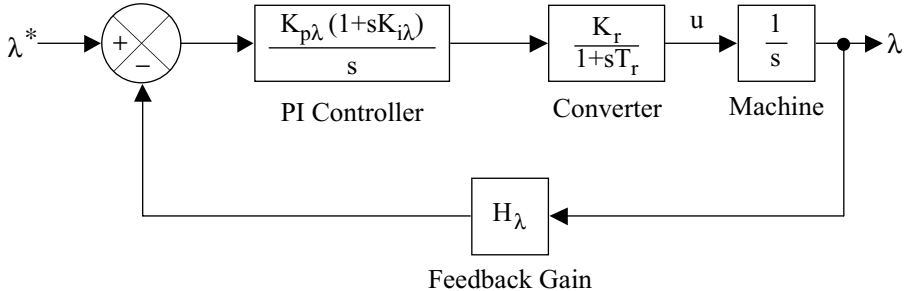


**FIGURE 5.28** Flux linkage feedback control.

given flux linkage bandwidth of  $\omega_\lambda$  and damping ratio  $\zeta_\lambda$ , the controller gains are derived as:

$$K_{p\lambda} = \frac{2\zeta_\lambda\omega_\lambda}{\sqrt{(1+2\zeta_\lambda^2)} + \sqrt{(1+2\zeta_\lambda^2)^2 + 1}} \cdot \frac{1}{H_\lambda K_r} \quad (5.73)$$

$$K_{i\lambda} = \frac{\omega_\lambda^2}{2\zeta_\lambda\sqrt{(1+2\zeta_\lambda^2)} + \sqrt{(1+2\zeta_\lambda^2)^2 + 1}} \quad (5.74)$$

The gains of the flux linkage controller are constants and not functions of rotor position. It is important to note the difference between current and flux linkage control. The current controller requires a gain scheduling to counter the effect of varying rotor position, whereas the flux linkage controller does not require gain scheduling which is of enormous significance in implementation and performance.

## 5.6 TORQUE CONTROL

Airgap torque is precisely regulated in all electrical machines with the control of current. In many machines, such as in ac and dc machines, the airgap torque is directly proportional to the excitation current or a transformed current variable. Therefore, the torque control is fairly straightforward in these machines, resulting in the system being converted into a linear torque amplifier. The direct consequence, then, is that the drive system offers very high performance in its speed control. In the case of the SRM drive system, the airgap torque has no such linear relationship with the excitation current because of the three-dimensional relationship between the flux linkages, excitation current, and rotor position contributing to nonlinear three-dimensional relations between the airgap torque, excitation current, and rotor position. Extraction of the excitation current reference from the airgap torque reference is made using the three-dimensional relationship. This is in contrast to the two-dimensional relationships required for all other motor drives. The complexity of the control task in an SRM drive when making a linear torque amplifier is greater. Many methods can be found

in the literature to obtain a high-performance linear torque amplifier out of the SRM drive. They will be briefly described in this section but one of the most elegant methods is presented in detail, including the effects of mutual coupling and saturation.

### 5.6.1 METHODS OF TORQUE CONTROL

Methods of torque control are dependent on how many phases are excited at a given instant and the current control capability of the system. For example, consider a single-phase excitation control method in which only one phase winding is energized at a time.<sup>5</sup> During the commutation of one phase and initiation of another phase, the current flows in two phases. If the current is not controlled in the outgoing phase and only controlled in the incoming phase, the sum of the airgap torques contributed by the outgoing and incoming phases during this interval need not be a constant. The resultant torque usually has a trough during this interval known as a commutation interval that increases the torque ripple. Torque ripple is undesirable in a high-performance drive system as it may lead to speedier ripple and higher machine losses. The performance of a linear SRM with a single-phase excitation scheme is shown in Figure 5.29. A number of observations deserve merit here: (1) The stator current

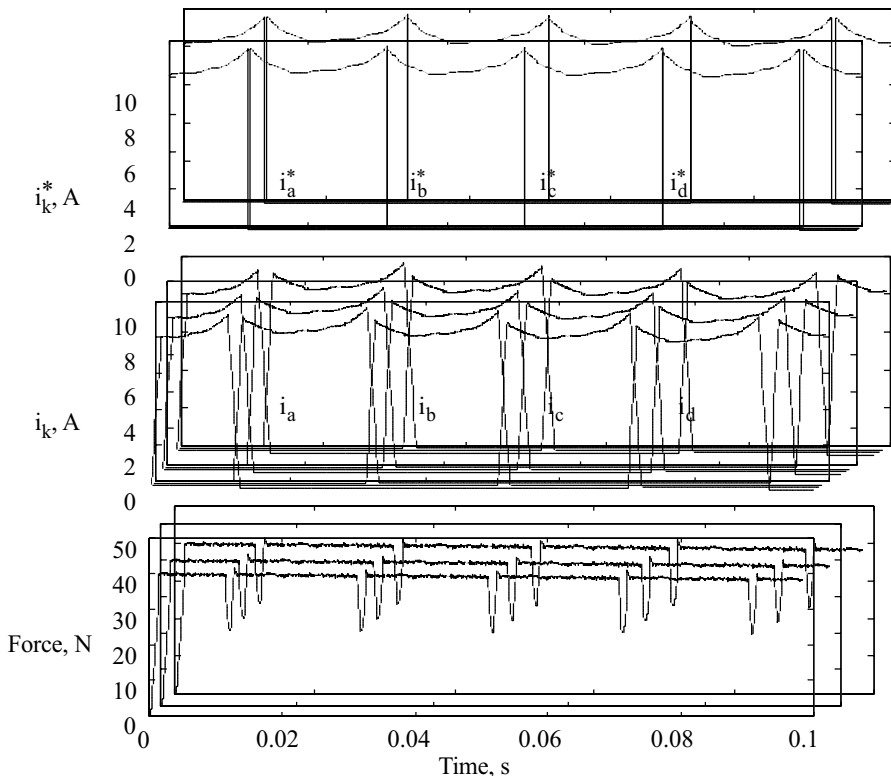


**FIGURE 5.29** Linear SRM performance with one phase excitation at a time.

references have zero rise and fall times that are impossible to generate in a real machine with inductances. (2) The currents are adaptively controlled to yield a constant torque, but the current is not constant during any interval other than the commutation; therefore, a very high-performance current controller is required to enforce the continuously varying phase currents. (3) Because the actual currents have finite rise and fall times, and as the torque constants are not equal for the outgoing and incoming phases, the airgap torque generated during the commutation interval will not equal the reference torque.

A number of techniques have been suggested in the literature to overcome some of the problems facing the torque control.<sup>5,6,7,8,13,14</sup> During the commutation interval, linearly varying currents can be coordinated in the two phases, resulting in smooth current control, but that does not guarantee a constant airgap torque as the torque constants are different for the two phases. But, it does avoid the problem of demanding steep currents in the phases. Instead of using a single-phase excitation, two phases can be coordinated for the torque control but will require greater than normal phase conduction periods. For example, a four-phase machine may require more than 15° conduction in each of its phases using this technique. It may be as much as 30° for the four-phase machine in order to maintain the current control during the commutation interval and to keep the airgap torque equal to its request. The basis of such techniques is that the torque request is distributed to two phases during the commutation interval. The torque may then be written as the sum of, say, phases  $x$  and  $y$  as:

$$T_e^* = T_x^* + T_y^* \quad (5.75)$$

where

$$T_x^* = T_e^* f_x(\theta) \quad (5.76a)$$

$$T_y^* = T_e^* f_y(\theta) \quad (5.76b)$$

where the functions  $f_x(\theta)$  and  $f_y(\theta)$  are the torque distribution functions to phases  $x$  and  $y$ , respectively. Note that they are made functions of the rotor position. For instance, when  $T_e^* \geq 0$  and  $0^\circ \leq \theta < 15^\circ$  for a four-phase, 8/6 SRM,

$$0^\circ < \theta_i < \theta_f < 15^\circ \quad (5.77)$$

where  $\theta_i$  and  $\theta_f$  are the initial and final angle of the commutation region, respectively. These angles are chosen based on the inductance profile of a specific motor. The excitation interval of a phase is smaller than 30° and the phase conduction period

of  $30^\circ$  is not fully utilized in these approaches. Husain et al.<sup>17</sup> proposed following a torque distribution function denoted as TDF I:

$$f_x(\theta) = \begin{cases} 1 & \text{for } 0^\circ \leq \theta < \theta_i \\ (1 + \cos k(\theta - \theta_i))/2 & \text{for } \theta_i \leq \theta < \theta_f \\ 0 & \text{for } \theta_f \leq \theta < 15^\circ \end{cases} \quad (5.78a)$$

$$f_y(\theta) = \begin{cases} 1 & \text{for } 0^\circ \leq \theta < \theta_i \\ (1 - \cos k(\theta - \theta_i))/2 & \text{for } \theta_i \leq \theta < \theta_f \\ 0 & \text{for } \theta_f \leq \theta < 15^\circ \end{cases} \quad (5.78b)$$

where

$$k = 180/(\theta_f - \theta_i) \quad (5.79)$$

Ilic-Spong et al.<sup>6</sup> proposed following a torque distribution function denoted as TDF II:

$$f_x(\theta) = \begin{cases} 1 & \text{for } 0^\circ \leq \theta < \theta_i \\ e^{-(\theta - \theta_i)/k^2} & \text{for } \theta_i \leq \theta < \theta_f \\ 0 & \text{for } \theta_f \leq \theta < 15^\circ \end{cases} \quad (5.80a)$$

$$f_y(\theta) = \begin{cases} 1 & \text{for } 0^\circ \leq \theta < \theta_i \\ 1 - e^{-(\theta - \theta_i)/k^2} & \text{for } \theta_i \leq \theta < \theta_f \\ 0 & \text{for } \theta_f \leq \theta < 15^\circ \end{cases} \quad (5.80b)$$

where

$$k = (\theta_f - \theta_i)/5 \quad (5.81)$$

Both these torque distribution functions are shown in [Figures 5.30](#) and [5.31](#) for initial and final angles of  $6^\circ$  and  $12^\circ$ , respectively.

The first torque distribution function (TDF) has much greater rise and fall times for the phase torque and for the currents compared to the second TDF and therefore may be easier to realize in practice for the chosen initial and final angles of commutation. The currents need not follow the profiles of the torque, as they have a square relationship to the torque; hence, steep variations in them may be required to obtain a constant torque using these TDFs.

A newer method of generating torque distribution functions that allows smooth and gradual variations of the currents has been selected for detailed presentation here. Torque distribution to two phases at any time for the entire possible conduction interval is attempted. Such a feature allows gradual variations of the currents, thus enabling their generation under all conditions in the machine. Three particular cases of torque control are considered: (1) Torque distribution neglecting mutual coupling

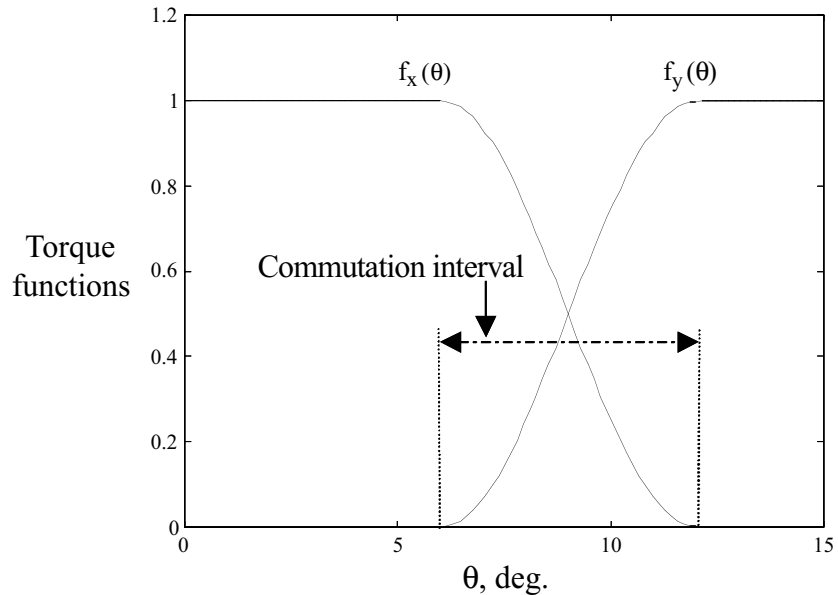


**FIGURE 5.30** First torque distribution functions.

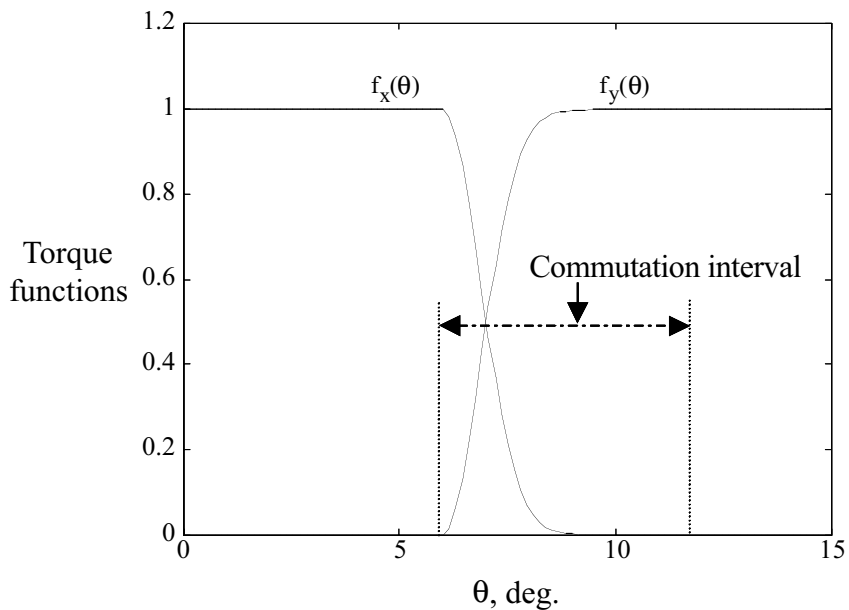


**FIGURE 5.31** Second torque distribution functions.

between the phase windings and saturation, (2) torque distribution considering mutual inductance but ignoring saturation, and (3) torque distribution considering mutual inductance and saturation.

### 5.6.1.1 Torque Distribution Neglecting Mutual Inductance and Saturation

Torque distribution is derived here based on phase currents because the output torque equation in terms of phase currents is elegant and simple. This approach to torque distribution is readily applicable to the model based on flux linkage due to the fact that there are no dynamics involved in the relationship between the phase currents and flux linkages. The method ignores mutual coupling between phases and also the saturation.<sup>13,14</sup> By ignoring saturation, the inductances in the machine phases are only dependent on rotor position and not the excitation currents. The partial derivatives of inductances with respect to rotor position are denoted as  $g$ , with subscripts  $x$  and  $y$  indicating that they are the corresponding self-inductances of phases  $x$  and  $y$ . When  $g$  appears with subscript  $xy$ , it corresponds to the derivative of the mutual inductance with respect to position.

Stator currents  $i_x$  and  $i_y$  track current commands  $i_x^*$  and  $i_y^*$  due to the high-performance current controller, described in earlier sections and therefore can be denoted by:

$$i_x^* \equiv i_x, \quad i_y^* \equiv i_y \quad (5.82)$$

Then the airgap torque is written as:

$$T_e^* = \frac{1}{2}g_x(i_x^*)^2 + \frac{1}{2}g_y(i_y^*)^2 + g_{xy}i_x^*i_y^* \equiv \frac{1}{2}g_xi_x^2 + \frac{1}{2}g_yi_y^2 + g_{xy}i_xi_y = T_e \quad (5.83)$$

Under the assumption of no tracking error, the airgap torque and its reference are equal and so also are the currents and their references. Therefore, the variables and their references are merged into the variables and are given as such from this point on. The torque can be distributed to  $x$  and  $y$ , the two conducting phases of the machine, at any time such that their sum is equal to the airgap torque request. It may be represented as:

$$T_e = T_x + T_y \quad (5.84)$$

where

$$T_x = \frac{1}{2}g_xi_x^2 = f_x T_e \quad (5.85a)$$

$$T_y = \frac{1}{2}g_yi_y^2 = f_y T_e \quad (5.85b)$$

Here, the mutual coupling term is neglected by assuming  $g_{xy}$  is zero. The airgap torque functions  $f_x$  and  $f_y$  have to be determined for two-phase excitation. They can be determined based on many criteria, such as: (1) minimum of the integral of the square of the rate of change of current, (2) minimum rate of change of current, (3) minimum peak current, and (4) minimum stator losses. The currents satisfying one of these criteria can be determined by analytical or numerical methods.

Some constraints can be derived based on the observations that to ensure that the sum of  $T_x$  and  $T_y$  is equal to  $T_e$ ,  $T_x$  and  $T_y$  have the same sign as  $T_e$ , the waveforms of the phase currents or flux linkages are smooth, and the torque distribution functions should satisfy the following constraints:

$$\begin{aligned} f_x(\theta) + f_y(\theta) &= 1 \\ 0 \leq f_x(\theta) \leq 1 &\quad f_x(\theta_i) = 1 \quad f_x(\theta_f) = 0 \quad \text{for } \theta_i \leq \theta \leq \theta_f \\ 0 \leq f_y(\theta) \leq 1 &\quad f_y(\theta_i) = 0 \quad f_y(\theta_f) = 1 \end{aligned} \quad (5.86)$$

where

$$(\theta_i, \theta_f) \in \{(0^\circ, 15^\circ), (15^\circ, 30^\circ), (30^\circ, 45^\circ), (45^\circ, 60^\circ)\}$$

for a four-phase machine. The reference angles  $\theta_i$  and  $\theta_f$  are the initial and final angles of the commutation region, respectively.

Noting the fact that if a larger share of the torque is distributed to a phase whose self-torque function is larger, the magnitude of phase currents can be reduced and the fact that  $g_x$  and  $g_y \geq 0$  for  $\theta_i \leq \theta \leq \theta_f$  and  $g_x(\theta_f) = 0$ ,  $g_y(\theta_i) = 0$ , the following TDFs, denoted hereafter as TDF III, emerge:

$$f_x = \frac{g_x^2}{g_x^2 + g_y^2} \quad (5.87a)$$

for  $\theta_i \leq \theta \leq \theta_f$

$$f_y = \frac{g_y^2}{g_x^2 + g_y^2} \quad (5.87b)$$

It is evident that TDF III satisfies the constraints given in Eq. (5.86). From Eqs. (5.81) and (5.87), the phase currents then are calculated from the torque equation as:

$$i_x = \sqrt{\frac{2g_x T_e}{g_x^2 + g_y^2}} \quad (5.88a)$$

for  $\theta_i \leq \theta \leq \theta_f$

$$i_y = \sqrt{\frac{2g_y T_e}{g_x^2 + g_y^2}} \quad (5.88b)$$

When mutual inductance is neglected, the phase flux linkages are calculated as:

$$\lambda_x = L_x i_x = L_x \sqrt{\frac{2g_x T_e}{g_x^2 + g_y^2}} \quad (5.89a)$$

for  $\theta_i \leq \theta \leq \theta_f$

$$\lambda_y = L_y i_y = L_y \sqrt{\frac{2g_y T_e}{g_x^2 + g_y^2}} \quad (5.89b)$$

**Table 5.1** summarizes TDF III in an excitation period for a four-phase, 8/6 SRM (also shown in [Figure 5.32](#)). The resultant phase currents, flux linkages, and torque error caused by TDF III for a torque request in the first quadrant of operation are shown in [Figures 5.33](#) and [5.34](#), respectively. If  $f_k$  is equal to zero, to avoid unnecessary switching of devices, the corresponding phase is turned off instead of regulating  $i_k$  to zero. Operations in other quadrants are similar to operation in the first quadrant. The rates of change of the phase currents and flux linkages are significantly reduced, but, in spite of them, there exists a torque ripple with a magnitude of 7% peak to peak. This can be solely attributed to the effect of mutual coupling between the phases.

### 5.6.1.2 Torque Distribution Including Mutual Inductance and Neglecting Saturation

For precision applications, the torque ripple induced by the mutual coupling effects is unacceptable. A case in point may be servo drives and electronically controlled steering motor drives using SRM. Note that the SRMs are designed for minimum mutual inductance. As the pole numbers and pole arcs on the stator or rotor increase, mutual coupling between phases invariably comes into effect. In order to eliminate or minimize the effects of mutual coupling appearing in the form of torque ripple in the SRM, the torque distribution functions have to be modified. Such a procedure is given in the following discussion, along with an appropriate torque distribution function derivation referred to as TDF IV.<sup>16</sup>

Including mutual inductance, the airgap torque has three components of torque due to two self-inductances of the two conducting phases and a third due to the mutual coupling of the two phases, represented as:

$$T_e = T_x + T_y + T_{xy} \quad (5.90)$$

where

$$T_x = \frac{1}{2} g_x i_x^2 = f_x T_e \quad (5.91a)$$

$$T_y = \frac{1}{2} g_y i_y^2 = f_y T_e \quad (5.91b)$$

$$T_{xy} = g_{xy} i_x i_y = f_{xy} T_e \quad (5.92)$$

**TABLE 5.1**  
**TDF III in an Excitation Period**

	$T_e^* \geq 0$	$T_e^* < 0$
$f_a$	$\frac{g_a^2}{g_d^2 + g_a^2}$ for $0^\circ \leq \theta < 15^\circ$ $\frac{g_a^2}{g_a^2 + g_b^2}$ for $15^\circ \leq \theta < 30^\circ$ 0 for $30^\circ \leq \theta < 45^\circ$ 0 for $45^\circ \leq \theta < 60^\circ$ 0 for $0^\circ \leq \theta < 15^\circ$ $\frac{g_b^2}{g_a^2 + g_b^2}$ for $15^\circ \leq \theta < 30^\circ$ $\frac{g_b^2}{g_b^2 + g_c^2}$ for $30^\circ \leq \theta < 45^\circ$ 0 for $45^\circ \leq \theta < 60^\circ$ 0 for $0^\circ \leq \theta < 15^\circ$ $\frac{g_c^2}{g_b^2 + g_c^2}$ for $15^\circ \leq \theta < 30^\circ$ $\frac{g_c^2}{g_c^2 + g_d^2}$ for $30^\circ \leq \theta < 45^\circ$ 0 for $45^\circ \leq \theta < 60^\circ$ 0 for $0^\circ \leq \theta < 15^\circ$ $\frac{g_d^2}{g_c^2 + g_d^2}$ for $15^\circ \leq \theta < 30^\circ$ 0 for $30^\circ \leq \theta < 45^\circ$ $\frac{g_d^2}{g_d^2 + g_a^2}$ for $45^\circ \leq \theta < 60^\circ$	0 for $0^\circ \leq \theta < 15^\circ$ 0 for $15^\circ \leq \theta < 30^\circ$ $\frac{g_a^2}{g_d^2 + g_a^2}$ for $30^\circ \leq \theta < 45^\circ$ $\frac{g_a^2}{g_a^2 + g_b^2}$ for $45^\circ \leq \theta < 60^\circ$ $\frac{g_b^2}{g_b^2 + g_c^2}$ for $0^\circ \leq \theta < 15^\circ$ 0 for $15^\circ \leq \theta < 30^\circ$ 0 for $30^\circ \leq \theta < 45^\circ$ $\frac{g_c^2}{g_b^2 + g_c^2}$ for $45^\circ \leq \theta < 60^\circ$ $\frac{g_c^2}{g_c^2 + g_d^2}$ for $0^\circ \leq \theta < 15^\circ$ 0 for $15^\circ \leq \theta < 30^\circ$ 0 for $30^\circ \leq \theta < 45^\circ$ 0 for $45^\circ \leq \theta < 60^\circ$ 0 for $0^\circ \leq \theta < 15^\circ$ $\frac{g_d^2}{g_c^2 + g_d^2}$ for $15^\circ \leq \theta < 30^\circ$ 0 for $30^\circ \leq \theta < 45^\circ$ $\frac{g_d^2}{g_d^2 + g_a^2}$ for $45^\circ \leq \theta < 60^\circ$
$f_b$		
$f_c$		
$f_d$		

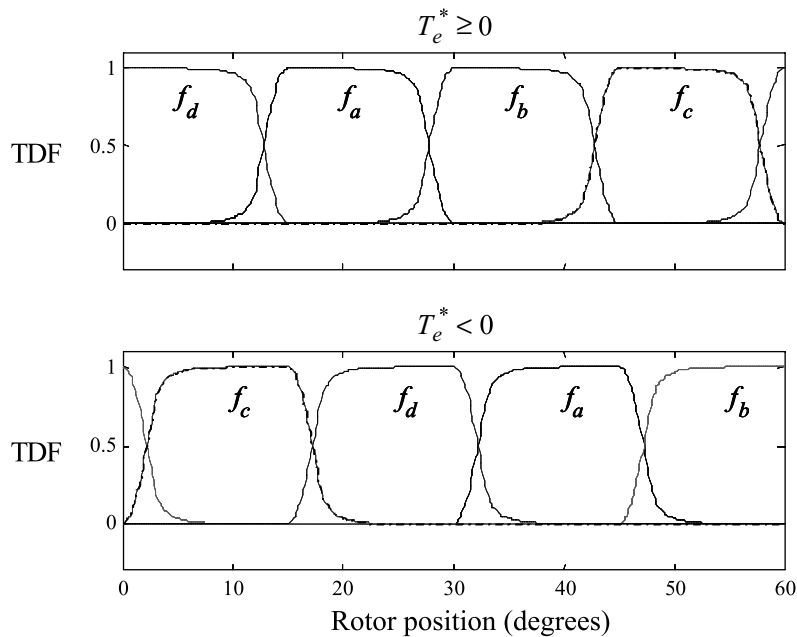


**FIGURE 5.32** TDF III in an excitation period.

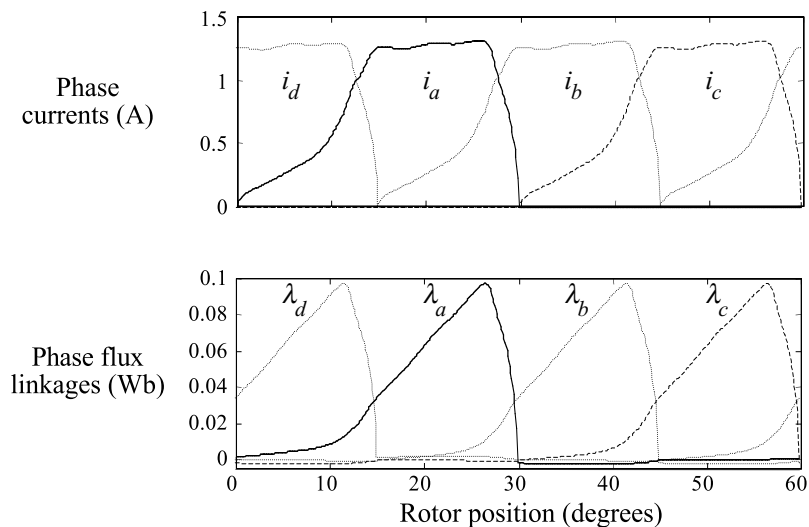


**FIGURE 5.33** Resultant phase currents and flux linkages for TDF I at  $T_e^* = 0.2 \text{ N}\cdot\text{m}$ .

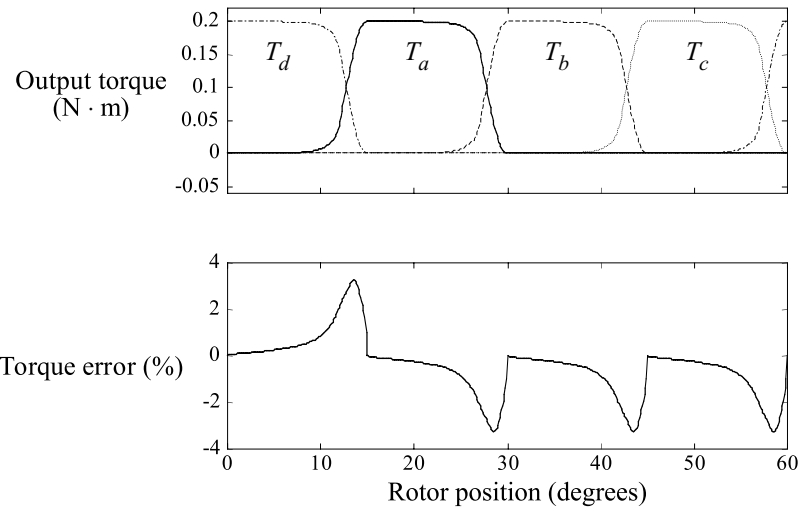


**FIGURE 5.34** Resultant airgap torque and its error for TDF III at  $T_e^* = 0.2 \text{ N}\cdot\text{m}$ .

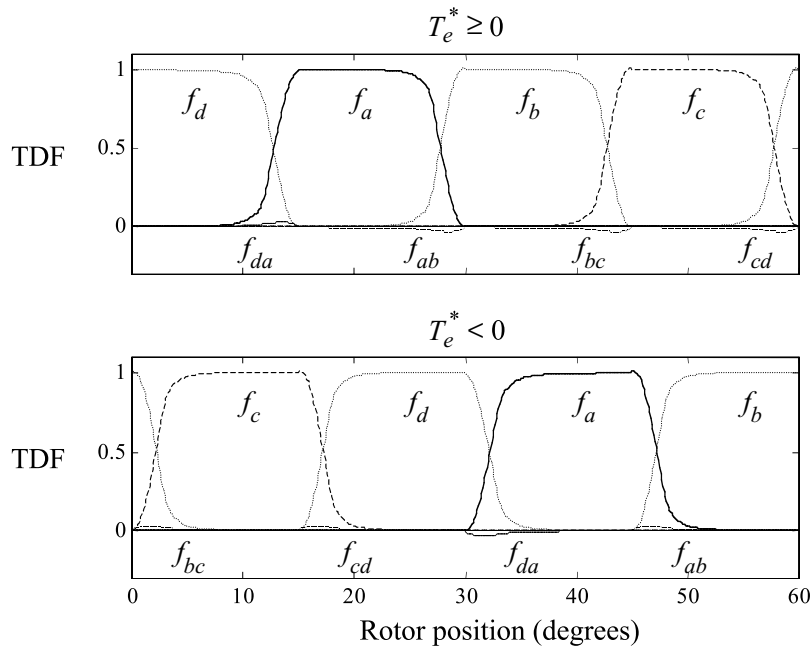


**FIGURE 5.35** TDF IV in an excitation period.

The constraints for new TDF are similar to the constraints derived for the previous TDF but slightly modified as follows:

$$\begin{aligned} f_x(\theta) + f_y(\theta) + f_{xy}(\theta) &= 1 \\ 0 \leq f_x(\theta) \leq 1, \quad f_x(\theta_i) &= 1, \quad f_x(\theta_f) = 0, \quad f_{xy}(\theta_i) = f_{xy}(\theta_f) = 0 \quad \text{for } \theta_i \leq \theta \leq \theta_f \\ 0 \leq f_y(\theta) \leq 1, \quad f_y(\theta_i) &= 0, \quad f_y(\theta_f) = 1, \quad f_{xy}(\theta_i) = f_{xy}(\theta_f) = 0 \end{aligned} \quad (5.93)$$

where

$$(\theta_i, \theta_f) \in \{(0^\circ, 15^\circ), (15^\circ, 30^\circ), (30^\circ, 45^\circ), (45^\circ, 60^\circ)\}$$

for a four-phase machine. TDF III is slightly modified to obtain TDF IV. Because of the quadratic form of TDF III,  $f_x$ ,  $f_y$ , and  $f_{xy}$  can be of the following form to satisfy the constraints given above:

$$f_x = \frac{g_x^2}{g_x^2 + g_y^2 \pm h_{xy}^2} \quad (5.94a)$$

$$f_y = \frac{g_y^2}{g_x^2 + g_y^2 \pm h_{xy}^2} \quad (5.94b)$$

$$f_{xy} = \frac{h_{xy}^2}{g_x^2 + g_y^2 \pm h_{xy}^2} \quad (5.95)$$

where  $h_{xy}$  is the unknown variable to be solved. Note that in the denominator a plus sign applies when the output torque is positive and a minus sign applies when the output torque is negative. From the individual torque component expressions, the phase currents are derived as:

$$i_x = \sqrt{\frac{2T_x}{g_x}} = \sqrt{\frac{2T_e g_x}{g_x^2 + g_y^2 \pm h_{xy}^2}} \quad (5.96a)$$

$$i_y = \sqrt{\frac{2T_y}{g_y}} = \sqrt{\frac{2T_e g_y}{g_x^2 + g_y^2 \pm h_{xy}^2}} \quad (5.96b)$$

Substituting Eq. (5.96) into Eq. (5.92) yields:

$$T_{xy} = \frac{2g_{xy}\sqrt{g_x g_y}}{g_x^2 + g_y^2 \pm h_{xy}^2} T_e \quad (5.97)$$

From Eqs. (5.92), (5.95), and (5.97),

$$h_{xy}^2 = 2g_{xy}\sqrt{g_x g_y} \quad (5.98)$$

Substituting Eq. (5.98) into Eqs. (5.94) and (5.95) yields the torque distribution function, TDF IV, as:

$$f_x = \frac{g_x^2}{g_x^2 + g_y^2 \pm 2g_{xy}\sqrt{g_x g_y}} \quad (5.99a)$$

$$f_y = \frac{g_y^2}{g_x^2 + g_y^2 \pm 2g_{xy}\sqrt{g_x g_y}} \quad \text{for } \theta_i \leq \theta \leq \theta_f \quad (5.99b)$$

$$f_{xy} = \frac{2g_{xy}\sqrt{g_x g_y}}{g_x^2 + g_y^2 \pm 2g_{xy}\sqrt{g_x g_y}} \quad (5.99c)$$

TDF IV satisfies the constraints given in Eq. (5.93); therefore, phase currents are calculated as:

$$i_x = \sqrt{\frac{2g_x T_e}{g_x^2 + g_y^2 \pm 2g_{xy}\sqrt{g_x g_y}}} \quad (5.100a)$$

for  $\theta_i \leq \theta \leq \theta_f$

$$i_y = \sqrt{\frac{2g_y T_e}{g_x^2 + g_y^2 \pm 2g_{xy}\sqrt{g_x g_y}}} \quad (5.100b)$$

And phase flux linkages are calculated as:

$$\lambda_x = L_x \sqrt{\frac{2g_x T_e}{g_x^2 + g_y^2 \pm 2g_{xy}\sqrt{g_x g_y}}} + M_{xy} \sqrt{\frac{2g_y T_e}{g_x^2 + g_y^2 \pm 2g_{xy}\sqrt{g_x g_y}}} \quad (5.101a)$$

for  $\theta_i \leq \theta \leq \theta_f$

$$\lambda_y = M_{xy} \sqrt{\frac{2g_x T_e}{g_x^2 + g_y^2 \pm 2g_{xy}\sqrt{g_x g_y}}} + L_y \sqrt{\frac{2g_y T_e}{g_x^2 + g_y^2 \pm 2g_{xy}\sqrt{g_x g_y}}} \quad (5.101b)$$

TDF IV in an excitation period is summarized in [Table 5.2](#) and plotted in [Figure 5.36](#). The phase currents and flux linkages for 0.2 N·m torque shown in [Figure 5.37](#) are easily realizable in practice because of the gradual variations. [Figure 5.38](#) shows the output torque of each phase containing the self and mutual components. The resultant torque error for TDF IV is zero. So far the saturation has been neglected in the torque control and its inclusion is described in the next section.

### 5.6.1.3 Torque Distribution Including Mutual Inductance and Saturation

In the current controller section, the saturation effects have been included and system equations have been derived. Based on the same understanding, relevant expressions for airgap torque are derived in the following.<sup>14</sup> There is hardly any difference between the approach described in the previous section and the one that follows.

**TABLE 5.2**  
**TDF IV in an Excitation Period**

	$T_e^* \geq 0$	$T_e^* < 0$
$f_a$	$\frac{g_a^2}{g_d^2 + g_a^2 + 2g_{da}\sqrt{g_d g_a}}$ for $0^\circ \leq \theta < 15^\circ$	0 for $0^\circ \leq \theta < 15^\circ$
	$\frac{g_a^2}{g_a^2 + g_b^2 + 2g_{ab}\sqrt{g_a g_b}}$ for $15^\circ \leq \theta < 30^\circ$	0 for $15^\circ \leq \theta < 30^\circ$
	0 for $30^\circ \leq \theta < 45^\circ$	$\frac{g_a^2}{g_d^2 + g_a^2 - 2g_{da}\sqrt{g_d g_a}}$ for $30^\circ \leq \theta < 45^\circ$
	0 for $45^\circ \leq \theta < 60^\circ$	$\frac{g_a^2}{g_a^2 + g_b^2 - 2g_{ab}\sqrt{g_a g_b}}$ for $45^\circ \leq \theta < 60^\circ$
	0 for $0^\circ \leq \theta < 15^\circ$	$\frac{g_b^2}{g_b^2 + g_c^2 - 2g_{bc}\sqrt{g_b g_c}}$ for $0^\circ \leq \theta < 15^\circ$
$f_b$	$\frac{g_b^2}{g_a^2 + g_b^2 + 2g_{ab}\sqrt{g_a g_b}}$ for $15^\circ \leq \theta < 30^\circ$	0 for $15^\circ \leq \theta < 30^\circ$
	$\frac{g_b^2}{g_b^2 + g_c^2 + 2g_{bc}\sqrt{g_b g_c}}$ for $30^\circ \leq \theta < 45^\circ$	0 for $30^\circ \leq \theta < 45^\circ$
	0 for $45^\circ \leq \theta < 60^\circ$	$\frac{g_b^2}{g_a^2 + g_b^2 - 2g_{ab}\sqrt{g_a g_b}}$ for $45^\circ \leq \theta < 60^\circ$
$f_c$	0 for $0^\circ \leq \theta < 15^\circ$	$\frac{g_c^2}{g_b^2 + g_c^2 - 2g_{bc}\sqrt{g_b g_c}}$ for $0^\circ \leq \theta < 15^\circ$
	0 for $15^\circ \leq \theta < 30^\circ$	$\frac{g_c^2}{g_c^2 + g_d^2 - 2g_{cd}\sqrt{g_c g_d}}$ for $15^\circ \leq \theta < 30^\circ$
	$\frac{g_c^2}{g_b^2 + g_c^2 + 2g_{bc}\sqrt{g_b g_c}}$ for $30^\circ \leq \theta < 45^\circ$	0 for $30^\circ \leq \theta < 45^\circ$
	$\frac{g_c^2}{g_c^2 + g_d^2 + 2g_{cd}\sqrt{g_c g_d}}$ for $45^\circ \leq \theta < 60^\circ$	0 for $45^\circ \leq \theta < 60^\circ$
$f_d$	$\frac{g_d^2}{g_d^2 + g_a^2 + 2g_{da}\sqrt{g_d g_a}}$ for $0^\circ \leq \theta < 15^\circ$	0 for $0^\circ \leq \theta < 15^\circ$
	0 for $15^\circ \leq \theta < 30^\circ$	$\frac{g_d^2}{g_c^2 + g_d^2 - 2g_{cd}\sqrt{g_c g_d}}$ for $15^\circ \leq \theta < 30^\circ$
	0 for $30^\circ \leq \theta < 45^\circ$	$\frac{g_d^2}{g_d^2 + g_a^2 - 2g_{da}\sqrt{g_d g_a}}$ for $30^\circ \leq \theta < 45^\circ$
	$\frac{g_d^2}{g_c^2 + g_d^2 + 2g_{cd}\sqrt{g_c g_d}}$ for $45^\circ \leq \theta < 60^\circ$	0 for $45^\circ \leq \theta < 60^\circ$

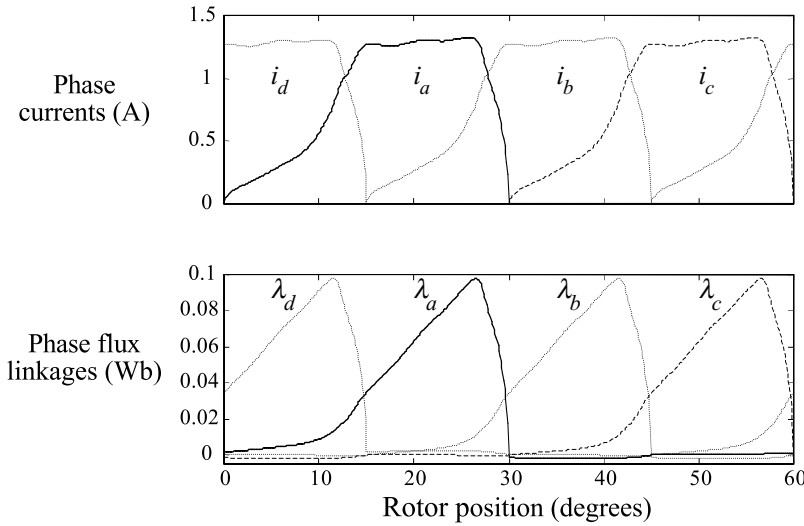


**FIGURE 5.36** Resultant phase currents and flux linkages for TDF IV at  $T_e^* = 0.2 \text{ N}\cdot\text{m}$ .

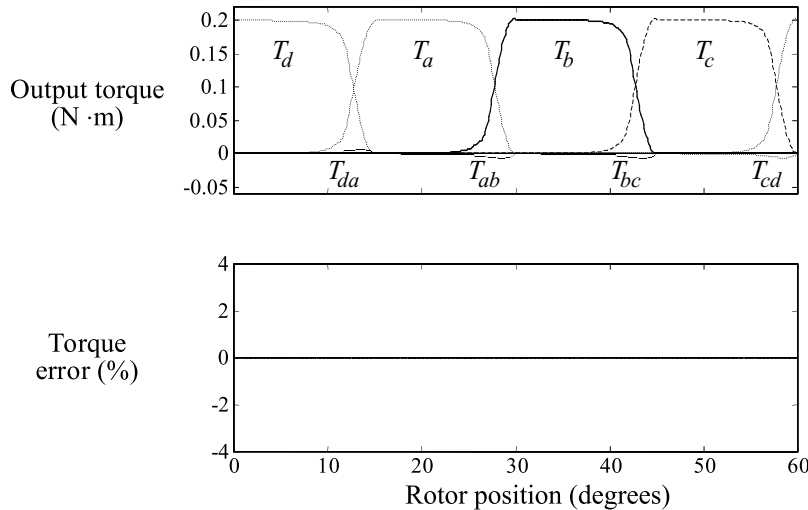


**FIGURE 5.37** Resultant output torque and torque error for TDF II at  $T_e^* = 0.2 \text{ N}\cdot\text{m}$ .

The definition of the torque constants and inductances to include the effect of saturation depends not only on the rotor position but also excitation currents. The complexity of handling the three-dimensional relationship among the airgap torque, current (or flux linkages), and rotor position is increased to include saturation.

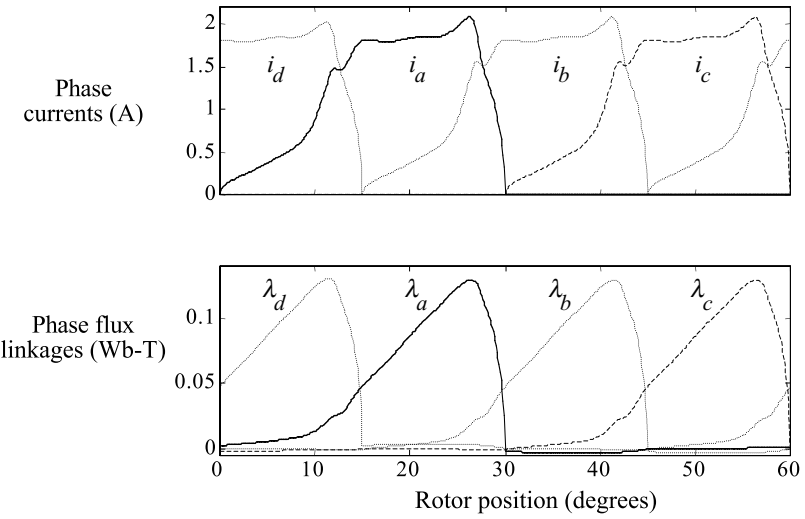


**FIGURE 5.38** Phase currents and flux linkages for TDF V at  $T_e^* = 0.4$  N·m.

The coenergy is derived<sup>10</sup> as:

$$\begin{aligned}
 W_c(i_x, i_y, \theta) &= \int_0^{i_y} \lambda_y(0, \xi, \theta) d\xi + \int_0^{i_x} \lambda_x(\xi, i_y, \theta) d\xi \\
 &= \int_0^{i_y} L_y(\xi, \theta) \xi d\xi + \int_0^{i_x} (L_x(\xi, \theta) \xi + M_{xy}(\xi, i_y, \theta) i_y) d\xi \\
 &= \int_0^{i_x} L_x(\xi, \theta) \xi d\xi + \int_0^{i_y} L_y(\xi, \theta) \xi d\xi + \int_0^{i_x} M_{xy}(\xi, i_y, \theta) i_y d\xi \quad (5.102)
 \end{aligned}$$

where  $\xi$  is an integration variable. The coenergy has three distinct components, each representing the coenergy related to the corresponding self-inductances of two current-conducting phases and the mutual inductance between these two phases, as expected. To have a form similar to the output torque expressions in the earlier sections, the torque components are expressed as:

$$\int_0^{i_x} L_x(\xi, \theta) \xi d\xi = \frac{1}{2} K_x(i_x, \theta) i_x^2 \quad (5.103a)$$

$$\int_0^{i_y} L_y(\xi, \theta) \xi d\xi = \frac{1}{2} K_y(i_y, \theta) i_y^2 \quad (5.103b)$$

$$\int_0^{i_x} M_{xy}(\xi, i_y, \theta) i_y d\xi = K_{xy}(i_x, i_y, \theta) i_x i_y \quad (5.103c)$$

where  $K_x(i_x, \theta)$ ,  $K_y(i_y, \theta)$ , and  $K_{xy}(i_x, i_y, \theta)$  are functions determined by each integral given in Eq. (5.103). Then,  $T_e$  is calculated as:

$$T_e = \frac{\partial W_c(i_x, i_y, \vartheta)}{\partial \theta} \Big|_{i_x, i_y \text{ fixed}} = T_x(i_x, \theta) + T_y(i_y, \theta) + T_{xy}(i_x, i_y, \theta) \quad (5.104)$$

where

$$T_x(i_x, \theta) = \frac{1}{2} \frac{\partial K_x(i_x, \theta)}{\partial \theta} i_x^2 \quad (5.105a)$$

$$T_y(i_y, \theta) = \frac{1}{2} \frac{\partial K_y(i_y, \theta)}{\partial \theta} i_y^2 \quad (5.105b)$$

$$T_{xy}(i_x, i_y, \theta) = \frac{\partial K_{xy}(i_x, i_y, \theta)}{\partial \theta} i_x i_y \quad (5.105c)$$

The new torque functions are defined as:

$$g'_x(i_x, \theta) = \frac{\partial K_x(i_x, \theta)}{\partial \theta} \quad (5.106a)$$

$$g'_y(i_y, \theta) = \frac{\partial K_y(i_y, \theta)}{\partial \theta} \quad (5.106b)$$

$$g'_{xy}(i_x, i_y, \theta) = \frac{\partial K_{xy}(i_x, i_y, \theta)}{\partial \theta} \quad (5.106c)$$

Note that  $g'_x$  and  $g'_y$  are the self-torque functions and  $g'_{xy}$  is the mutual torque function. These torque functions can be evaluated from: (1) the machine three-dimensional relationships through numerical integration and partial differentiation using Eqs. (5.103) and (5.106), respectively; and (2) computing the individual torque components  $T_x(i_x, \theta)$ ,  $T_y(i_y, \theta)$ , and  $T_{xy}(i_x, i_y, \theta)$  for two known phase currents and using Eq. (5.105).

The torque distribution functions are derived using the same procedure given previously. They are the same as given in [Table 5.2](#) except that the torque function  $g$  is replaced by the new torque function  $g'$  given above.

The phase currents and flux linkages at  $T_e^* = 0.4$  N·m for this TDF are shown in [Figure 5.38](#). The rising phase currents and hence flux linkages have steeper gradients where the two adjacent phase currents or flux linkages intersect. The performance of the current controller or the flux linkage controller can be degraded by this phenomenon.

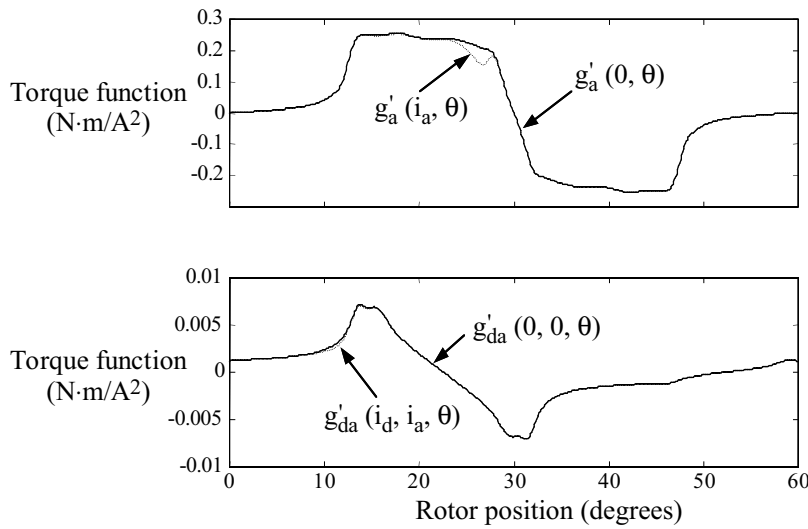


**FIGURE 5.39** Torque functions in an excitation period at  $T_e^* = 0.4$  N·m.

Figure 5.39 shows the self and mutual torque functions for an excitation period using TDF V. Variation in the self-torque function is very slight but in the mutual torque function it is so small that it may be ignored in practice. The implication in implementation is that a simple table of mutual torque function vs. rotor position can be used in the controller regardless of current magnitude. The dependence of the mutual torque function on two-phase currents and rotor position necessitating a three-dimensional table can be dispensed with by using a simple two-dimensional table in the torque controller.

### 5.6.2 SIMULATION RESULTS<sup>14</sup>

Figures 5.40 and 5.41 give airgap torque and phase currents for four different conditions when the phase currents are the controlled states. Figures 5.42 and 5.43 illustrate the drive performance for the same conditions when flux linkages are the controlled states. At low speeds, both controllers show good performance because the current and flux linkage controllers can track commands with negligible error due to smooth reference waveforms. At higher speeds, the current or flux linkage control loop bandwidth is not high enough to track the steep current or flux linkage command due to the presence of a larger induced emf which curtails the reserve voltage available to generate the required current and flux linkage. At lower current, the torque control based on phase currents shows better performance at all speeds than the torque control based on phase flux linkages due to the smaller harmonic distortion in its commands. However, at higher current, the latter shows better performance due to the abrupt changes in the two adjacent current commands around their intersection. At higher current and speed, both  $di/dt$  and  $d\lambda/dt$  become too steep to track the commands. As a result, the torque errors become substantial. This shows that tracking error is

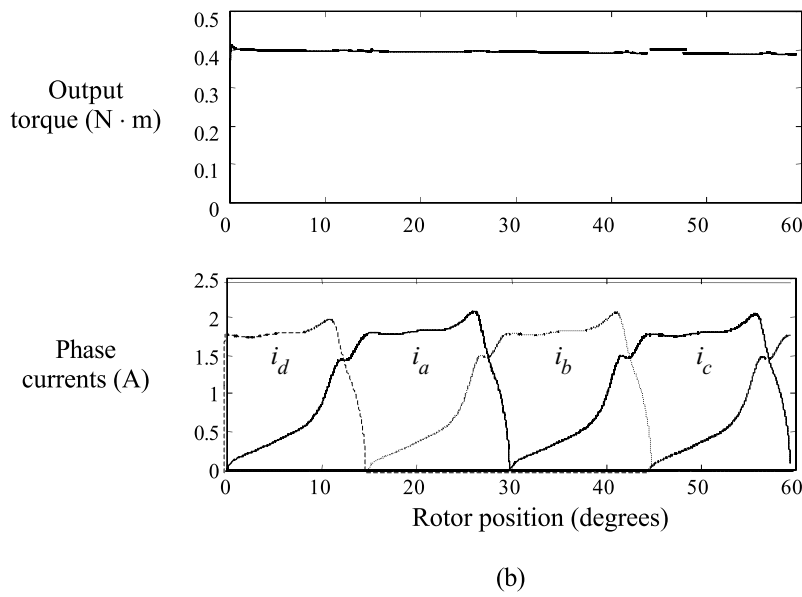
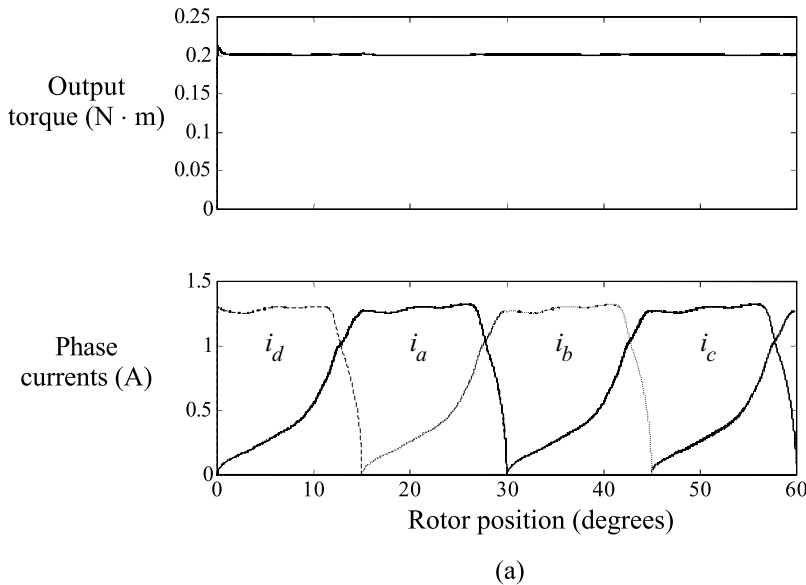
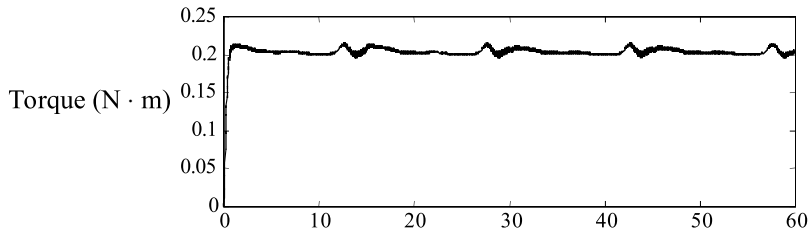
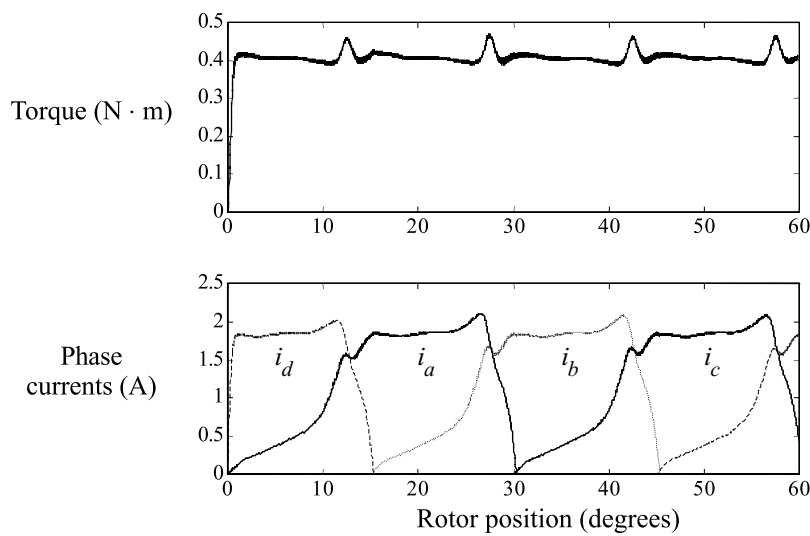


**FIGURE 5.40** Torque control based on phase currents at 100 rpm. (a)  $T_e^* = 0.2 \text{ N}\cdot\text{m}$ ; (b)  $T_e^* = 0.2 \text{ N}\cdot\text{m}$ .

inevitable because of the limited bandwidth of the control loops. To further reduce the torque ripple, this practical limitation should be considered in designing the SRM because overall system performance is determined by the characteristics of the machine as well as by the controller.

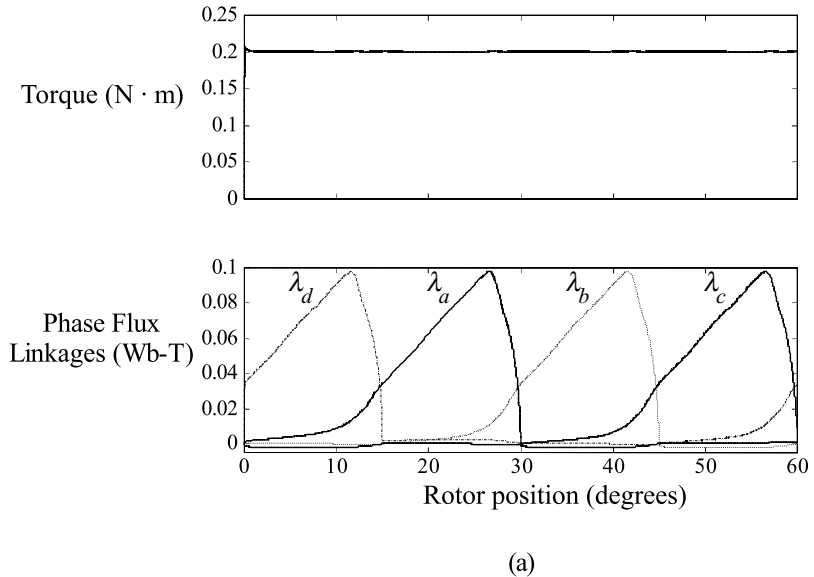


(a)

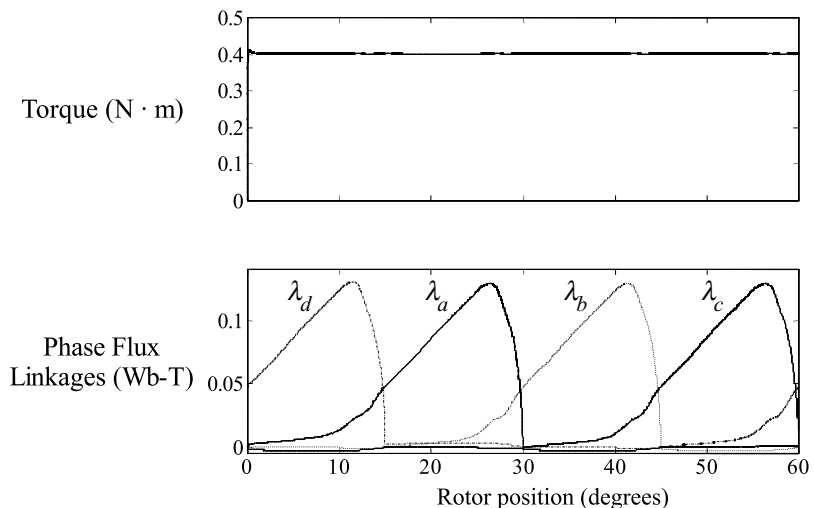


(b)

**FIGURE 5.41** Torque control based on phase currents at 1000 rpm. (a)  $T_e^* = 0.2 \text{ N}\cdot\text{m}$ ; (b)  $T_e^* = 0.4 \text{ N}\cdot\text{m}$ .

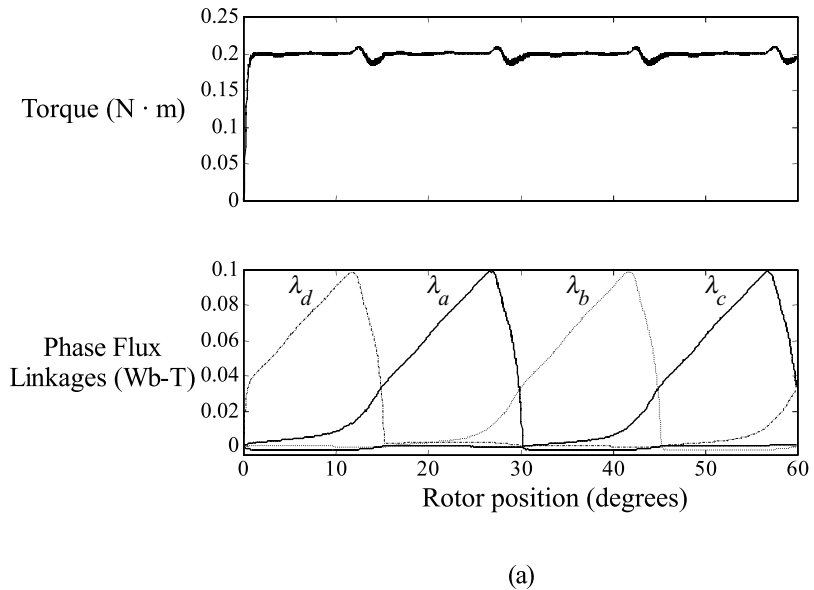


(a)

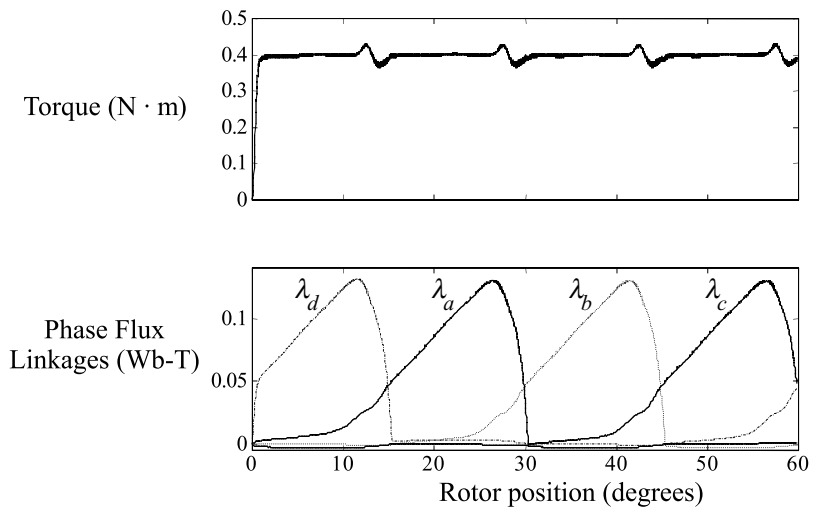


(b)

**FIGURE 5.42** Torque control based on phase flux linkages at 100 rpm. (a)  $T_e^* = 0.2$  N·m; (b)  $T_e^* = 0.4$  N·m.

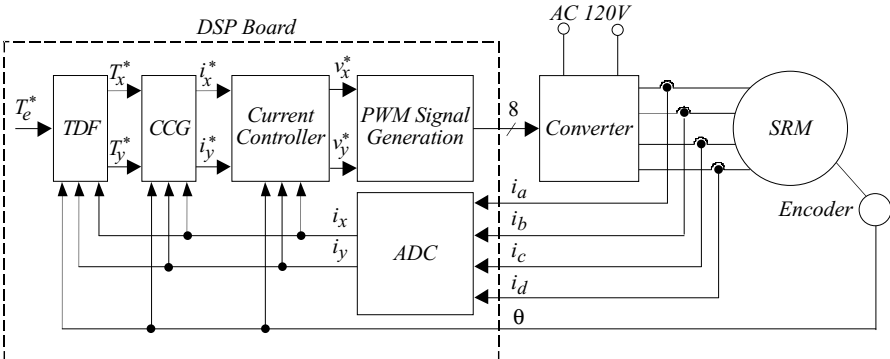


(a)



(b)

**FIGURE 5.43** Torque control based on phase flux linkages at 1000 rpm. (a)  $T_e^* = 0.2$  N·m; (b)  $T_e^* = 0.4$  N·m.



TDF : Torque Distribution Function

CCG : Current Command Generation

ADC : Analog to Digital Converter

**FIGURE 5.44** Implementation of the torque controller.

### 5.6.3 IMPLEMENTATION OF TORQUE CONTROLLER<sup>15</sup>

A block diagram schematic of the torque controller implementation is shown in Figure 5.44 with a four-phase SRM. It is assumed that rotor position and stator instantaneous currents are obtained through appropriate sensors or estimators for this implementation. The feedback currents are processed, conditioned, and converted to digital form through an analog-to-digital conversion (ADC) circuit. It only provides the two conducting-phase current signals to the current and other controllers. When a torque is requested, the torque distribution function controller provides the phase torque commands. It is obtained using the rotor position, phase currents, and TDF tables developed earlier. These phase torque commands are taken in the current command generator block, which, based on the currents and rotor position, provides the phase current commands, which then serve as inputs to the current controller. The current controller, described in previous sections, depending on the algorithm chosen, provides the phase voltage commands. The pulse width modulation block converts these voltage commands into gate-drive signals of the power converter, which, when impressed on the converter, amplifies the commands to the desired levels for application to the machine phases.

### 5.7 DESIGN OF THE SPEED CONTROLLER<sup>15</sup>

Various speed controllers are available in literature.<sup>3,4,15</sup> For industrial use, a proportional plus integral speed controller is presented in this section.<sup>15</sup>

To simplify the design of the speed control loop, it is assumed that the delay of the current loop is negligible due to the fact that usually the speed of response of the current loop is at least ten times faster than the response of the speed loop. To further simplify the design equations, the current loop gain is approximated as unity and its time delay is neglected as it is very, very small compared to all other time constants. Normally, the delay due to the speed feedback may be neglected, which

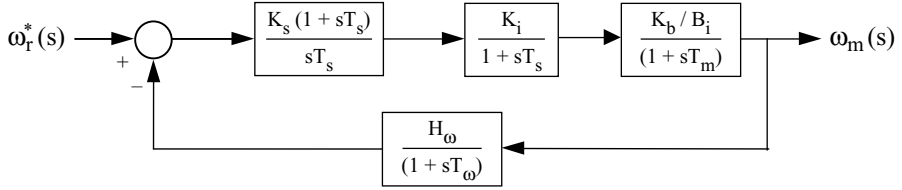


**FIGURE 5.45** Approximated speed loop block diagram.

would reduce the system to a second-order system, but when the speed feedback delay is comparable to the delay of the other subsystems it must be considered in the design process. Given in Figure 5.45 is the block diagram of the approximated speed loop.

Consider the speed loop transfer function given as:

$$GH_\omega(s) = \frac{K_s(1+sT_s)}{sT_s} \cdot \frac{K_b/B_t}{(1+sT_m)} \cdot \frac{H_\omega}{(1+sT_\omega)} \quad (5.107)$$

Near the gain crossover frequency, as  $T_m$  is large compared to other time constants, the following approximation is made:

$$(1+sT_m) \approx sT_m \quad (5.108)$$

This results in the speed loop transfer function as:

$$GH_\omega(s) \approx \frac{K_2 \cdot K_s}{T_s} \cdot \frac{(1+sT_s)}{s^2(1+sT_\omega)} \quad (5.109a)$$

where

$$K_2 = \frac{K_b H_\omega}{B_t T_m} \quad (5.109b)$$

From this, the closed loop speed-transfer function is approximately derived as:

$$\frac{\omega_m(s)}{\omega_r^*(s)} \approx \frac{1}{H_\omega} \left[ \frac{GH_\omega(s)}{1+GH_\omega(s)} \right] = \frac{1}{H_\omega} \cdot \frac{a_0 + a_1 s}{a_0 + a_1 s + a_2 s^2 + a_3 s^3} \quad (5.110)$$

where the coefficients of the polynomials are

$$a_0 = \frac{K_2 K_s}{T_s} \quad (5.111)$$

$$a_1 = K_2 K_s \quad (5.112)$$

$$a_2 = 1 \quad (5.113)$$

$$a_3 = T_\omega \quad (5.114)$$

To optimize the gain of the closed-loop, speed-transfer function, the denominator of the magnitude response function is minimized to provide a flat frequency response (i.e., symmetric optimum). Such a condition gives a relationship between the coefficients of the characteristic polynomial leading to evaluation of the speed controller constants as given below:

$$\left| \frac{\omega_m(j\omega)}{\omega_r^*(j\omega)} \right| = \frac{1}{H_\omega} \sqrt{\frac{a_0^2 + a_1^2 \omega^2}{[a_0^2 + a_1^2 - (2a_0a_2)\omega^2 + (a_2^2 - 2a_1a_3)\omega^4 + a_3\omega^6]}} \quad (5.115)$$

from which the coefficients are related by:

$$a_1^2 = 2a_0a_2 \quad (5.116)$$

$$a_2^2 = 2a_1a_3 \quad (5.117)$$

to give a flat frequency response. From the above two conditions, the speed controller constants are evaluated as:

$$K_s = \frac{1}{2K_2 T_\omega} \quad (5.118)$$

$$T_s = 4T_\omega \quad (5.119)$$

### 5.7.1 FEATURES OF THE SYMMETRIC OPTIMUM FUNCTION<sup>1</sup>

Substituting for  $K_s$  and  $T_s$  we can obtain the closed-loop, speed-transfer function in terms of  $T_\omega$  as:

$$\frac{\omega_m(s)}{\omega_r^*(s)} = \frac{1}{H_\omega} \cdot \frac{1 + 4T_\omega s}{1 + 4T_\omega s + 8T_\omega^2 s^2 + 8T_\omega^3 s^3} \quad (5.120)$$

For the open-loop gain function, the corner points are  $1/4T_\omega$  and  $1/T_\omega$  with a gain crossover frequency of  $1/2T_\omega$ . In the vicinity of the gain crossover frequency the slope of the magnitude response is  $-20$  dB/decade, which is the most desirable characteristic for good dynamic behavior. Because of its symmetry at the gain crossover frequency, this transfer function is known as a symmetric optimum function. Further, this transfer function has the following features:

1. Approximate time constant of the system is  $4T_\omega$
2. The step response is given by:

$$\omega_r(t) = \frac{1}{H_\omega} \{ (1 + e^{-t/2T_\omega}) - 2e^{-t/4T_\omega} \cos(\sqrt{3}t/4T_\omega) \} \quad (5.121)$$

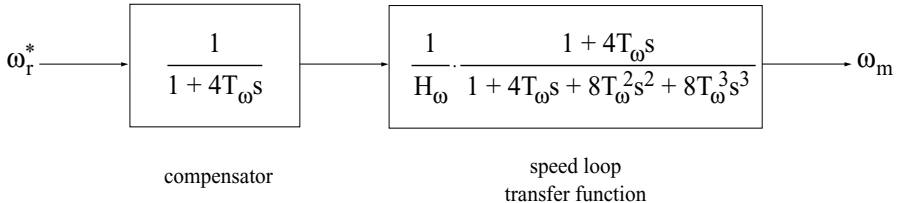


**FIGURE 5.46** Smoothing of the overshoot with a compensator.

with a rise time of  $3.1T_\omega$ , maximum overshoot of 43.4%, and a settling time of  $16.5T_\omega$ .

3. Because the overshoot is high, it can be reduced by compensating for its cause (i.e., the zero by a pole in the speed command path, as shown in the [Figure 5.46](#)). The resulting transfer function of the speed to its command is

$$\frac{\omega_m(s)}{\omega_r^*(s)} = \frac{1}{H_\omega} \left[ \frac{1}{1 + 4T_\omega s + 8T_\omega^2 s^2 + 8T_\omega^3 s^3} \right] \quad (5.122)$$

whose step response is

$$\omega_r(t) = \frac{1}{H_\omega} \left\{ \left( 1 - e^{-t/4T_\omega} - \frac{2}{\sqrt{3}} e^{-t/4T_\omega} \sin(\sqrt{3}t/4T_\omega) \right) \right\} \quad (5.123)$$

with a rise time of  $7.6T_\omega$ , maximum overshoot of 8.1%, and a settling time of  $13.3T_\omega$ . Even though the rise time has increased, the overshoot has been reduced to approximately 1/5th of its previous value, and the settling time has come down by 19%.

4. The poles of the transfer function are

$$s = -\frac{1}{2T_\omega}; \quad -\frac{1}{4T_\omega} \pm j \frac{\sqrt{3}}{4T_\omega} \quad (5.124)$$

As the real part of the poles are negative and there are no repeated poles at the origin, the system is asymptotically stable. Hence, in the symmetric optimum design, the system stability is guaranteed and there is no need to check for it in the design process. Whether this is true for the original system without approximation will be explored in the following example.

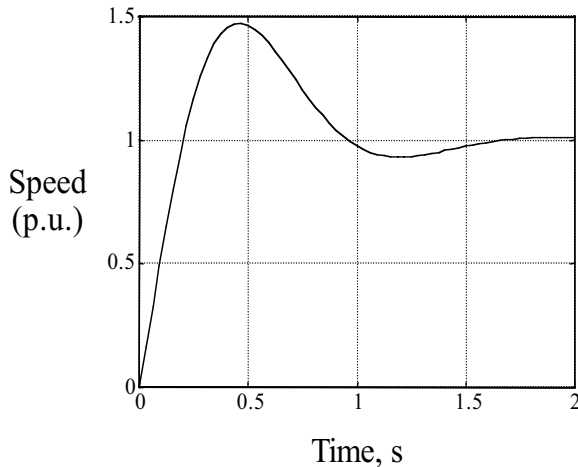


**FIGURE 5.47** Step response of the speed loop.

- Symmetric optimum eliminates the effects due to the disturbance very rapidly compared to other optimum techniques employed in practical systems such as linear and modulus optimum, etc. This approach indicates one of the possible methods to synthesize the speed controller. The judicious choice of approximation is based on the physical constants of the motor, converter, and transducer gains and delays.

### 5.7.2 SIMULATION RESULTS

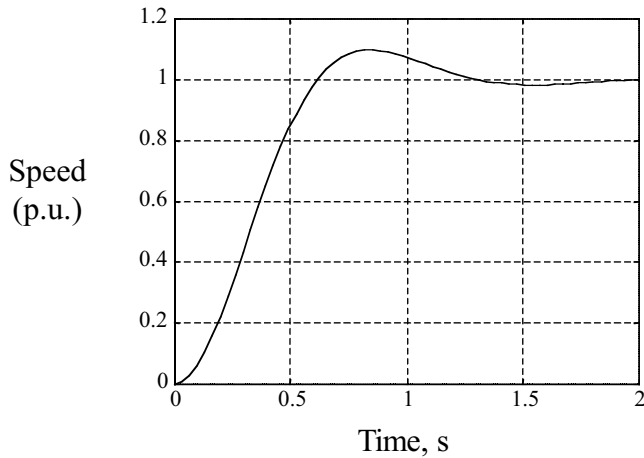
An SRM drive given in Example 1 (Section 5.4.4.1) is instrumented with a speed controller with gain constant  $K_s = 0.223$  and time constant  $T_s = 0.308$  sec. Shown in [Figure 5.47](#) are the step and frequency response of the unapproximated speed loop. The bandwidth of the resulting speed loop is approximately 15.9 Hz, and the overshoot for the step response is large.

To reduce the overshoot in the speed response, a soft start is placed between the reference command and the SRM drive system, which has a time constant of the same magnitude as the speed controller time constant. The following is the transfer function of the soft start:

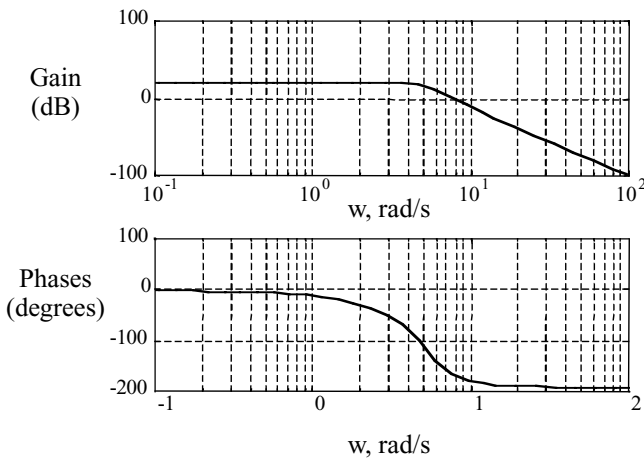
$$S(s) = \frac{1}{1 + 0.3808 s} \quad (5.125)$$

Shown in [Figure 5.48](#) are the step and frequency responses of the SRM drive system with a soft start. Even though the bandwidth of the system is reduced to approximately 6.37 Hz, the overshoot is very small compared to the previous response.

[Figure 5.49](#) shows the dynamic simulation of the speed loop. Shown in the first plot is the speed command at 1 p.u. and its response and the torque command and



(a)



(b)

**FIGURE 5.48** Step and frequency response of speed loop with soft start. (a) Step response of speed loop transfer function with soft start; (b) frequency response of speed loop with soft start.

its response. The response is oscillatory during settling. Torque does not particularly track its command at high speeds. Also, it has a large torque ripple. Note that this drive has a low-performance current controller with no torque control. High-performance speed control can be obtained when a linearized and decoupled current controller with torque control using torque distribution functions is implemented.

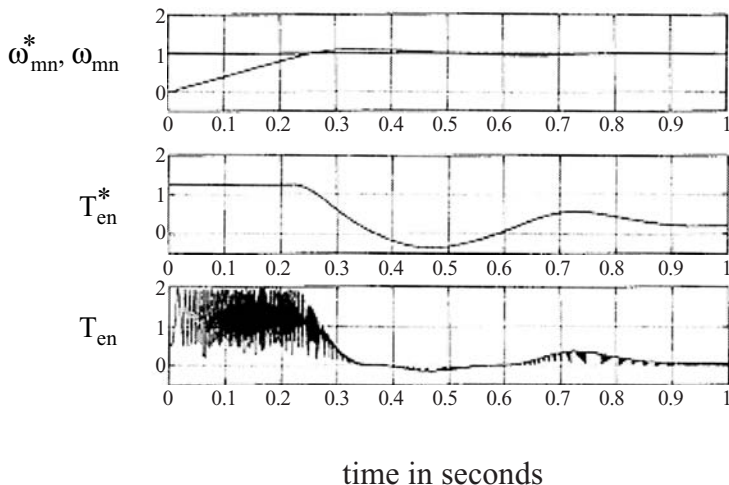


**FIGURE 5.49** Speed loop simulation results in normalized variables for a step speed command.

## REFERENCES

1. Krishnan, R., *Electric Motor Drives*, Prentice-Hall, Englewood Cliffs, NJ, 2001.
2. Krishnan, R., X. Mang, and A.S. Bharadwaj, A low-cost SRM analog controller, *Electronic Motortechnics*, Feb/March 1990, pp. 19–23.
3. John, G. and A.R. Eastham, Speed control of SRM using slide mode control strategy, *Conf. Rec. IEEE IAS Ann. Mtg.*, Oct. 1995, pp. 263–270.
4. Buja, G.S., R. Menis, and M.I. Valle, Variable structure control of an SRM drive, *IEEE Trans. on Industrial Electronics*, 40(1), 56–63, 1993.
5. Schramm, D.S., B.W. Williams, and T.C. Green, Torque ripple reduction of switched reluctance motors by phase current optimal profiling, *IEEE Power Electronics Specialist Conf.*, 1992, pp. 857–860.
6. Ilic-Spong, M., T.J.E. Miller, S.R. MacMinn, and J.S. Thorp, Instantaneous torque control of electric motor drives, *IEEE Trans. on Power Electronics*, 2(1), 55–61, 1987.
7. Wallace, R.S. and D.G. Taylor, A balanced commutator for switched reluctance motors to reduce torque ripple, *IEEE Trans. on Power Electronics*, 7(4), 617–626, 1992.
8. Kim, C.H. and I.J. Ha, A new approach to feedback-linearizing control of variable reluctance motors for direct-drive applications, *IEEE Trans. on Control Syst. Technol.*, 4(4), 348–362, 1996.
9. Pillay, P., Y. Liu, W. Cai, and T. Sebastian, Multiphase operation of switched reluctance motor drives, *IEEE Ind. Appl. Soc. Ann. Mtg. Conf. Rec.*, 1997, pp. 310–317.
10. Krause, P.C., *Analysis of Electric Machinery*, McGraw-Hill, 1986.
11. Bae, H.K. and R. Krishnan, A study of current controllers and development of a novel current controller for high performance SRM drives, *IEEE Ind. Appl. Soc. Ann. Mtg. Conf. Rec.*, 1996, pp. 68–75.
12. Slotine, J.J.E. and W. Li, *Applied Nonlinear Control*, Prentice-Hall, Englewood Cliffs, NJ, 1991.

13. Bae, H.K., B.S. Lee, P. Vijayraghavan, and R. Krishnan, A linear switched reluctance motor: converter and control, *IEEE Trans. Ind. Appl.*, Vol. 36, No. 6, Nov./Dec. 2000, pp. 1351–1359.
14. Bae, H.K., Control of Switched Reluctance Motors Considering Mutual Inductance, Ph.D. thesis, The Bradley Department of Electrical and Computer Engineering, Virginia Tech., Blacksburg, VA, August 2000.
15. Jackson, T.W., Design and development of a low-cost controller for SRM drive, M.S. Thesis, The Bradley Department of Electrical and Computer Engineering, Virginia Tech., Blacksburg, VA, July 1996.
16. Bae, H.K. and R. Krishnan, A novel approach to control of switched reluctance motors considering mutual inductance, *IEEE Ind. Electronics Conf.*, Oct. 2000, Nagoya, Japan, pp. 369–374.
17. Husain, I. and M. Ehsani, Torque ripple minimization in switched reluctance motor drives by PWM control, *IEEE Trans. on Power Electronics*, Vol. 11, No. 1, 1996, pp. 83–88.
18. Rim, Guen-hie., Variable speed constant frequency power conversion with permanent magnet synchronous and switched reluctance generators, Ph.D. Thesis, The Bradley Department of Electrical and Computer Engineering, Virginia Tech., Blacksburg, VA, February 1992.

---

# 6 Modeling and Simulation of the SRM Drive System

## 6.1 INTRODUCTION

The SRM drive system simulation is much more complex than ac and dc motor drives because its operational region is mostly nonlinear. The nonlinearity is introduced by the following three factors:

1. The nonlinear B-H characteristics of the magnetic material
2. The dependence of phase flux linkages on both the rotor position and current magnitude; in other machines, it is dependent only on the current magnitude as the rotor position dependence is eliminated artificially with trigonometric transformations not feasible with an SRM
3. The single source of excitation

Consider the separately excited dc machines and synchronous machines having two sources of excitation, one for its field and the other to the armature. In these, the torque is proportional to the product of the armature and field currents. The system is made linear by keeping the magnetization (field) current constant, thus making the torque-producing part of the (armature) current a variable to provide a variable air gap torque as in the case of dc and ac machines. The implication of the excitation source being single is that the machine's torque is proportional to the square of the excitation current, among other things, resulting in a nonlinear system through the coupling of the air gap torque to the load through the mechanical system. The inability to separate the excitation current into a magnetizing or flux-producing part and a torque-producing part makes it difficult to obtain a high-performance control in the SRM drives.

The earlier chapters developed a procedure for designing an SRM, selecting a suitable converter topology to drive it, and designing a current controller, torque-smoothing controller, and speed controller. The controllers integrate the machine, converter, and load to deliver a specified performance for the entire motor drive system. A dynamic simulation of the drive system enables verification of the analytical designs and ability of the motor drive system to match the load torque over its entire speed range both in its steady state and during transients. With such a verification, time and cost of product development are minimized by avoiding a trial-and-error approach to prototype construction that may lead to repetitive testing and redesign until specifications are met. Such a trial-and-error process in design is very costly and time consuming.

Simulation of the drive system requires models for the SRM drive subsystems and their interconnections. This chapter contains the subsystem models and their derivation and a procedure for simulation of the drive system. The simulation procedure

is also illustrated with many cases of SRM operation. Single-quadrant and four-quadrant drive system dynamic performances are illustrated. Also included is load compensation of the drive system for compressor load.

## 6.2 MODELING

A general schematic of a drive system<sup>14,15,17,20</sup> shown in [Figure 6.1](#) is considered. Practical drive systems may vary from this general schematic. Variations from this block diagram may be minor, are usually confined to the controller section, and are specific to applications. Therefore, only common but essential elements of the drive system are given consideration to generalize the procedure. Application-specific controller blocks can be modeled similar to the modeling process developed in the controller subsection. The modeling of various subsystems of the SRM drive is considered in this section. The modeling procedure for the machine in terms of its three-dimensional relationships of flux linkages, current, and rotor positions and air gap torque, current, and rotor position is derived. Given a torque command, the current reference for a particular rotor position is found from these three-dimensional relationships. When the current reference is enforced through a converter, one or more phases of the machine windings are impressed with a voltage. The machine equations, the input voltages, and the machine characteristics captured in the three-dimensional relationships are used to determine the phase currents, air gap torque, rotor speed, and rotor position. With the available computed currents and rotor speed, their respective errors are then found for use in the controller to determine the reference current and torque. This almost completes the tasks of the controller for speed and average torque enforcement. For an instantaneous torque controller, the torque reference to current reference generation is a function of rotor position, and various algorithms discussed in Chapter 5 may be used.

### 6.2.1 MACHINE MODEL

The magnetization characteristics of the machine can be obtained from finite element simulation of the machine given the B-H characteristics of the lamination material, machine dimensions, and winding data. Alternatively, they can be computed from the analytical approach<sup>5,16,18</sup> outlined in Chapter 2 using finite element analysis methods<sup>9,10,11</sup> or measured.<sup>21</sup> However they may be obtained, a large data set in the form of three-dimensional relationships results for flux linkages vs. current vs. rotor position and air gap torque vs. current vs. rotor position. These characteristics are shown for an 8/6 machine<sup>36</sup> in [Figures 6.2](#) and [6.3](#), respectively, for a finite set of currents and rotor position. For currents and rotor positions within the given finite sets there could be infinite sets, and for these sets a procedure is required to compute the flux linkages and air gap torque. Further, the handling of such large data sets is a formidable problem in the modeling process. Some methods are discussed here to model the machine characteristics. Only one phase is considered, and its extension to other phases is achieved considering the appropriate position shift between the phases and applying it to the known phase characteristics.

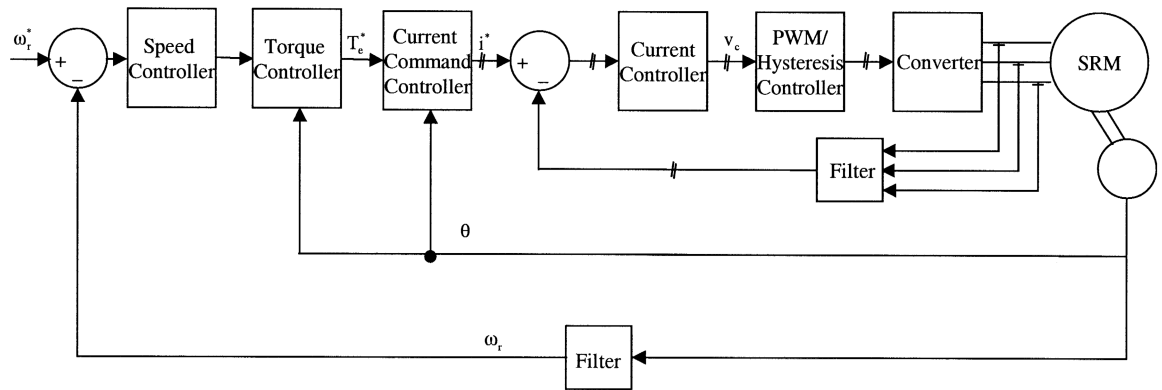


**FIGURE 6.1** Closed-loop, speed-controlled SRM drive system.

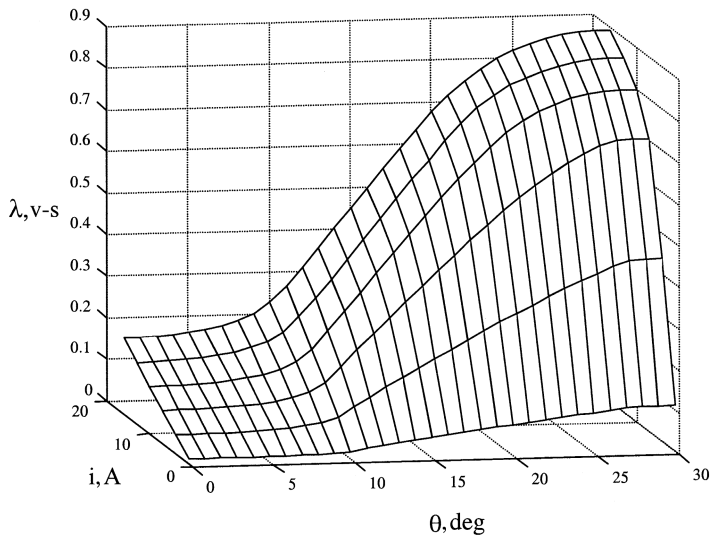


**FIGURE 6.2** Flux linkages vs. current vs. rotor position characteristics of an 8/6 SRM.

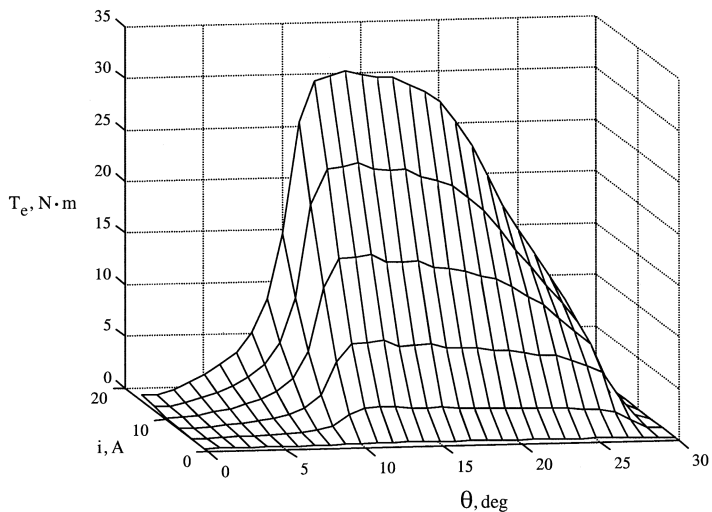


**FIGURE 6.3** Air gap torque vs. current vs. rotor position characteristics of an 8/6 SRM.

#### 6.2.1.1 Per Phase Model

The voltage equation for one phase of the SRM assuming that there is no mutual coupling to other phases is given by:

$$v = R_s i + \frac{d\lambda(\theta, i)}{dt} \quad (6.1)$$

where  $i$  is the phase current,  $R_s$  is the resistance of the phase,  $v$  is the voltage applied across the phase winding, and  $\lambda(\theta, i)$  is the phase flux linkages for a given rotor position  $\theta$  and excitation current  $i$ . The rate of change of flux linkages with respect to time can be obtained in many ways<sup>3,4</sup> assuming that:

$$\lambda(\theta, i) = L(\theta, i)i \quad (6.2)$$

$$p\lambda(\theta, i) = L(\theta, i)|_{\theta=\text{const}} \frac{di}{dt} + i \frac{dL(\theta, i)}{dt} \Big|_{i=\text{const}} \quad (6.3)$$

where  $p$  is the derivative operator,  $d/dt$ . The inductance  $L$  is the self-inductance of the machine phase, and it is available as a function of excitation current and rotor position. Also, the derivative of flux linkages can be obtained using partial derivatives as:

$$p\lambda(\theta, i) = \frac{\partial\lambda(\theta, i)}{\partial i} \frac{di}{dt} + \frac{\partial\lambda(\theta, i)}{\partial\theta} \frac{d\theta}{dt} = \ell(\theta, i) \frac{di}{dt} + \omega_m \frac{\partial\lambda(\theta, i)}{\partial\theta} \quad (6.4)$$

where  $\ell(\theta, i)$  is the incremental inductance, so-named because it is the ratio between the incremental flux linkages and incremental excitation current. The incremental inductance is again referred to in Chapter 8 on sensorless SRM drives. The relationship between the self-inductance and incremental inductance is given by:

$$L(\theta, i) = \frac{1}{i} \int_0^i \ell(\theta, i) di \quad (6.5)$$

Note that the self-inductance is different from the incremental inductance when the operating condition is not linear, which is usually the case in an SRM drive system.

### 6.2.1.2 Representation of Machine Magnetic Characteristics<sup>33</sup>

Equations (6.3) and (6.4) give different ways of computing the rate of change of flux linkages and are determined by how the machine data can be arranged in a form suitable to realize them through these equations. Whichever may be the equation used in the final solution of the flux linkages and current for a given voltage input, one thing becomes clear upon a cursory glance of the flux linkage equations—it requires a large amount of discrete data. The data are discrete in terms of the current vs. rotor position vs. flux linkages, and by using a cubic spline fit, given current and rotor position, the flux linkages can be retrieved. Consider a set of flux linkage vs. phase excitation current vs. rotor position characteristics shown in [Figure 6.4](#). The data may have excitation currents of interest (say, from zero to 2 p.u. in usual circumstances and more for specific applications). The rotor position it may cover is from a completely unaligned to fully aligned position given as  $\theta_u$  and  $\theta_a$ , respectively. The retrieval of flux linkages can be achieved in many ways, as discussed in the following. The three-dimensional fit of  $\lambda(\theta, i)$  is accomplished by first creating two sets of two-dimensional natural cubic splines. One set contains spline fit curves

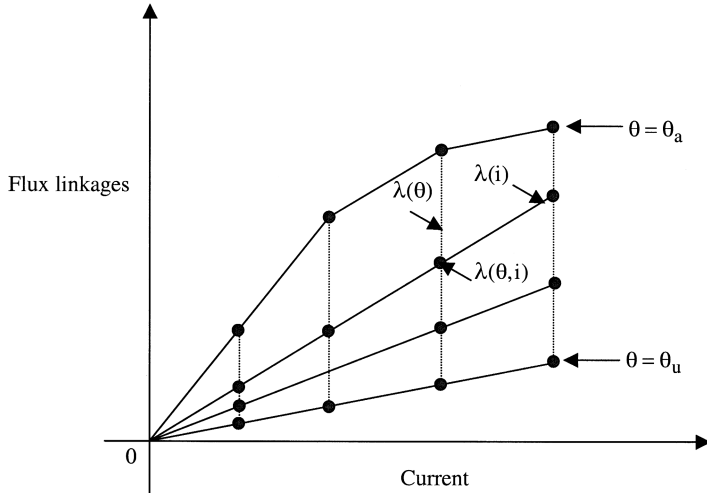


**FIGURE 6.4** Phase flux linkages vs. current for varying rotor positions.

of  $\lambda(\theta)$  for each value of  $n_i$  current values and the second set contains the curves of  $\lambda(i)$  for each of the  $n_\theta$  rotor positions. The two sets are then described as:

$$\lambda(\theta)|_{i=i(j)}, \quad \text{for } j = 0, 1, \dots, n_i \quad (6.6)$$

$$\lambda(\theta)|_{\theta=\theta(k)}, \quad \text{for } k = 0, 1, \dots, n_\theta \quad (6.7)$$

### 6.2.1.3 Method 1

From these two sets of two-dimensional spline fits, the flux linkages for any position and current can be extracted by using the following algorithm.<sup>33,34</sup> Given the excitation current at a rotor position, the algorithm uses a linear interpolation to find flux linkages. Accuracy can be improved with nonlinear algorithms for interpolation but will require additional computational steps. The accuracy of the solution vs. computational burden needs to be considered for final implementation of the search algorithm to find the flux linkages.

Consider the required flux linkages for a current and rotor position in the space enclosed by four flux linkage points defined by the combination of two currents  $i_1$  and  $i_2$  and two rotor positions  $\theta_1$  and  $\theta_2$ . Only that part of the data set is displayed in Figure 6.5 for clarity. It is noted that the data points are unequally spaced but the algorithm is general to cover both the equal and unequal spacing in data sets. The flux linkages for a current  $i$  such that  $i_1 < i < i_2$ , using linear interpolation, can be derived as:

- Given the current  $i$ , find  $i_1$  and  $i_2$  such that  $i_1 < i < i_2$ , where  $i_1$  and  $i_2$  are the two neighboring currents to the given current  $i$  for which the flux linkages data are available.

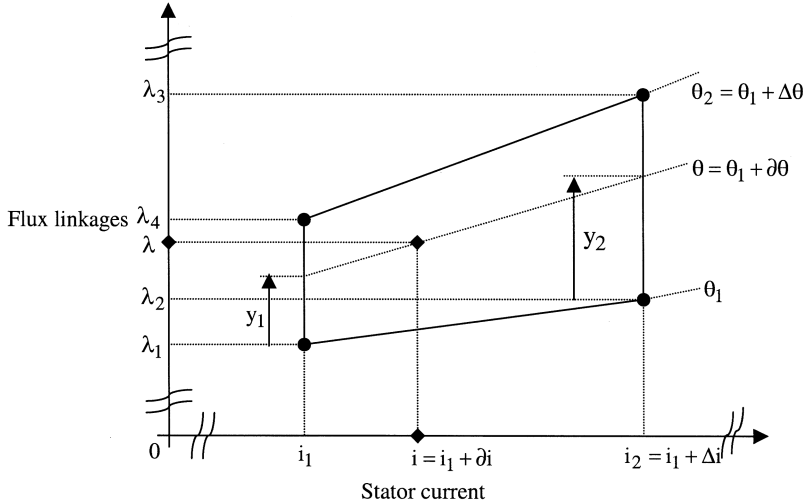


**FIGURE 6.5** Flux linkages retrieval for current  $i$  and rotor position  $\theta$ .

2. Similarly, given rotor position  $\theta$ , find  $\theta_1$  and  $\theta_2$  such that  $\theta_1 < \theta < \theta_2$ , where  $\theta_1$  and  $\theta_2$  are two neighboring positions to the given position  $\theta$  for which the flux linkages data are available.
3. Find the incremental current and rotor position of the desired point from the lowest data set point as  $\delta i = i - i_1$  and  $\delta\theta = \theta - \theta_1$ .
4. Compute current and rotor position data set intervals as  $\Delta i = i_2 - i_1$  and  $\Delta\theta = \theta_2 - \theta_1$ .
5. Compute flux linkage ordinates for the currents  $i_1$  and  $i_2$  for rotor position  $\theta_1$  as:

$$y_1 = \frac{\lambda_4 - \lambda_1}{\Delta\theta} \delta\theta \quad \text{and} \quad y_2 = \frac{\lambda_3 - \lambda_2}{\Delta\theta} \delta\theta$$

6. The flux linkages are then derived using linear interpolation:

$$\lambda = (\lambda_1 + y_1) + \left[ \frac{(\lambda_2 + y_2) - (\lambda_1 + y_1)}{\Delta i} \right] \delta i$$

The data sets can be spaced at unequal intervals in the linear and deeply saturated regions of the machine characteristics where the variations are linear and therefore memory requirement may be drastically reduced for data storage. Equal but smaller spacing of current and rotor position is chosen in the quasilinear or knee region of the machine characteristics to improve the accuracy of the prediction. Dataset spacing has implications in the computational effort. For example, there are 16 algebraic operations involved in the computation of the flux linkages for a given current and rotor position with unequally spaced data sets, while 14 algebraic operations are required with an equally spaced data set. This reduction arises because  $\Delta i$  and  $\Delta\theta$

are constants in equally spaced data sets. Over and above the algebraic operations, search steps to find where the arbitrary current at a rotor position lies between which two currents and two rotor positions, respectively, have to be counted for online computation in a control loop.

If the current intervals and rotor position intervals in the data sets are small, linear interpolation suffices. When those intervals are larger, nonlinear interpolation is essential for accuracy in flux linkages prediction. The nature of nonlinearity is very well defined as it is due to the magnetic material characteristic. The relationship for the material B-H curve is known to lend itself to very simple analytical models,<sup>8,12,26,27,28</sup> thereby making a nonlinear interpolation algorithm easy to formulate.

#### 6.2.1.4 Method 2

Another alternative is to use neural networks to find the stator flux linkages for any given rotor position and stator current. There may not be savings in computational steps with this method compared to the previous methods. Further, additional effort is involved in training the neural network. The error in the flux linkages by this method may be even more than for conventional methods, given the same number of computational steps.

#### 6.2.1.5 Torque Representation and Its Computation

So far, given the discrete data set of flux linkages vs. current vs. rotor position, the extraction of flux linkages for any current and rotor position has been developed. The next step in the computation of machine performance is determining the electromagnetic torque that can be obtained from the change in coenergy,  $\delta W'_f(\theta, i)$ ,<sup>3,4,12</sup> given as:

$$\delta W'_f(\theta, i) = \int_{i_1}^{i_2} \lambda(\theta, i) di \quad (6.8)$$

where the flux linkages are integrated with respect to the phase current for each rotor position. The air gap torque, then, can be calculated for a constant current from the equation as:

$$T_e = \frac{\partial W'_f(\theta, i)}{\partial \theta} \quad (6.9)$$

Taking a derivative with a finite set of data numerically can introduce significant error. Further, the performance computation by this algorithm requires a substantial amount of data and their handling, thus making storage and retrieval time-consuming processes, particularly for online computation and control. A number of efficient methods exist to compute the electromagnetic torque of the system. An adequate method uses spline fit to create three-dimensional relationships among air gap torque vs. current vs. rotor position. These relationships can then be accessed using the algorithm similar to that developed earlier to retrieve the flux linkages from the stator current and rotor position. Other methods such as neural or fuzzy computation are equally applicable for online retrieval.

### 6.2.1.6 Mutual Inductance

In the derivation so far, the mutual flux linkages between phases have been ignored. This is justifiable for well-designed machines where their effects may be within 3 to 5% of the phase flux linkages. Neglecting their effects barely affects the air gap torque estimation except in the ripple torque estimation, but ripple torque estimation is only necessary for a few high-performance applications and those applications hardly come in the way of switched reluctance motor drives. In many high-performance and high-speed switched reluctance machines, the currents in adjacent machine phases overlap for a significant portion of the conduction cycle, as much as 30 to 40% of the period. The mutual flux linkages between windings can then rise as high as 10% of the self flux linkages of a phase. Their effects in such instances are not negligible and therefore need to be incorporated for a better prediction of the machine performance. The machine model including the mutual flux linkages is given in the following.

In general, adjacent phases have overlapping current conduction; therefore, there are mutual flux linkages between these adjacent phases that result in mutual inductance between the windings. For example, in a four-phase machine, the mutual inductance between phases *ab*, *bc*, *cd*, and *da* are shown in [Figure 6.6](#) for currents of 1 to 16 A in step increments of 3 A. The characteristics for 1 and 4 A vary little and are shown as one curve only.

The mutual inductances between nonadjacent phases such as *ac* and *bd* are negligible as the currents in phases *a* and *c* and phases *b* and *d* do not overlap in

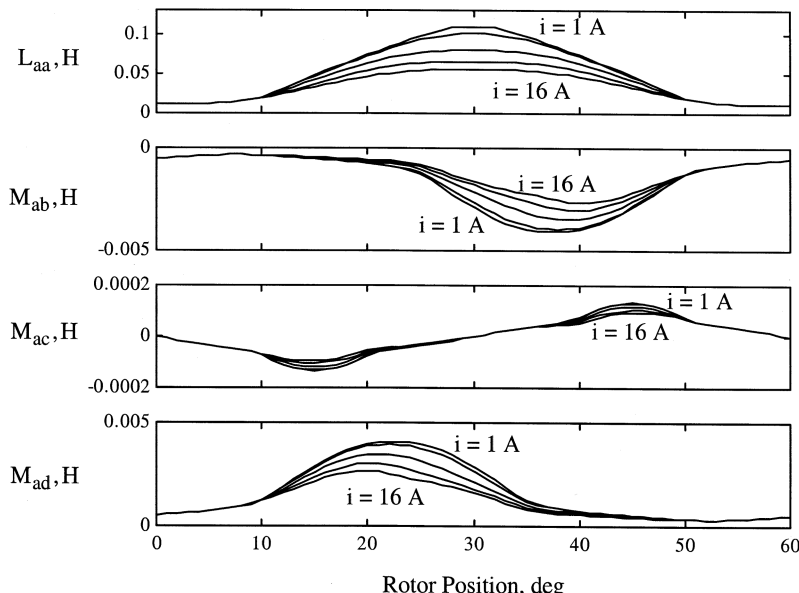


**FIGURE 6.6** Mutual inductance vs. rotor position for rated current.

general. Even when they overlap, they overlap a smaller duration of time for smaller currents so mutual flux linkages are very small compared to mutual flux linkages between adjacent phases. The voltage and flux equations for four-phase SRM,<sup>36</sup> then, can be expressed in terms of phase currents and phase resistances and inductances that are positions of current and rotor position (even though they are not indicated as such in the symbols) as follows:

$$\begin{bmatrix} v_a \\ v_b \\ v_c \\ v_d \end{bmatrix} = \begin{bmatrix} R_s & 0 & 0 & 0 \\ 0 & R_s & 0 & 0 \\ 0 & 0 & R_s & 0 \\ 0 & 0 & 0 & R_s \end{bmatrix} \cdot \begin{bmatrix} i_a \\ i_b \\ i_c \\ i_d \end{bmatrix} + \frac{d}{dt} \begin{bmatrix} \lambda_a \\ \lambda_b \\ \lambda_c \\ \lambda_d \end{bmatrix}$$

where

$$\begin{bmatrix} \lambda_a \\ \lambda_b \\ \lambda_c \\ \lambda_d \end{bmatrix} = \begin{bmatrix} L_a & M_{ba} & 0 & M_{da} \\ M_{ab} & L_b & M_{cb} & 0 \\ 0 & M_{bc} & L_c & M_{dc} \\ M_{da} & 0 & M_{cd} & L_d \end{bmatrix} \cdot \begin{bmatrix} i_a \\ i_b \\ i_c \\ i_d \end{bmatrix} \quad (6.10)$$

and

$$M_{ab} = M_{ba}, M_{bc} = M_{cb}, M_{cd} = M_{dc} \text{ and } M_{da} = M_{ad}$$

where  $R_s$  is the stator resistance per phase.  $L$  represents the self-inductance of the phase indicated by the subscript;  $M$  is the mutual inductance between phases indicated by the subscripts; and  $v$ ,  $i$ , and  $\lambda$  are the voltage, current, and flux linkages, respectively, in the phase indicated by their subscripts.

Usually currents in adjacent phases overlap for a fraction of the conduction period of one phase. Hence, the four-phase equations of the machine need not be solved all the time as currents in two phases are zero at any time. Therefore, only machine equations for the two phases that conduct current are considered here. They are compactly represented as a set consisting of phases  $x$  and  $y$  and the set can be from one of the available combinations of current-conducting phases  $a$  and  $b$ , phases  $b$  and  $c$ , phases  $c$  and  $d$ , and phases  $d$  and  $a$  for the four-phase machine. This combination of phases is true only, say, for first-quadrant operation. Considering only the first- and third-quadrant operation consisting of forward and reverse motor-ing, the equations are given below. Note that for the other two quadrants of forward and reverse regeneration, the equations are similar.

$$\begin{bmatrix} v_x \\ v_y \end{bmatrix} = \begin{bmatrix} R_s & 0 \\ 0 & R_s \end{bmatrix} \cdot \begin{bmatrix} i_x \\ i_y \end{bmatrix} + \frac{d}{dt} \begin{bmatrix} \lambda_x \\ \lambda_y \end{bmatrix} \text{ for } (x, y) \in \begin{cases} \{(a, b), (b, c), (c, d), (d, a)\} \text{ for } T_e \geq 0; \omega_m \geq 0 \\ \{(d, c), (c, b), (b, a), (a, d)\} \text{ for } T_e < 0; \omega_m \leq 0 \end{cases} \quad (6.11)$$

where

$$\begin{bmatrix} \lambda_x \\ \lambda_y \end{bmatrix} = \begin{bmatrix} L_x & M_{xy} \\ M_{xy} & L_y \end{bmatrix} \times \begin{bmatrix} i_x \\ i_y \end{bmatrix} \text{ for } (x, y) \in \begin{cases} \{(a, b), (b, c), (c, d), (d, a)\} \text{ for } T_e \geq 0; \omega_m \geq 0 \\ \{(d, c), (c, b), (b, a), (a, d)\} \text{ for } T_e < 0; \omega_m \leq 0 \end{cases} \quad (6.12)$$

The first element in the set denotes the outgoing phase and the second element denotes the incoming phase of the machine. The voltage and torque equations can be expressed in terms of phase currents or fluxes. Phase currents are chosen as state variables because they can be easily measured with galvanic isolation by current sensors, and the voltage and torque equations are simpler when expressed in terms of phase currents. The differentiation of Eq. (6.12) gives:

$$\begin{aligned} \frac{d}{dt} \begin{bmatrix} \lambda_x \\ \lambda_y \end{bmatrix} &= \frac{d}{dt} \left( \begin{bmatrix} L_x & M_{xy} \\ M_{xy} & L_y \end{bmatrix} \cdot \begin{bmatrix} i_x \\ i_y \end{bmatrix} \right) \\ &= \frac{d}{dt} \left( \begin{bmatrix} L_x & M_{xy} \\ M_{xy} & L_y \end{bmatrix} \right) \cdot \begin{bmatrix} i_x \\ i_y \end{bmatrix} + \begin{bmatrix} L_x & M_{xy} \\ M_{xy} & L_y \end{bmatrix} \cdot \frac{d}{dt} \begin{bmatrix} i_x \\ i_y \end{bmatrix} \\ &= \frac{\partial}{\partial \theta} \left( \begin{bmatrix} L_x & M_{xy} \\ M_{xy} & L_y \end{bmatrix} \right) \cdot \frac{d\theta}{dt} \cdot \begin{bmatrix} i_x \\ i_y \end{bmatrix} + \begin{bmatrix} L_x & M_{xy} \\ M_{xy} & L_y \end{bmatrix} \cdot \frac{d}{dt} \begin{bmatrix} i_x \\ i_y \end{bmatrix} \\ &= \frac{\partial}{\partial \theta} \left( \begin{bmatrix} L_x & M_{xy} \\ M_{xy} & L_y \end{bmatrix} \right) \cdot \omega_m \cdot \begin{bmatrix} i_x \\ i_y \end{bmatrix} + \begin{bmatrix} L_x & M_{xy} \\ M_{xy} & L_y \end{bmatrix} \cdot \frac{d}{dt} \begin{bmatrix} i_x \\ i_y \end{bmatrix} \end{aligned} \quad (6.13)$$

Substituting Eq. (6.13) in Eq. (6.11), the state variable formulation of the equations in the currents is obtained as:

$$\begin{aligned} \frac{d}{dt} \begin{bmatrix} i_x \\ i_y \end{bmatrix} &= - \begin{bmatrix} L_x & M_{xy} \\ M_{xy} & L_y \end{bmatrix}^{-1} \left( \begin{bmatrix} R_s & 0 \\ 0 & R_s \end{bmatrix} + \frac{\partial}{\partial \theta} \begin{bmatrix} L_x & M_{xy} \\ M_{xy} & L_y \end{bmatrix} \cdot \omega_m \right) \cdot \begin{bmatrix} i_x \\ i_y \end{bmatrix} \\ &\quad + \begin{bmatrix} L_x & M_{xy} \\ M_{xy} & L_y \end{bmatrix}^{-1} \begin{bmatrix} v_x \\ v_y \end{bmatrix} \end{aligned} \quad (6.14)$$

This formulation necessitates too many algebraic operations of multiplications and additions to evaluate the stator currents and also requires too many variables such as the rotor speed and partial derivatives of self- and mutual inductances with respect to rotor position. The computational burden is very high with this approach, hence an alternative is suggested in the following. Consider the flux linkages as variables.

They can easily be calculated for the current time interval from the stator currents and applied voltages of the previous sampling interval. Using the present flux linkages and rotor position, the stator currents can be extracted from the three-dimensional data set of flux linkages vs. current vs. rotor position. Note that this approach does not involve the rotor speed variable, partial derivatives, and many algebraic operations. An additional advantage of this approach is that control of the flux linkages leads to perfect decoupling and simpler controller design compared to the current feedback control approach shown in the previous chapter.

### 6.2.2 CONVERTER

Simulation of the drive system has many objectives, such as validation of the drive system performance, design verification of the machine, and design verification of the converter,<sup>1,6,22,25,29,30,31</sup> especially during transients. For drive system performance validation both in steady-state and for dynamic conditions, it can be assumed that the converter is robust between the switching transients, hence the converter power devices can be treated as ideal switches by neglecting the switching transients and voltage drops during conduction. The disadvantage of such an approach is that as the voltage drops across the converter switches an error will be introduced in the switch duty cycle as well as in the power input to the drive system. Their magnitudes will depend on the operational speed of the drive system. At low speeds, the error introduced by the converter switch voltage drop can be significant, while at higher speeds it is negligible. Negligence of the switching transients hardly interferes with the steady state but can have an impact on the evaluation of switch losses. Therefore, depending on the objective, the converter model can be simple or complex.

In the simple model, the power devices can be assumed to be ideal during turn-on and turn-off instants, and the device voltage drops during conduction are negligible. The last assumption is based on the fact that the source voltage is much larger than the nominal device voltage drop. The device conduction drop in some cases, such as in low-voltage, battery-operated drives, is a significant proportion of the voltage source itself. It then is factored in the simulation model during conduction phase as:

$$v_a = V_{dc} - nV_t \quad (6.15)$$

where  $n$  is the number of power devices in series with the phase,  $v_a$  is the applied voltage to the phase,  $V_{dc}$  is the source voltage, and  $V_t$  is the device conduction voltage drop. Consider an asymmetric converter for this illustration. During freewheeling, the phase applied voltage is

$$v_a = -V_d - V_t \quad (6.16)$$

where  $V_d$  is the conduction drop of the freewheeling diode. Note that during this mode the current flows in the machine phase, one diode, and one power switch. When the phase current is being commutated with source voltage, the phase voltage is given by:

$$v_a = -V_{dc} - 2V_d \quad (6.17)$$

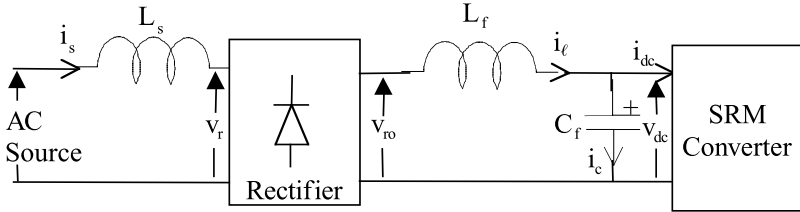


**FIGURE 6.7** Schematic of source side of the SRM converter.

since the current flows in the machine phase, two diodes, and source voltage during this mode.

#### 6.2.2.1 Effect of Source Impedance and dc Link Filter

The source is considered infinite and is maintained as a constant in the model. The voltage source is derived from an ac source by rectification or is obtained with a battery. In both cases, there are source impedances. In the case of a battery, the impedance is referred to as *internal resistance*. When the voltage source is derived from an ac source, the ac source impedance, diode bridge rectifier, and dc link filter have to be modeled,<sup>22,29,30</sup> as shown in Figure 6.7.

The relevant equations for this schematic are obtained by considering zero source impedance and an ideal rectifier:

$$v_{ro} = |V_m \sin(\omega_s t)| \quad (6.18a)$$

$$i_\ell = i_c + i_{dc} \quad (6.18b)$$

$$L_f \frac{di_\ell}{dt} = v_{ro} - v_{dc} \quad (6.18c)$$

$$v_{dc} = \frac{1}{C_f} \int i_c dt \quad (6.18d)$$

It is fairly straightforward to incorporate ac source impedance and device conduction drops in this model. For the study of power device transients, device dynamic modeling is required.

#### 6.2.2.2 Device-Transient Model

When the objective of the simulation is to determine the peak device voltage and current stresses, switching losses, and electromagnetic interference (EMI) due to switching, then the device has to be modeled dynamically. Such a need can be met by using circuit simulation packages (SPICE or SABER, for example), or by embedding the device-transient equivalent models in simulation software. For that purpose, refer to literature on power devices.

### 6.2.3 LOAD

A generic load for simulation consists of inertia, friction, and load torque, all of which are usually assumed to be constants. The load determines the machine rotor acceleration, speed, and position. It is given symbolically as:

$$J \frac{d\omega_m}{dt} + B \omega_m = T_e - T_\ell = T_a \quad (6.19)$$

where  $J$  is the combined moment of inertia of the motor and load,  $B$  is the combined friction coefficient of the motor and load,  $T_e$  is the electromagnetic torque,  $T_\ell$  is the load torque, and  $T_a$  is the acceleration torque. Note that the electromagnetic torque is a function of the rotor position and excitation current. The rotor position is therefore crucial to the control of the machine excitation and is obtained from the speed as:

$$\omega_m = \frac{d\theta}{dt} \quad (6.20)$$

In many applications, the inertia and load torques vary during a load cycle and can be functions of rotor position. The load equation has ignored the windage losses, which are proportional to the square of the speed. For speeds higher than 5000 rpm, it is important to incorporate these losses to obtain a realistic load equation, a better estimate of speed and rotor position, and a better performance prediction of the SRM. For example, machines running at 50,000 rpm can have windage and friction losses as high as 2 to 5% of the total input power.

Accurate modeling of the rotor-position-dependent load is essential to study the effect of rotor speed ripples, rotor shaft fatigue, and its longevity. For example, consider the effect of a compressor load on the rotor speed when the load is a function of rotor speed as shown in [Figure 6.8](#).

The acceleration torque is periodically triangular with an offset when the generated electromagnetic torque is assumed to be constant. Because of that, the rotor speed is not a smooth ramp during acceleration. When the air gap torque is made to match the load torque but with a dc offset, then the acceleration torque becomes constant, resulting in a smooth ramping of the speed without oscillations, as shown in [Figure 6.9](#). The discussion so far has pertained to a dynamic situation. During steady state, the rotor speed will have a cyclic variation when the air gap torque is not modified to match the load torque. These cyclic variations of the acceleration torque during steady-state and dynamic conditions lead to increased audible noise and shaft fatigue, contributing to faster wear and tear of the mechanical subsystem and consequently a reduced life span for the shaft.

### 6.2.4 CONTROLLER

The control of an SRM requires an inner current control loop and an outer speed feedback control loop, which is commonly encountered in ac and dc drives. The manner in which the torque and current commands are generated is different in tune

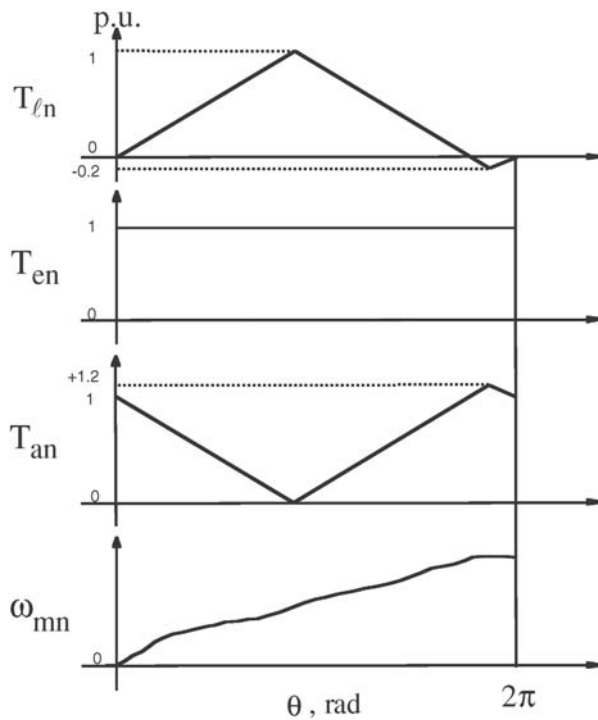


**FIGURE 6.8** Effect of a cyclic load on the rotor speed when the air gap torque is constant in normalized units.

with the peculiarities of this machine. The controller considered in this section is capable of giving fine torque control in regard to its ripple content and therefore may be considered to correspond to a high-performance drive system control. Simple applications may not require controllers with torque and current shaping, so the torque command and current command controller blocks can be removed. The simulation of various controllers, such as speed, torque command, current command, current, pulsed width modulation (PWM), and hysteresis current, is described briefly in this section. Synthesis of these controllers can be found in the previous chapter and some in the early part of this chapter. In the simulation, the relevant equations are derived from the outer to inner loops of the drive system, and the reverse is also feasible.

#### 6.2.4.1 Speed Controller

It is assumed that the speed signal is available and is processed through a filter. The speed signal may be measured directly or obtained from measured rotor position pulses or extracted from estimated rotor position. By whichever manner it is obtained, a number of factors surrounding its acquisition have to be captured in the simulation to reflect the reality: (1) time delay, (2) attenuation or gain, (3) error characteristics if they are obtained through estimation, and (4) linearity, if it is measured, as the error characteristics can handle this aspect in the estimated speed

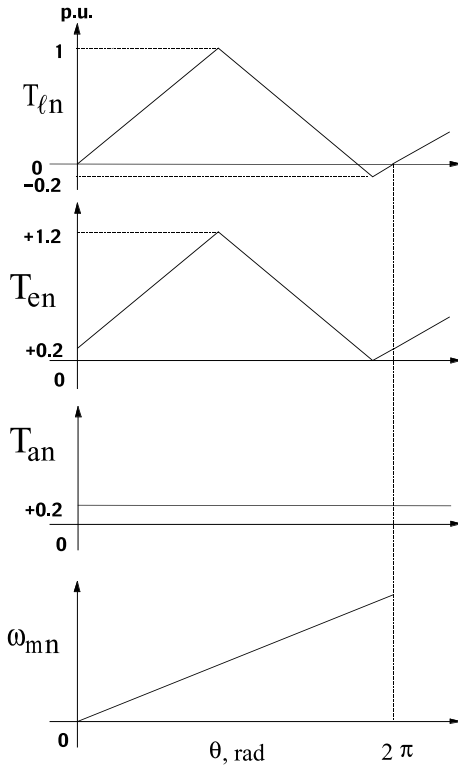


**FIGURE 6.9** Effect of a cyclic load with modified air gap torque on the rotor speed in normalized units.

signal case. Usually the time delay and gain are fairly constant over the entire frequency range of interest; the error and linearity are variables and have to be measured or estimated and stored for simulation.

The speed controller's input is the speed error that is the difference between the speed reference and the filtered speed feedback signals and its output is the unmodified torque command. In order for the integral part of the speed controller not to be deeply saturated and to provide a responsive operation, an anti-windup controller usually is built into the speed controller in the integral controller path. Individual block diagrams for the speed filter and the speed controller, including the anti-windup controller, are given in the following discussion, and differential, algebraic, and conditional relationships are derived from them for inclusion in the simulation.

For the speed feedback filter, for purposes of illustration, the feedback of the speed signal is processed through a generic block whose transfer function is a first-order lag with gain  $H_\omega$  and time delay  $T_\omega$ . [Figure 6.10](#) shows the speed feedback filter. The transfer function of the filter and tachogenerator can be represented as:

$$G_\omega(s) = \frac{\omega_{mr}(s)}{\omega_m(s)} = \frac{H_\omega}{1 + sT_\omega} \quad (6.21)$$

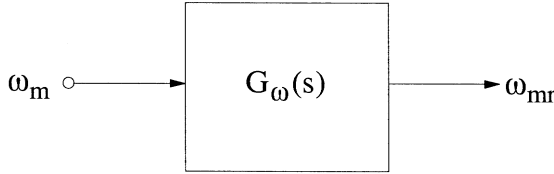


**FIGURE 6.10** Speed feedback filter.

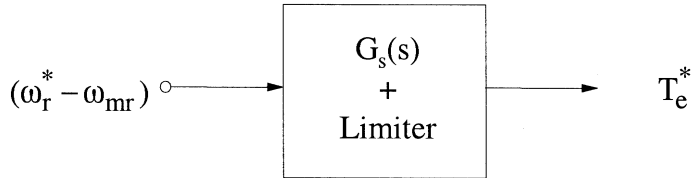


**FIGURE 6.11** Speed controller block diagram.

In the time domain, this can be rearranged by letting

$$x_4 = \omega_{mr} \quad (6.22)$$

resulting in:

$$\dot{x}_4 = \frac{1}{T_\omega}(H_\omega x_3 - x_4) \quad (6.23)$$

where  $\dot{x}_4$  is the derivative of  $x_4$ .

The state variable  $x_4$  forms one of the inputs to the speed error/controller block and is considered next. Note that  $x_3$  denotes the rotor speed, and  $x_1$  and  $x_2$  are the currents in two phases of the machine.

For the speed controller, a block diagram is shown in Figure 6.11. The transfer function of the speed controller considered in our analysis is a proportional-plus-integral (PI) controller given as:

$$G_s(s) = K_{ps} + \frac{K_{is}}{s} \quad (6.24)$$

The state diagram of this block is shown in Figure 6.12. Letting

$$\dot{x}_5 = \omega_r^* - \omega_{mr} = \omega_r^* - x_4 \quad (6.25)$$

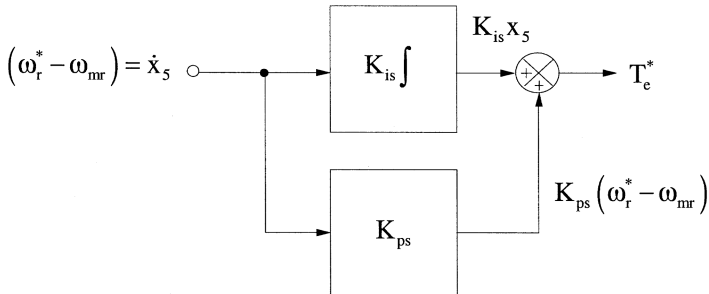


**FIGURE 6.12** State diagram of the speed controller.

the torque command signal is derived as:

$$T_e^* = K_{ps}(\omega_r^* - x_4) + K_{is}x_5 \quad (6.26)$$

To maintain the drive system in the safe operating region, the torque reference is limited to allowable maximum limits determined by the converter and motor peak capabilities. In this case, let it be  $+T_{\max}$ , assuming the drive is for a one-quadrant operation. This torque reference limit is integrated in the simulation as:

$$0 \leq T_e^* \leq +T_{\max} \quad (6.27)$$

Because of the large integral gain in the speed controller, its output will saturate in time. When the integral controller's output is saturated, the speed error required to change the torque command is very large. Therefore, the speed control is sluggish and the rotor speed will experience large undesirable transients during speed reference changes or load torque disturbances. An anti-windup circuit is necessary to overcome the saturation in the integral controller part to keep the speed controller responsive. The anti-windup circuit may be realized in many ways. One of the implementations<sup>35</sup> is shown in Figure 6.13.

In the case of an anti-windup controller, the saturation due to the integral action alone is countered. It is achieved by negative feedback control of the integral controller output through a dead-zone circuit. This dead-zone circuit only produces an output when the output of the integral controller exceeds a preset absolute maximum (i.e., when the controller output saturates). This feedback is subtracted from the speed error and the resulting signal constitutes the input to the integrator. When the output of the integral controller saturates, the input to the integral controller is reduced. This action results in the reduction of the integral controller's output, thus pulling the integral controller from saturation and making the controller very responsive. If there is no saturation in the integral controller output, then the feedback is zero due to the dead-zone circuit so the anti-windup circuit is inactive in this implementation. The output of the integral and proportional controller is summed and is then limited to generate the torque reference signal. By keeping the outputs of the proportional and integral controllers separate, their individual tuning and the beneficial effects of the high proportional gain are maintained.

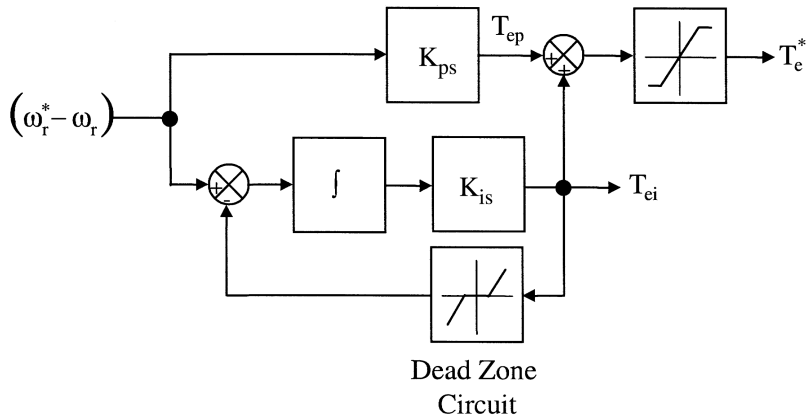


**FIGURE 6.13** Anti-windup circuit in the PI speed controller.

#### 6.2.4.2 Torque Controller

In low-performance controllers, there is no special torque controller. In that case, the output of the speed controller can be treated as the torque command signal. The disadvantage of such an approach is that the torque command is not conditioned to the peculiarities of the load, such as the cyclic load described in an earlier section, and the transient and steady-state limits are not embedded in the torque command signal. The former disadvantage has the deleterious effects of speed oscillations and reduced shaft life, whereas the latter can compromise reliable operation. Therefore, it is prudent to modify the torque command with a torque controller in a high-performance drive system. Then the factors that may influence the torque controller design are

1. Continuous and intermittent operational limits
2. Load peculiarities, such as continuously varying cyclic loads
3. Individual phase torque command generation primarily to mitigate or eliminate the torque ripple by coordination of individual phase currents

The third factor merits further attention here. Torque ripple reduction is absolutely necessary in SRM drives if they are to find applications in high-performance environments. The reduction is achieved in many ways but most of them are based on the premise that the sum of the air gap torques produced by the outgoing phase and the incoming phase has to be equal to the overall torque command. Therefore, the individual phase torque commands for the outgoing and incoming phases have to be identified for each operating point that is a function of the rotor position. In this method, the slope of the outgoing current is controlled and the radial force can be controlled to mitigate the acoustic noise. A number of advantages can accrue with this torque command modification in the torque controller. Hereafter, the output of

the torque controller will be labeled as a modified torque command. The modeling of this block is then based on the three factors discussed. The first two factors are easy to incorporate: the first factor as a torque limiter with time constraints, and the second factor in the load torque as a function of rotor position and/or speed. The third factor uses one of the algorithms discussed in Chapter 5 to mitigate the ripple torque. The latter is usually a function of rotor position and sometimes also magnitude of current.

#### 6.2.4.3 Current Command Controller

The current command is generated in a straightforward manner when there is a torque controller in the system. The current controller takes the modified phase torque commands and generates the phase current commands as a function of rotor position. This is achieved using the three-dimensional torque vs. current magnitude vs. rotor position characteristics of the machine stored in tables and recovered using the algorithm developed earlier. The modeling of the current command controller is likewise accomplished by use of tables containing the machine characteristics.

In low-performance systems, the torque controller is usually absent. In this case, the current command is generated in a slightly different way. The magnitude of the current command is generated from the predetermined steady-state characteristics of the machine. Then, positioning of this stator phase current command with respect to the rotor pole is very crucial. Realizing that the current command needs to be initiated well in advance of the overlap instant of the stator and rotor poles to gain higher speed operation and the current command must be forced to zero well ahead of complete alignment of the poles to minimize or eliminate generation of air gap torque counter to the request, determination of the advance and fall angles is critical to operation of the machine. The inputs to the current controller then consist of torque magnitude, absolute rotor position, and advance and fall angles of the phase current. The reference for advance angle is the angle at which the leading rotor pole tip just comes into alignment with the lagging stator pole tip. The fall angle reference is when the stator and rotor poles align. The advance and fall angles usually are predetermined by simulation and programmed into the controller as a function of speed. More of the effects of these angles may be referred to in Chapter 3. The advance and fall angles can be controlled in such a way that the input power is minimized by measuring the input power and incrementally adjusting the angles to determine the local minimum. The search for the minimum input power operating point can be vastly improved by fuzzy control.

#### 6.2.4.4 Current Controller

Current control is achieved with closed-loop control with either a PWM or hysteresis switching control of the converter. The current controller structure is different depending on the switching strategy chosen. The PWM- and hysteresis-based current controllers are therefore discussed separately and modeled in the following sections.<sup>35</sup>

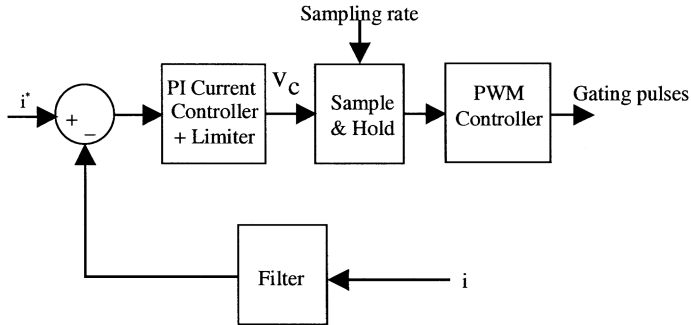


**FIGURE 6.14** PWM-based current controller.

#### 6.2.4.4.1 PWM Current Controller

The PWM current controller consists of the following control blocks: current error generator, a PI current controller, sample-and-hold block, and a PWM controller as shown in [Figure 6.14](#). Each phase current control loop has identical controller structure. The filter in the current feedback path can include the model of the current sensor and can be modeled as a gain with a first-order time lag. The modeling of the PI controller is very similar to the PI speed controller discussed earlier. As the controller is an integral part, an anti-windup controller is advisable in this part, also. Note that values of the control voltage,  $v_c$ , higher than the carrier signal's maximum amount to a duty cycle of one. If  $v_c$  is negative, the duty cycle is zero, thus initiating a drastic reduction of current, applying a negative voltage across the phase winding, and transferring the energy from the phase winding to the dc link. These subtleties have to be built into the logic of the gate drive and are dictated by the polarity of the control signal,  $v_c$ , and PWM controller output pulse signals. The control signal,  $v_c$ , is sampled and held at a rate determined by the sampling rate input into the system. The sampling rate usually determines the switching frequency. The PWM controller takes the output of the sample-and-hold circuit and computes the duty cycle and therefore the on and off times in a PWM period for implementation. In hardware implementation, the on- and off-time gating pulses are generated by comparing the output of the sample-and-hold circuit with a triangular carrier signal. From a modeling point of view, it is easier to consider the analytical computation of the duty cycle and use that information in the generation of gating pulses and applied voltage to the phase windings.

#### 6.2.4.4.2 Hysteresis Current Controller

In the hysteresis switching-based current controller, the current control is much simpler. The current error is computed from which the switching is generated depending on its relationship to the hysteresis current window. Even here, the phase winding energization corresponding to on time, demagnetizing of the winding corresponding to off time, and freewheeling corresponding to the interim off times

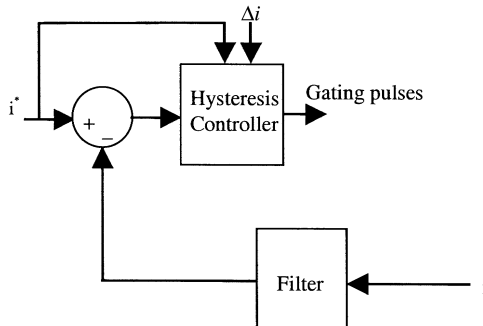


**FIGURE 6.15** Block diagram schematic of the hysteresis current controller.

during phase conduction time have to be discriminated and coordinated with the current command and outputs of the hysteresis current controller. The modeling is as follows: The current command  $i_a^*$  will be compared to the motor phase current,  $i_a$ . The switching logic of the hysteresis controller is summarized as:

$$\text{If } (i_a^* - i_a) \geq \Delta i, \quad \text{then} \quad V_a = V_{dc} \quad (6.28a)$$

$$\text{If } (i_a^* - i_a) \leq -\Delta i, \quad \text{and} \quad i_a^* > 0, \quad \text{then} \quad V_a = 0 \quad (6.28b)$$

$$\text{If } (i_a^* - i_a) \leq -\Delta i, \quad \text{and} \quad i_a^* \leq 0, \quad \text{then} \quad V_a = -V_{dc} \quad (6.28c)$$

where  $\Delta i$  is the hysteresis window and  $V_{dc}$  is the link voltage. It is assumed that the power devices in the converter are ideal in this illustration, hence their voltage drops and switching times are neglected. The applied voltage is 0 or  $-V_{dc}$ , depending on the converter configuration and switching strategy for negative current error. An earlier section contains the modeling method for the effect of device voltage drop and switching times, which may be incorporated here, too, depending on the level of accuracy necessary in the simulation. Note that when the current error is less than the negative of the hysteresis current window, the applied voltage to the machine phase is zero when the current command is positive, and the applied voltage to the machine phase is negative when the current command is negative. Discrimination between the freewheeling and demagnetization instances has to be built into the modeling and simulation. A block diagram of the hysteresis current controller is shown in Figure 6.15.

### 6.3 SIMULATION

By combining various blocks of the drive system described in detail, system equations are assembled which contain differential, algebraic, and conditional equations. The differential equations are solved for a given instant of time starting from zero with small time intervals for integration using one of the standard techniques such as the Runge–Kutta fourth-order integration method. For faster computation of the system solution, the simpler Euler integration method may be resorted to. It is

assumed that the variables are constant over the integration interval and then with the updated values. The algebraic and conditional equations are embedded in the system solution. Because of the large amount of data handling in the system, the task of simulation may initially be daunting. Proceeding systematically and assembling the system equations with the help of a flow chart will make the code assembly a fairly straightforward chore. Some sample results of the simulation are considered in the following section.

### 6.3.1 SIMULATION RESULTS<sup>33,34</sup>

**Figure 6.16** corresponds to a torque-controlled drive system in which the speed of the drive system is maintained at a fixed speed and a torque command is applied to the SRM drive. The various drive variables are displayed for a typical drive system.

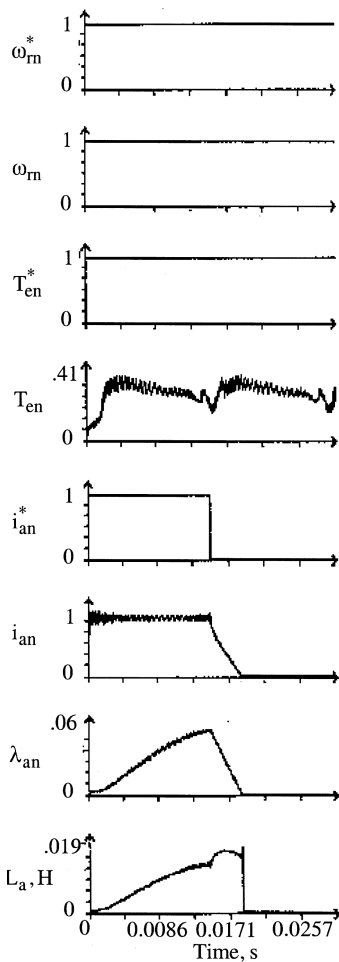


**FIGURE 6.16** Torque drive simulation in normalized units: direct method.

It is evident that when a constant amplitude current is commanded, the torque is not a constant as in the case of other motor drives. This requires a control technique to modify the current command so that the resulting torque is uniformly constant.

The torque request and rotor position are inputs into the table containing the corresponding phase current magnitudes. This current forms the reference for enforcement in the machine phase. It is to be noted that this current reference has to be obtained for each torque request and rotor position. Because the torque request is a constant for a given steady-state operating point, the current reference is identified for the rotor position and can be initiated in advance to compensate for the time delay of the converter and the time lag due to the machine phase. Such an implementation in software simulation results in obtaining almost smooth and constant torque in the SRM, as shown in [Figure 6.17](#) for a speed-controlled drive system.

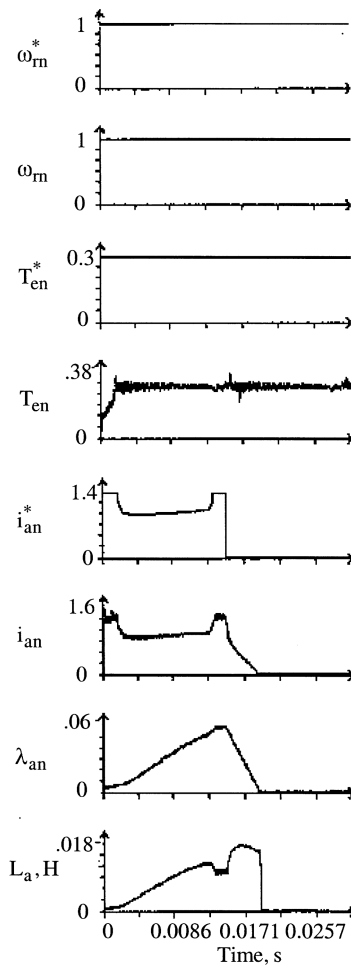


**FIGURE 6.17** Torque drive simulation in normalized units: torque smoothing.

A more demanding application of this technique is in load compensation and is demonstrated here with a compressor load. Without and with load compensation dynamic simulation results are shown in Figures 6.18a and b, respectively. Consider that the electromagnetic torque of the motor is constant, resulting in a varying acceleration torque, which, in turn, produces an oscillatory speed response for an inertial load as shown in Figure 6.18a. Such oscillatory speed behavior fatigues the shaft, increases its wear and tear, and results in audible noise generation. These effects reduce the life of the compressor and cause discomfort to the users. They could be overcome if the electromagnetic torque is made to match the load torque and to generate the required acceleration torque uniformly as shown in Figure 6.18b,

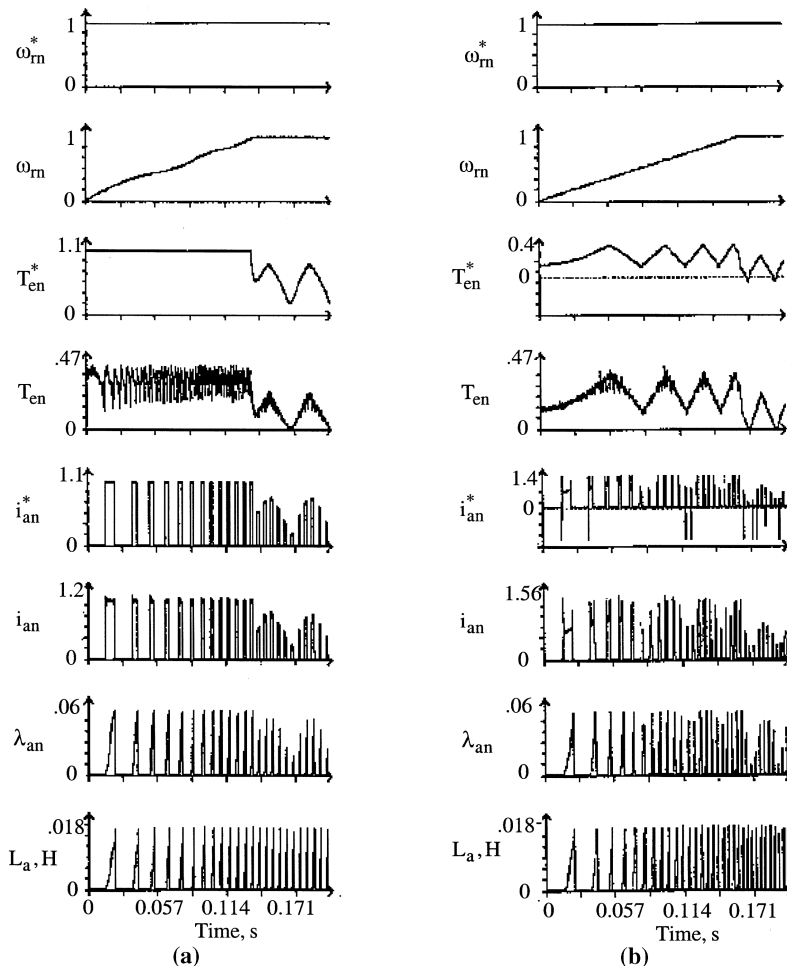


**FIGURE 6.18** (a) Performance of the speed controlled drive with speed matching; (b) performance of the speed drive without load matching.

resulting in a smooth speed response. Note that compensation by modifying the electromagnetic torque is achieved to match the load torque during both steady and transient states. The speed oscillations are eliminated with load compensation, as can be seen from the simulation results.

## REFERENCES

1. Ray, W.F. and R.M. Davis, Inverter drive for doubly salient motors: its fundamental behavior, linear analysis and cost implications, *IEE Proc. B. Electr. Power Appl.*, 2(6), 185–193, 1979.
2. Lawrenson, P.J. et al, Variable speed switched reluctance motors, *IEE Proc. B*, 127(4), 253–265, 1979.
3. Stephenson, J.M. and J. Corda, Computation of torque and current in doubly salient reluctance motors from non-linear magnetization data, *IEE Proc.*, 126(5), 393–396, 1979.
4. Harris, M.R., A. Hughes, and P.J. Lawrenson, Static torque prediction in saturated doubly salient machines, *IEE Proc.*, 122(10), 1121–1127, 1975.
5. Corda, M. and J.M. Stephenson, Analytical estimation of the minimum and maximum inductances of a double-salient motor, in *Proc. of Int. Conf. on Stepping Motors and Systems*, Sept. 1979, Leeds, pp. 50–59.
6. Davis, R.M., W.F. Ray, and R.J. Blake, Inverter drive for switched reluctance motor: circuits and component ratings, *IEE Proc. B*, 128(2), 126–136, 1981.
7. Finch, J.W., M.R. Harris, A. Musoke, and H.M.B. Metwally, Variable speed drives using multi-tooth per pole switched reluctance motors in *Proc. 13th Ann. Symp. Incr. Mot. Contr. Syst. and Dev.*, May, 1984, pp. 293–301.
8. Krishnan, R., R. Arumugam, and J.F. Lindsay, Design procedure of switched reluctance motors, *IEEE Trans. on Ind. Appl.*, IA-24(3), 456–461, 1988.
9. Arumugam, R., D.A. Lowther, R. Krishnan, and J.F. Lindsay, Magnetic field analysis of a switched reluctance motor using a two-dimensional finite-element model, *IEEE Trans. on Magnetics*, 21(5), 1883–1885, 1985.
10. Lindsay, J.F., R. Arumugam, and R. Krishnan, Finite-element analysis characterization of switched reluctance motor with multitooth per stator pole, *IEE Proc. B*, 133(6), 347–353, 1986.
11. Arumugam, R., J.F. Lindsay, and R. Krishnan, A comparison of the performance of two different types of switched reluctance motors, *Electrical Machines and Power Systems*, 12, 281–286, 1987.
12. Krishnan, R., A.S. Bharadwaj, and P.N. Materu, Computer aided design of electrical machines for variable speed applications, *IEEE Trans. on Industrial Electronics*, 36(4), 560–571, 1988.
13. Materu, P.N. and R. Krishnan, Steady state analysis of the variable speed switched reluctance motor drive, *IEEE Trans. on Industrial Electronics*, 36(4), 523–529, 1989.
14. Oza, A.R., R. Krishnan, and S. Adkar, A microprocessor control scheme for switched reluctance motor, in *IEEE Ind. Electronics Conf.*, Nov. 1987, Boston, MA.
15. Mang, X., R. Krishnan, S. Adkar, and G. Chandramouli, Personal computer based controller for switched reluctance motor drives, in *IEEE Ind. Electronics Conf.*, Nov. 1987, Boston, MA.
16. Materu, P.N. and R. Krishnan, Analytical prediction of SRM inductance profile and steady-state average torque, in *Conf. Rec. IEEE IAS Ann. Mtg.*, Oct. 1990, Seattle, WA, pp. 214–223.

17. Krishnan, R., X. Mang, and A.S. Bharadwaj, Design and performance of a micro-controller-based switched reluctance motor drive system, *Electrical Machines and Power Systems*, 18(4), 359–373, 1990.
18. Krishnan, R., M. Abou-Zeid, and X. Mang, A design procedure for axial field switched reluctance motor, in *Conf. Rec. IEEE IAS Ann. Mtg.*, Oct. 1990, Seattle, WA, pp. 241–246.
19. Krishnan, R., Switched reluctance motor drive applications, *Motortechnics*, 25–32, 1989.
20. Krishnan, R., X. Mang, and A.S. Bharadwaj, A low cost SRM analog controller, *Motortechnics*, 19–23, 1990.
21. Krishnan, R. and P.N. Materu, Measurement and instrumentation of a switched reluctance motor, in *Conf. Rec. IEEE IAS Ann. Mtg.*, Oct. 1989, San Diego, CA, pp. 116–121.
22. Krishnan, R. and P.N. Materu, Analysis and design of a low cost converter for switched reluctance motor drives, in *Conf. Rec. IEEE IAS Ann. Mtg.*, Oct. 1989, San Diego, CA, pp. 561–567.
23. Materu, P.N. and R. Krishnan, Estimation of switched reluctance motor losses, in *Conf. Rec. IEEE IAS Ann. Mtg.*, Oct. 1988, Pittsburgh, PA, pp. 79–90.
24. Arumugam, R., J.F. Lindsay, and R. Krishnan, Sensitivity of pole arc/pole pitch ratio on switched reluctance motor performance, in *Conf. Rec. IEEE IAS Ann. Mtg.*, Oct. 1988, Pittsburgh, PA, pp. 50–54.
25. Pollock, C. and B.W. Williams, Power converter circuits for switched reluctance motors with the minimum number of switches, *IEE Proc. B*, 137(6), 373–384, 1990.
26. Brauer, J.R., Simple equations for the magnetization and reluctivity curves of steel, *IEEE Trans. on Magnetics*, 11(1), 81, 1975.
27. El-Sherbiny, S.K., Representation of the magnetization characteristics by sum of exponentials, *IEEE Trans. on Magnetics*, 9(1), 60–61, 1973.
28. Trutt, F.C., E.A. Erdelyi, and R.E. Hopkins, Representation of magnetization characteristics of dc machines for computer use, *Trans. on IEEE-PAS*, 87, 665–669, 1968.
29. Krishnan, R. and S. Lee, Effect of power factor correction circuit on switched reluctance motor drives for appliances, in *Conf. Proc. APEC '94*, Feb. 1994, Orlando, FL, pp. 83–89.
30. Krishnan, R. and S. Lee, Analysis and design of a single switch per phase converter for switched reluctance motor drives, in *Conf. Proc. PESC*, 1994, pp. 485–492.
31. Krishnan, R. and S. Lee, Uninterruptible motor drives: A case study with switched reluctance motor drives, in *Conf. Proc. IECON*, 1994, 220–225.
32. Gharpure, V.S., R. Krishnan, and S. Lee, Analysis and design of energy recovery snubbers for switched reluctance motor drives, in *Conf. Proc. IAS*, 1994, pp. 1055–1062.
33. Bedingfield, R.A., Development of CAE system for switched reluctance motor drive systems, M.S. Thesis, The Bradley Department of Electrical and Computer Engineering, Virginia Tech., Blacksburg, VA, July 1991.
34. Krishnan, R. and R.A. Bedingfield, Dynamic analysis of an SRM drive system, *IEEE-IAS Annual Meeting*, Conf. Record, Dearborn, MI, Oct 1991, pp. 265–271.
35. Krishnan, R., *Electric Motor Drives: Modeling, Analysis and Control*, Prentice-Hall, NJ, Feb. 2001.
36. Bae, H.K., Control of switched reluctance motors considering mutual inductance, Ph.D. Thesis, The Bradley Department of Electrical and Computer Engineering, Virginia Tech., Blacksburg, VA, Aug. 2000.

---

# 7 Acoustic Noise and Its Control in SRMs

## 7.1 INTRODUCTION

Vibration and the resulting acoustic noise in SRMs have generated intense interest from the time they became commercially competitive with dc and ac drives. Earlier SRM designs and their controls allowed discontinuous torque for most of the speed control range for the sake of implementing extremely simple control schemes. Further, such discontinuous torque control enabled high-efficiency operation in switched reluctance machines. Moreover, construction of the SRM presented opportune circumstances to generate acoustic noise due to its specific magnetic configurations and manufacturing tolerances. The need for the smallest air gap to maximize torque and power output, fewer poles (say, 6/4 or 8/6), and uneven machining or punching of diametrically opposite poles, which created uneven magnetic pull in the radial direction, exacerbated the problem of acoustic noise. In addition to these manufacturing tolerances and magnetic shapes, converter- and controller-related events, such as the drastic variation in rate of fall of current in the machine phases by applying dc source voltage of negative polarity, resulted in immense radial vibrations. Negative voltage is applied to turn off the current faster to avoid generating torque of opposite polarity that is undesirable for the quadrant of operation of the SRM as it reduces the average torque. An understanding of many of these factors developed in the last few years led to many ameliorative measures in the design of the SRM and in its control. This chapter outlines the causes of acoustic noise and some measures to overcome this problem. It must be noted that many laboratories claim to have produced SRM drives which are quieter than equivalent converter controlled induction motor drives.

This chapter includes a basic description of noise sources in electrical machines in general and in particular SRM drive systems, noise cancellation or mitigation using the converter control, and qualitative design measures that could be implemented at the design stage of the SRM itself to reduce the noise. Even though an analytical relationship between the acoustic noise and various motor and converter variables is very difficult to formulate given the complexity of the process of noise generation, an approximate implicit or explicit relationship can be of immense help for design of a quiet SRM drive system. Many applications require a stringent upper limit on the acoustic noise of the motor drive, and most of the prototype development is iterated based on past knowledge and current practical work.

## 7.2 SOURCES OF ACOUSTIC NOISE IN ELECTRICAL MACHINES

In order to understand the acoustic noise in general, the various noise sources in electrical machines are presented briefly. Then, based on the special features of the SRM, only relevant items are considered in detail. Identification of noise sources and cancellation or mitigation of noise in electric machines have been in vogue since the 1940s due to the introduction of new materials which helped to revise designs of machines, such as induction and synchronous machines with a wound rotor, permanent magnet rotor, or salient rotor. With the advent of newer topologies such as switched reluctance and synchronous reluctance machines and axial field machines for variable-speed-drive applications, the interest in noise and its cancellation perked up even more vigorously. Some of the sources of noise and techniques for its cancellation or mitigation are different for newer machines as they have a single or a doubly salient structure and, in addition, have no windings or magnets on the rotor. This is in contrast to ac machines with distributed windings on the stator and rotor or distributed windings on the stator and permanent magnets on the rotor. The stringent regulations governing noise in electrical machines require a careful consideration of all possible noise sources and their mitigation methods. Reference 6 gives a list of publications and abstracts only, while References 2 and 5 are excellent starting points for information on acoustic noise sources and mitigation.

### 7.2.1 NOISE SOURCES

Noise sources can be divided into four broad categories: magnetic, mechanical, aerodynamic, and electronic. [Figure 7.1](#) shows the broad classification of noise sources in electric machines. The various sources of noise are described below.

#### 7.2.1.1 Magnetic Sources of Noise

The magnetic flux in the machine passes across the air gap in an approximate radial direction producing radial forces on the stator and rotor, resulting in magnetic noise and vibrations. A description of the radial forces in electrical machines is given in References 2 and 5. It is critical to know the frequencies at which various components of the radial forces are produced. If one of the radial force frequencies coincides with the natural frequency of the machine, resonance occurs, leading to an increase in the acoustic noise.

The radial, tangential, and lateral forces in the SRM, as in any other machine, may be calculated by finite element analysis techniques using standard commercial software. To determine the relationships between these forces and the machine dimensions, the machine is assumed to be operating in the linear region. [Figure 7.2](#) illustrates the various dimensions involved in the derivation of these forces. The forces generated in the SRM are derived from first principles with the assumption of magnetic linearity.

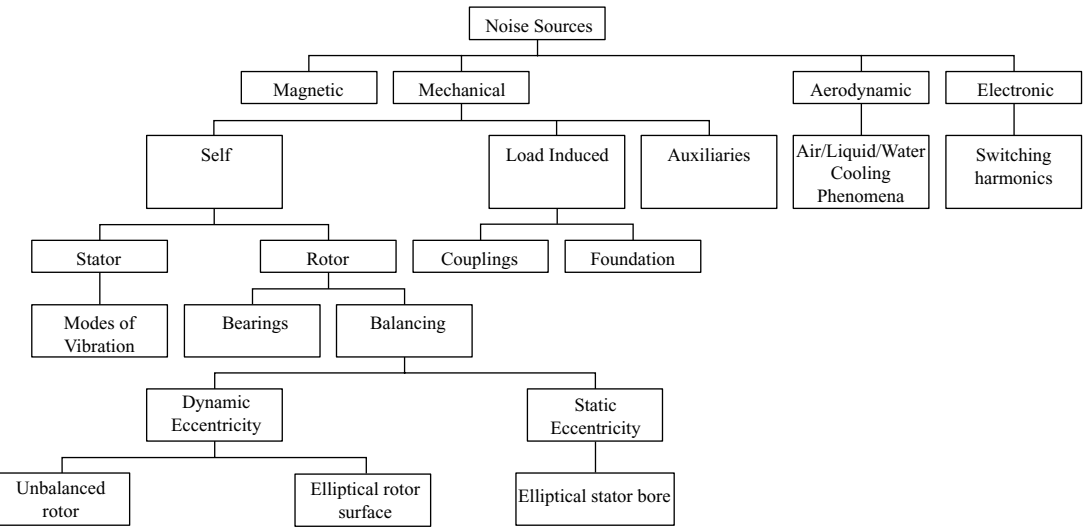


**FIGURE 7.1** Sources of noise in electric machines.

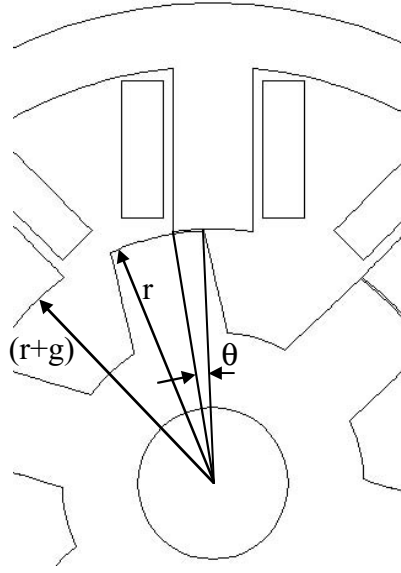


**FIGURE 7.2** Relevant dimensions of the SRM.

Consider that iron is infinitely permeable and has zero reluctance which leaves only the air gap to provide reluctance in the circuit. The air gap flux density at a given stator and rotor pole overlap angle  $\theta$ , air gap  $l_g$ , and current  $i$  is given as  $B_g(\theta, l_g, i)$ . Let  $r$  be the outer radius of the rotor,  $L$  be the stack length or iron length in the  $z$  direction,  $T_{ph}$  be the number of turns in one phase of the machine,  $i$  be the current in the winding,  $H_g$  be the magnetic field strength,  $\Phi$  be the flux, and  $\mu_o$  be the permeability of air. Then the following variables are derived as:

$$B_g(\theta, l_g, i) = \frac{\Phi}{Lr\theta} = \mu_o H_g = \mu_o \frac{T_{ph}i}{l_g} \quad (7.1)$$

$$T_{ph}i = \frac{l_g}{\mu_o Lr} \frac{\Phi}{\theta}$$

The incremental electrical input energy  $dW_e$  is given by:

$$dW_e = id\lambda = id(T_{ph}\Phi) = T_{ph}id\Phi = T_{ph}i = \frac{l_g}{\mu_o r L} \frac{\Phi}{\theta} d\Phi \quad (7.2)$$

The stored energy in the magnetic field  $dW_s$  is

$$W_s = \frac{l_g L r \theta}{2 \mu_o} B_g^2(\theta, l_g, i) = \frac{l_g}{2 \mu_o r L} \frac{\Phi^2}{\theta} \quad (7.3)$$

where the term  $gLr\theta$  gives the volume of the air gap contained by the stator and rotor pole overlap. Note that  $r\theta$  gives the arc of the overlapping region between the stator and rotor poles. The energy balance equation neglecting losses is

$$dW_e = dW_s + dW_m \quad (7.4)$$

where  $dW_m$  is the incremental mechanical energy and  $dW_s$  is the incremental field energy. To find the tangential, radial, and lateral forces, note that the incremental field energy for that directional variable has to be taken and substituted in Eq. (7.4). As the electrical input energy is given in Eq. (7.2), the mechanical energy is computed by subtracting the incremental field energy from the incremental input energy. For example, to calculate the tangential force that is in the direction of rotor pole arc and is a function of the varying rotor position, the incremental field energy is obtained from Eq. (7.3) as:

$$dW_s = -\frac{l_g}{2\mu_o Lr} \frac{\Phi^2}{\theta^2} d\theta + \frac{l_g}{\mu_o Lr} \frac{\Phi}{\theta} d\Phi \quad (7.5)$$

The second term on the right side of Eq. (7.5) is due to the fact that  $\Phi$  is a function of rotor position,  $l_g$  and  $i$ , as is the air gap flux density.

Then, substituting Eqs. (7.2) and (7.5) in Eq. (7.4), the incremental mechanical energy is obtained as:

$$dW_m = \frac{l_g}{2\mu_o Lr} \frac{\Phi^2}{\theta^2} d\theta \quad (7.6)$$

From which the tangential torque, or what is known as the electromagnetic torque, is obtained as:

$$T_e = \frac{dW_m}{d\theta} = \frac{l_g}{2\mu_o Lr} \frac{\Phi^2}{\theta^2} = \frac{l_g r L}{2\mu_o} B_g^2(\theta, l_g, i) \quad (7.7)$$

The tangential force is obtained by dividing the tangential torque by the radius of the rotor pole, yielding:

$$F_t = \frac{T_e}{r} = \frac{l_g L}{2\mu_o} B_g^2(\theta, l_g, i) \quad (7.8)$$

Similarly, the normal force, which is the radial force in the direction of the air gap, is obtained from considering the incremental field energy with respect to the air gap and the incremental mechanical energy as:

$$dW_m = -\frac{1}{2\mu_o r L} \frac{\Phi^2}{\theta} dl_g \quad (7.9)$$

and the radial force is given by:

$$F_n = \frac{dW_m}{dl_g} = -\frac{1}{2\mu_o rL} \frac{\Phi^2}{\theta} = -\frac{rL\theta}{2\mu_o} B_g^2(\theta, l_g, i) \quad (7.10)$$

Similarly, the lateral force can be derived as:

$$F_y = \frac{l_g r \theta}{2\mu_o} B_g^2(\theta, l_g, i) \quad (7.11)$$

From a cursory glance at the forces, it can be stated that lateral force and tangential force are of similar magnitude but the radial force is not. The ratio between the radial and tangential force from Eqs. (7.8) and (7.10) is

$$\frac{F_n}{F_t} = -\frac{r\theta}{l_g} \quad (7.12)$$

The rotor angle can be assumed to be equal to the one-phase conduction angle which in terms of the rotor and stator poles is given as:

$$\theta = \frac{4\pi}{P_s P_r}, \text{ rad} \quad (7.13)$$

where  $P_s$  and  $P_r$  are the number of stator and rotor poles. Considering, for example, an 8/6 SRM with a ratio of radius to air gap equaling 100, the ratio between the radial and tangential forces is found to be 26.19; therefore, the radial force is always multiple times that of the tangential force in the SRM and the same can be said for other electrical machines. Such a large force, though it is symmetric and nulls out in the final analysis (only for uniform air gap), has an impact on the machine because the forces cancel each other only through the rotor and stator bodies, causing stator vibrations. This is the most dominant source of noise generation in an SRM as well as in other electrical machines.

### 7.2.1.2 Mechanical Sources of Noise

The mechanical sources of noise can be divided into many subsections as follows.

#### 7.2.1.2.1 Self

One of the main sources of noise is the stator structure. The stator of the machine has a natural frequency. When one of the frequencies of the exciting forces coincides with the stator natural frequency, resonance occurs, leading to acoustic noise. Therefore, it is imperative to calculate the stator natural frequency accurately. A number of methods are described in literature, but only one method is discussed here.

Similar to other machines, SRM has radial forces producing vibrations that result in acoustic noise. This is mostly at the fundamental mode frequency of the SRM

structure. If the phase frequency or its odd harmonics coincide with that of the SRM, then a resonance occurs, resulting in peaking of stator vibration. The phase frequency is given by:

$$f_p = \left( \frac{\omega_m}{2\pi} \right) P_r, \quad (7.14)$$

where  $\omega_m$  is the speed in rads/sec and  $P_r$  is the number of rotor poles. Vibration is maximum if any of the frequencies,

$$f_n = nf_p, \quad n = 1, 3, 5, 7, \dots \quad (7.15)$$

are coincident with the natural frequency,  $f_n$ , of the stator.<sup>14</sup> Vibrations seem to diminish for even harmonics of phase frequency coinciding with natural frequency  $f_n$  of the SRM structure. Then, to control the acoustic noise, the natural mode frequency of the SRM has to be evaluated. It could be calculated using finite element analysis software for structures or using analytical expression.<sup>14</sup>

Consider the stator lamination stack as a uniform cylindrical shell. Its thickness is  $b_{sy}$  (i.e., the back iron thickness itself), and the stack length is  $L$ . When a vertical load  $w$  is applied on this ring structure, a deflection results, making the ring into an ellipse. The potential energy due to the load application must be equal to the kinetic energy arising out of deflection for energy conservation of the structure. The derivation of  $f_n$  for any material characteristics is given in Appendix 7A.<sup>14</sup> From this, the angular natural frequency can be obtained as:

$$\omega^2 = \frac{2}{12\pi(1-\gamma^2)\left(\frac{\pi}{4}-\frac{2}{\pi}\right)} \cdot \left(\frac{E}{\rho}\right) \cdot \left(\frac{b_{sy}^2}{r_y^4}\right) \quad (7.16)$$

where  $b_{sy}$  is the stator back iron thickness (m),  $\gamma$  is the Poisson ratio,  $\rho$  is the mass density of the material ( $\text{kg}/\text{m}^3$ ),  $r_y$  is the geometric mean radius of the stator shell (m) given by  $r_{sy} = (D_o - b_{sy})/2$ , and  $D_o$  is the outer diameter of the stator lamination (m).

From Eqs. (7.14) and (7.16) it can be seen that the fundamental mode frequency is primarily influenced by back iron thickness and to a lesser extent by the outer diameter of the stator lamination because  $D_o$  usually is a constant for a given power and speed in industrial production. That leaves the back iron thickness as a design parameter to select its first mode frequency. A higher modal frequency is desirable to place the maximum phase frequency at a small fraction of the  $f_n$ . The penalty then is a large back iron thickness that increases the weight, reduces the available area for windings, and increases the current density and copper losses. Note that power density will be reduced. A compromise value of the back iron thickness is based on its flux density being not less than half of the stator pole flux density. This helps to reduce the core losses and could be very useful in high-speed operation.

The stator natural frequency expression is derived under the assumption that the stator core and the outer frame together constitute a single ring, but this may not

hold in many cases. A different approach is required in machines with a stator thickness to radius ratio greater than 0.2. Girgis and Verma<sup>7</sup> derived the general frequency equation of the stator based on the energy method and the principle of Rayleigh–Ritz, considering rigorously the yoke, frame, teeth, windings, and cooling ribs. The procedure is too elaborate to describe here. Verma et al.<sup>10–12</sup> also considered machines with varying stator lengths and their effects on the natural frequency of the machines. The effects of windings and their impregnation on the resonant frequencies of machines are given in Reference 13. A number of other publications outline methods to obtain the approximate resonant frequencies with varying degrees of success. All of these studies are based on induction and synchronous machines, but it is possible to derive relevant relationships for the switched reluctance machines using similar procedures.

Yongxiao et al.<sup>15</sup> have developed a method of calculating natural frequencies for SRMs based on the energy method, similar to induction motors, and have also demonstrated the effects of varying pole arcs and windings on the natural frequencies. Neglect of stator windings on the calculation of natural frequency results in 20 to 30% error in SRMs.

#### 7.2.1.2.2 Load-Induced

The load-induced sources of noise include noise due to coupling of the test machine with a load and due to mounting of the machine on the foundation.

#### 7.2.1.2.3 Auxiliaries

The auxiliary mechanical sources of noise include noise due to bearings, brush commutators, and rotor unbalance.<sup>2,5</sup> Noise due to brush commutators is not considered further as it is not relevant to SRMs. Manufacturers usually choose between sleeve bearings and rolling bearings. Sleeve bearings are not contributors to noise but are more expensive than rolling bearings. The causes of noise due to sleeve bearings are the roughness of the sliding surfaces, lubrication, stability of the oil film in the bearing, and manufacturing faults. The exciting forces are produced at frequencies of  $N/60$  (due to rotor unbalance and/or eccentricity) and  $N_g N/60$  (due to axial grooves), where  $N$  is the speed in rpm, and  $N_g$  is the number of grooves in the sleeve bearing.

Noise from rolling bearings results due to track geometry and spherical accuracy problems, dirt and other foreign matters, lubrication conditions, natural frequencies of the outer ring, running speed, load, temperature, and alignment. The exciting forces are produced at frequencies of  $N/60$  (due to rotor unbalance and/or eccentricity),  $\frac{N}{60} \frac{r_i}{r_i + r_o}$  (due to irregularities in the ball cage),  $Z_b \frac{N}{60} \frac{r_i}{r_i + r_o}$  (due to defects in the outer ring of the bearing), and  $i \cdot Z_b \frac{N}{60} \frac{r_i}{r_i + r_o}$  (due to variation of the stiffness of the bearing), where  $i$  is a positive integer;  $r_i$  and  $r_o$  are the radius of the inner and outer contact surfaces, respectively; and  $Z_b$  is the number of balls in the ball bearing.

#### 7.2.1.2.4 Rotor Unbalance

Rotor unbalance is one of the major causes of noise. It gives rise to dynamic rotor vibration, eccentricity, and an exciting force due to rotor unbalance and occurs at a frequency of  $N \cdot i/60$ .

### 7.2.1.3 Aerodynamic Sources of Noise

Cooling of machines by air, water, or oil with fans<sup>2,5</sup> is one of the major sources of acoustic noise. Fans create discrete noise components at frequencies of  $f_v \pm f_f$ , where  $f_v$  and  $f_f$  are the vortex and pure tone blade frequencies, respectively, given by:

$$f_v = 0.185 \frac{v}{D_f} \text{ Hz} \quad (7.17)$$

$$f_f = N_b \frac{N}{60} \quad (7.18)$$

where  $D_f$ ,  $N_b$ , and  $v$  are the fan-mounting-arm diameter, the number of fan blades, and the airstream velocity, respectively. The frequency of the pure tone due to cooling air passing through rotor ducts is given by:

$$f_{rt} = Z_r \frac{N}{60} \quad (7.19)$$

where  $Z_r$  is the number of rotor slots which in the case of SRMs equals the rotor poles.

### 7.2.1.4 Electronic Sources of Noise

The electronic sources of noise arise due to the harmonics contained in the applied voltage and in the current. The current in the SRM is determined by the winding inductance vs. rotor angle for a given current and the controller algorithm. The winding current is not steady during operation of the machine, thus the inductance varies continuously, resulting in generation of harmonic flux linkages. This is a particular feature of the SRM itself. The impact of various control and system variables on vibration and acoustic noise are summarized below:<sup>19</sup>

1. At a given rotor position with the same maximum current, the single pulse mode induces a higher peak vibration than the current limited mode.
2. At a given rotor position, a higher rate of change of current causes larger vibrations.
3. Vibration is greater near the aligned position relative to the unaligned position.
4. Higher current induces larger vibrations.
5. Vibrations are larger during turn-off in both single-pulse and current-limited modes because of the higher rate of change of current and because turn-off occurs near the aligned position where vibration is maximum.
6. Turn-off before full alignment reduces vibrations.
7. Vibrations induced behind a stator pole 90° away from the excited pole are exactly 180° out of phase with the vibrations of the excited pole (8/6 machine).
8. The largest vibrations were induced when the speed was such that an odd harmonic frequency component of the exciting phase current coincided with the resonant frequency, and smaller vibrations were found when the even harmonic frequency component coincided with the resonant frequency of the stator.

## 7.3 NOISE MITIGATION

A summary of noise mitigation methods is provided in this section.

### 7.3.1 MAGNETIC NOISE MITIGATION

The radial forces in a machine are directly proportional to the square of the flux density in the air gap. One of the obvious ways to reduce noise would be to reduce the flux density by enlarging the air gap. The power density is then reduced, resulting in lower utilization of materials.

Skewing the stator or rotor slots reduces the average radial forces in small machines, leading to a considerable reduction in noise, whereas in large machines it may lead to torsional vibrations and an increase in acoustic noise. Skewing is also helpful in eliminating standstill locking and crawling in induction machines. Experimentation has shown that skewing of the rotor by about one stator slot pitch produces the best results with regard to reducing noise and vibrations.<sup>20</sup>

Skewing is not relevant in the SRM for the reasons that it will remove the advantage of manufacturing simplicity and will lower the ratio between the aligned and unaligned inductances, thus reducing the power output and power density of the machine. The number of poles influences the dominant harmonic torque ripple but seems to have no apparent impact on the magnitude of radial forces and hence on the acoustic noise.

Following standard rules to select slot numbers reduces or eliminates unbalanced magnetic pull, locking, and crawling in ac machines and vastly helps in reducing noise and vibrations in machines. A comprehensive list of rules for construction of ac machines can be found in Reference 5. Locking and crawling problems have not been reported in SRM studies so far; therefore, no guidelines exist as to selection of the number of slots or poles from the point of view of such problems. Magnetic noise produced by rotor eccentricity can be reduced by using parallel paths in the stator phase windings.<sup>2</sup>

Magnetic noise due to rotor eccentricity will exacerbate the radial forces unevenly, resulting in additional noise generation. Manufacturing the rotor with tight tolerances will mitigate the problem.

### 7.3.2 MECHANICAL NOISE MITIGATION

As mentioned before, the exciting force frequencies and the natural frequency of the machine structures have to be mismatched. Hence, the natural frequencies of the machine must be calculated accurately either by some of the methods described earlier or by finite element analysis, and they must be compared with the main exciting forces. However, this will not ensure complete noise mitigation, especially in variable-speed drives, where some resonance is bound to occur. Proper adjustments of couplings and a proper foundation may reduce or eliminate noises of load-induced origin. Bearing noise<sup>2</sup> can be reduced by applying an axial pre-load by means of coil springs, adding elastic damping elements in the bearing housing, mismatching natural frequencies of the bearing outer ring and bearing housing with the natural frequencies of the machine and exciting forces, and keeping bearing

misalignment to a minimum. Using bearings having shields or seals to prevent dirt from entering the bearing may help reduce noise. Dynamic rotor balancing is done routinely in industry to eliminate noise due to rotor unbalance.

### 7.3.3 AERODYNAMIC NOISE MITIGATION

Vortex frequency is no longer detectable if the shape of the fan blades is changed from a circular to an aerofoil cross section. In addition, research has shown that the minimum distance between the fan blades and a stationary obstacle should be  $\geq(u^2/30)$ , where  $u$  is the blade speed in m/sec.<sup>25</sup> This will avoid the appearance of the pure tone component in the ventilation noise spectrum. Reducing the number of rotor vents and lining air chambers with sound-absorbent insulation provide noise mitigation. Noise from the cooling fan is decreased using unevenly spaced fan blades, reducing the diameter of the fan, and using porous materials for the fan blades.

### 7.3.4 ELECTRONIC NOISE MITIGATION

Various pulse width modulation (PWM) schemes are in force to eliminate lower order harmonics. The higher order harmonics can be neglected completely, as their forces are small.

Modulation of phase voltages while varying switching frequency or the pulse position randomly is referred to as random pulse width modulation (RPWM). A number of publications have established that RPWM causes the power spectrum of the output voltage to acquire a continuous part, while the harmonic part is significantly reduced, which in turn reduces very marginally acoustic noise and vibrations while the sound pressure is not affected.<sup>22</sup> This strategy has been applied to induction motor drives, and a few attempts have been made to adapt it to SRM drives.<sup>21,23,24</sup>

Spectral analysis of the PWM voltage output to obtain the amplitudes and frequencies of the harmonics and then spreading the spectrum over the entire frequency range by pulse frequency modulation while avoiding the natural frequencies of the stator can lead to significant reduction in noise.<sup>25</sup> Both induction and switched reluctance motor drives demonstrate considerably less noise if the torque ripple is minimized. A number of publications give methods to minimize the torque ripple.

Active noise reduction methods have been proposed for both induction and switched reluctance motors. A current harmonic injected into the stator windings will cause additional stator flux density components and force waves to be generated. If the force wave has the same magnitude, frequency, and mode number as the natural force wave but is of opposite phase, the two force waves will nullify, causing the corresponding magnetic noise to disappear.<sup>27</sup> Similar methods have also been proposed for SRMs.<sup>26</sup>

A number of electronic noise-reduction methods for SRMs have been summarized in Reference 28. Current shaping is utilized so the resulting magnetic attraction of the stator to the rotor does not contain any harmonics that can excite the stator resonance.<sup>21</sup> Current shaping, however, introduces the possibility of a lower electro-mechanical efficiency and a trade-off may have to be considered between acoustic

noise and efficiency. It has been shown that maximum vibrations occur in SRMs during current commutation,<sup>19</sup> so the current commutation procedure can be modified to lower the rate of change of voltage during turn-off and to lower the resulting acoustic noise and vibrations.<sup>28</sup>

All the prevailing analyses assume that the rise and fall of the current are left to circuit conditions rather than being actively shaped; therefore, the nature of the air gap torque in relation to its ripple magnitudes and harmonic numbers is not considered. This is bound to have consequences on noise reduction. Hence, the discussion needs to be cautiously interpreted in light of very limited studies and results.

### 7.3.5 ACTIVE NOISE-CANCELLATION TECHNIQUES

The relationship between acoustic noise due to vibration of the stator and phase current commutation initiation with negative bus voltage application to phase has been documented.<sup>19</sup> A large negative rate of change of current is suddenly realized with voltage polarity reversal across the machine winding. This induces high-magnitude vibration at the first mode frequency of the SRM. A few switching techniques to reduce the vibrations and resulting noise have been proposed as follows.<sup>19</sup>

#### 7.3.5.1 Two-Stage Commutation Method

In this method, the winding voltage is reduced from positive dc bus voltage to zero by letting the current freewheel in the machine winding. After half a resonant cycle, the voltage across the winding is changed from zero to a negative dc source voltage and maintained at that until the current is reduced to zero, as shown in [Figure 7.3](#). This produces a vibration  $180^\circ$  out of phase with that due to the first vibration and thus cancels it. To apply this method, the SRM converter must be capable of applying positive, zero, and negative voltage across the machine phases. Note that the asymmetric converter and  $(q + 1)$  switch topologies could meet this requirement. Two additional methods for noise reduction proposed for converters with no zero-voltage capability are given in the following text.

#### 7.3.5.2 Voltage-Smoothing Method

In this method, the applied voltage is gradually reduced by decreasing the duty cycle prior to applying constantly the negative bus dc voltage across the machine phase winding. The time taken to change the duty cycle of one to zero can be applied in many resonant frequency cycles (say, as many as 20). The disadvantage of this method is that it may take considerable time and may interfere with optimum torque production and its control. The method is illustrated in [Figure 7.4](#) with single-voltage pulse operation. This method requires converters with positive and negative voltage capability such as C-dump, etc. Note that the rate of change of current at the onset of commutation is very low due to duty cycle reduction and then becomes greater when the voltage applied is a constant negative dc bus value. This method is found to reduce the acoustic noise but is not able to effectively cancel as much as the two-stage commutation method. Hence, a three-stage commutation method has been introduced.

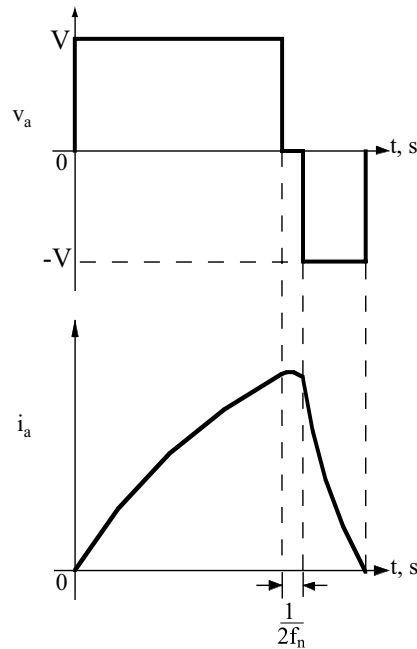


**FIGURE 7.3** Two-stage commutation method for single-voltage pulse operation.

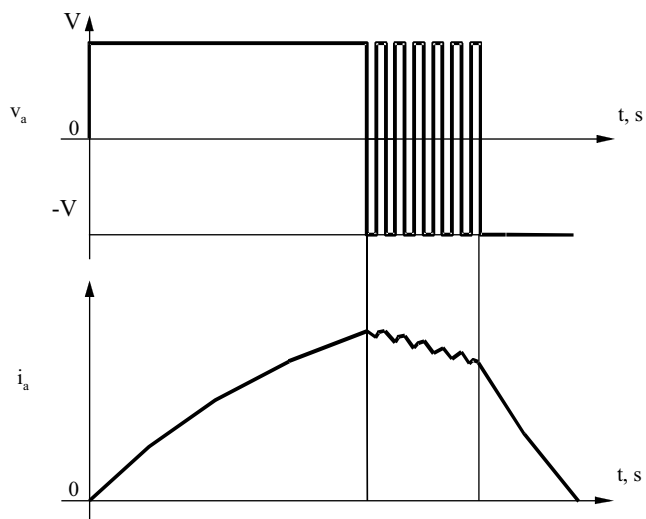


**FIGURE 7.4** Voltage smoothing method for single-voltage pulse operation.

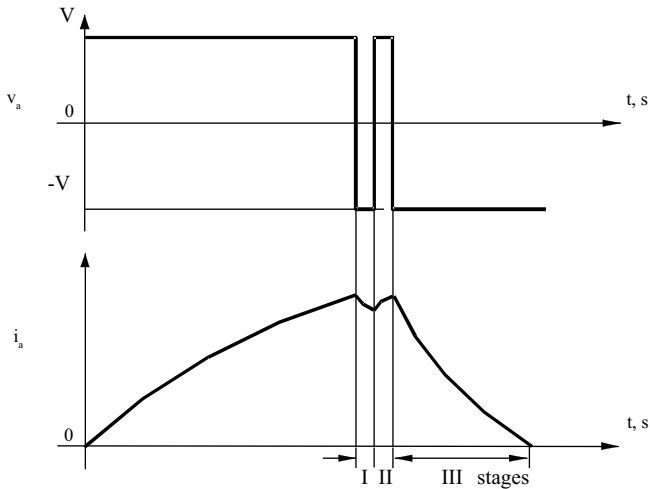


**FIGURE 7.5** Three-stage commutation illustrated with a single-voltage pulse operation.

### 7.3.5.3 Three-Stage Commutation Method

This method has three stages. In the first stage, at the onset of commutation, a negative voltage is applied to produce a first vibration with a negative acceleration. After some time, the applied voltage to the machine phase is reversed to positive which produces a vibration in opposition to the first one. After some time, the applied voltage is again reversed to a negative bus value and maintained at it until the current is made zero (see Figure 7.5). Here, again, note that only the positive and negative voltage capability of the converter is required. This method is better than the voltage-smoothing method. It still requires at least half a resonant cycle to cancel the noise by accomplishing stages one and two. The initial negative acceleration at the onset of commutation, which was attenuated considerably in the two-stage commutation method, persists in this method. The time durations for stages one and two must be arrived at by trial and error, and there seems to be no direct way of evaluating them for practical implementation.

### 7.3.5.4 Extended Freewheeling Method

In this method, near the onset of commutation, freewheeling of the current within the winding is attempted. Note that the applied voltage across the phase winding is approximately zero. This freewheeling is allowed for an extended period of time unlike in the two-stage commutation method where freewheeling is permitted for only half the resonant cycle. After a considerable time or zero voltage operation, negative voltage is switched across the machine phase to finally commute the current. This method attenuates the vibrations but does not cancel as much as two-stage and three-stage commutation methods do. This method is illustrated with a single-voltage pulse operation in Figure 7.6. Note that the implementation of this

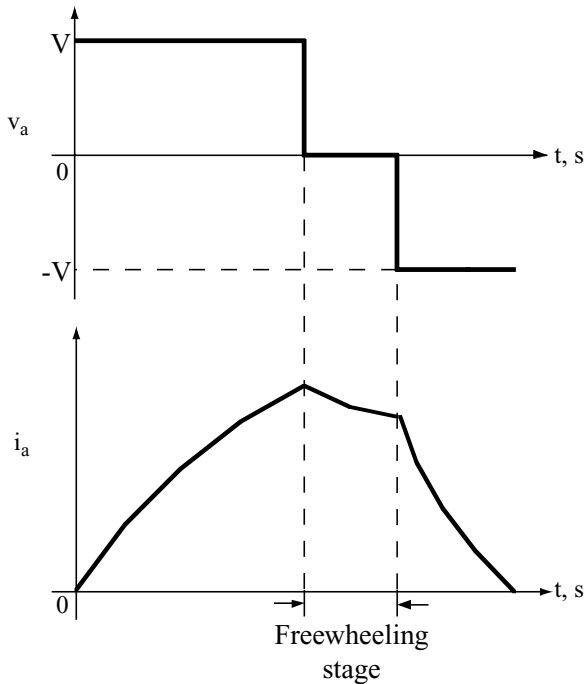


**FIGURE 7.6** Extended freewheeling method illustrated with single-voltage pulse operation.

algorithm requires a converter with positive, zero, and negative voltage output capability such as an asymmetric converter or other topologies.

### 7.3.5.5 Disadvantages of Noise-Cancellation Techniques

In spite of attenuation of the acoustic noise of the SRM due to noise-cancellation techniques, there are some disadvantages:

1. Even the best method (two-stage commutation) requires at least half a resonant cycle. That, for example, in a machine with 1.5-kHz frequency at the first mode, amounts to a time of 0.333 msec. In comparison to a phase period at 6000 r/min in an 8/6 machine, two-stage commutation time constitutes 20% of the phase period. This is very considerable and will adversely affect the torque generation and power output along with dynamic control of the drive system. Therefore, these techniques may be more suitable at very low speeds than at high speeds.
2. If the drives operate with PWM switching, then for speeds much lower than the full speed the two-stage or extended freewheeling method could be incorporated, because at lower speeds the duty cycle of the switching will be much less than one. Results are not available for high speeds where the noise is a particularly serious problem, as the third harmonic of the phase frequency excites the first-mode vibration.

## 7.4 QUALITATIVE DESIGN MEASURES TO REDUCE NOISE

In the absence of theoretical relationships to describe the impact of design and control variables on the noise reduction, some qualitative design measures have evolved based on empirical data obtained over a good many years of practice. They are considered in the following.

### 7.4.1 MACHINE DESIGN CONSIDERATIONS

Back iron thickness, air gap length, notches and holes in the laminations, and bearing locations play an important role in noise control. Each one of these factors is considered below.

1. *Back iron thickness*: Higher thickness is favorable as it increases the first mode frequency and gives higher mechanical strength, both of which are helpful to reduce vibration. But, it has design consequences and a trade-off has to be achieved, as discussed elsewhere.
2. *Air gap*: Smaller air gaps tend to give higher inductance slopes at the beginning and ending of pole overlaps. This may not have much impact on rate of change of current but can produce a sharp rate of rise in the torque. Higher inductance slopes tend to produce higher acoustic noise. Extension of the rotor pole area with pole shoes reduces the inductance slope, resulting in lower acoustic noise.<sup>42</sup> With a smaller air gap, punching tolerances and machining tolerances of the lamination are amplified with the consequence of high, uneven magnetic pull. A slightly larger air gap is preferred from the noise and manufacturing points of view. Further, a smaller air gap also increases the flux density, thus increasing the severity of the radial forces.
3. *Notches and holes in the laminations*: They have to be judiciously chosen so as not to affect the mechanical robustness and not to create localized magnetic flux density increases which result in an increase in the magnetic noise.
4. *Bearings*: These have to be located very close to the rotor laminations so as to minimize eccentricity in the rotor and minimize lateral deflection of the rotor. A stiff bearing is highly recommended for the same reasons.
5. *Punching of laminations*: Tight tolerances on the stator and rotor poles and its angles help to reduce the uneven radial forces.

### 7.4.2 TORQUE-SMOOTHING CONTROL

Torque smoothing results in uniform air gap torque generation, and noise associated with the torque ripple and commutation torque ripple is eliminated which leads to a significant reduction in acoustic noise.

### **7.4.3 CONVERTERS WITH A HIGH DEGREE OF FREEDOM**

To prevent large ripples in the current, it is important to have converters with the capability to output positive, zero, and negative voltages for application to machine phases. If freewheeling is used for current control before the commutation initiation, not only is smooth and low ripple current control achieved but the duty cycle of the switching is also very much reduced. It also reduces the circulating energy from the dc bus and the machine phases and increases efficiency but most of all avoids frequent energy reversals in the machine phases. Energy reversals are associated with a large rate of fall of current that is clearly a noise source. Elimination of these energy reversals during the phase cycle eliminates noise associated with them altogether.

### **7.4.4 VARYING INPUT VOLTAGE**

As the induced emf is directly proportional to rotor speed, the input voltage to the machine can be programmed to be a function of the speed. At speeds lower than the rated speed, the rate of change of current is reduced as the available input voltage is made lower than the source voltage. Studies have indicated that noise reduction is considerable when the speed is below the rated value.<sup>41</sup> The only disadvantage with this technique is that it may require an additional converter stage such as a buck or buck-boost converter to vary the input voltage to machine phases.

## **7.5 MEASUREMENT OF ACOUSTIC NOISE AND VIBRATIONS**

Measurement of motor noise can be made using an A-weighted sound level meter that is of either analog or digital type. The meters directly output the readings in decibels, and measuring the acoustic noise at a number of positions around the machine, as dictated by ISO R1680-1970, leads to very reliable results. Accurate motor noise results can be obtained only if noise measurements are made in an anechoic chamber after properly calibrating the noise measuring equipment and having a very large number of measuring points. If an anechoic chamber is not available, then measurements can be made in an ordinary large room after measuring the ambient noise and making corrections for the ambient noise. This is an inexpensive way of measuring the noise.

The audible noise caused by vibrations in electrical machines is also measured in the method described above. However, there may be a requirement to measure the actual vibrations in the test machine. Many international standards, such as ISO 2372-1974,<sup>31</sup> ISO 2373-1974,<sup>32</sup> and ISO 3945-1977<sup>33</sup> describe the procedure.

The standards define the types of mounting bases, operating conditions, measurement points, and measurement equipment and give recommendations on the limits of vibration severity. Timar<sup>5</sup> describes the use of non-contact and contact transducers for measurement of vibrations. A simple method of measuring actual vibrations of a machine would be using piezoelectric accelerometers, which can be directly mounted on the machine. Their output is directly proportional to the

vibrations and can be amplified and recorded. A detailed description of piezoelectric accelerometers and methods of using them to obtain accurate vibration measurements are given in Reference 5. Other researchers<sup>8</sup> also describe the piezoelectric accelerometer measuring systems. Stuhler and El-Kafrawy<sup>34</sup> describe the use of laser doppler vibrometers, fiberoptic vibrometers, non-contacting displacement transducers, and piezoforce vibrometers.

ISO R1680-1970 is the primary international standard governing the acoustic noise performance of electric machines and can be applied to all rotating electrical machines of all sizes without limitations to power output and voltage. The test environment and mounting of the test machine are clearly defined, as is the effect of background noise. ISO R1680 acknowledges that the machine should be operated under the rated load, speed, and excitation conditions while measuring airborne noise, but it also mentions that when the effects of load are known or if the machine noise is independent of loading, then noise measurements under no-load conditions will usually suffice. ISO R1680 also defines the type of measuring instruments to be used, methods of measurements, location of the measuring points, calculations, and interpretation of results. It also accounts for measuring airborne noise in reverberant and semi-reverberant field conditions.

There are many limitations to the measurement methods and procedures outlined by ISO R1680. Lisner and Timar<sup>35</sup> have investigated these limitations for induction motors. Noise under no-load conditions is smaller than under load conditions. Speed variations may cause resonance at some frequencies known as critical frequencies; therefore, noise may increase or decrease with changes in speed and may be higher when the machine is operated at speeds greater than the nominal speed. Slightly excess supply voltage may also cause a large increase in noise. Also, supplying power from inverters may increase noise as the input voltages are not pure sinusoids with the higher order harmonics injected from switching control of the inverters. This may require that machines be supplied with inverters, tested over the full range of operating speed, and tested at 110% of nominal voltage and at various loads from no load to full load.

Craggs<sup>36</sup> reviews many methods to measure the acoustic noise of loaded machines. One method is to obtain the ambient noise of all the auxiliary equipment used to load a machine and then load the machine and obtain the noise measurement. Obviously, if the ambient noise of auxiliary equipment is very high, then obtaining accurate readings for the loaded machines will be difficult. Another method for obtaining the noise of a loaded machine is to construct a noise-testing enclosure.<sup>36</sup> A third method is to use sound-intensity measurements to obtain the noise of loaded machines (see Yang and Ellison<sup>3</sup> and Craggs<sup>37</sup>).

## 7.6 FUTURE DIRECTIONS

One of the approaches available for research in acoustic noise is a parametric study to evaluate the decisive influence of leading variables on the noise. That does not help in the design of quiet machines, as the relationship between the machine dimensions and excitation conditions is not explicitly or implicitly established. Alger<sup>1</sup> derived a relation for induction machines but subsequent work has demonstrated that

it is not adequate. While realizing that the models relating the machine dimensions and operating conditions determined by converter and load to the noise will be extremely complex, nevertheless simple models can enable understanding of the phenomenon of noise generation. Such models are being researched for SRMs.<sup>29</sup> If such simpler models are experimentally correlated, then these models can be handy in the minimization of noise at the design stage itself. Also, the constraints involved in low-noise machines in terms of lower utilization of the materials in the machine and control of the converter and drive system could be studied to provide clear insight into the cost implications for the motor drive system under consideration to achieve a certain noise specification.

## APPENDIX 7A: DERIVATION OF FIRST-MODE FREQUENCY OF AN SRM

The following derivation is from Reference 14 and is obtained without substituting the Poisson value in the equation. A Poisson value of 0.3 is used in the reference.

### POTENTIAL ENERGY

Let  $W$  be a vertical load on a plain ring. Then, the change in vertical part of the diameter is

$$D_y = \frac{Wr_y^3}{E \cdot I} \left( \frac{\pi}{4} - \frac{2}{\pi} \right) \quad (7A.1)$$

where  $r_y$  is the geometric mean radius of the ring; that is,

$$r_y = \frac{(D_o - b_{sy})}{2} \quad (7A.2)$$

In Eq. (7A.2),  $D_o$  is the outer diameter of the stator lamination stack, and  $b_{sy}$  is the back iron thickness. In Eq. (7A.1),  $E$  is the modulus of elasticity, and  $I$  is the polar moment of inertia. The product of  $E$  and  $I$  for a rectangular section with length  $L$  and thickness  $b_{sy}$  and Poisson ratio  $\gamma$  is

$$EI = \frac{ELb_{sy}^3}{12(1 - \gamma^2)} \quad (7A.3)$$

Substituting Eq. (7A.3) in (7A.1) gives:

$$D_y = \left( \frac{W}{L} \right) \cdot \left( \frac{r_y}{b_{sy}} \right)^3 \cdot \frac{1}{E} \cdot \left( \frac{\pi}{4} - \frac{2}{\pi} \right) [12(1 - \gamma^2)] \quad (7A.4)$$

Let  $K$  be the spring constant per unit length defined as:

$$K = \frac{W/L}{D_y} = \left( \frac{b_{sy}}{r_y} \right)^3 \cdot \frac{E}{12(1 - \gamma^2) \left( \frac{\pi}{4} - \frac{2}{\pi} \right)} \quad (7A.5)$$

The radial deflection is then derived to be

$$\Delta = \frac{D_y}{2} \quad (7A.6)$$

and the potential energy per unit length is

$$E_p = 2K\Delta^2 = 2\left(\frac{b_{sy}}{r_y}\right)^3 \cdot \frac{E\Delta^2}{12(1-\gamma^2)\left(\frac{\pi}{4} - \frac{2}{\pi}\right)} \quad (7A.7)$$

## KINETIC ENERGY

Due to the load, assume that the ring is deformed into an ellipse with radius,

$$r_y(\theta) = r_y + \delta(t) \cos(2\theta) \quad (7A.8)$$

where the time variation of the radius  $\delta(t)$  is given by:

$$\delta(t) = \delta \sin(\omega t) \quad (7A.9)$$

The local velocity of a point on the ring is

$$v = \frac{dr_y}{dt} = \omega \delta \cos(\omega t) \cos(2\theta) \quad (7A.10)$$

Using this, the kinetic energy of the ring is derived as:

$$E_k = \int_0^{2\pi} (vr_y b_{sy} L \rho) d\theta \quad (7A.11)$$

where  $\rho$  is the mass density of the lamination material. Substituting Eq. (7A.10) into (7A.11) and simplifying,

$$E_k = \pi \rho \delta^2 r_y b_{sy} \omega^2 \quad (7A.12)$$

## NATURAL FREQUENCY

For a ring, it is found that the vertical deflection in terms of horizontal deflection  $D_x$  is

$$D_y = 1.086 D_x \quad (7A.13)$$

The average of the deflection in diameters is 1.0445, by taking the average of the  $D_x$  and  $D_y$  coefficients. Let the variation in radius be

$$\delta = \frac{\Delta}{1.0445} \quad (7A.14)$$

Equating potential and kinetic energy in Eq. (7A.14), the resonant frequency is

$$\omega^2 = \frac{2}{12\pi(1-\gamma^2)\left(\frac{\pi}{4} - \frac{2}{\pi}\right)} \cdot \left(\frac{E}{\rho}\right) \cdot \left(\frac{b_{sy}^2}{r_y^4}\right) \quad (7A.15)$$

## REFERENCES

1. Alger, P.L., *Induction Machines*, Gordon & Breach, New York, 1970.
2. Yang, S.J., *Low-Noise Electrical Motors*, Clarendon Press, Oxford, 1981.
3. Yang, S.J. and A.J. Ellison, *Machinery Noise Measurement*, Clarendon Press, Oxford, 1985.
4. Belmans, R., K.J. Binns, W. Geysen, and A. Vandenput, *Vibrations and Audible Noise in Alternating Current Machines*, NATO ASI Series, Kluwer Academic, Dordrecht/Norwell, MA, 1988.
5. Timar, P.L., *Noise and Vibrations of Electrical Machines*, Elsevier, Amsterdam/New York, 1989.
6. Bonnet, A., L. Wittman, and J.G. Miller, Motor vibes: noise and vibration bibliographies and abstracts, in *1993 Pulp and Paper Ind. Tech Conf.*, Hyannis, MA, pp. 184–205, 1993.
7. Girgis, R.S. and S.P. Verma, Method for accurate determination of resonant frequencies and vibration behavior of stators of electrical machines, in *IEEE Trans. on Electrical Power Apparatus B*, 128(1), 1–11, 1981.
8. Verma, S.P. and R.S. Girgis, Experimental verification of resonant frequencies and vibration of stators of electrical machine. Part 1. Model, experimental procedure and apparatus, in *IEEE Trans. on Electrical Power Apparatus B*, 128(1), 12–21, 1981.
9. Verma, S.P. and R.S. Girgis, Experimental verification of resonant frequencies and vibration of stators of electrical machines. Part 2. Experimental investigations and results, in *IEEE Trans. on Electrical Power Apparatus B*, 128(1), 22–32, 1981.
10. Verma, S.P., K. Williams, and R.K. Singal, Vibrations of long and short laminated stators of electrical machines. Part I. Theory, experimental models, procedure and set-up, *J. Sound Vibration*, 129, 1–13, 1989.
11. Williams, K., R.K. Singal, and S.P. Verma, Vibrations of long and short laminated stators of electrical machines. Part II. Results for long stators, *J. Sound Vibration*, 129, 15–29, 1989.
12. Singal, R.K., S.P. Verma, and K. Williams, Vibrations of long and short laminated stators of electrical machines. Part II. Results for short stators and validity of simplified frequency equations, *J. Sound Vibration*, 129, 31–44, 1989.
13. Singal, R.K., K. Williams, and S.P. Verma, The effect of windings, frame and impregnation upon the resonant frequencies and vibrational behavior of an electrical machine stator, in *Experimental Mechanics*, 30, 270–280, 1990.
14. Colby, R.S., F.M. Mottier, and T.J.E. Miller, Vibration modes and acoustic noise in a four-phase switched reluctance motor, in *IEEE Trans. on Ind. Appl.*, 32(6), 1357–1364, 1996.
15. Yongxiao, C., W. Jianhua, and H. Jun, Analytical calculation of natural frequencies of stator of switched reluctance motor, in *8th Int. Conf. on Electrical Machines and Drives*, Conf. Publ. No. 444, pp. 81–85, 1997.

16. Yang, S.J., Effects of voltage/current harmonics on noise emission from induction motors, in *Vibrations and Audible Noise in Alternating Current Machines*, R. Belmans, K.J. Binns, W. Geysen, and A. Vandenput, Eds., Kluwer Academic, Dordrecht/Norwell, MA, 1988, pp. 457–468.
17. Belmans, R.J.M., L. D'Hondt, A. Vandenput, and W. Geysen, Analysis of the audible noise of three phase squirrel cage induction motors supplied by inverters, *IEEE Trans. on Ind. Appl.*, 23, 842–947, 1987.
18. Belmans, R.J.M., D. Verdyck, W. Geysen, and R.D. Findlay, Electro-mechanical analysis of the audible noise of an inverter-fed squirrel-cage induction motor, *IEEE Trans. on Ind. Appl.*, 27(3), 539–544, 1991.
19. Wu, C.Y. and C. Pollock, Analysis and reduction of vibration and acoustic noise in the switched reluctance drive, Conf. Record, *IEEE IAS Ann. Mtg.*, 93CH3366-2, 1993, pp. 106–113.
20. Nau, S.L., The influence of the skewed rotor slots on the magnetic noise of three-phase induction motors, in *8th Int. Conf. on Electrical Machines and Drives*, Conf. Publ. No. 444, 1997, pp. 396–399.
21. Cameron, D.E., J.H. Lang, and S.D. Umans, The origin and reduction of acoustic noise in doubly salient variable-reluctance motors, in *IEEE Trans. on Ind. Appl.*, 28(6), 1250–1255, 1992.
22. Trzynadlowski, A.M., F. Blaabjerg, J.K. Pedersen, R.L. Kirlin, and S. Legowski, Random pulse width modulation techniques for converter fed drive systems—A Review, Conf. Record, *IEEE IAS Ann. Mtg.*, 93CH3366-2, 1993, pp. 1136–1143.
23. Blaabjerg, F. and J.K. Pedersen, Digital implemented random modulation strategies for ac and switched reluctance drives, in *Proc. of IECON '93*, 93CH3234-2, 1993, pp. 676–682.
24. Blaabjerg, F., J.K. Pedersen, P. Nielsen, L. Andersen, and P.C. Kjaer, Investigation and reduction of acoustical noise from switched reluctance drives in current and voltage control, in *Proc. of Int. Conf. on Electrical Machines*, 1994, pp. 589–594.
25. Stemmler, H. and T. Eilinger, Spectral analysis of the sinusoidal PWM with variable switching frequency for noise reduction in inverter-fed induction motors, in *Proc. 1994 Power Electronics Specialist Conf.—PESC '94*, Vol. 1, Taipei, Taiwan, 1994, pp. 269–277.
26. Michaelides, A. and C. Pollock, Reduction of noise and vibrations in switched reluctance motors: new aspects, in *Proc. IEEE IAS Ann. Mtg.*, 96CH25977, 1996, pp. 771–778.
27. Belkhayat, D., D. Roger, and J.F. Brudny, Active reduction of magnetic noise in asynchronous machine controlled by stator current harmonics, in *8th Int. Conf. on Electrical Machines and Drives*, Conf. Publ. No. 444, 1997, pp. 400–405.
28. Krishnan, R. and P. Vijayraghavan, State of the art: acoustic noise in switched reluctance motor drives, in *Proc. of IECON '98*, Aachen, Germany, 1998, pp. 929–934.
29. Rasmussen, P.O., F. Blaabjerg, and T.J.E. Miller, *Acoustic Noise Simulation for Switched Reluctance Motors with Audible Output*, private communication.
30. International Organization for Standardization, ISO R1680-1970: test code for the measurement of the airborne noise emitted by rotating electrical machinery, in *ISO Standards Handbook. 4. Acoustics, Vibration, and Shock*, 1985, pp. 150–166.
31. International Organization for Standardization, ISO 2372-1974: mechanical vibration of machines with operating speeds from 10 to 200 rev/s—basis for specifying evaluation standards, in *ISO Standards Handbook. 4. Acoustics, Vibration, and Shock*, 1985, pp. 560–568.

32. International Organization for Standardization, ISO 2373-1974: mechanical vibration of certain rotating electrical machinery with shaft heights between 80 to 400 mm—measurement and evaluation of the vibration severity, in *ISO Standards Handbook. 4. Acoustics, Vibration, and Shock*, 1985, pp. 569–573.
33. International Organization for Standardization, ISO 3945-1977: mechanical vibration of large rotating machines with speed range from 10 to 200 rev/s—measurement and evaluation of the vibration severity *in situ*, in *ISO Standards Handbook. 4. Acoustics, Vibration, and Shock*, 1985, pp. 580–585.
34. Stuhler, W. and A. El-Kafrawy, Measurements of vibrations for electrical machines, in *Vibrations and Audible Noise in Alternating Current Machines*, R. Belmans, K.J. Binns, W. Geysen, and A. Vandenput, Eds., Kluwer Academic, Dordrecht/Norwell, MA, 1988, pp. 425–446.
35. Lisner, R. and L. Timar, A new approach to electric motor acoustic noise standards and test procedures, in *IEEE Int. Electric Machines and Drives Conf. Rec.*, Milwaukee, WI, pp. 6.1–6.3, 1997.
36. Craggs, J.L., Measuring the noise level of loaded electric motors, in *Rec. of 1991 Ann. Pulp and Paper Ind. Tech. Conf.*, Montreal, Canada, pp. 239–245.
37. Craggs, J.L., Specifying and measuring the noise level of electric motors in operation, in *Rec. IAS 38th Ann. Petroleum and Chemical Ind. Conf.*, 1991, Toronto, Canada, pp. 79–83.
38. Pulle, D.W.J., J.C.S. Lai, J.F. Milthorpe, and N. Huynh, Quantification and analysis of acoustic noise in switched reluctance drives, in *Fifth European Conf. on Power Electronics and Applications*, Conf. Publ. No. 377, 1993, Brighton, UK, pp. 65–70.
39. Tang, Y., Characterization, numerical analysis, and design of switched reluctance motors, *IEEE Trans. on Ind. Appl.*, 33(6), 1544–1552, 1997.
40. Vijayraghavan, P. and R. Krishnan, Noise in electric machines: a review, *IEEE Trans. on Ind. Appl.*, Vol. 35, No. 5, pp. 1007–1013, Sept. Oct., 1999.
41. Panda, D. and V. Ramnarayanan, Low-noise switched reluctance drive, in *Int. Conf. on Power Electronics, Drives, and Energy Systems (PEDES'98) for Industrial Growth*, Dec. 1–3, 1998, Perth, Australia, pp. 627–633.
42. Kim, K.-B., Field analysis of low acoustic noise switched reluctance motor, *IEEE Trans. on Magnetics*, 33(2), pp. 2026–2029, 1997.

---

# 8 Sensorless Operation of SRM Drives

## 8.1 INTRODUCTION

The control of SRM drives depends on the phase current, absolute rotor position, and rotor speed signals to obtain closed-loop control of current (torque) and speed. Depending on the quality of performance required for a particular application, such as for a low performance, the phase current and speed signals may be dispensed within the control system. The feedback signals are usually measured with transducers, which increase the cost of the electronic controller and its packaging size. In the case of a rotor position/speed transducer, the size of the motor housing and the cost are increased significantly. Emerging high-volume applications in heating, ventilation, and air conditioning (HVAC); fans; pumps; home appliances; automobile accessory drives; and many others are cost sensitive. The performance requirements for such applications are not high as is required for machine tool servo drives. The requirement of low cost with high performance for motor drives has placed the agenda of low-cost, sensor-based or sensorless technology at the forefront of present-day research and development of motor drives. SRM drives are no exception to this trend, as seen from the high degree of interest shown by industrial and academic researchers worldwide on this topic.

This chapter considers the study of a low-cost, sensor- or sensorless-based, current- and speed-controlled SRM drive system. The current and position sensorless algorithms and schemes are reviewed with some new unpublished schemes for low-cost, current-sensor-based controls. While no attempt has been made to cover all the schemes proposed in the literature, an attempt is made to present the most useful, fairly accurate, cost-effective, and industrially relevant algorithms and schemes in the following sections.

## 8.2 CURRENT SENSING

### 8.2.1 CURRENT-SENSING METHODS

Current control could be inexpensively achieved both with sensors and without sensors. A number of options emerge as indicated in the flow diagram shown in [Figure 8.1](#). Direct measurement with galvanically isolated current transducer is still an expensive solution. Noninductive, low-ohmic resistors can be used to monitor the current by measuring the voltage drop across them. They are not galvanically isolated, as in many applications galvanic isolation is not a strict requirement. This method provides the most accurate current measurement with the least amount of investment in materials and processing circuitry, but it does introduce an external

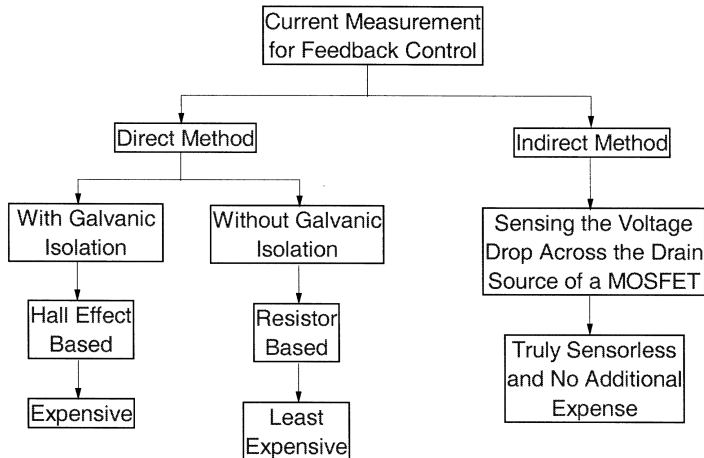


**FIGURE 8.1** Classification of current measurement for feedback control.

resistor component in the circuit that consumes power on the order of a watt or less. The indirect method, such as the one utilizing the resistive nature of the drain-to-source conduction path of a MOSFET for monitoring the current, is an attractive alternative. It also does not require any additional components to serve as a transducer, as the phase power switches could be used for monitoring indirectly<sup>28</sup> the currents. Special MOSFETs, called senseFETs, are available with processed current signals that minimize additional control electronic circuitry to transform the drain–source conduction voltage drop to the control level and keep it isolated during its off state from the control circuit. Otherwise, the drain voltage at turn-off will be at least equal to the dc source voltage, which is multiple times greater than the control supply voltage and will damage the control circuitry.

### 8.2.2 CURRENT SENSING WITH RESISTORS

Two different implementations of resistor-based current measurement are possible. Only one resistor could be used in the path from all the bottom switches to the negative dc bus rail (say, for an asymmetric converter), as shown in Figure 8.2. The phase-current measurement is not available with this implementation during freewheeling of a phase. More or less an average current can be obtained with this setup. If two phases are simultaneously conducting, then it is not possible to separate each phase current in this method. Therefore, it is useful when no overlapping conduction occurs in the machine phases and average current control is acceptable.

In the second arrangement, each phase current is sensed independently with one resistor, as shown in Figure 8.3. Including the resistor in the freewheeling path allows the monitoring of phase currents continuously except when the current is being turned off (commutated) once and for all at the end of the phase cycle. In most of the control arrangement, the decaying current need not be monitored. If torque smoothing control

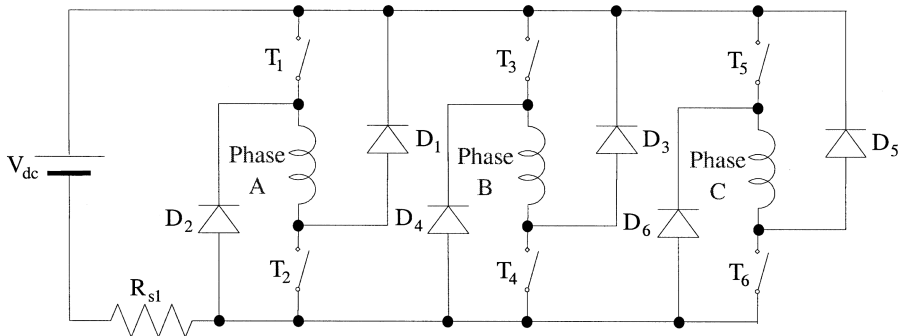


**FIGURE 8.2** Single-resistor-based, current-sensing arrangement in the SRM drive.

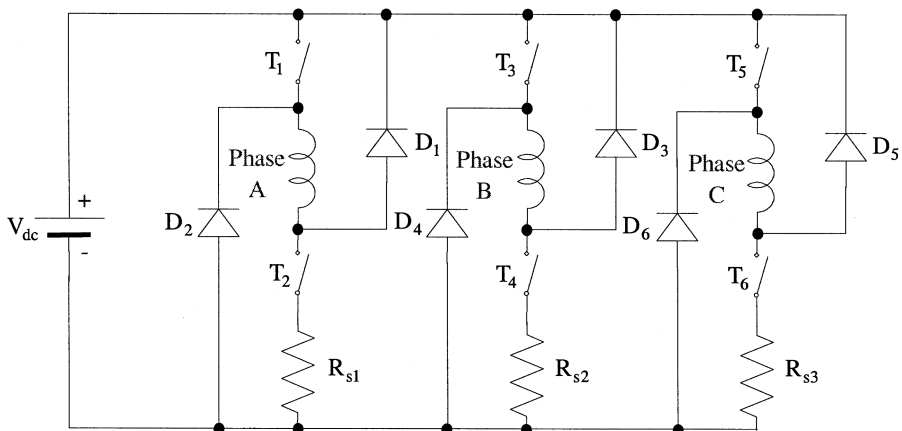


**FIGURE 8.3** Current sensing of individual phases with one resistor per phase.

is implemented, then coordination of phase currents at all times is essential, but this arrangement is unsatisfactory only for this reason. If the machine is intended for generation but not for motoring, then this scheme is also not useful because most of the time, in generation mode, both the phase switches have to be turned off to enable both the diodes to reverse the current flow in the dc link to transfer energy from the machine to the dc bus. The current then bypasses the sensing resistor. Alternatively, the resistor can be connected in that path or one common resistor in the dc rail may be more satisfactory, as shown in [Figure 8.4](#).

Sensing resistor  $R_{s1}$  (say, for phase A) provides the excitation current drawn from the dc source to provide magnetization of the machine to set up the generation. When switches  $T_1$  and  $T_2$  are opened, the phase current is diverted through diode  $D_1$ , the phase-A winding,  $D_2$ , the dc source, and the sensing resistor  $R_{s4}$ . With the measurement common at the anode of  $D_2$ , the voltage signal measured across  $R_{s4}$  has to be reversed to indicate that the dc source is receiving the current from the machine.

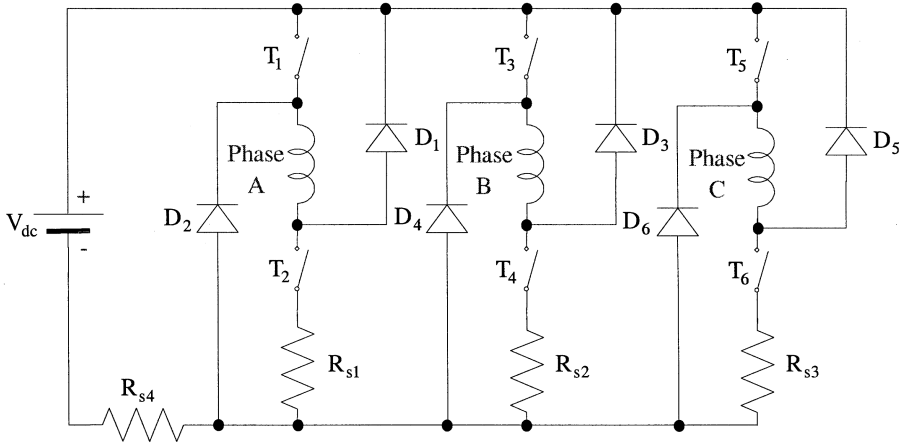


**FIGURE 8.4** Current-sensing resistor arrangement for both motoring and generating action.

Overlapping phase currents in generation mode are still difficult to measure in this arrangement. Note that in both the arrangements considered the current signal is obtained with respect to the negative dc bus rail, and this could be the common for control circuitry. The gate-drive amplifiers for the upper power switches can be isolated from the power bus by any one of the conventional techniques.

### 8.2.3 DRIVE SCHEME WITH CURRENT LIMITER

If feedback current control is not required for an application but only current limiting is needed to protect the power devices and ensure that the machine current is within the prescribed limit, then the devices themselves could be exploited to provide the current limit signal. Their collector-to-emitter or anode-to-cathode conduction voltages, whatever the case may be, could be monitored for desired maximum currents through their gate drivers. Many commercial gate drivers are equipped to do this task. In one or two microseconds, the device will turn off, thereby limiting the current in the machine phase. Note that this will not provide instantaneous current control, in that tracking of a reference is not possible, but serves as an over-current signal. Motor drives catering to applications such as pumps and fans with no great dynamic performance requirements can utilize this technique. A control schematic using current limiting is shown in [Figure 8.5](#) for a speed controlled drive system.

The speed error obtained from the difference between the rotor speed and its reference is amplified and limited in the speed controller, which usually is a proportional-plus-integral (PI) controller. Its output, the torque command signal is compared with a triangular carrier frequency to generate the pulse width modulated (PWM) logic signals to drive the power converter's devices. Depending on the rotor position, phase energization instants are generated which are known as phase position pulses. The PWM signals are steered into the appropriate phases of the converter with the help of the phase position pulses. The converter power devices are equipped with current-limiting circuits through their gate-drive amplifiers. If the phase current

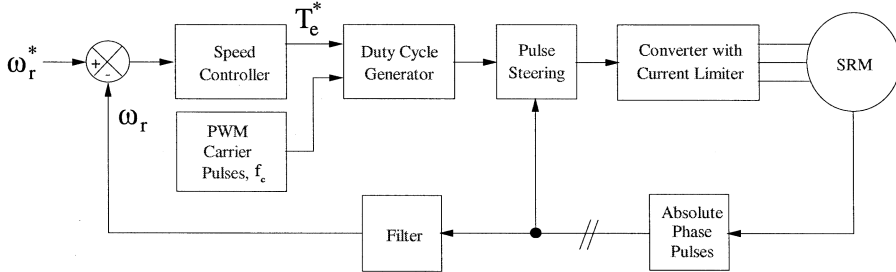


**FIGURE 8.5** Speed-controlled drive schematic with current limiter.

exceeds the set current limit, the device is turned off only for that carrier cycle. Again, in the next carrier cycle, the phase will be energized for its turn-on duration and so on.

### 8.3 ROTOR POSITION MEASUREMENT AND ESTIMATION METHODS

The control of an SRM is dependent on knowledge of the relative and absolute rotor position and is explained as follows. As seen for the control aspects of SRM in Chapter 6, the current reference is dependent on the advance turn-on angle and commutation angle to maximize the air gap torque. Hence, an incremental rotor angle is required to vary these control angle variables. But, the control angles are developed with respect to a constant or fixed rotor position for each stator phase (a set of poles). Therefore, the absolute rotor position information must position the advance turn-on and commutation angles to generate the final current command.

Various methods of measuring absolute and incremental rotor position with sensors or without sensors are classified and shown in Figure 8.6. Rotor position measurement and estimation can be broadly classified into the two categories of acquisition schemes: continuous or discrete. Within these two categories, they can be further subdivided into sensor- and sensorless-based methods of rotor position measurement and estimation. Considering each stream of acquisition methods, a description of various schemes for rotor position measurement and estimation is given in the following discussion.

For **continuous acquisition**, the methods with sensors can provide either absolute or relative rotor position. The absolute rotor position can be obtained with an absolute encoder or a resolver with an accompanying resolver-to-digital converter. These are usually expensive and are not recommended for low-performance applications. The incremental or relative position can be measured with incremental encoders and magnetic pickups which may be less expensive than the absolute position sensors but still are not very inexpensive. The sensorless methods of estimation can be classified into modern control-based and inductance-based estimation schemes. The inductance-based estimation methods exploit the inherent unique characteristic of the three-dimensional relationships among the flux linkages or inductance, current, and rotor position, and the availability of the first two variables leads to resolution of the third unknown, which is the rotor position. A number of

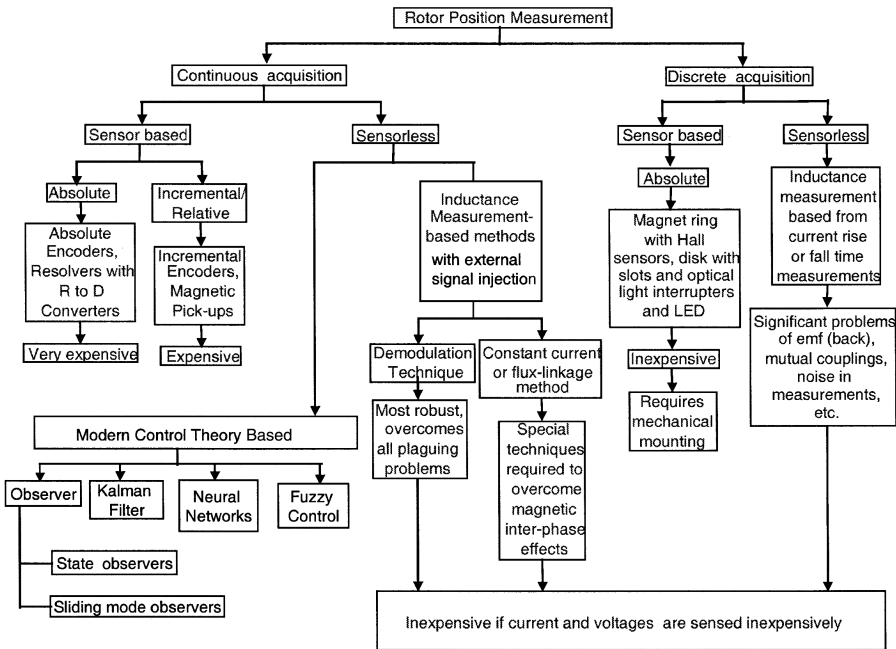


**FIGURE 8.6** Rotor position measurement and estimation methods.

methods exist using inductance-based estimation. They in turn can be further divided into direct and indirect forms of inductance measurement. The salient difference between these methods lies in which either the inductance is measured directly or by monitoring other variables. The modern control methods are based on observer and intelligent control techniques. The observer-based methods use a state observer or a sliding mode observer, both of which essentially depend to an extent on the inductance slope for their convergence and functioning. The observers are computationally intensive and have the problem of convergence in terms of the time taken to converge to the correct estimates. The intelligent control methods encompass estimators based on artificial neural networks and fuzzy control. These methods are computationally less intensive compared to observer methods but due to their learning capability provide adaptive control. The accuracy of the rotor position estimation is not sufficient for high-performance applications, such as a position servo control application, but is acceptable in many other industrial applications. Most of the sensorless methods require phase currents and applied voltages for their estimation. The current can be sensed inexpensively, but the commercial voltage sensors with high bandwidth are expensive. Alternatively, a low-cost voltage sensor or estimator is realizable using control-level, isolated-gate drive signals and a dc source voltage magnitude.

For **discrete acquisition**, the rotor position measurement is possible with hall sensors and disks with optical light interrupters. They are inexpensive but are still unacceptable in applications requiring low cost. The sensorless estimation scheme uses current rise and fall times to estimate the incremental inductance of the machine

phase from which the rotor position is extracted. This method works well in the low-speed region and is fairly inexpensive to realize in the controller. All the methods briefly introduced here are elaborated in the following sections.

### 8.3.1 SENSOR-BASED MEASUREMENT

Absolute encoders or resolvers with resolver-to-digital (R-to-D) converters give continuous measurement of absolute position of the rotor. Both these methods are very expensive and not suitable for high-volume, low-cost applications. While incremental encoders and magnetic pickups give relative position measurements, they have to be indexed to obtain the absolute position. At the time of starting, the index pulse may not be coincidental, so some form of memory to remember the previously stalled position has to be in place to acquire the absolute part of the rotor position. These incremental devices are still expensive but not as much as the absolute encoders or resolvers with R-to-D converters.

A discrete absolute rotor position to indicate the unaligned and aligned position for each phase can be obtained with a magnet ring and Hall sensor assembly, as in the case of the permanent magnet brushless dc machines. Or, alternatively, a slotted disk with infrared light emitters and diodes could be inexpensively built. These two methods provide the least expensive ways of acquiring absolute rotor position using sensors.

Almost all the position sensors require mechanical mounting arrangements on the rotor shaft which invariably takes up space, increasing the total volume of the motor and housing. Further, some sensors are temperature sensitive, such as the optical methods of sensing, or are limited in their resolution in spite of the high cost associated with these devices, as well as the mechanical labor required for their installation. For many applications, the discrete sensor-based rotor position measurements are satisfactory, such as for the control of fans and pumps.

## 8.4 SENSORLESS ROTOR POSITION ESTIMATION

A mechanical sensorless rotor position estimation is considered desirable because of compactness in weight and volume, lower cost due to elimination of the mechanical assembly and mounting associated with a rotor position sensor, and no rotating parts and no wear and tear, thus no maintenance requirements for its life. The driving factor behind sensorless operation of any electrical drive including that of SRMs is the quest for low-cost drives with high performance. Three broad classes of rotor position estimation have emerged in research and development:

1. Observer-based schemes give a continuous estimation of rotor position.
2. Incremental inductance-based measurement uses current rise time or fall time or its magnitude to obtain discretely the rotor position.
3. Inductance-based estimation of rotor position uses the two different techniques of demodulation and constant current or constant flux linkage applied to sensor signals and sensing phases, respectively, to give a continuous estimation.

These methods are described briefly in the following sections.

## 8.4.1 INDUCTANCE-BASED ESTIMATION

The relationship between inductance and rotor position for each excitation current is unique over half a rotor pole pitch regardless of the rotor speed. This particular feature of an SRM is then used to find the rotor position from the estimated or measured inductance of a machine phase winding from the stored information of inductance vs. rotor position for each current in the control circuit. The burden of storing the inductance vs. rotor position information for all currents could be simplified in many ways and is discussed elsewhere.

### 8.4.1.1 Incremental Inductance Measurement

This method uses the fact that the current rise and fall times are proportional to the incremental inductance, and under certain assumptions the rise and fall times reflect the incremental inductance and hence the rotor position itself. Both these techniques are described in detail and their merits and demerits are discussed. The only advantage of this method is that it only needs to measure the current and its rise or fall time to predict the rotor position and can use the active phase itself. Therefore, it can be implemented in real time and online with very little or no extra cost other than some software codes required in the controller.

#### 8.4.1.1.1 Current Rise Time Method

For every on time of a hysteresis or carrier cycle, the phase current varies from a minimum value  $i_o$  to a maximum value  $i_1$ , say, in  $t_r$  sec., as shown in Figure 8.7.

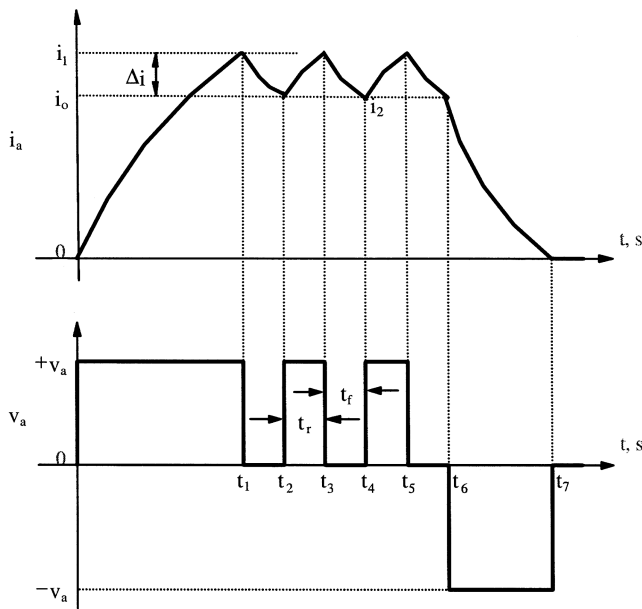


**FIGURE 8.7** Voltage and current in a machine phase applied from the two-switches-per-phase converter.

The voltage applied to the machine phase is the difference between the source voltage and the voltage drops in the connecting cables and power devices in series with the phase during this on interval. The currents at the beginning of the on time and off time are measured, and their difference is the incremental current rise given by  $\Delta i$ . The time for current rise is denoted as  $t_r$ . The applied voltage is known, from which the flux linkages are estimated. The basis for this method is as follows. The applied phase voltage is given by:

$$v_a = R_s i_a + \frac{d\lambda_a}{dt} = R_s i_a + \frac{\delta\lambda_a}{\delta\theta} \cdot \frac{d\theta}{dt} + \frac{\delta\lambda_a}{\delta i_a} \cdot \frac{di_a}{dt} \quad (8.1)$$

The rate of rise of current for one carrier or PWM or switching cycle is written as:

$$\frac{di}{dt} = \frac{i_1 - i_o}{t_3 - t_2} = \frac{\Delta i}{t_r} \quad (8.2)$$

Combining Eq. (8.1) with Eq. (8.2), the rise time is evaluated as:

$$t_r = \left( \frac{\delta\lambda}{\delta i} \right) \cdot \left[ \frac{\Delta i}{v_a - R_s i_a - e} \right] \quad (8.3)$$

where the induced emf is given by:

$$e = \frac{\delta\lambda}{\delta\theta} \cdot \omega_m \quad (8.4)$$

The term  $\delta\lambda/\delta i$  is incremental inductance and can be written as  $\delta L$  and evaluated as:

$$\delta L = \frac{\delta\lambda}{\delta i} = \left[ \frac{v_a - R_s i_a - e}{\Delta i} \right] \cdot t_r \quad (8.5)$$

From the right-hand side of Eq. (8.5), the incremental inductance is estimated which enables the recovery of the rotor position from stored data (say, in a memory). Examining the right-hand side of Eq. (8.5) reveals the difficulties of this method in implementation:<sup>1-3</sup>

1.  $v_a$ ,  $\Delta i$ , and  $t_r$  can be measured accurately but it is not possible to predict the resistive voltage drop due to resistance variation caused by skin effect and temperature rise, and the induced emf which requires the rotor speed and  $\delta L/\delta\theta$ , which itself is yet to be evaluated. Therefore, inaccuracies in this approach are inherent and will affect the estimation accuracy.
2. This approach does not consider mutual coupling of phases. The mutual coupling effect comes into play when currents are overlapping in the machine phases, introducing errors in the estimation.

3. Switching noise will corrupt the measurements even if inactive phases are utilized for sensing.
4. Magnetic losses are not considered in this approach; therefore, their effects in introducing significant error in estimation are neither isolated nor compensated.
5. This method provides discrete estimates of rotor position as the sample takes at least one PWM or hysteresis cycle during which time no updating of estimation is possible. This is not a serious drawback at low speeds where one phase conduction period will have many PWM cycles and many estimates of rotor position. At high speed, however, the number of PWM cycles contained in a phase conduction period may be very small and the number of updates is also limited. This severely limits the resolution of the relative rotor position estimates and this scheme is not acceptable in high-speed drives. All the same, the rotor position estimation at high speed can be used for a simpler control strategy, such as single-pulse voltage control.
6. The incremental inductance is bi-valued even within half a rotor pole pitch (cycle) at currents equal to or greater than 50% of the nominal rated current. This requires discrimination in the interpretation of results for use in the drive system.

The difficulty in computing the incremental inductance has been highlighted. An alternative way of looking at the incremental inductance equation is beneficial in that the incremental inductance is directly proportional to the current rise time. Therefore, the rise time is an indicator of incremental inductance and the rotor position, assuming that the current rise is small and the voltage differential between the applied source voltage on the one hand and the resistive voltage drop and induced emf on the other hand is constant. Such a technique has been suggested for estimating rotor position and its potential use in the control of the SRM. The drawbacks of such a technique become obvious by examining the assumptions. The accuracy of this method very much depends on the rotor speed and supply voltage fluctuations and the average current at which the measurements are being made.

In spite of some salient drawbacks to this method, its ability to perform at low speeds is very good as the induced emf is small at low speeds and its impact on the overall accuracy is thus minimized. It also suffers from low resolution in the relative rotor position at high speeds which restricts the control strategy to a low-performance one in this speed region. Despite ambiguity in the rotor position estimation near the aligned rotor position, as there are four rotor positions possible for one value of incremental inductance, it can be noted that there is only one unique measurement at the exact aligned and unaligned rotor positions. The measurements are precisely the absolute rotor positions required for commutation and initiation of current in a phase winding, and can be obtained without any ambiguity. While such a result is useful in low-performance drives, note that high-performance drives also require the relative rotor position information for finer control.

In spite of the drawbacks of the current rise or fall time method, it has the advantage of not using any additional transducer or external circuitry to estimate the rotor position.

The processing of measured current and rise or fall time alone delivers the rotor position estimate. In contrast to this, other methods require one or more of the following: special circuits to inject the test signals into the machine windings, voltage transducers, high computational power, and additional complex processing circuits to process the test signals and their responses.

#### *8.4.1.1.2 Current Fall Time Method*

Similarly, it is possible to estimate the inductance and hence rotor position from the time taken for the current to fall from  $i_1$  to  $i_2$ , denoted as  $-\Delta i$ , in time  $(t_4 - t_3)$ , denoted as fall time,  $t_f$ , as indicated in [Figure 8.7](#). The incremental inductance is given by:

$$\delta L = \left[ \frac{-Ri_a - e}{-\Delta i} \right] \cdot t_f \quad (8.6)$$

This method has the advantage of zero sensitivity to dc source voltage variation and requires no voltage sensor, but it requires precise estimates of stator resistive voltage drop and induced emf and measurement of  $\Delta i$  and  $t_f$ . The first part of this task is difficult to accomplish and the latter part of the task is achievable only with high precision. The complexity of computing induced emf with the required precision makes this method more difficult to realize, particularly at high speed, so the range of operational speeds for this method is very limited. Again, an alternative method similar to the current rise time method can be employed here by noting that the fall time is likewise directly proportional to the incremental inductance. Then, the fall time itself could be an indicator of the incremental inductance and the rotor position. This method has disadvantages similar to the current rise time scheme discussed earlier. This technique gives usable results when applied to inactive phases.

#### **8.4.1.2 Sensing with Inactive Phases**

To overcome the measurement or estimation of induced emf, different methods have been suggested.<sup>4-6</sup> One such scheme involves, in general, the use of inactive phases for current or voltage injection to measure the electrical time constant of the phase from which inductance and position could be estimated. By applying a voltage pulse of very small duration to keep the current small, it is noted that the induced emf is small due to the fact that  $\delta L/\delta i$ ,  $\delta L/\delta\theta$ , and current are small. Hence, its effect is negligible, making the measurement technique more robust compared, for example, to using the online current rise or fall methods discussed earlier. To get a reliable measurement in the presence of switching noise due to the active phase, it is necessary to have at least 10% of the rated current injected into the sensing phase. This produces a considerable negative torque, which, in turn, generates a knocking sound in the machine. This is unacceptable in many applications.

#### **8.4.1.3 Estimation Based on Constant Current/Flux Linkages**

This method exploits the linear characteristics of the machine when excitation current and flux linkages are small.<sup>7,8</sup> Under these conditions, the induced emf is negligible and there is no need to estimate the induced emf for this strategy. Also, it employs

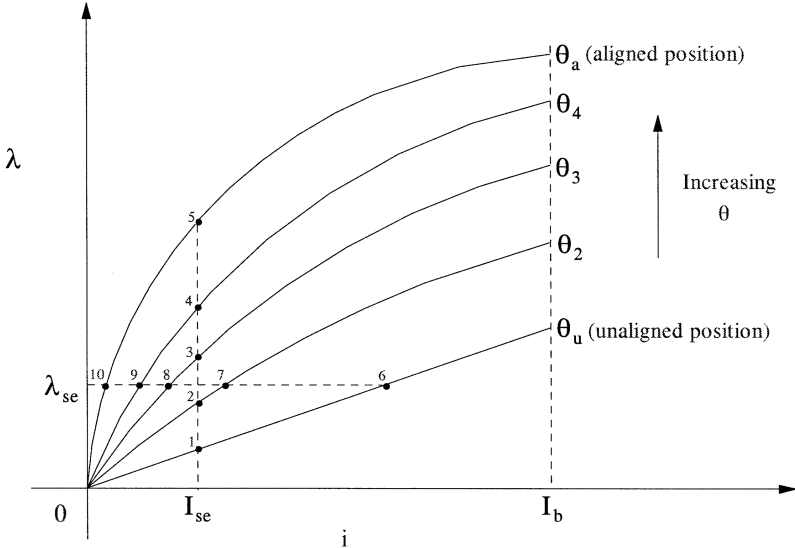


**FIGURE 8.8** Typical  $\lambda$  vs.  $i$  for various  $\theta$  characteristics of a switched reluctance machine.

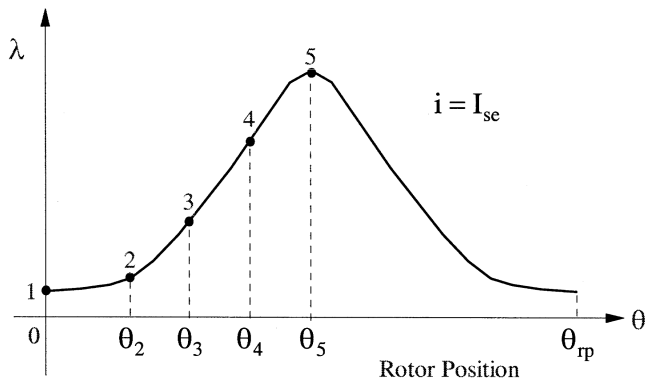


**FIGURE 8.9** Flux linkage vs. rotor position at constant current  $I_{se}$ .

the inactive phases for sensing. Consider the flux linkages vs. phase current for various rotor positions shown in Figure 8.8 for small currents. The current and flux linkages are indicated as  $I_{se}$  and  $\lambda_{se}$ , respectively. For the constant  $I_{se}$ , the flux linkages vs. rotor position is extracted from Figure 8.8, and, similarly for constant  $\lambda_{se}$ , the current vs. rotor position is extracted as shown in Figures 8.9 and 8.10, respectively. Between these two characteristics, it is more practical to use the fairly linear flux linkages vs. rotor position characteristic at constant current than the highly nonlinear current vs. rotor position characteristics at constant flux linkages. Then, the implementation schematic using  $\lambda$  vs.  $\theta$  for  $I_{se}$  is derived as shown in Figure 8.11.

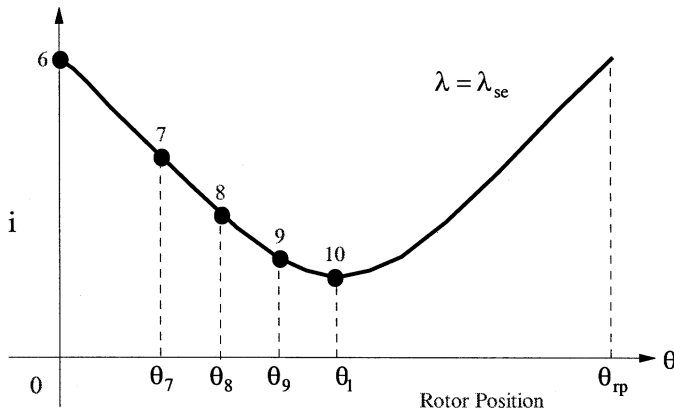


**FIGURE 8.10** Phase current vs. rotor position at constant flux linkages.

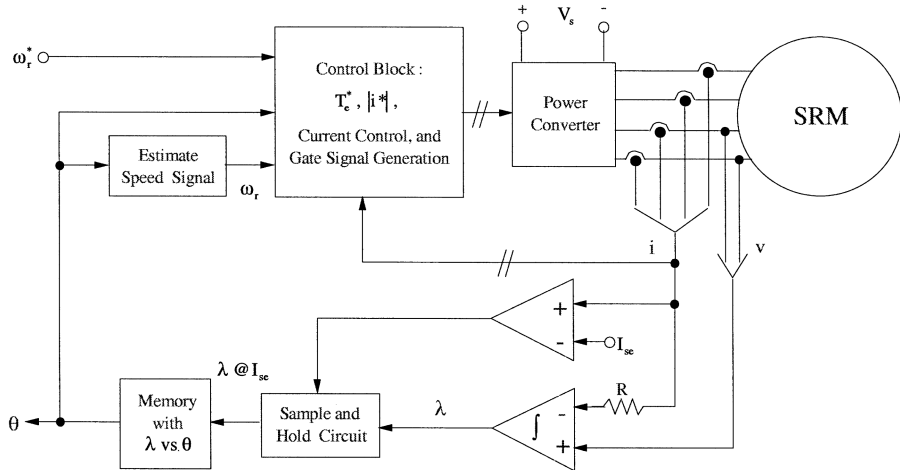


**FIGURE 8.11** SRM drive schematic with sensorless rotor position estimation from flux linkages vs. rotor position at constant current.

Note that the flux linkages is

$$\lambda = \int (v - R_s i) dt \quad (8.7)$$

It is sampled and held when the phase current is equal to  $I_{se}$ , and this flux linkage is used as the input to the memory where the corresponding rotor position from Figure 8.9 is stored. The output from the memory circuit then is the rotor position. Once the rotor position is available, speed is estimated for closing an external speed loop to enforce speed control in the SRM drive system. The estimated rotor position and speed, measured currents, and external speed reference are input into a control

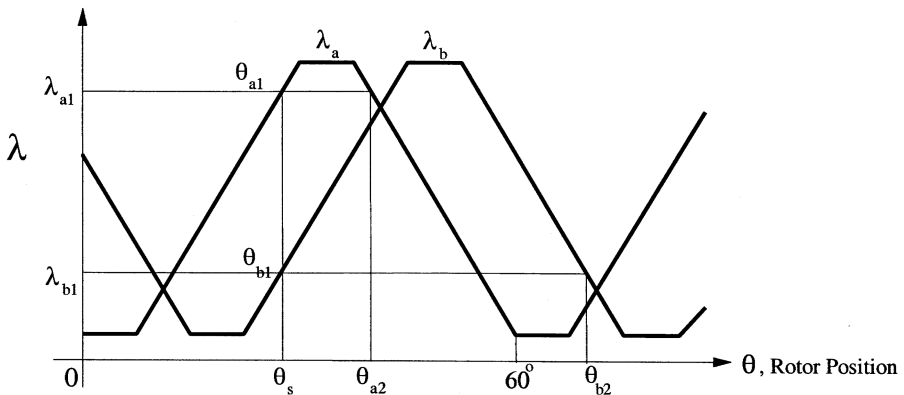


**FIGURE 8.12** Initial rotor position (absolute) detection by exciting two phases.

block where the speed error generates a torque command from which the current magnitude command is generated using any one of the algorithms developed in Chapter 5. The individual phase current commands are generated using the rotor position determined using the inactive phases. The phase current command is enforced with an inner current control loop for each phase by using PWM switching in the converter.

At the time of starting, since the  $\lambda$  vs.  $\theta$  characteristic is double valued, it is necessary to use two phases to identify the rotor position by looking at the common rotor position reading for both phases. This is shown in Figure 8.12 for excitation of phases A and B in a four-phase SRM. Let the initial rotor position be  $\theta_s$  and the flux linkages for the current  $I_{se}$  be  $\lambda_{a1}$  for phase A and  $\lambda_{b1}$  for phase B. This gives two rotor positions  $\theta_{a1}$  and  $\theta_{a2}$  and  $\theta_{b1}$  and  $\theta_{b2}$  for phases A and B, respectively. The common rotor position reading for both the phases is  $\theta_{a1}$  and  $\theta_{b1}$  which corresponds to the initial starting position. The readings that do not match  $\theta_{a2}$  and  $\theta_{b2}$  are rejected.

Once starting is achieved, sensing with one inactive phase is sufficient. To reduce the interference due to the switching noise of the active phase on the sensing phase, a different switching frequency for sensing than that for the active phase can be effectively employed.

This method suffers at high loads due to mutual inductance between phases and saturation effects on the back iron. Note that the back iron is shared by the sensing and active phases. The currents in the active phases introduce a component of flux linkages in the sensing phases by mutual coupling that leads to an error in rotor position estimation. The saturation of the back iron changes the magnetic characteristics, thus introducing an error in the flux linkages of the sensing phases. Compensation for these errors based on the excitation current and flux linkages in the sensing phases has been shown to be possible using memory tables or using analog function generators to provide a correction signal. However these are cumbersome to implement and are yet to be applicable over a very wide speed range. Within its limited speed range of operation, this method of sensing rotor position could be useful in applications such as fans, pump drives, appliances, and direct drives, to

name a few. This method is better than many methods discussed earlier both in its novelty and in its exploitation of the inherent linear characteristics of the SRM at very low excitation.

#### 8.4.1.4 Resonant Circuit Method

In this method, a signal is injected into an inactive phase at a frequency to produce resonance at the unaligned position of the rotor.<sup>9</sup> The impedance measured only reflects the resistive component and the reactance component given by the difference between the aligned and unaligned inductive reactance. This resonant frequency has to be smaller than the frequencies at which the equivalent reactance becomes capacitive and usually is the case. The reactance at very high frequencies is capacitive because of the inter-turn winding capacitance.

In order to appreciate the effects of the frequency on the measured equivalent resistance and reactance of the circuit in the inactive phase, consider the per-phase equivalent circuit of the SRM with core losses. The core losses are modeled through a resistive element,  $R_c$ , across the inductor and motional emf. The core loss resistor may be considered a constant. Note that the motional emf is given by:

$$e = i_o \omega_m \frac{dL}{d\theta} = R_{em} i_o \quad (8.8)$$

The term given by the product of the speed and rate of change of inductance with respect to rotor position resembles a resistor,  $R_{em}$ . This resistor part of the motional emf is small compared to the inductive reactance of the machine, particularly at a resonant frequency that is in the range of a few kHz to tens of kHz. Neglecting then this component, the resulting equivalent circuit is shown in [Figure 8.13](#). From this circuit, the series equivalent circuit may be derived with a resistance  $R_{eq}$  and inductance  $L_{eq}$  as shown in [Figure 8.14](#). In terms of the circuit parameters  $R_s$ ,  $L(\theta)$ , and

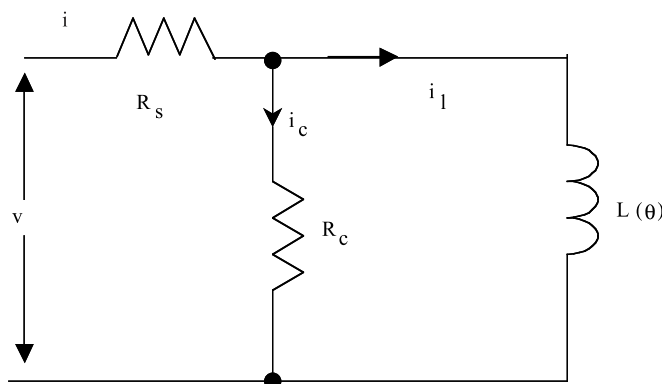


**FIGURE 8.13** Simplified per-phase equivalent circuit of the SRM.

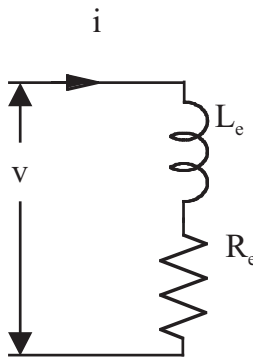


**FIGURE 8.14** Series per-phase equivalent circuit of the SRM.

excitation frequency  $\omega_c$ , they are derived as:

$$R_e = R_s + \frac{\omega_c^2 \tau_c^2}{1 + \omega_c^2 \tau_c^2} R_c \quad (8.9a)$$

$$L_e = \frac{L(\theta)}{1 + \omega_c^2 \tau_c^2} \quad (8.9b)$$

where

$$\tau_c = \frac{L(\theta)}{R_c} \quad (8.10)$$

For a given frequency, as the inductance increases when the rotor poles move from the unaligned to the aligned position with the stator poles, the time constant  $\tau_c$  increases and the equivalent resistance increases, whereas the equivalent inductance decreases. The effect of an increase in the excitation frequency  $\omega_c$  as seen from the derived relationships is that, for the same rotor position, there is a significant increase in the equivalent resistance but a decrease in equivalent inductance. Therefore, using only a measurement of inductance in this circuit will not yield measurements with high resolution as the equivalent inductance becomes a constant over a larger portion of the region between the unaligned and aligned rotor positions.

Alternatively, the resonant method increases resolution of the measured impedance by designing resonance at the unaligned position by selecting a capacitor to be connected in series with the machine phase. Here, the impedance is measured against the inductance. Note that at the unaligned position the measured impedance equals only the equivalent resistance of the circuit, whereas at the aligned position the impedance will be due to the equivalent resistance and the differential inductance between the aligned and unaligned positions. This increases the resolution of the

impedance significantly compared to the method without the capacitor. The resonant frequency is given by:

$$\omega_{rs} = \frac{1}{\sqrt{CL_e}}, \text{ rad/sec} \quad (8.11)$$

where  $C$  is the value of the external capacitor included in series with the inactive phase.

The impedance, inductance, and rotor position are obtained by demodulating the current and locking on its peak in each excitation period. With the proper locking arrangement, the noisy interference from the switching phase can be excluded. One such arrangement may be devised by setting the switching frequency of the active phase very differently from the resonant frequency of the inactive phase.

#### 8.4.1.5 Synchronous Demodulation Method

From the method discussed earlier, it could be summarized that the problems of inter-phase coupling, eddy current losses, switching noise interference, and estimation error in the motional emf are the major sources of error in inductance/flux linkages and in rotor position estimation. They are avoided in this method<sup>10</sup> by using synchronous demodulation of the applied fundamental voltage and resulting current in the sensing winding. The synchronous demodulation of these signals provides the quadrature components by taking the integral of the voltage and using it as a reference ( $v_{ref}$ ) in the synchronous demodulators to obtain the magnitudes of the quadrature components of current and voltage:

$$v_1(t) = V_m \cos(\omega_{cs}t) \quad (8.12)$$

$$i_1(t) = I_m \cos(\omega_{cs}t - \phi) \quad (8.13)$$

where  $v_1$  and  $i_1$  are the fundamentals of the applied voltage and resulting current in the inactive phases;  $\omega_{cs}$  is the PWM switching frequency of the inactive phase which is different from the PWM switching frequency of the active phase to eliminate switching interference. The modulation signals are

$$V_{1q} = \frac{1}{2}|v_{1q}| = \frac{V_m}{2\omega_{cs}} \quad (8.14)$$

$$I_{1q} = \frac{1}{2}|i_{1q}| \quad (8.15)$$

This quadrature component of the current is a function of  $L(\theta)$  and can be derived from the equivalent circuit of the SRM shown in [Figure 8.15](#), in which  $R_c$  is the

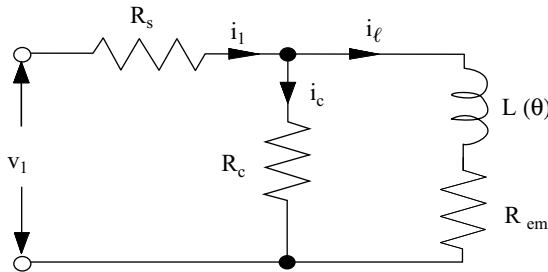


**FIGURE 8.15** Single-phase equivalent circuit of the SRM.

iron loss resistance and  $R_{em}$  is the effective resistance due to induced emf given by:

$$R_{em} = \omega_m \frac{dL(\theta, i)}{dt} \quad (8.16)$$

Assuming  $\omega_{cs}$  is fairly high and on the order of 90,000 rad/sec and above,

$$\omega_{cs}L(\theta) \gg R_{em} \quad (8.17)$$

making  $R_{em}$  negligible compared to the reactance and thus introducing very little error in estimation. Therefore,  $i_\ell$  represents the reactive (quadrature) component of the input phase current  $i_1$  which must be equal to  $2I_{1q}$  and is given as:

$$i_\ell = \frac{v_1}{\omega_{cs}L(\theta)} = 2I_{1q} \quad (8.18)$$

Dividing Eq. (8.14) by Eq. (8.18), the inductance is obtained as:

$$L(\theta) = \frac{V_{1q}}{I_{1q}} \quad (8.19)$$

The realization of this method is shown in [Figure 8.16](#). This method overcomes the major problems in the following manner:

1. *Magnetic losses:* Because only the reactive component of the sensing current is used for inductance estimation, it is entirely independent of the core loss component of the current.
2. *Mutual coupling effects:* These effects are avoided by having different frequencies for the active and sensing phases. As the synchronous demodulators deal only with the fundamental components of the sensing phase voltage and current, they reject the mutual coupling effect of the active phase appearing at a different frequency.
3. *Phase resistance:* The phase resistance could be accounted for by subtracting its voltage drop from the applied fundamental voltage to obtain

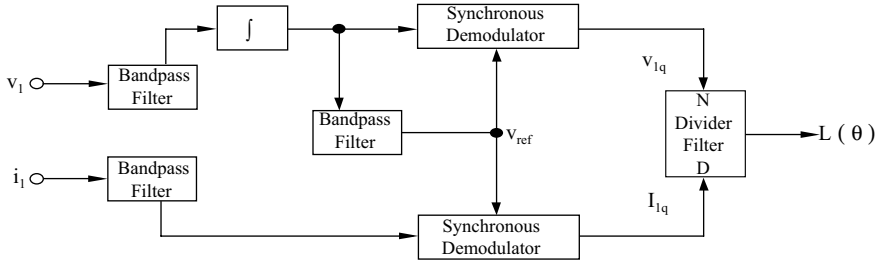


**FIGURE 8.16** Inductance estimation schematic with synchronous demodulator.

the voltage applied to the inductance, but note that the effect of the voltage drop across the phase resistance is negligible as the phase current is small.

4. *Motional emf*: The motional emf is very small compared to the inductive reactance voltage drop at a high switching frequency and is negligible.

The bandpass filter frequencies have to be chosen based not only on the PWM switching frequency of the sensing phases but also on the harmonic spectrum of the inductance profiles. The inductance profiles have a fundamental frequency of rotor poles. The criterion for the design consideration of the filters is derived as follows:

$$H(\theta) = \frac{1}{L(\theta)} \quad (8.20)$$

which could be written as a Fourier series by:

$$H(\theta) = \sum_{k=0}^{\infty} H_k \cos(kP_r\theta) \quad (8.21)$$

In terms of time,

$$H(t) = \sum_{k=0}^{\infty} H_k \cos(kP_r\omega_m t) \quad (8.22)$$

The quadrature component of current is written in terms of  $H(\theta)$  as:

$$i_\ell(t) = \frac{v_1}{\omega_{cs}} \sum_{k=0}^{\infty} H_k \cos(kP_r\omega_m t) \quad (8.23)$$

This shows that  $i_\ell$  is modulated by each harmonic of  $H(t)$ . It is usually sufficient to have only four harmonics to model the position harmonic of the inductance profile. If the mechanical rotor frequency is  $f_m$  and the switching frequency is  $f_{cs}$ , then side bands will exist from  $(f_s - 4f_m P_r)$  to  $(f_s + 4f_m P_r)$ , assuming that  $k = 4$ , and these side

bands exist in steps of  $f_m P_r$ . Therefore, the bandpass filters in the detection part of the fundamental voltage and current must have the bandpass characteristic over these limits to correctly reproduce the inductance profile for the entire speed range of the machine specified by  $f_m$ .

Synchronous demodulated filters introduce a phase shift in the inductance profiles almost linearly with respect to the rotor speed which can be compensated for in practice. This method provides continuous and precise rotor position estimates and does not require as many corrections as do other methods. It has fundamentally no restrictions in its application over a wide speed range. It is insensitive to all problems associated with inductance measurement, unlike other methods. The one problem for this scheme lies in injecting test signals in the active phases and their measurements, similar to the constant current method. When a high-frequency but low-voltage test signal is required, we need to have a means of connecting such a source to the inactive phases through a power switch with the same voltage rating as the other switches but with a small current rating. This increases the complexity of the implementation on the test circuit side and the cost equals those of some sensor-based measurements. In spite of this disadvantage, it is one of the best methods for rotor position estimation in SRMs.

#### **8.4.1.6 Variation of the Demodulation Method**

A derivative of this method is possible without an external circuit arrangement for feeding the test signal into the inactive phases.<sup>5</sup> The main power converter itself can be used to excite the inactive phases with a small duty cycle at low frequencies such as 1 kHz. Analyzing the input test signal, it may be found that it has a dc value and a fundamental component and a host of harmonics. If the current response is measured and demodulated for the fundamental and other harmonics of interest then the phase inductance can be recovered from it using the demodulation technique. Note that this technique has the disadvantage of injecting a steady dc current into the inactive phases, resulting in a small torque of undesirable polarity. High-frequency testing may not be possible with this technique because of the converter switching frequency and loss limitations. Pure sinusoidal inputs cannot be generated and impressed with this technique as required in the demodulation method, thus much more sophisticated processing circuitry and software are necessary.

#### **8.4.1.7 Mutual Flux Linkages Method**

Mutual coupling of the machine phases produces an induced emf from which on integration yields the mutual flux linkages between the active and inactive phases.<sup>11</sup> Well-designed SRMs have mutual inductances of only 2 to 3% of the aligned phase inductances. The effect is usually very negligible except in high-performance drives. The inactive phases can be used as sensors to measure the mutual flux linkages, thus the mutual inductance between the phases from which the rotor position can be extracted is similar to that found in the methods employing the self-flux linkages. Note that the mutual flux linkages are not only a function of the rotor position but also excitation current, which complicates the solution for rotor position as it has a three-dimensional relationship. Because the mutual induced emf is very small and appears

across the inactive phase, its extraction for signal processing is very difficult unless voltage transducers are employed, thus making the scheme very expensive to implement. Further, the gain of the transducer has to be high enough to get a good measure of the mutually induced emf but low enough when the phase becomes active so that its transmission does not harm the control-level electronics on the signal processing side. The only option then is to disconnect the transducer by active power devices, thus making it more expensive to implement. Due to these disadvantages, the method is not popular.

### 8.4.2 DIRECT INDUCTANCE-SENSING METHODS

In the following schemes, the inductance is estimated using the active phase to estimate the self-inductance. Note that this is different from the incremental inductance method.

#### 8.4.2.1 Current Gradient Method

Many of the open-loop control schemes in the SRM vary the duty cycle of the PWM control signals depending on the speed of the machine to a larger degree and to a smaller extent on the load. If the PWM duty cycle is kept constant during one conduction period of a phase, then the current behavior has a certain pattern. This method exploits the current pattern under this condition to estimate the rotor position.<sup>12</sup> It is assumed that the phases are energized when they have zero inductance slopes. That means that the machine phases are triggered with an advance angle. Such a requirement is very important for this technique to work and in almost all the control strategies it is incorporated in some manner to achieve high performance. The pattern of the phase current can be inferred from an elementary circuit analysis. The phase current will keep increasing until the inductance starts to increase from its unaligned position. Thereafter, it declines slowly until commutation is initiated, leading to a rapid decrease of the current. This pattern is shown in [Figure 8.17](#). By removing the switching noise from the phase current through a filter, the resulting current can be differentiated to obtain its rate of change or gradient. Note that the gradient is zero where the inductance starts to change its slope from zero to positive. From this point onward, the SRM can generate a torque of positive polarity until the inductance slope reaches zero (i.e., when the rotor pole completely aligns with the stator pole). As this instant is desired for the control of each phase, the zero phase current gradient instances can be generated for all the phases from only the dc link input current to the converter. In that case, the zero current gradients are clearly identified when the phase currents are not overlapping with each other. When they overlap, there will be instances of two zero current gradients for each phase with the use of the dc link current: the first one contributed by the decaying current of the previous phase and the second one from the rising current of the current phase. Therefore, the first signal is ignored and the second one is considered for control purposes.

Even though there is only one signal for each phase conduction cycle that provides absolute position information, it is possible to generate the relative position information by multiplying the frequency of the zero current gradient signals with

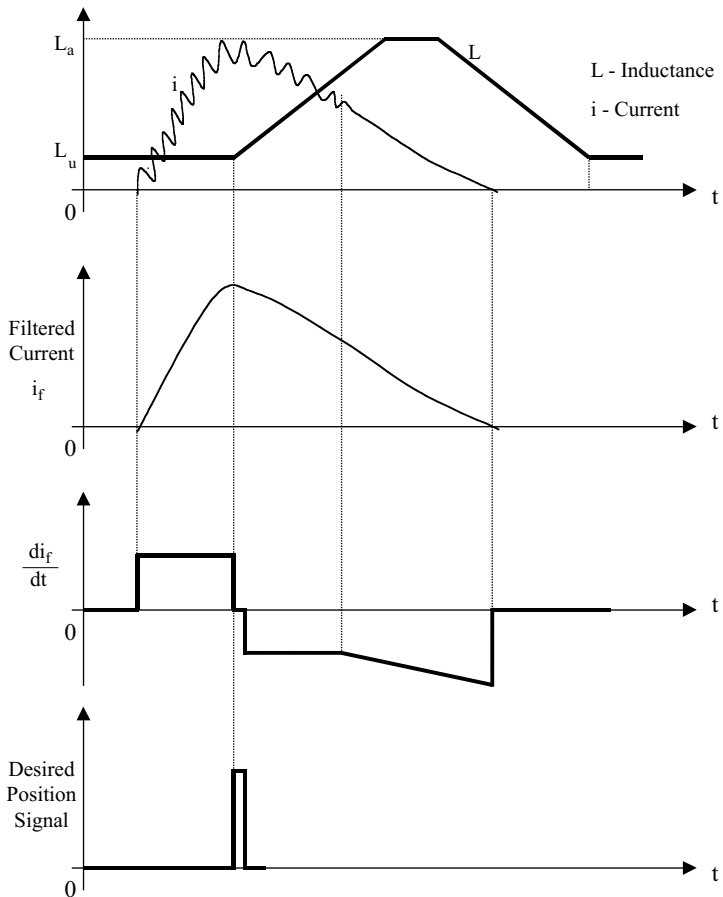


**FIGURE 8.17** Derivation of current gradient and its relationship to rotor position.

phase-locked-loop techniques (say, 32 times). This increases the resolution of the position signals and places the gate-drive control signals with the desired advanced turn-on and commutation angles in each phase. They are essential in the optimization of machine torque and efficiency. The rotor position estimation may be off to an extent at low speeds but seems to provide very high accuracy at higher speeds. This is due to the current processing circuitry and can be improved with proper circuit design procedures. With the availability of high-resolution rotor position signals by a phase-locked-loop technique, the rotor speed can be extracted and can be used for closure of the speed feedback loop for speed control. This enables the realization of a speed-controlled SRM drive system.

One drawback of this method is that the current gradient signals are not available at the time of starting; therefore, a separate starting procedure has to be incorporated with the current gradient method. Such a step is very similar to the starting of permanent magnet brushless dc machine drives without a position sensor. The SRM, likewise, can be started on an open loop with a preprogrammed frequency vs. time feature

until the machine reaches a speed sufficient to provide the current gradient signals. Optimization of the SRM drive system performance in this region from zero to the threshold speed is not possible except that it can spin the machine with a load. Many applications do not require such optimized performance, and examples can be found in appliance and automotive accessory drives, to name a few.

The major advantage of the current gradient method of position estimation is that it does not require voltage transducers and highly computationally intensive processing circuitry to obtain the position information. It is realizable with simple hardware and thus lends itself to low-cost applications. It is also not important that the zero current gradient has to be detected, but its polarity change, which is easier to detect than the zero current gradient instant, is sufficient to pinpoint the instant when the torque-producing region starts in the machine.

#### 8.4.2.2 Flux Linkages Estimation Method Based on Reference Position

This method uniquely combines both the low-speed and high-speed operational ranges by using a diagnostic pulse from the main converter in the former region and using actual power signals in the latter region.<sup>13</sup> It is an extension of the method by Hedlund. This method still relies on flux linkage estimation from the terminal machine phase voltage and current. The method requires that the flux linkages at a reference rotor index or angle (say,  $\theta_{rf}$ ) as a function of excitation current is known. From the instant a phase winding is energized, an estimate of the time required to reach the reference rotor angle is made from previous estimates of the rotor and speed and then a timer is set to run. When the estimated time to reach the reference rotor angle elapses, the current in the machine phase  $i_m$  is measured. Also phase flux linkage  $\lambda_m$  is computed from the applied voltage to the phase and resistive voltage drop. From the current  $i_m$ , the expected flux linkage  $\lambda_e$ , if it is at the reference rotor position, is obtained from the stored static characteristics shown in [Figure 8.18](#).

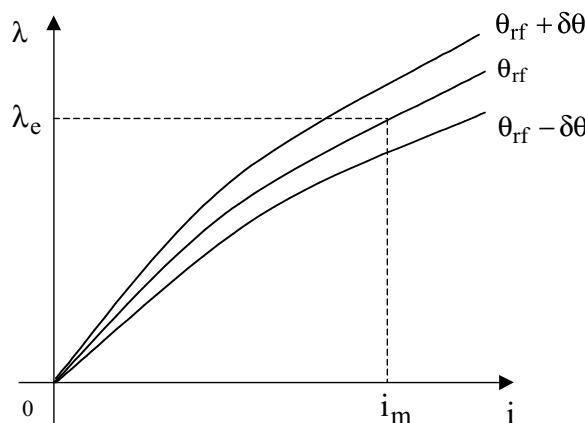


**FIGURE 8.18** Flux linkages vs. excitation current for small variations in rotor position.

Assuming that the actual rotor position is only away from the reference position by a small measure (i.e., for a small variation around the reference rotor position), the small variation in the flux linkages is derived as:

$$\delta\lambda = \left\{ \frac{\partial\lambda}{\partial\theta} \Big|_{i=i_m} \right\} \delta\theta \quad (8.24)$$

where, in general,

$$\delta\theta = k(\theta, \lambda) \delta\lambda \quad (8.25)$$

and

$$k_m(\theta, \lambda) = \left. \frac{\partial\theta}{\partial\lambda} \right|_{i=i_m}; \delta\lambda = \lambda_m - \lambda_e; \delta\theta = \theta_m - \theta_{rf} \quad (8.26)$$

Then, the actual rotor position is obtained as:

$$\theta_m = \theta_{rf} + k_m(\theta, \lambda)(\lambda_m - \lambda_e) \quad (8.27)$$

The  $k(\theta, \lambda)$  vs. excitation current characteristic can be derived from the static tests and is shown in [Figure 8.19](#). Note that  $k_m(\theta, \lambda)$  is the value of  $k(\theta, \lambda)$  for the measured current  $i_m$ . It can be stored in an array form for retrieval and use in the calculation of actual rotor position.

The guideline for placing the reference rotor angle is where the current has a reasonable value for measurement and well before the commutation need to be initiated. It is usually placed in the region where the rotor and stator poles partially overlap.

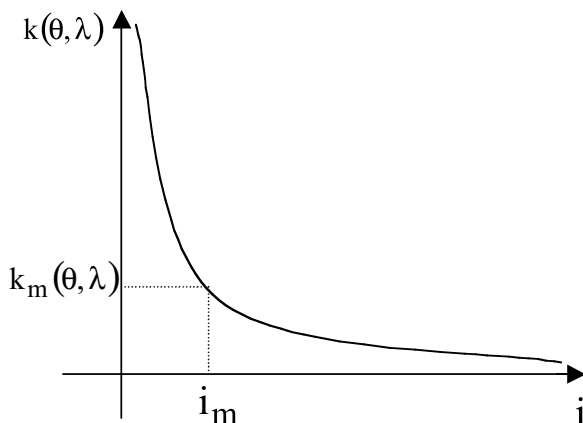


**FIGURE 8.19**  $k(\theta, \lambda)$  vs. current characteristic.

The procedure also works for the regeneration region with the reference rotor position angle located in the falling inductance region, and  $k(\theta, \lambda)$  vs. current will have negative values. Multiple PWM switching can create problems in estimation of the flux linkages with this technique but can be minimized if the required number of PWM switchings is small before the rotor reaches its reference position or the close neighborhood. If the resistive voltage drop is small compared to the input voltage to the converter, then the flux linkages can be estimated by taking the area of the voltage over time from the time of energizing the phase. That would reduce the computational steps required for the flux linkages estimation.

For low-speed operation, instead of probing the active phase, inactive phases are used to estimate the rotor position for the simple reason that multiple switching will occur by the time the reference rotor angle will be reached and estimation of the flux linkages will become difficult. With the inactive phase, a timer initiates a diagnostic pulse based on the estimated rotor position and turns off the diagnostic pulse in a small interval of time. The pulse duration is greater than one PWM time period so as to have a significant current for measurement. At the end of the diagnostic pulse, the phase current is measured and the phase flux linkages are computed. Then, similar to the motoring region, the actual rotor position is estimated except that the  $k(\theta, \lambda)$  vs. current characteristic will have negative values as the inactive phase is operating in the negative inductance region.

The effect due to mutual coupling between the windings is minimized with having a substantial current in the diagnostic phase only for a short duration. Note that it may produce counterproductive torque and may result in a knocking sound in the machine. It has been demonstrated that this method has sufficient accuracy and stability, and it is considered suitable for a general-purpose drive. The method requires simple computational steps and does not involve extensive signal-processing circuitry. The diagnostic signal is applied using the power converter for the SRM and dispenses with the need for a separate signal source and additional power devices to connect the signal source to the machine windings. The scheme has a minor drawback in that it is unable to achieve starting. Therefore, it requires an alternative control technique to spin it to a threshold speed, at which point the algorithm takes over the position estimation and its use in the control system. The technique for starting is given in Section 8.4.2.1.

#### **8.4.2.3 Flux-Linkages-Based Method with Hesitation-Free Starting**

In order to avoid hesitation during starting of the SRM without a position sensor, a clever algorithm has been developed.<sup>14</sup> One way to know for certain the standstill rotor position is by exciting one phase to align the rotor to its stator phase. If the load is significant, then it may not work until a combination of two or three phases is excited. Or, alternatively, as suggested in this method, all the phases can be excited for a short duration and the currents in them are monitored. The phase with the second highest current can be chosen to identify the rotor position. The reason that the phase with the highest current is not chosen is that its inductance will be the

lowest among all of them and therefore that phase is not in the torque-generating region of the inductance vs. rotor position characteristic. Hence, the phase with the next highest current is chosen and its current will be sufficient for rotor position estimation. Let voltage  $v$  be applied to the windings for a duration of  $t_d$ , during which the current increases from zero to  $I$ . Noting that the induced emf is zero at standstill leads to a simple calculation of flux linkages as:

$$\lambda = \int_0^{t_d} (v - R_s i) dt = \left( v - \frac{R_s I}{2} \right) t_d \quad (8.28)$$

From the flux linkages of the phase, the rotor position can be determined from the machine's magnetization characteristics. Then, a voltage pulse of considerable duration (say, 4 to 5 times the PWM time period or about 200  $\mu$ sec) is applied to start the machine.

As for running the SRM after its starting, all the phases are excited for a short duration to find the phase that has the maximum current. That phase is then chosen for rotor position estimation. The reason for this is that most of the high-performance control schemes require setting up a current in the phase well in advance of the changing inductance slope region to extract the maximum torque from the machine. The flux linkages of the phase can be estimated from the following discrete relationship as:

$$\lambda(k) = \lambda(k-1) + \left[ v(k-1) - \frac{R_s}{2} (i(k) + i(k-1)) \right] T_s \quad (8.29)$$

where  $\lambda(k)$  and  $\lambda(k-1)$  are the flux linkages at the sampling instants of  $k$  and  $(k-1)$ . The currents at the sampling instants of  $k$  and  $(k-1)$  are  $i(k)$  and  $i(k-1)$ , respectively;  $v(k-1)$  is the voltage applied at the  $(k-1)$ th instant of sampling; and  $T_s$  is the sampling time. As this computation is iterative, it is easy to mechanize in the processor.

This sensorless scheme gives a very good overall performance, including four-quadrant performance. It requires voltage transducers in addition to the usually required current sensors. The only drawback of this scheme is that all phases may have to carry a current during the probing to determine the best phase to latch onto for rotor position estimation. It can be overcome by probing only one or two phases.

#### 8.4.3 OBSERVER-BASED ROTOR POSITION ESTIMATION

Consider an SRM model assuming that the motor parameters and inputs are known. The motor parameters consist of phase inductances that are functions of excitation current and rotor position and phase resistances. To obtain the rotor position, we require the rotor speed dynamics, obtained through the electromechanical equation coupling the air gap torque to the mechanical system with rotor inertia and friction constants. The air gap torque is a function of the excitation currents and inductances. The real-time solution of the SRM system equations gives estimates of the current, speed, and rotor position. For example, an error current is developed by comparing the measured current and estimated current, and this error current can then be used

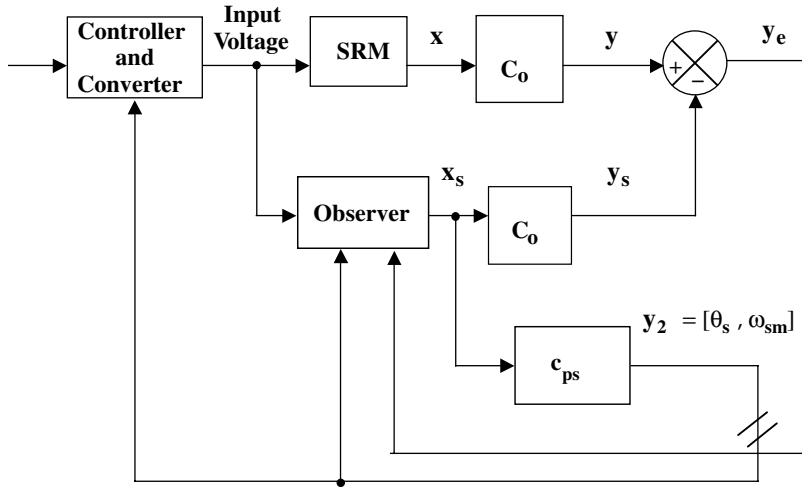


**FIGURE 8.20** An observer for SRM drive system.

to adjust the system model until the estimated value of current is equal to its measured value. The current error is zero only when all the variables and their estimates are equal; the case that may be of interest here under this circumstance is that the estimated position is equal to the actual rotor position. Therefore, the position estimate is available continuously for use in feedback control of the drive system. In essence, with the available measured feedback, the error in estimation is computed and then used to adjust the model until the model matches the SRM system. The system model can be adapted to the actual system (i.e., adaptive control). Model reference adaptive control is one of the prevalent techniques used to adapt the model to its actual system. Alternatively, one could observe the system from its model, an approach known in modern control theory as estimation. For estimation, the machine model incorporating the error variables with their gain adjustment feature constitutes what is known as an observer. The observer with its error feedback is shown in Figure 8.20. Here, the system or state variables are labeled as  $X$ , and  $y$  is the output variable. Note that the number of outputs is less than the number of state variables. For the SRM system, the outputs are the phase currents. The rotor position and speed are obtained from the state variables of the observer for use in the controller. A simple observer is considered for illustration in the following.<sup>15</sup>

The linear SRM system equations are

$$\frac{d\lambda_n}{dt} = -R_s L^{-1}(\theta) \lambda_n + v_n; n = 1, 2, \dots, m \quad (8.30a)$$

$$\frac{d\omega_m}{dt} = -\frac{B}{J} \omega_m + \frac{1}{J} \sum_n \frac{1}{2} \lambda_n^2 \frac{dL(\theta)}{d\theta} - \frac{T_\ell}{J} \quad (8.30b)$$

$$\frac{d\theta}{dt} = \omega_m \quad (8.30c)$$

$$i_n = L^{-1}(\theta)\lambda_n \quad (8.30d)$$

For the observer model, only the current error is considered to be available and is incorporated in the machine model. To distinguish the actual model from the observer system, an additional subscript  $s$  in front of any existing subscript is added. The observer is then given by:

$$\frac{d\lambda_{sn}}{dt} = -R_s L^{-1}(\theta)\lambda_{sn} + v_n + k_1(i_n - i_{sn}); n = 1, 2, \dots, m \quad (8.31a)$$

$$\frac{d\omega_{sm}}{dt} = -\frac{B}{J}\omega_{sm} + \frac{1}{J} \sum_n \frac{1}{2} \lambda_{sn}^2 \frac{dL_s(\theta)}{d\theta} - \frac{T_{s\ell}}{J} + k_2(i_n - i_{sn}) \quad (8.31b)$$

$$\frac{d\theta_s}{dt} = \omega_{sm} + k_3(i_n - i_{sn}) \quad (8.31c)$$

$$i_{sn} = L^{-1}(\theta)\lambda_{sn} \quad (8.31d)$$

where  $k_1$ ,  $k_2$ , and  $k_3$  are gains to adjust the observer which can be functions of both rotor position and current. Thus, they are equivalently dependent on the flux linkage (which is one of the state variables). The errors between the actual and observer variables are then defined as:

$$i_{en} = i_n - i_{sn} \quad (8.32a)$$

$$\lambda_{en} = \lambda_n - \lambda_{sn} \quad (8.32b)$$

$$\omega_e = \omega_m - \omega_{sm} \quad (8.32c)$$

$$\theta_e = \theta - \theta_s \quad (8.32d)$$

Using the error variables, we find the error dynamics of the system by substituting from the system and observer equations:

$$\frac{d\lambda_{en}}{dt} = -R_s L^{-1}(\theta)\lambda_{en} + v_n + k_1 i_e; n = 1, 2, \dots, m \quad (8.33a)$$

$$\frac{d\omega_e}{dt} = \frac{1}{J} \sum_n \frac{1}{2} \left[ \lambda_{sn}^2 \frac{dL_s(\theta)}{d\theta} - \lambda_n^2 \frac{dL(\theta)}{d\theta} \right] - \frac{B}{J}\omega_e - \frac{T_{\ell e}}{J} + k_2 i_e \quad (8.33b)$$

$$\frac{d\theta_e}{dt} = \omega_e + k_3 i_e \quad (8.33c)$$

The gains  $k_1$ ,  $k_2$ , and  $k_3$  are chosen to guarantee stability and convergence of the errors to zero. The selection of these gains may be based on a number of factors. They could be found using the Lyapunov stability criterion or other methods such as switching gains based on the trajectory of the errors using sliding mode control theory.

Further, the error current need not be the only feedback variable, estimation of load torque, speed, and rotor position, for example, can also be included to enhance the drive system dynamics. An observer that includes all these estimations is a full-order observer.<sup>16,17</sup>

These methods require considerable computational power for their implementation using dedicated software. A problem with this method is that at the time of starting it can have significant errors as it may take some time for the observer to converge and provide the correct position for operating the SRM drive. It has no self-starting capability. Studies are incomplete for these schemes, particularly in regard to variation in speed, operation at full-load torque, mutual coupling of phases, and core losses. Variations of observer-based estimators have been tested with a sliding mode observer scheme<sup>18</sup> and with a Kalman filter.<sup>19</sup>

#### 8.4.4 INTELLIGENT-CONTROL-BASED ESTIMATION

A spurt of activity in the intelligent control methods encompassing artificial neural networks (ANN) and fuzzy control also found application in SRM control. The intelligent control methods are not model dependent, even though they learn from the simulation or experimental results consisting of input and output data sets. Because they are not model dependent, the estimation is freed from dependencies of the parameters and disturbances, unlike all other modern control methods. The computational requirements for the intelligent control methods vary. Their ability to handle uncertainties in both parameters and disturbances is much better compared to other methods as the smoothing characteristics enable avoidance of sharp changes in the output variables. Briefly, both methods are described in this section.

##### 8.4.4.1 Artificial Neural Networks

Neural networks have the inherent capability for identification. Rotor position estimation can be viewed as an identification process given the set of current and flux linkages from the three-dimensional relationships that exist between them. Such an approach is used in the ANN-based rotor position estimator. Earlier, the neural network has been used for torque ripple minimization control to find the current command from the torque reference and rotor position, which is a three-dimensional relationship.<sup>20,21</sup> A similar approach is used here, except the rotor position is unknown.

The neural network consists of basic elements of neurons modeled as a nonlinear combination of inputs with added bias. The gain in the path of each input, known as the synaptic weight, is given as  $k_1, k_2, \dots, k_n$  and shown in [Figure 8.21](#). The weighted inputs are summed and processed through a nonlinear function, the activation function  $f(x_{im})$ . The activation function can be chosen from a host of available functions but it is usual to choose the one with continuity and differentiability to yield a smooth output. In a typical neural network, many such neurons are used in layers, as shown in [Figure 8.22](#). The layers in between the output and input layers are referred to as

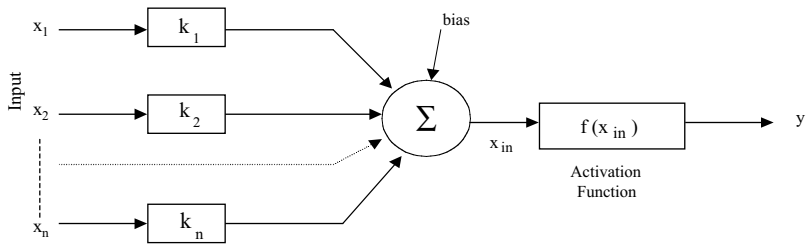


**FIGURE 8.21** Neuron model.

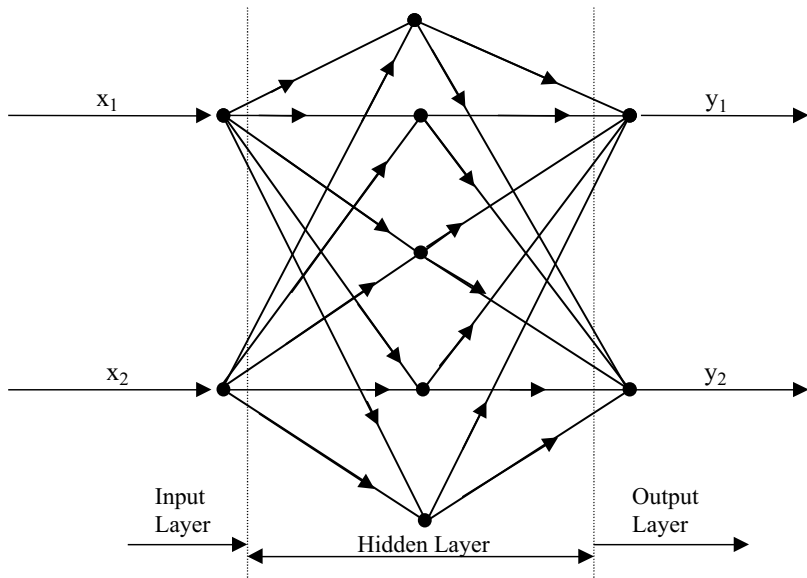


**FIGURE 8.22** A generic neural network.

hidden layers. For nonlinear systems, the hidden layers become necessary to implement identification. The inputs consist of currents and flux linkages, whereas the output is the rotor position. The number of layers is usually one, and the neurons in the hidden layers can be from 9 to 15. The number of neurons in the hidden layer is influenced by factors such as the activation function and the basis functions. The literature so far indicates that for SRM application the number of neurons in the hidden layer is from 9 to 15, which imposes a significant number of computational steps to find an output from the set of inputs. With zero bias, 37 multiplication operations with 24 additions for the nine neuron hidden layer and 61 multiplication operations with 42 additions for a 15 neuron hidden layer are required to compute one output. The number of computations is large compared to all other methods other than that of the observer based methods is to be recognized. A dedicated processor may be required to implement this scheme.

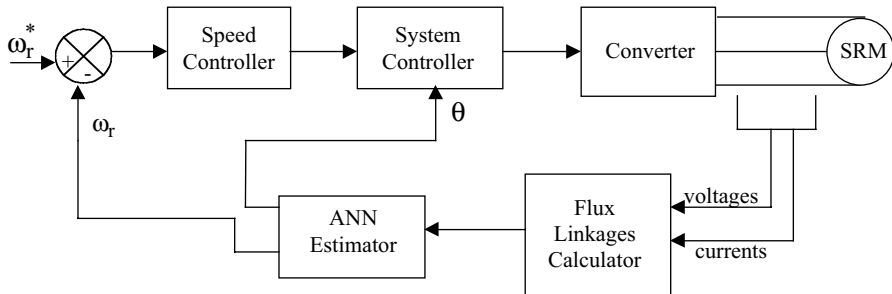


**FIGURE 8.23** ANN-based SRM drive system.

The weights in the neurons are determined during the process of training when the neural network is applied with known test data and the error in the output is propagated back to the network to adjust and to fine-tune the weights. The process uses a back propagation algorithm to minimize the error rapidly. Once the network is trained off line, then it is ready to be incorporated in to the closed loop speed controlled drive system as shown in [Figure 8.23](#). It has been demonstrated that this system is capable of rotor position identification and running the drive system. As to its accuracy, resolution and operable speed range, the scheme is yet to be studied to address these concerns.

The ANN method can be seen as a way of implementing a three dimensional table with a dynamic network in contrast to a static memory based realization which is incapable of adaptation if parameters change. If the continual learning feature is incorporated, then the ANN system becomes adaptive and can easily accommodate load and motor parameter changes. That is where the advantage may lie with the neural network based estimation methods.

#### 8.4.4.2 Fuzzy Control Estimator

Fuzzy control uses a linguistic-based, approximated human reasoning to provide the solution to the problem of identification. The inputs are the estimated flux linkages and measured currents, and the output is the rotor position from which the speed is derived. The fuzzy controller also requires a training phase to teach itself the machine flux linkages vs. current vs. rotor position relationships. Because of this, the method may be seen as another type of dynamic mapping of these relationships. The system has yet to be comprehensively studied in regard to its performance, even though basic operation with the estimated position has been shown to be satisfactory.<sup>22-24</sup>

#### 8.4.5 SENSING COIL APPROACH

All the approaches described above use the SRM windings for actuation and sensing the inductances. The sensing part is complicated because the current and voltage measurements must be isolated, thus increasing the cost of that part pertaining to the sensors. Another viable approach is to have a set of sensing coils of a few turns that provide galvanic isolation and access to inject signals independently of the main

power converter, thus freeing the main converter solely for the SRM actuation. Such an approach has been attempted.<sup>25,26</sup> This method has the disadvantage of cross-coupling from power signals and requiring extra connections from the sensing coils to the controller board which may not be acceptable in many high-volume applications such as hermetically sealed compressor pump motors.

In the first method, the inductances of the sensing coils are measured.<sup>25</sup> The inductance of the sensing coils change as the rotor moves and is measured by connecting the winding as a part of the oscillator and obtaining a variable frequency output as a function of the varying inductance of the sensing coils. The frequency is then converted into a voltage. From this voltage, which is proportional to the machine inductance, the rotor position can be recovered from a table stored in the memory. An advantage of this method is that the measurement can be made at all speeds, including zero, and there is no adverse effect of the sensor coils on the performance of the motor drive system as they are not excited.

In the second method, the sensor voltage can be integrated to obtain the flux linkages of that phase winding.<sup>26</sup> It is then compared to the flux linkages of a particular rotor position at which the commutation of the phase is desired. When the sensor-based flux linkages exceed the estimated flux linkages, then commutation is initiated for that phase. This approach suffers from the disadvantage that at low excitation current it introduces errors in the instrumentation. Also, at zero speed, this method does not work to energize the drive system, as it requires excitation to find the position; therefore, some means of starting has to be incorporated into the system.

## REFERENCES

1. Acarnley, P.P., B.J. Hill, and C.W. Hooper, Detection of rotor position in stepping and switched motors by monitoring of current waveforms, *IEEE Trans. on Industrial Electronics*, 32(3), 215–222, 1985.
2. Panda, S.K. and G.A.J. Amaralunga, Waveform detection technique for indirect rotor position sensing of switched reluctance motor drives. Part 1. Analysis, *IEE Proc. B*, 140(1), 80–88, 1993.
3. Panda, S.K. and G.A.J. Amaralunga, Waveform detection technique for indirect rotor position sensing of switched reluctance motor drives. Part 2. Experimental results, *IEE Proc. B*, 140(1), 89–96, 1993.
4. Harris, W.D. and J.H. Lang, Simple motion estimator for VR motors, *Conf. Rec. IEEE Ind. Appl. Soc.*, Oct., 387–393, 1988.
5. Brosse, A., G. Henneberger, M. Schniedermeyer, R.D. Lorenz, and N. Nagel, Sensorless control of a SRM at low speeds and standstill based on signal power evaluation, *Conf. Rec. IEEE Ind. Appl. Soc.*, Oct., 1538–1543, 1998.
6. Kirchhoff, F. and R. Hanitsch, A sensorless SRM drive without A/D and D/A converters, *Conf. Rec. Int. Conf. on Electrical Machines*, 3, 314–317, 1994.
7. Mvungi, N.H., M.A. Lahoud, and J.M. Stephenson, A new sensorless position detector for SR drives, in *Proc. of IEE 4th Int. Conf. on Power Electronics and Variable Speed Drives*, 1990, pp. 249–252.
8. Mvungi, N.H. and J.M. Stephenson, Accurate sensorless rotor position detection in an SR motor, *Proc. Eur. Power Electronics Conf.*, 390–393, 1991.

9. Laurent, P., M. Gabsi, and B. Multon, Sensorless rotor position analysis using resonant method for switched reluctance motor, *Conf. Rec. IEEE Ind. Appl. Soc.*, Oct., 687–694, 1993.
10. Egan, M.G., M.B. Harrington, and J.M.D. Murphy, PWM-based position sensorless control of variable reluctance motor drives, *Proc. Eur. Power Electronics Conf.*, 4, 024–029, 1991.
11. Ehsani, M. and I. Husain, Rotor position sensing in switched reluctance motor drives by measuring mutually induced voltages, *Conf. Rec. IEEE Ind. Appl. Soc.*, Oct., 422–429, 1992.
12. Gallegos-Lopez, G., P.C. Kjaer, and T.J.E. Miller, A new sensorless method for switched reluctance motor drives, *IEEE Trans. on Ind. Appl.*, 34(4), 832–840, 1998.
13. Ray, W.F. and I.H. Al-Bahadly, A sensorless method for determining rotor position for switched reluctance motors, in *Proc. of IEE Power Electronics and Variable Speed Drives Conf.*, Conf. Publ. No. 399, Oct. 1994, pp. 26–28.
14. Bu, J. and L. Xu, Eliminating starting hesitation for reliable sensorless control of switched reluctance motors, *Conf. Rec. IEEE Ind. Appl. Soc.*, Oct., 693–700, 1998.
15. Lumsdaine, A. and J.H. Lang, State observers for variable-reluctance motors, *IEEE Trans. on Industrial Electronics*, 37(2), 133–142, 1990.
16. Gentili, F. and S. Nicosia, Observer based control system design for switched reluctance motors, in *Proc. of the 34th Conf. on Decision and Control*, Dec. 1995, pp. 115–120.
17. Elmas, C. and H. Zelaya-De La Parra, Application of a full-order extended Luenberger observer for a position sensorless operation of switched reluctance motor drive, *IEEE Proc. on Control Theory Appl.*, 143(5), 401–408, 1996.
18. Zhan, Y.J., C.C. Chan, and K.T. Chau, A novel position and velocity observer for robust control of switched reluctance motors, *Conf. Rec. IEEE Ind. Appl. Soc.*, Oct., 1998.
19. Brosse, A. and H. Henneberger, Sensorless control of a switched reluctance motor using a Kalman filter, in *Proc. of the European Power Electronics Conf.*, 1997, Trondheim, pp. 4,561–4,566.
20. Bellini, A., F. Filippetti, G. Franceschini, C. Tassoni, and P. Vas, Position sensorless control of a SRM drive using ANN-techniques, *Conf. Rec. IEEE Ind. Appl. Soc.*, Oct., 709–714, 1998.
21. Mese, E. and D.A. Torrey, Sensorless position estimation for variable-reluctance machines using artificial neural networks, *Conf. Rec. IEEE Ind. Appl. Soc.*, Oct., 540–547, 1997.
22. Xu, L. and J. Bu, Position transducerless control of a switched reluctance motor using minimum magnetizing input, *Conf. Rec. IEEE Ind. Appl. Soc.*, Oct., 533–539, 1997.
23. Cheok, A. and N. Ertugrul, A model free fuzzy logic based rotor position sensorless switched reluctance motor drive, *Conf. Rec. IEEE Ind. Appl. Soc.*, Oct., 76–83, 1996.
24. Panda, D. and V. Ramanarayanan, Fuzzy logic based control of a switched reluctance motor, in *Proc. of the Canadian Conf. on Electrical and Computer Engineering*, 1998.
25. Liou, S.P. and W. Wang, Indirect rotor position sensing for switched reluctance motor using search coil, in *Proc. of the Canadian Conf. on Electrical and Computer Engineering*, 1996, pp. 938–942.
26. Richardson, K.M., C. Pollock, and J.O. Flower, Design and performance of a rotor position sensing system for a switched reluctance machine propulsion unit, *Conf. Rec. IEEE Ind. Appl. Soc.*, Oct., 168–173, 1996.
27. Lyons, J.P., S.R. MacMinn, and M.A. Preston, Flux/current methods for SRM rotor position estimation, *Conf. Rec. IEEE Ind. Appl. Soc.*, Oct., 482–487, 1991.

28. MacMinn, S.R., P.M. Szczesny, W.J. Rzesos, and T.M. Jahns, Application of sensor integration techniques to switched reluctance motor drives, *Conf. Rec. IEEE Ind. Appl. Soc.*, Oct., 584–588, 1988.
29. Ray, W.F. and I.H. Al-Bahadly, Sensorless methods for determining the rotor position of switched reluctance motors, in *Proc. of the European Power Electronics Conf.*, 1993, Brighton, U.K., pp. 7–13.
30. Kawamura, A., Survey of position sensorless switched reluctance motor control, *Conf. Rec. IEEE Conf. on Ind. Electronics*, Nov., 1595–1598, 1994.
31. Husain, I., Indirect rotor position estimation techniques for switched reluctance motors: a review, *Electromotion*, 94–102, 1996.
32. Rehman, S.U. and D.G. Taylor, Issues in position estimation of SR motors, *Conf. Rec. Power Electronics Specialist Conf.*, 337–343, 1996.
33. Krishnan, R. and P. Materu, Measurement and instrumentation of a switched reluctance motor, *Conf. Rec. IEEE Ind. Appl. Soc. Ann. Mtg.*, Oct., 116–121, 1989.

---

# 9 Application Considerations and Applications

## 9.1 INTRODUCTION

Newer motor drives are faced with a lag in acceptance in the marketplace, as well as a lag in the research and development arena. Historically, a 20-year lapse between the research and product development of a motor drive and its widespread acceptance for applications in industries is common. Such has been the case with permanent magnet synchronous and brushless dc motor drives and induction motor drives for high-performance applications. Further, when the ac drives are entrenched in the marketplace, it is difficult to dislodge them from existing applications due to customer reluctance to replace a good working system of which they are knowledgeable with another that requires the retraining of their personnel at great expense. Also, manufacturers of the motor drives are hesitant to install additional, new manufacturing lines that can lead to cannibalization of their existing product line, require capital investment, and decrease profitability in the short term. But, progress happens only by discarding the old for the new, and the field of motor drives is no exception. When it comes to newer applications for which a variable-speed motor drive has to be found, manufacturers and users can be persuaded to consider a new motor drive if it offers substantial cost reduction, performance enhancement (but certainly no performance degradation compared to available dc and ac motor drives), higher or comparable reliability, improved packaging compactness, higher or equivalent efficiency, and ease of manufacture and maintenance. Given this, switched reluctance motor drives have found some applications, which are described in this section. The key advantages of the SRM drives are summarized, leading to their facilitation in some applications.

## 9.2 REVIEW OF SRM DRIVE FEATURES FOR APPLICATION CONSIDERATION

The suitability of an SRM for a given application will be determined by the application considerations. Even though all the considerations cannot be exhaustively listed here, the most salient ones are included and may be considered as general. Special considerations may accompany each and every application, over and above the general considerations, that need to be addressed. They can be ambient temperature,

submersibility of the motor drive in liquid or water, intermittent and peak ratings, type of cooling, insulation class, weight and volume constraints of the entire package, and regeneration, to name a few. These additional application considerations can exclude one or more drives for an application from further consideration. The salient features of the SRM drive systems are reviewed here for application consideration.

## 9.2.1 MOTOR

### 9.2.1.1 Advantages

- Windings are on the stator only, with no windings or magnets on the rotor, thus saving materials on the rotor.
- The windings are concentric around a pole, leading to a greater manufacturing economy compared to distributed windings on ac machines or even dc machines.
- The concentric windings also reduce the end-turn buildup, thus minimizing the inactive part of the materials and resulting in lower resistance and copper losses compared to the distributed winding structure of other machines.
- The rotor is the smallest of any machine and has the lowest moment of inertia, thus giving a large acceleration rate for the motor.
- It is a brushless machine, like other ac machines, and therefore is superior from a maintenance point of view compared to dc machines.
- Because the rotor does not have windings or magnets, it is highly mechanically robust and therefore naturally suited for high-speed operation.
- The major sources of heat are on the stator, so cooling is simpler as the stator is easier to access than the rotor. The rotor losses are much smaller compared to the stator, unlike the case for dc and induction machines. Permanent magnet synchronous and brushless dc machines would be comparable in this respect.
- Skewing is not required to decrease cogging torque or crawling torque, as it is for induction and permanent magnet synchronous and brushless dc machines. This machine does not produce cogging or crawling torques.
- The power density is comparable to and even slightly higher than that for induction machines but is lower than that of the permanent magnet synchronous and brushless dc machines with high-energy, rare-earth magnets. This statement is true only for low speeds (i.e., below 20,000 rpm); for higher speeds, the switched reluctance motor offers equivalent or higher power density.
- As the windings are electrically separate from each other and as they have negligible mutual coupling, electrical fault in one phase does not affect other phases, in general. Such a feature is unique to the switched reluctance motor. For some permanent magnet brushless dc machines, such a concentric winding with one slot pitch is being introduced and may bestow some of the benefits of the SRM.

- The induced emf is a function of the phase current; hence, when there is no current in the winding, there is no induced emf in the SRM, and a phase winding fault cannot be sustained if the input current is cut off. Such is not the case for induction or permanent magnet synchronous and brushless dc machines. This leads to higher reliability in an SRM compared to any other electrical machine.
- The freedom to choose any number of phases is inherent in the SRM and lends itself to high reliability if one or more phases fails during operation. Note that all the phases are electrically independent.
- The machine is an inherent position transducer, as its inductance is uniquely dependent on rotor position and excitation current. During the inactive period of each phase winding, the rotor position can be extracted by measuring the inductance. Such a feature is difficult to exploit with induction and permanent magnet synchronous machines as there is no inactive period for the windings. The rotor position information is extracted in these machines in other ways, but all of the methods are fraught with complexities in implementation and signal processing. Extraction of discrete rotor position information is possible with a permanent magnet brushless dc machine because there is an inactive period for each winding in this machine, but a direct relationship between rotor position and a measurable quantity such as inductance is not available with the brushless dc machine as it is in the case of the SRM.

#### **9.2.1.2 Disadvantages**

- Torque ripple is high but can be reduced by controlling the overlapping phase currents.
- Acoustic noise is high, but its causes are being studied and some recommendations have resulted in considerable noise reduction compared to the first-generation machines.
- Friction and windage losses are high due to the salient rotor at high speeds. They can be reduced by making the rotor surface smooth by filling in the rotor interpolar space with inert material.
- The SRM requires an electronic power converter to run and does not have line-start capability; therefore, it is difficult to compete in an application requiring this aspect, where an induction motor is an asset. Permanent magnet synchronous and brushless dc machines have the same disadvantages of the SRM in this regard.
- Position information is required to control the SRM, as is the case for permanent magnet synchronous and brushless dc machines. Induction and dc machines are exceptions to this rule. To compete for applications requiring no position sensor and absolutely low cost, the SRM must incorporate sensorless position control. Induction and dc machines are superior in this regard, at least for low-performance applications.
- Radial forces are high at aligned positions and minimum at unaligned positions; variation over half the rotor pole pitch can contribute to faster

wear and tear of the bearings if there are rotor eccentricities and uneven air gap, which is the major source of noise in SRMs. Such a phenomenon is not present in other machines.

## 9.2.2 CONVERTER

### 9.2.2.1 Advantages

- The SRM requires only unidirectional current for its four-quadrant operation; therefore, many power converter topologies with less than two switches per phase are feasible to operate the SRM. A variety of such power converter topologies is also available.
- Because the power switches are always in series with the phase winding and together they are in parallel to the dc source voltage, at no time could a shoot-through fault occur, as in the case of the six-switch H-bridge inverters. This assures high reliability for this converter compared to other converters.
- Failure of one switch in a converter phase need not interrupt operation of the remaining phase legs of the converter and hence the SRM drive system operation. That is not the case with the ac motor drives under the same circumstance.
- Because the number of power switches can be reduced in the SRM drive, a considerable saving can accrue from a reduction in the number of logic power supplies and gate drivers and reduced heatsink area and volume, resulting in great reduction in the converter packaging and enclosure size. In high-volume applications, this could lead to considerable savings of transportation costs and overall material and manufacturing labor costs. Such a distinct advantage is generally not available for other ac drives.

### 9.2.2.2 Disadvantages

- A separate freewheeling diode for each switch is necessary in all SRM converter topologies, which cannot use anti-parallel diodes in the switches, as in the case of the H-bridge inverters. This may increase the cost if two switches per phase converter are employed for an SRM in comparison to other inverter-driven machines. This may be mitigated by reducing the number of switches and also by a special converter module developed for high-volume applications so that the overall converter cost can be reduced.

## 9.2.3 CONTROL

The control implications can be discussed from the point of view of sensors for feedback and signal processing requirements:

- Control is a consequence of the machine characteristics, the chosen converter topology, and feedback variables. Consider the case of the feedback requirement for the SRM drive system. It requires at least one current

sensor sensing the dc link current from which the phase currents can be derived. Similar is the case for ac drives. Therefore, there is not much difference between the current sensor requirement between the drives. The absolute rotor position information is essential for SRM control as it is for permanent magnet synchronous and brushless dc motor drives, whereas induction motor drives require such feedback only when high performance is required of them. Like other drives, position information can be estimated for the SRM drives but much more easily and at all speeds.

- In regard to a processor-based controller, there are no separate or special burdens for the SRM drive in comparison to other drives. Even though the torque characteristics are strongly dependent not only on the rotor position but also on the excitation current, they can be stored in the form of tables for easier control processing. Doing so may require additional memory, but other drives may require the same if parameter sensitivities are taken into consideration.

## 9.3 APPLICATIONS

Some of the industrial applications<sup>1</sup> are described in this section. It is very difficult to pinpoint the reasons for their development as they are mired in industrial and business-related decisions made by companies and not available to the public or in the literature. Therefore, only general observations are made where possible. Many of the applications are categorized as low-, medium-, and high-power and high-speed drives for rotary motor drives. Some emerging applications and underwater applications are given. Very limited but definite applications for linear SRMs have developed over a long period in machine tool XY tables.

### 9.3.1 Low-Power Drives

In this category, drives less than 3 hp are considered. This has been a successful range for many applications of SRM drives. While many of these applications have the potential to be high volume, their current sales position is in the range of up to 20,000 units and above per year.

1. *Plotter drive:* Hewlett-Packard developed and uses an SRM as a servo drive in a plotter that produces about 0.1275 N·m. torque at 4000 rpm and a maximum power of 53 W. It is a three-phase machine with six stator and eight rotor poles. Such a pole combination is not usual in other applications.
2. *Air-handler motor drive:* A.O. Smith has developed a 0.5-hp air handler, for the market.
3. *Hand fork lift/pallet truck motor drive:* Radio Energie, a French company, has developed an SRM drive for this application. Its ratings are 1.8 kW at 1500 rpm with four times the full torque for braking. It has a measured efficiency of 82% at 3200 rpm. A MOSFET four-quadrant converter drive has been chosen for this application, which has the potential to become high volume.

4. *Door actuator system*: Besam produces a door actuator with a three-phase, 12/8 pole motor delivering 5 N·m. at 300 rpm. It is a position control system that requires low-speed operation with high accuracy. This is a fairly high-volume application.
5. *Washers and dryers*: Two companies have introduced SRM drives for their washer and dryer lines, primarily for economic considerations.

### **9.3.2 MEDIUM-POWER DRIVES**

This segment is generally in the range of less than 300 kW. Initially, the SRM entered this market in the tens of hp range for general-purpose, variable-speed application but for various reasons did not gain a strong foothold in the market. Some reasons may be found in the entrenchment of ac and dc drives in existing applications, with only new applications offering an entry point for new drives. New applications do not come in large numbers and do not create huge markets for SRM drives in the medium-power range. Some selective applications seem to do better in this sector than the general-purpose industrial drives.

1. *Industrial general-purpose drives*: A number of companies produce general-purpose drives with a rating of up to 140 hp for industrial applications.
2. *Train air-conditioning drives*: Normalair Garrett markets 40-kW at 30,000 rpm, three-phase, 6/4 SRM drives for driving compressors in air-conditioning systems in trains.
3. *Mining drive*: British Jeffrey Diamond offers mine drives at 150 and 300 kW at 1500 rpm. They are all three-phase SRM drives with a 12/8 pole combination and are designed as four-quadrant drives.

### **9.3.3 HIGH-POWER DRIVES**

There has been some effort to develop SRM drives up to 1000 hp for fan and pump applications but they have yet to enter the marketplace. At this high power level, the SRM converter is very competitive, as the freewheeling diodes have to be separately mounted, similar to inverter freewheeling diodes. At high power levels, the inverter switches do not come with anti-parallel diodes as a single package. This is a significant factor, as the cost of the additional freewheeling diodes is the same for both the SRM and ac drives, thus creating a level playing field for the SRM drives in regard to the converter cost. The cost of the switched reluctance machine is certainly less than that of the ac and dc machines due to their winding and lamination form. Therefore, the SRM drives at high power may be much more attractive than the dc and ac drives.

### **9.3.4 HIGH-SPEED DRIVES**

The SRM is a natural choice for high-speed application primarily due to its robust rotor construction and its high power density.<sup>2</sup> In the permanent magnet (PM) synchronous motor drive system, the magnets have to be retained in place by a sleeve, which increases eddy current losses and tends to heat the magnets, which in turn affect the operating flux density and hence the output torque and power.

Further, the assembly of the rotor itself is made difficult due to the magnets which increases the cost. Rotor construction in the induction motor has accuracy problems in machining for high-speed operation, thus limiting its suitability for this application. Note that its performance sensitivity to high temperatures is minimal compared to permanent magnet synchronous and brushless dc motor and induction motor drive systems, as the SRMs have neither magnets nor windings on the rotor, both of which are sensitive to temperature variations. Some existing products are described in the following.

1. *Screw rotary compressor drive*: Many companies have developed SRM drives for this application. A two-phase, 8/4 SRM delivering 75 kW at 4500 rpm has been marketed by CompAir BroomWade.
2. *Centrifuge for medical applications*: Beckman Instruments, markets a high-speed SRM centrifuge drive system. It is a three-phase, 6/4 pole combination delivering 2.5 kW at 30,000 rpm.
3. *Aerospace applications*: SRM drives are ideal for aircraft applications such as a jet engine starter motor generator.<sup>3</sup> The SRM drive can be used initially to start the jet engine and run it at 27,000 rpm; once the jet engine is started, the SRM drive is driven in the regeneration mode to supply electric power to the aircraft. The regeneration speed range is from approximately 27,000 rpm to 50,000 rpm. The SRM drive system is good for applications where it is integrally mounted onto the jet engine; therefore, it must have high thermal capability and an ability to perform with one or more phase windings short-circuited in both the motoring and regeneration modes. Note that the SRM drive system can be designed to have a large number of independent phases, unlike the other machines, thus short circuit of a few phases will still leave a considerable number of healthy phases. Due to the insignificant mutual coupling between phases, the operation of healthy phases is not affected by the short-circuited phases insofar as they are electrically isolated. The electrical isolation of the short-circuited phases is achieved with the individual phase switches in series with the phase windings. The reliability of the SRM drive system is certainly higher than other drive systems in the area of shoot-through faults, as the SRM phases are in series with the switches so the rate of rise of current is limited by inductance of the phase winding. The power range for this application was initially 30 kW and then sized up to 250 hp.

Another application is a 5-hp, fuel-lube pump motor drive for a gas turbine engine for aerospace applications.<sup>4</sup>

## 9.4 EMERGING APPLICATIONS

A number of product developments are described under this heading, but the ability for these products to emerge in the market is dependent on many factors, only one of which is the technical superiority of the SRM drives over others in technical and cost-related comparison factors. These product developments are classified as

high-volume and underwater applications using rotary SRM drive systems and as applications for linear SRM drive systems.

#### **9.4.1 HIGH-VOLUME APPLICATIONS**

Due to its simplicity of construction and resulting economy in its manufacture, SRMs are expected to gravitate toward high volume but inexpensive variable-speed applications. They can be found in hand power tools, fans, pumps, drives for freezers and refrigerators, automotive applications such as antilock brake drives and ripple-torque-minimized electronically controlled steering systems, and transportation and machine tool spindles where torque ripple is not a serious concern.

#### **9.4.2 UNDERWATER APPLICATIONS**

This drive system is also under consideration for underwater propulsion applications. The main features sought after for marine propulsion systems for surface, submersible, and flexible-steering propulsion units are the enhanced control, greater efficiency, reduced acoustic noise, high reliability, and equipment layout flexibility. Even though some form of position information is necessary for successful operation of the SRM drive, it is noted that a primitive form of position encoder is sufficient for many applications as well as a sensorless position scheme that has been found sufficient for this application with sensing coils. One such application involves a 7.5-kW drive system with a partial stator with a sector arc of  $72^\circ$  on the periphery and a cylindrical rotor completely in water with 3 and 72 poles, respectively.<sup>5</sup> The other application is an underwater marine drive unit for propulsion of remotely operated vehicles.

#### **9.4.3 LINEAR DRIVE APPLICATIONS**

Up to this point, a few applications using the rotary SRM drives have been discussed. The linear SRM is emerging for select applications. The trend is to use direct-drive systems whereby the rotary-to-linear mechanical converters, such as the lead screw, gears, etc., can be dispensed with both to reduce the cost of the system and to make the system compact and highly reliable. The linear SRMs have been in long use in XY table-drive systems. Many possible applications may be found in direct-drive-based elevator door openers, semiconductor fabrication plants for material handling, other material handling applications, low-speed direct-propulsion drive transit systems,<sup>7,8</sup> automatic direct-drive-based door openers in office and commercial environments, machine tools, slide tables, and in futuristic levitation systems for urban transit systems.

### **REFERENCES**

1. Lloyd, J., SR drive applications, in *Tutorial Course on Switched Reluctance Motor Drives*, organized by R. Krishnan, *Conf. Rec. IEEE Ind. Appl. Soc. Ann. Mtg.*, Oct., 210–245, 1996.
2. Krishnan, R. and A.S. Bharadwaj, A comparative study of various motor drive systems for aircraft applications, *Conf. Rec. IEEE Ind. Appl. Soc. Ann. Mtg.*, Oct., 252–258, 1991.

3. Radun, A.V., High power density switched reluctance motor drive for aerospace Applications, *IEEE Trans. on Ind. Appl.*, 113–119, 1992.
4. Ferreira, C.A., S.R. Jones, B.T. Drager, and W.S. Heglund, Design and implementation of a five horsepower, switched reluctance fuel-lube, pump motor drive for a gas turbine engine, *Conf. Rec. IEEE Appl. Power Electronic Conf.*, 56–62, 1994.
5. Richardson, K.M., C. Pollock, and J.O. Fowler, Design and performance of a rotor position sensing system for a switched reluctance marine propulsion unit, *Conf. Rec. IEEE Ind. Appl. Soc. Ann. Mtg.*, Oct., 168–173, 1996.
6. Mauch, K. and F. Peabody, A compact thruster for industrial submarines, *Conf. Rec. IEEE Ind. Appl. Soc. Ann. Mtg.*, Oct. 242–247, 1985.
7. Lee, B.S., H.K. Bae, P. Vijayraghavan, and R. Krishnan, Design of a linear switched reluctance machine, *Conf. Rec. IEEE Ind. Appl. Soc. Ann. Mtg.*, Oct. 2267–2274, 1999.
8. Bae, H.K., B.S. Lee, P. Vijayraghavan, and R. Krishnan, A linear switched reluctance motor: converter and control, *Conf. Rec. IEEE Ind. Appl. Soc. Ann. Mtg.*, Oct., 547–554, 1999.